NASA TECHNICAL TRANSLATION

NASA TT F-626

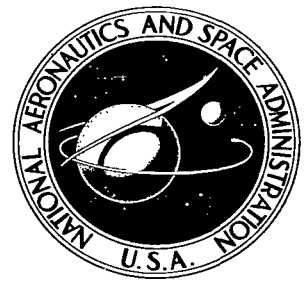

NASA TT F-626

2.1

TECH LIBRARY KAFB, NM
0069171

LOAN COPY: RETURN
AFWL (DOGL)
KIRTLAND AFB, N. M

THERMAL SENSING OF THE ATMOSPHERE FROM SATELLITES

by K. Ya. Kondrat'yev and Yu. M. Timofeyev

Gidrometeorologicheskoye Press
Leningrad, 1970

NATIONAL AERONAUTICS AND SPACE ADMINISTRATION • WASHINGTON, D. C. • JUNE 1971

Document Processing Errors

Document: NASA-TT-F-626

Document Problems:

TEXT CUT

Pages 235, 237

TECH LIBRARY KAFB, NM
0069171
NASA TT F-626

THERMAL SENSING OF THE ATMOSPHERE FROM SATELLITES

By K. Ya. Kondrat'yev and Yu. M. Timofeyev

Translation of "Termicheskoye zondirovaniye atmosfery so sputnikov"
Gidrometeorologicheskoye Press, Leningrad, 1970

NATIONAL AERONAUTICS AND SPACE ADMINISTRATION

For sale by the National Technical Information Service, Springfield, Virginia 22151
$6.00

TABLE OF CONTENTS

Foreword 1

Chapter 1. Fundamentals of the Theory of Infrared and Microwave Radiative Transfer in the Atmosphere. 4

§1. The equation of thermal-radiation transfer 4
§2. Absorption of radiation by gases 11
§3. Transmission functions of atmospheric gases. 24
§4. Approximate methods of the theory of infrared radiative transfer in the atmosphere. 35

Chapter 2. Angular and Spectral Distributions of the Outgoing Thermal radiation. 48

§1. Rocket- and satellite-borne radiation equipment. . . 48
§2. Results of experimental studies of the angular and spectral distributions of the outgoing thermal radiation. 81
§3. Results of theoretical calculations of angular and spectral distributions of the outgoing thermal radiation. 98

Chapter 3. Determination of Temperatures of Underlying Surface and Cloud Tops. 108

§1. Certain optical characteristics of the atmosphere, the underlying surface, and the clouds in the transparency-window regions. 108
§2. Optimum selection of atmospheric transparency windows for determination of underlying-surface and cloud temperatures from satellites 131
§3. A method of introducing corrections for the influence of atmospheric thickness in determining underlying-surface temperatures 139
§4. Joint solution of the problems of determining underlying-surface temperature and tropospheric moisture content. 150
§5. Conditions for detection of cloudage from thermal contrasts in the atmospheric transparency windows. 157
§6. Certain results from study of underlying-surface temperature, cloud-top temperature and height, and tropospheric moisture content. 172
§7. Possibilities for interpretation of measured data on the outgoing thermal radio emission. 184

Chapter 4. Semiempirical Interpretation of Measured Data on the Outgoing Thermal Radiation 191

§1. Correlation links between the outgoing radiation and certain meteorological parameters. 191
§2. Determination of stratosphere temperature. 205

Chapter 5. Thermal Sensing of the Atmosphere. 216
§1. Formulation and general characterization of the problem 216
§2. Mathematical aspects of solution of the inverse problems. 229
§3. Certain information on the absorption characteristics of atmospheric gases 249
§4. Results of numerical experiments to determine the temperature profile in the atmosphere 261
§5. Influence of errors in assignment of integral-equation kernels on accuracy of temperature-profile reconstruction. 279
§6. Thermal sounding under conditions of a cloudy atmosphere. 286
§7. Examples of reconstruction of the thermal-structure characteristics of the atmosphere under real conditions. 297
§8. Examples of interpretation of satellite measurements 308
§9. Certain problems in routine processing of radiation data. 311
Chapter 6. Reconstruction of Atmospheric Humidity Distribution. 316
§1. General characteristics of the problem. Properties of water-vapor absorption 316
§2. Methods of solving the problem of atmospheric-humidity-distribution reconstruction. Examples of numerical experiments 324
§3. Examples of reconstruction of humidity distribution in the atmosphere under real conditions 331
Conclusion. 335
References. 337

THERMAL SENSING OF THE ATMOSPHERE FROM SATELLITES

/2*

K.Ya. Kondrat'yev and Yu.M. Timofeyev

ABSTRACT: The monograph summarizes the results of Soviet and foreign experimental, theoretical, and instrumentation developments with a bearing on the utilization of the outgoing thermal radiation to study the earth's atmosphere. The angular and spectral distributions of the outgoing radiation and problems in determining the temperatures of the underlying surface and the upper cloud boundary, stratosphere temperatures, and troposphere moisture are analyzed in detail. Data related to theoretical and experimental aspects of atmospheric thermal sensing and determination of vertical moisture profiles from satellites are presented. The possibilities of a complex approach to solution of the set of inverse problems and the prospects for further research are briefly discussed in conclusion. It is hoped that the book will be useful to scientific workers specializing in the field of atmospheric physics, astrophysicists, and representatives of astronautics and other related sciences.

FOREWORD

/3

The solid progress in satellite meteorology that has taken expression in the development of experimental space weather systems by the USSR and USA with the object of acquiring meteorological information on the planetary scale is being slowed by the predominantly qualitative manner in which the data are analyzed. The great potential inherent in interpretation of television and infrared pictures of the cloud cover is almost never exploited beyond qualitative (or, at best, semiquantitative) synoptic analyses. The need for numerical methods of short-term forecasting and numerical simulation of the general atmospheric circulation in terms of planetary three-dimensional temperature, pressure, and wind fields has not yet been satisfied. For precisely this reason, the development of methods of securing quantitative meteorological information with satellites has become the first order of business in connection with the further development of satellite meteorology.

*Numbers in the margin indicate pagination in the foreign text.

The possibilities inherent in indirect methods of determining meteorological parameters and underlying-surface characteristics from outgoing-radiation measurements (the solutions of the inverse problems of satellite meteorology) are many and varied. However, there is no doubt that the problem of determining the vertical temperature profile from the outgoing thermal radiation spectrum in various wavelength bands (the carbon dioxide bands in the infrared, the oxygen bands in the microwave range) is of the greatest interest from the standpoint of practical feasibility. The numerous theoretical studies concerned with fundamental possibilities for solution of this problem that have appeared in recent years justify the statement that all fundamental questions have now been set forth with sufficient clarity. Numerical simulation and experimental aerostat and satellite tests of the thermal-sensing technique (which required far-reaching instrumentation developments) have demonstrated its practical promise. We may conclude from all this that the time is now ripe, and the groundwork laid, for a summation of the research that has been done toward solving the problem of thermal sensing from satellites and the related inverse problems of satellite meteorology. The present monograph represents a first attempt in this direction.

It should be noted that the content of the monograph is not limited to examination of the atmospheric thermal sensing problem. With a view to the complex nature of the subject matter discussed, the authors have made an effort to include examination of the related problems whose solution is closely related to the thermal-sensing problem. This refers primarily to determination of the moisture content and vertical water-vapor concentration distribution in the atmosphere. /4

Solution of these problems will depend basically on the state of our knowledge of the laws governing transfer of infrared and microwave radiation in the atmosphere. For this reason, Chapter 1 is devoted to the theory of infrared and microwave radiative transfer, with a special detailed analysis of the present state of the problem of determining the atmosphere's transmission functions in various regions of the spectrum.

Chapter 2 discusses the set of problems involved in development of instrumentation and information on the laws governing the angular and spectral distributions of the outgoing thermal radiation, which is basic to solution of the thermal-sensing problem.

Chapter 3 examines progress made toward determination of underlying-surface or cloud-top temperatures from outgoing-radiation measurements made in the atmosphere's transparency windows. In addition to theoretical developments, a large amount of experimental material from satellite measurements has already been accumulated in this field. In this context, the chapter discusses the various possibilities open for interpretation of data on the outgoing infrared field, the fundamental problems of acquiring and

analyzing infrared pictures of the cloud cover and underlying surface, determination of moisture content in the lower atmosphere, etc.

Chapter 4 is concerned with the problem of semiempirical interpretation of measured outgoing thermal radiation on the basis of correlations between the outgoing radiation and the various meteorological parameters, as well as with the purpose of determining stratosphere temperatures.

Chapter 5 is devoted to problems in the theoretical interpretation and practical solution of the general problem of determining the atmosphere's vertical temperature profile from the outgoing thermal radiation spectrum. Chapter 6 examines the problem of determining moisture distribution within a similar framework.

Chapters 2-4 were written by K.Ya. Kondrat'yev and Chapters 1, 5, and 6 by Yu.M. Timofeyev (§2 of Chapter 5 was prepared by O.M. Pokrovskiy).

The authors express their heartfelt gratitude to B.D. Panin and V.G. Boldyrev for their careful review of the manuscript and to G.M. Shved, A.P. Gal'tsev, and O.V. Afanas'yeva, who examined certain chapters and offered a number of valuable comments.

The authors thank in advance any readers who direct comments and criticisms to Leningrad, B-53, 2-ya liniya, d. 23, Gidrometeoizdat.

Chapter 1

/5

FUNDAMENTALS OF THE THEORY OF INFRARED AND MICROWAVE RADIATIVE TRANSFER IN THE ATMOSPHERE

Many monographs have been devoted to the theory of radiative transfer in planetary atmospheres. For a detailed study of radiative transfer in the earth's atmosphere, we refer the reader to the specialized literature [1-6]. The present chapter will present only the information necessary for understanding of the book's basic content, apart from giving attention to certain special problems in the theory of thermal radiative transfer in the atmosphere (the problem of transmission functions, approximate methods of thermal radiative transfer theory) that play an important role in solution of the problems to be considered later.

§1. THE EQUATION OF THERMAL-RADIATION TRANSFER

A radiation field is characterized by a number of quantities among which the radiant intensity J_ν is basic. If dE_ν is the radiant energy passing per unit time dt through unit area dσ perpendicular to the propagation direction in the frequency range dν (from ν to ν + dν) in a solid angle dΩ, the intensity is determined by the expression

$$dE_\nu = J_\nu \, dt \, d\sigma \, d\nu \, d\Omega. \tag{1.1}$$

Other quantitative characteristics of a radiation field (flux, flux density, etc.) can easily be found if the intensity is known. For example, the radiant flux in a solid angle Ω is

$$\Phi_\nu = \int_\Omega J_\nu \, d\Omega. \tag{1.2}$$

In the general case, radiant intensity depends on the time t, /6 the space point under examination M(x, y, z), and the direction r, i.e., $J_\nu = f_\nu(t, M(x, y, z), \mathbf{r})$. However, we shall be concerned below only with a stationary radiation field, i.e., we shall assume that $J \neq f(t)$.

It is quite often necessary to deal with radiation characteristics that are referred not to a unit frequency interval, but to an arbitrary interval $\Delta\nu = \nu_2 - \nu_1$, whose limits are ν_1 and ν_2. We then have

$$J_{\Delta\nu} = \int_{\nu_1}^{\nu_2} J_\nu \, d\nu. \tag{1.3}$$

Radiation characteristics referred to the entire spectrum are conventionally known as integral characteristics, although this term is also frequently applied to quantities defined for specific absorption bands. Apart from frequency, the wavelength $\lambda = c/\nu$ (here c is the velocity of light) and the wave number $\nu' = 1/\lambda$ are used to characterize radiation, the latter particularly often.

In space, where there is no interaction between the radiation and the medium, the radiant intensity J_ν remains constant along a given line of sight. The radiation-medium interaction can be described by the radiative-transfer equation. The derivation of this equation can be found in [1-6].

Absorption and emission coefficients are usually introduced to characterize the interaction between the radiation and the medium in the macroscopic approach. The absorption coefficient is defined by the expression

$$dJ_\nu = -k_\nu \rho J_\nu \, ds, \tag{1.4}$$

where dJ_ν is the change in the original intensity J_ν along path ds, ρ is the density of the absorbing gas, and k_ν is the absorption coefficient calculated per unit mass of the absorbing gas. Relation (1.4) can be written in slightly different forms, depending on the units used [3].

Various factors may cause the radiant intensity to change along path ds. We shall be interested basically in true absorption, which consists in the transformation of radiant energy into internal energy of the gas molecules. In the general case, radiation may also be attenuated by scattering. However, we shall assume that the contribution of scattering can be disregarded for the spectral region (infrared and microwave) and propagation conditions under consideration. This assumption is at variance with reality only in certain cases, which will be discussed in greater detail below.

The relationship defining the emission coefficient takes the /7
form

$$dE_\nu = \varepsilon_\nu \, dm \, d\Omega \, dt \, d\nu = \varepsilon_\nu \rho \, dv \, d\Omega \, dt \, d\nu. \tag{1.5}$$

As we see from (1.5), the emission coefficient ε_ν is the amount of energy radiated per unit time in a unit frequency interval and a unit solid angle by a unit of mass. For the conditions of interest to us, the emission coefficient will be governed basically by the transformation of gas-molecule internal energy to radiant energy.

In the absence of scattering, the equation of thermal radiative transfer can be written

$$\frac{1}{\rho}\frac{dJ_\nu}{ds} = -k_\nu J_\nu + \varepsilon_\nu. \tag{1.6}$$

If the absorption and emission coefficients are given as functions of the coordinates, the transfer equation can easily be obtained in integral form, the specific form depending on the geometry of the medium in which the radiation is transferred and on boundary conditions. For example, in the case of the plane-parallel model of the atmosphere with the boundary condition at the ground surface

$$J_\nu(0, \theta) = J_{0\nu}(\theta) \tag{1.7}$$

we have for the radiant intensity into the upper hemisphere at height z

$$J_\nu(z, \theta) = J_{0\nu}(\theta) \exp\left[-\frac{1}{\cos\theta}\int_0^z k_\nu(z')\rho(z')dz'\right] + \\ + \int_0^z \frac{\varepsilon_\nu(z')}{\cos\theta} \exp\left[-\frac{1}{\cos\theta}\int_{z'}^z k_\nu(z'')\rho(z'')dz''\right]\rho(z')dz', \tag{1.8}$$

where z is the vertical coordinate reckoned from the ground surface and θ is the angle between the propagation direction and the z-axis.

The physical significance of the terms in (1.8) is quite simple: the first term represents the surface radiation that has reached height z and the second the radiation generated by the atmospheric layer from 0 to z. The quantity

$$\exp\left[-\frac{1}{\cos\theta}\int_z^{z'} k_\nu(z'')\rho(z'')dz''\right] = P_\nu(0, z, z') \tag{1.9}$$

is known as the monochromatic transmission function and characterizes the fraction of the radiation that has passed through the atmospheric layer between levels z and z' in direction θ with respect to the vertical.

The specific form of the absorption and emission coefficients /8 depends on the interactions between the radiation and the medium. As we have noted, we assume in our problems that the scattering effect can be disregarded. There is sufficient basis for this assumption in the case of a cloudless atmosphere over almost the entire infrared region of the spectrum. This is because the intensity of Rayleigh scattering (particle sizes much smaller than the wavelength of the scattered radiation) is inversely proportional to the fourth power of the wavelength λ. Rayleigh scattering can be a significant factor only in the near infrared. However, scattering cannot be totally disregarded for clouds and fogs under conditions of high aerosol turbidity of the atmosphere. Sufficient data has now been accumulated to indicate the necessity of allowing for scattering on large particles in such cases, especially in those spectral regions in which radiation is not absorbed. Consideration of scattering in these regions of the spectrum greatly complicates solution of the problems in which we are interested and the scattering effect is taken into account approximately at best.

Another important problem involving scattering is the need to take account of the sunlight scattered by the atmosphere in various regions of the spectrum. Theoretical and experimental estimates indicate that the intensity of the intrinsic thermal radiation of the earth-atmosphere system becomes equal to the intensity of atmosphere-scattered sunlight in the wavelength range from 4 to 5 μm. At λ > 5 μm, scattered sunlight can be practically disregarded in all problems. By way of example, Fig. 1.1 shows spectral curves of the outgoing radiation at the upper boundary of the atmosphere as they result from scattering of sunlight and the atmosphere's intrinsic thermal radiation [7]. Figure 1.1 clearly shows that at λ > 5 μm, the influence of scattered sunlight is negligible, and the basic contribution to the outgoing radiation is made by the atmosphere's thermal radiation. This conclusion is of no little importance in selecting bands in the infrared for solution of a number of

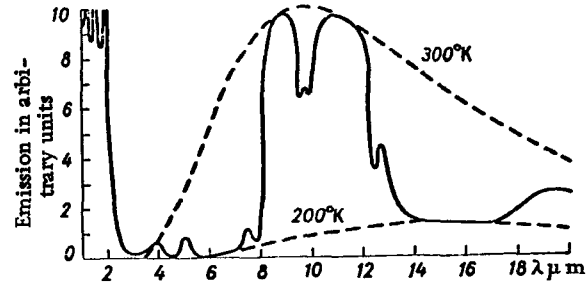

Figure 1.1. Schematic Spectral Curve of Brightness of Sunlit Side of the Earth as Observed from Satellites. The dashed curves indicate the black-body brightnesses at 300 and 200°K.

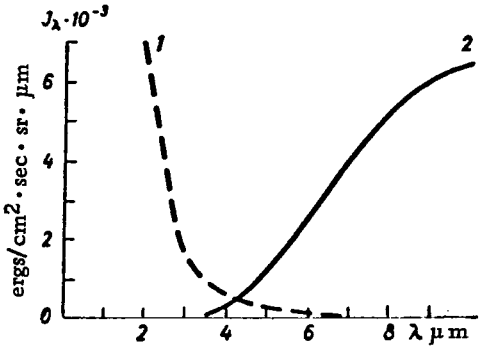

Figure 1.2. Spectral Curves of Reflected Sunlight at 0.40 Earth Albedo (1) and Intrinsic Atmospheric Thermal Radiation (2).

satellite-meteorology problems.

The data of O.I. Popov et al. [8] indicate that the influence of reflected sunlight is discerned all the way to wavelengths of 4.6-4.7 μm. Figure 1.2, which has been borrowed from R. McClatchey [9], characterizes the contributions made to the outgoing radiation as measured on a satellite by reflected sunlight (dashed curve) at a mean earth albedo of 0.40 and by the atmosphere's intrinsic radiation (solid curve) at an emission temperature of 275°K.

All of this indicates that special research must be carried out to solve the problem of allowing for scattered sunlight in the range around 4-5 μm in interpreting radiation data. /9

Disregarding the influence of scattering greatly simplifies solution of the atmospheric radiative transfer equation. Another highly important simplification that is used in study of thermal radiative transfer is the assumption that local thermodynamic equilibrium obtains [1-4, 10]. Failure to take account of scattering and the existence of the local thermodynamic equilibrium (l.t.e.) has as a consequence that the emission coefficient does not depend on radiant intensity. It is also important that Kirchhoff's law applies under l.t.e. conditions, assuming satisfaction of the following relation between the emission and absorption coefficients: /10

$$\frac{\varepsilon_\nu}{k_\nu} = B_\nu[T], \tag{1.10}$$

where

$$B_\nu[T] = \frac{2h\nu^3}{c^2} \frac{1}{\exp\left[\frac{h\nu}{kT}\right] - 1}, \tag{1.11a}$$

is the intensity of absolute black-body emission, which is a universal function of temperature and frequency.

The Wien approximation

$$B_\nu(T) = \frac{2h\nu^3}{c^2} e^{-\frac{h\nu}{kT}} \qquad (1.11b)$$

for B(ν, T) is valid with high accuracy in the near infrared, and the Rayleigh-Jeans approximation

$$B_\nu(T) = \frac{2kT\nu^2}{c^2}. \qquad (1.11c)$$

in the microwave region.

We note that in the microwave region, (1.11c) is commonly used to characterize the spectral radiant intensity J_ν in terms of the radio brightness temperature [11]. By definition, T_r is the temperature of the absolute black-body emission whose intensity equals J_ν, i.e.,

$$T_r = \frac{c^2 J_\nu}{2k\nu^2}. \qquad (1.12)$$

The question as to whether l.t.e. conditions can be satisfied for the earth's atmosphere has been discussed in a number of papers [12, 13]. Because of the low frequency of molecular collisions and the short lifetimes of excited molecular states, we should expect the excited-state distribution of the molecules in the upper atmospheric layers, beginning at certain altitudes, to be determined not by collision processes, but by external radiation, whose radiation temperature may differ from the kinetic temperature of the gas. In this case, the emission processes depend, as when scattering is taken into account, on the unknown radiant intensity, and this greatly complicates the radiative-transfer problem. For the spectral region of interest to us, deviations from l.t.e. are best observed for the oscillatory states of the gas molecules. Even for oscillatory transitions, however, Eq. (1.10) is best applicable up to 50-70 km above the earth's surface. When we consider that it is precisely the lowermost 50-kilometer layer of the atmosphere that is responsible for the thermal emission of the earth-atmosphere system in most of the problems with which we are concerned, we can hardly expect the deviations from l.t.e. that are observed in the upper layers of the atmosphere to be a substantial factor in solution of the problems examined in this book. It might be supposed that deviations from the existence conditions of l.t.e. would be important in shaping emission at high altitudes at large nadir and zenith angles, i.e., for paths that are largely in the atmospheric layers

/11

above 50 km. However, the reduction of rocket infrared measurements on the assumption that l.t.e. exists [14] failed to indicate any marked deviations of radiation temperature from the kinetic temperature of the atmosphere up to 70-80 km (Reference [14] analyzed the results of measurements in the 15-μm carbon dioxide band). Thus, it may be assumed that Expressions (1.10) and (1.11) are good approximations of the real situation for our particular problems.

Applying (1.10), (1.11), and, for example, (1.8), and having data on the distribution of temperature T, the density ρ of the absorbing matter, and the absorption coefficient as a function of z, we can calculate the radiant intensity at any point in space and in any direction θ (here and below, we shall assume azimuthal symmetry of the thermal emission field and, consequently, $J \neq f(\phi)$, where ϕ is the azimuth angle). Nor does the calculation of J_ν present fundamental difficulties with other geometries of the radiating medium (e.g., spherical atmosphere) or boundary conditions other than (1.7), although the volume of the calculations is sometimes substantially larger.

The following boundary condition at the lower limit of the atmosphere (earth's surface or upper limit of cloudage) is most frequently used in calculations of outgoing thermal radiation:

$$J_\nu(0, \vartheta) = B_\nu[T(0)].$$

This condition signifies that the surface of the earth or cloudage radiates as an absolutely black body at the surface temperature. Although this assumption is justified in many cases, it is far from accurate for certain radiating surfaces (see Chapter 3). The concept of emissivity is introduced to take account of the nonblackness of the surfaces; it is defined as the ratio of the energies emitted by the real and black bodies at the same temperature. Here it is necessary to distinguish spectral emissivities ε_ν, integral emissivities ε, which are referred to the entire emission spectrum, and hemispherical emissivities $\bar{\varepsilon}$, which are defined for radiant fluxes. Generally speaking, emissivity depends on the type and form of the surface, wavelength, and the angle between the surface normal and the line of sight. In this case, if the emissivity /12

$$\varepsilon_\nu = f(\nu, \vartheta), \tag{1.13}$$

the body is said to be grey. Naturally, $\varepsilon_\nu < 1$ for all bodies. In actuality, the approximation of (1.13) is not always satisfied with sufficient accuracy. This is manifested in dependence of

emissivity on both frequency and sighting angle. Substantial anisotropy of emission is observed for a number of surfaces. These bodies radiate much less energy at large sighting angles than at small ones. This effect is most pronounced for smooth water surfaces. It was for this case that the influence of the angle dependence of emissivity on the outgoing radiation was evaluated in K.Ye. Yakushevskaya's paper [15]. It was found that $\varepsilon_\nu(\theta)$ may play a substantial role in shaping the angular structure of the outgoing thermal radiation in the spectral intervals of weak absorption. The differences from blackness are not very large for the hemispherical emissivity [1, 16].

Appreciable deviations from the properties of absolutely black radiators are observed for clouds, and especially for intermediate and high-level clouds [16, 17] (see Chapter 3). In spite of all the above, the processes in which radiation interacts with the surface are seldom taken into account in all their complexity in thermal radiation calculations. In solution of the problems constituting the subject matter of this book, the deviations of the radiating surface from blackness are an important factor in determining underlying-surface temperature (for greater detail, see Chapter 3).

§2. ABSORPTION OF RADIATION BY GASES

Knowledge of the absorption coefficients and the manner in which they depend on physical variables — temperature and pressure — enables us to calculate all necessary characteristics of the radiation field. The most reliable information on absorption coefficients or quantities related to them (transmission functions) are obtained by experiment. Analysis of the interactions between the radiation and the gaseous atmosphere is required for theoretical study of the absorption coefficients. Among the many processes that result in absorption, we shall be interested only in those that determine absorption in the infrared and microwave regions.

It is known that the basic gaseous constituents of the atmosphere — N_2 and O_2 — have practically no absorption bands in the region of the spectrum in which we are interested. This is because they have no electrical dipole moments. However, oxygen has bands governed by magnetic dipole transitions around $\lambda = 1$ μm /13 and an absorption band in the microwave region. Despite the low absorption probability for these transitions, the presence of the large amount of oxygen in the earth's atmosphere makes these bands quite important in the transformation of radiation in the corresponding spectral regions.

However, most of the absorption in these spectral regions is governed by the vibrational-rotational and purely rotational absorption spectra of water vapor, carbon dioxide, and ozone. Detailed descriptions of the infrared spectra of these molecules can

be found in [1-5, 18-20]; the microwave absorption of the gases is discussed in [11, 21, 22]. Various data on the absorption characteristics will be examined below as the solutions of specific problems are handled. We note here only that the most important water-vapor bands are those centered at wavelengths of 1.3, 2.7, and 6.3 μm and the rotational band whose influence is felt in a broad region of the spectrum from $\lambda \sim 10$ μm to the radio region. The most intense CO_2 absorption bands are found around 4.3 and 15μm; ozone has an intense band at around 9.6 μm.

The role of the various gases in transforming thermal radiation depends not only on the presence of strong absorption bands in the appropriate spectral region, but also on the content of the absorbing gas in the atmosphere. Details on the composition of the atmosphere can be found in [2, 23]. Here we note only that absorption by water vapor is decisive in the troposphere, where it is commensurate with the carbon dioxide absorption in the stratosphere. In the mesosphere, transformation of radiation is governed primarily by carbon dioxide. Ozone is of appreciable importance in the stratosphere and mesosphere. Aside from these gases, secondary absorbing atmospheric components such as CO, CH_4, N_2O [15, 24] and, as we indicated above, oxygen may have a certain influence on the outgoing radiation in certain narrow spectral intervals.

The following may also be sources of absorption under certain conditions in the wavelength range under consideration: absorption by dimers, induced absorption, aerosol absorption. The dimer mechanism of absorption begins to come into evidence at high densities of the absorbing gas. For example, water-vapor molecules may form substantial amounts of dimers by hydrogen bonding even under high-humidity conditions in the lower layers of the earth's atmosphere (according to estimates by A.A. Viktorova and S.A. Zhevakin [26], the number of dimers may run to about 0.1% of the number of monomers). Calculations carried out in [25] indicate that the contribution of dimers to absorption in the transparency windows for wavelengths $\lambda > 1$ mm is approximately the same as the monomer contribution. Only at $\lambda < 0.7$ mm does the dimer contribution become negligible. The influence of dimers on infrared absorption has been almost totally neglected (an exception is [27], where the influence of oxygen complexes on absorption in the visible and near infrared is investigated). /14

The absorption mechanisms to which the term "induced" is usually applied begin to appear at high pressures in the gaseous atmosphere. They are manifested in the absorption of radiation in forbidden vibrational frequency regions (for example, in the region of the symmetrical ν_1 vibration for the CO_2 molecule) as a result of reciprocal deformation of electric-charge distributions in the molecules during collisions and the appearance of an electrical dipole moment. The induced absorption is approximately proportional to the square of gas pressure [28] and is therefore

easily distinguished from absorption due to magnetic dipole and electrical quadrupole transitions. Induced absorption may also be manifested in the appearance of absorption bands in the spectra at frequencies equal to the sum and difference of vibrational frequencies of two different molecules. One possibility is the appearance of simultaneous vibrational transitions in CO_2-H_2, CO_2-O_2, CO_2-N_2, and other mixtures. This mechanism may acquire particularly great importance in the atmosphere of Venus, where the pressures range to several tens of atmospheres. Induced absorption is of no practical importance under terrestrial conditions.

Aerosol absorption is capable of exerting a much stronger influence on the transformation of radiation under terrestrial conditions. We now have rather large bodies of experimental and theoretical data on the laws governing absorption of infrared radiation by various types of aerosols. For example, some information on this problem can be found in V.Ye. Zuyev's monograph [5].

Consideration of additional mechanisms of interaction between radiation and gaseous environment greatly complicates solution of the problems to be discussed below, and this is why these mechanisms are disregarded in many problems. However, the possible effects of these factors will be evaluated below in the appropriate cases.

The frequency dependence of the absorption coefficient governed by vibrational-rotational transitions of molecules is determined by the position of the spectral line ν_0, its intensity S, its half-width α, and the shape of the spectral line. The absorption coefficient can usually be presented in the form

$$k(\nu) = Sf(\nu_0, \nu),$$

where $f(\nu_0, \nu)$ is a function that characterizes the contour of the line.

The spectral-line positions are determined from the familiar Planck relationship /15

$$h\nu_0 = E_2 - E_1. \qquad (1.14)$$

Here, E_1 and E_2 are the initial and final energy levels of the molecules the transition between which results in the appearance of a spectral line at frequency ν_0. Solution of the Schrödinger equation [15, 16] yields sets of possible energy values corresponding to stationary states of the particular molecule. The

selection rules and Relation (1.14) determine the frequency at the center of the i-th spectral line ν_{0i}. In first approximation, the vibrational-rotational levels of molecules are determined by adding the vibrational and rotational energies after finding them separately. The theory of these problems is analyzed in detail in the works on theoretical spectroscopy [18, 19]. We might note that there is now a large amount of experimental material for both vibrational and rotational levels of various molecules. The position accuracy of spectral lines obtained by first-approximation calculation without considering the interaction of the vibrational and rotational energies usually satisfies the requirements that arise in the majority of infrared radiative transfer problems. The problem of laser-light transfer in the atmosphere is an exception [29]. Substantial progress has been made in recent years in computing spectral-line positions with consideration of the vibrational-rotational energy interaction [9, 19]. There are a number of methods for highly accurate experimental determination of the line positions. On the one hand, this gives an independent source of the necessary line-position information, and, on the other, it permits us to verify and improve the theory by which these parameters were calculated. Table 1.1 gives certain characteristics of the accuracy of spectral-line position calculations in the 15-μm carbon dioxide band, comparing data obtained experimentally and theoretically (columns 1 and 4).

The intensity of the spectral line associated with the transition between a lower state 1 and a higher state 2 can be represented as follows:

$$S_{12} = \frac{c^2 g_2 A_{21}}{8\pi\nu^2 Z(T)}\left(1 - e^{-\frac{h\nu}{kT}}\right)e^{-\frac{E_1}{kT}}. \qquad (1.15)$$

Here ν is frequency, E_1 is the energy of the lower level, g_2 is the statistical weight of the higher state, A_{21} is the Einstein coefficient for spontaneous emission, Z(T) is the partition function, and h and k are the Planck and Boltzmann constants. The term in parentheses determines the induced emission and is close to unity for the spectral region under consideration and the temperatures observed in the atmosphere.

In turn, the Einstein coefficient can be expressed in terms of the square of the dipole-moment matrix element P_{12} corresponding to the transition in question: /16

$$A_{21} = \frac{64\pi^4\nu^3}{3c^3h}|P_{12}|^2. \qquad (1.16)$$

TABLE 1.1. COMPARISON OF MEASURED [30] AND CALCULATED [31] POSITIONS AND INTENSITIES OF SEPARATE SPECTRAL LINES IN THE 15-μm CO_2 BAND

Measurement results [30]			Calculated data [31]			
ν_{0l} cm^{-1}	s_l' cm^{-2}·atm^{-1}	Experimental error, %	ν_{0l} cm^{-1}	s_l'' cm^{-2}·atm^{-1}	$s_l' - s_l''$ cm^{-2}·atm^{-1}	$\frac{s_l' - s_l''}{s_l'} \cdot 100\%$
664,29	1,00	6	664,3	0,992	0,008	0,8
661,52	0,106	15	661,5	0,121	—0,015	12,4
661,18	2,24	6	661,2	2,088	0,152	7,3
660,81	0,140	15	660,7	0,138	0,002	1,4
641,65	0,105	20	641,6	0,0846	0,0204	24,1
641,65	0,095	20	640,9	0,0765	0,0185	24,2
629,46	0,143	7	629,4	0,132	0,011	8,3
628,91	0,0750	7	629,1	0,0707	0,0043	6,1
627,99	0,101	7	627,9	0,0932	0,0078	8,4
627,38	0,0695	7	627,5	0,0655	0,0040	6,1
626,51	0,0704	7	626,4	0,0647	0,0057	8,8
625,83	0,0613	7	625,9	0,0578	0,0035	6,0
625,05	0,0481	7	625,0	0,0441	0,0040	9,1
612,56	0,0565	3	612,6	0,0468	0,0097	20,7
611,00	0,0627	3	611,0	0,0562	0,0065	11,6
609,42	0,0682	3	609,5	0,0633	0,0049	7,7
607,84	0,0712	3	607,9	0,0679	0,0033	4,9
606,27	0,0715	3	606,4	0,0701	0,0014	9,6
604,70	0,0692	3	604,8	0,0699	—0,007	1,0
603,13	0,0656	3	603,3	0,0678	—0,0022	3,2
601,56	0,0614	3	601,8	0,0641	—0,0027	4,2
599,98	0,0668	3	600,2	0,0591	—0,0023	3,3
598,40	0,0522	3	598,7	0,533	—0,0011	2,1

Translator's Note: Here and in other tables reproduced from Russian, commas represent decimal points.

The matrix element is related to the molecule's dipole moment M as follows:

$$P_{1\,2} = \int \varphi_1^* M \varphi_2 \, dv, \tag{1.17}$$

where ϕ_1 and ϕ_2 are the wave functions of the molecule in the respective quantum states and dv is a unit volume; integration is extended over the entire configuration space.

Spectral-line intensities in vibrational-rotational bands are now usually calculated as follows [32]. The intensity of any line /17 at frequency ν can be written formally

$$S = S_{\text{vib}} S_{\text{rot}} \frac{\nu}{\nu_0} F. \tag{1.18}$$

Here S_{vib} is the intensity of the vibrational transition of the nonrotating molecule, S_{rot} is a factor characterizing the particular rotational transition (relative rotational intensity) of the

rigid nonvibrating molecule, ν_0 is the center of the vibrational band, and the factor F takes account of the fact that the two types of motion (vibration and rotation) are observed simultaneously.

TABLE 1.2. COMPARISON OF MEASURED AND CALCULATED INTENSITIES AND HALF-WIDTHS OF INDIVIDUAL SPECTRAL LINES OF WATER VAPOR

Band type	Identification of transition		Line center ν_0, cm^{-1}	$S_E \alpha$ $cm^{-3} \cdot atm^{-2}$	S_E $cm^{-2} \cdot atm^{-1}$	α_E $cm^{-1} \cdot atm^{-1}$	α_T $cm^{-1} \cdot atm^{-1}$	S_T $cm^{-2} \cdot atm^{-1}$
	J'_T	J''_T						
1	2	3	4	5	6	7	8	9
b	9_{-1}	10_{-1}	1280,01	0,0122	0,0270	0,45	0,374	0,0125
b	8_{-1}	9_1	1287,40	0,0190			0,328	0,0300
b	8_2	9_2	1288,89	0,057	0,0197	0,29	0,296	0,0077
b	7_{-2}	8_0	1308,21	0,0156	0,0410	0,38	0,382	0,0215
b	9_{-3}	10_{-3}	1323,35	0,090	0,0225	0,40	0,396	0,0189
b	8_{-2}	9_{-2}	1329,90	0,0101	0,0240	0,42	0,402	0,0140
c	4_{-1}	5_1	1351,56		0,0051		0,434	
b	11_{-7}	12_{-7}	1352,36	0,0025	0,0096	0,26	0,253	0,0100
b	6_0	7_0	1354,84	0,0376			0,397	0,0625
c	2_1	3_3	1408,52	0,0060	0,0175	0,34	0,439	
b	3_0	4_2	1429,96	0,1600			0,400	0,3300
b	5_{-3}	6_{-3}	1447,38	0,3470			0,456	0,7500
b	12_{-7}	11_{-7}	1901,82	0,0084	0,0310	0,27	0,253	0,0390
b	7_0	6_0	1907,96	0,0390			0,397	0,2220
b	7_{-1}	6_{-3}	1909,95	0,0620			0,419	0,3800
b	12_{-5}	11_{-5}	1957,69	0,0034	0,0093	0,365	0,316	0,0172
b	8_{-2}	7_{-4}	1961,19	0,0063	0,0191	0,33	0,405	0,0445
b	7_3	6_1	1967,41	0,0610			0,328	0,0050
b	8_1	7_1	1988,41	0,0367			0,357	0,3450
b	9_0	7_0	2007,74	0,0054	0,0163	0,335	0,366	0,0560

F = 1 for a rigid top. The value of S_{rot} can be obtained from available tables and simple relationships. S_{vib} is selected on the basis of comparison with measured radiation-absorption data. Calculation of line intensities in the rigid-top approximation often results in large errors [33, 38]. Table 1.2 compares experimental water-vapor line intensities with those calculated on the basis of /18 the rigid-top approximation. Column 1 gives the band index: b for the ν_2 band and c for the $2(\nu_2-\nu_2)$ band, columns 2 and 3 identify the spectral line, column 4 gives the central frequency of the line, column 5 the product of the experimental value S_E by the line half-width α, column 6 the experimental line intensity for T = 400°K, and column 9 the theoretical value S_T. We see from the table that the disagreement between S_T and S_E sometimes exceeds 100%.

TABLE 1.3. COMPARISON OF VALUES OF THE FACTOR F OBTAINED THEORETICALLY AND EXPERIMENTALLY FOR VARIOUS WATER VAPOR LINES [37]

Line cen., cm^{-1}	F_{theor}	F_{exp}	
		$S_v^0 = 1{,}1 \cdot 10^4$ $cm^{-1}/g \cdot cm^{-2}$	$S_v^0 = 1{,}33 \cdot 10^4$ $cm^{-1}/g \cdot cm^{-2}$
1	2	3	4
3777,97	0,41	0,55	0,46
3638,09	1,10	1,25	1,04
3598,11	1,34	1,61	1,34
3579,33	1,48	1,53	1,27
3574,47	1,50	1,78	1,48
3563,61	1,57	1,78	1,48
3557,14	1,59	1,82	1,51
3530,75	1,82	2,14	1,78
3496,63	2,11	2,83	2,35
3495,16	1,99	2,79	2,32

The departure of F from unity is due to a number of factors, of which the most important are examined, for example, in [32].

Theoretical determination of F permits considerable refinement of the calculated line intensities. As an example, we present a table from the work of H. Babrov and F. Casden [37], which compares values of F that were obtained theoretically (considering only the effect of centrifugal scattering) and experimentally for the ν_1 band of water vapor.

Table 1.3 lists F_{exp} values obtained under two assumptions as to the total intensity of the vibrational band. The agreement between theory and experiment is good for $S_V^0 = 1.33 \cdot 10^4$ $cm^{-1}/g \cdot cm^{-2}$. Similar results have also been obtained for other absorption bands, for example, by K.P. Vasilevskiy, V.A. Kazbanov, and T.Ye. Dervich [34].

Theoretical and experimental values of the intensities of certain lines were recently compared for a number of absorption bands of various atmospheric gases [31, 33-38, 63]. The following /19 conclusions may be drawn from these comparisons.

1. To calculate the intensities of individual spectral lines accurately, it is necessary to correct for various energy interactions of the molecule.

2. When the various types of vibrational-rotational interactions are taken into account, the accuracy of intensity calculations for individual spectral lines approaches the experimental accuracy of intensity determination for individual vibrational transitions. At the present time, the latter is about 5-10%.

Table 1.1 (columns 5, 8, 10) list data characterizing the accuracy of theoretical line-intensity determinations for the 15-μm carbon dioxide band [31].

Without consideration of the interaction between vibrational and rotational energies, the partition function in (1.15) can be presented in the form

$$Z(T) \approx Z_{\text{vib}}(T) Z_{\text{rot}}(T); \tag{1.19}$$

under atmospheric conditions, Z_{vib} is close to unity, so that

$$Z(T) \approx Z_{\text{rot}}(T) \sim \begin{cases} T - \text{for linear molecules,} \\ T^{3/2} - \text{for nonlinear molecules.} \end{cases} \tag{1.20}$$

Accordingly, the following formula is often used in the calculations to characterize the temperature dependence of line intensity:

$$S(T) = S_0 f(T) = S_0 \left(\frac{T_0}{T}\right)^n e^{\frac{E_1}{k}\left(\frac{1}{T_0} - \frac{1}{T}\right)}. \tag{1.21}$$

Here n = 1.0 for linear molecules (for example, CO_2) and n = 3/2 for nonlinear molecules (for example, H_2O); E_1 is the energy of the lower state of the molecule and S_0 is the line intensity under normal conditions.

The Planck formula (1.14) can be used to determine the central frequencies of spectral lines. However, even a completely isolated and quiescent molecule absorbs and emits electromagnetic energy in a certain spectral interval. The lower limit of this interval is the so-called natural width of the spectral line. The natural width is governed (from the classical point of view) by effects in which the vibrations of the oscillator emitting the energy are damped. From the quantum-theoretical viewpoint, it is due to diffusion of the molecular energy levels and hence to the nonzero lifetime of the molecule in any given state. Under atmospheric conditions, however, the natural line width is negligibly small by comparison with the line widths due to other causes, and primarily the Doppler effect and effects of the interaction /20 of the emitting molecules with one another and foreign particles (pressure effects). A derivation of the absorption-line contour shape as determined by molecular-interaction effects is given in [3, 4].

The absorption coefficient of a Doppler line takes the following form under conditions such that the molecules can have a Maxwellian velocity distribution:

$$k_\nu = \frac{S\sqrt{\ln 2}}{\alpha_D\sqrt{\pi}} \exp\left[-\frac{(\nu-\nu_0)^2}{\alpha_D^2}\ln 2\right], \qquad (1.22)$$

where

$$\alpha_D = \frac{\nu_0}{c}\sqrt{\frac{2kT}{m}\ln 2} \qquad (1.23)$$

is the Doppler half-width, which depends, as is evident from (1.23), on the type of the molecules, temperature, and the region of the spectrum (m is the mass of the molecule).

The pressure broadening is much more complex from the theoretical standpoint [3, 4, 39-45]. The emitting molecule is not isolated; it is acted upon by surrounding molecules. From the standpoint of collision broadening of the spectral lines, this action manifests in collisions between the emitting molecule and other particles. Statistical theory treats this interaction as influence exerted on the emitting molecule by an external field created by the surrounding particles. This external field shifts the molecular energy levels and, consequently, broadens the spectral lines. The collision and statistical theories give totally different expressions for the contour shapes of absorption lines. The coarsest approximation in collision theory gives the Lorentzian expression widely used in atmospheric optics:

$$f(\nu_0, \nu) = \frac{1}{\pi}\frac{\alpha}{(\nu-\nu_0)^2+\alpha^2}. \qquad (1.24)$$

The Lindholm formula [42-45], which is a generalization of (1.24), has the same structure, but takes account of the line's central-frequency shift. The line shift is not normally taken into consideration in radiative-transfer theory for the earth's atmosphere. (Its influence is evaluated by G. Plass [46]). The prime reason for this is that no change in ν_0 was observed experimetally in the infrared, indicating that this shift is small or nonexistent. Collision theory is usually applied for the line central frequencies and the statistical theory for the wings of the lines. Finally, the collision mechanism of line broadening is the decisive factor in shaping the entire line contour at low pressures and high molecule velocities, but at high pressures and

low velocities, collision theory gives incorrect contours even for /21
the central frequencies. In the latter case, the statistical shape of the line must be used for the entire contour [42].

Major difficulties stand in the way of experimental verification of spectral-line contour shapes. This is felt particularly acutely for frequencies remote from the center of the line. The primary cause is the overlapping of the lines. Existing experimental data tend to indicate that the contour shape at the center of a line closely resembles that determined by the Lorentz expression. This conclusion is arrived at both on the basis of experimental studies of line contours and by comparing the atmospheric transparency calculated theoretically by the Lorentz expression with experimental transparency data. The situation is more complex for the wings of the lines. There is as yet no theoretical expression that correctly describes the spectral-line contours for frequencies far from the line center. Results indicating that the Lorentz expression gives high values of the absorption coefficients in the line wings have been obtained in a number of studies. For example, B. Winters, S. Silverman, and W. Benedict [47] proposed the following empirical relationship for the line contour from analysis of data pertaining to the 4.3-μm carbon dioxide band:

$$f(\nu, \nu_0) = \frac{1}{\pi} \frac{\alpha}{(\nu - \nu_0)^2 + \alpha^2}, \quad |\nu - \nu_0| \leqslant \Delta\nu^*,$$

$$f(\nu, \nu_0) = \frac{1}{\pi} \frac{\alpha \exp\{-a|\nu_0 - \nu|^m\}}{(\nu - \nu_0)^2}, \quad |\nu - \nu_0| \geqslant \Delta\nu^*, \tag{1.25}$$

where a and m are empirical constants.

A number of expressions for $f(\nu, \nu_0)$ are used in the microwave region of the spectrum:

the complete Lorentz expression

$$f(\nu, \nu_0) = \frac{\nu}{\pi\nu_0}\left[\frac{\alpha}{(\nu_0 - \nu)^2 + \alpha^2} - \frac{\alpha}{(\nu_0 + \nu)^2 + \alpha^2}\right]; \tag{1.26}$$

the Van Vleck-Weiskopf formula

$$f(\nu, \nu_0) = \frac{\nu^2}{\pi\nu_0^2}\left[\frac{\alpha}{(\nu_0 - \nu)^2 + \alpha^2} + \frac{\alpha}{(\nu_0 + \nu)^2 + \alpha^2}\right]; \tag{1.27}$$

and the Zhevakin-Naumov contour

$$f(\nu, \nu_0) = \frac{\nu^2}{\pi} \frac{4\alpha}{(\nu_0^2 - \nu^2)^2 + 4\nu^2\alpha^2}. \qquad (1.28)$$

However, none of these formulas gives full agreement between the theoretical values of the water-vapor rotational-band absorption coefficients in the transparency windows with experimental data. We note that the Zhevakin-Naumov contour substantially reduces the disagreement between the theoretical and experimental values over a broad wavelength range [36, 48-50]. For example, it gives correct atmospheric-transparency values for $\lambda \approx 10$ μm, unlike other absorption-line forms. /22

Expressions (1.26)-(1.28) yield approximately the same values for the absorption coefficient at the center of the line, but differ substantially in the wings. The validity of a given contour can be confirmed only on the basis of high-precision absorption measurements far out in the wings of the lines. S.A. Zhevakin and A.P. Naumov [50] showed that Expressions (1.26) and (1.28) give practically identical absorption-coefficient values (with an error <5%) for a broad range of λ, from 10 μm to the radio region. At the present time, therefore, the uncertainty of data on the contours of spectral lines may be the most serious source of error in calculations of the absorption characteristics of atmospheric gases in those intervals of the spectrum where absorption is determined to a substantial degree by the wings of the lines.

Obviously, the most reliable information on transmission in spectral intervals where absorption is governed basically by the remote wings of the lines can be obtained from experimental data.

When the contour shape of a spectral line is governed by both the Doppler and pressure effects, it is necessary to use the so-called Lorentz-Doppler contour (Voight contour). We then have

$$k_\omega = k_0 H(a, \omega), \qquad (1.29)$$

where

$$k_0 = \sqrt{\frac{\ln 2}{\pi}} \frac{S}{\alpha_D},$$

$$H(a, \omega) = \frac{a}{\pi} \int_{-\infty}^{\infty} \frac{e^{-x^2}}{a^2 + (\omega - x)^2} dx,$$

$$a = \sqrt{\ln 2} \frac{\alpha_L}{\alpha_D}, \quad \omega = \sqrt{\ln 2} \frac{\nu - \nu_0}{\alpha_D}. \qquad (1.30)$$

Numerous studies have been devoted to the problem of calculating the function H (a, ω) [51-57]; the function itself is

tabulated in [58, 59].

Another important problem in the theory of spectral-line contours is calculation of line half-widths. Such calculations have recently been made for a series of bands in the infrared and microwave regions on the basis of Anderson's theory [60, 61]. The /23 calculations employ various experimental data obtained for specific bands, which make it possible to determine the unknown parameters that figure in the theoretical analysis. Theoretically calculated line half-widths have been compared with experimental half-widths in a number of papers. For example, A. Mason and A. Nielsen [62] showed that experimental half-widths for a number of lines in the rotational spectrum of gaseous hydrogen fluoride are close to the theoretical values calculated in the resonant-dipole approximation of the hard-elastic-ball model. Satisfactory agreement of the experimental and theoretical values has also been obtained for the ν_2 water-vapor band [33]. The results of a comparison for this band, which we have borrowed from [33], appear in Table 1.2 (columns 7 and 8). Here it must be noted that the experimental data often contain rather large errors. For example, T. McCubin and T. Mooney [63] make reference to the fact that different methods of determining line half-widths (the growth-curve and laser methods) give results that differ systematically. The contrary is observed for the half-widths of water-vapor rotational band, which were calculated theoretically by B. Benedict and L. Kaplan. Table 1.4, which gives the experimental values of the line half-widths and the ratio $\alpha_{exp}/\alpha_{theor}$, indicates that the differences between α_{theor} and α_{exp} may reach 100% [36].

TABLE 1.4. EXPERIMENTAL VALUES OF SPECTRAL-LINE HALF-WIDTHS AND COMPARISON WITH THEORETICAL VALUES [36]

Quantum transition	ν_{0i}, cm^{-1}	α_{exp}, cm$^{-1}\cdot$atm^{-1}	$\frac{\alpha_{exp}}{\alpha_{theor}}$
$5_{-1}-6_{-5}$	0,74	0,084	
2_2-3_{-2}	6,12	0,095 ± 0,001	0,99
		0,107 ± 0,005	1,18
		0,1025 ± 0,0035	1,13
		0,108 ± 0,006	1,21
4_0-5_{-4}	10,86	1,106 ± 0,009	1,25
		0,106 ± 0,009	1,25
3_1-4_{-3}	12,67	0,106 ± 0,004	1,21
$1_{-1}-1_{+1}$	18,58	0,05 ± 0,01	0,5
$1_{+1}-2_1$	92,54	0,182	1,78
3_1-4_1	170,33	0,122	1,40
4_0-5_0	188,27	0,129	1,45
5_1-6_5	536,36	0,12	1,84
$8_{-3}-9_4$	625,44	0,11	2,07
$12_{-1}-13_5$	914,03	0,047 ± 0,002	1,06

It is a characteristic peculiarity of the line-broadening mechanism under the conditions of the earth's atmosphere that the broadening results both from collisions among molecules of the absorbing gas themselves and from collisions with molecules of a foreign broadening gas. The two types of collisions are not equally effective. For a two-component mixture consisting of N_a absorbing particles and N_b foreign-gas particles per unit volume (for the earth's atmosphere, the broadening due to nitrogen is usually considered), we can write the following expression for the line half-widths: /24

$$\alpha = \frac{1}{4\pi}\sqrt{2\pi kT}\left\{N_a(D_{a,a})^2\sqrt{\frac{2}{m_a}} + N_b(D_{a,b})^2\left[\frac{m_a+m_b}{m_a\cdot m_b}\right]^{1/2}\right\}. \qquad (1.31)$$

Here the D are the optical collision diameters for the different molecules and the m are the masses of the colliding molecules (the subscript a pertains to the absorbing gas and b to the broadening gas).

Converting to the partial pressures p_a and p_b, we obtain

$$\alpha = \frac{1}{4\pi}\left(\frac{2\pi}{kT}\right)^{1/2}(c_{a,a}p_a + c_{a,b}p_b) = \frac{1}{4\pi}\left(\frac{2\pi}{kT}\right)^{1/2}c_{a,b}(Bp_a + p_b), \qquad (1.32)$$

where $B = C_{a,a}/C_{a,b}$ and $C_{a,a}$ and $C_{a,b}$ are constant coefficients.

Relation (1.32) can be recast in the form

$$\alpha = A(T)p_l, \quad A(T) = \frac{1}{4\pi}\left(\frac{2\pi}{kT}\right)^{1/2}c_{a,b}, \qquad (1.33)$$

where $p_l = Bp_a + p_b = p + (B-1)p_a$ is the equivalent (effective) pressure, which takes account of the differing broadening effects of the separate gases.

The values of the self-broadening coefficient B have been investigated experimentally and theoretically in many papers [1-3, 5, 64-71]. For example, according to the theoretical study by B. Benedict and L. Kaplan [65], the values of B for the rotational band of water vapor lie in the range from 4.5 to 6.0. This is quite consistent with the values obtained experimentally for B. Both theory and experiment indicate that B also varies within individual absorption bands. These variations are small in some cases, but in others range into the tens of percent [66, 67, 69-71]. The hypothesis has been advanced that substantial variations

of the self-broadening coefficient might be observed within a single absorption line. The basis for this hypothesis was the expectation that the spectral-line contour shape would differ substantially between self-broadening and broadening by foreign molecules [47, 71]. /25

The phenomenon of self-broadening is easily taken into account approximately in calculating atmospheric absorption characteristics by introducing the equivalent pressure p_1. However, it is very often assumed in the calculations that $p_b >> p_a$ and $p_1 \approx p$. This assumption may not be satisfied in consideration of water-vapor absorption, both because of the large value of the self-broadening factor B and because of the relatively high water vapor partial pressure at high atmospheric humidities. Values of the self-absorption coefficient for the principal absorbing gases of the atmosphere can be found in [3, 5, 67, 69].

§3. TRANSMISSION FUNCTIONS OF THE ATMOSPHERIC GASES

With the assumptions that we have adopted for the infrared part of the spectrum, the integral form of the radiative-transfer equation (1.7) can be presented as follows:

for the incoming radiant intensity in spectral interval $\Delta\nu$ (which is narrow enough to permit disregarding the frequency dependence of B_ν) at the level with pressure p_1

$$J^{\downarrow}_{\Delta\nu}(p_1,\ 0) = \int_{p_1}^{0} B_{\bar{\nu}}[T(p)]\,\frac{\partial P_{\Delta\nu}(p_1,\ p,\ \theta)}{\partial p}\,dp; \tag{1.34}$$

for the outgoing radiation at the level with pressure p_1

$$J^{\uparrow}_{\Delta\nu}(p_1,\ 0) = \int_{p_0}^{p_1} B_{\bar{\nu}}[T(p)]\,\frac{\partial P_{\Delta\nu}(p_1,\ p,\ \theta)}{\partial p}\,dp + B_{\bar{\nu}}[T(p_0)]\,P_{\Delta\nu}(p_1,\ p_0,\ \theta). \tag{1.35}$$

The boundary condition $J^{\downarrow}_{\Delta\nu}(0,\ 0)=0$ was used in deriving the first relationship, and $J^{\uparrow}_{\Delta\nu}(p_0,\ 0)=B_{\bar{\nu}}[T(p_0)]$ in deriving the second. In (1.34) and (1.35), $P_{\Delta\nu}(p_1,\ p,\ 0)$ is the transmission function for the layer of the atmosphere bounded by levels with pressures p_1 and p, and θ is the angle between the direction of propagation and the vertical. The static equation

$$dp = -\rho g\, dz \tag{1.36}$$

was used in deriving (1.34) and (1.35).

For sufficiently narrow spectral intervals ($\Delta\nu < 50$ cm^{-1}), the expression for the transmission function can be written with high accuracy as follows: /26

$$P_{\Delta\nu}(p_1, p, \theta) = \frac{1}{\Delta\nu}\int_{\Delta\nu}\exp\left[-\frac{\sec\theta}{g}\int_{p_1}^{p} q(p')\times k_\nu[p', T(p'), q(p')]\,dp'\right]d\nu. \tag{1.37}$$

Here g is the acceleration of gravity, T(p) is the atmospheric temperature distribution, and $q(p) = \rho_a(p)/\rho(p)$ is the ratio of the densities of the absorbing gas and the air. The dependence of the coefficient $k_\nu[q(p)]$ is governed by self-broadening and can be taken into account by introducing the equivalent pressure. Very often, however, the self-broadening effect is not taken into account in radiation calculations. As we noted in §2, this may result in appreciable errors for water vapor in many cases. A more general definition of the transmission function that takes account of the frequency dependence of black-body radiation is valid for broader spectral intervals [15]. The transmission function defined by (1.37) pertains to propagation conditions in an inhomogeneous atmosphere, i.e., to the case in which both pressure and temperature vary along the ray path. For homogeneous media (p = = const, T = const, and, in the general case, p_1 = const), the transmission function can be written thus:

$$P_{\Delta\nu}(u, p_1, T, \theta) = \frac{1}{\Delta\nu}\int\exp\left[k_\nu[p_1, T]\,u\right]d\nu. \tag{1.38}$$

Here u is the content of absorbing matter, expressed in various units [3]. The units are usually centimeters of precipitation for water vapor and atm·cm for carbon dioxide.

The transmission functions of infrared radiation are of fundamental importance in the theory of radiative transfer in the atmosphere. They can be used to solve a wide variety of problems: determination of atmospheric transparency for various propagation paths, calculation of intrinsic-radiation fields and the rates of radiative temperature change in the atmosphere. Information on transmission functions is needed to solve the inverse problems of atmospheric optics. Transmission functions have been the subject

of an enormous number of studies, both experimental and theoretical [1-3, 5]. Thorough study of transmission functions is a complex problem. Transmission of radiation depends on many factors: the position of the spectral interval under consideration, the absorbing-gas content, the pressures of the absorbing and broadening gases, and temperature. Major difficulties arise in investigation of transmission an inhomogeneous medium (in this case, /27 the transmission function is a complex functional of the functions q(p), T(p)) or under the conditions of a multicomponent absorbing medium.

We now have a large body of information on the transmission functions of various gases (especially for H_2O, CO_2, O_3) with various spectral resolutions for pressures from ~0.001 to ~1 atm. Temperature curves of the transmission functions have not been studied in sufficient detail. Most frequently, the work is concerned with transmission functions (or absorption functions $A_{\Delta\nu}$, which are linked with the transmission functions by the simple relationship $P_{\Delta\nu} = 1 - A_{\Delta\nu}$) of whole absorption bands. The reader who would familiarize himself with these data in detail is referred to [1-3, 5]. We note that despite the tremendous number of published papers, it cannot be said that there is no longer any need for further intensive research in this field. This is not only because of the complexity of the radiation-transformation processes in the real atmosphere, but also because of the continuously growing range of problems that require more and more detailed and precise characteristics of this transformation.

Methods of acquiring transmission functions can be classified as experimental and theoretical.

1. Experimental Methods

a. **Laboratory studies of the transmission of infrared and microwave radiation in gas cuvettes.** This method usually yields transmission functions for a homogeneous medium at fixed values of p and T. However, transmission measurements made in a sequenced set of gas cuvettes [72, 73] in which the pressure and the content of absorbing substance (and, in the general case, temperature) can be varied independently permits laboratory study of the basic laws governing transfer of radiation in the inhomogeneous medium as well. In investigating transmission functions, it is necessary to solve a series of complex experimental problems. Laboratory research is presently underway in a broad range of pressures (0.001-10 atm) and temperatures (280-1500°K).

The spectral emissivities of gases are measured at high temperatures [3, 20].

b. **Invesitgation of transmission functions under natural conditions.** This method can be used to study the transmission

functions of both homogeneous and inhomogeneous media. However, this advantage is largely cancelled by the inadequate accuracy of control of the physical conditions observed along the ray paths, and slant paths in particular.

The experimental methods have an advantage in that, assuming /28 that the experimental conditions are accurately controlled, they yield real data on the transmission of radiation by gases and do not require the numerous unjustified assumptions characteristic of a number of theoretical calculation methods. Among the deficiencies of these methods are the facts that the laboratory experiment pertains basically to homogeneous media and neither of them can produce absorption characteristics with sufficient accuracy for all conditions observed in the atmosphere. This applies primarily to the transmission functions for small $\underline{u}$ and $\underline{p}$.

The experimental results are often presented in an analytical form that is convenient for calculation of various radiation-field characteristics [74-77, 99]. We note here that the result of an experiment is not the transmission function as defined by (1.38), but the transmission function for a specific spectral measuring instrument:

$$P'_{\Delta\nu}(u,\ p,\ T,\ \nu') = \frac{\int_{\nu'-\Delta\nu}^{\nu'+\Delta\nu} J_{0\nu}\varphi(\nu-\nu')\exp[-k_\nu u]\,d\nu}{\int_{\nu'-\Delta\nu}^{\nu'+\Delta\nu} J_{0\nu}\varphi(\nu-\nu')\,d\nu'}, \qquad (1.39)$$

where $J_{0\nu}$ is the intensity of the radiation source and $\phi(\nu - \nu')$ is an instrumental function.

If $|\sim 2\Delta\nu|\ J_{0\nu} \approx$ const in the instrument's spectral-sensitivity range, we have

$$P'_{\Delta\nu}(u,\ p,\ T,\ \nu') = \frac{1}{2\Delta\nu}\int_{\nu'-\Delta\nu}^{\nu'+\Delta\nu}\varphi(\nu-\nu')\exp[-k_\nu(p,\ T)u]\,d\nu. \qquad (1.40)$$

This last expression is derived with normalization of the instrumental function $\phi(\nu - \nu')$, which characterizes the influence of the instrument on the measured variable:

$$\frac{1}{2\Delta\nu}\int_{-\infty}^{\infty}\varphi(\nu-\nu')\,d\nu = 1. \qquad (1.41)$$

In the infrared, the instrumental functions are usually approximated by the following expressions:

the rectangular instrumental function

$$\varphi(\nu-\nu')=\begin{cases}1 & \text{For } |\nu-\nu'|\leqslant\Delta\nu,\\ 0 & \text{For } |\nu-\nu'|>\Delta\nu\end{cases} \tag{1.42}$$

and the triangular instrumental function /29

$$\varphi(\nu-\nu')=2\begin{cases}1-\frac{1}{\Delta\nu}(\nu-\nu') & \text{For } \Delta\nu>(\nu-\nu')\geqslant 0,\\ 1+\frac{1}{\Delta\nu}(\nu-\nu') & \text{For } -\Delta\nu<(\nu-\nu')\leqslant 0,\\ 0 & \text{For } |\nu-\nu'|>\Delta\nu.\end{cases} \tag{1.43}$$

In computing radiation characteristics for the real atmosphere, it is necessary to use the transmission functions (1.38), which characterize the transformation of radiation without instrumental distortions. On the other hand, when it is necessary to deal with measured radiation fluxes (comparison of theory with experiment, solution of inverse problems), it is necessary to use (1.40) with the $\phi(\nu - \nu')$ corresponding to the instrument used. This rule is often overlooked, although the differences between (1.38) and (1.40) are at times appreciable. The instrumental function may influence the absorption characteristics particularly strongly for specific intervals within a spectral-line contour [20]. For broad spectral intervals, on the other hand (for example, for individual absorption bands), (1.38) and (1.40) may agree or differ insignificantly.

2. Theoretical Methods

a. **Simulation of infrared absorption bands.** Even in the case of a homogeneous medium, the general expression for the transmission function is extremely cumbersome. This becomes obvious when we remember that the absorption coefficient appearing in (1.38) is determined by the contributions of many lines:

$$k_\nu(p,\ T)=\sum_{l=1}^{N}k_{l\nu}(p,\ T). \tag{1.44}$$

The summation must often consider hundreds and thousands of spectral lines. Even when the rather simple Lorentz expression is used for the contour shape of an absorption line, it is an extremely complex task to obtain analytical expressions connecting

$P_{\Delta\nu}$ with $\underline{u}$, $\underline{p}$, and T. In order to obtain comparatively simple expressions for the transmission functions, therefore, it is necessary to sacrifice some of the accuracy with which the real structure of the absorption bands is reflected and introduce various simplifying assumptions. Use of the various absorption-band models is based on this principle [1-3, 5].

Without dwelling in detail on the various models, let us briefly describe those that are used most frequently in transmission-function calculations [1-3, 5]. /30

1. The isolated-line model. It is assumed in these models that overlapping of the lines can be disregarded. The expression for the equivalent width of the isolated Lorentz line, which is known as the Ladenburg-Reiche formula, and asymptotic representations (approximation of weak and strong lines) are used extensively in the various calculations. Isolated-line models are usually applicable at low pressures of the gaseous atmosphere; their limits of applicability are examined in [78, 79]. Analytical expressions by which overlapping of two Lorentz lines can be taken into account have been derived in a number of papers.

2. The Elsasser model. This model of the band consists of an infinite set of lines with identical intensities and half-widths situated at equal distances from one another. The Elsasser model is usually used to describe absorption in the bands of linear molecules, e.g., carbon dioxide, which have regular structure. The basic parameters of the model are the distance δ between the spectral lines and the line intensity S. The absorption of the real band is often described by superimposing Elsasser bands with different δ and S.

3. "Stochastic" models. These models assume that the positions of the spectral lines, their intensities, and their half-widths have various stochastic distributions. Various conceptions as to the probability distributions of the line intensities, half-widths, and positions result in various transmission-function forms. The "stochastic" models are used to good effect in describing absorption in the absorption bands of water vapor and ozone.

4. The quasistochastic model. This model was developed for transmission-function calculations in relatively narrow spectral intervals. In it, the interval $\Delta\nu$ for which transmission is determined is broken up into narrower intervals $D \ll \Delta\nu$. It is assumed that the lines are distributed at random within these narrow intervals. This makes possible considerably more accurate localization of the strong lines that play a major role in absorption (the error of localization $\sim D$). Other features of the quasistochastic model are the use of individual spectral lines in the calculations, correct allowance for the influence of the line wings, and the use of an expression for the equivalent line width for finite spectral intervals in the calculations.

5. Overlapping regular and stochastic bands. When the structure of the bands bears little resemblance to those of regular or randomly structured bands, use of combined models is justified. /31

Two methods of using models should be noted. In the former case, the expressions defined by the model are used for analytical representation of the experimental data. Here the parameters of the model (for example, average intensity, half-width, distance between lines, or combinations of these parameters) are used as fitting parameters.

However, there is a definite difference between this approach and simple representation of the experimental data with empirical approximations. This is because a given absorption-band model presupposes a given and sometimes quite general structure of the band. If in this case these properties of the model are closely similar to the real properties of the band (and this condition must be satisfied if the models are to be used correctly), the model expressions not only closely approximate the transmission function in the range of the experimental data, but are also a natural and physically grounded instrumental extrapolation of the transmission functions to a broader range of physical conditions. Simple empirical relationships very often give gross errors when used outside the range of the measured data.

Models can also be used in another way. Such models as the quasistochastic model [80] take close account of the real structure of the absorption bands, making use of theoretical data on the fine-structure parameters ν_{0i} and S_i of the absorption bands to obtain quantitative results. This approach also requires experimental data, but in a different form: for example, it uses experimental intensity values for individual oscillatory transitions to obtain absolute line intensities. Other experimental information is also used for computation of other parameters.

Model representations of transmission functions have a disadvantage in that they distort the real structure of the absorption bands to some degree. This distortion is often minor or unimportant in analyses of transmission in whole absorption bands or broad spectral ranges, but it sometimes becomes essential in study of transformations of radiation in narrow zones of the spectrum. Even a model as detailed as the quasistochastic model does not always yield the required accuracy of transmission-function calculation [81-83]. On the other hand, we might cite examples [84] in which the model gives a very good representation of real band structure.

Another deficiency of models, which are of definite value for many problems, is the fact that most of the results of the model approach pertain to uniform propagation conditions. In addition, /32 one of the basic advantages of the model approach – the relative simplicity of the calculations – is lost in complex models.

b. **Direct method of transmission-function calculation.** Progress in the development of electronic computers that operate at high speed and have large memory capacities and the appearance of comparatively accurate calculated data for the fine-structure parameters of absorption bands have made it possible to undertake extensive calculations of transmission functions based on numerical integration of (1.37) and (1.38).

No explicit recommendations can be given as to the applicability of the various transmission functions in all problems of radiative transfer theory. This is because of the varying requirements made of the transmission functions in different problems. Specific problems require different spectral resolutions, different accuracies of the transmission functions themselves, and information on transmission under different physical conditions. In the problems considered in the present volume, use of the direct method of calculating transmission functions is especially promising. (However, this does not exclude the use of a number of other methods to obtain absorption characteristics.) We shall therefore dwell on this method in somewhat greater detail.

Knowledge of the fine-structure parameters and contour shapes of the absorption lines enables us to compute transmission functions by direct integration over frequency. Applying (1.37-1.38) and (1.44), let us rewrite the transmission functions in the forms:

for a homogeneous medium

$$P_{\Delta\nu}(u,\ p,\ T)=\frac{1}{\Delta\nu}\int\limits_{\Delta\nu}\exp\left[-\sum_{i}k_i(\nu,\ p,\ T)u\right]d\nu, \tag{1.45}$$

for an inhomogeneous medium

$$P_{\Delta\nu}[p_1p_2,\ \theta,\ T(p),\ q(p)]=$$
$$=\frac{1}{\Delta\nu}\int\limits_{\Delta\nu}\exp\left[-\frac{\sec\theta}{g}\sum_{i}\int\limits_{p_1}^{p_2}k_i[\nu,\ p,\ T(p)]\,q(p)\,dp\right]d\nu. \tag{1.46}$$

In summing over the i, it is necessary to consider all lines that make contributions to the absorption coefficient at all frequencies in the interval $\Delta\nu$ under examination. Their number may range into the thousands. However, far fewer lines can be considered in less-than-exact calculations. Despite the cumbersomeness of the direct method of calculating transmission functions, which requires a large amount of machine time, especially for complex absorption-line contours, and despite the fact that successful use of this method depends entirely on the accuracy with /33

which the initial data are assigned — which is inadequate for a number of absorption bands —, a number of advantages of the direct method have encouraged stepped-up use of this method in solving various problems involving infrared radiative transfer. The following may be cited among the basic advantages of the direct calculation method.

1. The possibility of obtaining transmission functions for all spectral intervals, while a number of the absorption-band models have fundamental limitations in this respect.

2. The real structure of the band, i.e., the most reliable data on ν_{0i}, S_i, α_i and $f(\nu - \nu_{0i})$, is used in the calculations. The method does not involve the use of any simplifying assumptions as to the positioning of the spectral lines, the intensity and half-width distributions of the lines in the band, etc.

3. The possibility of obtaining transmission functions for any set of physical conditions, inhomogeneous and homogeneous media, and any path in the atmosphere. Naturally, the fine-structure characteristics of the absorption bands must be known for the particular conditions of interest. The fact that the direct method can yield transmission functions for an inhomogeneous medium without using approximate methods to correct for atmospheric inhomogeneity is of importance in certain problems of atmospheric optics (see §4 of this chapter).

4. Unlike many of the model approaches, this method makes it easy to allow for the effects of the instrument, which are important in some problems.

The direct-integration method cannot, of course, supplant all other methods of obtaining transmission functions, but its use in solving a number of problems may offer substantial advantages. These include acquisition of absorption characteristics for narrow or complex-structured spectral intervals and calculation of transmission functions for conditions that are practically inaccessible for experimental study.

All of the above advantages of the direct method can be exploited only if the initial data are assigned with sufficiently high accuracy. Otherwise, the refinements obtained in the direct method, e.g., by accurate correction for atmospheric inhomogeneity, will be nullified by the inaccuracy with which the transmission functions are calculated on the basis of approximate data. The real accuracy of direct calculations must also be taken into account in determining whether one or another approximate method of infrared radiative transfer theory can be used, and in determining the necessary accuracy of radiation calculations.

The real accuracy with which transmission functions are computed by the direct method depends primarily on the accuracy of

assignment of the spectral-line parameters: the positions, intensities, half-widths, and contour shapes of the lines and the pressure and temperature dependences of these parameters. The problem of the accuracy of these data was discussed briefly in §2 of this chapter. The errors of assignment of the line parameters are quite variable from line to line and from one absorption band to another. At the present time, we can only estimate the approximate range of parameter-assignment errors for specific bands and parameters. The upper limit of line-parameter assignment accuracy is the experimental accuracy with which the fundamental characteristics of the molecule and absorption band under consideration have been determined. For example, when modern calculation methods are applied for the intensity of a spectral line, this upper limit is the accuracy of determination of the individual vibrational-band intensities. Apart from the errors of statement of the fundamental constants, the accuracy of line-parameter determination is also adversely affected by the various hypotheses and simplifications used in theoretical calculation of the quantities required. /34

The real accuracy with which transmission functions are computed by the direct method also depends on many subsidiary factors: the nature of the initial-data error, features of spectral structure in the interval under consideration, and the values of absorbing-substance content, pressure, and temperature. It is therefore possible to indicate only a range of accuracy that can be expected from the calculations when the initial-data assignment errors are known.

With a line-intensity assignment error $\delta_S = \Delta S/S = \pm(5\text{-}15)\%$ and a line-half-width assignment error $\delta_\alpha = \Delta\alpha/\alpha = \pm(10\text{-}30)\%$, the real accuracy of transmission-function calculation lies in the range from 0.01 to 0.10 of the absolute transmission values. Substantially larger errors can be expected in transmission-function calculations for a number of specific calculating conditions. For example, much more serious errors may be incurred when transmission functions are computed for spectral intervals in which absorption is basically governed by the wings of outlying spectral lines. This is because of the lack of accurate data on the line contour at large distances from the center.

The direct method may also be helpful in studying the laws governing infrared radiative transfer with consideration of the real fine structure of the spectrum, determining the accuracy of the various approximate methods of radiative-transfer theory, and ascertaining the relative importance of the various factors that influence the transmission functions.

Calculation using formulas such as (1.45) and (1.46) with consideration of the real spectral structure presents certain computational difficulties and is accomplished to advantage on high- /35

speed electronic computers. First of all, it is necessary to consider a large number of spectral lines in the summations in Formulas (1.45) and (1.46). This applies in particular to calculations for high temperatures, when the numerous lines associated with transitions between excited levels come to play an important role in radiative transfer. Thus, $2.3 \cdot 10^6$ lines in the interval from 800 to 12,500 cm^{-1} were considered in J. Auman's calculations [85] of the absorption characteristics of hot water vapor at temperatures of 1680-3360°K. (We note that the spectral lines were approximated by rectangles in these calculations, which simplified the calculations substantially.) The number of spectral lines that must be taken into account in the calculations depends on the specific region of the spectrum and the necessary accuracy of the results. A.G. Pokrovskiy [86] proposed a method by which those lines that must be taken into account in calculating transmission functions for a given spectral interval can be separated out of the entire ensemble of lines. Another approach, which was used in [81, 82, 87], consists in a preliminary analysis of the absorption spectrum and calculation of the over-all absorption coefficient for all lines situated remote from the interval under consideration. This over-all absorption coefficient is then taken into account with the absorption characteristics of nearby lines in calculating the transmission functions. The advantages of this approach are that the calculation takes account of all spectral lines and there is no danger of introducing systematic errors resulting from failure to consider very faint but numerous lines.

Selection of the optimum method of frequency integration in Expressions (1.45) and (1.46) is an important problem. Since the monochromatic transmission P_ν is a rapidly varying function, it is quite obvious that the integration step must be variable to take account of the manner in which the integrand varies as a function of frequency. The calculations would otherwise be inaccurate or uneconomical. A number of integration methods were proposed in [81, 82, 86].

Finally, selection of an economical method of calculating the absorption coefficient governed by the combined action of the Doppler and pressure effects is of great importance, especially in expanded calculations. An appreciable number of recent papers have been devoted to methods of computing the function $H(a, \omega)$, and detailed tables of this function have been published [51-59].

The direct method of calculating transmission functions is currently being used in a wide variety of problems [88]. Some of them have a direct bearing on the problems under consideration here and will subsequently be discussed in greater detail.

§4. APPROXIMATE METHODS OF THE THEORY OF INFRARED RADIATIVE TRANSFER IN THE ATMOSPHERE /36

Calculations of various characteristics of the radiation field of the earth-atmosphere system are often quite cumbersome when they are based on exact relationships. For example, a number of integrations must be performed in computing the infrared radiation flux for a specified spectral interval (over the space variable, over frequency, and over angles). When we consider that all of these operations must be repeated each time for each specific state of the atmosphere, the need for and importance of approximate methods capable of sharply reducing the volume of calculations become understandable. However, the accuracy of the calculations must also meet the requirements that arise in the various problems.

A method based on introduction of a coefficient of diffusivity is often used to facilitate integration over the angles [1-3]. For a given spectral interval, integration over frequency is accomplished by introducing the transmission function. Integration over the space variable (in computing transmission functions for an inhomogeneous atmosphere) is aided by approximate methods of taking atmospheric inhomogeneity into account. We noted above that use of transmission functions in the form of Relationships (1.37) and (1.38) does not introduce large errors in the radiation-field-characteristic values calculated for the spectral ranges in which we are interested. The accuracy of the diffusivity-approximation method is also quite adequate for many problems, but is almost never used in those of interest to us.

Naturally, use of one or another approximate method results in additional inaccuracies in the calculations. We shall therefore give somewhat more detailed attention to a number of approximate methods that are extensively used in our range of problems.

Approximate consideration of atmospheric inhomogeneity. The basic methods of obtaining transmission functions give absorption characteristics for a homogeneous atmosphere. On the other hand, radiative transfer in the real atmosphere is effected along paths on which pressure and temperature vary. The inhomogeneity of the medium can be taken into account accurately in direct transmission-function calculations and by simpler methods in a number of idealized cases. (For example, for an isolated Lorentz line under the conditions of an isothermal atmosphere with constant volume concentration of the absorbing gas [3].) Most frequently, however, specific calculations make use of approximate methods of accounting for the inhomogeneity; they reduce the problem of radiative transfer in the inhomogeneous medium to a problem of homogeneous-medium transfer. Let us examine some of these methods. /37

a. The reduced-mass (RM) method [1-3]. It is assumed in this method that the transmission function of the real inhomogeneous

atmosphere (for example, a layer with pressures p_1 and p_2 at its boundaries) can be replaced by the transmission function of a homogeneous medium at pressure p_0 and temperature T_0 for a reduced-absorbing-mass value

$$\tilde{u} = \frac{\sec\theta}{g}\int_{p_1}^{p_2}\left(\frac{p}{p_0}\right)^n\left(\frac{T}{T_0}\right)^m q(p)\,dp. \qquad (1.47)$$

Here, $\underline{n}$ and $\underline{m}$ are empirical constants determined by analyzing data on the $\overline{P_{\Delta\nu}(p)}$ and $P_{\Delta\nu}(T)$ curves for homogeneous conditions.

The RM method actually assumes that the transmission functions can be represented as certain functions of the product $up^{\underline{n}}T^{\underline{m}}$, where the constants $\underline{n}$ and $\underline{m}$ found on conversion from one set of homogeneous conditions to another can be used to take account of the pressure and temperature variations of absorption in the real atmosphere. Certain experimental confirmations of this premise were obtained in [72, 73]; these results are also analyzed in [89, 90]. On the other hand, use of the RM method requires that it be possible to separate the variables in the optical-density expression $\tau = k(\nu, p, T)u$, i.e., it is assumed that

$$\tau(\nu, p, T) = \varphi(\nu)\,p^n T^m. \qquad (1.48)$$

In the general case, neither of these assumptions is satisfied, and this makes the RM method quite crude. One manifestation of this is that the constants $\underline{n}$ and $\underline{m}$ do not remain constant for broad ranges of variation of the pressure, temperature, and content of the absorbing substance. The values of $\underline{n}$ and $\underline{m}$ also depend on the structure of the spectral interval under consideration. A particularly strong dependence on these factors can be observed for the parameter $\underline{n}$. Let us demonstrate this with the example of an isolated Lorentz line. Equating optical densities for the homogeneous and inhomogeneous atmospheres, we have

$$\tilde{u}k_\nu(p_0, T_0) = \frac{1}{g}\int k_\nu(p, T)\,q(p)\,dp. \qquad (1.49)$$

Relation (1.49) yields the following expression:

$$\tilde{u} = \frac{1}{g}\int\frac{k_\nu[p, T(p)]}{k_\nu[p_0, T_0]}\,q(p)\,dp = \frac{1}{g}\int f(\nu, p, T)\,g(p)\,dp. \qquad (1.50)$$

The function f for the Lorentz contour can be written

$$f(\nu, p, T(p)) = \frac{S[T(p)]}{S(T_0)} \frac{\alpha[p, T(p)]}{\alpha(p_0, T_0)} \frac{(\nu-\nu_0)^2 + \alpha_0^2(p_0, T_0)}{(\nu-\nu_0)^2 + \alpha^2[p, T(p)]}; \quad (1.51)$$

Disregarding the temperature variation of spectral-line half-width as small by comparison with that of the intensities, we have:

for the center of a line ($\nu = \nu_0$)

$$f(\nu_0, p, T) = \frac{S[T(p)]}{S(T_0)} \left(\frac{p}{p_0}\right)^{-1}, \quad (1.52)$$

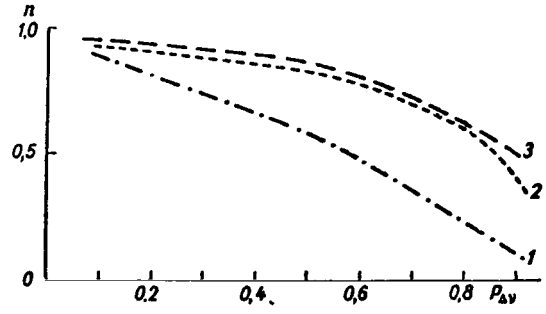

Figure 1.3. Exponent n (Formula (1.47)) as a Function of Transmission. 1) Spectral interval around $\nu = 669$ cm^{-1}; 2) around $\nu = 709$ cm^{-1}; 3) around $\nu = 703$ cm^{-1}.

for the wings of a line ($(\nu - \nu_0) >> \alpha$)

$$f(\nu_{wg}, p, T) = \frac{S[T(p)]}{S(T_0)} \frac{p}{p_0}. \quad (1.53)$$

Thus, the exponent n varies from -1 to 1 within an isolated Lorentz line. In the real spectrum, the exponent n is determined by many spectral lines for each frequency. In addition to the smoothing of n by contributions from many lines, there is also smoothing as a result of averaging over the spectral interval considered. The result of all this is that the exponent n becomes somewhat less variable than in the case of an isolated Lorentz line. (For the case of so-called weak absorption ($\tau_0 << 1$), absorption does not depend on the pressure of the absorbing medium after averaging over frequency ($n = 0$).) Figure 1.3 shows curves of the exponent n for a number of specific spectral intervals in the carbon dioxide band at $\lambda = 15$ μm as a function of transmission [91].

If the effect of temperature on absorption is either negligible or disregarded, the reduced content of the absorbing substance is found from the relation

$$\tilde{u} = \frac{\sec\theta}{g} \int_{p_1}^{p_2} \left(\frac{p}{p_0}\right)^n q(p)\, dp. \quad (1.54)$$

Taking the temperature dependence into account is sometimes difficult because of the lack of data on $P_{\Delta\nu}(T)$, especially for narrow spectral intervals. Attention should be drawn to the fact that the temperature dependence in Relations (1.52) and (1.53) for the two extreme cases is determined by the ratio of the line intensities at various temperatures. This and the similar expressions that can be obtained for the temperature dependence when the model approach is used serve as a basis for approximation of a function that accounts for $P_{\Delta\nu}(T)$ in the form

$$\eta(T)=\frac{\sum_i S_i(T)}{\sum_i S_i(T_0)}. \qquad (1.55)$$

The results of [91] indicate that $\eta(T)$ is a correct first approximation of the function $(T/T_0)^m$ and, most importantly, the true temperature dependence of the transmission functions. By way of example, Fig. 1.4 compares the function $\eta(T)$ calculated on the basis of (1.55) and the $\eta(T)$ obtained by analysis of the temperature curve $P_{\Delta\nu}(T)$. The same figure shows curves of $(T/T_0)^m$ for $m = 5.0$ and $m = 3.5$. The example pertains to a spectral interval 5 cm^{-1} wide (706.5-711.5 cm^{-1}) in the 15-μm CO_2 band.

Successful application of the RM method actually depends on optimum selection of the average values of $\underline{n}$ and $\underline{m}$ and the reference pressure and temperature values p_0 and T_0. The basic advantage of the RM method is its simplicity. To find the real-atmosphere transmission functions, it is necessary to know only how the transmission function depends on the absorbing-substance content, $P_{\Delta\nu}(u)$ and the values of the constants $\underline{n}$ and $\underline{m}$. We note that data needed for application of the RM method for many infrared bands are given in the work of N.I. Moskalenko [75] and B.M. Golubitskiy and N.I. Moskalenko [76].

Despite the extensive use of the RM method in calculating various characteristics, its accuracy has not been studied adequately. /40

Major errors may obviously be incurred under certain conditions as a result of use of a constant coefficient $\underline{n}$. In fact, even a small error in the exponent $\underline{n}$ may result in large errors in the reduced-mass values if the reference pressure p_0 differs greatly from the pressure in the atmospheric layer under consideration [92]. Hence the first prerequisite for successful use of the RM method is the availability of propagation data for conditions as close as possible to the conditions of transfer in the real atmosphere. Figure 1.5 presents a typical comparison of transmission functions obtained by various methods for a narrow /41

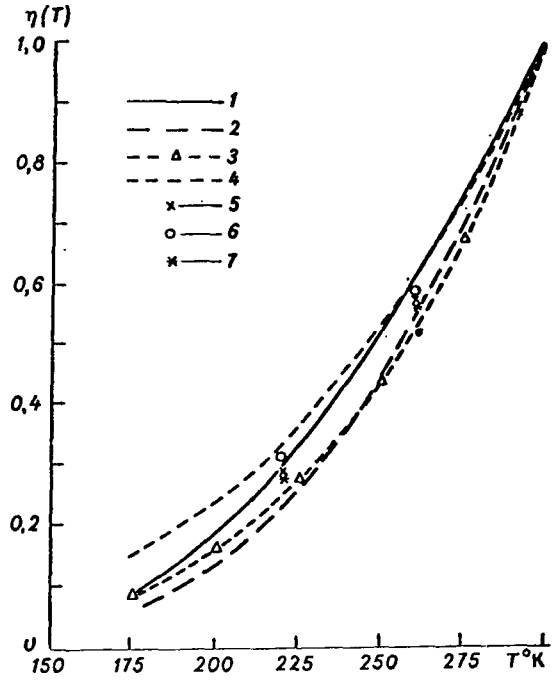

Figure 1.4. Function $\eta_i(T)$ for 709-cm^{-1} Interval.

$1-\eta_i(T)$; $2-\eta'(T)$; $3-\eta(T)=\left(\frac{T}{T_0}\right)^{5,0}$; $4-\eta(T)=\left(\frac{T}{T_0}\right)^{3,5}$; 5, 6, 7) functions $\eta(T)$ obtained from analysis of temperature dependence $P_{\Delta\nu}(T)$ for P of 0.9, 0.5, and 0.2.

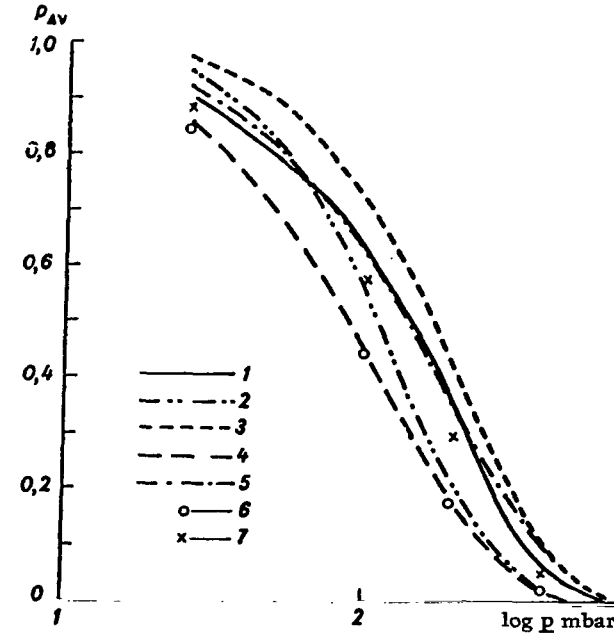

Figure 1.5. Comparison of Exact and Approximate Transmission Functions (Interval Around ν = 709 cm^{-1}). 1) Exact transmission function; 2) transmission function obtained by RM method (n = 1.0) for p_0 = = 1000 mbar, T_0 = 300°K; 3) for p_0 = 1000 mbar, T_0 = 220°K; 4) for p_0 = 100 mbar, T_0 = = 300°K; 5) for p_0 = 100 mbar, T_0 = 220°K; 6) transmission-function values obtained by the Curtis-Godson method without consideration of T-dependence; 7) with consideration of T-dependence.

spectral interval in the 15-μm carbon dioxide band. Table 1.5 presents the results of a comparison of various methods for approximating the influence of atmospheric inhomogeneity for other spectral intervals of various bands. The exact and approximate transmission functions were calculated by the direct method. The approximate methods were applied both with and without consideration of the temperature variation of the transmission functions. Yu.M. Timofeyev [92] compares transmission functions obtained for rather narrow spectral intervals by application of various absorption-band models. It can be concluded from analysis of the available data that the errors of the RM method may range up to 0.2-0.3 of the absolute transmission in calculation /42

TABLE 1.5. COMPARISON OF TRANSMISSION FUNCTIONS OBTAINED BY VARIOUS APPROXIMATE METHODS WITH EXACT VALUES OF $P_{\Delta\nu}$ (10 mbar, p)

p mbar	$P_{\Delta\nu}$ (10 mbar, p)	Effective-mass method: Without corr. for $\overline{P}_{\Delta\nu}(T)$, $n=1$, $T_0=300°$ K, $p_0=1000$ mbar	Effective-mass method: Without corr. for $\overline{P}_{\Delta\nu}(T)$, $n=1$, $T_0=220°$ K, $p_0=1000$ mbar	Effective-mass method: With corr. for $\overline{P}_{\Delta\nu}(T)$, $n=1$, $T_0=300°$ K, $p_0=1000$ mbar	Effective-mass method: With corr. for $\overline{P}_{\Delta\nu}(T)$, $n=0{,}5$, $T_0=300°$ K, $p_0=1000$ mbar	C-G method: Without corr. for $P_{\Delta\nu}(T)$	C-G method: With corr. for $P_{\Delta\nu}(T)$	Spectral intervals, cm^{-1}
25	0,962	0,987	0,976	0,996	0,971	0,929	0,959	
100	0,861	0,825	0,855	0,949	0,813	0,707	0,848	706,5—
200	0,712	0,555	0,714	0,803	0,597	0,471	0,691	711,5
400	0,388	0,230	0,461	0,431	0,267	0,195	0,365	
600	0,169	0,088	0,289	0,184	0,100	0,072	0,157	
800	0,058	0,030	0,172	0,063	0,032	0,023	0,054	
25	0,942	0,975	0,957	0,991	0,935	0,899	0,936	
100	0,789	0,705	0,779	0,888	0,662	0,592	0,771	700,5—
200	0,570	0,370	0,574	0,653	0,376	0,304	0,541	705,5
400	0,196	0,080	0,266	0,215	0,085	0,064	0,175	
600	0,043	0,010	0,122	0,045	0,011	0,010	0,036	
50	0,999	0,999	—	0,999	—	0,999	0,999	
170	0,993	0,996	—	0,989	—	0,989	0,990	
310	0,936	0,940	—	0,960	—	0,917	0,937	
510	0,798	0,778	—	0,804	—	0,770	0,798	434,3—
615	0,635	0,654	—	0,672	—	0,647	0,664	442,4
750	0,451	0,469	—	0,459	—	0,462	0,452	
850	0,271	0,317	—	0,283	—	0,311	0,277	
990	0,134	0,182	—	0,137	—	0,179	0,136	
50	0,999	0,999	—	0,999	—	0,999	0,999	
170	0,996	0,992	—	0,997	—	0,993	0,996	
310	0,957	0,927	—	0,957	—	0,921	0,957	407,2—
510	0,615	0,537	—	0,620	—	0,528	0,612	412,5
615	0,275	0,239	—	0,282	—	0,234	0,276	
750	0,030	0,033	—	0,031	—	0,032	0,031	

of real-atmosphere transmission functions. The accuracy of the method is improved when the temperature dependence is taken into account, but even then the RM method cannot be recommended as a means of acquiring highly accurate transmission functions. However, it is fully justified for calculation of both transmission functions and other characteristics in problems requiring moderate accuracy.

Kh.Yu. Niylisk [93] proposes a new method of introducing the /43 reduced mass $\tilde{u}$.

This method requires knowledge of the transmission functions over a broad range of pressures and temperatures. Preliminary estimates of its accuracy have indicated that it yields real-atmosphere transmission functions with a small error.

b. The Curtis-Godson (C-G) method [2, 3, 5]. In this method, the real-atmosphere transmission function is replaced by that of a homogeneous medium with a constant temperature T at a pressure

$$\tilde{p} = \frac{\int \eta [T(p)]\, q(p)\, p\, dp}{\int \eta [T(p)]\, q(p)\, dp} \tag{1.56}$$

and an absorbing-substance content

$$\tilde{u} = \frac{1}{g} \int \eta(T)\, q(p)\, dp. \tag{1.57}$$

It can be shown that the C-G method is accurate in the two extreme cases of weak and strong absorption [3]. Expression (1.55) or the relation

$$\eta'(T) = \left[\frac{\sum_i S_i^{1/2}(T)}{\sum_i S_i^{1/2}(T_0)} \right]^2 \tag{1.58}$$

is usually used for the function η. Calculations for a series of spectral intervals [91] have shown that the functions $\eta(T)$ and $\eta'(T)$ are quite closely similar and, most importantly, correctly describe the temperature variation of the transmission functions. When the temperature curve of absorption is not considered in the calculations, $\eta(T) \equiv 1$.

The accuracy of the C-G method has been studied on many occasions [81, 82, 91, 92, 94-98]. One group of these studies has been concerned with investigation of the accuracy of the method with various model conceptions of the transmission functions, and another with testing its accuracy against directly calculated transmission functions. Very many papers of the first group have worked with the isolated spectral line model [81, 82, 98]. It is shown here that the maximum errors of the C-G method do not exceed 6% of the absolute transmission in transmission-function calculations for the case of an atmosphere with heightwise constant concentration by volume of the absorbing substance. Interestingly, this value is reduced to about two-thirds when the influence of the Doppler effect on absorption is taken into account.

C. Walshaw and C. Rodgers [94] and R. Goody [95] studied the accuracy of the C-G method in calculation of various radiation-field characteristics for the 15-μm CO_2 band, the 9.6-μm O_3 band, /44

and the rotational band of water vapor. Both papers pronounce the method quite accurate for the CO_2 and H_2O bands. It is much less accurate and often unsatisfactory for the ozone band. This is due both to the specific structure of this band and to the altitude distribution of ozone in the atmosphere (most of the absorbing gas is at low pressures). Calculations made by K.Ya. Kondrat'yev and Yu.M. Timofeyev [91, 96] for specific spectral intervals in the 15-μm carbon dioxide band and the water-vapor rotational band showed that when the temperature variation of the transmission functions is taken into account with theoretical functions $\eta(T)$, the accuracy of the C-G method is often quite satisfactory for solution of most problems in atmospheric optics.

Table 1.5 presents data on the accuracy of the method for specific cases. The errors of the C-G method as applied to the ozone band gave impetus to the development of more accurate methods for consideration of atmospheric inhomogeneity. Thus, for example, R. Goody [95] proposed a three-parameter method. In this method, the inhomogeneous layer of atmosphere is actually replaced by two homogeneous layers with constant pressures p_1 and p_2 that contain amounts u_1 and u_2 of the absorbing substance. (Only three, and not all four parameters are independent in this method.) Use of this method improves the accuracy of the resulting characteristics in all cases. For ozone, for example, accuracy is improved by a factor of 3 to 12. B. Armstrong [97] analized the errors of the C-G method and the more exact methods of considering atmospheric inhomogeneity in detail.

Let us now dwell on the possibilities of using the direct method to obtain inhomogeneous-atmosphere transmission functions. For a stated stratification of the atmosphere, the transmission functions can be obtained on the basis of (1.46). However, it is impossible, because of the large volume of the calculations, to make them for all sets of $T(p)$ and $q(p)$ that are encountered in nature and characterize the state of the atmosphere at a fixed point in time.

This gives rise to the problem of converting from transmission functions for the state $q_0(p)$, $T_0(p)$ to those for neighboring states. The following method might be proposed for the conversion or correction of transmission functions. Suppose, for example, that $P_{\Delta\nu}[p, q_0(p), T_0(p)]$ is the transmission function of spectral interval $\Delta\nu$ of the layer of atmosphere from the upper boundary to the level with pressure p (other layers of the atmosphere could also be considered similarly). Expanding the functional $P_{\Delta\nu}$ in Taylor series [100, 101] for the transmission function, for example, with an artibrary absorbing-substance distribution, we have /45

$$P_{\Delta\nu}[p, q(p), T(p)] = P_{\Delta\nu}[p, q_0(p), T(p)] + \int_0^p \left.\frac{\delta P_{\Delta\nu}(p, p')}{\delta q(p')}\right|_{q_0(p)} \delta q(p')\,dp'. \qquad (1.59)$$

Here, $\left.\frac{\delta P_{\Delta\nu}[p, p']}{\delta q(p')}\right|_{q_0(p)}$ is the variational derivative of the transmission function calculated at point p' for the standard distribution $q_0(p)$. It equals

$$\left.\frac{\delta P_{\Delta\nu}(p, p')}{\delta q(p')}\right|_{q_0(p)} = \frac{1}{\Delta\nu}\int_{\Delta\nu} k[\nu, p', T_0(p)] \exp \times$$

$$\times\left[-\frac{1}{g}\int_0^p k[\nu, p'', T) q(p'') dp''\right] d\nu \qquad (1.60)$$

and

$$\delta q(p) = q_0(p) - q(q).$$

Relations (1.59) and (1.60) can be used to calculate transmission functions for arbitrary q(p) distributions. Naturally, q(p) must be quite close to $q_0(p)$ to obtain high accuracy in the $P_{\Delta\nu}$ calculations. The corresponding expressions for temperature correction of the transmission functions can be written similarly.

As we see from (1.59) and (1.60), the proposed correction method requires additional calculations. In addition to values of the transmission function itself, it is necessary to calculate the variational derivatives, which are functions of the two variables p and p'. Naturally, this complicates the already cumbersome calculations. However, calculation of the variational derivatives is based on calculations of the same absorption and monochromatic-transmission coefficients as are used for the transmission functions themselves. Another possible approach is a compromise in which the first term in (1.59) is calculated exactly by the direct methods, while the second, correcting term is found with the aid of approximate methods of considering atmospheric inhomogeneity. Since the approximate methods will be used to find not the transmission functions themselves, but a small correcting term, the error resulting from use of these methods will be of the second order of smallness by comparison with the errors incurred when they are applied directly.

Transmission of a gas mixture. The absorption bands of various atmospheric gases are observed to overlap in various regions in the infrared. For example, those of carbon dioxide and water vapor overlap in the 13-18 and 2.7-μm regions. This poses the problem of obtaining transmission functions for a mixture of different gases. Gas-mixture transmission and its relation to the transmissions of the individual components have been studied in a /46

number of experiments. Reference [102] arrived at the important conclusion that the following relationship is satisfied quite accurately under certain conditions:

$$P_{1+2}=P_1P_2. \tag{1.61}$$

Here P_{1+2} is the transmission of the gas mixture and P_1 and P_2 are the transmission functions of the two gases under consideration.

This relationship is exact for the transmission of monochromatic radiation. We might note one more trivial case in which (1.61) may be satisfied for nonzero spectral intervals. The multiplication method is valid if at least one of the absorbing gases has a frequency-independent absorption coefficient in the spectral range considered. A situation similar to this case is observed for relatively narrow spectral intervals in which the absorption of one of the gases is due basically to the wings of remote spectral lines — to a continuum in which the absorption coefficient depends rather weakly on frequency. Other conditions under which (1.61) is applicable are indicated in [3, 103, 104]. Most important among these are overlapping of bands with random line positions in each band and overlapping of regular bands with different values of the intervals between lines. However, we stress that these conditions are applicable only to rather broad spectral intervals.

The high accuracy of (1.61) has recently been confirmed experimentally not only for the conditions stated above, but also for other real situations in which absorption bands overlap. D. Burch, J. Howard, and D. Williams [102] studied transmission in the 2.7-μm region. Here we encounter a water-vapor band corresponding to ν_1 and ν_3 vibrations and a CO_2 band formed by a combination of resonant levels. A low-resolution spectrometer was used to verify the multiplication method for spectral intervals containing large numbers of spectral lines. The accuracy of (1.60) for a broad temperature range (400-1000°K) was investigated by E.S. Kuznetsova and M.V. Podkladenko [105]. These authors concluded that for spectral intervals of width $\Delta\nu \sim 25$ cm^{-1}, the multiplication method is valid with a relative error of $\Delta P/P \leq 10\%$. It is noted that transmission calculations using (1.60) usually give values that are somewhat on the high side; this evidently cannot be explained completely in terms of measurement errors. /47

The accuracy of the multiplication method was investigated further in [103, 104], which are especially important in that they were concerned with substantially narrower spectral intervals. The overlapping ranges of the CO and NO_2 bands ($\nu \sim 2200$ cm^{-1}) and the CH_4 and NO_2 bands ($\nu \sim 1300$ cm^{-1}) were investigated. The deviations from (1.61) that were observed at low resolutions

($\Delta\nu \approx 10$-15 cm^{-1}) did not exceed 5% of the absolute transmission. The method usually gave low-side transmission values. Approximately the same results were obtained in a numerical investigation of multiplication-method accuracy for the overlapping range of the 15-μm CO_2 band and the H_2O-vapor rotational band. The transmission functions were computed directly for intervals 5-10 cm^{-1} wide in the 15-20-μm region [87].

High-resolution measurements produced discrepancies between the values determined by the multiplication method and the exact gas-mixture transmission values; they ranged up to 10% of the absolute transmission, but the authors of [104] feel that measurements with more sophisticated instruments will be necessary to arrive at a final judgement as to the accuracy of (1.61).

On the basis of available experimental data and theoretical considerations, we should expect marked deviations from (1.61) for rather narrow spectral intervals containing closely spaced lines of various gases. This was checked by direct calculation of transmission functions for spectral intervals of various widths. The errors of transmission-function determination by the multiplication method increase with diminishing distance between the spectral lines and may reach values around 10% of absolute transmission [106].

Thus, high accuracy may be expected in the results obtained with (1.61) when the following conditions are satisfied:

1) the spectral intervals $\Delta\nu$ must be broad enough to include several absorption lines;

2) the quantity of absorbing substances in the gas mixture and in absorption by the isolated components must be the same;

3) the pressures at which the transmissions of the gas mixture and its components were determined must be the same (substitution of equivalent-pressure equality for this last condition improves the accuracy of (1.61) by a factor of 2-3 [104]).

Let us pause on yet another problem whose solution does much to determine the volume of calculations needed for theoretical acquisition of the various characteristics. As we know, the absorption coefficient is expressed as follows under the combined influence of two line-broadening factors that are extremely important for the earth's atmosphere — the Doppler effect and molecular collisions: /48

$$k_\omega = k_0 H(a, \omega),$$

where the function $H(a, \omega)$ and the parameters a, ω, and k_0 are

those defined earlier (page 21).

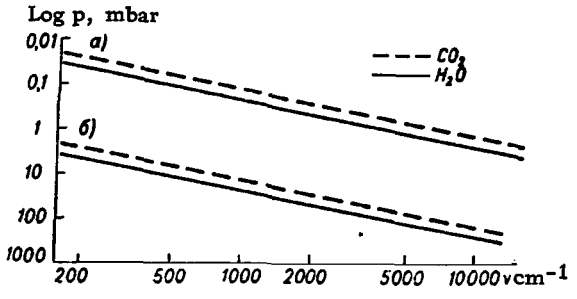

Figure 1.6. Limits of Applicability of Various Spectral-Line Contours in Calculation of Equivalent Widths with Error no Greater than 5%. a) Doppler contour; b) Lorentz contour.

Although calculation of the function H(a, ω) no longer involves any fundamental difficulties, it is desirable to use the much simpler Lorentz expression whenever possible in large-volume calculations. Thus, we encounter the problem of ascertaining the physical conditions calling for use of one or another of the spectral-line contours. This problem has been discussed in a number of papers in connection with solution of various problems [81, 107-109]. First of all, it must be noted that the limits of applicability of a given contour depend on the accuracy required in calculation of the transformation characteristic of interest to us, the region of the spectrum, and the species of the absorbing gas.

The simplest way of estimating the limits of usefulness of a given contour is to compare the half-widths of the Lorentz and Doppler lines. It is usually considered unnecessary to take account of the Doppler effect if $\alpha_L > \alpha_D$. On the other hand, if $\alpha_L \leq \alpha_D$, Doppler broadening is important. In spite of the simplified approach, which does not take account of atmospheric radiative transfer processes in all their complexity, this estimate gives, in first approximation, the regions of the atmosphere in which the composite Lorentz-Doppler contour must be used. However, it must be noted that even if the condition $\alpha_L \leq \alpha_D$ is satisfied, consideration of Doppler broadening is superfluous in many cases (e.g., under conditions of weak and strong absorption) [107].

To determine quantitatively the physical conditions under which the mixed contour must be used, a number of authors have compared equivalent spectral-line widths for various pressures and absorbing-substance contents [110-112]:

$$W = \int_{-\infty}^{\infty} [1 - \exp[-k_\nu u]]\, d\nu.$$

Figure 1.6 indicates the regions in which the mixed contour must be used to calculate W with an error no greater than 5%. We note that the actual errors may be much smaller even in these ranges, and that they can easily be determined with the results of [85, 86]. In real-atmosphere calculations, it is necessary to deal with propagation paths along which the pressure varies and consideration of the Doppler broadening may be necessary for one segment and superfluous for another. The results of [112] may be used to resolve the contour question in this case. This study gives estimates of the error resulting from neglect of the Doppler effect in calculating equivalent widths for the atmospheric layer from the upper boundary to the level with pressure p. The case of an isothermal atmosphere with constant volume concentration of the absorbing substance was studied. We note that for real spectral intervals consisting of many overlapping lines in which absorption in the Lorentz wings is significant, use of the pure Lorentz contour is justified at lower pressures than Fig. 1.6 would indicate.

/49

Chapter 2 /50

ANGULAR AND SPECTRAL DISTRIBUTIONS OF THE OUTGOING THERMAL RADIATION

As we have already noted, the initial data for solution of atmospheric temperature sounding problems are the results of measurements of the spectral and/or angular distributions of the outgoing thermal radiation. It is therefore important to discuss the presently available information on the laws governing the spectral and angular distribution of the earth's thermal radiation into the cosmos. Until quite recently, there was almost no such experimental information available. Over the last five to ten years, however, the situation has changed substantially: a comparatively large number of aircraft, aerostat, rocket, and satellite measurements has made it possible to assemble a rather complete picture of the outgoing thermal radiation field that is observed in reality. The substantial progress that has been made in experimental study of the outgoing radiation has been due primarily to advances in the development of the appropriate rocket- and satellite-borne instruments. For this reason, we shall turn our attention first of all to the basic types of radiation instruments that have been developed for experimental study of the outgoing thermal radiation field and acquisition of the data necessary to solve the thermal-sensing problem.

§1. ROCKET- AND SATELLITE-BORNE RADIATION EQUIPMENT

Soviet investigators have developed a wide variety of radiometer and spectrometer types for measurement of the angular and spectral distributions of the outgoing radiation [1-18]. A.M. Kasatkin [2] described the design of a high-altitude optical station (HOS) designed for multiinstrument rocket studies of the radiation field in the upper layers of the atmosphere. The /51
scientific instrument package of the HOS, which had a three-axis automatic orientation mechanism, also included such instruments as a solar-position and corona sensor, telescopic photometers with color filters, telescopic spectrometers, spectral analyzers, etc. However, the HOS was used primarily to investigate short-wavelength radiation.

The first rocket measurements of the earth's thermal radiation in a broad region of the spectrum (0.8-40 μm) at altitudes up to 500 km were undertaken in the USSR in 1958 by A.V. Liventsov, M.N. Markov, Ya.I. Merson, and M.R. Shamilev [4]. A diagram of the experiment, which was carried out with a geophysical rocket on 27 August 1958 (as part of the program of the International

Geophysical Year), appears in Fig. 2.1. Differential radiometer B, which has two lenses, is rotated continuously as the rocket rises and descends, thus effecting circular scanning in the vertical plane. As many as 50 successive circular scanning series can be obtained during the flight of the rocket (on the ascending and descending branches of its trajectory), which takes about 10 minutes. The lenses have a field about 0.02 radian wide.

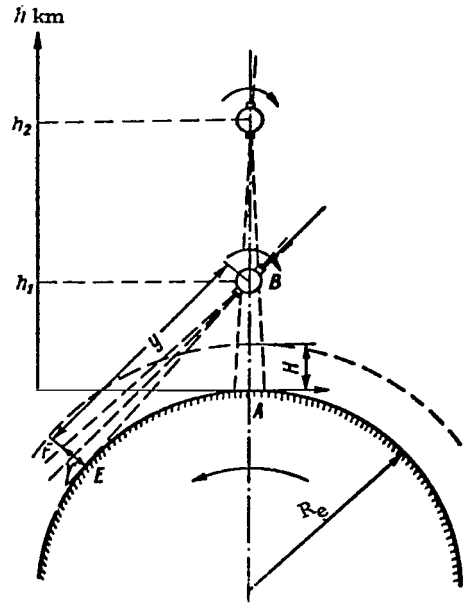

Figure 2.1. Diagram of Rocket Experiment (in Scanning Plane) to Measure Integrated Outgoing Thermal Radiation.

Figure 2.2 presents a block diagram of the radiometer. When the optical head is in working position, the two Cassegrain objectives are aimed in opposite directions. During the scanning process (the scanning speed is about 6°/sec), the lenses are pointed toward the earth and into space by turns. After passing through the objectives 1 and 2 and being reflected from the mirrors, the radiation is modulated by a chopper (frequency 80 Hz) and falls onto bolometers 3. The radiometer's sensitivity is monitored during its operation by means of a standard radiation source (incandescent lamp). Bolometers with a receiving area of about 3 mm^2 are used in the instrument; they have a sensitivity of 15 V/W when connected into a bridge circuit, and a time constant of about 5 msec. In this case, the sensitivity threshold is 10^{-9} W/Hz at the 80-Hz modulation frequency. A variable-temperature black body was used for preflight calibration of the radiometer (liquid nitrogen served to model the null signal from space). The radiometer's readings were recorded on standard 6.3-mm-wide magnetic tape. A similar radiometer was also used on aerostats to measure infrared-radiation angular distributions [3]. The modified rocket radiometer mounted on the high-altitude optical station differed in that its reference objective was always pointed at the zenith. /52

References [30-33] describe the infrared and actinometric instrumentation designed for measurement of outgoing radiation fluxes in various regions of the spectrum on Soviet weather satellites.

The television-type infrared scanning apparatus provides for acquisition of images of both the daytime and nighttime sides of the planet. The scanning unit, which is provided with a sensor

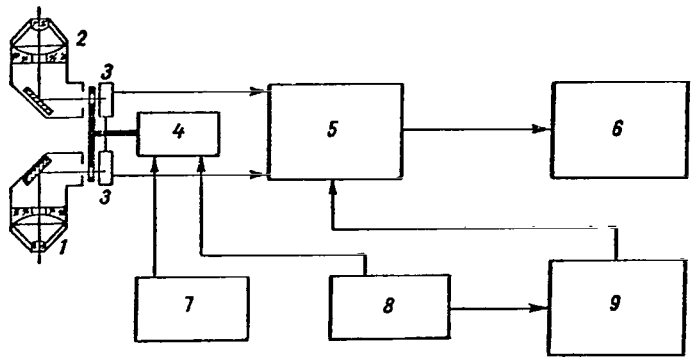

Figure 2.2. Block Diagram of Radiometer for Measurement of Integrated Thermal Radiation. 1) Optical scanning head; 2) optical null-signal head; 3) bolometers; 4) scanning mechanism; 5) amplifier; 6) telemetry; 7) motor power source; 8) on-board command unit; 9) power source (self-contained).

responsive to the 8-12-μm band, can be used to construct infrared images for later conversion to visible images. The working principle of the infrared instruments is based on the fact that the thermal radiation from the earth's surface or clouds, whose maximum lies in the 8-12-μm band, is determined by the temperature of the radiating surface. On /53 the other hand, it is in this band of the transparency window that the atmosphere absorbs almost none of the radiation. Since the temperatures of the earth's surface and the clouds differ (clouds are usually colder and therefore do not radiate as strongly), this creates thermal contrasts that make it possible to distinguish clouds against the background of the earth's surface. The strip covered on the ground by the infrared apparatus is about 1000 km wide, and its spatial resolution at the subsatellite point is 15 × 15 km. This equipment can register temperature contrasts no smaller than 2-3° at above-freezing temperatures and 7-8° at below-freezing temperatures.

The actinometric apparatus, whose function is to acquire information on the thermal balance (heat influx and efflux) of the earth as a planet, includes two scanning narrow-angle radiation receivers with an instantaneous field of 4 × 5° and two wide-angle instruments (with fields of 136-140°), that cover the entire disk of the earth as seen from satellite altitude. One of the narrow-angle sensors measures the solar radiation reflected by the earth into space (wavelength range from 0.3 to 3 μm). The other measures the earth's thermal radiation into space: in the 3-30-μm region of the spectrum during scanning in one direction and in the 8-12-μm interval during scanning in the opposite direction (see diagram of actinometric-data collection in Fig. 2.3). The actinometric instruments cover a strip about 2500 km wide on the earth's surface and have a spatial resolution of 50 × 50 km at the subsatellite point.

The optical system of the long-wave channel in the narrow-angle scanning radiometer (Fig. 2.4) incorporates the following elements [32]:

1) a cylindrical fairing made of KRS-5, which seals the instrument and permits scanning and calibration;

2) a conical scanning mirror, which compensates the divergence of the beam after it has passed through the fairing;

3) a three-lobe mirror modulator, which interrupts the radiation flux at a frequency of 80 Hz;

4) color filters for isolation of the spectral zones mentioned above and for calibration;

5) an off-axis parabolic mirror;

6) a bolometer;

7) a KRS-5 space window;

8) a standard-light-source unit.

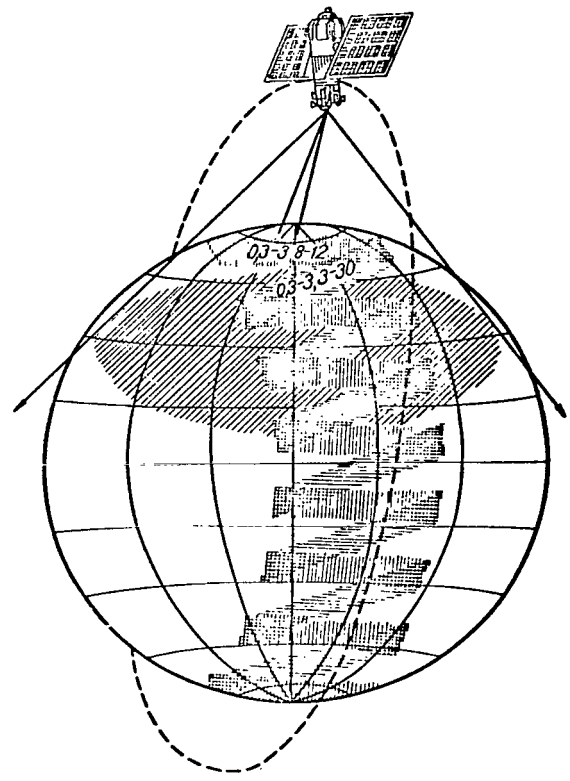

Figure 2.3. Diagram Showing Collection of Actinometric Data.

In the double-beam (differential) system used here, radiation strikes the receiver from the earth and from space by turns.

The optical system of the short-wavelength channel is simpler /54 (in this case it is unnecessary to use the double-beam system and there is no switching between optical filters). Scanning takes place in the plane perpendicular to the satellite's direction of motion. The two channels are synchronized.

Figure 2.5 explains the optical system used in the wide-angle radiometer (in this case, the optical systems are identical for both channels). Devices that permit varying not only the temperature of the reference black body, but also that of the radiometer case under conditions simulating those of outer space are used for preflight calibration of the radiometer's long-wave channels (L.B. Krasil'shchikov [33] gives details of the calibration procedure). Incandescent lamps were used as standards for monitoring /55 radiometer sensitivities on board the satellite.

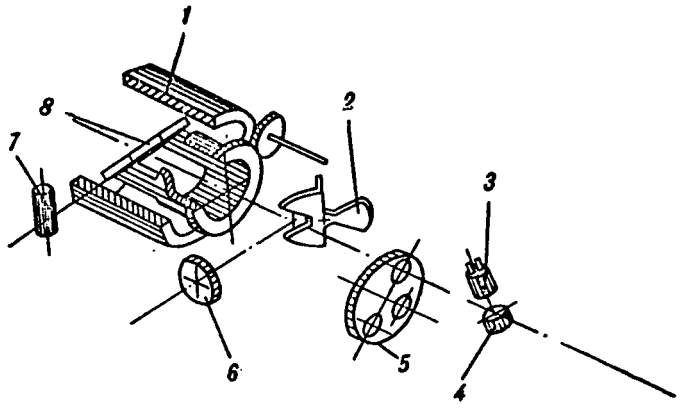

Figure 2.4. Optical Train of Narrow-Angle Radiometer Long-Wave Channel. 1) Cylindrical fairing; 2) modulator; 3) bolometer; 4) off-axis parabolic mirror; 5) color filters; 6) space window; 7) standard light-source unit; 8) scanning mirror.

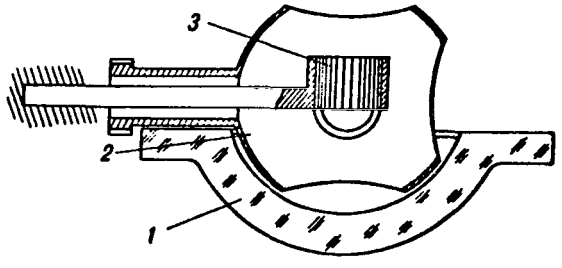

Figure 2.5. Optical Diagram of Wide-Angle Radiometer. 1) Color-filter fairing; 2) modulator; 3) bolometer.

P.A. Bazhulin, A. V. Kartashev, and M.N. Markov [5, 7] developed rocket and satellite spectrometer models for measurement of the outgoing infrared radiation. In this case, scanning is spectral as well as in angle. Space scanning is the function of scanning mirror 1 (Fig. 2.6), which rocks through an angle of ±90° (an angle of 180° is scanned in 100 sec). With mirrors 7 and 8, /56 the spherical Cassegrain objective concentrates the radiation on short-lag bolometer 4. This bolometer, which has a receiving area of 0.3×9 mm^2, a resistance of 1000 ohms, and a time constant of 5-7 msec, has conversion efficiencies up to 40 V/W and a detection coefficient $D^* = 1.5 \cdot 10^9$ at a modulation frequency of 30-40 Hz. The signals go from the bolometer to a broad-band amplifier (passband 0.5-200 Hz, gain greater than 10^5) and thence to the earth via telemetry system or for registration on the on-board loop oscillograph (the latter is one of the satellite measurements).

Spectral scanning is accomplished by introducing absorbing plates with successively shifted long-wave limits into the radiation path. These plates are mounted in the disk of modulator 3, rotation of which modulates the input signal. The use of four plates, three of which are partially transparent (lithium fluoride, calcium fluoride, and quartz), while the fourth is an opaque metal plate, makes it possible to measure the radiation in broad intervals of the spectrum and to find the radiation localized in much narrower spectral intervals from the differences between the readings. /57 Figure 2.7 shows transmission curves for the "direct" and differential channels of the spectrometer according to [7]. The four narrow bands of the spectrum selected in [4] were centered

around the following wavelengths: 3.59 ± ± 0.49 μm; 4.28 ± 0.29 μm; 4.69 ± 0.26 μm; 6.3 ± 0.35 μm. The plates were mounted unsymmetrically in the modulator disk to code the positions of the signals from the separate optical filters on the time scale. All units of the device that contain moving parts are sealed (the entrance window is made from KRS-5 crystal).

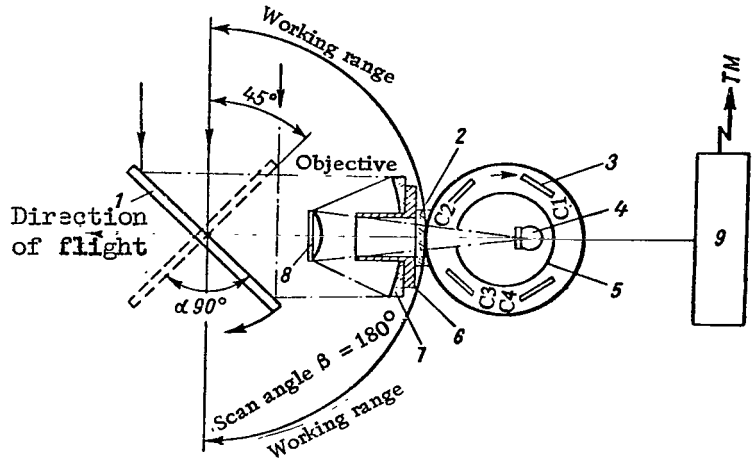

Figure 2.6. Block Diagram of Rocket-Borne Infrared Pulse Spectrometer to Register Angular Distrubition of Outgoing Radiation. 1) Scanning mirror; 2) sealed window; 3) modulator; 4) bolometer; 5) slit diaphragm; 6) inner barrel; 7) first spherical mirror; 8) second spherical mirror; 9) electronic amplifier.

A variable-temperature black body was used to calibrate the spectrometer in the laboratory. The sensitivity threshold for the 4.5-38-μm channel, expressed in terms of radiation temperature, varied from 0.36 to 2.7°K. Since the quantity measured directly in this case is the earth-modulator radiant-flux difference, and modulator temperature was not monitored accurately enough, the corresponding errors (including stray radiation from the windows, etc.) were excluded by feeding a standard radiant flux to the output one or more times during each scanning cycle. The radiation from space, as recorded in nearly horizontal directions, was used as the reference (null) flux. In some cases, ionospheric radiation was observed in this direction, and then the reference flux was recorded at a zenith angle of 45°. To monitor sensitivity constancy of the receiving and amplifying system, the signal from a standard incandescent lamp was applied periodically to the input of this system. This was done with the scanning mirror in its horizontal position, which corresponds to the "dead zone" of the scanning cycle. /58

A.I. Lebedinskiy et al. [10-16] designed the diffraction-grating satellite spectrophotometer that was carried on the Kosmos-series satellites for measurement of the spectral composition of the outgoing thermal radiation in the 7-38-μm wavelength band. Since these satellites had a three-axis orientation system, the instrument's optical axis was always pointed at the nadir. A differential measurement scheme was employed in the spectrophotometer: the directly measured quantity is the difference between the

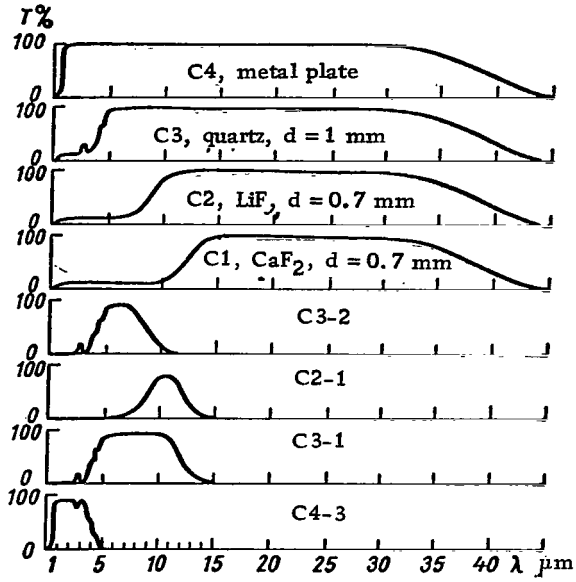

Figure 2.7. Transmission Curves of Pulse-Spectrometer Channels.

unknown outgoing radiation in the vertical direction and the hypothetical space null radiation in the horizontal direction. Cloudage conditions in the subsatellite region were monitored with a photometer that measured the brightness of the radiation at the nadir in the 0.6-0.8-μm zone of the spectrum (the photometer's resolution at the ground is about 30 km; in this context, we note that, for example, the Kosmos 45, which carried one of these spectrometers, had a perigee of 206 km and an apogee of 327 km).

The entire spectral range of the instrument is divided into two intervals: 7-20 and 14-38 μm. The dispersing element for the first of these intervals is a diffraction grating with 24 lines/mm; for the other it is a grating with 12 lines/mm (the energy-concentration maxima occur at about 10 μm and 20 μm, respectively). For the first of these intervals, the spectral resolution varies from 1.4 μm at a wavelength of 7 μm to 1.1 μm at 18 μm. The corresponding figures for the second interval are from 2.8 μm at 14 μm to 2.1 μm at 38 μm. The spectrophotometer's instantaneous field is 1°46' × 2°20', which corresponds to a 7.5 × 10-km area on the ground for a satellite 250 km high. Provision is made for scanning around the nadir in an angle of ±8°30'. The radiation detector was a bolometer with a sensitive area of 1 × 1 mm.

The spectrophotometer's complete operating cycle, which takes 81 seconds (including transition periods), contains the following series of measurements:

1) measurement of energy distribution in the spectrum from 7 to 20 μm within 18.5 sec;

2) scanning along the satellite's trajectory at a wavelength of 9 μm for 14.4 sec; /59

3) measurement of the energy distribution in the spectrum from 14 to 38 μm for 18.5 sec;

4) scanning at the 18.5-μm wavelength for 14.4 sec.

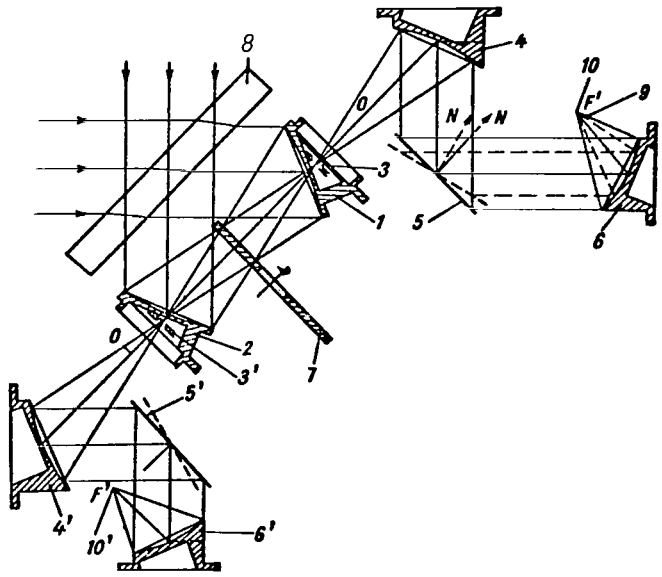

Figure 2.8. Optical System of Satellite Spectrophotometer. 1, 2) Mirror objectives; 3, 3') entrance slits; 4, 4') collimator objectives; 5, 5') diffraction gratings; 6, 6') objectives; 7) modulator; 8) entrance window; 9) color filter; 10, 10') bolometers.

All measured data were registered on the 35-mm motion-picture film of a six-loop oscillograph, which was housed in a recoverable container. The spectrophotometer is sealed and has a KRS-5 window.

Figure 2.8 shows the optical system of the spectrometer. After passing through sealed window 8, the radiation strikes the two-sided, four-bladed gold-plated modulator 7, which directs it by turns (at a frequency of 27 Hz) onto the measured- and null-radiant-flux entrance slits. Mirror objective 1 focuses images of the surface zones of interest onto entrance slit 3. The identical objective 2 is aimed at the comparison background (outer space). Both of the monochromators represented on the diagram have collimators and chambers with identical objective mirrors (4 and 4', 6 and 6'). All objectives are gold-plated off-axis paraboloids (except for 4', which is made of lithium fluoride and not coated). The positions of objectives 1 and 2 are such (see Fig. 2.8) that the radiation from the surface under study and the radiation from the comparison background pass through the same area of /60 the entrance window, thus eliminating the influence of inhomogeneities of the window.

Plate 9, which is made from indium antimonide and 0.15 mm thick, serves as an optical filter for removal of wavelengths shorter than 7 μm in the 7-20-μm channel. For the 14-38-μm channel, the functions of the "cutoff" filter are provided by the lithium-fluoride collimator objective 4', which does not reflect radiation at wavelengths shorter than 14 μm.

After dispersion into a spectrum by diffraction gratings 5, 5', the radiant fluxes are focused by objectives 6, 6' onto the sensitive areas of radiation detectors 10 and 10'. The functioning of the spectrophotometer is such that if radiation from the target surface strikes the receiver in the first channel, radiation from the comparison background is incident on the second-channel receiver and vice versa. The diffraction gratings are rotated for spectral scanning. Nadir-angle scanning is by rotation of objective mirrors 1, 2 about axis OO through an angle of ±12°. Two black bodies positioned at a 90° angle are used for preflight calibration of the instrument. The comparison-channel black body was at room temperature, while the temperature of the other black body was varied. It was reported in [10] that the second-order spectra were superposed for the 28-30-μm and 14-17-μm spectral intervals.

A package of radiometers and photometers with color filters for measurement of the outgoing radiation in various regions of the spectrum was mounted on the Kosmos 149 satellite, which was launched on 21 March 1967 into an orbit with an apogee of 297 km, a perigee of 248 km, and an equatorial inclination of 48.8° [104, 105]. This satellite, which is an orbiting optical station, has a three-axis aerogyroscopic orientation system that ensures orientation in space with an error no greater than 5° (orientation was monitored from the readings of the scientific equipment). One of the main objectives in the scientific program of the satellite is determination of the statistical spatial-structure characteristics of cloud fields and other ground formations from brightness measurements made of the planet in three zones of the spectrum outside the absorption bands (wavelengths 0.34, 0.47, and 0.74 μm). Such measurements also enable us to acquire information on the angular and spectral distributions of the absolute reflected solar radiation, which was based until recently almost exclusively on calculated results.

Another problem was to determine the altitude of the cloudage upper boundary from measurements of reflected-solar-radiation brightness in the absorption band of molecular oxygen (0.76 μm) and outside this band (0.74 μm). Plans also called for determi- /61
nation of the water vapor content deep in the atmosphere from similar measured brightness data in the region of the weak water-vapor band (0.72 μm) and on a comparison segment (0.74 μm).

The program included measurements of the outgoing radiation in the 8-12-μm atmospheric transparency window with the purpose of

determining the radiation temperature of the underlying surface or the upper cloud boundary with errors no greater than 1-2°, as well as measurements of the solar radiant flux reflected by the earth (0.3-3 μm) and the outgoing long-wave radiant flux (3-40 μm) with a view to investigating the planet's radiation balance.

For acquisition of cloudage information, the satellite carried a television system that could produce television pictures with 30° coverage at the nadir simultaneously with a picture of the transitional zone between space and the earth in four directions (the latter permitted visual monitoring of the satellite's attitude).

The scientific equipment consisted of two scanning telescopic photometers for measurement of shortwave brightness (field angle 3°; one of the telephotometers scanned along the flight path, the other in the perpendicular plane); a radiometer pointed at the nadir (field 2°) for measurement of the outgoing radiation in the 8-12-μm transparency window; two radiation-balance instruments (field 180°). All of this scientific equipment functioned on a planned schedule, and the measured quantities were found to be in the expected ranges. The aerogyroscopic stabilization system provided for geographic connection of the results with acceptable accuracy (the deviations from the vertical did not exceed 2-3°, which corresponds to a distance of 10-15 km on the ground).

For reasons that are as yet unclear, the sensitivities of the telephotometers and radiation-balance instruments varied with time, but this was taken into account using the on-board calibration results during reduction of the data. It is interesting to note that the data registered for the angular distribution of the earth's brightness in various regions of the spectrum showed anomalously high brightness values in the 0.72-μm water vapor absorption band (this may be explained by the daytime luminescence of the atmosphere, whose intensity is comparable with that of the reflected solar radiation).

American specialists have developed an extensive and varied series of radiometers and spectrometers for rocket and satellite outgoing-radiation measurements. Most of this equipment was designed for installation aboard weather satellites. Ten years of experience in the development of radiation apparatus in the USA brought out the need for a variety of radiometer and spectrometer models that would take account of the specifics of solutions of /62
the various problems that arise in data interpretation. The monographs [34-36] give rather detailed descriptions of such instruments as the hemispherical sensors designed by V.E. Suomi, which were carried aboard the Explorer VII satellite (1959), and the wide-angle conical-aperture and five-channel radiometers of the Tiros satellites. Here we shall only describe in brief some of the later models developed (or in preparation) primarily for the Nimbus and ESSA weather satellites.

TABLE 2.1. RADIOMETERS AND SPECTROMETERS ON AMERICAN WEATHER BALANCE AND SOLUTION OF THE INVERSE

/64

No. n/n	Instrument	Satellite	Channels (spectral-sensitivity ranges, μm
1	Wide-angle radiometers	Explorer VII, Tiros III, IV, VII, ESSA 3, 5, ...	1) "Black" (long- and short-wave radiation), 2) "White" (long-wave radiation)
2	Wide-angle radiometer with conical aperture	Tiros II, III, IV	1) "Black" (Long- and short-wave radiation) 2) "White" (long-wave radiation)
3	Five-channel scanning radiometer (SFR)	Tiros II, III, IV, VII	1) 6.0-6.5 (Tiros II, III, IV). 14.8-15.5 (Tiros VII) 2) 8.0-12.0 3) 0.2-6.0 4) 8.0-30.0 (except Tiros IV) 5) 0.55-0.75
4	High-resolution scanning infrared radiometer (HRSIR)	Nimbus I, II, III	1) 3.5-4.1 (Nimbus I, II); 3.5-4.1 (night); 0.7-1.3 (day) (Nimbus III)
5	Scanning five-channel medium-resolution radiometer (SFMRR)	Nimbus II, III	1) 6.4-6.9 2) 10.0-11.0 3) 14.0-16.0 (Nimbus II) 14.5-15.5 (Nimbus III) 4) 5.0-30.0 (Nimbus III) 20.0-23.0 (Nimbus III) 5) 0.2-4.0
6a	Infrared interference spectrometer (ILS)	Nimbus III	5-20 – spectral scanning with 5-cm^{-1} resolution (0.1 μm at 15-μm wavelength)

SATELLITES DESIGNED FOR INVESTIGATION OF THE EARTH'S RADIATION PROBLEMS OF SATELLITE METEOROLOGY /65

Radiation detectors	Instantaneous field	Linear resolution at subsatellite point, km (orbit altitude in parentheses, (km)	Problems to be solved
Hemispherical or flat plates - semiconductor bolometers	Entire visible disk of planet	50% of radiation from 1400 (700) (Explorer, Tiros), 2400 (1400) (ESSA)	Radiation budget (outgoing long-wave radiation, albedo)
Semiconductor bolometers	50°	670 (700)	Radiation budget
Semiconductor bolometers	5°	60 (700)	Cloudage distribution and cloud-top height, underlying-surface and stratosphere temperatures, troposphere humidity, radiation budget
Lead selenide photoresistor radiant-cooled to 200°K	0.46°	9 (1100)	Cloudage distribution (infrared pictures) and cloud top altitude, underlying-surface temperature (at night)
Semiconductor bolometers	2.9°	55 (1100)	Same as in line 3 (SFR)
Semiconductor bolometers	8°	150 (1100)	Vertical profiles of temperature and concentrations of water vapor, ozone, etc.

TABLE 2.1 (Cont'd.)

/66

No. n/n	Instrument	Satellite	Channels (spectral-sensitivity ranges, μm
6b	Infrared interference spectrometer (IIS-M)	Nimbus D	6.3-50.0, spectral scanning with 3-cm^{-1} resolution (0.07 μm at 15-μm wavelength)
7a	Satellite infrared spectrometer (SIRS)	Nimbus D	8 channels; 7 in the 15-μm CO_2 band and 1 in the transparency window around 11 μm. Spectral distribution 5 cm^{-1}
7b	Satellite infrared spectrometer, modified (SIRS-M)	Minbus D	14 channels; 7 in the 15-μm CO_2 band, 6 in the H_2O rotational band, and 1 in the transparency window at 11 μm. Spectral resolution 5 cm^{-1}
8	High-resolution scanning radiometer (HRSR)	Tiros M. Improved Tiros Operational Satellites ITOS A, B, ...	1) 10.5-12.5 2) 0.52-0.75
9	Selective modulation radiometer (SMR)	Nimbus D	6 channels in 15-μm CO_2 band with provision for switching one to the 11 μm window
10	Wedge filter spectrometer (WFS)	Nimbus D	1) 1.2-2.4; and 3.2-6.4 Spectral scanning with resolution $\lambda/\Delta\lambda = 100$ (0.05 μm at 5-μm wavelength)

Radiation detectors	Instantaneous field	Linear resolution at subsatellite point, km (orbit altitude in parentheses, km)	Problems to be solved
Semiconductor Bolometer	5°	90 (1100)	Same as in line 6a (IIS)
Semiconductor bolometers	12°	230 (1100)	Vertical temperature profile
Semiconductor bolometers	12°	230 (1100)	Vertical profiles of temperature and water vapor concentration
Semiconductor bolometer	0.30° 0.16°	7 4 (1100)	Distribution of cloudage (pictures) and cloud-top height, underlying-surface temperature, albedo
Semiconductor bolometer	10°	190 (1100)	Vertical temperature profile
Lead selenide photoresistor radiant-cooled to 160°K	2°	38 (1100)	Wetness and ice content in clouds (1.2-2.4 μm), vertical profiles of temperature (4.3-μm CO_2 band) and H_2O-vapor concentration (6.3-μm water vapor band)

TABLE 2.1 (Cont'd.)

/68

No. n/n	Instrument	Satellite	Channels (spectral-sensitivity ranges, μm
11	Scanning infrared radiometer (SIR)	Nimbus D	1) 10.5-12.5 2) 6.5-7.0
12	Radiometer for determination of vertical temperature profile (RVTP)	ITOS ('70's)	8 channels: 6 in the 15-μm CO_2 band, 1 in the H_2O rotational band, and 1 in the 11-μm window
13	Very high resolution scanning radiometer (VHRSR)	ITOS ('70's)	1) 10.5-12.5 2) 0.6-0.7
14	Very high resolution scanning radiometer for synchronous satellites (VHRSR-S)	Synchronous satellite	10.5-12.5

Note. Launching dates (actual or proposed) of the weather Nimbus I, 28 August 1964; Nimbus 3, 14 April 1969; Tiros II, 23 1969; Tiros III, 12 June 1961; ESSA 3, 2 October 1966; ITOS-A, April 1967; Nimbus D, first quarter of 1970; Tiros VII, 19 June ESSA satellites).

Radiation detectors	Instantaneous field	Linear resolution at subsatellite point, km (orbit altitude in parentheses, km)	Problems to be solved
Lead selenide photoresistor radiant-cooled to 160°K	0.40° 1.20°	8 23 (1100)	Cloudage distribution and top altitude, underlying-surface temperature, vertical movements and jet streams, identification of air masses
Semiconductor bolometers	2°	50 (1400)	Vertical temperature profile
Photoresistor radiant cooled in two stages to 80°K. Photodiode	0.034°	0.8 (1400)	Cloudage distribution (pictures) and top altitudes, underlying-surface temperature, albedo
Photoresistor cryogenically cooled to 80°K	0.023°	15 (3500)	Cloudage distribution (pictures) and top altitude, underlying-surface temperature

satellites listed in the table: Explorer VII, 17 October 1959; November 1960; Nimbus II, 15 May 1966; Tiros M, first quarter of third quarter of 1969; Tiros IV, 8 February 1962; ESSA-5, 20 1963 (wide-angle sensors will be mounted on all odd-numbered

Table 2.1, which was compiled by W.R. Bandeen [37], lists characteristics of sixteen varieties of radiometers and spectrometers designed for acquisition of data for study of the radiation balance of the ground/atmosphere system and solution of various inverse problems in satellite meteorology. The first inference to be drawn from this table is that wide-angle radiometers (with "black" and "white" hemispherical or flat sensors [95-98]) and five-channel radiometers with comparatively narrow fields [61] are recognized as the most promising instruments for study of the earth's radiation balance. It is proposed that instruments of the former type be installed on all odd-numbered ESSA satellites (since they were used on ESSA 3 and ESSA 5). Reference was made in this case to sensors with flat receiving surfaces. Modifications of this instrument in which the field is limited by use of conical optics may also be used [37].

As for the Nimbus satellites, which have a three-axis ground orientation system, and satellites of the Improved Tiros Operational System (ITOS), they have been provided with a modified scanning five-channel medium-resolution radiometer (SFMRR).

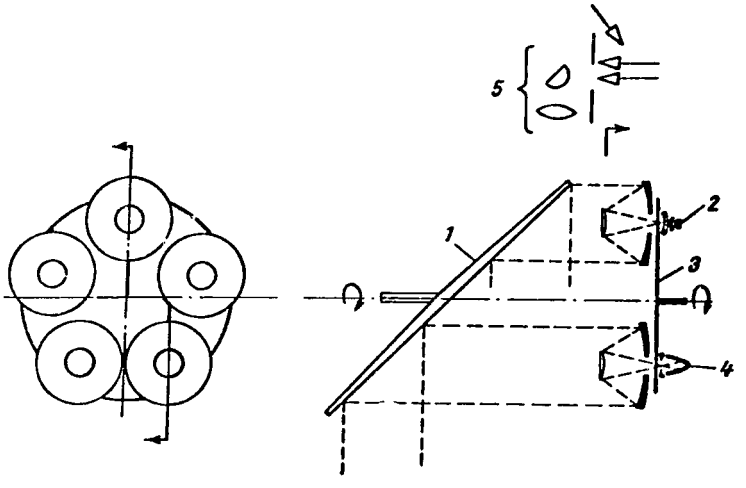

Figure 2.9. Scanning Five-Channel Radiometer with Medium Spatial Resolution. 1) Scanning mirror; 2) immersion receiver; 3) modulator; 4) receiver without immersion optics; 5) optics for sun calibration.

While it is fundamentally an analog of the radiometer carried on the Tiros satellites, the modified five-channel radiometer is a totally redesigned instrument [38]. The analogy in principle consists in the use of approximately the same spectral sensitivity ranges (channels) of the instrument: 6.4-6.9, 10-11, 14-16, 5-30, and 0.2-0.4 μm. It will be recalled that the following channels

were used in the original model of the five-channel radiometer: 6.0-6.5 μm (replaced by 41.8-15.5 μm in the case of Tiros VII), 8.0-12.0, 0.2-6.0, 8.0-30.0, and 0.55-0.75 μm. Naturally, selection of the 5-30 and 0.2-4.0-μm channels for the SFMRR was dictated by the need to find the optimum solution to the problem of measuring integrated long-wave and short-wave outgoing-radiation fluxes. The change in the limits of the spectral range in the 6.3-μm water-vapor band was required to optimize conditions for /63
determination of tropospheric moisture content. The 14-16-μm interval was selected because of the success with which data measured in this channel had been used (Tiros VII) to determine stratosphere temperature [36]. The object of narrowing the spectral region in the atmospheric transparency window to 10-11 μm was to reduce the influence of the lower atmosphere on the results of underlying-surface or cloud-upper-margin temperature calculation from measured outgoing-radiation data in this spectral region.

One of the most important design features of the SFMRR is the use of scanning mirror 1 (Fig. 2.9), which rotates in a position in which it is inclined 45° to the radiometer optical axis. This makes it possible to scan the earth in the plane perpendicular to the satellite's direction of motion from one limb to the other (obviously, this scanning regime is suitable only when three-axis attitude control is available). Since the mirror turns through 360°, both the earth and space are scanned. During scanning of space, various elements of the satellite's construction also come into the instrument's field. The radiant flux to be measured is modulated by mechanical chopper 3 before /68
it strikes radiation receivers 2 and 4. When the radiant flux is interrupted in this manner, the measured quantity is the difference between the earth and modulator radiations. Since modulator temperature varies with time, provision is made for compensating these variations in such a way that the output voltage will always be the same at a given temperature. After amplification of the signal and synchronous detection, the voltage at the output varies from 0 to 6.4 V. The analog signals are converted to digital and registered on eight-track recorder tape.

The radiometer is calibrated under laboratory (preflight) /69
conditions against a black body (infrared channels) and a diffuse-reflecting screen illuminated by a standard incandescent lamp (short-wavelength radiation) with the instrument case at various temperatures in a vacuum. The laboratory technique used for calibration of the short-wave channels is discussed in detail in L.F. Bartman's paper [39]. The null signal from space and a signal generated when satellite structural elements come into the field are used for on-board calibration of the radiometer (more precisely, control of its sensitivity). The channels centered on 6.6 /70
and 15 μm are provided with an electronic interlock that shuts off the sensors when the source temperature exceeds 270°K (this corresponds to the values observed in reality). Thus, a fixed

voltage is applied for sensitivity control in these channels. The short-wave channel is calibrated on board with respect to the sun (Fig. 2.9).

The development of a modified five-channel radiometer for thermal sensing of the atmosphere is highly interesting [61]. The modified five-channel radiometer that was originally to be tested on manned spacecraft at the end of 1969 has the following channels: 1) 825-975 cm^{-1}; 2) 740-780 cm^{-1}; 3) 730-770 cm^{-1}; 4) 717.5-757.5 cm^{-1}; 5) 500-570 cm^{-1}. The first of these spectral intervals, which lies in a transparency window of the atmosphere, will be used to determine the temperature of the underlying surface or the upper cloudage boundary and to characterize the amount of cloudage in the radiometer field in the presence of broken cloud cover. The second, third, and fourth intervals, which lie on the short-wave side of the 15-μm carbon dioxide band, were selected for determination of the tropopsheric vertical temperature profile. The fifth channel, which lies in the rotational water-vapor band, is provided for determination of total tropospheric moisture content. The five-channel radiometer will function in the nadir-angle scanning mode in the plane perpendicular to the spacecraft's direction of motion, figuring on the possibility of acquiring 10 elements along each scan with an area of about 32.5 km^2 at ground level. Ten successive scans will cover an area of about 32.5 km^2, and 100 readings will be obtained in each of the channels for this purpose.

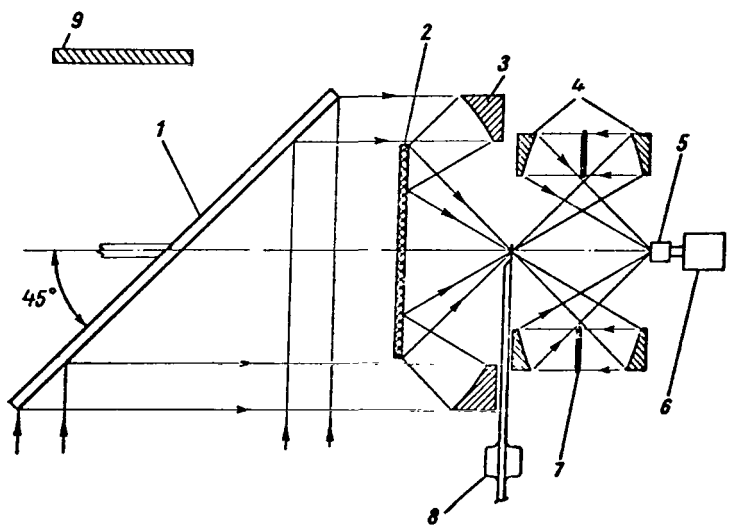

Figure 2.10. Scanning Infrared Radiometer with High Spatial Resolution. 1) Scanning mirror; 2) secondary mirror; 3) primary mirror; 4) transfer mirror; 5) radiation detector; 6) cryogenic device; 7) optical filter; 8) modulator; 9) black body.

The high-resolution scanning infrared radiometer (HRSIR) (Table 2.1) performs the important functions of acquiring infrared images of the cloud cover and absolute measurements of the outgoing radiation in the 3.5-4.1-μm region of the spectrum. A diagram of this instrument appears in Fig. 2.10. As we see, the rotary-mirror scanning feature is the same as in the five-channel radiometer. The lead selenide photoresistor, which can be cooled (radiation cryogen) to -75°C, makes it possible to measure radiation temperature in the range from 210 to 330°K with a "noise" temperature of 1° for a radiation temperature of 250°K. The radiant flux is modulated at the focus of a four-inch Cassegrain telescope (see Fig. 2.10). The scanning rate is 44.7 rpm, which makes it possible to obtain contiguous scanning strips at the subsatellite point (with increasing overlapping in the direction of the horizon). /71 Calibration is carried out in the same way as in the five-channel radiometer. Thus, for example, the Nimbus 1 radiometer was graduated against a black body whose temperature was varied from 190 to 340°K at various photoresistor temperatures. The results of a recalibration of the radiometer eight months later, when the instrument was on the satellite and ready to launch, gave good agreement. The radiometer casing was thermostated aboard the satellite at 11°C, and the deviations from this temperature in flight did not exceed ±2.5°. The sensitivity of the radiometer underwent no discernible change during the entire time for which it functioned under space conditions. The temperature resolution actually obtained was 2°K.

The images were constructed (rendered visible) and subjected to automatic geographic connection by ground apparatus. The photofacsimile recorder used here has a device for automatic calibration based on ten brightness gradations.

As we see from the eighth line of Table 2.1, a two-channel HRSR, which makes it possible to acquire both infrared and visible /72 light images of the cloud cover and underlying surface by means of a scanning measuring apparatus, is under development for the Tiros M and ITOS satellites. The field of this instrument is so narrow that the spatial resolution of the images should approach the resolution limit of television photographs. At the same time, this means a substantial increase in the probability that the radiometer field will be completely filled by clouds or underlying surface in the presence of partial cloud cover; this is highly important from the standpoint of reliability of temperature determination for the underlying surface or upper cloudage limit. Selection of the 10.5-12.5-μm long-wave channel (instead of 3.5-4.1 μm) is also very important, since it makes it possible to obtain infrared images not only during the night, but also during the day (the simultaneous presence of the short-wave 0.52-0.75-μm channel will make it possible to establish quite confidently whether clouds were present or absent in the field of view). It is proposed that the HRSR readings in the 10.5-12.5-μm channel not only be registered by the on-board storage unit, but also be

transmitted in the direct (real-time) mode.

A distinctive feature of the scanning infrared radiometer (line 11 of Table 2.1) is the use of the 6.5-7.0-μm channel in the 6.3-μm water-vapor band with extremely high spatial resolution.

The very high resolution scanning radiometer (line 13 of Table 2.1) is similar in principle to the HRSIR (line 4) and the HRSR (line 8), but is designed to obtain exceptionally high spatial resolution. The limited capacity of the on-board storage system presents a serious difficulty in this connection. For this reason, direct data transmission is planned.

A modification that belongs to the same group is the very high resolution scanning radiometer for synchronous satellites (VHRSR-S) (Table 2.1, line 14). It is designed for installation on the ATS-FG synchronous satellites, which have a three-axis orientation system, and is a scanning instrument with the following basic components [80]: a scanning mirror, a 20-cm Cassegrain telescope, a radiant-flux modulating system, a solid-state bolometer, and a bolometer cooling system. Its effective solid angle of $4 \cdot 10^{-3}$ radian gives a ground-level spatial resolution of 15 km (the detection coefficient of the bolometer is $D^* = 1.5 \cdot 10^{10}$ $cm \cdot Hz^{1/2}W^{-1}$). The time to acquire one image, which consists of 1000 lines, is 20 minutes.

Use of spectral apparatus is most promising for solution of /73
the various inverse problems of satellite meteorology [40]. Since one of the most pressing inverse problems is determination of the vertical temperature profile from spectral measurements of the outgoing thermal radiation in the 15-μm carbon dioxide band [41], a whole series of spectrometer models has been developed in recent years for solution of this (and related) problems (Table 2.1).

Let us first briefly describe the satellite infrared spectrometer (SIRS), which was developed by the U.S. Weather Bureau Meteorological Satellite Laboratory [37, 42, 43, 44, 48, 88, 90].

It was originally proposed [42] that the outgoing infrared radiation be measured in four narrow segments of the spectrum (5 cm^{-1} wide) in the 15-μm carbon dioxide band for approximate determination of the vertical temperature profile. Later, plans were changed to include similar measurements of the outgoing radiation around the absorption maximum of the 15-μm band, so that data could be obtained on temperatures at high altitudes in the atmosphere and used as a basis for studying, for example, sudden warmings of the stratosphere. In addition, it was planned from the very beginning to include measurements in a narrow spectral interval (7 cm^{-1} wide) around the 11.1-μm wavelength, where the atmosphere is most transparent in the infrared (these data would permit acquisition of the planetary temperature distribution of the underlying surface).

The spectrometer has a field of 0.04 steradian, which, for a satellite at an altitude of about 1000 km, corresponds to localization of ground areas of about 200 × 200 km at the nadir. It should be noted that, chiefly because of inadequate sensitivity of the radiation receivers, the spectrum-scanning time is about 10 seconds, which means a "blur" zone of about 100 km. W. Nordberg [57] predicts that with the development of deep-cooled receivers, it will be possible to increase the scanning rate to 10 scans/second, and improve spatial resolution to 1 km. Use of highly sensitive receivers will also permit substantial improvement of spectral resolution.

The satellite infrared spectrometer is of the Fasti-Ebert type and uses a 12.5 × 12.5-cm diffraction grating with 500 lines/cm. The focusing mirror, which is 40 cm in diameter (focal length 62.5 cm), points the outgoing earth radiation at a two-sectored modulator disk placed at a 45° angle to the spectrometer optical axis. As the disk rotates, radiations from the earth and from space (null signal) fall alternately onto the spectrometer entrance slit, since the instrument has a second entrance aperture pointed in the direction away from the earth. The directly measured difference between the earth and space signals is practically equivalent to the radiation outgoing from the earth. /74

To check sensitivity during measurements, the focusing mirror is rotated in such a way that it directs the radiation of a black body at known temperature onto the entrance slit (in this case, the difference between the black-body and space radiations is measured). The temperature of the black body is not regulated, and it can vary from 0 to 60°C.

Behind the entrance slit, the radiation strikes a collimator mirror and is then back-reflected by the diffraction grating onto the same mirror, which focuses the spectrum onto five entrance slits corresponding to the five spectral regions under study (four in the carbon dioxide band and the fifth in the transparency window). The radiant fluxes are measured simultaneously in the five spectral regions by means of immersion-type solid-state bolometers placed directly behind the exit slits. The spectrometer is designed to measure radiant fluxes in the range from 25 to 180 ergs/$cm^2 \cdot sec \cdot sr \cdot cm^{-1}$, which corresponds to effective temperatures from -70 to +70°C. Radiant-flux variations no smaller than 0.25 erg/$cm^2 \cdot sec \cdot sr \cdot cm^{-1}$ should then be registered; this corresponds to a temperature change of 0.25°C at the effective temperature of -70°C. The time constant is about 6 seconds. Provision is made for controlling the spectral calibration of the spectrometer by insertion of an interference filter into the beam from the black body to the exit slit (a change in the expected signal level on insertion of the filter indicates that the wavelength calibration has shifted).

Laboratory tests of the spectrometer showed that it registers 0.2°C changes in the temperatures of objects at room temperature.

The SIRS has since been slightly modified [43, 44] and further tested.

The modified spectrometer, which was tested by sending the instrument up on an aerostat during the daytime of 11 August 1964 at Palestine, Texas [44], permits measurement of the outgoing radiation in six 5-cm^{-1}-wide spectral intervals, which are centered at the wave numbers 669, 677.5, 691, 697, 703, and 709 cm^{-1} (region of the 15-μm carbon dioxide band) and in an interval 7 cm^{-1} wide at a wave number of 899 cm^{-1}.

We note that the following channels were ultimately selected for the on-board version of the SIRS [4]: 669.0, 677.5, 692.0, 699.0, 706.0, 714.0, 750.0, and 8.9.0 cm^{-1} (so that the SIRS acquired eight channels).

The optical axis of the spectrometer, which has a 12° field, /75
points at the nadir. The directly measured quantity is the difference between the radiant intensities of the "earth-atmosphere" system and the absolute black body (a comparison source simulating space) at 77°K.

The aerostat reached a maximum altitude of about 31 km and then drifted above the 30-km level for 7.5 hours. The sky was cloudless at the beginning of the flight; then the aerostat passed over regions with cumulus clouds and, on part of its path, over a squall zone with cloud cover up to an altitude of 10.5 km. The error of outgoing-radiation measurement was about 0.5 $erg/cm^2 \times$ $\times sec \cdot sr \cdot cm^{-1}$ (which corresponds to a relative error of about 1%). The two examples of measured-data reduction given in [44] (for the cases of cloudless sky and cloudage with an upper-boundary temperature of 233°K) indicate that the indirectly acquired vertical temperature profiles agree quite satisfactorily with the results of direct measurements (see Chapter 5). These and other tests subsequently led to the decision to install the SIRS on Nimbus III.

Improved models of the multichannel infrared spectrometer and other apparatus are being prepared for the Nimbus D (Nimbus IV) weather satellite. As W. Nordberg [91] and W.P. Porter [93] note in their surveys, this satellite, which is to be launched in the first quarter of 1970, has four features that distinguish it from the Nimbus III: 1) the radioisotope thermoelectric generator is eliminated; 2) it uses a new "modularized" monitoring system; 3) provision is made for four new weather experiments; 4) certain improvements have been made in various satellite subsystems.

The improved instruments include a dissector television camera, which delivers an 800-line image. This camera can produce images in the form of a continuous strip 2594 km wide with a nadir resolution (at ground level) of 1.5 km. Another instrument is a two-channel infrared scanning radiometer with high spatial resolution (10.6 km on the ground at the nadir); it is sensitive

in the wavelength intervals from 10.5 to 12.5 and 6.5 to 7 μm. This instrument was designed to determine underlying-surface temperature, the temperature (and altitude) of the upper cloudage boundary, and atmospheric moisture content. The two-channel radiometer is expected to distinguish very fine cirrus clouds and moist air masses.

An interference spectrometer (of the Michelson interferometer type) will make it possible to register the outgoing-radiation spectrum in the 8-40-μm band with a 93-km nadir spatial resolution. This information is to be used to determine vertical temperature profiles, moisture, and ozone. Since the time to register the spectrum is 13.1 sec, "blur" is to be eliminated (as on the Nimbus III) by slow rotation of the mirror that directs the radiation into the instrument through 4° in the backward direction. /76

Another instrument designed for thermal sensing of the atmosphere is a multichannel diffraction spectrometer (Ebert-Fasti type), which permits simultaneous registration of the outgoing radiation in a series of spectral intervals in the 11-35-μm wavelength band (six intervals in the 15-μm carbon dioxide band and several in the water-vapor bands and transparency windows). The rotary mirror at the entrance to the instrument provides for influx of radiation from the nadir and six other directions on either wide of the satellite's direction of motion.

In the measurement procedure envisaged, the spectrometer sights the earth for one minute in the nadir angle range from 25 to 39° to the left of the satellite's direction of motion, is then pointed at the nadir, and, during the third minute, ranges from 25 to 39° to the right of the direction of motion. This stepwise scanning cycle is repeated continuously. The variation of the lateral sighting angle is programmed in such a way as to vary the nadir angle from 39° at the equator to 25° at high latitudes, thus keeping spatial resolution constant and, consequently, making it easier to use the standard coordinate grid in reducing the data.

The spectrometer's field is a square cone with a vertex angle of 12.5°. The instrument gives data on the vertical temperature profile to an altitude of 30 km and the moisture contents to 11 km.

A third instrument, a radiometer with selective modulation, is designed to acquire information on the vertical temperature profile not only in the troposphere, but also in the stratosphere. Data measured in six spectral zones of the 15-μm carbon dioxide band will be used for this purpose. Spatial resolution on the ground at the nadir is 185 km.

Plans call for the use of a spectrometer with a wedge filter to measure the spectral distribution of the reflected solar radiation in the wavelength band from 1.2 to 2.4 μm and the infrared

outgoing radiation in the 3.2-6.4-μm interval (the scanning time for each of the intervals is 16 seconds). The instrument's field is 2.5 × 2.5°. Spectral resolution varies from 600 to 200 cm^{-1}. /77
On-board black-body calibration is provided for all of the spectrometers listed above.

The vertical ozone profile will be determined from measured data on the outgoing ultraviolet radiation in twelve spectral intervals of the 2500-3400-Å band obtained with a double diffraction grating monochromator (spectral resolution 10 Å, field 0.044 sr). An auxiliary component of this instrument is a photometer with an interference filter (passband 50 Å), which is to measure the radiation around 3800 Å, where there is no ozone absorption. The instrument is calibrated on-board using a Cerenkov radiator and a mercury-argon lamp as radiation sources. The instrument will measure the direct solar radiation reflected by a diffusing screen once during each orbit. The sunlight reflected by the moon is to be measured on the night segments of the orbit. Five simple photometers with photodiodes (these instruments have a 90° field oriented horizontally backward, and can therefore register solar radiation as the satellite passes from the daytime to the nighttime side of the earth in the region of the North Pole) will be used for special extended-term measurements of the ultraviolet solar radiation at wavelengths of 1216, 1600, 1800, 2100, and 2600 Å. The Nimbus D will also carry such apparatus for collection and transmission of data from sounding balloons and buoys at sea.

In connection with our remarks on prospects for the development of scientific apparatus for specific weather satellites, we should note that R.M. Rados [92] gives a complete summary characterizing the scientific equipment and programs not only of all previously launched American weather satellites, but also of those planned for the immediate future (as of January 1969).

Like the SIRS described above, the classical diffraction-grating spectrometer is a rather heavy and cumbersome instrument. Interference spectrometers are more suitable from this standpoint. Such spectrometers also have extremely important advantages in "photographic" registration of the spectrum and their high light grasp. For these reasons, a great deal of attention has been devoted to the development of interference spectrometers for weather satellites in recent years [45-49, 85]. An infrared interference spectrometer (IIS) (see lines 6a and 6b in Table 2.1) was developed in [45-47] with the object of solving the problem of atmospheric thermal sensing from satellites; it is capable of measuring the spectral distribution of the outgoing thermal radiation in the 500-2000 cm^{-1} region of the spectrum with a resolution of /78
5 cm^{-1} and an error not exceeding ±0.5 $erg/cm^2 \cdot sec \cdot sr$. As we have already noted, instruments of this type are to be mounted on Nimbus weather satellites. As concerns calibration of the IIS aboard the satellites, the procedure is the same as for the SIRS (against

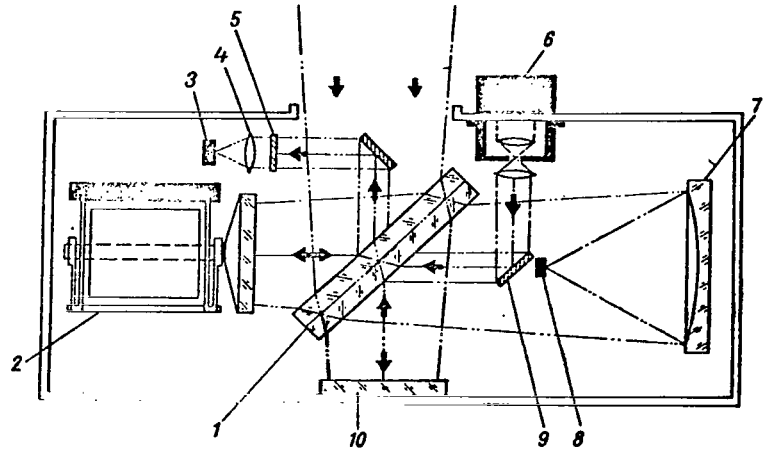

Figure 2.11. Infrared Interference Spectrometer. 1) Radiant flux divider and compensating plate; 2) moving mirror; 3) receiver; 4) lens; 5) interference filter; 6) monochromatic radiation source; 7) infrared collimator; 8) infrared receiver; 9) mirror; 10) stationary mirror.

space and a black body).

The infrared interference spectrometer is a Michelson interferometer (Fig. 2.11). An important element of this instrument is the divider 1, which splits the radiant flux entering the instrument into two approximately equal components. After reflection from vibrating and stationary mirrors 2 and 3, respectively, the two beams interfere with a path difference determined by the difference between the distances traveled by the two beams. The resultant radiant flux is focused on radiation detector 5 and registered in the form of a plot of the signal $\underline{i}$ against the path difference δ.

In the case of monochromatic radiation, the recorded signal is obviously sinusoidal, while in the presence of a continuous spectrum, many amplitudes corresponding to the various frequencies will be superimposed in the form of an interferogram. The amplitudes are proportional to the radiant intensities $J(\nu)$, and the frequencies to the wave numbers ν. Leaving out the constant term, the result of the measurements can be represented in the form /79

$$i(\delta) = \int_{\nu_1}^{\nu_2} J(\nu)\cos(2\pi\nu\delta)\,d\nu,$$

where ν_1 and ν_2 are the limits of the spectral region studied.

Reduction of the data consists in performance of the inverse transformation

$$J_\nu = \int_{-\delta_{max}}^{+\delta_{max}} i(\delta)\cos(2\pi\nu\delta)\,d\delta.$$

The true radiant intensity J_ν can be obtained only with certain restrictions applying to the accuracy of the absolute value and spectral resolution. These limitations stem from the limited size of the interval $i(\delta)$, the instrument's field of view, and receiver noise. The spectral resolution $\nu/\Delta\nu$ is identical to the number of periods observed on the interferogram for the particular frequency. Thus, for example, to obtain a resolution of 5 cm^{-1} at ν = 665 cm^{-1}, it is necessary to have no fewer than 133 periods, which requires an optical path difference of 2 mm. The interferometer described above has a 4-mm interval from $-\delta_{max}$ to $+\delta_{max}$, and this requires shifting the mirror by 2 mm. The limitation on the instrument's solid angle Ω is governed by the requirement that the phases of the off-axis and axial rays differ only insignificantly (accordingly, we have the criterion $\Omega \leqslant \frac{2\pi\Delta\nu}{\nu}$). In this case, the field-cone vertex angle is 8°. According to the Shannon theorem, the interferogram must be registered at least twice during the period corresponding to the highest-frequency component. Registration is twice as often in the IIS. The required registration frequency is determined with the aid of an auxiliary interferometer with a neon source 9 (wavelength 5852.5 Å) and radiation detector 6.

The basic disadvantages of interference spectrometers stem from the following circumstances: 1) the need for the inverse Fourier transformation of the interferogram (use of electronic computers makes these calculations considerably easier and faster); 2) the radiation source used must be stable during the time required to register the interferogram (under satellite conditions, this requires compensation of "blur"); 3) the stiffness of requirements made of the instrument's mechanical and optical stability; 4) the need for a wide dynamic range for the data-transmission channel (2000:1) and the need for linearity.

Test results obtained during an aerostat launching of the IIS on 8 May 1966 during cloudless weather (the balloon drifted at the 33.5-km level) were encouraging (see Chapter 5 for details). /80

Preparation of the modified IIS-M (line 6b in Table 2.1) for the Nimbus D includes broadening of the spectral range at the long-wave end (water-vapor rotational band) and increases in spectral and spatial resolution.

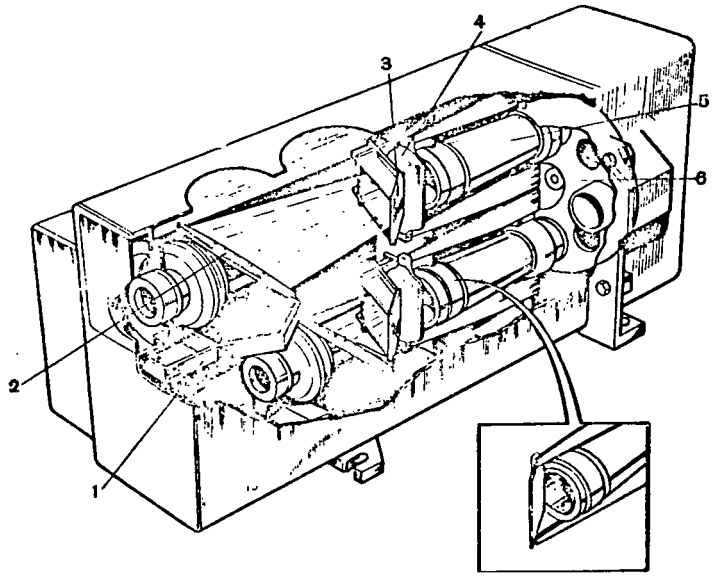

Figure 2.12. Radiometer with Selective Modulation. 1) Black body; 2) moving mirror; 3) stationary mirror; 4) modulators; 5) cuvettes (in front end); 6) interchangeable filters.

A team of specialists headed by J.T. Houghton of the Oxford University Clarendon Laboratory has done interesting developmental work on spectrometers for thermal sensing problems [50-55]. For example, this group has designed a so-called selective modulation radiometer (SMR) (Table 2.1, line 9) for the Nimbus D satellite [55].

Figure 2.12 shows a diagram of the selective-modulation radiometer. The device has a two-element receiving system consisting of two cuvettes 5, which the radiation enters after reflection from moving mirrors 2, which are set at a 45° angle to the optical axis. The radiant-flux modulators 4, which execute /81
flywheel-like oscillatory motions, are set up in front of the cuvettes. A system of germanium lenses directs the radiant fluxes into the cuvettes and thence through interference filters 6 and a light conductor to the radiation detectors (semiconductor bolometers), which are situated at the extreme right end of the radiometer. Mirrors 3 serve to point the instrument at space. The differential operating principle of the SMR consists in measurement of the difference between the earth and space radiations. The radiation of black body 1, which is directed into the instrument by moving mirrors 2 through the "earth" channel, is used for onboard monitoring of radiometer sensitivity.

The radiation is monochromatized in the SMR by combined use of very narrow-band interference filters and selective modulation. The latter is accomplished by means of the cuvettes, which are filled with carbon dioxide. One of the cuvettes contains a very small amount of CO_2 at low pressure, while the other is filled with carbon dioxide. The radiation entering the instrument is "split" in each of the channels into two beams, which pass through the corresponding cuvettes. In this case, the signal at the radiometer output is determined by the radiation in very narrow spectral intervals centered on strong absorption lines (the centers themselves are excluded by absorption in the nearly empty cuvette). The two-element receiving system makes it possible to isolate two narrow spectral segments in the region of strong absorption in which the stratosphere makes the basic contribution to the outgoing radiation.

The four radiometer channels whose function is to determine the vertical temperature profile in the troposphere function with a single absorbing cuvette, which eliminates the radiation around the line centers. The radiation in the wings of the lines is measured in this case. One of the six channels described can be switched for measurement of radiation in the interval around 11 μm. Aerostat tests of the SMR made in 1966 confirmed the feasibility of using this instrument.

The wedge filter spectrometer (WFS) described in [37] was also designed for the Nimbus D satellite (Table 2.1, line 10). The principal element of the WFS is a combination interference filter consisting of halves of two variable-thickness filters — one for the 1.2-2.4-μm spectral range and one for 3.2-6.4 μm. The theory and experimental technique of making interference filters with variable-thickness coatings for monochromatization and coverage of a broad spectral range (by rotating the filter with successive passband measurements) are described in [59, 60]. The /82
radiation detector is a lead selenide photoresistor cooled to 160°K. The WFS can produce a continuous spectrum with a resolution $\lambda/\Delta\lambda = 100$ in both spectral ranges. The basic goals in use of this instrument, which has been tested successfully in an aircraft version, are as follows: a) differentiation between ice and water clouds (from the radiation minimum of ice clouds around $\lambda = 2$ μm; b) determination of the vertical temperature profile from measured outgoing-radiation data for the 4.3-μm carbon dioxide band; c) determination of the vertical water-vapor distribution from data measured for the 6.3-μm band.

The radiometer for determination of vertical temperature profile (Table 2.1, line 12) is a modified SIRS. Although the spectral channels of this instrument have not yet been finally selected, the following have been proposed [4]: six channels in the 15-μm carbon dioxide band (669-750 cm^{-1}), one channel (around 532 cm^{-1}) in the region of the water vapor rotational band, and one in the atmosphere's transparency window, around $\nu = 899$ cm^{-1}.

Spectral resolution will be about 5 cm^{-1}. The instrument will be very light (4 kg) and require very little electric power as compared with similar earlier models (for example, the SIRS weighs 37 kg and draws 20 W).

In his monograph, W. Corliss [62] describes various types of spectral equipment used on American satellites for measurement of solar radiation (chiefly in the ultraviolet), as well as research on the spectral composition of the outgoing infrared radiation. For example, the instruments used for outgoing-radiation measurements include the interference spectrometer launched in 1962 on a USAF satellite, which was patterned after the Michelson interferometer. This instrument, which operated in the 1.8-15-μm wavelength range, attained a spectral resolution of 40 cm^{-1}. A diffraction-grating spectrometer capable of scanning the 1600-3100 Å wavelength range in 20 seconds with a resolution of about 5 Å was developed for outgoing ultraviolet radiation measurements.

Table 2.1 does not list instruments that are in various stages of development for measurement of the solar constant. Omitting description of R. Hanel's highly interesting radiometer, which is described in the monograph [35], let us examine the twelve-channel solar radiometer developed at the Appley Laboratory [56, 87].

This twelve-channel radiometer, which uses optical filters and thermoelectric radiation detectors, can be used for aircraft /83
and satellite measurements of the solar constant. In its original version, the radiometer was designed for tests on jet aircraft and the X-15 rocket airplane (in this case, the instrument weighed 5 kg). The comparatively tolerant requirements for the accuracy of aiming at the sun (±2°), which result from the instrument's wide field (15°), made it possible to dispense with automatic tracking devices. Of the radiometer's twelve channels, two were used to measure the integrated solar radiant flux. Eight specially designed interference filters (which are capable of sustaining g-forces and operating under hard-vacuum conditions) isolate the following spectral intervals: 220-320, 274-330, 295-365, 375-404, 408-472, 445-503, 510-595, 1250-1975 nm. Two broad-band Schott-glass filters for 535-2800 and 697-2800 nm were also used. The radiometer has an average temperature coefficient of sensitivity of 0.05% per 1°C. Since the instrument's temperature may vary from -50 to +30°, it is important to take the temperature variation into account. It is also necessary to allow for the pressure dependence of the instrument's readings.

The instrument's functioning was investigated by tests in a temperature- and pressure-controlled chamber. Various standard sources were used for laboratory calibration. The radiometer was also calibrated against the sun and compared with the standard pyrheliometer at Davos Observatory (the international pyrheliometer scale was reproduced to within 0.1-0.2%). The errors of

measurement of the integrated solar radiation do not exceed 0.5-1%, increasing to 1-2% in the case of the broad-band filters and perhaps to 5% in measurements using the interference filters. The first tests on the X-15, which climbed to 76.5 km, were made in Nevada on 14 September 1966. The results of these measurements could not be processed because of the strong external noise. Tests on a B-57B aircraft were more successful.

Satellites of the Orbiting Solar Observatory series carried equipment for measurement of the solar radiation reflected by the earth in specific spectral zones in the ultraviolet, visible, and near-infrared regions. A six-channel spectroradiometer — a photoelectric photometer with a set of optical filters — was used for this purpose. Each channel of this radiometer has two inputs — one for measurements of the reflected radiation within a 5° field, and another for periodic on-board calibration against the sun. Reference [86] describes the procedure for calibrating the radiometer, which includes five steps: 1) measurement of the spectral transparency of neutral filters used in the sun calibration channel; 2) a test of channel linearity; 3) determination of the /84
field for each channel; 4) determination of the relative spectral sensitivity of each channel; 5) absolute calibration of the channels. The principal source of error in the absolute calibration was the instability of the standard radiation source (a xenon lamp), which varied from ±8% at 2500 Å to ±2% at λ = 7500 Å. For this reason, the calibration errors for the various channels varied from ±11 to ±6%.

An extensive complement of optical instruments of various types, designed for measurement of the outgoing radiation in the 0.25-30-μm region, was carried on a USAF satellite launched on 30 March 1966 into an orbit with an apogee at 1054 km and perigee at 980 km [58]. The radiometric and optical apparatus of this satellite includes the following types of instruments: 1) an interference spectrometer for the 1-12-μm wavelength interval with a lead sulfide bolometer used as the radiation detector; 2) a radiometer with the same detector for the 2.2- and 2.7-μm wavelengths; 3) a radiometer with a similar bolometer for measurement of the fluctuating radiation at frequencies from 50 to 5000 Hz (all of the above instruments were pointed at the nadir); 4) a radiometer with a lead sulfide bolometer for the wavelength range from 0.28 to 15 μm; 5) an interference spectrometer for the 8-15-μm interval. The last two instruments were oriented toward the horizon. Good measured data were obtained for the atmospheric transparency windows at 1.5, 2.2, and 8-12 μm, the 2.7-μm water vapor absorption band, and the 0.25-0.30-μm ozone absorption range.

Table 2.2 presents a summary borrowed from T.P. Condron [63], which lists rocket and satellite experiments to investigate the earth's outgoing infrared radiation field that have been carried out or planned in connection with the development of infrared target detection methods.

TABLE 2.2. APPLIED EXPERIMENTAL STUDIES OF THE OUTGOING INFRARED RADIATION FIELD (1966-1968) /85

Booster	Launch date	Number of Flights	Instruments
	Rockets		
Centaur	7 April 1966 29 Oct 1966	2	Spectroradiometer (2.4-3.0 μm)
Saturn 1B	5 July 1966	1	Double spectroradiometer (1.1-4.4 μm)
Atlas SSP-A-201	10 Feb 1966	1	Five ten-channel radiometers (0.5-4.3 μm). High resolution spectroradiometer (2.6-2.8 μm)
AVCO-RVIP-2	1968	3	Two ten-channel radiometers (0.2-4.5 μm). Double spectroradiometer (0.2-2.8 μm).
	Satellites		
Agena	1967 Aug	1	Interferometer with thermoelectrically cooled PbS detector (2.4-30 μm). Radiometer for 2.7-μm wavelength
OV-1 Series	30 March 1966 27 July 1967	2	OV-1-5: scanning interferometer, double interferometer, two-channel radiometer (2.2 and 2.7 μm) OV-1-86: cooled PbSe interferometer (2.1-4.25 μm), double radiometer (2.2 and 2.7 μm)

Obviously, the results of these experiments are of great interest from the meteorological standpoint. However, the results of the measurements still remain unpublished.

We note in conclusion that the staggering variety of radiation instruments used to measure the outgoing radiation makes comparisons of instruments of different types a matter of exceptional urgency. There is no question but that some degree of unification of the devices would be expedient on the basis of selection of the

most suitable instruments.

It must also be stressed that, despite the variety of radiation apparatus, the requirements made as to the spectral and spatial resolution and sensitivity attainable with them remain unsatisfactory in many cases (especially from the standpoint of the thermal-sensing problem).

Implementation of the Nimbus III experimental program represents a major advance in this respect. /86 As was reported in one of the first publications on the launching of this satellite [84], the principal achievement of the Nimbus III weather satellite, which was built by General Electric under contract to NASA and launched on 14 April 1969, has been successful thermal sensing of the atmosphere. During the first week of operation of the satellite's infrared spectrometer, about 30,000 sensings were acquired. Comparison of the satellite sensing data with the results of radiosonde measurements indicated close agreement (for details, see Chapter 5).

A diffraction-grating spectrometer weighing about 36.5 kg measures the outgoing thermal radiation in seven wavelength intervals in the 15-μm carbon dioxide band. The vertical temperature profile is computed from these data. The underlying-surface temperature is determined (in the absence of clouds) from data measured in an eighth spectral interval around 11 μm. In the presence of cloud cover, the measurement data in this interval can be used to find the temperature (and altitude) of the upper cloudage boundary. The Nimbus III also carried a 14-kg interference spectrometer (with a Michelson interferometer) having a field (on the ground) of about 160 km for solution of the analogous problem of thermal sensing of the atmosphere at altitudes up to 25 km. This instrument, which permits measurement of the energy distribution in the outgoing-radiation spectrum from 6 to 20 μm, can also be used to determine the vertical ozone (up to 25 km of altitude) and water-vapor (up to 9 km) profiles. Registration of the continuous spectrum of the outgoing radiation yields information on the atmosphere's contents of carbon dioxide, nitric oxide, and methane. The interference spectrometer delivered about 25,000 sensings during its first week of operation.

The scientific-instrument package of the Nimbus III also includes a number of other instruments. A dissector-type scanning television system weighing about 5.5 kg delivers images of the cloud cover with resolution (on the ground) of about 1.6 km. This system operates both in a storage mode and with real-time image transmission. A scanning infrared radiometer with high spatial resolution (about 8 km), which is sensitive in the wavelength interval from 3.4 to 4.2 μm and fitted with a lead selenide photoresistor cooled to -83°C as a radiation detector, is used to acquire images of the cloud cover on the night side of the earth. During the day, this radiometer is used to produce images of the

earth in the spectral region around 1 μm. The scanning radiometer operates in storage and direct image-transmitting modes. /87

Analysis of daytime near-infrared pictures of the earth showed that they can be used to distinguish underlying surface areas with and without vegetation, as well as moist and arid zones. A similar instrument having higher resolution is to be mounted on an experimental satellite being built by NASA for study of the earth's natural resources. The Nimbus III carries a five-channel scanning radiometer of medium spatial resolution (weighing about 8.5 kg) for measurements of the radiation-balance components of the earth-atmosphere system (plans also call for using these data to study large-scale air currents, e.g., the jet streams). An ultraviolet photometer weighing about 3.5 kg will permit registration of solar radiant fluxes in five broad spectral intervals; this is of importance from the standpoint of study of the processes in the ionosphere and ozone layer and heating of the upper layers of the stratosphere.

Equipment designed for collection and transmission of weather data from sounding balloons drifting in the atmosphere along constant-pressure levels and successive localization of these sounding balloons for determination of wind speed was tested on the Nimbus III. Processing of the first data indicated that the accuracy of localization is about 1.6 km. This apparatus can also be used to collect and transmit data from unmanned ground stations and ocean buoys. Along with solar-battery current sources, the NASA satellites were the first to use radioisotope thermoelectric generators — 19 in number — delivering a continuous 50 W of power. During the first week of the satellite's operation, there was only one case of instrument failure: one of the storage-system tape recorders failed on the tenth orbit.

All of these instrumental developments with the purpose of solving the problem of sounding the atmosphere from satellites are oriented to the use of satellites launched into circular quasi-polar orbits about 1000 km high. The use of synchronous satellites (orbital altitudes about 35.8 thousand km) is of great interest from the standpoint of continuous monitoring of atmospheric processes. Estimates published in a report by W. Suomi, R. Krauss, and T.V. Haar [94] indicate that the acquisition of outgoing infrared radiation spectral measurements of the necessary accuracy and adequate spatial resolution is possible in principle (at the present level of the technique) even in this case.

§2. RESULTS OF EXPERIMENTAL STUDIES OF THE ANGULAR AND SPECTRAL DISTRIBUTIONS OF THE OUTGOING THERMAL RADIATION /88

Recent years have witnessed a whole series of detailed experimental investigations of the spectral and angular structures of the outgoing thermal radiation field by means of the rocket and satellite instruments described in the preceding section. Although

only a small fraction of the results obtained have been reduced and analyzed, published data can be used to develop a conception of the basic laws governing the angular and spectral distributions of the outgoing thermal radiation on the basis of experiment.

Beginning in 1958, M.N. Markov, I.Ya. Merson, and M.R. Shamilev [6] conducted systematic studies of the outgoing infrared radiation with instruments launched on rockets and aerostats. The angular intensity distribution of the outgoing radiation was measured in the 0.8-40-μm region of the spectrum at altitudes from 100 to 400 km from rockets and simultaneously in the lower atmosphere up to the 30-km level from geophysical aerostats (in a total of about 50 instrument launchings). The angular resolution of the equipment was $2 \cdot 10^{-3}$ rad. Reference [6] drew the following basic conclusions from the studies: 1) the agreement between the measured data and calculations is satisfactory; 2) it is found that the contribution of the upper atmospheric layers to the outgoing radiation is substantially larger than had hitherto been assumed (the radiating thickness of the atmosphere may reach heights up to 150 km, and the altitude distribution of the contributions to radiation is stratified; for example, radiating layers at altitudes of 280, 430, and 500 km are observed for the 2.5-8-μm region of the spectrum); 3) the angular distribution of the outgoing radiation does not contain small-scale inhomogeneities; 4) there is no marked diurnal variation of the outgoing-radiation angular distribution (meteorological conditions at the particular point in time are the determining factor).

In later reports, the above conclusions were quite thoroughly detailed on the basis of analysis of experimental data not only on the angular, but also on the spectral distribution of the outgoing radiation. An interference spectrometer carried aboard a USAF satellite [27] delivered our first information on the spectrum of the outgoing thermal radiation.

P.A. Bazhulin, A.V. Kartashev, and M.N. Markov [5, 7, 9] studied the angular and spectral distributions of the long-wave outgoing radiation with equipment launched on geophysical rockets to altitudes up to 500 km on 18 October 1962 and 6 and 18 June 1963; M.N. Markov et al. [1, 4, 6, 8, 17, 18] made simultaneous satellite measurements of the spectral composition (wavelength interval from 4 to 38 μm) and angular distribution (angle range ±90° around the nadir) of the outgoing radiation. The rocket measurements were made on both the ascending and descending segments of the rocket trajectory using a pulsed infrared rocket spectrometer (see §1 of this chapter). /89

The measured data indicate that the shape of the outgoing radiation angular distribution curves is weakly dependent on altitude in the 200-500-km altitude range. The angular distribution is nearly isotropic for broad regions of the spectrum, with almost no small-scale fluctuations. The intensity fluctuations of

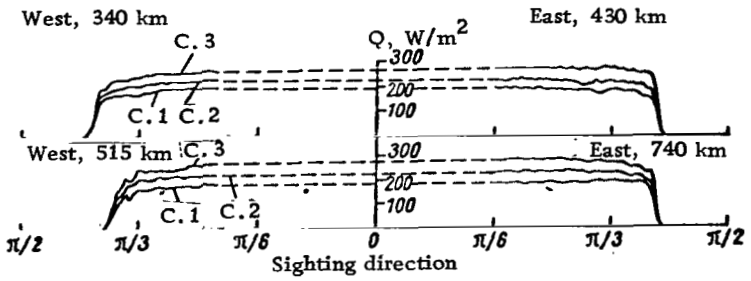

Figure 2.13. Angular Distribution of the Earth's Infrared Radiation in Three Regions of the Spectrum: 12.5-38 μm (channel 1); 8.5-38 μm (channel 2); and 4.5-38 μm (channel 3). Based on data from 6 June 1963 rocket launching.

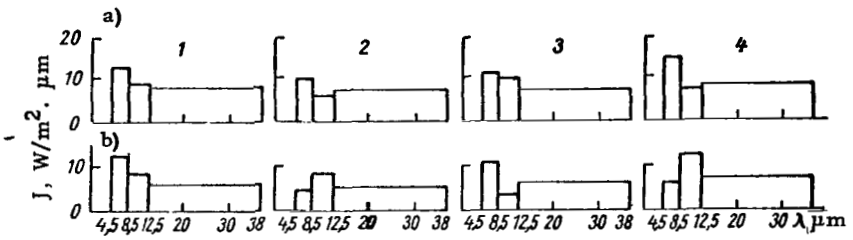

Figure 2.14. Spectral Distribution of the Earth's Infrared Radiation from Data of Rocket Launchings on 6 and 18 June 1963 for Two Sighting Directions: 0.5 rad (a) and 1.2 rad (b) off the nadir. 1) 6 June 1963, east, 450 km; 2) 6 June 1963, west, 510 km; 3) 6 June 1963, west, 310 km; 4) 18 June 1963, north, 200 km.

the outgoing radiation are substantially greater (up to 50%) in narrow spectral zones. In most cases, the maximum of the spectral distribution lies in the 4.5-8.5-μm band, where the effective temperature reaches 270-280°K, while it is about 240°K in the transparency window (weather conditions are characterized by the presence of variable cloudiness ranging from 1-2 to 7-8 points on the scale, with the lower boundary at altitudes from 1 to 7 km). Figure 2.13 shows an example of the results of rocket measurements of the outgoing-radiation angular distribution in three regions of the spectrum as obtained in the 6 June 1963 launching. Since these data pertain to the peak of the trajectory, the altitude of the rocket did not change very greatly during scanning, averaging about 400 km for the lower curves and about 500 km for the upper curves.

Figure 2.14 presents data on the spectral distribution of the outgoing radiation for these three regions of the spectrum and sighting directions of 0.5 and 1.2 rad from the nadir.

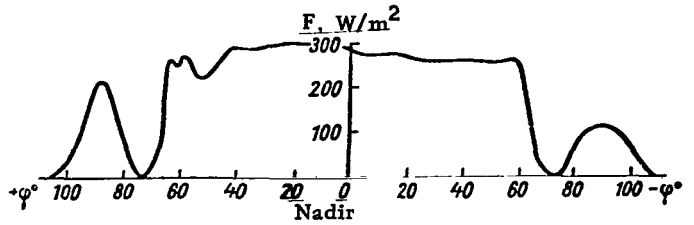

Figure 2.15. Radiating Layers of the Ionosphere.

Comparison of the radiation temperatures with the real temperature values at the various levels showed that the effective temperature for the integrated radiation corresponds to the air temperature at the 6-km level. For the region of the water vapor absorption band (4.5-8.5 μm), this level lies at an altitude of 2 km. /90
However, the interpretation to be put on the high radiation-temperature values in this case is that the upper layers of the atmosphere are the source of the radiation, so that this correspondence is of only formal significance. It should be noted in this context that the detection of intense ionospheric infrared radiation in [6, 9, 18] is highly important. Figure 2.15 presents an example of ionospheric radiation layers according to data from the 18 June 1963 rocket experiment.

Strong infrared radiation from layers of the atmosphere in the 250-300, 420-450, and 500-km altitude ranges has been detected in observations under various conditions. This radiation is for the most part concentrated in the 2.5-3-μm band and in the sunlit part of the atmosphere. The radiant flux reaches $(3-7) \cdot 10^2$ W/m² when the line of sight is tangential and passes through about 1000 km of atmosphere. The intensity of the radiation increases during the solar-activity maximum. /91

Table 2.3 is a summary, based on M.N. Markov's data [9], of the results of the experiments that led to detection of the ionospheric thermal layers. Here, K_p is the planetary magnetic disturbance index, which characterizes the variations of solar activity. All of the instruments listed in the table (except for the MS-2) were rocket-borne radiometers. /92

The measured data indicate that the radiating layers are observed both during the day and at night at practically all latitudes (±65°). Careful analysis of equipment operating conditions showed that these findings could not be the result of some sort of measurement error, but are quite objective in nature.

As for the nature of the radiation, it is concluded in [9, 18] that it is due to excitation of the molecules of certain atmospheric gases by the solar corpuscular radiation. It appears

TABLE 2.3. RADIATING LAYERS OF THE IONOSPHERE

Experiment	Date (Moscow time)	Layer altitudes, km	Radiated flux, W/m^2	Spectral sensitivity of range instrument, μm	K_p
RIZ-1	27 Aug 1958 8h 06m	290 425	690 650	0,8—40	5,0
RIZ-5	18 Oct 1962 11h 30m	240 430 495	150 180 160	0,8—40	4,0
	6 July 1963 4h 36m	320 400	<20	2,5—40	0
	18 June 1963 4h 20m	280 420 505	250 220 220	2,5—40	3—4
MR-1	18 Oct 1962 11h 30m	400	150	4,5—8,5	4,0
	6 June 1963 4h 36m	320	<20	4,5—8,5	0
MS-2	13 Sept 1964 17-19h	280	100 <25	4,5—8,5 0,8—4,5	1—2
	17 April 1965 13-18h	150 320	30 <10	4,5—8,5	0
	18-22h	250 320	<10 <20	4,5—8,5	4,0
RIZ-10	1 Oct 1965 6h 57m	250—300 400 500	<10 <10 <10	0,8—40	0
Anthony and Smiley [26]	1962	160	0,5	4,45—4,95	

that NO might be one of these gases (this applies in any event to the 280-km altitude). Estimates indicate that the effective temperature should be about 2000°K at the radiant intensity observed. In this case, however, it is not possible to establish correspondence between the effective and kinetic temperatures owing to the absence of thermodynamic equilibrium.

It must be stressed that no convincing theoretical interpretation of the radiating layers has as yet been found. This circumstance occasionally gives rise to arguments as to whether they really exist. Thus, for example, V.I. Krasovskiy [106] advanced the hypothesis that the intense infrared radiation may be due to secondary processes associated with pollution of the atmosphere by rocket-fuel combustion products and other factors.

A.I. Lebedinskiy et al. [10-16] measured the spectral composition of the outgoing thermal radiation in the 7-38-μm band using a diffraction-type scanning spectrometer on the Kosmos 45, Kosmos

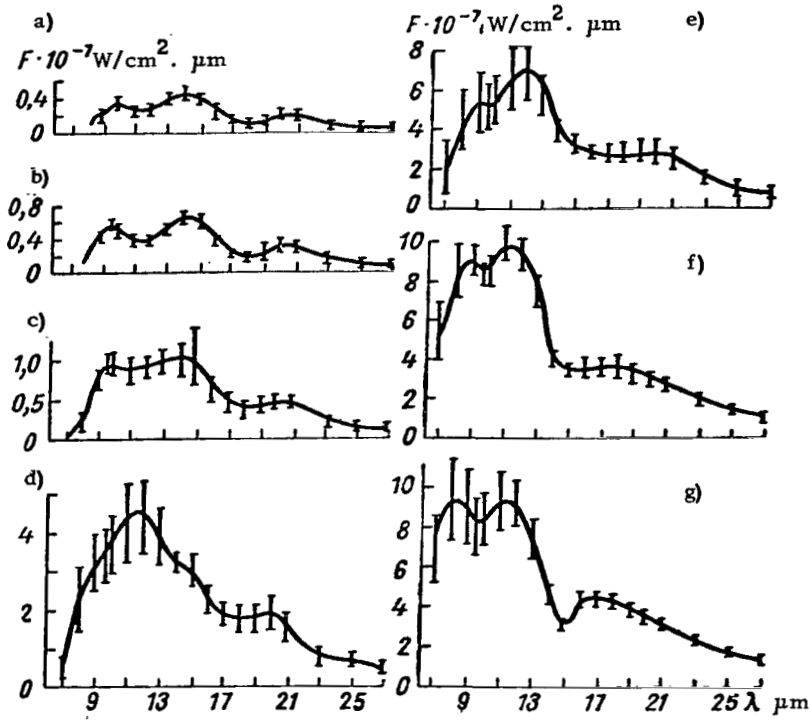

Figure 2.16. Spectral Distribution of the Earth's Infrared Radiation Near the Limb of the Planet and at the Nadir. a) θ° = 1-1.5; b) θ° = 0.5-1.0; c) θ° = 0-0.5; d) θ° = 0 to -1; e) θ° = -1 to -3; f) θ° = -3 to -6; g) nadir.

65, and Kosmos 92 satellites (see the description of this instrument in §1 of the present chapter). Analysis of the measured outgoing-radiation spectral-distribution data for cloudy and clear skies clearly brings out the 9.6-μm ozone band, the 15-μm carbon dioxide band, and other emission bands separated by transparency windows. This is clearly illustrated, for example, by the results of measurements made with the spectrophotometer's 1°46' × 2°20' field oriented to the nadir and in the direction of the horizon [16]. The orientation of the instrument's optical axis with respect to the horizon was determined from scans across the horizon at the 10- and 19-μm wavelengths.

The results of reduction of 222 spectrograms obtained in April 1965 for the latitude belt from 45 to 15° South over the Atlantic and Pacific Oceans on the daytime side of the earth were analyzed in [16]. Some of the results appear in Fig. 2.16. Here, θ is the angle of deflection of the spectrophotometer's optical axis from the limb of the earth (positive θ imply that the optical /93

axis was pointed above the earth's visible horizon). The scattering of the points, which is indicated by the vertical lines, characterizes the real dispersion of the outgoing radiation rather than errors of measurement.

As we see from Fig. 2.16, the outgoing radiation increases rapidly, especially in the transparency windows, as the sighting line approaches the horizon from the space side ($\theta > 0$). As it moves onto the disk of the planet, the maxima are reconstructed into distinct minima in the ozone and carbon dioxide emission bands because of the appearance of the "warm" radiation of the earth's surface in the transparency windows. At distances of 3-6° from the horizon (above the earth's disk), the outgoing radiation is practically identical to that observed at the nadir. It is important to note here that the nature of the infrared "darkening" toward the limb varies substantially as a function of wavelength (Fig. 2.17). A "brightening" effect toward the limb is observed for the 15-μm wavelength. A similar phenomenon was reported in [19] on the basis of rocket measurements using a three-channel radiometer (effective wavelengths of 10.97, 14.76, and 24.79 μm with interval widths of 1.41, 1.51, and 10.94 μm, respectively) having an extremely narrow field (0.2-0.4°), and in the studies of A. Girard [22, 89]. Rocket measurements of the angular distribution of the outgoing radiation at 3.5, 4.3, 4.7, and 6.3 μm near the horizon are also described in [26]. /94

J.H. Lienesh and D.Q. Wark [23] used statistical methods to reduce measurements made with a five-channel radiometer on the Tiros II, Tiros III, Tiros IV, and Tiros VII weather satellites and found that the radiant intensity varied greatly at a given nadir angle. The authors of [23] plotted angular-distribution curves of outgoing-radiation intensity for data samples corresponding to various fractions (expressed in tenths) of the total number of measured values for a particular nadir angle (e.g., from the values corresponding to 0.1 of all cases, etc.). The angular-distribution curves were normalized with reference to the 45° angle, for which the measured data were most numerous. A small fraction of the cases (0.1) pertains to the conditions of warm and generally cloudless regions (high outgoing-radiation values). For 0.9 of cases, the data pertain to cold arctic regions with dense unbroken cloudage having high-altitude upper boundaries (low outgoing-radiation values). For the 8-12-μm atmospheric transparency window, the range of variation of the outgoing radiation fluxes is 0-57 W/m^2.

Theoretical calculations made previously to determine the infrared darkening for schematic cloudless-sky and unbroken-cloudage cases indicated that the degree of darkening depended on the absolute radiant intensity. Statistical analysis of the experimental data indicated that this conclusion was in error. However, substantial variations of the infrared darkening were detected as functions of latitude and season; this can be explained by the

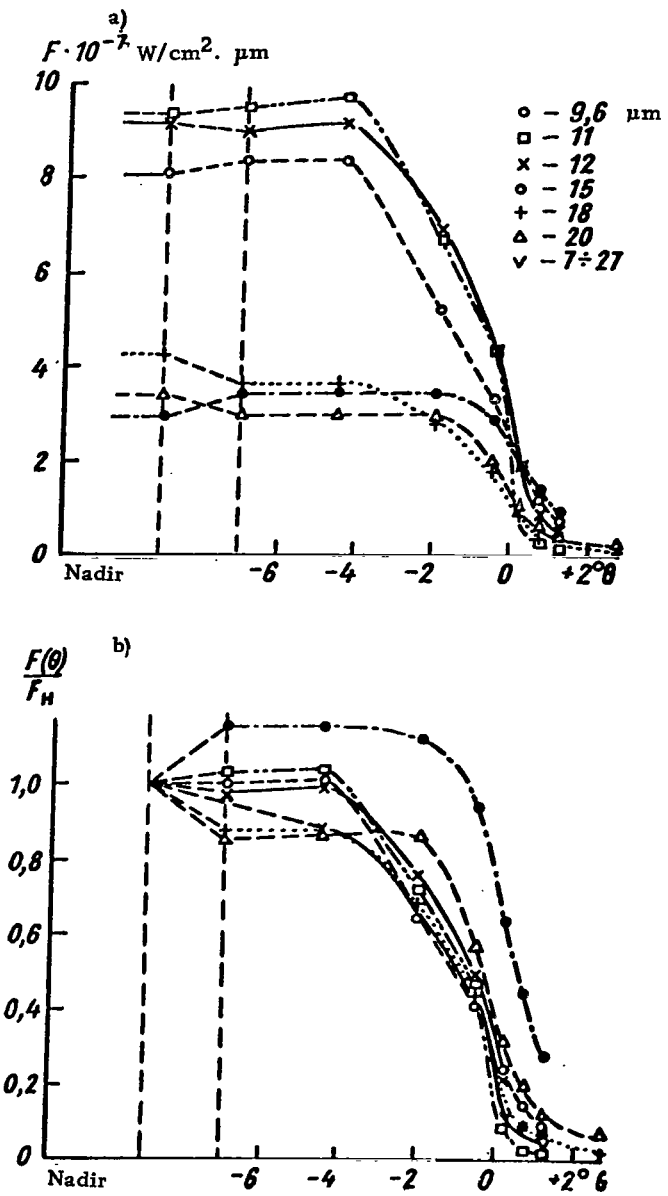

Figure 2.17. Angular Distribution of the Earth's Infrared Radiation at Various Wavelengths. a) Absolute values; b) relative values.

variations of the air and underlying-surface temperatures and of the cloudage characteristics and conditions. As a rule, the infrared darkening observed in the polar and tropical regions is stronger than that at temperate latitudes.

J.H. Lienesh and D.Q. Wark [23] and the authors of [102] derived empirical relationships that describe the angular distribution of the outgoing-radiation intensity (infrared darkening) as a function of latitude and time of year (empirical orthogonal functions were used to smooth the outgoing-radiation fields), but noted that all of the results require improvement as experimental data are accumulated. /96

J.R. Thomas, E.E. Jones, and R.E. Peterson [102] proposed a method for analytical approximation of computed data on the angular intensity distribution of the thermal radiation that the earth radiates into space in the 14-16-μm band, which were represented as the dependence of the radiant intensity on a line parallel to the tangent to the earth's surface on the height of that line above the earth's surface. The initial data took the form of 20 "climatological" (computed for various atmospheric-stratification models in order to take account of the latitude and annual variations) angular distributions pertaining to ray heights from -30 to +80 km and monthly-average data on the stratification for January, April, July, and October at Northern latitudes of 20, 30, 45, 60, and 75° along the 90° meridian west of Greenwich (the east-central sector of the North American continent).

Reference [102] gives 24 functional representations of data on the radiant intensity angular distribution, which were analyzed as corresponding to the shapes of the angular-distribution curves. Detailed consideration was given to the possibilities of applying two approximations based on the use of: 1) the ratio of two ten-term power polynomials; 2) a trigonometric series with five terms. The best approximation is selected by the Tschebyscheff linear programming method. It is shown that the accuracy of the approximation depends strongly on the number of terms in the expansion. Use of the ratio of polynomials with ten terms makes it possible to reduce the error to ±2-4% (with respect to the intensity maximum) for altitudes from -30 to 50 km. In the 50-80 km altitude range, the errors increase to 6-42%. The five-term trigonometric series yields an error of ±5% (increasing the number of terms to eleven reduces the error by a factor of 3-5). The accuracy of the trigonometric approximation improves if we drop the assumption of zero radiant intensity at a ray distance of 80 km from the ground.

We note that a similar statistical investigation of the reflected solar radiation angular distribution was made in [24] in the 0.55-0.75-μm band (on the basis of Tiros IV data). The results of outgoing longwave radiation measurements made with the Tiros III and Tiros IV weather satellites were used in [28, 29] for analysis of individual infrared angular distribution curves and comparison with calculated results. Similar data from aerostat measurements for the 0.55-0.75-μm and 0.2-5.0-μm intervals are given in [99]. /97

According to [10], a distinct negative correlation is observed between the readings of a photometer sensitive in the 0.6-0.8-μm band and the results of measurements for the 8-12-μm transparency window, reflecting the contrary effects of cloudage on the outgoing shortwave and longwave radiation. A similar negative correlation also occurs for the outgoing radiation at 18.5 μm. Here it is found that the influence of cloudage is strongly manifested in all of the spectral regions studied. This is because the lower half of the troposphere makes the basic contribution to the outgoing radiation in the 7-38-μm range of wavelengths. The infrared radiation may vary in many different ways as a function of cloudage. P.A. Bazhulin, A.V. Kartashev, and M.N. Markov [6] showed that the nature of this dependence is determined primarily by the proportions of clouds at the various levels.

A.I. Lebedinskiy et al. [10] found that the radiation varies widely with time in the region of the 9.6-μm ozone absorption band owing to variations of the atmosphere's ozone content. It is assumed in this context that the contribution of radiation in the region of the 14.1-μm ozone band to the outgoing radiation corresponding to this wavelength may also be substantial.

Reference [14] analyzes the results of spectral measurements of the outgoing thermal radiation in the 7-26-μm wavelength band that were made with the Kosmos 45 (September 1964) and Kosmos 65 (April 1965) satellites for the zone from 65° S. lat. to 65° N. lat. with the object of studying the latitude variation of the outgoing radiation.

The latitude curves of outgoing radiation shown in Figs. 2.18 and 2.19 for a continuous set of spectral intervals 1 μm wide indicate that the radiant intensities are minimum at high latitudes and increase toward the tropics; this dependence is most strongly manifested in the 8-13 and 16-20-μm ranges (the atmosphere's transparency windows). In the 8-13-μm band, the tutgoing radiation increases from (1-1.5) $\cdot 10^3$ W/cm$^2\cdot$μm at latitude 65° to (2-2.5)$\cdot$ $\cdot 10^3$ W/cm$^2\cdot$μm in the subtropics. The radiation at 14-16 and 22-26 μm is virtually independent of latitude, amounting to (0.5-0.7)$\cdot$ $\cdot 10^{-3}$ W/cm$^2\cdot$μm. Cloud cover strongly influences the latitude variation of the outgoing radiation (especially in the transparency windows); this is manifested in the existence of a radiation minimum in the region of the equator (due to the increased amount of cloud cover in the intertropical convergence zone). In September 1964, the equatorial minima were north of the equator around the clock; in April 1965, they were north of it at night and south of it in the daytime (the distances of the minima from the equator were 5-10°). There are also marked shifts of the subtropical outgoing-radiation maxima. The outgoing radiation is most variable in the region of the equatorial minima and least variable in the region of the subtropical maxima. /98

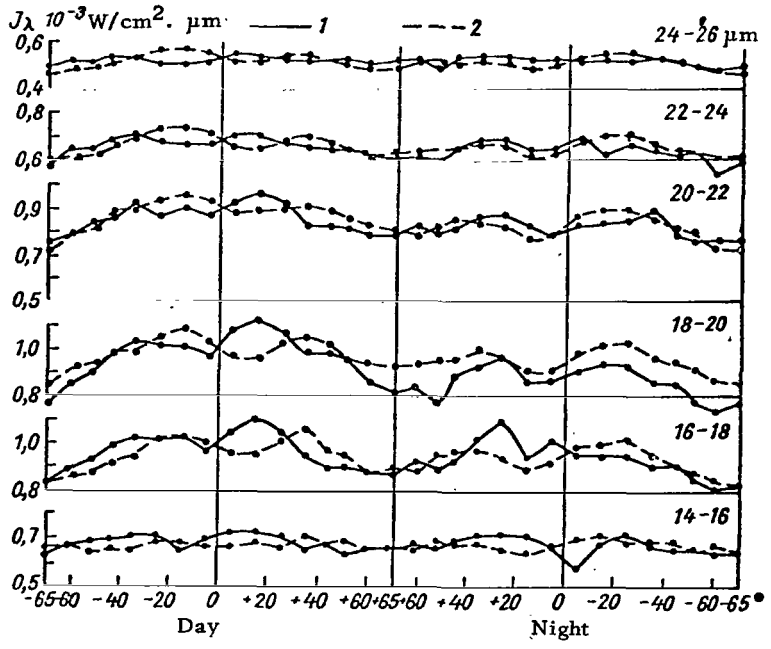

Figure 2.18. Latitude Variations of Outgoing Radiation in Various Regions of the Spectrum. 1) Kosmos 65; 2) Kosmos 45.

Comparison of the outgoing-radiation figures for the same latitude on the nighttime and sunlit sides of the earth showed that in September, the daytime values exceed the nighttime values in the zone from the equator to latitudes of 40-50°. At higher latitudes, the night and day values are almost identical. The diurnal variation presents a more complex picture in April.

The meridional radiation distribution is found to be asymmetrical about the equator. Determination of the integrated outgoing radiation values and comparison with similar data from Tiros VII showed close agreement. Determination of the averaged (for various seasons) meridional integral outgoing radiation distributions showed that they vary only very slightly in time (see also [101, 103]). /100

Reference [15] makes an interesting comparison of the measured outgoing thermal radiation spectra with data from ground meteorological measurements. For example, it was shown by analyzing 70 spectra that the radiation temperature for the 12-μm wavelength corresponds to most closely to the temperature of the air at the ground (the deviations do not exceed 5°C in 70% of cases). As a rule, the highest radiation temperature is observed at this wavelength (in 70% of cases, the radiation-temperature maximum falls in the 11.5-12.4-μm wavelength interval).

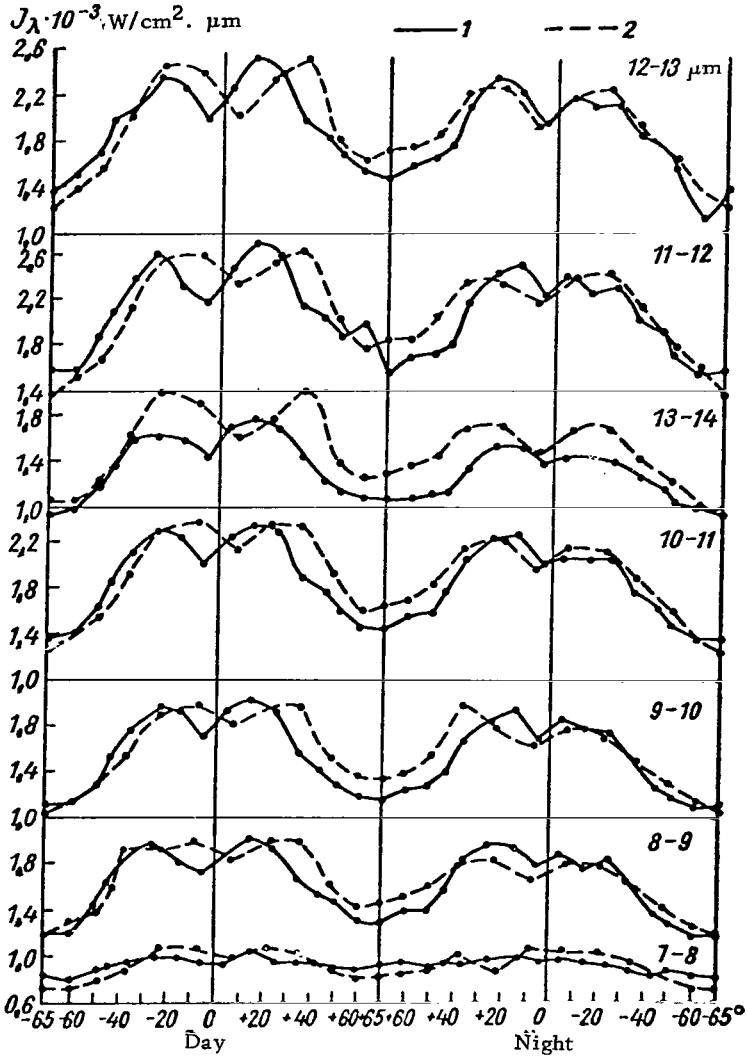

Figure 2.19. Latitude Variations of Outgoing Radiation in Various Regions of the Spectrum. 1) Kosmos 65; 2) Kosmos 45.

The outgoing-radiation maximum is shifted toward longer wavelengths with respect to the 10-11-μm interval of maximum atmospheric transparency; this can be explained by the distorting effect of the instrument.

Comparison of measured and calculated outgoing radiation spectra for the 8-35-μm wavelength range and consistently cloudless situations indicates that the differences are largest in the absorption-band regions and are due to a defect of the calculation method and incompleteness of the starting meteorological data.

Figure 2.20 presents an example in which calculated and measured spectra are compared for three points in the middle latitudes of the northern hemisphere.

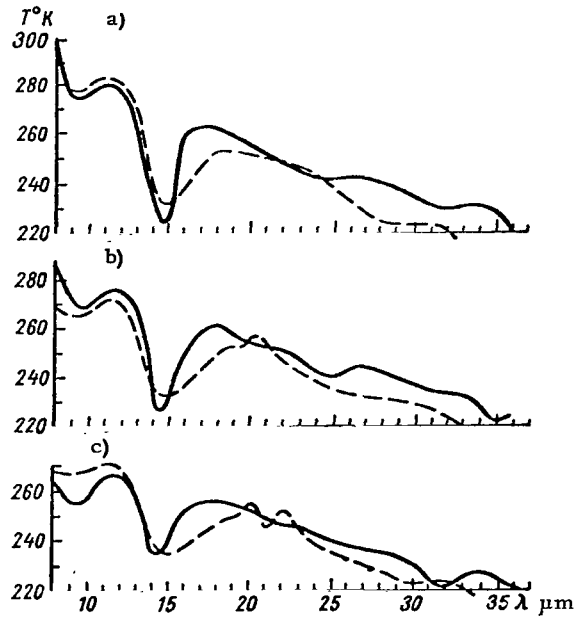

Figure 2.20. Comparison of Measured (Solid Curves) and Calculated (Dashed Curves) Outgoing Radiation Spectra. a) 61° N, 59° E; b) 54° N, 140° E; c) 46° N, 151° E.

Comparison of the variations of cloudage, temperature at various levels, and radiation temperatures for various wavelengths along the satellite's path led to the conclusion that the influence of cloudage on the outgoing radiation can be traced distinctly not only in the transparency windows (where it is strongest), but also in other (practically all) spectral intervals. Thus, for example, the radiation-temperature distribution for the 17-20-μm interval resembles the variability of temperature for the 8-12-μm window. Here the absolute temperatures for the 8-12-μm range are approximately 5-7° higher in the absence of clouds, and the differences diminish to zero in the presence of clouds.

The altitude variations of the effective radiation levels were investigated for various wavelengths in [15] on the basis of aerological sounding data and results of outgoing-radiation measurements. These variations depend strongly on wavelength. Thus, for the 12- and 18-μm wavelengths, which lie in transparent segments, level altitude fluctuates from the top to the bottom of the troposphere. For other wavelengths, where absorption is stronger, these variations are much smaller: 5-8 km at 14 μm, 4-8 km at 23 μm, and 5-11 km at 32 μm. Naturally, such wide variations of effective-level height make it impossible to establish direct correspondence between radiation and actual temperatures at any fixed level, as has been shown earlier by theoretical calculations [20]. /101

In view of the strong variability of the outgoing radiation, great interest attaches to statistical analysis of the data. Without restating the results obtained in this problem, which are discussed in [21], we note that in a recent study [13], spectral measurements of the outgoing thermal radiation made in the 7-15-μm

band with a diffraction-type scanning spectrometer on the Kosmos 45 satellite were used to construct two-dimensional radiant intensity distribution laws for several spectral intervals in this band. The radiation from ground areas of 75 km^2 was registered from an average satellite altitude of 250 km. Various pairs of spectral intervals were selected for calculation of the correlation moments and coefficients of correlation. A total of 1176 spectrograms was processed. /102

The highest correlation is observed between the radiant intensities in the emission bands of the same atmospheric gas at closely similar absorption-coefficient values. This applies, for example, to the 8-9 and 10-11-μm and 8-9 and 11-12-μm bands, for which the correlation coefficients are 0.91 and 0.87, respectively. The lowest correlation occurs when we consider the radiant intensities in the bands of different gases. Thus, for example, the correlation coefficient for the 7-8-μm (water vapor) and 14-15-μm (carbon dioxide) intervals is 0.17. Such low correlation can be explained by the fact that the radiation in these intervals is generated in different layers of the atmosphere. The results may have been influenced substantially by the fact that the values were not measured simultaneously at the various wavelengths (it takes 7 seconds to scan the 7-15-μm band in question). This problem is examined in [100].

Reference [12] discusses the possibilities of smoothing statistical series compiled from measured outgoing-radiation data by using a universal system of Pearson curves; this makes it possible to exclude the influence of the limited scope of the observations in arriving at a statistical generalization of the measured results. Each Pearson curve depends on four parameters A_1, A_2, M_1, and M_2 (or $\underline{m}$, ν, $\underline{a}$, and α), which are so selected as to preserve the first four moments of the statistical distribution.

Let us examine the following two Pearson equations for the probability density f(x) of the random variable $\underline{x}$ (the quasimonochromatic radiant flux expressed in $W/cm^2 \cdot \mu m$):

$$f(x) = y_0^* \left(1 + \frac{x - M}{A_1}\right)^{M_1} \left(1 - \frac{x - M}{A_2}\right)^{M_2}, \tag{2.1}$$

$$f(x) = y_0 \left[1 + \frac{(x - \alpha)^2}{\alpha^2}\right]^{-m} \exp\left[-\nu \operatorname{arctg} \frac{x - \alpha}{a}\right]. \tag{2.2}$$

Here M is the most probable value (mode) of random variable $\underline{x}$:

$$M = \bar{x} - \frac{\mu_3 (r + 2)}{2\mu_2 (r - 2)}, \tag{2.3}$$

where $\bar{x}$ is the mathematical expectation of the variable $\underline{x}$

$$\bar{x} = \sum_{i=1}^{m_0} x_i p_i, \tag{2.4}$$

and μ_2 is the second central moment (dispersion) of the random variable $\underline{x}$ /103

$$\mu_2 = \sum_{i=1}^{m_0} (x_i - \bar{x})^2 p_i, \tag{2.5}$$

and m_0 is the number of categories into which the entire range of observed $\underline{x}$-values is broken up.

The quantity μ_3 is the third central moment, which characterizes the asymmetry or skewness of the distribution:

$$\mu_3 = \sum_{i=1}^{m_0} (x_i - x)^3 p_i, \tag{2.6}$$

$$M_{1,2} = \frac{1}{2}\left[r - 2 \pm (r+2) r \left(\frac{\beta_1}{\beta_1 (r+2)^2 + 16 (r+1)}\right)^{1/2}\right], \tag{2.7}$$

$$r = \frac{6(\beta_2 - \beta_1 - 1)}{6 + 3\beta_1 + 2\beta_2}, \quad \beta_1 = \frac{\mu_3^2}{\mu_2^3}, \quad \beta_2 = \frac{\mu_4}{\mu_2^2}. \tag{2.8}$$

Here, μ_4 is the fourth central moment of the random variable $\underline{x}$ and characterizes the sharpness or flatness of the peak of the distribution,

$$\mu_4 = \sum_{i=1}^{m_0} (x_i - \bar{x})^4 p_i. \tag{2.9}$$

If $\mu_3 < 0$, the negative root is taken as M_2 in Formula (2.7):

$$\begin{gathered} A_1 + A_2 = \frac{\sigma}{2} \sqrt{\beta_1 (r+2)^2 + 16 (r+1)}, \\ A_1 = \frac{A_1 + A_2}{1 + \frac{M_2}{M_1}}, \quad y_0^* = \frac{y_0}{N}, \end{gathered} \tag{2.10}$$

where $\sigma = \sqrt{\mu_2}$ is the root-mean-square deviation for $\underline{x}$.

The remaining nomenclature is explained as follows:

$$\begin{gathered} y_0 = \frac{M_1^{M_1} M_2^{M_2}}{(M_1 + M_2)^{M_1 + M_2}} \frac{N}{A_1 + A_2} \frac{\Gamma(M_1 + M_2 + 2)}{\Gamma(M_1 + 1)\Gamma(M_2 + 1)}, \\ \alpha = M + \frac{\mu_3 r}{4\mu_2}, \quad a = \frac{\sigma}{4} \sqrt{16(s-1) - \beta_1 (s-2)^2}. \end{gathered} \tag{2.11}$$

$$s = -r, \quad a > 0, \quad m = -\frac{1}{2}(r-2) = \frac{1}{2}(s+2), \qquad (2.11)$$
(Cont'd.)
$$\nu = -\frac{\mu_1 s(s+2)}{4\mu_2 a}.$$

$\Gamma(x)$ is the gamma function of the corresponding arguments, and N is the total number of spectra to be processed. /105

For Eq. (2.2)

$$y_0^* = \frac{1}{aF(s, \nu)}, \quad F(s, \nu) = \int_{-\pi/2}^{\pi/2} \cos\theta e^{-\nu\theta} d\theta. \qquad (2.12)$$

Applying the system of formulas (2.3)-(2.12) to determine the coefficients in the Pearson equations (2.1) and (2.2), the authors of [12] obtained values of the parameters (Table 2.4) from Kosmos 45 data obtained with the spectrophotometer described in §1 of the present chapter. Only the 7-15-μm (N = 1176) and 14-26-μm (N = 1278) regions of the spectrum, which are free from superposed second-order spectra, were processed. The measured data pertain to a wide variety of observational conditions (cloud cover, time of day, land and sea, etc.).

The asterisks (*) in this table mark those spectral regions for which the Pearson equation (2.2) was used. In these cases, m, ν, a, and α are indicated instead of the parameters M_1, M_2, A_1, and A_2.

This table indicates that the smallest outgoing radiant flux values (x and M) and radiation fluctuations (σ) correspond to emission bands (the 9.6-μm ozone band and the 15-μm carbon dioxide band), especially in the case of the latter. A low level of variability of the outgoing radiation is typical for the long-wave part of the spectrum (λ > 14 μm). The outgoing radiation varies through a wider range (maximum σ) in the atmospheric transparency window. In this case, the distribution function corresponds closely to the uniform-density law.

Table 2.5 presents the results of a statistical analysis of the data obtained on the same Kosmos 45 satellite on 13 September 1964 using the pulse spectrometer [5].

These data confirm the qualitative inferences that proceed from the preceding table, indicating substantial variability of the outgoing radiation.

In summarizing the results of experimental study of the outgoing thermal radiation field, it can be stated that the angular and spectral distributions of radiant intensity are highly

TABLE 2.4. VALUES OF COEFFICIENTS IN PEARSON EQUATIONS ACCORDING TO SPECTROPHOTOMETRIC MEASUREMENTS OF THE OUTGOING RADIATION ON KOSMOS 45

/104

λ μm	$x \cdot 10^{-3}$ W·cm^{-2}·μm^{-1}	$s \cdot 10^{-3}$ W·cm^{-2}·μm^{-1}	$\mu_2 \cdot 10^{-6}$ W^2·cm^{-4}·μm^{-2}	$\mu_3 \cdot 10^{-11}$ W^3·cm^{-6}·μm^{-3}	$\mu_4 \cdot 10^{-1}$ W^4·cm^{-8}·μm^{-4}	$M \cdot 10^{-3}$ W·cm^{-2}·μm^{-1}	$y_0^* \cdot 10^{-3}$ cm^2·μm·W^{-1}	M_1	M_4	$A_1 \cdot 10^{-3}$ W·cm^{-2}·μm^{-1}	$A_4 \cdot 10^{-3}$ W·cm^{-2}·μm^{-1}
7—8	0,88	0,25	0,062	—1,09	0,18	1,01	1,59	6,09	1,31	1,57	0,34
8—9	1,60	0,41	0,17	—3,1	0,94	1,69	0,99	1,76	14,3	19,6	1,59
9—10	1,54	0,44	0,19	0,64	1,1	1,53	0,99	46,7	71,8	3,9	6,02
10—11	1,88	0,55	0,30	—4,0	2,02	2,1	0,62	1,16	0,57	1,62	0,8
11—12	2,07	0,64	0,41	—8,05	3,54	2,77	0,55	0,68	0,13	2,1	0,42
12—13	1,81	0,61	0,37	—4,2	2,79	2,23	0,53	0,52	0,23	1,66	0,72
13—14	1,45	0,53	0,28	5,37	2,02	1,32	0,71	3,06	6,94	1,25	2,83
14—15*	0,79	0,18	0,034	0,0693	0,18	0,75	0,18	2,98	6,76	0,28	0,47
14—16	0,67	0,09	0,0082	0,11	0,0039	0,59	6,64	0,24	15,7	0,023	1,52
16—18	0,93	0,11	0,012	—0,03	0,0035	0,95	3,60	13,4	7,04	0,71	0,37
18—20*	0,98	0,12	0,014	—0,017	0,011	1,02	0,4810	47,15	19,81	0,26	1,39
20—22	0,84	0,1	0,01	—0,07	0,0035	0,88	3,94	13,1	2,38	0,93	0,17
22—24*	0,65	0,073	0,0053	—0,01	0,0011	0,66	4,56	5,74	2,45	0,21	0,7
24—26*	0,51	0,057	0,0032	—0,0064	0,0006	0,52	6,85	3,48	1,56	0,11	0,54

TABLE 2.5. STATISTICAL CHARACTERISTICS OF OUTGOING RADIATION (KOSMOS 45, 13 SEPTEMBER 1964)

Radiant fluxes (W/m^2), radiation temperature (^oK)	Region of spectrum, μm			
	4,5—38	4,5—8,5	8,5—12,5	12,5—38
F_{max}	320	75	95	165
F_{min}	175	15	25	80
$\overline{F}$	245	45	62	137
$F_{msq}=\sqrt{\overline{(F-\overline{F})^2}}$	35	14,8	17,5	19,5
$T_{r\,max}$	275	298	304	262
$T_{r\,min}$	233	240	235	210
$\overline{T_r}$	255	277	276	245
$T_{r\,msq}=\sqrt{\overline{(T_r-\overline{T_r})^2}}$	8,8	14,8	17,7	11,7
$\frac{F_{max}-F_{min}}{F_{msq}}$	4,15	4,05	4,0	4,35
$\frac{T_{r\,max}-T_{r\,min}}{T_{rmsq}}$	4,8	3,9	3,9	4,45

variable, although a high degree of stability is characteristic for the average radiation values. For a clear sky, the outgoing thermal radiation is determined by the vertical distributions of temperature and the atmospheric components that emit the radiation. The appearance of clouds works a change in the outgoing radiation in almost all parts of the spectrum (even in certain absorption bands).

The experimental data examined above were obtained with instruments of comparatively modest angular and spectral resolution. /106
The volume of these data is not yet sufficient for any inferences of a climatological nature. From these two aspects, great interest attaches to presently available results of theoretical calculations of the angular and spectral distributions of the outgoing thermal radiation. Let us continue now with a brief discussion of these results.

§3. RESULTS OF THEORETICAL CALCULATIONS OF ANGULAR AND SPECTRAL DISTRIBUTIONS OF OUTGOING THERMAL RADIATION

The need for solution of a whole series of important applied problems (interpretation of radiation data from weather satellites, the problem of orienting satellites by the infrared contrast at the limb of a planet, etc.) has stimulated lively interest in data on the angular and spectral distributions of the outgoing thermal radiation field. This explains the comparatively large number of /107
papers that have been devoted to the corresponding calculations [64-79]. A detailed survey of the results can be found in [20]. Thus we shall limit ourselves here to a very brief examination,

devoting most of our attention to the most recent data.

Angular distribution. As the experimental data examined in the preceding section imply, the angular intensity distribution of the outgoing thermal radiation is almost always characterized by a decrease in intensity toward the limb of the planet (there is a so-called infrared darkening effect), and this results from the decrease in temperature with increasing altitude. The temperature rise in the stratosphere produces the opposite effect — infrared brightening toward the horizon — only at the centers of very intense absorption bands (for example, the 15-μm carbon dioxide band), where the radiant intensities become appreciable even at low concentrations of the absorbing (emitting) atmospheric component and the influence of the temperature increase with altitude "outweighs" the decrease in the concentration of the emitting component.

Almost all theoretical calculations of outgoing radiation angular distribution have been made using model stratifications of the atmosphere, and this endows them with a certain climatological importance. Thus, for example, D.Q. Wark, G. Yamamoto, and J.H. Lienesch [74] calculated angular distributions for 106 models of the atmosphere that covered the full range of climatic conditions.

By way of illustration, let us examine certain results calculated for model atmospheres by K.Ya. Kondrat'yev and K.Ye. Yakushevskaya [64-66]. These calculations, which were made for the various spectral segments listed in Table 2.6, assumed three midseason, middle-latitude stratifications of the atmosphere: equator (latitude $\phi = 0°$, summer) and $\phi = 65°$ N. lat. (summer and winter). The calculations pertain to cases of cloudless skies and solid cloud cover with the cloud tops at the 3- and 9-km levels.

Although these calculations were made for a point 300 km above the earth's surface, they are quite universal, since the conversion to the angular distribution of outgoing radiant intensity $U(\theta_H)$ at any other altitude H (θ is the nadir angle) from the angular distribution $U(\theta)$ at a fixed level is easily accomplished with the aid of the formulas (which are valid in the absence of an azimuthal dependence of the outgoing radiation:

$$U(\theta) \to U(\theta_H); \quad \sin\theta_H = \frac{(R+300)\sin\theta}{R+H}. \tag{2.13}$$

where R = 6371 km is the radius of the earth.

The results of the calculations are presented in Fig. 2.21. /108
In these figures, the curves marked with the letters "s" and "w" pertain to summer and winter conditions at 65° N. lat., and the unmarked curves to conditions at the equator. The horizontal

arrows at the right sides of the figures indicate the clear-sky radiant intensity at the zenith (nadir) angle subtended by the limb of the earth from an altitude of 300 km (θ = 72°45').

Figures 2.21-2.22 clearly demonstrate the predominance of the /110 darkening effect toward the earth's limb. Only in a few cases (see spectral segments 6, 7, and 11, which correspond to zones of strong absorption) do we have a distinct increase in radiant intensity near the limb of the earth. However, a weak brightening effect may be observed in segments 4 and 5, in which absorption is not as strong (and even in the 8-12-μm transparency window) in the presence of unbroken cloudage with high (9 km), cold tops and a relatively humid stratosphere.

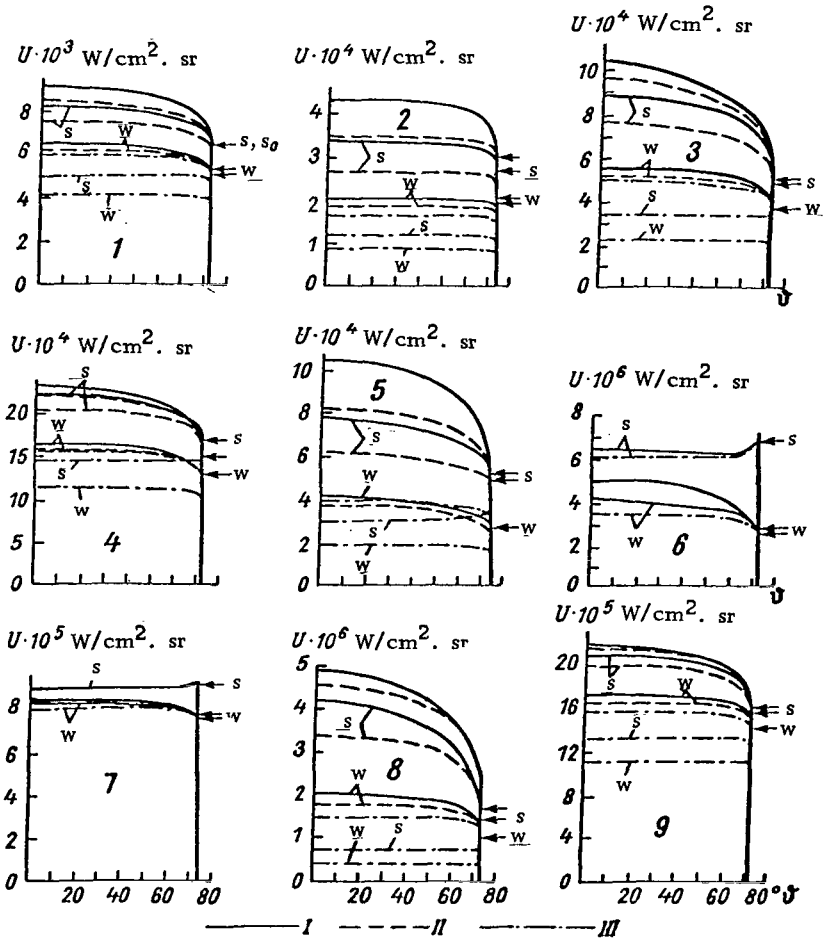

Figure 2.21. Angular Distribution of Outgoing Radiant s_0) Summer, equator; s) summer, 65° N. lat.; w) winter, altitude h_t = 3 km; III) h_t = 9 km.

Naturally, the outgoing-radiation field is highly sensitive to changes in cloudage conditions. Table 2.7 presents values of the ratio $A = \frac{U_0 - U_\vartheta}{(U_\vartheta)_{\vartheta=0}}$, which characterizes the sensitivity of outgoing radiation to cloudage in various regions of the spectrum. Here U_ϑ and $(U_\vartheta)_{\theta=0}$ are the intensities of the outgoing radiation in the presence of clouds with tops at 9 km in the direction of the nadir angle θ and the nadir, respectively; U_0 is the outgoing radiation intensity of a cloudless sky in the direction θ relative to the nadir.

Obviously, the parameter A characterizes the uniformity of /111
the outgoing radiation angular distribution under conditions of variable cloudage: small A signify a weak dependence of the angular distribution on cloudage conditions. As we see from Table 2.7, the cloud sensitivity of the outgoing-radiation field varies very strongly as a function of wavelength. While A << 1 in the absorption bands (for example, segments 6 and 11), cloud cover affects the outgoing radiation very strongly in the transparency windows. Naturally, the influence of cloudage diminishes with increasing nadir angle. It is also important that the near infrared is more sensitive to clouds than the far region; this is because of the stronger dependence of the Planck function on temperature in the near infrared. This is why the outgoing radiation is quite sensitive to cloudage conditions even in most of the absorption bands at $\lambda < 18$ μm (disregarding narrow intervals in the centers of the bands).

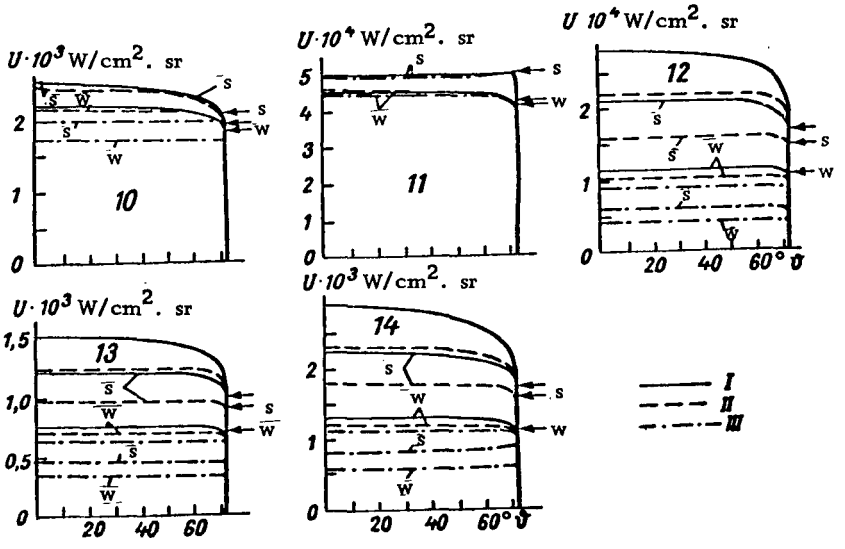

Intensity for Spectral Segments 1-14 (see Table 2.6). 60° N. lat.; I) clear sky; II) unbroken clouds, top

TABLE 2.6. SPECTRAL INTERVALS STUDIED IN PAPERS BY K.YA. KONDRAT'YEV AND K.YE. YAKUSHEVSKAYA [64, 55] /109

Spectral Segment No.	Spectral Interval Studied	Limits of Spectral Interval, μm	Principal Absorbing Gases
1	Integrated radiation	0-∞	H_2O, CO_2
2	Segment in atmospheric window	10.55-11.01	H_2O
3	6.3-μm water vapor absorption band	4.88-8.70	H_2O
4	15-μm carbon dioxide absorption band	12-18	CO_2, H_2O
5	9.6-μm ozone absorption band	9.01-10.29	O_3, H_2O
6	Segment with very strong absorption	6.494-6.579	H_2O
7	Segment with very strong absorption	41.67-45.45	H_2O
8	Segment with weak absorption	5.00-5.05	H_2O
9	Segment with weak absorption	17.86-18.52	H_2O
10	Region of 80-μm water vapor absorption band	18-40	H_2O
11	Region of 80-μm water vapor absorption band	40-120	H_2O
12	Segment in atmospheric window	8.70-9.01	H_2O
13	Same	10.29-12.00	H_2O
14	"	8.70-12.00	H_2O, O_3

Data on the cloudage dependence of the radiation field and its angular structure near the limb of the planet are of great interest from the standpoint of technical utilization of information on the outgoing thermal radiation angular distribution (for example, for orientation of spacecraft with respect to the earth). Calculations made for this purpose by D.Q. Wark, J. Alishouse, and G. Yamamoto [75] indicate that the outgoing radiation is most variable on the disk of the planet in the region of maximum atmospheric transparency (10.5-11.0 μm) (where it varies from 300 to 5100 units). There is similar wide variability in the outgoing radiation in one of the regions of strongest absorption (6.56-6.67 μm), where the radiation varies very strongly as a function of temperature (in this case, the Planck function is proportional to the eighth power of temperature).

Although absorption is also very strong in the region of the water vapor rotational band (30.8-33.3 μm), the variability of the

TABLE 2.7. ILLUSTRATING DEPENDENCE OF OUTGOING RADIATION ANGULAR DISTRIBUTION ON CLOUDAGE CONDITIONS

(RATIO $A=\frac{U_0-U_\vartheta}{(U_\vartheta)_{\vartheta=0}}$)

Boundaries of spectral segment, μm	$\vartheta=0°$			$\vartheta=70°$		
	0°	∠ 65°N. lat.		0°	65°N. lat.	
	Summer	Summer	Winter	Winter	Summer	Winter
0—∞	0,506	0,617	0,529	0,317	0,430	0,400
10,55—11,01	1,58	1,81	1,25	1,21	1,64	1,07
4,88—8,70	1,07	1,60	1,43	0,495	0,943	1,05
12—18	0,494	0,542	0,350	0,231	0,299	0,313
9,01—10,29	1,62	1,59	1,10	0,818	0,906	0,754
6,49—6,58	$0,404\cdot10^{-2}$	0,0528	0,210	0	0,0111	0,0111
41,67—45,45	0	0,0101	0,0277	0	0	0,002
5,00—5,05	2,22	4,36	3,73	0,954	2,06	2,80
17,85—18,52	0,404	0,575	0,560	0,199	0,343	0,444
18—40	0,149	0,245	0,278	0,058	0,123	0,171
40—120	0,0009	0,008	0,0244	0	0,0002	0,0101
8,70—9,01	2,08	2,47	1,68	1,48	2,12	1,65
10,29—12,00	1,44	1,72	1,20	1,03	1,50	1,18
8,70—12,00	1,56	1,73	1,30	0,989	1,33	1,13
4,88—40,00	0,628	0,698	0,543	0,340	0,451	0,399
4,88—120	0,578	0,631	0,486	0,313	0,407	0,358

outgoing radiation is comparatively small here (from 940 to 1600 units), since the Planck function is proportional to the square of temperature on this segment of the spectrum. The same applies to the central part of the carbon dioxide absorption band (14.8-15.4 μm), where the outgoing radiation varies from 980 to 2030 units over the disk of the planet and "brightening" is always observed toward the limb. Thus, the outgoing radiation around the center of the 15-μm carbon dioxide band and the rotational band of water vapor is most suitable for location of the earth's limb.

In connection with a study of the possibilities for orientation of satellites with respect to the earth on the basis of the thermal radiant intensity contrast at the limb of the planet and /112
the fact that the most stable contrasts are observed in the region of the 15-μm carbon dioxide band, J.S. Bates [82] undertook calculations of the angular distribution of thermal outgoing radiation intensity in the 13.8-16.7-μm (600-725-cm^{-1}) spectral interval, which he divided into 10 narrow segments ranging from 10 to 20 cm^{-1} in width. It was assumed that the atmosphere is 90 km thick and that carbon dioxide is the only absorbing and emitting component. The calculations were made for two vertical temperature profiles, one of which is typical for low latitudes (distinct tropopause), while the other typifies high latitudes (almost isothermic lower stratosphere).

The angular distribution, which was represented in the form of the radiant intensity in the direction of the tangent to the earth's surface as it depends on altitude above the surface,

demonstrates the rather strong influence of atmospheric temperature stratification and the location of the spectral segment on the outgoing radiation. The data obtained for all ten segments on the vertical weighting-function (transmission-function derivative) profiles, which characterize the contributions of various atmospheric layers to the outgoing radiant intensity as functions of altitude above the earth's surface (varied from -30 to +60 km), indicate that the weighting functions have a very sharp maximum (peak) for high altitudes above the earth's surface, at a level corresponding to the height of the ray above the earth's surface. With decreasing altitude, this maximum becomes increasingly indistinct. The "sharpness" of the weighting function also depends strongly on the location of the spectral segment (absorption intensity).

As we have already noted, the problem of thermal sensing of the atmosphere from satellites can, in principle, be solved equally well on the basis of either spectral or angular-distribution data on the radiation. However, the results examined above, which characterize the strong dependence of the outgoing radiation on cloudage conditions, practically exclude the use of angular-distribution data, since in the presence of clouds, this distribution will, generally speaking, be determined not so much by the influence of the vertical temperature profile as by cloudage conditions. There is no doubt that cloudage effects will also create serious difficulties in interpreting measured data on the spectral composition of the outgoing radiation. Only in the far infrared (wavelengths longer than 18 μm) is the radiation field practically independent of cloudage conditions, since it is formed for the most part in the stratosphere.

In our analysis of the factors that determine the angular distribution of the outgoing radiation, it is interesting to note that the absolute latitude variations of radiant intensity for most segments of the spectrum (for a given set of cloudage conditions) are much smaller than the radiation changes that take place on a transition from clear sky to a cloudy sky with the cloud tops at an altitude of 9 km. This fact is one more indication of the strong dependence of outgoing-radiation field on cloudage conditions. /113

All of these calculated results for the outgoing radiation angular distribution have been obtained without consideration of the azimuth-angle dependence of the radiation. However, climatological estimates made in [64] showed that the azimuthal dependence is relatively unimportant. Needless to say, the azimuthal dependence may become very substantial for specific synoptic situations in which the cloud cover shows strong three-dimensional "mottling."

Spectral distribution. There have been comparatively few calculations of the spectral distribution of the outgoing thermal

radiation [66, 67, 71, 72, 74]. Data (Fig. 2.22) from a paper by D.Q. Wark, G. Yamamoto, and J.H. Lienesch [74] may be cited as an example of calculated outgoing-radiation spectra obtained with quite high wavelength resolution.

Calculations of K.Ye. Yakushevskaya [67] have shown that within the limits of the planet's disk, the relative spectral distribution of the outgoing radiation depends strongly on cloudage conditions and atmospheric stratification, but is virtually independent of nadir angle. Under the conditions of a cold atmosphere and in the presence of high clouds, we observe smoothing of the spectral radiation distribution in the wavelength range from 8 to 18 μm and a substantial increase in the importance of radiation at wavelengths longer than 18 μm. The spectral composition of the outgoing radiation undergoes substantial variations in the range of zenith angles beyond the critical value corresponding to the direction of the tangent to the earth's surface. Here the contribution of the 12-18, 18-40, and 40-120-μm regions of the spectrum to the integrated radiant intensity increases substantially, while the fraction of radiation at wavelengths shorter than 12 μm — except for the 9.6-μm ozone band — diminishes rapidly, amounting to less than 5% at zenith angles larger than 73°10'. This means, for one thing, that the long-wave limit of the

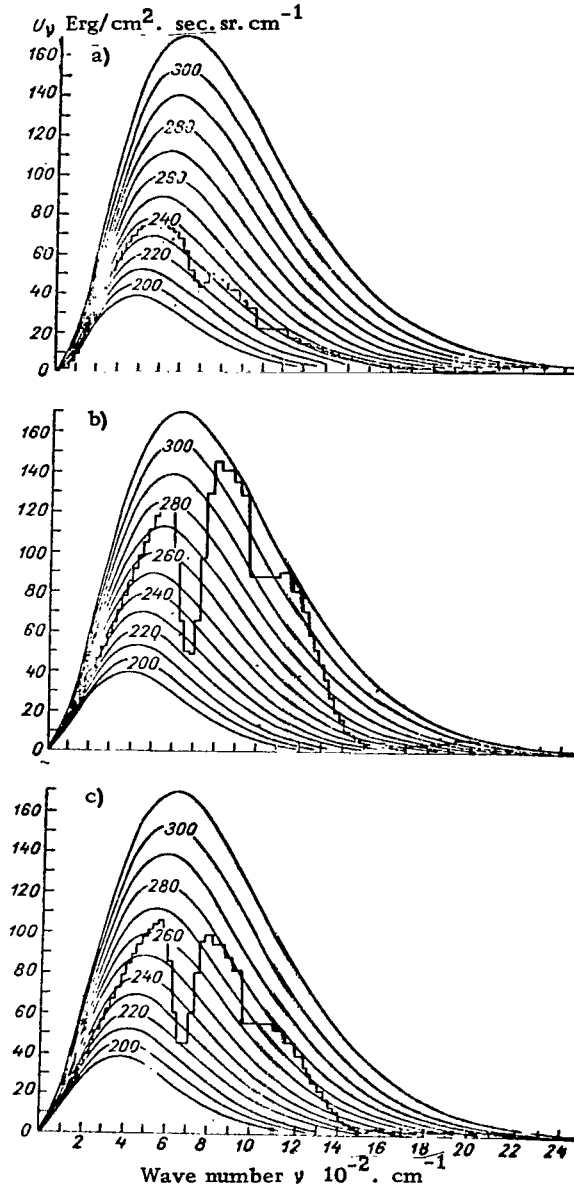

Figure 2.22. Spectral Distribution of Outgoing Radiation in Direction of Nadir. a) Clear sky, winter, Arctic; b) clear sky, summer, western USA; c) unbroken clouds, summer, tropics.

integrated radiation cannot be put at 40 μm for large zenith angles, as is often done.

From the standpoint of the thermal-sensing problem, interest attaches to K.Ye Yakushevskaya's calculated results [81] for the contributions of the earth's surface, clouds (tops at 9-km level) and certain layers of the atmosphere (0.3 km, 3-9 km, 9 km-∞) to the outgoing thermal radiation in various segments of the spectrum for the 0-72°45' zenith-angle range and various stratifications of the atmosphere. These results indicate that in the nadir-angle range below 50°, the fraction of the radiation due to the radiating surface or specific atmospheric layers is practically independent of nadir angle. /115 There is accordingly no change in the proportional contributions of radiation in various segments of the spectrum, especially in the case of the integrated radiation. This means that only large zenith angles can be used effectively in solving the problem of atmospheric thermal sensing from satellites by the angle-scanning method. In this case, however, the influence of the horizontal inhomogeneity of the atmosphere may be rather strongly in evidence, and the atmosphere's curvature must be taken into account.

The principal factors determining the contribution of the earth's surface or any given layer of the atmosphere to the outgoing radiation at small nadir angles are the position of the spectral segment considered and the stratification of the atmosphere. Thus, for example, in the tropics (humid atmosphere), the atmospheric-radiation fraction is 30% even in the most transparent segment of the spectrum from 10.55 to 11.01 μm. The contribution of the lowermost three kilometers of the atmosphere is greatest in the 5.00-5.05 and 17.85-18.52-μm segments of the spectrum, except for zenith angles around 70°. The fraction of radiation from the 3-9-km layer is largest for the 18-40-μm interval. The contribution of ground-surface radiation and individual atmospheric layers depends most strongly on the humidity of the air mass in the wings of the 15-μm carbon dioxide band. This makes evident the importance of taking account of absorption by water vapor in the wings of the 15-μm band in solving the thermal-sensing problem by frequency scanning.

Unfortunately, no acceptable comparisons have as yet been made between calculated and measured outgoing-radiation spectra. At the same time, solution of this problem is highly important. Comparisons made in recent years between calculations and ground measurements of the atmosphere's back radiation indicate wide disagreement, which is due chiefly to the imperfection of the calculation methods.

This can be illustrated by the results obtained by F.-W Bertram [83]. The radiation spectra of the day and night skies were measured with a diffraction-grating spectrometer (spectral slit width from 3 to 5 cm^{-1}) for a band extending from 3.1 to 4.2 μm

near Munich in June 1966 and March 1967 and the corresponding figures were calculated. Temperature, absolute air humidity, and aerosol size distribution were measured simultaneously. The calculated profile of the band differs markedly in shape from the measured profile; this can be attributed to failure to consider the influence of selective carbon dioxide emission. The absolute radiation values are also observed to disagree; this can be explained by failure to consider aerosol radiation. Calculations of the thermal radiation due to water vapor and carbon dioxide in the 3.7-3.85-μm interval showed the calculated values to be low by factors of 1.3-5.0. Calculations based on the hypothesis that this disagreement is due entirely to aerosols yielded aerosol absorption coefficients representing 3 to 10% of the total attenuation coefficients. /116

Thus, the data of [83] testify to the effect that calculated spectral distributions of the thermal radiation cannot yet be regarded as fully dependable.

Chapter 3

/117

DETERMINATION OF TEMPERATURES OF UNDERLYING SURFACE AND CLOUD TOPS

During recent years, a substantial amount of research has been devoted to development of a method for determining the temperature of the underlying surface or the upper boundary of the cloud cover from outgoing-radiation data measured aboard satellites.

The possibility of determining the temperature of the underlying surface or the cloud tops from measured outgoing thermal radiation data is determined by the existence of transparency windows in the atmosphere, where the earth's surface or the clouds make the basic contribution to the outgoing radiation. Information on the emissivities of the atmosphere, the underlying surface, and the clouds are of great importance for correct interpretation of measured data of this type.

We shall examine the results of research in this field exclusively on the basis of data for the optical infrared wavelength band (great interest also attaches to the microwave band; see §7 of this chapter).

§1. CERTAIN OPTICAL CHARACTERISTICS OF THE ATMOSPHERE, THE UNDERLYING SURFACE, AND THE CLOUDS IN THE TRANSPARENCY-WINDOW REGIONS

1. **The atmosphere's transparency windows.** Figure 3.1 shows atmospheric transparency as a function of wavelength according to aerostat measurements made by a Leningrad University team [1] for the 3-14-μm wavelength range at various altitudes of the sun, which is the extraatmospheric radiation source. The following obvious conclusions proceed from these data: 1) the underlying-surface or cloud-top temperature can be determined by use of /119 either the transparency windows on etiher side of the 4.3-μm carbon dioxide absorption band or the broad 8-12-μm transparency window (in this case, the presence of the 9.6-μm ozone absorption band introduces a certain amount of interference); 2) the absolute transmission values depend strongly on depth of atmosphere (at the same time, this implies the need to consider the variation with sighting angle). Even in the most weakly absorbing segments of the transparency windows, the absorption of radiation by the full thickness of the atmosphere at low sun altitudes (which corresponds to slant paths from the satellite; in the case corresponding to

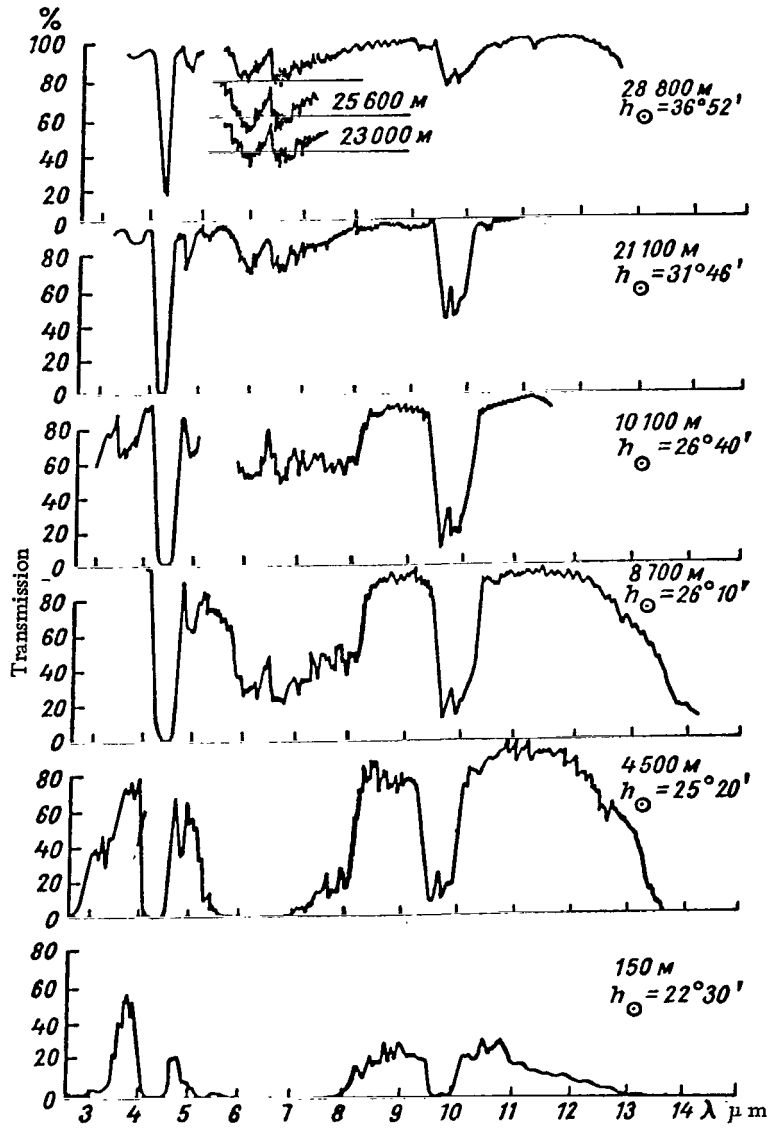

Figure 3.1. Transmission (%) of Infrared Radiation by the Atmosphere at Various Elevations Above Sea Level.

the lower curve in Fig. 2.1, a 67.5° nadir angle) is so strong that corrections for attenuation by the lower atmosphere will obviously be necessary in determining the temperature of the radiating surface. On the other hand, the existence of strong absorption indicates strong emission from the lower atmosphere in the same regions of the spectrum. In actuality, therefore, we must concern ourselves with correction not only for absorption (more

precisely, attenuation), but also for a more complex transformation of the underlying-surface (or cloudage) emission by the lower atmosphere. This, in turn, would require the availability of data on absorption and emission by the full thickness of the atmosphere.

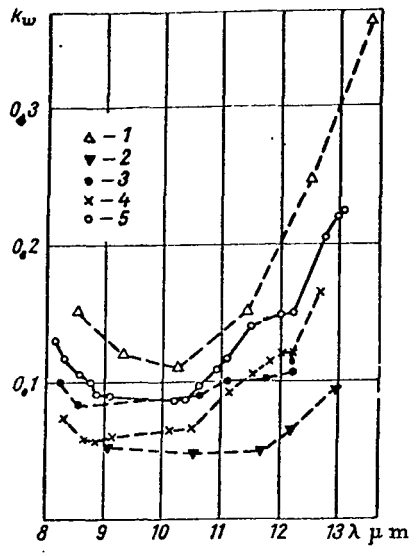

Figure 3.2. Logarithmic Water Vapor Absorption Coefficients According to K.Ya. Kondrat'yev (1), Anthony (2), Gebbie et al. (3), Saiedy (4), and I.Ya. Badinov (5) (see [4]).

The quantitative absorption characteristics of the atmosphere's transparency windows have been the subject of many investigations (see [2, 3]). Figure 3.2 presents the results of a comparison made in [4] of logarithmic absorption coefficients obtained in recent years for the 8-13-μm window. We note here that the possibility of determining the absorption coefficients k_w is determined by the fact that an exponentially decreasing transmission function $P_w = e^{-k_w w}$ approximates the experimental data quite satisfactorily in this transparency window (w is the water-vapor content in the thickness of the atmosphere expressed in g/cm^2, which is equivalent to 1 cm of precipitated water). The rather wide scattering of the measured absorption coefficients results both from differences in the observation conditions and from systematic errors of certain data. As for the differences in the observation conditions, an important factor here is aerosol attenuation, which varies strongly as a function of atmospheric turbidity. The contribution of absorption by hydrocarbons and nitrogen oxides is also highly important for the near infrared.

Table 3.1 presents data from [4] on the logarithmic absorption coefficients of water vapor and compares them with values of the residual optical thickness τ_a of the atmosphere (computed for a unit air mass), which is determined both by the influence of aerosol attenuation and by absorption by minority components of the atmosphere. These data were obtained both under alpine conditions with high atmospheric transparency (Terskol Peak) and near sea level (Mineral'nyye Vody, Leningrad); here it is important to note that the observations made at the two latter stations were made on days with relatively high transparency. Despite all this, the residual optical thicknesses were found to be considerable. This result is quite discouraging from the standpoint of correct interpretation of measured data on the outgoing radiation

/120

/121

TABLE 3.1. LOGARITHMIC WATER VAPOR ABSORPTION COEFFICIENTS AND RESIDUAL OPTICAL THICKNESSES OF THE ATMOSPHERE IN THE INFRARED

λ, μm	k_w см$^{-1}$	τ_a (per unit air mass)		
		Terskol Peak	Mineral 'nyye Vody	Leningrad
3,58	0,070 ± 0,01	0,06 ± 0,02	0,08 ± 0,02	0,10 ± 0,02
3,70	0,062 ± 0,007	0,04 ± 0,02	0,06 ± 0,02	0,08 ± 0,02
8,15	0,15 ± 0,02	0,04 ± 0,02	0,09 ± 0,03	0,17 ± 0,03
8,30	0,12 ± 0,01	0,04 ± 0,2	0,08 ± 0,02	0,11 ± 0,03
8,53	0,10 ± 0,01	0,01 ± 0,02	0,08 ± 0,02	0,12 ± 0,03
8,76	0,10 ± 0,01	0,04 ± 0,02	0,07 ± 0,02	0,14 ± 0,03
8,86	0,095 ± 0,01	0,03 ± 0,02	0,06 ± 0,02	0,11 ± 0,03
9,10	0,090 ± 0,01	0,05 ± 0,02	0,08 ± 0,03	0,13 ± 0,04
10,18	0,085 ± 0,01	0,03 ± 0,01	0,06 ± 0,02	0,09 ± 0,02
10,40	0,085 ± 0,01	0,02 ± 0,01	0,01 ± 0,02	0,01 ± 0,02
10,62	0,090 ± 0,01	0,02 ± 0,01	0,01 ± 0,02	0,07 ± 0,02
10,92	0,11 ± 0,01	0,02 ± 0,01	0,05 ± 0,02	0,07 ± 0,02
11,11	0,12 ± 0,01	0,01 ± 0,01	0,01 ± 0,02	0,06 ± 0,02
11,51	0,15 ± 0,02	0,01 ± 0,01	0,03 ± 0,01	0,01 ± 0,02
11,98	0,15 ± 0,02	0,01 ± 0,01	0,03 ± 0,01	0,03 ± 0,01
12,18	0,16 ± 0,02	0,01 ± 0,01	0,03 ± 0,01	0,03 ± 0,01
12,72	0,21 ± 0,02	0,02 ± 0,01	0,06 ± 0,02	0,09 ± 0,03
12,95	0,22 ± 0,02	0,01 ± 0,02	0,06 ± 0,02	0,09 ± 0,03
13,95	0,225 ± 0,02	0,05 ± 0,02	0,08 ± 0,02	0,11 ± 0,03

by introducing corrections that take account of atmospheric thickness, since the presently available data on the atmosphere's aerosol composition and its contents of hydrocarbons and nitrogen oxides are too spotty.

References [5-7] report quite detailed experimental data on the peculiarities of the vertical aerosol distribution at altitudes up to 30 km. They give a detailed analysis of the results of 1961-1965 measurements of the vertical profile of integrated direct solar radiation, which were made to obtain information on the vertical optical inhomogeneity of the atmosphere (and especially of its aerosol layers). The atmosphere was found to have a stratified aerosol structure. Thus, according to the data for 1 October 1965, aerosol levels were registered at altitudes of 12, 7-14, 15-17, ≈19, 21.5-22.5 km, etc. An anomalously low value of the solar radiant flux was obtained on this date at the level of the sounding ceiling (28 km); it was only 1.82 cal/cm^2·min, indicating the presence of strong aerosol attenuation in the upper stratosphere, apparently as a result of the eruption of Taal volcano.

The aerosol layers are unstable and short-lived in the layer from the tropopause to 20 km. In several cases, the solar radiation attenuation maxima coincide with maxima of ozone concentration. Similarity between the vertical profiles of aerosol attenuation and relative humidity is usually observed in the lower stratosphere.

According to data from ten aerostat ascents in 1963-1965, layers of increased attenuation of the direct solar radiation occur in the troposphere at average altitudes of 2-4 km and between 6 and 10 km (6.0-7.8 km and 3.4-10.3 km); this corresponds to the layers in which clouds are formed. In the lower stratosphere (up to 25 km), attenuating layers generally form at three levels: most frequently above the tropopause (12.3-17.0 km) and in the 18.6-22.4-km and 23.2-25.0-km layers. The thickest attenuating layers are observed below and above the tropopause. The stratospheric layers are usually under inversions. /122

This complex picture of variable vertical aerosol distribution makes it much more difficult to allow for aerosol attenuation of infrared radiation, leaving approximate estimates pertaining to conditions of a defined standard atmosphere as the only possibility. The work of L. Elterman [8] may be cited as an example of construction of such an optical model of the standard atmosphere for the atmospheric windows in the 0.4-4.00-μm wavelength region.

Unfortunately, the optical characteristics of aerosols in a cloudless atmosphere have been almost totally neglected. In this context, infrared absorption spectrum measurements made by G.B. Hoidale and A.J. Blanco [141] on samples of atmospheric dust collected in the ground layer of the atmosphere are quite interesting.

From May 1966 through October 1967, the absorption spectrum was studied in the 2.5-4.0-μm region for aerosol samples collected at four stations in south central New Mexico (USA). The samples were collected on membrane filters mounted 3.5 m above the ground during the period from sunrise to sunset (16-18 hours), during which 0.3 to 3 mg of dust settled out of an air volume of about 100 m^3. Almost all samples (265 out of 287) were collected at a station with an elevation of 1311 m above sea level. For comparison, 22 samples were taken at elevations of 1220, 2472, and 2730 m. To exclude the influence of scattering in the absorption measurements, the dust particles were "packed" into a "matrix" having the same index of refraction but high and uniform transparency (potassium bromide met these requirements).

Investigation of these 265 absorption spectra showed that they all have similar features. The most intense absorption bands occur at wavelengths of 7.0, 9.7, and 21.4 μm, with the 9.7-μm band strongest. Comparison with the absorption spectra of various minerals made it possible to identify the various bands. The most intense 9.6-μm band belongs to silicates (illite, montmorillonite, kaolinite). The 7.0-μm band is due to carbonates (chiefly calcite).

The dust absorption spectra showed two kinds of time variation: 1) redistribution of the band intensities; 2) sporadic

appearance of bands. For example, the 7.0- and 9.7-μm bands were found to be strongly variable (intensity redistribution). Their depth ratio varies from 1 to 10. On the average, the silicate band is more intense than the carbonate band. The occasional (sporadic) absorption bands were weak and of sulfate origin (sulfates of calcium, ammonium, and potassium). The absorption spectra obtained from the data at the four stations (simultaneously in almost all cases) were found to be highly similar. Only the band intensities varied. The spectra of ground soil samples taken at various stations (particle sizes about 37 μm) were investigated to determine the origin of the atmospheric dust. With certain exceptions, these spectra were found to be almost identical to those of the atmospheric dust. Compounding of "synthetic" dusts to match the real dust indicated that a mixture of particles consisting of 80% by weight of silicates, 16% carbonates, and 4% nitrates produced the best reproduction of the real spectrum. /123

The presence of substantial aerosol attenuation in the 10-11-μm wavelength band was clearly demonstrated by aircraft measurements of the ascending radiant flux made by B.A. Sparkman, G.T. Cherrix, and M.S. Tobin [143] over Southern California with a five-channel radiometer. In this case, the attenuation was due to a layer of haze lying below 3 km. Estimates of the attenuation effect indicated that failure to take it into account in underlying-surface temperature measurements from satellites might lower the temperature values by as much as 9°K.

J.T. Peterson [148] made an interesting set of aircraft radiaton soundings over northwestern India, where the atmosphere is extremely dusty just before the monsoon. Simultaneous measurements of the vertical radiant-flux profiles (short-wave and long-wave radiation), vertical concentration distribution, composition, and particle-size distribution of the aerosol made possible a detailed and quite rigorous study of the influence of aerosols on transfer of long-wave radiation. Comparison of the observational data with theoretical calculations showed that the agreement is satisfactory only when the aerosol is taken into account (in the case under consideration, the aerosol consisted primarily of quartz-dust particles).

Naturally, aerosols influence transfer of long-wave radiation noticeably only when they are present in sufficiently high concentration. In many cases, calculations of only the "gas" component of the long-wave radiant fluxes agree closely with experiment.

For example, M. Griggs [149] compared the results of aircraft measurements and calculations of the thermal radiant intensity of the ground surface/atmosphere system in the 8-12-μm transparency window. The aircraft measurements were made at altitudes ranging from 0.015 to 6.40 km above various underlying surfaces (ocean, stratus clouds, snow, ice, desert) with two instruments, which had 18° fields and were pointed at the nadir: 1) an integrating /124

radiometer for the 8-14-μm region; 2) a Fourier spectrometer, which measured the spectral distribution of radiation in the 6-15-μm wavelength band.

The radiant intensities in the 5.05-16.67-μm range were computed for the conditions of the flights. The instrumental function of the radiometer was taken into account in comparing its data with the calculated values. The entire thickness of the atmosphere that was covered by the measurements was broken up into ten layers for the calculations. They were also made for a number of levels above 6.4 km and extending up to 50 km (outgoing radiation). The agreement between the measured and calculated radiation-temperature values for the integral radiation in the transparency window was found to be quite close. The agreement of experiment with theory was less satisfactory when the spectra were compared, apparently for the most part because of measurement errors.

The vertical radiation-temperature profiles thus obtained make it possible to characterize the influence of atmospheric thickness in determinations of underlying-surface temperature and indicate variability of the transformation of underlying-surface radiation by the lower atmosphere. According to measured data for the 5.49-km level, the radiation temperature is usually about 4° lower than the true underlying-surface temperature. However, the opposite situation, in which temperature increased with altitude, was also observed on occasion. The transformation of surface radiation by the layer of atmosphere may even be quite substantial at 0.05-km altitude.

F.F. Hale [144] calculated the atmospheric back-radiation in the presence of cirrus clouds 200 m thick for a particle concentration of $5 \cdot 10^5$ m^{-3}, an average radius of 50 μm, and an average cloud temperature of 238°K. These calculations showed that in the presence of cirrus clouds, the back-radiation varies substantially in the 8-13-μm transparency window, where the complex refractive index of ice varies from 1.17-0.03i to 1.58-0.12i.

V. Zdunkowski, D. Henderson, and J.V. Hales [33] made theoretical calculations with the object of studying the influence of thin layers of cirrus clouds that are invisible to the eye on the outgoing long-wave radiation, considering the following spectral intervals: 6-6.5, 8.75-12.25, and 13.5-16.5 μm and the integrated long-wave ascending radiation. It was assumed that the haze was formed by a layer of spherical ice particles of uniform size (radius 120 μm and concentration from $5.0 \cdot 10^{-4}$ to $1.0 \cdot 10^{-1}$ cm^{-3}) 1 km thick, and that its upper boundary was 1 km below the tropopause. It was assumed in the outgoing-radiation calculations that the upper boundary of the atmosphere was at 45 km in the presence of the haze layer. Reference [33] discusses the calculated latitude variation of the outgoing radiation along 80°W. long. In /125 both the absorption band (wavelengths 6-6.5 μm) and the

transparency window (8-12 μm), the influence of the haze layer on the outgoing radiation was found to be quite substantial, especially at particle concentrations above 10^{-2} cm^{-3}. At a concentration of 10^{-1} cm^{-3}, the latitude variation even reverses: the outgoing radiation decreases southward instead of increasing, as it is observed to do at low ice-particle concentrations. The influence of haze on the integrated outgoing radiation is just as strong, as confirmed by actinometric sounding data. Estimates indicated that invisible cirrus clouds may reduce the integral outgoing radiation by about 10%. When measured data on the outgoing radiation in the transparency window are used to determine underlying-surface temperatures, failure to take the haze into account may lower the temperature by 3-4° in the case of a tropical air mass or by 2-3° under winter conditions in middle latitudes. It was reported that for observations made at zenith angles from 0 to 45°, the transition from invisible to visible reflection from the clouds takes place as the particle concentration increases from $1.5 \cdot 10^{-3}$ to $1.5 \cdot 10^{-2}$ cm^{-3}. In the infrared, the transition from partly transparent to almost black clouds takes place in the 10^{-2}-10^{-1} cm^{-3} concentration range. Estimates of the influence of a stratospheric aerosol layer (assuming that it consists of carbon particles) in the 10-30-km altitude range on long-wave radiative transfer showed no appreciable effects.

P.M. Kuhn and V.E. Suomi [32] analyzed the results of two nocturnal actinometric soundings made over a desert region (California) on 20 February 1964 at a time when the sky was cloudless and the atmosphere very dry, with simultaneous visual observations of jet-airplane smoke trails at an altitude of about 12.9 km. Independent underlying-surface temperature measurements were made with thermistors and a ground radiometer. A surface emissivity of 0.95 was obtained on the basis of comparison of the radiometer and thermistor readings. Analysis of the data from the first ascent of the actinometric radiosonde revealed the presence of a continuous cloud or haze layer at altitudes of 10.5-12.9 km; this was also confirmed by visual observations from an airplane. The ascending radiant flux calculated for the ceiling of the radiosonde from the sounding data without considering the haze layer was found to be 0.041 $cal/cm^2 \cdot min$ higher than the measured flux. The calculated values agree with the measured values if the layer of haze is taken into account and a relative emissivity of 0.11 is used. Similar agreement is also observed if 3.0°C instead of the observed 8.7°C is taken for the underlying-surface temperature; at the same time, this characterizes the error (5.7°) that can arise in determinations of surface temperature from satellite outgoing radiation measurements without consideration of aerosol-layer effects. It is noted that the air temperature in the Stevenson shelter was 12.2°C. Only residues of the thin clouds observed during the first sounding were detected during the second (later) ascent. /126

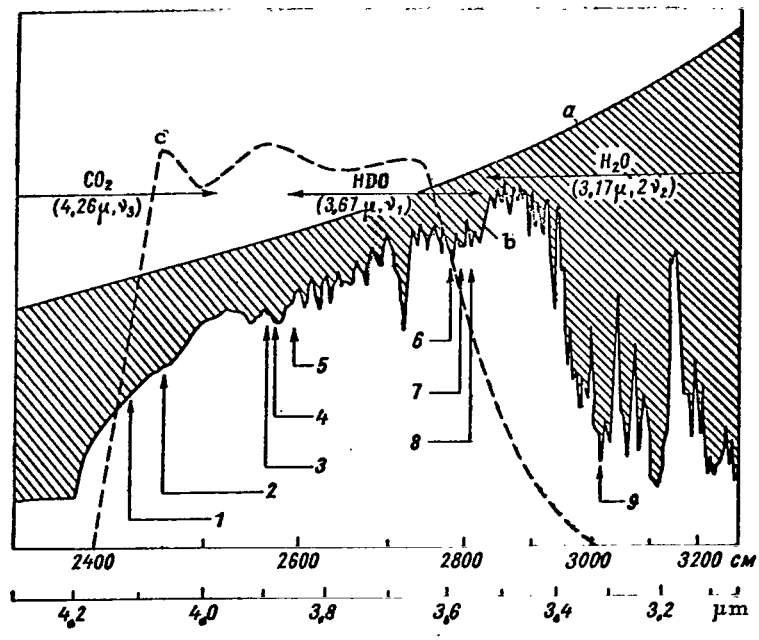

Figure 3.3. Absorption of Radiation in 3-4-μm Transparency Window. 1) CO_2 band (center at $\lambda = 4.06$ μm, $\nu_1 + \nu_3$); 2) N_2O band ($\lambda = 4.06$ μm, $\nu_1 + 2\nu_2$); 3) N_2O band ($\lambda = 3.90$ μm, $2\nu_1$); 4) N_2O band ($\lambda = 3.88$ μm; $2\nu_1 + \nu_2$); 5) CH_4 band ($\lambda = 3.85$ μm, $2\nu_4$); 6) HDO band ($\lambda = 3.59$ μm, $2\nu_2$); 7) N_2O band ($\lambda = 3.57$ μm, $\nu_2 + \nu_3$); 8) CH_4 band ($\lambda = 3.55$ μm, $\nu_2 + \nu_4$); a) energy distribution in solar spectrum ($T = 6000°K$); the shaded area characterizes the absorption of the solar radiation; b) solar spectrum; c) effective spectral sensitivity curve of high-resolution radiometer carried on Nimbus I satellite.

The atmospheric transparency window in the 3-4-μm wavelength range was investigated in detail in [9-11, 29, 30]. In this case, carbon dioxide, methane, and nitric oxide make substantial contributions to absorption along with water vapor. It is important to consider aerosol attenuation. Figure 3.3 gives a semiquantitative characterization of absorption in the 3-4-μm window according to [29, 30]. /127

To obtain approximate calculated results, the authors of [12] used the analytical approximations of the transmission function P given in Table 3.2 for various transparency windows. The nomenclature is as follows: w_{H_2O}, w_{CO_2}, and u_{O_3} are the water vapor, carbon dioxide, and ozone contents, k_w is the absorption

TABLE 3.2. APPROXIMATION OF TRANSMISSION FUNCTIONS FOR VARIOUS ABSORBING SUBSTANCES OF THE ATMOSPHERE IN VARIOUS REGIONS OF THE INFRARED

Interval, μm	Absorbing substance	Approx. of trans. functions
3—4	Water vapor	$P=1-\Phi\left(\sqrt{\frac{p_{av}}{p_0}\frac{l_\lambda w_{H_2O}}{2}}\right)$
4—5	Water vapor, Carbon dioxide	$P=\left[1-\Phi\left(\sqrt{\frac{p_{av}}{p_0}\frac{l_\lambda w_{H_2O}}{2}}\right)\right]\times\left[1-\Phi\left(\sqrt{\frac{p_{av}}{p_0}\frac{l_\lambda w_{CO_2}}{2}}\right)\right]$
5—8	Water vapor	$P=1-\Phi\left(\sqrt{\frac{p_{av}}{p_0}\frac{l_\lambda w_{H_2O}}{2}}\right)$
8—9,1	Water vapor	$P=\exp\left(-\frac{p_{av}}{p_0}k_w w_{H_2O}\right)$
9,1—10,2	Water vapor, ozone	$P=\exp\left(-\frac{p_{av}}{p_0}k_w w_{H_2O}\right)\times\left[1-\Phi\left(\sqrt{\frac{p_{av}}{p_0}\frac{l'_\lambda u_{O_3}}{2}}\right)\right]$
10,2—13	Water vapor	$P=\exp\left(-\frac{p_{av}}{p_0}k_w w_{H_2O}\right)$
13—18	Water vapor, carbon dioxide	$P=\left[1-\Phi\left(\sqrt{\frac{p_{av}}{p_0}\frac{l_\lambda w_{H_2O}}{2}}\right)\right]\times\left[1-\Phi\left(\sqrt{\frac{p_{av}}{p_0}\frac{l'_\lambda w_{CO_2}}{2}}\right)\right]$

coefficient of water vapor, $\underline{l}_\lambda$, $\underline{l}'_\lambda$, and $\underline{l}''_\lambda$ are generalized absorp- /129
tion coefficients (in Elsasser's sense) for water vapor, carbon dioxide, and ozone; p_0 and p_{av} are the ground and average atmospheric pressures; Φ is the error probability integral. Table 3.3 lists values of the generalized absorption coefficients for intervals 0.1 μm wide in the 3-18-μm range.

The intrinsic radiation of the atmosphere in the transparency windows has been investigated in a whole series of experimental studies during recent years. Data on the spectral and angular distributions of the outgoing radiation are discussed in detail in the monograph [1.13].[1]

[1]When a source listed in the bibliography for another chapter is cited, the first numeral in the brackets indicates the chapter number and the second the reference number.

TABLE 3.3. GENERALIZED ABSORPTION COEFFICIENTS OF WATER VAPOR, CARBON DIOXIDE, AND OZONE FOR 0.1-μm INTERVALS IN THE 3-18-μm SEGMENT OF THE SPECTRUM

λ μm	Absorption coefficient			λ μm	Absorption coefficient		
	H_2O	CO_2	O_3		H_2O	CO_2	O_3
3,0	2,350	—	—	7,7	0,70	—	—
1	1,250	—	—	8	0,50	—	—
2	0,610	—	—	9	0,35	—	—
3	0,220	—	—	8,0	0,32	—	—
4	0,085	—	—	1	0,17	—	—
5	0,020	—	—	2	0,14	—	—
6	0,004	—	—	3	0,126	—	—
7	0,002	—	—	4	0,117	—	—
8	0,0006	—	—	5	0,110	—	—
9	0,003	—	—	6	0,106	—	—
4,0	0,006	0,000005	—	7	0,106	—	—
1	0,007	0,002	—	8	0,100	—	—
2	0,008	0,910	—	9	0,096	—	—
3	0,008	0,165	—	9,0	0,090	—	—
4	0,009	0,0001	—	1	0,086	—	0,050
5	0,010	0,000002	—	2	0,084	—	0,965
6	0,014	0,000002	—	3	0,083	—	0,200
7	0,020	0,000009	—	4	0,083	—	2,100
8	0,030	0,00003	—	5	0,084	—	0,910
9	0,110	0,000002	—	6	0,085	—	2,730
5,0	0,250	—	—	7	0,086	—	1,900
1	0,520	—	—	8	0,087	—	1,180
2	1,040	—	—	9	0,088	—	0,570
3	3,320	—	—	10,0	0,089	—	0,230
4	7,000	—	—	1	0,090	—	0,060
5	18,0	—	—	2	0,092	—	—
6	44,0	—	—	3	0,095	—	—
7	105,0	—	—	4	0,098	—	—
8	201,5	—	—	5	0,100	—	—
9	270,0	—	—	6	0,103	—	—
6,0	246,0	—	—	7	0,104	—	—
1	155,0	—	—	8	0,104	—	—
2	54,50	—	—	9	0,106	—	—
3	160,0	—	—	11,0	0,115	—	—
4	409,0	—	—	1	0,118	—	—
5	450,0	—	—	2	0,125	—	—
6	284,0	—	—	3	0,131	—	—
7	147,0	—	—	4	0,137	—	—
8	92,0	—	—	5	0,141	—	—
9	62,0	—	—	6	0,142	—	—
7,0	28,0	—	—	7	0,145	—	—
1	12,75	—	—	8	0,147	—	—
2	10,3	—	—	9	0,149	—	—
3	6,5	—	—	12,0	0,153	—	—
4	3,45	—	—	1	0,159	—	—
5	1,90	—	—	2	0,169	—	—
6	1,10	—	—	3	0,184	—	—

2. **Underlying-surface emissivity.** Consideration of the true emissivity of the underlying surface in determining the surface temperature is important for two reasons: 1) the conversion from radiant flux to temperature requires information on the "nonblackness" of the radiating surface; 2) the atmosphere's intrinsic emission background depends on the reflectivity (emissivity) of the underlying surface. G.N. Kostyanoy [13] derived formulas that /130

λ μm	Absorption coefficient			λ μm	Absorption coefficient		
	H_2O	CO_2	O_3		H_2O	CO_2	O_3
12,4	0,200	—	—	15,2	0,470	4,500	—
5	0,216	—	—	3	0,510	3,260	—
6	0,233	—	—	4	0,540	1,950	—
7	0,249	—	—	5	0,570	0,980	—
8	0,260	—	—	6	0,600	0,640	—
9	0,270	—	—	7	0,630	0,450	—
13,0	0,276	0,0013	—	8	0,670	0,310	—
1	0,280	0,0023	—	9	0,700	0,220	—
2	0,284	0,0044	—	16,0	0,730	0,150	—
3	0,288	0,0101	—	1	0,770	0,110	—
4	0,292	0,0194	—	2	0,810	0,090	—
5	0,296	0,030	—	3	0,850	0,080	—
6	0,293	0,050	—	4	0,910	0,060	—
7	0,300	0,085	—	5	0,970	0,050	—
8	0,303	0,120	—	6	0,020	0,040	—
9	0,307	0,190	—	7	1,110	0,025	—
14,0	0,313	0,290	—	8	1,170	0,016	—
1	0,320	0,420	—	9	1,230	0,0076	—
2	0,325	0,630	—	17,0	1,300	0,0030	—
3	0,340	0,910	—	1	1,380	0,0016	—
4	0,360	1,290	—	2	1,450	0,0010	—
5	0,360	1,890	—	3	1,500	0,0008	—
6	0,370	2,760	—	4	1,600	0,0006	—
7	0,380	4,170	—	5	1,650	0,0005	—
8	0,400	6,280	—	6	1,720	0,0004	—
9	0,410	6,610	—	7	1,800	0,0003	—
15,0	0,430	5,950	—	8	1,900	0,0002	—
1	0,450	5,350	—	9	1,980	0,0001	—

define the ascending integrated long-wave radiant flux in the atmosphere with consideration of underlying-surface emissivity for the cases of diffuse and specular reflection. These formulas were used to estimate the contribution of reflected radiation for various stratifications of the atmosphere; the results indicated that the fraction of reflected radiation in the ascending radiant flux diminishes beginning at an altitude of the order of a few tens of meters, and that this decrease is stronger in the case of diffuse reflection. Above 300-500 m, the contribution of reflected radiation is nearly constant at 20-40% for 100% (specular) reflection or 10-30% (diffuse reflection) of the ascending radiant flux corresponding to an absolutely black underlying surface. Under real conditions, when the albedo is about 10%, the correction for the reflectivity of the underlying surface does not exceed 4% (specular reflection) or 3% (diffuse reflection). Considering the modest accuracy of present-day methods for measuring long-wave radiation, this would imply that the reflection correction can be disregarded for all practical purposes (D. Lorenz arrived at the same conclusion [34, 135, 146]). However, the situation may not be as simple in calculations of the spectral radiant fluxes. In occasional cases in which the albedo is large enough, it may be necessary to take reflection into account.

As concerns direct allowance for surface nonblackness in the conversion from measured radiant flux to temperature, it is the

relative stability of emissivity that is important here.

According to W.A. Hovis [14, 15, 31, 133] and M. Griggs [139], who measured the reflectivities of various minerals and natural underlying surfaces in the wavelength range from 0.5 to 22 μm, reflectivity is strongly selective in all cases, and varies with the nature of the reflecting surface. The 10-12-μm interval is most suitable for radiometric surface-temperature determinations, since it lies in a transparency window of the atmosphere and the relative emissivity of the surfaces is comparatively constant and near unity in this interval.

To investigate the factors that determine the emissivities of natural suraaces, J.E. Conel [145] made laboratory measurements and constructed theoretical models of the thermal radiation from various powdered media. Another proposed application of the results is use of emission spectroscopy in the 8-14-μm transparency window of the earth's atmosphere for petrographic study of the moon and Mars, since the infrared thermal-radiation spectra of continuous and powdered silicates depend on composition, surface roughness, and particle size. /131

The results of the foregoing studies showed that the emission spectrum becomes more and more structureless with decreasing particle size (for example, it loses structure completely in the case of Al_2O_3 at particle diameters smaller than 0.02 μm). In this context, the emission spectra of films of powdered silicates (about 30 μm thick) of various compositions were studied in the laboratory. Measurements were made with a Beckmann spectrophotometer fitted with an auxiliary radiation source and a calibration black body. Specimen temperatures were varied from 400 to 450°K.

Analysis of the measured data made it possible for the first time to detect broad emission minima near frequencies where strong absorption occurs and emission maxima in regions of anomalous dispersion (where the real part of the complex refractive index approaches unity). In the case of certain basic and ultrabasic rocks in the powdered state (at micron particle sizes), these spectral features may dominate, causing the spectrum to differ from that determined by the characteristic bands of "residual" rays.

To explain the observed phenomena, Reference [145] proposes a theoretical model of the emission spectra of powdered substances in the form of the spectrum of a semiinfinite cloud consisting of scattering and absorbing particles. The spectral emission features are determined in this case chiefly by the dependence of particle albedo on particle size (emissivity also depends on the asymmetry of the scattering indicatrix).

A detailed analysis of the data for quartz indicated that the theory explains the experimental results quite well; for example,

it was found that the distribution of temperature in the powder layer is of no substantial importance. Thus, the change in the emission spectra of powdered solids with particle size should be attributed primarily to the dependence of particle albedo and scattering-indicatrix asymmetry on particle dimensions. It was also shown that the fundamental Christiansen frequencies obtained by measuring the transmission of silicate-powder films have diagnostic value for study of minerals and correspond to the emissivity maxima of the powders (these conclusions are illustrated by the data for quartz). /132

Table 3.4 presents a summary of the emissivities measured in the 8-12-μm transparency window according to [16-18, 142]. We note that the authors of [19] performed extensive calculations of the spectral and angular distributions of the emissivity of water.

Reduction of outgoing-radiation measurements obtained in the 8-12-μm transparency window from the Tiros III satellite [18] gave an emissivity very close to unity for the surface of the Mediterranean Sea. According to observations made above the Sahara, the emissivity there varies from 0.79 to 1.00.

Analysis of the reflectivity variations of the underlying surface in the 3.4-4.2-μm transparency window according to aircraft measurements showed [15] that this variability is no obstacle to determination of underlying-surface temperature with adequate reliability.

H. Arlt and H.-J. Bolle [93] recently completed extensive laboratory measurements of the angular and spectral dependences of emissivity for various natural formations (sand, water, humus, asphalt, wood, etc.). The principal conclusion to be drawn from the results of these measurements is that substantial deviations from isotropic reflection (Lambert's law) are observed, especially in the case of high reflectivities. This fact will undoubtedly complicate correct allowance for the emissivities of natural surfaces. On the other hand, the specific nature of the angle dependence of reflection raises the question as to the possibility of identifying surfaces from data on the nature of the reflection anisotropy. /133

Study of the reflectivities of dispersed media (sand, etc.) showed a strong dependence on particle size (microstructure).

3. **Emissivity of clouds.** Only very few experimental studies have thusfar been made of cloud emissivities. The most detailed theoretical calculations of radiative transfer in clouds have been made by Ye.M. Feygel'son [20]. Table 3.5 presents the results of Ye.M. Feygel'son's calculations of the albedo of stratus clouds as a function of wavelength (for various segments of the spectrum), the water content ρ_v of the cloud, cloud temperature $\underline{t}$, and a

TABLE 3.4. MEASURED EMISSIVITIES δ IN REGION OF 8-12-μm TRANSPARENCY WINDOW (EMISSIVITY EXPRESSED AS A FRACTION OF UNITY)

Surface	δ	Surface	δ
Fine dry sand	0.949	Wet snow, 0°C	0.997
Fine sand, thoroughly moistened	0.962	Quartz	0.712
Sandy loam, dry	0.954	Granite	0.815
Sandy loam, thoroughly moistened	0.968	Rough granite	0.898
Dry peat	0.970	Feldspar	0.870
Thoroughly moistened peat	0.983	Obsidian	0.862
Thick green grass	0.986	Rough obsidian	0.837
Patchy green grass on moist sandy loam	0.975	Basalt	0.904
Pine needles	0.971	Rough basalt	0.934
Freshly fallen snow	0.986	Dunite	0.856
Dirty snow	0.969	Rough dunite	0.892
Melting snow	0.995	Dolomite	0.929
Ice	0.980	Rough dolomite	0.958
Dry snow, -2.5°C	0.996	Dolomite, fragments (0.5 cm)	0.959
		Quartz sand, coarse	0.914
		Same, moistened with water	0.936
		Pure water	0.993
		Water coated with film of motor oil	0.972

coefficient c_1, which characterizes the shape of the scattering indicatrix.

It follows from this table that albedo depends quite strongly on the shape of the scattering indicatrix. Usually, the coefficient c_1 varies from 0.5 to 3.0. A reduction of the albedo by about half corresponds to the increase in c_1 in this range. There is a distinct dependence of albedo on wavelength: maximum reflectivity is observed in the 8-12-μm transparency window. Naturally, this indicates the substantial nonblackness of the thermal radiation from stratus clouds. Another property of the albedo for the 8-12-μm transparency window is the fact that it is practically independent of water content and temperature. In other spectral intervals, albedo increases with increasing water content and declining temperature. Since the albedo seldom exceeds 15% in all regions of the spectrum other than the 8-12-μm window (for $t \geq -10°C$ and a water content $\rho_v \geq 0.1$ g/m^3), the stratus cloud may be regarded in approximation as a black body in these intervals. However, this inference will require improvements when we consider segments of the spectrum narrower than those considered in Table 3.5.

These improvements are called for by the highly selective reflectivities of clouds, which are evident from Tables 3.6 and 3.7, where we have listed 8-12-μm and 3-4-μm transparency-window

TABLE 3.5. ALBEDO OF A STRATUS CLOUD IN THE INFRARED (IN FRACTIONS OF UNITY)

t °C	ρ_v g/m^3			ρ_v g/m^3		
	0,1	0,2	0,5	0,1	0,2	0,5
			$c_1=0,5$			
	4—8 μm			16—20 μm		
0	0,09	0,14	0,2041	0,09	0,10	0,12
—5	0,12	0,17	0,2252	0,10	0,11	0,12
—10	0,14	0,19	0,2424	0,10	0,12	0,12
	8—12 μm			20—24 μm		
0	0,27	0,27	0,27	0,05	0,08	0,10
—5	0,27	0,27	0,27	0,07	0,09	0,11
—10	0,27	0,27	0,27	0,08	0,10	0,13
	12—16 μm			24—28 μm		
0	0,11	0,11	0,11	0,03	0,05	0,08
—5	0,11	0,11	0,11	0,04	0,06	0,09
—10	0,11	0,11	0,11	0,06	0,08	0,10
			$c_1=1$			
	4—8 μm			16—20 μm		
0	0,08	0,12	0,18	0,08	0,09	0,10
—5	0,10	0,14	0,20	0,08	0,10	0,11
—10	0,13	0,17	0,22	0,09	0,10	0,11
	8—12 μm			20—24 μm		
0	0,24	0,24	0,24	0,05	0,07	0,10
—5	0,24	0,24	0,24	0,06	0,08	0,10
—10	0,24	0,24	0,24	0,07	0,09	0,11
	12—16 μm			24—28 μm		
0	0,09	0,09	0,10	0,03	0,05	0,07
—5	0,09	0,09	0,10	0,04	0,06	0,08
—10	0,09	0,09	0,10	0,05	0,07	0,09
			$c_1=2$			
	4—8 μm			16—20 μm		
0	0,06	0,09	0,14	0,05	0,06	0,07
—5	0,07	0,11	0,15	0,06	0,07	0,08
—10	0,09	0,13	0,17	0,06	0,07	0,08
	8—12 μm			20—24 μm		
0	0,19	0,19	0,19	0,03	0,05	0,06
—5	0,19	0,19	0,10	0,04	0,05	0,07
—10	0,19	0,19	0,19	0,05	0,06	0,08
	12—16 μm			24—28 μm		
0	0,07	0,07	0,07	0,02	0,03	0,05
—5	0,07	0,07	0,07	0,03	0,04	0,06
—10	0,07	0,07	0,07	0,03	0,05	0,06
			$c_1=2,5$			
	4—8 μm			16—20 μm		
0	0,04	0,06	0,11	0,04	0,04	0,06
—5	0,06	0,08	0,12	0,04	0,06	0,06
—10	0,07	0,10	0,14	0,04	0,05	0,06
	8—12 μm			20—24 μm		
0	0,15	0,15	0,15	0,02	0,04	0,04
—5	0,15	0,15	0,15	0,03	0,04	0,06
—10	0,15	0,15	0,15	0,04	0,04	0,06
	12—16 μm			24—28 μm		
0	0,06	0,06	0,06	0,02	0,02	0,04
—5	0,06	0,06	0,06	0,02	0,03	0,04
—10	0,06	0,06	0,06	0,02	0,04	0,04

TABLE 3.6. ALBEDO OF A STRATUS CLOUD IN THE 8-12-μm TRANSPARENCY WINDOW OF THE ATMOSPHERE

λ, μm	8	9	10	11	12
A, %	41	18	12	5	5

TABLE 3.7. ALBEDO OF A STRATUS CLOUD IN THE 3-4-μm TRANSPARENCY WINDOW OF THE ATMOSPHERE

λ μm	t °C		
	−15	−5	+15
3	9	6	5
3,4	12	12	11
4	24	22	21

albedos calculated by Ye.M. Feygel'son for a water content of 0.2 g/cm^2 and various temperatures (for the 3-4-μm window).

Using the Monte Carlo method, G.W. Kattawar and G.N. Plass [147] made detailed calculations of the radiation fields of sunlit clouds and haze in the near infrared (for selected wavelengths from 1.07 to 6.05 μm). The angular radiant intensity and radiant flux distributions at the boundaries of the cloud or haze layers were calculated for various scattering indicatrices, optical thicknesses, microstructure models, underlying-surface albedos, and angles of sunlight incidence. It was shown that for weak absorption (for example, for the 1.7-μm wavelength), the cloud albedo increases rapidly with increasing optical thickness from 0.1 to 10.0. For intervals of strong absorption (for example, around 2.96 μm), there is practically no dependence on the optical thickness τ for τ > 1. Cloud albedo (at zero underlying-surface albedo) varies in this region of the spectrum from 0.00035 (λ = = 2.8 μm, τ = 0.1, sunlight incidence angle $\vartheta_\odot = 0$) to 0.685 (λ = = 1.7 μm, $\tau = 10$, $\cos\vartheta_\odot = 0{,}15$). The albedo of haze was found to be higher than that of clouds, since a more elongated scattering indicatrix was assumed for haze. /135 /136

G. Yamamoto, M. Tanaka, and K. Kamitani [22, 91] made a circumstantial theoretical study of radiative heat transfer in the region of the 8-12-μm atmospheric transparency window (taking 10 μm as the reference wavelength) in water clouds. The model of cloud microstructure and information on the scattering indicatrix of the droplets and the ratio of scattering coefficient to attenuation coefficient were borrowed from the work of D. Dermendzhan. The cloud is regarded as isothermal and homogeneous, and the radiant-field intensity as independent of azimuth angle. The influence of water vapor on radiative transfer in the cloud is assumed to be negligible and is taken into account (in the case of semitransparent clouds) only in the layer of atmosphere between the earth's surface and the lower boundary of the cloud.

The results of calculations for the 10-μm wavelength indicate that in the case of a thin cloudage layer (optical thickness 0.1),

the outgoing radiant intensity at the cloud-top level is determined chiefly by radiation passing through the cloud from below and decreases with increasing zenith angle (in a "darkening" effect near the horizon). This effect is most distinct at a cloud optical thickness of 1.0 (although the contribution of cloud radiation naturally increases in this case). When the optical thickness reaches 10, there is practically no transmitted radiation, and the radiation field is almost isotropic. A "brightening" effect is always observed for the descending radiant intensity at cloud-bottom level; it decreases with increasing optical thickness of the cloud.

Analysis of calculated data for the emissivity, reflectivity, and transmission of clouds for the 8-12-μm interval as functions of the droplet content in a vertical unit-cross-section column of cloud (which characterizes the cloud's geometrical thickness) showed a substantial increase in emissivity and a sharp decrease in transmission with increasing thickness (Fig. 3.4). As we see, the curve of the reflectivity increase with increasing cloud thickness is smoother. The important point is that these characteristics are practically independent of the cloud and ground-surface temperatures. Thus, for known values of these temperatures and cloud thickness, the radiant fluxes at the boundaries of a cloud can be calculated from the reflectivity, emissivity, and transmission values. In a later study [91], G. Yamamoto discussed the results of calculations for cloud emissivity as a function of wavelength in the 5-20-μm band. Figure 3.5 illustrates these reuults as calculated for a semiinfinite cloud. As we see, emissivity depends strongly on wavelength, diminishing considerably in the region of the 8-12-μm transparency window. A sharp emissivity drop takes place in the region of the shortwave wing of the 6.3-μm water vapor band. It is interesting to note that emissivity does not reach unity even in the region of the absorption-band maxima, an effect that can be explained by multiple scattering of the radiation in the cloud. The emissivity averaged over the entire spectral region considered is 0.95.

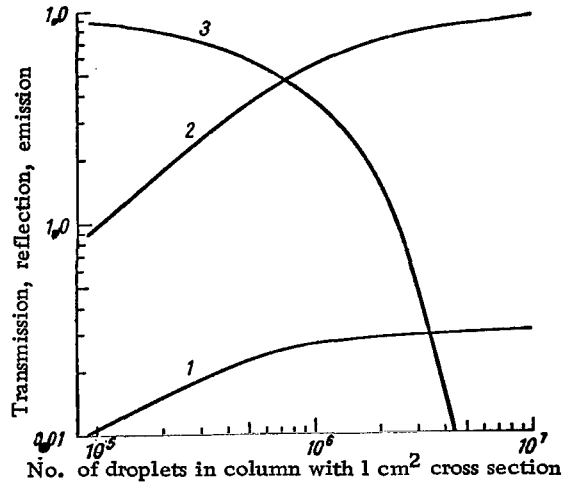

Figure 3.4. Transmission (1), Emissivity (2) and Reflectivity (3) of a Cloud for 10-μm Wavelength as Functions of Water-Droplet Content in a Unit-Cross-Section Column of the Cloud.

/137

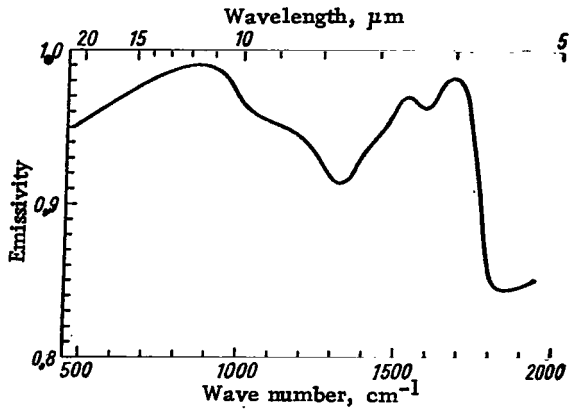

Figure 3.5. Emissivity of a Cloud as a Function of Wavelength.

V.L. Gayevskiy [22] made cloud-top thermal-radiation measurements in the 8-12-μm region, which can be used to estimate cloudage albedos in this spectral interval. The measurements were made in winter (December-January) from an airplane flying at an altitude of 50-100 m above the upper edges of the clouds (in this case, the influence of the intervening atmospheric layer can be disregarded). Simultaneously, the atmosphere was sounded vertically to determine the thickness of the cloud cover and the temperature profile inside the cloud, as well as the vertical profile of radiation temperature throughout the entire thickness of the cloud.

Thermodynamic equilibrium was observed inside the clouds when /138 their optical thicknesses were great enough: the radiation temperature determined from the outgoing radiation was close to the air temperature. For water clouds, the average albedo was 0.03-0.04, and no differences were noted between stratus and altostratus clouds. Mixed stratocumulus clouds have albedos of 0.08-0.09. With small cloud thicknesses (about 150 m), the influence of radiation from the cool underlying surface becomes pronounced. Comparison with the results of theoretical albedo calculations indicates that the calculated water-cloud albedos were on the high side.

Aircraft measurements of stratocumulus-cloud reflectivities made by W.Hovis and M. Tobin [15] in the near infrared also yielded albedo values much smaller than those given in Table 3.7. Thus, for example, the albedo estimated by the authors of [15] for the 3.7-μm wavelength is about 4.5%. The calculated results of E. Bauer [21] agree closely with the data of Table 3.7: he obtained albedos of 10.9% for 3.7 μm and 15.7% for λ = 4.3 μm. It must, of course, be emphasized that comparison of albedo values obtained by different authors cannot be altogether correct, since albedo is variable and the observing (calculating) conditions were dissimilar.

The results considered above pertain almost exclusively to lower-level stratus clouds. There are almost no similar data for clouds of the middle and upper levels (and ice clouds in particular). Only in Ye.P. Novosel'tsev's paper [24] are relative emis- /139 sivities (blacknesses) of upper- and middle-level clouds

calculated theoretically in various spectral intervals and for the entire thermal range of the spectrum on the basis of the "two-flux" approximation of the theory of radiative transfer in clouds (with an estimate of the errors of this approximation).

TABLE 3.8. EMISSIVITY OF UPPER-LEVEL CLOUDS

Δλ μm	On Normal		Into hemis.		Δλ μm	On Normal		Into hemis.	
	Cl	Cs	Cl	Cs		Cl	Cs	Cl	Cs
4—8	0,68	0,69	0,74	0,78	20—22	0,80	0,82	0,90	0,91
8—12	0,16	0,26	0,27	0,40	22—26	0,95	0,96	0,98	0,99
12—18	0,19	0,28	0,31	0,43	26—∞	1	1	1	1
18—20	0,69	0,73	0,82	0,85	0—∞	0,46	0,53	0,56	0,64

TABLE 3.9. EMISSIVITY OF MIDDLE-LEVEL CLOUDS

Δλ μm	On Normal		Into hemis.		Δλ μm	On Normal		Into hemis.	
	Ac	As	Ac	As		Ac	As	Ac	As
4—8	0,83	0,91	0,92	0,96	18—∞	1	1	1	1
8—12	0,40	0,73	0,56	0,85	0—∞	0,74	0,90	0,83	0,94
12—18	0,70	0,93	0,83	0,97					

According to [24], the emissivities of upper-level clouds are determined in approximation by their transmission functions and optical thicknesses. Because of the large sizes of the ice particles in these clouds and the fact that optical thickness is independent of wavelength, the latter can be determined from the attenuation of sunlight by upper-level clouds. The optical thicknesses found in this way proved to be extremely small: 0.32 for cirrus and 0.6 for cirrostratus clouds. As a result, the emissivities of upper-level clouds are substantially smaller than unity, especially in the 8-12-μm transparency window (the minimum for normally directed radiation is 0.16). Table 3.8 presents calculated results for an upper-level cloud 2 km thick (water-vapor content $1.2 \cdot 10^{-2}$ g/cm^2) at -50°C.

Table 3.9 presents analogous data for middle level clouds.

L.P. Grant and G.E. Hunt [94] calculated emissivities for various models of a monodisperse cirrus cloud consisting of ice spheres with radii of 5, 10, 20, and 40 μm with particle concentrations of 10^5, 10^6, and $5 \cdot 10^6$ m^{-3}. The calculations, which were made for the wavelength range from 50 to 120 μm, showed that the emissivity is markedly smaller than unity and depends on particle dimensions and concentration. For a cloudless sky in the radiation-temperature range from 220 to 230°K, the appearance /140

of cirrus clouds results in a 20-30°K drop in radiation temperature. This effect is even more distinct in the 8-13-μm transparency window.

From a U-2 airplane, F. Valovcin [92] made the first measurements of ascending thermal radiant fluxes in the 8-13-μm transparency window above and within cirrus clouds formed in jet-stream zones. Simultaneously, the clouds were photographed, air temperatures were measured, and visual estimates were made of the boundary positions and thicknesses of the cloudage layers. The measurements were conducted using three radiometer modifications with semiconductor radiation detectors (all radiometers had the same 2 × 2° field). The radiometers were calibrated on board the airplane (during the measurements) against a variable-temperature black body.

Analysis of data from 23 flights above the eastern USA during the period from April 1964 through February 1966 indicates that the emissivities of cirrus clouds vary over a very broad range, from 5 to 100%. The difference between the measured radiation temperature and the air temperature at cloud-top level varied from 0 to 68°, averaging 30-36° (this means that the hypothesis that the clouds are absolutely black may result in errors up to 10 km when it is used to determine cloud-top heights from radiation temperature).

Reference [92] proposes a classification of cirrus clouds into three categories in accordance with the radiation temperature T_{rad}: 1) radiometrically thick clouds ($T_{rad} < 244°K$, which corresponds to an emissivity $\delta_c = 0.80 \pm 0.20$); 2) an intermediate case ($T_{rad} \approx 244\text{-}260°K$, $\delta_c = 0.50 \pm 0.15$); 3) radiometrically thin clouds ($T_{rad} > 260°K$, $\delta_c = 0.20 \pm 0.15$). This classification can be used to introduce corrections for cloud nonblackness (in accordance with the measured radiation temperature) and thus obtain a more reliable determination of cloud-top altitude.

F.F. Hall [95] made interesting ground-based studies of the influence of cirrus clouds on the atmosphere's thermal radiation. It had been observed previously that the measured intensity of the atmosphere's back radiation at the zenith often substantially /141
exceeds the intensity computed from radiation nomograms. It was assumed that this was due to the influence of cirrus clouds, which frequently go unnoticed. Ground measurements were therefore made in [95] using a two-channel bolometer with optical filters to determine the intensity and polarization of the atmosphere's thermal radiation in the region of its 8-13-μm transparency window and the 9.6-μm ozone band for clear skies and cirrus clouds in the daytime. The back-radiation intensity was measured near the sun with the object of detecting the inner corona in the infrared (since the ice crystals of cirrus clouds are substantially larger

than the wavelength, strong forward scattering of the solar radiation will be expected).

Evaluation of aerosol radiation for haze with a meteorological visibility of 1 km yielded a value of 1.2 $mW/cm^2 \times sr$. Here the contribution of ground-surface radiation back-scattered by the aerosol exceeds 21% of this emission value. At 50-km visibility, the influence of the aerosol is negligible.

As for the microstructure of cirrus clouds, measured data indicate that a typical particle is a prism 200 μm long and 30 μm thick; this corresponds to an equivalent sphere with a radius of 50 μm. The crystal concentration may be taken equal to $5 \cdot 10^5$ m^{-3}.

Comparison of the measured zenith back-radiations with those computed for this cloud model indicated that in the presence of a strong corona around the sun, the measured values are considerably larger because of cirrus clouds that cannot be detected visually. Here the back-radiation intensity may rise by 0.1 $mW/cm^2 \cdot sr$ at the zenith and twice as much at a 60° zenith angle. In the case of visible, but thin cirrus clouds, the "additional" radiation may amount to 1 $mW/cm^2 \cdot sr$ at the zenith and be 1.4 times larger at a zenith angle of 60°.

In the case of a dense cirrostratus cloud cover, no polarization is detected.

For a clear sky, the radiation in the 8-13.5-μm transparency window is found to be weakly polarized at large zenith angles. Polarization of the back radiation may be explained as due to scattering of thermal radiation from the earth's surface by cirrus clouds.

In the context of the cloud-emissivity problem, considerable interest attaches to the experimental studies of L.I. Chapurskiy [25] and R.P. Espinola and H.H. Blau [26] on the optical properties of clouds in the visible and near infrared regions of the spectrum. /142

L.I. Chapurskiy made aircraft measurements of the spectral brightnesses of clouds, atmospheric haze, and the underlying surface using high-speed spectrometers in the 0.3-0.9-μm and 0.6-2.25-μm wavelength bands. The spectral contrasts between lower- and middle-level clouds and freshly fallen snow were studied on the basis of data obtained from flights in February-March 1962 and 1964 at an altitude of about 2.7 km during the noonday hours. The snow averaged brighter than the clouds in the 0.3-1.1-μm wavelength band, but the reverse was the case between 1.4 and 2.5 μm. The reflected radiation is observed to depend weakly on the vertical thickness of the clouds in the 1.4-2.5-μm spectral segment. The maximum contrasts occur in the 0.3-1.4-μm interval, and the

minimum contrasts from 1.4 to 2.5 μm; in either case, they correspond to clouds from which snow fell. A diminution of the contrasts is observed in the region of the water absorption bands. There is a certain decrease in the contrasts with altitude for the entire spectral region studied.

Analysis of the cloud-reflectivity determinations as compared with theoretically calculated data indicated that the general trends of the experimental and theoretical curves agree satisfactorily, but that there are also appreciable differences (disagreement of the absolute values, a shift of the albedo minima). In the 1.4-2.5-μm interval, the basic contribution to the ascending shortwave radiation over snow is made by atmospheric haze.

Data from 1964-65 winter flights were used to ascertain the possibility of determining crystalline and liquid-drop clouds from the amount of reflected solar radiation in the 0.6-2.5-μm band. The albedo curves of thick crystalline cloudage and snow are identical in this spectral interval. For the 1.4-2.5-μm wavelength range, the albedo of liquid-drop clouds is more than four times the reflectivity of thick crystalline cloudage and snow, while the brightnesses of snow and crystalline and liquid-drop clouds are similar in absolute value in the 0.6-1.1-μm interval. Comparisons of the measured and computed vertical atmospheric haze brightness profiles above water in the 0.3-0.7-μm range indicated that the agreement between the experimental and theoretical data is satisfactory.

The results of angular-distribution measurements of the ascending radiant intensity above a large mass of stratus clouds with an extremely level top indicate that the reflection indicatrix of the cloud is elongated in the direction of the sun at a small angle to the horizon.

An approximate evaluation of the spectral polarization characteristics of clouds in the 0.3-2.5-μm interval showed that the degree of polarization may range from 15 to 30% and decreases markedly with increasing wavelength. The polarization plane lies between 45 and 75° of the direction to the sun. /143

R.P. Espinola and H.H. Blau [26] used an aircraft infrared spectrometer to study the spectra of solar radiation scattered by various types of clouds in the 1.2-3.6-μm wavelength range. Measurements of the brightness angular distribution were also made for various wavelengths in the range of angles from 45 to 150° with respect to the direction of the incident light. In the 2.6-2.9-μm band, where water and ice strongly absorb the radiation and single scattering therefore dominates, the brightnesses of the clouds in this angle range vary through a factor of approximately ten. Where absorption is slight, the angular variability of brightness is about 300%.

Considerable absorption of radiation inside clouds at wavelengths of 1.38, 1.87, and 2.7 μm was observed. Brightness minima at 1.5, 2.0, and 2.8 μm are characteristic for ice clouds; they are absent in the case of clouds consisting of water droplets.

The differences found in [25, 26] in the reflection spectra of water and ice clouds can be used to identify them from satellites.

The principal conclusion to be drawn from all of the studies discussed above is substantial variability and selectivity of underlying-surface and cloudage emissivities. It will be necessary to complete a broad program of further experimental and theoretical studies before the corresponding information can be regarded as adequate from the standpoint of underlying-surface and cloud-top temperature determination based on measurements of outgoing radiation in the atmosphere's transparency windows. It would be most expedient to implement this program within the framework of a complex radiation experiment [27].

§2. OPTIMUM SELECTION OF ATMOSPHERIC TRANSPARENCY WINDOWS FOR DETERMINATION OF UNDERLYING-SURFACE AND CLOUD TEMPERATURES FROM SATELLITES

The analysis of the optical characteristics of the atmosphere, underlying surface, and clouds that was developed in the foregoing section clearly indicates that the 3.0-4.0- and 8.0-12.0-μm transparency windows (or narrower intervals within these segments of the spectrum) are most suitable for determination of surface temperatures from satellites. Having drawn this inference, however, /144 it is important to attempt a solution of the problem of using a defined spectral segment in an unequivocal manner. This brings us to the problem of optimum and unique selection of an atmospheric transparency window that is most suitable for determination of radiating-surface temperature.

Optimality of this selection consists in finding the most favorable combination of the following conditions: 1) minimum transformation of the surface radiation by the thickness of the atmosphere, 2) maximum sensitivity of the radiation to surface-temperature variations, 3) maximum blackness of the surfaces and minimum emissivity variability, 4) equal utility of the selected spectral range during the day and at night, and 5) technical feasibility of outgoing-radiation measurements in the corresponding spectral region with minimum errors. Working from the results of [35, 36], let us analyze whether these conditions can be met.

First of all, we should note that the 8-12-μm transparency window has an unquestionable advantage from the standpoint of equal daytime and nighttime utility, since the outgoing shortwave (reflected solar) radiation in this region of the spectrum is negligibly small under all observing conditions. This cannot

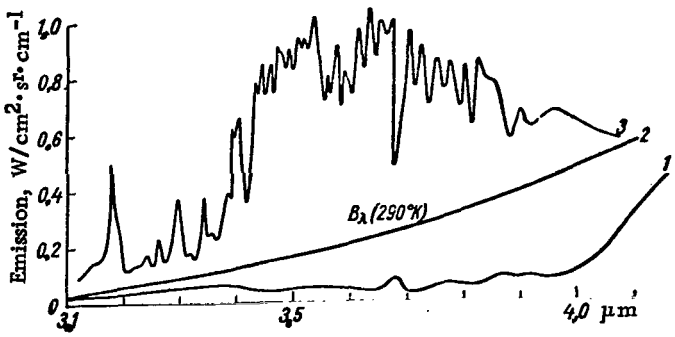

Figure 3.6. Energy Distribution in Emission Spectra of Day and Night Skies (3-4 μm). 1) Thermal emission at night: Maysach (West Germany), 4 June 1966, 1 hour 46 min-1 hour 56 min Central European Time, western sector of sky at altitude of 10° above horizon; 2) black body radiation at 290°K; 3) daytime emission: Maysach (West Germany), 4 May 1966, 17 hours 00 min-17 hours 03 min Central European Time, western sector of sky at altitude of 5° above horizon, $h_\odot$ -24°.

be said of the 3-4-μm interval, where the contribution of shortwave (reflected solar) radiation is often not only significant, but even dominant. The validity of this statement is obvious from Fig. 3.6, which shows curves of energy distribution in the day and night sky emission spectra according to ground measurements made by F.-W. Bertram [9] for the 3-4-μm wavelength band. Even at comparatively low sun altitudes (24°), the shortwave radiation is several times the thermal radiation, which totally precludes determination of temperature from the thermal radiation of the surface.

To solve the problem of optimum transparency-window selection, the authors of [35, 36] calcu-

TABLE 3.10. VALUES OF EXPONENT n_s AT VARIOUS BLACK-BODY TEMPERATURES T AS FUNCTIONS OF WAVELENGTH λ

λ μm	T °K					
	213	233	253	273	293	313
2,5	27,1	24,8	22,8	21,1	19,8	18,5
3,0	22,6	20,6	19,0	17,6	16,4	15,4
4,0	16,9	15,5	14,3	13,2	12,3	11,5
5,0	13,6	12,4	11,4	10,6	9,9	9,2
6,0	11,3	10,3	9,5	8,8	8,2	7,7
7,0	9,7	8,6	8,2	7,6	7,0	6,6
8,0	8,5	7,8	7,1	6,6	6,2	5,8
9,0	7,5	6,9	6,3	5,9	5,5	5,1
10,0	6,8	6,2	5,7	5,3	4,9	4,6
12,0	5,6	5,2	4,8	4,4	4,1	3,8
15,0	4,5	4,1	3,8	3,5	3,3	3,1

lated the outgoing radiation for the 3.5-4.0- and 8.0-12.0-μm spectral bands from aerological sounding data obtained at 24 stations in the USSR (the calculation method used in these studies

permitted determination of the outgoing radiation accurate to 0.6% or better).

Let us present the radiant intensity of the underlying surface for an interval $\Delta\lambda$ in the form

$$J_s = gT_s^{n_s},$$

where g is a certain coefficient, T_s is the surface temperature, and n_s is an exponent that depends on the selection of $\Delta\lambda$ and temperature (see Table 3.10).

The radiation temperature T_{rad} measured from a satellite differs from T_s by an amount ΔT that characterizes the influence of surface nonblackness and transformation of the surface radiation by the thickness of the atmosphere: /145

$$T_{rad} = T_s - \Delta T.$$

Thus, we have for the outgoing radiation J_∞ /146

$$J_\infty = g(T_s - \Delta T)^{n_1} = gT_s^{n_1}\left(1 - \frac{\Delta T}{T_s}\right)^{n_1}.$$

Since ΔT is small (T_{rad} and T_s are closely similar), we may assume that $n_s = n_1 = n$. We then obtain

$$J_\infty = g(T_s - \Delta T)^n = gT_s^n\left(1 - \frac{\Delta T}{T_s}\right)^n = J_s\left(1 - \frac{\Delta T}{T_s}\right)^n.$$

We introduce the nomenclature

$$\frac{J_\infty}{J_s} = \psi = \left(1 - \frac{\Delta T}{T_s}\right)^n.$$

From this

$$\ln\psi = n\ln\left(1 - \frac{\Delta T}{T_s}\right).$$

Since $\frac{\Delta T}{T_s} \ll 1$,

$$\ln\left(1 - \frac{\Delta T}{T_s}\right) \approx -\frac{\Delta T}{T_s}.$$

Consequently,

$$\Delta T = -\frac{T_s}{n}\ln\psi.$$

We see from this formula that the correction for the influence of atmospheric thickness (or the error of underlying-surface-temperature determination if this correction is not introduced) depends not only on transformation of radiation by the thickness of the atmosphere $\left(\ln\psi=\ln\frac{J_\infty}{J_s}\right)$, but also on the transparency window selected (exponent n). Since the exponent n is considerably larger for the shortwave transparency window at 3-4 μm than for the longwave window, this means that the shortwave window has a major advantage from the standpoint of stronger variability of the radiation as a function of surface temperature.

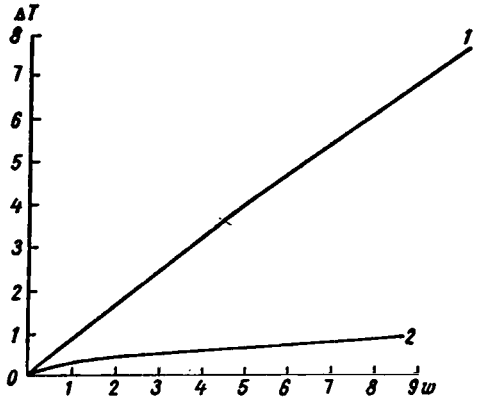

Figure 3.7. ΔT as a Function of Water Vapor Content in the Atmosphere in the 10.55-12.0-μm (1) and 3.5-4.0-μm (2) Regions.

On the other hand, the strong variability of the outgoing radiation calls for apparatus that functions in a broad range of measured radiant fluxes. We note that the black-body radiation at 293°K is almost two orders greater than the radiation corresponding to 233°K (this corresponds exactly to the observed range of underlying-surface temperatures). Such a broad range is without question inconvenient for measurements. Further, it is pointed out in [36] that at low temperatures, the radiation in the near infrared is so weak as to approach the sensitivity threshold of existing radiation detectors. All this indicates the inexpediency of using the 3-4-μm window at low temperatures. Observance of this recommendation also makes it possible to narrow the range of measured values considerably. /147

In evaluating the influence of atmospheric thickness, it is interesting first to study the dependence of the correction ΔT on moisture content, since water vapor is the principal component of the atmosphere responsible for the transformation of surface radiation.

Figure 3.7 shows ΔT as a function of water vapor content in the thickness of the atmosphere for the 10.55-12.0 and 3.5-4.0-μm spectral intervals according to [36]. As we see, the 3.5-4.0-μm window is much more transparent. The fact that the exponent n is

much larger for this segment of the spectrum than in the 10.55-12.0-μm long-wave window is also an important consideration. It should be recalled that carbon dioxide and ozone, in addition to water vapor, make a certain contribution to absorption in the 8-12-μm transparency window. For the 3-4-μm shortwave window, the picture is even more complex (see Fig. 3.3, which was borrowed from [30]). Here it is necessary to consider the various hydrocarbons and nitrogen oxides (primarily ammonia and nitric oxide). Table 3.11 presents calculated results of J. Tannhäuser [11], which characterize the contributions made by the various atmospheric components to the outgoing radiation in the 3.4-4.2-μm wavelength band (this corresponds to the spectral sensitivity range of the scanning infrared radiometer on the Nimbus I satellite) for various surface emissivities δ and varying surface elevation h above sea level. Relationships of the type ΔT (CO_2, CH_4) = $\overline{T}_{rad}(H_2O, CO_2, CH_4) - T_{rad}(H_2O)$ were used to calculate certain corrections ΔT. In this case, $T_{rad}(H_2O, CO_2, CH_4)$ and $T_{rad}(H_2O)$ are the radiation temperatures calculated with consideration of water vapor, methane, and carbon dioxide and water vapor alone. /148

It follows from Table 3.11 that only in the case of clouds with high tops (8.5 km) does the correction $\Delta T(CO_2, CH_4, N_2O)$ become smaller than 1°.

Figure 3.8 shows spectral distributions of radiation temperature (outgoing radiant flux) in the 2190-2290-cm^{-1} range as calculated by J. Tannhäuser [11, 150] for the following concentrations of the atmospheric components considered (cm^3/m^3) and their total contents (atm·cm) in the 1013-10-mbar atmospheric thickness (the total content is indicated in parentheses): /149

	CO_2	CO	N_2O
а)	314 (246,7)	0,2 (0,158)	0,5 (0,393)
б)	313 (246,2)	0,2 (0,158)	0,3 (0,236)

The symbol m> in Fig. 3.8 corresponds to variant а); m< pertains to variant б). The m>f curve was obtained by using erroneous (deviant) transmission-function parameters.

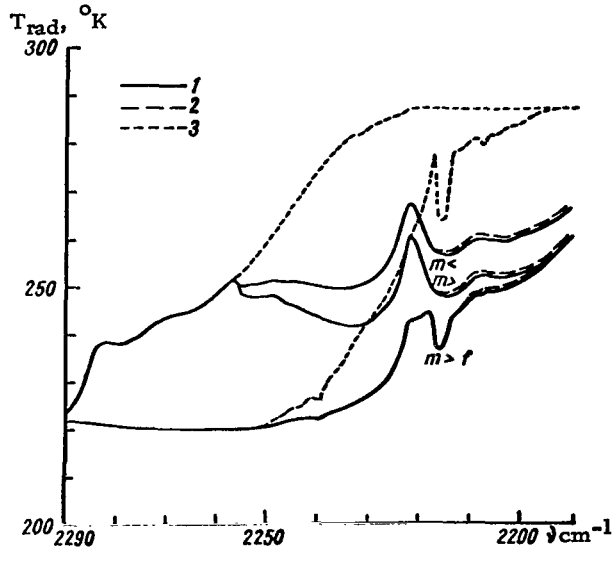

Figure 3.8. Energy (Radiation Temperature) Distribution in Spectrum of Outgoing Radiation from 2190-2290 cm^{-1}. 1) $CO_2 \cdot N_2O \cdot CO$; 2) $CO_2 \cdot N_2O$; 3) CO_2.

TABLE 3.11. INFLUENCE OF VARIOUS ATMOSPHERIC COMPONENTS ON OUTGOING RADIATION (RADIATION TEMPERATURE) IN 3.4-4.2-μm WAVELENGTH BAND

h km	$T(H_2O)$	$T(H_2O+CO_2)$	$T(H_2O+CO_2+CH_4)$	$T(H_2O+CO_2+CH_4+N_2O)$	$\Delta T(CO_2)$	$\Delta T(CO_2+CH_4)$	$\Delta T(CO_2+CH_4+N_2O)$
			$\delta=1,0$				
0,00	268,1	266,4	265,6	263,6	1,7	2,5	4,5
1,05	262,6	261,1	260,4	258,7	1,5	2,2	3,9
2,65	253,8	252,6	252,1	250,7	1,2	1,7	3,1
5,15	239,7	238,9	238,6	237,7	0,8	1,1	2,0
8,50	220,3	220,0	219,9	219,5	0,3	0,4	0,8
			$\delta=0,8167$				
0,00	264,6	263,0	262,4	260,5	1,6	2,2	4,1
1,05	259,1	257,7	257,1	255,6	1,4	2,0	3,5
2,65	250,4	249,4	248,9	247,7	1,0	1,5	2,7
5,15	236,6	236,0	235,6	234,9	0,6	1,0	1,7
8,50	217,8	217,5	217,4	217,1	0,3	0,4	0,7
			$\delta=0,7631$ ·				
0,00	263,4	262,0	261,3	259,6	1,4	2,1	3,8
1,05	257,9	256,7	256,1	254,6	1,2	1,8	3,3
2,65	249,3	248,3	247,8	246,7	1,0	1,5	2,6
5,15	235,6	235,0	234,7	234,0	0,6	0,9	1,6
8,50	216,9	216,7	216,5	216,3	0,2	0,4	0,6

Examination of Fig. 3.8 shows how significant the N_2O contribution to the outgoing radiation is in this region of the spectrum. Correct allowance for the transmission-function parameters is also exceptionally important.

Table 3.12, which presents H.-J. Bolle's calculated results [10], clearly illustrates the roles of the various atmospheric components in determining the outgoing radiation in the 8-12-μm transparency window.

Outgoing-radiation values were calculated for the American Standard Atmosphere in 1962 using R. Penndorf's data on the vertical aerosol concentration distribution (aerosol emission was taken into account by using a mass aerosol emission coefficient of 0.0005 g/cm^2). The standard atmosphere involved has the following total contents of the various atmospheric components: 247.5 atm·cm of CO_2, 1.74 g/cm^2 of H_2O, and 0.213 atm·cm of O_3. The last column of Table 3.11 gives the corrections ΔT for conversion to the true temperature with consideration of a 0.75 emissivity of the earth's surface for this case ($A = 1 - \delta$). /150

TABLE 3.12. OUTGOING RADIANT INTENSITY IN WAVE-NUMBER RANGE FROM 903 to 1007 cm^{-1} IN THE DIRECTION OF THE NADIR FOR A CLOUDLESS AMERICAN STANDARD ATMOSPHERE, 1962

Radiator	Outgoing radiation, $W/cm^2 \cdot sr$		Relative value of outgoing radiation			Correction, °K		
				$A=0,25$			$A=0,25$	
	$A=0$	$A=0,25$	$A=0$	rel. $A=0$	relative surface radiation	$A=0$	T_{rad}	T_s
Earth's surface, (288.2°K)	0,9249	0,7673	1	0,830	1	0	0	—10,7
Earth's surface, H_2O	0,896	0,7455	0,969	0,806	0,971	—1,9	—1,8	—12,3
Earth's surface, H_2O, aerosol	0,8513	0,7326	0,920	0,792	0,955	—4,9	—2,8	—13,3
Earth's surface, H_2O, aerosol, CO_2	0,8478	0,7325	0,916	0,792	0,955	—5,1	—2,8	—13,3
Earth's surface, H_2O, aerosol, CO_2, O_3	0,8477	0,7325	0,916	0,792	0,955	—5,1	—2,8	—13,3

The data in Table 3.12 indicate that determination of underlying-surface temperature accurate to within 0.5° even in this most transparent part of the 8-12-μm window (the 903-1007-cm^{-1} range is equivalent to 10-11.1 μm) requires introduction of corrections that take account of transformation of the underlying-surface radiation by water vapor and aerosols. It is also important to consider the real albedo of the ground surface. This is also evident from inspection of Fig. 3.9 [36], which shows the correction ΔT for the nonblackness of the radiating surface as a function of emissivity δ. Aircraft measurements made by W. Marlatt [50], H.L. Clark [101], and D. Lorenz [102] and others have shown that even at small atmospheric-layer thicknesses, the correction ΔT is quite considerable for the 8-12-μm window. According to D. Lorenz [102], this correction becomes negligible only at distances of less than 150 m from the surface.

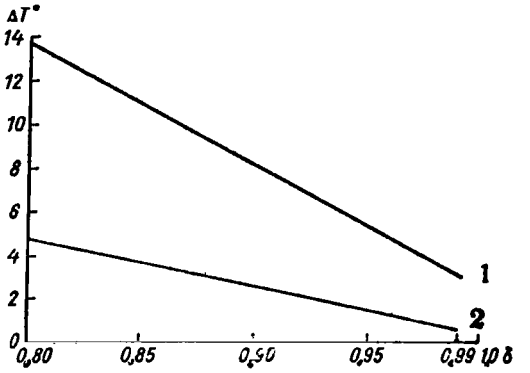

Figure 3.9. Error in Underlying-Surface-Temperature Determination for Various Surface Emissivities in the 10.55-12.0-μm (1) and 3.5-4.0-μm (2) Intervals. /151

As for the emissivity characteristics of the underlying surface and clouds in the various transparency windows, we know that they are highly variable and not at all well understood. If we consider only the underlying surface, we can state that its emissivity is less variable and larger (in many cases practically equal to unity) in the 8-12-μm range than in the near infrared.

Let us now examine the circumstances that have a bearing on analysis of the effects of measurement errors and certain other factors. It is shown in [36] that the error of an underlying-surface-temperature determination depends not only on measurement errors, but also on the exponent n, which characterizes the sensitivity of surface radiation to temperature. Since the exponent n decreases with increasing wavelength, it becomes obvious that for equal measurement errors, the data for the shortwave window should be more reliable.

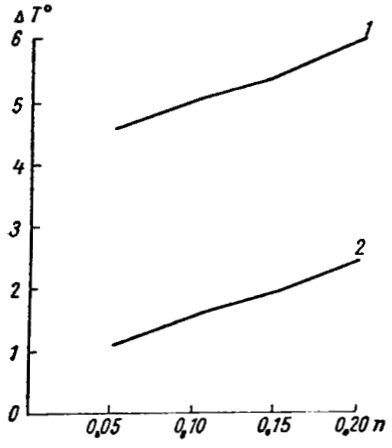

Figure 3.10. Error ΔT of Underlying Surface Temperature Determination as a Function of Amount of Cloudage in Radiometer Field in 10.55-12.0-μm (1) and 3.5-4.0-μm (2) Bands.

The authors of [36] estimated the influence of unrecorded partial cloud cover in the radiometer field on the error ΔT of underlying surface temperature determination from data measured in the 3.5-4.0- and 10.55-12.0-μm transparency windows. Figure 3.10 shows the results of these calculations (the abscissa is the amount of cloudage in the field, expressed as a fraction of unity). As we see, the influence of clouds is considerably weaker in the 3.5-4.0-μm band than in the 10.55-12.0-μm window. /152

In summarizing the above, we may conclude that the basic deficiencies of the 3.5-4.0-μm transparency window are as follows: 1) excessively small outgoing-radiation values at low temperatures (values near the sensitivity threshold of radiation detectors), 2) an excessively broad range of variation of the outgoing radiation as a function of surface temperature, and 3) the strong influence of reflected solar radiation during the daytime. These circumstances make the 3.5-4.0-μm window usable only during the night and when the temperatures are not very low. In other cases, preference must be given to the 10.55-12.0- or 8-12-μm interval, both of which are more universal, even though they are inferior in certain important respects to the short-wave transparency window.

Extensive calculations of radiation temperature were made in [36] for the 8-12- and 10.55-12.0-μm intervals for comparison with actual data on the underlying-surface and cloud-top temperatures from aerological sounding data obtained at 24 stations in the USSR; the variation of the difference between the actual and radiation temperatures was analyzed as a function of weather conditions. For a cloudless sky, this difference (and, consequently, the error of underlying-surface-temperature measurements uncorrected for the influence of atmospheric thickness) is greatest in the summer (reaching 9-10° at night and 12-17° during the day), when the moisture content of the atmosphere is high. The error of temperature determination for the surfaces of lower-level clouds is practically constant throughout the year, increasing slightly during the summer months. The errors of temperature measurement for the 10.55-12.0-μm interval are considerably smaller than for the 8-12-μm window (0.5-1.0° in winter, 1.5-2.0° at night and 3-6° during the day in summer). Climatological differences between the actual and radiation temperatures can be used as corrections to directly measured underlying surface radiation temperature values. /153

§3. A METHOD OF INTRODUCING CORRECTIONS FOR THE INFLUENCE OF ATMOSPHERIC THICKNESS IN DETERMINING UNDERLYING-SURFACE TEMPERATURES

Having discussed the various fundamental aspects of the determination of underlying-surface temperature from outgoing-radiation data measured in the atmosphere's transparency windows, let us now turn to concrete methods that have been proposed to account for the transformation of surface radiation by the thickness of the atmosphere.

The results cited in the two previous sections attest to the complexity of computing corrections for atmospheric thickness, which results from the inadequacy of the corresponding spectroscopic data and the sparsity of information characterizing the composition (including the aerosol composition) and structure of the atmosphere. The natural consequence is that experimental determination of these corrections is most reliable.

V.L. Gayevskiy and Yu.I. Rabinovich [37] made aircraft measurements of radiation temperatures in the Caspian Sea, Gulf of Finland, and White Sea areas and above a snow-covered surface in the Leningrad region with a view to solving the problem by precisely this approach. These measurements showed that for the 8-12-μm transparency window, the correction for atmospheric transformation of surface radiation (the airplane's ceiling was 6 km) reaches its 15° maximum at a 3.6-cm-layer content of water vapor in the thickness of the atmosphere. As we see from comparison with the calculated values presented earlier, the experiment yields slightly smaller corrections; the important point here is that the emissivities of water and snow surfaces are practically unity, so that the influence of surface nonblackness is excluded /154

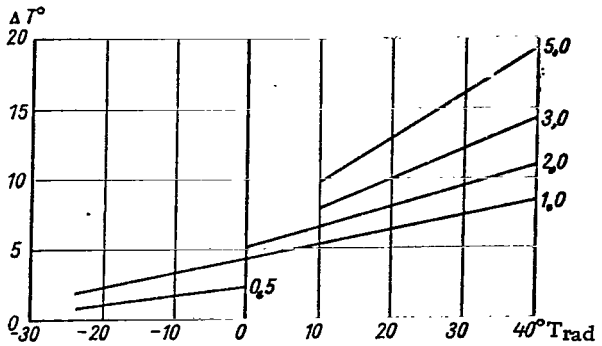

Figure 3.11. Diagram for Determination of True Underlying-Surface Temperature.

in this case.

Analysis of the experimental data showed quite satisfactory correlation between the corrections ΔT and the measured radiation temperatures T_{rad} for that particular atmospheric moisture content. The diagram shown in Fig. 3.11 can be plotted with an additional formula correction taking account of the ozone layer. It shows the correlation relationships ΔT (T_{rad}) for moisture contents of 0.5, 1.0, 2.0, 3.0, and 5.0 layer centimeters. The data of Fig. 3.11 can be used to apply the atmospheric-thickness corrections ΔT to the measured radiation-temperatures T_{rad} to obtain the true underlying-surface temperatures. The possible error of determination of the corrections is ±2.5°.

According to satellite measurements made by P.A. Bazhulin, A. V. Kartashev, and M.N. Markov [2.5] for the 8.5-12.5-μm transparency window, the difference between the radiation and actual temperatures of the earth's surface varies over a broad range, sometimes reaching (in 20% of cases) 30° and even (occasionally) 60-70°. In most cases (50%), $\Delta T \approx 15$-20°K. The authors of [5] concluded that the effective transparency of the atmosphere in the wavelength range considered averages about 50-75%. Although the maximum values of ΔT obtained in [5] are exaggerated, the data of this study generally established beyond a doubt that the thickness of the atmosphere is an essential factor.

The comparisons of data from simultaneous ground, aircraft, and satellite measurements that are made in [103, 104] are of substantial interest from the viewpoint of estimating the effects of atmospheric thickness and underlying-surface-temperature measurement errors. The chief conclusion drawn from these comparisons is that the observed discrepancies are quite large (here, of course, the impossibility of comparing the data altogether correctly is of major importance). What is essential, however, is the fact (which follows clearly from the analysis made in [134]) that the qualitative features of the temperature field are always brought out quite reliably. /155

M.S. Malkevich [38] proposed a theoretical method in which the influence of the intervening atmospheric layer is taken into account for the 8-12-μm window by introduction of a so-called transfer function. The transfer function is defined by the

relation [38-40]

$$P_{\Delta\nu}(w^*, m^*, T_0, \vartheta) = \frac{\int_{\nu_1}^{\nu_2} J_{\nu,\infty}(\vartheta)\,\varphi_\nu\,d\nu}{\int_{\nu_1}^{\nu_2} B_\nu(T_s)\,\varphi_\nu\,d\nu}. \qquad (3.1)$$

Here $J_{\nu,\infty}(\theta)$ is the outgoing radiant intensity at frequency ν at an angle θ to the vertical, ϕ_ν is a function characterizing the spectral sensitivity of the radiometer, $B_\nu(T_S)$ is the Planck function for the underlying-surface temperature T_S (it is assumed that the surface is absolutely black), and w* and m* are the effective water-vapor and ozone contents, respectively, in the thickness of the atmosphere, as computed by the formulas

$$w^* = \frac{1}{g}\int_p^{p_0} q\left(\frac{p}{p_0}\right)^a dp, \quad m^* = \frac{1}{g}\int_p^{p_0} \rho_{O_3}\left(\frac{p}{p_0}\right)^{a_1} dp,$$

where q is the specific humidity, p is the atmospheric pressure, and ρ_{O_3} is the ozone concentration. The parameter values are p_0 = = 1000 mbar, a = 0.6, and a_1 = 0.4. The limits of integration (ν_1, ν_2)are determined by the radiometer's spectral-sensitivity range.

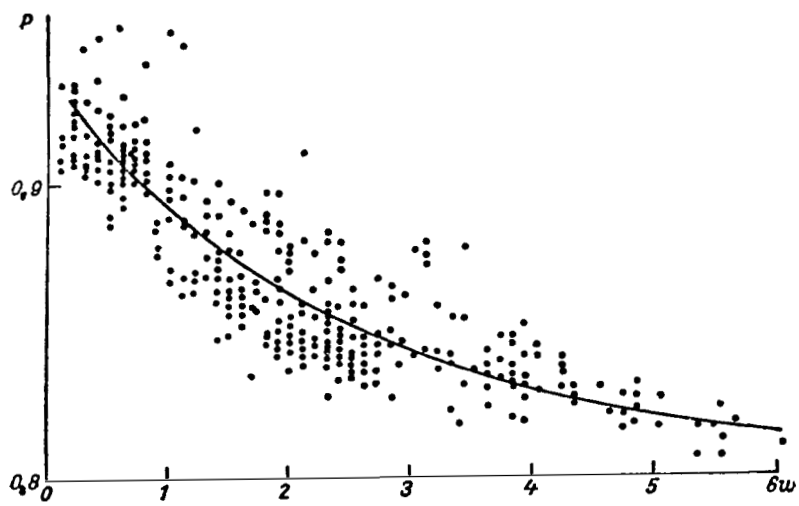

Figure 3.12. Transfer Function Plotted Against Atmospheric Moisture Content.

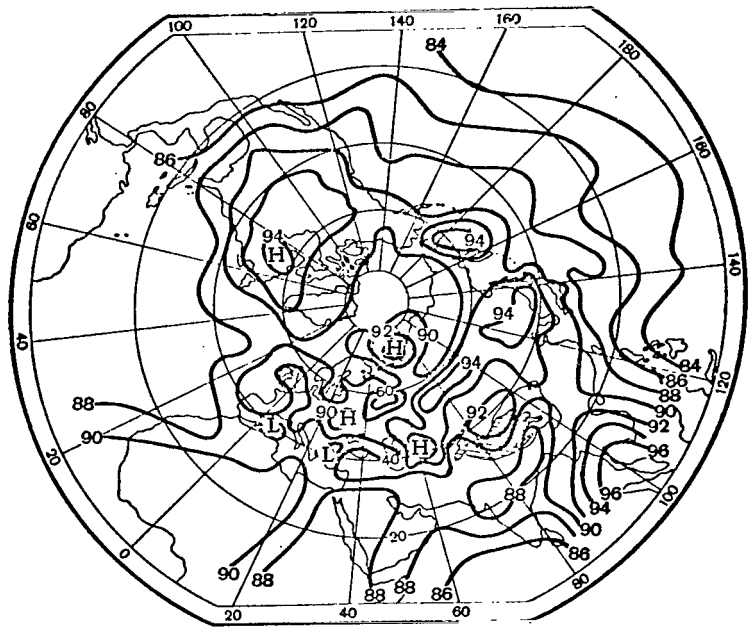

Figure 3.13. Map of Atmospheric Transfer Function. January (θ = 0°).

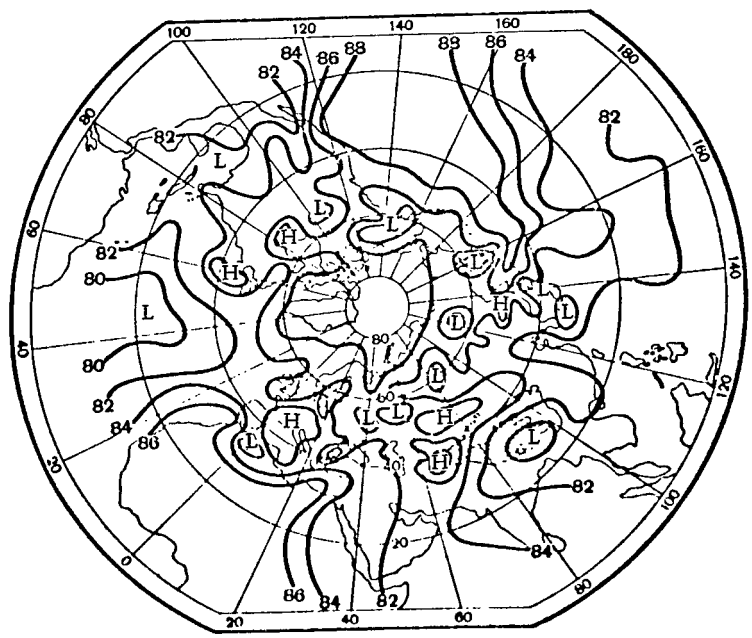

Figure 3.14. Map of Atmospheric Transfer Function. July (θ = 0°).

Since the function ϕ_ν appears in the numerator and the denominator of (3.1), it is clear that the dependence of $P_{\Delta\nu}$ on the form of ϕ_ν should be rather nonessential. As for the dependences of $P_{\Delta\nu}$ on w* and m*, the former should obviously dominate in the 8-12-μm window. We should therefore expect the transfer function to be determined with accuracy sufficient for practical purposes solely by atmospheric moisture content. This conclusion is confirmed by V.G. Boldyrev's calculations [40], the results of which appear in Fig. 3.12.

V.G. Boldyrev [39, 40] performed large-scale calculations of the transfer function for use in plotting a map of the geographic distribution of $P_{\Delta\nu}$ for the Northern Hemisphere at nadir angles θ /156
of 0, 30, 45, 60, 72, and 78°. Figures 3.13 and 3.14 present maps of this type for January and July and θ = 0 (the transfer-function values are expressed as percentages). The transfer-function values for any other nadir angle can be determined with sufficient accuracy by the following approximation formula:

$$\frac{P(\vartheta)}{P(\vartheta=0)} = 1 + a\vartheta + b\vartheta^2. \qquad (3.2)$$

Figures 3.13 and 3.14 illustrate the extremely complex geographic and seasonal variability of the transfer function. However, a definite dependence of $P_{\Delta\nu}$ on latitude is observed: in general, it diminishes with decreasing latitude, obviously as an effect of the atmosphere's increasing moisture content. The effects of the continents and oceans can be traced on the maps displayed, along with those of certain anomalies (thus, for example, there is a distinct low over Hindustan). The largest annual variation of $P_{\Delta\nu}$ is observed in middle latitudes (for example, its amplitude reaches 0.10-0.13 over the Urals and Siberia). Naturally, the substantial space-time variability of the transfer function makes it necessary to use the most concrete calculated $P_{\Delta\nu}$ available for the stations and seasons concerned. V.G. Boldyrev [42] developed a computer method for drawing underlying- /158
surface-temperature maps in which transfer-function data are used to apply atmospheric-thickness corrections.

The above calculated results for the transfer function were obtained by the use of climatological data on the stratification of the atmosphere. M.S. Malkevich [38, 41, 43] proposed a method of correcting the transfer function to take account of atmospheric stratification (vertical temperature and humidity profiles) as determined from a priori statistical information (the autocorrelation and mutual correlation functions of the temperature and specific-humidity fields) in combination with data from underlying-surface-temperature determinations (in the sense of a first approximation, i.e., at first without considering the influence

of stratification).

TABLE 3.13. TRANSFER FUNCTION ACCORDING TO MEASUREMENT DATA AND CALCULATIONS

Flight No.	Maximum altitude, meters	ΔT	Transfer Function			
			P	P_1	P_2	$\overline{P}$
1	3000	4	0,915	1,005	1,005	
2	4500	3,5	0,927	0,983	0,990	
3	4500	9	0,832	0,976	0,986	0,90
4	4500	9	0,837	0,942	0,990	
5	4500	12	0,792	0,959	0,962	

We must, however, stress the perhaps obvious fact that no calculated transfer function value can be considered altogether reliable because of the approximate nature of the calculations. This point is demonstrated convincingly, for example, by the aircraft measurements of outgoing radiant flux made in the 8-12-μm transparency window at altitudes up to 4500 m by A. K. Gorodetskiy, A.S. Gurvich, and A.V. Migulin [107]. Table 3.13 presents radiation-temperature differences ΔT measured by these authors at levels from 50 m up to the sounding ceiling together with transfer-function values obtained from experiment (P), calculated by two methods (P_1 and P_2), and taken from V.G. Boldyrev's climatological data [40] ($\overline{P}$).

The calculated transfer-function values are found to be systematically high, indicating that attenuation of the surface radiation by the thickness of the atmosphere was not fully taken into account. Another important point is that comparison of the measured and calculated vertical radiation-temperature profiles shows /159 much more smoothing of the calculated values (from the standpoint of the altitude depeneence) as compared with the experimental values.

The inadequacy (exaggeration) of the calculated transfer function for the 8-12-μm window as compared with the actual value was also detected by A.K. Gorodetskiy, Ye.F. Klimchuk, and M.S. Malkevich [151] in analysis of data measured on the Kosmos 149 satellite. Their conclusion was that the aerosol effect is the principal cause of the observed disagreements.

The aircraft measurements of A.V. Migulin [108] showed that the transformation of radiation from the underlying surface by the atmosphere drops off sharply if the measurements are made in the narrower 10-12-μm wavelength interval. Flights at altitudes up to 5 km over the Caspian Sea during atmospheric inversions showed that the radiation temperature remains practically constant in

this case up to the sounding ceiling.

D. Wark, G. Yamamoto, and J. Lienesch [44] developed a method for applying atmospheric-thickness corrections to the measured radiation temperature for reduction of measured outgoing-radiation data obtained in the 8-12-μm transparency window with the Tiros five-channel radiometer. This method is based on the use of calculated results for the outgoing radiation in the transparency window (with consideration of radiometer spectral sensitivity) for 106 different atmospheric stratification models. Analysis of the calculated data for the Tiros II weather satellite radiometer showed that the following approximation is fully satisfactory:

$$(\Delta T)_\vartheta = T_s - T_{\text{rad}}(\vartheta) = \frac{K}{\eta C - DT_{\text{rad}}(\vartheta)} - \zeta H. \qquad (3.3)$$

Here T_s is the true surface temperature, and $T_{\text{rad}}(\theta)$ is the radiation temperature measured at nadir angle θ. The coefficients η and ζ depend on θ (θ is expressed in degrees):

$$\eta = 1 - 1{,}018 \cdot 10^{-7} \cdot \vartheta^{3{,}1},$$
$$\zeta = 1 + 7{,}50 \cdot 10^{-7} \cdot \vartheta^{3{,}1}.$$

The parameter K = 516, C = 350, and H = 3.9. The coefficient D depends on atmospheric moisture content and varies in the range from 1.000 to 1.069, averaging 1.040.

Naturally, use of Formula (3.3) to reduce concrete data involves the use of excessively far-ranging averaging. The already noted variability of ΔT requires a large amount of detailing as a function of geographic conditions and time of year. This is done /160
in O. Lönnqvist's paper [45] by computing the corrections ΔT with the aid of a specially plotted radiation nomogram prepared for calculation of the outgoing radiation in the 7.5-13.5-μm transparency window (with consideration of radiometer spectral sensitivity). Table 3.14, which is borrowed from [45], characterizes the corrections $(\Delta T)_\theta$ as functions of atmospheric stratification.

From the standpoint of the results shown in Figs. 3.13 and 3.14, we may assume that it would be advisable in this case to construct maps of the geographic distribution of ΔT for various seasons (maps of this kind were prepared by V.G. Boldyrev for the Northern Hemisphere).

Statistical correlation links between the outgoing radiation in the 8-12-μm atmospheric transparency window, underlying-surface temperature, and other parameters were studied in a number of publications (for example, [60, 61]). Using data from aerological soundings over the USSR, V.V. Puchkov and S.I. Titov [61]

TABLE 3.14. CORRECTION $(\Delta T)_\theta$ AS A FUNCTION OF ATMOSPHERIC STRATIFICATION

Atmosphere model	T_s °C	$(\Delta T)_\theta$	
		$\theta=0°$	$\theta=60°$
A (0-10° N. lat.)	+27,7	11,6	15,0
B (30-40° N. lat.)	+13,0	7,2	9,3
C (5-60° N. lat.)	—5,0	4,3	5,5
D (desert)	+39,0	8,8	11,3
E (very high humidity)	+27,0	13,3	17,5

performed large-scale calculations of this type. Table 3.15 shows values that they obtained for the mutual correlation coefficients of a number of parameters. The nomenclature is as follows: T_S, T_2, and T_4 are the air temperatures at altitudes of 0, 2, and 4 km; $F_0^\uparrow$, $F_2^\uparrow$, $F_4^\uparrow$ are the ascending radiant fluxes from the surfaces at the same levels, F_∞ is the outgoing radiation, and w_∞ is the effective moisture content of the entire thickness of atmosphere.

As this table shows, the correlation coefficient between outgoing radiation and underlying-surface temperature is 0.92. In the presence of solid cloud cover radiating as a black body at the temperature at cloud-top level (2 or 4 km), the correlation coefficient increases to 0.95. This means that correlation links of this type can be used for approximate determination of underlying-surface temperature from measured outgoing-radiation values (with even better results when they are detailed for the specific observing conditions). It is shown in [61] that the errors of surface-temperature retrieval by this method do not exceed ±2.5° if the correlation coefficients are obtained from observational data acquired within a radius of no more than 50-100 km from the point in question (this condition is, of course, a very stiff one). /161

TABLE 3.15. MUTUAL CORRELATION COEFFICIENTS FOR A SERIES OF PARAMETERS

	T_s	T_2	T_4	$F_0^\uparrow$	$F_2^\uparrow$	$F_4^\uparrow$	F_∞	w_∞
T_s	1	0,56	0,42	0,92	—	—	0,92	0,73
T_2	0,56	0	0,62	0,47	0,95	—	—	—
T_4	0,42	0,62	1	0,44	—	0,95	—	—
$F_0^\uparrow$	0,92	0,47	0,44	1	0,68	0,58	0,76	0,72
$F_2^\uparrow$	—	0,95	—	0,68	1	0,91	—	—
$F_4^\uparrow$	—	—	0,95	0,58	0,91	1	—	—
$F_\infty^\uparrow$	0,92	—	—	0,76	—	—	1	0,61
w_∞	0,73	—	—	0,72	—	—	0,61	1

Table 3.15 shows that the correlation coefficient between outgoing radiation and effective atmospheric moisture content is also so large (0.73) as to permit approximate evaluation of w_∞ from the measured F_∞.

Practical tests of methods for applying atmospheric-thickness corrections in the 8-12-μm transparency window showed that the error of the final underlying-surface-temperature determination does not, as a rule, exceed ±5°. However, it must be stressed that the temperatures determined from satellite data were compared with the results of ground temperature measurements in a Stevenson screen. That this comparison method is not altogether correct cannot be disputed.

V. Kunde [30] developed a method similar to that proposed in [44] for correction in the shortwave 3.5-4.1-μm transparency window, which is used in the infrared scanning equipment of the Nimbus satellites. As was shown in §1 of the present chapter, the shortwave window is much more transparent than the 8-12-μm window. For this reason, $T = T_s - T_{rad}$ was calculated as a function of nadir angle θ for only three atmospheric models: tropical, arctic, and standard (ARDC-1959). The results of the calculations, which appear in Fig. 3.15, indicate, however, that even in this case the influence of atmospheric thickness remains substantial, especially at large nadir angles. While $\Delta T \approx 0.3°K$ at $\theta \leq 75°$ in the case of the arctic atmosphere, the correction increases to 8.0°K at $\theta = 75°$ under tropical-atmosphere conditions. If we limit ourselves to sighting directions near the nadir, then $\Delta T \leq 2°K$ in all cases, provided that the radiating surface is absolutely black. If the emissivity $\delta = 0.9$, ΔT increases by about 2° at small nadir angles.

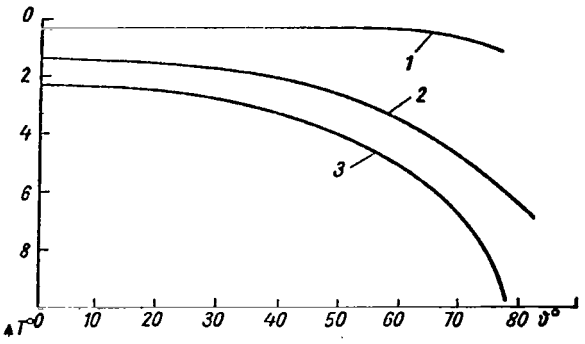

Figure 3.15. Correction ΔT as a Function of Nadir Angle for Various Atmospheric Models. 1) "Dry" arctic (T_s = 246°K); 2) standard ARDC-1959 (T_s = 288°K); 3) "moist" tropical (T_s = 305°K).

The advantages of the shortwave over the long wave transparency window are clearly evident from inspection of Fig. 3.16, which shown results calculated by V. Kunde [30] for the 3.5-4.1-μm (Nimbus I) and 8-12-μm (Tiros VII) transparency windows for the standard atmospheric stratification and an emissivity $\delta = 1$. As we see, ΔT varies from 1.4 to 4.8° in the case of the shortwave window, while the ΔT for the longwave window vary from 9.2 to 14.9° as the nadir angle varies in the 0-75° range. According to

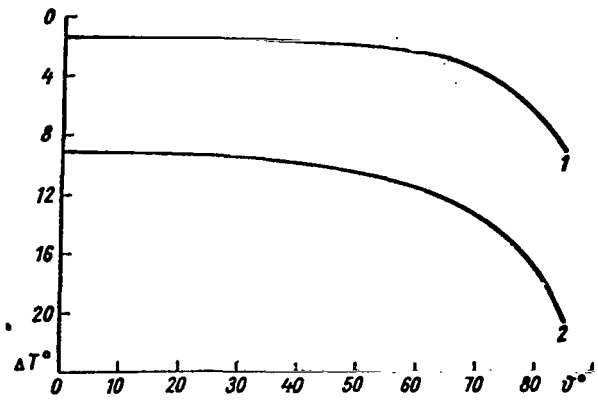

Figure 3.16. Corrections ΔT as Functions of Nadir Angle for the 3.5-4.1-μm (1) and 8-12-μm (2) Transparency Windows for Standard Atmospheric Stratification (ARDC-1959).

[100], the accuracy of underlying-surface temperature determinations with the radiometer on the Nimbus II satellite (3.4-4.2-μm window) ranged from ±1 to ±2°K with 1-5°K corrections for the intervening layer. Direct comparisons of satellite data with the results of radiometric measurements from low-flying aircraft yielded a root-mean-square deviation of 2.3° on averaging over 288 pairs of measured values. /163

F. Saiedy and D.T. Hilleary [53] used a satellite infrared spectrometer (the SIRS of Table 2.1) to determine underlying-surface temperature, selecting for the purpose an 8.75-cm^{-1}-wide spectral interval around the wave number 899 cm^{-1} (11.1 μm), where the selective absorption by water vapor is insignificant. There are only the two faint 896.6-cm^{-1} and 897.8-cm^{-1} spectral lines of the water-vapor band in this interval. The contribution of these lines to the continuous absorption coefficient, which equals 0.092 cm^2g^{-1}, is only 0.003, i.e., the over-all absorption coefficient is 0.095 cm^2g^{-1} (these data pertain to a temperature T = = 273°K). Figure 3.17 presents results obtained as the aerostat carrying the spectrometer drifted at an altitude of about 30 km. The balloon was launched at Palestine, Texas on 11 September 1964. Radiation temperatures were computed from the aerological-sounding data with the absorption coefficient stated above. Surface temperatures were measured simultaneously with a thermistor and radiometer.

Inspection of Fig. 3.17 shows that the agreement between the measured and computed radiation-temperature values is quite satisfactory. As the aerostat passed over a high cumulonimbus cloud, the transmission of radiation by the overlying thickness of atmosphere was practically unity (0.9997), so that curves 1 and 2 coincide in this case. The water-vapor content in the entire thickness of atmosphere amounted to 5.4 layer cm. As a result, the corrections to the measured radiation temperature were substantial even when this most transparent part of the 8-12-μm window was used. An attempt to use climatological aerological-sounding data to compute ΔT instead of the real stratification produced errors varying from 0.5° in the morning to 1.7° at noon. Variations of the absorption coefficient in a range of ±10% cause surface temperature determination errors not in excess of 1°. /164

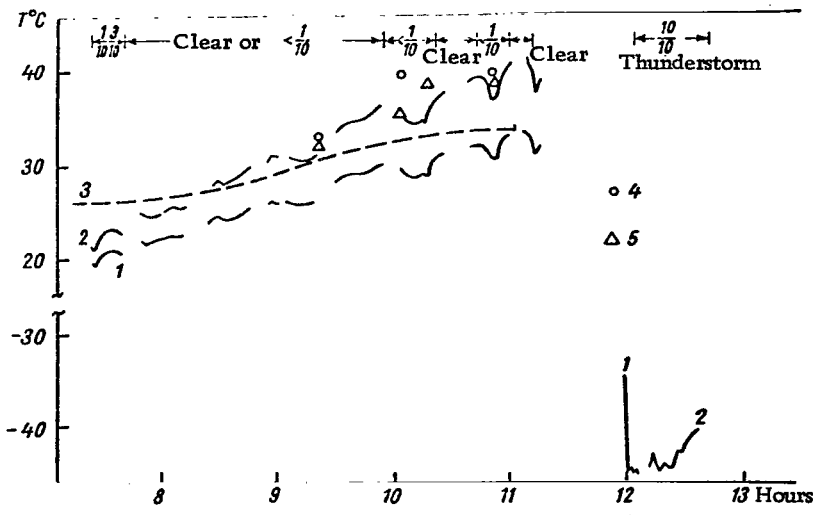

Figure 3.17. Determination of Underlying-Surface Temperature from Aerostat-Spectrometer Data. Palestine, Texas, 11 September 1964. 1) Measured radiation temperature; 2) radiation temperature computed theoretically with consideration of atmospheric-thickness effect; 3) air temperature in Stevenson screen; 4) temperature measured with thermistor at height of 1-2 mm above soil surface; 5) temperature measured with radiometer 30 cm above surface.

J. Adem [66] proposed an approximate method for determination of the monthly-average or seasonal anomalies of underlying-surface temperature and the mean-level temperature from analysis of the energy equation of the earth's surface/atmosphere system /165
using satellite data on the outgoing longwave radiation, the system's albedo, and the extent of cloud cover. It is assumed that the earth's surface, the clouds, and the atmosphere (except for the 8-13-μm transparency window) radiate as a black body. Since solution of the problem requires data on the temperature for the preceding month or season, it is proposed that the corresponding climatic values for the month or seaon in question be substituted for them.

In summarizing our discussion of the problem of allowing for atmospheric thickness in determining underlying-surface temperatures, it must be stressed that even when the most transparent segments of the transparency windows are selected, application of corrections for transformation of the surface radiation by the atmospheric thickness remains essential. Moreover, these corrections must be determined in all cases with the fullest possible consideration of the specific atmospheric stratification. The information that is used here on the emissivities of various

ground-surface types and the attenuation of infrared radiation by the thickness of the atmosphere is still admittedly inadequate.

§4. JOINT SOLUTION OF THE PROBLEMS OF DETERMINING UNDERLYING-SURFACE TEMPERATURE AND TROPOSPHERIC MOISTURE CONTENT

The results examined in the preceding section indicate that correct conversion from directly measured radiation temperatures T_{rad} to true underlying-surface temperatures T_s depends to a major degree on the availability of information on the moisture content of the atmospheric layer. This naturally suggests the expediency of finding a combined solution of the problem, with simultaneous determination of both temperature and moisture content. The first attempts at such a combination solution were made by F. Möller [46, 47, 152] and were later advanced further by E. Raschke [48-52]. B.D. Panin [96, 109] proposed an interesting solution to this problem.

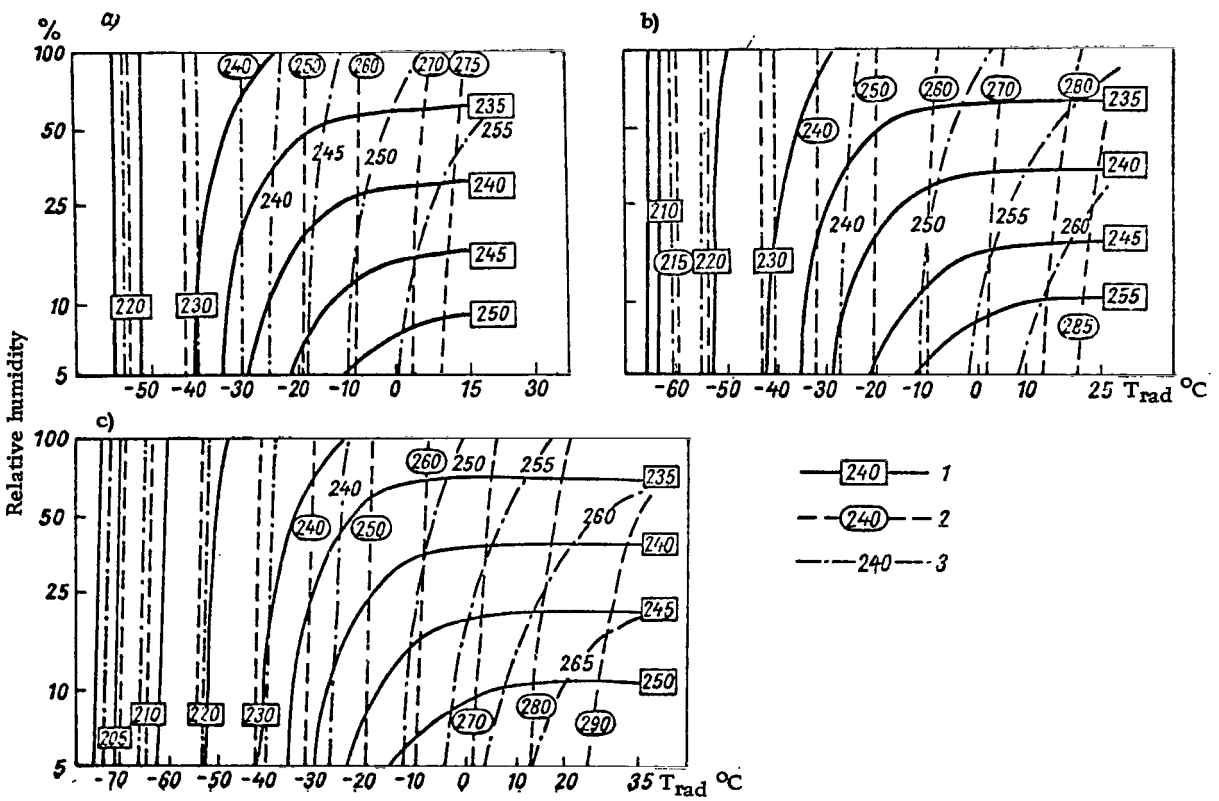

Figure 3.18. Nomograms for Calculation of Underlying-Surface Temperature and Relative Humidity. a) Atmosphere I (ARDC-1959); b) atmosphere II (subtropical); c) atmosphere III (tropical); 1) channel 1 (5.6-6.8 μm); 2) channel 2 (7.5-13.5 μm); 3) difference of readings (12-32.5 μm).

Available calculated outgoing-radiation data for the 5.8-6.8-μm (channel 1 of the five-channel radiometer on the Tiros satellites), 8-13-μm (channel 2), 7.5-32.5-μm (channel 4), and 12-32.5-μm regions of the spectrum (difference of readings for channels 4 and 2) can be used to plot isolines of calculated outgoing-radiation (or radiation-temperature) values with surface temperature and relative humidity as coordinates (Fig. 3.18). If relative humidity is plotted against the axis of ordinates and surface temperature against the axis of abscissas, the channel 2 isolines are found to be practically parallel to the axis of ordinates. Having the measured outgoing-radiation value (effective radiation temperature), we can therefore use this nomogram to find the surface temperature. Next, referring to the channel 1 isolines, we can use the known surface temperature value to determine the relative humidity in the upper half of the troposphere. The difference of the radiometer readings for channels 1 and 2 with respect to channel 4 gives the relative humidity for the lower part of the troposphere. /167

F. Möller and E. Raschke [48] showed that these isolines should be constructed for various models of the atmosphere pertaining to definite latitude belts and should then be applied to specific observational conditions. Figure 3.18 shows the corresponding nomograms for standard, subtropical, and tropical atmospheres. Using the described method of calculation, E. Raschke and J. Tannhäuser [52] used Tiros III data from the first six weeks of this satellite's active life to construct quasiplanetary distributions of underlying-surface temperature and relative humidity for the upper troposphere.

This method is also applicable for determination of water-vapor content in the atmospheric thickness by the formula

$$w = \int_{z}^{\infty} \frac{e_s(T(z))\, r(z)}{T(z)\, R^*/m_w}\, dz, \qquad (3.4)$$

where T(z) is the vertical temperature profile (the profile corresponding to the standard atmosphere for the temperature value at level z taken from observational data may be used here); $e_s(T(z))$ is the saturation water vapor pressure, r(z) is the relative humidity, R* is the unversal gas constant, and m_w is the molecular weight of water vapor.

The level of the 500-mbar surface can be taken as z in view of the fact that the outgoing radiation in the 6-6.5-μm region is shaped chiefly by the layers of the atmosphere above this level. Let us consider an example in which F. Möller's method is applied.

Let us assume that the following effective-temperature values have been obtained from observational data:

Channel	Temperature, °K
1	237.5 ± 2.5
2	272.5 ± 2.5
(4-2)	257.5 ± 2.5

Using the set of three nomograms constructed by E. Raschke for three atmosphere models, we obtain the results that appear in Table 3.16. /168

TABLE 3.16. EXAMPLE OF DETERMINATION OF SURFACE TEMPERATURE AND RELATIVE HUMIDITY

Atmosphere model	Surface Temperature, °C	Relative Humidity, %
	Channels 1 and 2	
I	9	40
II	8	45
III	7	55
	Channels 2 and (4-2)	
I	7	
II	6.5	
III	6	22

As we see, the surface temperature decreases slightly on transition from model I to model III, while relative humidity increases.

Using a statistical absorption-band model, T. Krishnamurti, A. Papetty, and M. Torres [65] analyzed outgoing-radiation data measured in the 6.3-μm water-vapor band with the five-channel radiometer on the Tiros III weather satellite with the object of determining the atmosphere's transmission of radiation in this region of the spectrum; they derived a simple formula expressing the transmission function in terms of the measured effective temperature and the underlying-surface temperature on the assumption that the layer of the atmosphere emitting radiation in the 6.3-μm band is at the average of these two temperatures. This formula was applied in [65] to obtain a relationship for determination of the total water-vapor content in the thickness of the atmosphere.

Comparison of moisture-content results calculated from outgoing-radiation measurements and aerological sounding data indicated that the atmospheric moisture content at 50% atmospheric transmission for the 6-6.5-μm band is 1.45 g/cm^2. It is important to note that the transmission of radiation in this band is highly variable with fluctuations in moisture content, diminishing, for example, from 45 to 30% as the water-vapor content rises from 1.5 to 3.0 g/cm^2.

S. Fritz and P.K. Rao [64] published a critique of the method proposed by F. Möller and E. Raschke [42-46] for determination of /169
underlying-surface temperature and tropospheric humidity in which they discussed the possibility of using the results of Nimbus II measurements in the 6.4-6.9-μm and 10-11-μm bands for a similar purpose, since the outgoing radiation in the first of these bands is determined by the vertical distributions of humidity and temperature above the ground surface (or the cloud tops), while that in the second is determined by the temperature of the radiating surface. The authors of [64] showed that in practice, serious obstacles arise to solution of this problem of determining relative humidity above the radiating surface by the "humidity diagram" method proposed by F. Möller and E. Raschke. The most formidable obstacle is that the frequently observed cirrus clouds are transparent for radiation in the 10-11-μm band. The assumption that the clouds are "black," on which the "humidity diagram" method is based, is met only in the region of the water-vapor band. The result is that calculated relative humidities above clouds are much too high, since the difference between the optical properties of the clouds in the two spectral channels determines the strength of outgoing-radiation contrast in these channels. It would therefore be much more correct to use outgoing-radiation data measured in these spectral bands to detect clouds on the basis of radiative contrast and to determine their properties, but not relative humidity (see also [162]). As for cloudless conditions, identification of zones with low relative humidity is possible in this case.

Satellite measurements for 22 June 1966 over the eastern half of the USA (16 hours 30 minutes Greenwich Mean Time) and the usual weather information were used to demonstrate these conclusions (maps showing the distributions of cloudage, relative humidity, and radiation temperature were prepared for both channels). S. Fritz and P.K. Rao also calculated the transmission of radiation at wavelengths of 6 and 10 μm as a function of the optical thickness and temperature of cirrus clouds (it was found that the dependence on cloud microstructure is very weak). For clouds that are completely opaque for radiation at 6 μm, the transmission for 10 μm may range up to 60%. If the cloud temperature is below 230°K, they also become partly transparent around 6 μm. An attempt to use humidity diagrams to determine relative humidity in the absence of clouds showed that the Nimbus II data for the 6.4-6.9-μm interval appeared to be unreliable.

Analyzing the method proposed by F. Möller with measured data and calculations, B.D. Panin [109] drew attention to the fact that the effective moisture content of the atmosphere $w^* = \int_{z_1}^{z_2} \rho_w \frac{p}{p_0} dz$ in the /170
layer of atmosphere above the "effective" level, at which the radiation temperature for the 6-6.5-μm band equals the actual temperature ($T_{rad} = T$), is always constant (ρ_w is the absolute

humidity, p_0 is the ground pressure, and p(z) is the vertical pressure profile in the layer from z_2 to z_1). It was found for data on approximately 1000 cases that $\overline{w^*} = 3.6 \cdot 10^{-3}$ g/cm^2 with a variance of $0.45 \cdot 10^{-8}$ (g/cm^2)^2. Here the height of the "effective" level undergoes considerable variations — in the cases considered, from the 600-mbar level (dry air) to the 100-mbar level (humid atmosphere).

Let us define the parameter $\zeta^* = p^*/p_0$ (p^* is the pressure at the level where $T = T_{rad}$) by the relation

$$\zeta^* = 0{,}4 \exp\left[\frac{2gT_{раз} - T_{0.4}}{R\gamma T_{раз} + T_{0.4}}\right], \qquad (3.5)$$

where g is the acceleration of gravity, $T_{0.4}$ is the air temperature at the 400-mbar level, R is the gas constant, and $\gamma = -\partial T/\partial z$.

This relationship is obtained from the barometric formula on the assumption that γ = const and the average temperature of the ζ^*-0.4 layer is $\overline{T} = (T_{rad} + T_{0.4})/2$, which can be accepted for the upper and middle troposphere in the absence of clouds (various possibilities can be used to determine $T_{0.4}$, the temperature at the 400-mbar level).

Using Tiros II and Tiros III measured data, B.D. Panin showed that there is a rather high correlation between the total effective atmospheric moisture content w_0 and ζ^* under cloudless conditions (the correlation coefficient is always above 0.70). This correlation link can be used to evaluate the total moisture content from measured outgoing-radiation data for the 6-6.5-μm band. The following empirical formula can also be used for rough estimates:

$$w_0 = 1{,}284 (\zeta^*)^{-0{,}373}. \qquad (3.6)$$

Estimation of the average absolute errors of calculation by this formula yielded 0.416 g/cm^2 (summer) and 0.112 g/cm^2 (winter).

In view of the constancy of w^*, B.D. Panin [109] also proposed the following method for determining water vapor partial pressure. Let us take an exponential law of variation of the water vapor partial pressure e with altitude: /171

$$e_2 = e_1 \left(\frac{p_2}{p_1}\right)^{3.7}, \qquad (3.7)$$

where p_1 and p_2 are the atmospheric pressures at the levels where the water vapor pressures are e_1 and e_2, respectively.

Applying (3.7), we obtain for the effective moisture content above the level $\zeta = p/p_0$

$$w_\zeta = w^* \left(\frac{\zeta}{\zeta^*}\right)^{4.7} \tag{3.8}$$

Selection of ζ is dictated by the condition that Relation (3.7) be satisfied above this level. We might, for example, take $\zeta = 0.5$.

We now have

$$e_\zeta = \frac{k_\zeta w^*}{(\zeta^*)^{4.7}}, \tag{3.9}$$

where k_ζ = const.

If ζ^* is determined from (3.5) using actual $T_{0.4}$ data, the water-vapor pressure at the 500-mbar level can be found with (3.9) with a relative error of about 10%. Knowing the water-vapor pressure at the $\zeta = 0.5$ level and having information on the spatial statistical structure of the water-vapor-pressure field, we can compute the vapor pressures at other altitudes in the troposphere.

With a view to (3.7), we can also derive the following simple formula for total moisture content:

$$w_0 = \frac{w^*}{(\zeta^*)^{4.7}}. \tag{3.10}$$

When $T_{0.4}$ and p_0 were determined from actual data, the mean absolute errors of computation of w_0 from (3.10) were 0.118 g/cm^2 (winter) and 0.433 g/cm^2 (summer).

B.D. Panin [96] also discussed the possibilities for combined use of data from outgoing-radiation measurements in the 8-12, 8-30, and 6-6.5-μm or 8-12 and 8-30-μm intervals for simultaneous determination of radiating-surface temperature (ground or cloud tops) and atmospheric moisture content (it is assumed that the cloud radiation is black-body). For this purpose, he used a simplified schematization of the radiative-transfer process based on use of an atmospheric model in which the vertical temperature profile is characterized by three radiation-temperature values for the 8-12, 8-30, and 6-6.5-μm channels. Certain further simplifications result in the following two-equation system for determination of the unknowns $\underline{x}$ and $\underline{y}$ from measured outgoing-radiation values J_{8-30} and J_{8-12}: /172

$$\begin{aligned} J_{8-30} &= 1.2xy + a_1 y + b_1, \\ J_{8-12} &= x(0.1 + 0.38y) + a_2 y + b_2. \end{aligned} \tag{3.11}$$

Here a_1, b_1, a_2, and b_2 are certain coefficients determined by the radiation-temperature values in the 8-12, 8-30, and 6-6.5-μm

channels. The quantity $x = B_{8-30}(T_\infty) = \int_8^{30} B_\lambda(T_s)\, d\lambda$, where B_λ is Planck's function and T_S is surface temperature, and $y = P_{8-30}(w_\infty)$, where P_{8-30} is the transmission function for the 8-30-μm band and w_∞ is the atmosphere's total moisture content.

The following relationships obtain for the coefficients of Eqs. (3.11):

$$\begin{aligned} a_1 &= 0{,}2B_{8-30}(T^*_{8-12}) - 0{,}7\left[B_{8-30}(T^*_{8-30}) + B_{8-30}(T^*_{6{,}5})\right], \\ b_1 &= 0{,}1B_{8-30}(T^*_{8-12}) + 0{,}4B_{8-30}(T^*_{8-30}) + 0{,}5B_{8-30}(T^*_{6{,}5}), \\ a_2 &= -0{,}62B_{8-12}(T^*_{8-12}) + 0{,}8B_{8-12}(T^*_{8-12}), \\ b_2 &= 0{,}33B_{8-12}(T^*_{8-12}) + 0{,}24B_{8-12}(T^*_{8-30}) + 0{,}03B_{8-12}(T^*_{6{,}5}), \end{aligned} \qquad (3.12)$$

where the T* are the radiation temperatures according to the measured data for the corresponding channels.

Application of the described method showed that it can be simplified even further and reduced to the use of only the measured data for T^*_{8-12} and T^*_{8-30}. In this case, the third terms in Formulas (3.12) drop out and the coefficients of the second terms assume the respective values 1.1, 0.7, 0.8, and 0.25.

Naturally, the method proposed by B.D. Panin is unsuitable in the presence of broken clouds of the middle and lower levels and cirrus clouds. It is also obvious that the prospects of the method will be determined only by large-scale tests in which extensive and reliable measured data are used.

The methods examined above for determination of underlying-surface temperature and atmospheric moisture content are based on the use of both direct physical (causal) links to the outgoing radiation and statistical correlation links. Correlation links between the integrated outgoing radiation and various parameters were used most extensively by L.R. Rakipova [110]. Using a large body of statistical material from outgoing-radiation calculations /173 with F.N. Shekhter's nomogram for various climatic regions and various seasons, L.R. Rakipova analyzed the correlations between the outgoing radiation and total cloud cover, cloud-top temperature and altitude, total water-vapor contents in the entire thickness of the atmosphere and the layer above the clouds, air temperature at the 500- and 200-mbar levels and in the tropopause, underlying-surface temperature, and the altitudes of the 500- and 200-mbar surfaces.

L.R. Rakipova's calculations indicate no correlation of the outgoing radiation with the total amount of cloudage (this means that no definite judgments can be drawn as to cloudage

distribution from the outgoing-radiation field), or with tropopause temperature, air temperatures at the 500- and 200-mbar levels, and the altitudes of the 500- and 200-mbar surfaces. The correlation with total atmospheric moisture content was found to be comparatively weak (a tendency toward increasing outgoing radiation with increasing moisture content is observed, especially at low humidities). Naturally, high correlation obtains between outgoing radiation and underlying-surface temperature (according to the data for Boyeykovo and Tashkent, the correlation coefficient varies from 0.56 to 0.84). The results of L.R. Rakipova's calculations indicate that the originally assumed correspondence between the radiation temperature determined from the integral outgoing radiation and the temperature of the level of average energy does not exist.

§5. CONDITIONS FOR DETECTION OF CLOUDAGE FROM THERMAL CONTRASTS IN THE ATMOSPHERIC TRANSPARENCY WINDOWS

Owing to the presence of thermal contrasts between cloud tops and the underlying surface, it has become possible to detect cloud fields from satellites through the inhomogeneities of the outgoing-radiation field in the transparency windows. The problem of optimum window selection is obviously solved in this case in the same way as for determination of underlying-surface temperature (see §2 of this chapter).

The outgoing thermal radiation in the 3-18-μm band was computed in [12] for various weather conditions (cloudless sky, cloudage at various levels, at various stations, and at various times of year) with the object of analyzing the variability of contrasts between underlying-surface radiation temperature and clouds of various levels and finding the spectral interval that is optimum from the standpoint of use for detection of clouds from satellites. The Ural-4 electronic-computer program provided for computation of the outgoing-radiation spectrum with a 0.1-μm wavelength step and /174
the radiant fluxes in the 3.5-4.0, 4.5-5.0, and 8-13-μm bands for a 22-layer model of the atmosphere. Water vapor, carbon dioxide, and ozone were considered as absorbing and radiating atmospheric components. When necessary, the nonblackness of the clouds as thermal radiators was taken into account.

Figures 3.19 and 3.20 illustrate calculations of the spectral distribution of the cloudless-atmosphere radiation temperature T_c for Leningrad in January and July (the line at the top characterizes the true underlying-surface temperature T_{true}). They also show the spectral curves of the energy and temperature contrasts between the tops of clouds of various levels and the underlying surface. Inspection of Figs. 3.19-3.20 shows that the radiation-temperature contrasts in the 3.5-4.0-μm interval are somewhat greater than the corresponding contrasts for the 8-13-μm band, but that the absolute outgoing-radiation values are so low in the

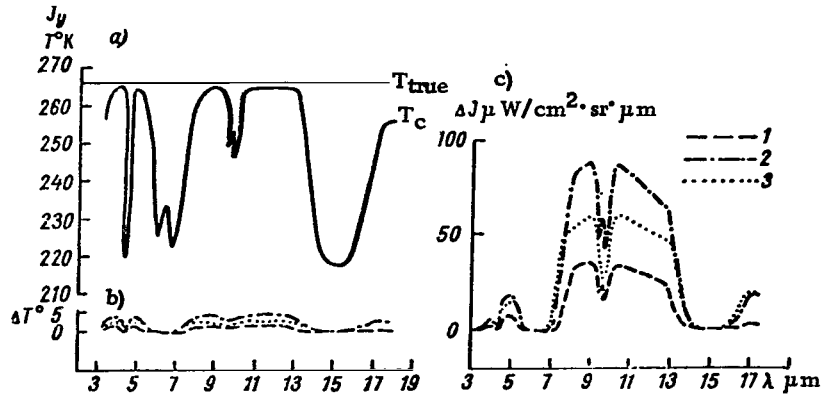

Figure 3.19. Spectral Variation of Cloudless-Sky Radiation Temperature (a), Radiation-Temperature Contrasts (b), and Outgoing-Radiation Intensity Contrasts (c). Leningrad, January. Cloud levels: 1) lower; 2) middle; 3) upper.

former case as to be at the spectral-sensitivity limits of the radiometers at subfreezing temperatures. Thus the 8-13-μm window must be considered more suitable for detection of clouds against the underlying-surface background at low temperatures. Moreover, the 8-13-μm band is more universal in the sense that it permits complete exclusion of brightening by earth-reflected solar radiation during the daytime. /175

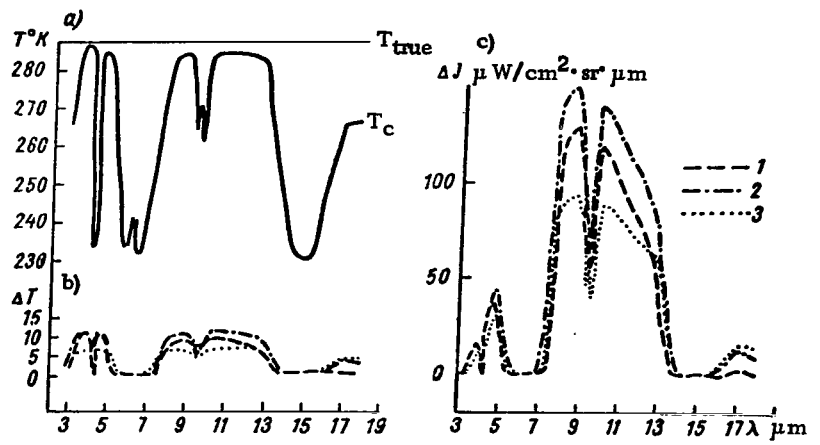

Figure 3.20. Spectral Variation of Cloudless-Sky Radiation Temperature (a), Radiation-Temperature Contrasts (b), and Outgoing-Radiation Intensity Contrasts (c). Leningrad, July. Cloud levels: 1) lower; 2) middle; 3) upper.

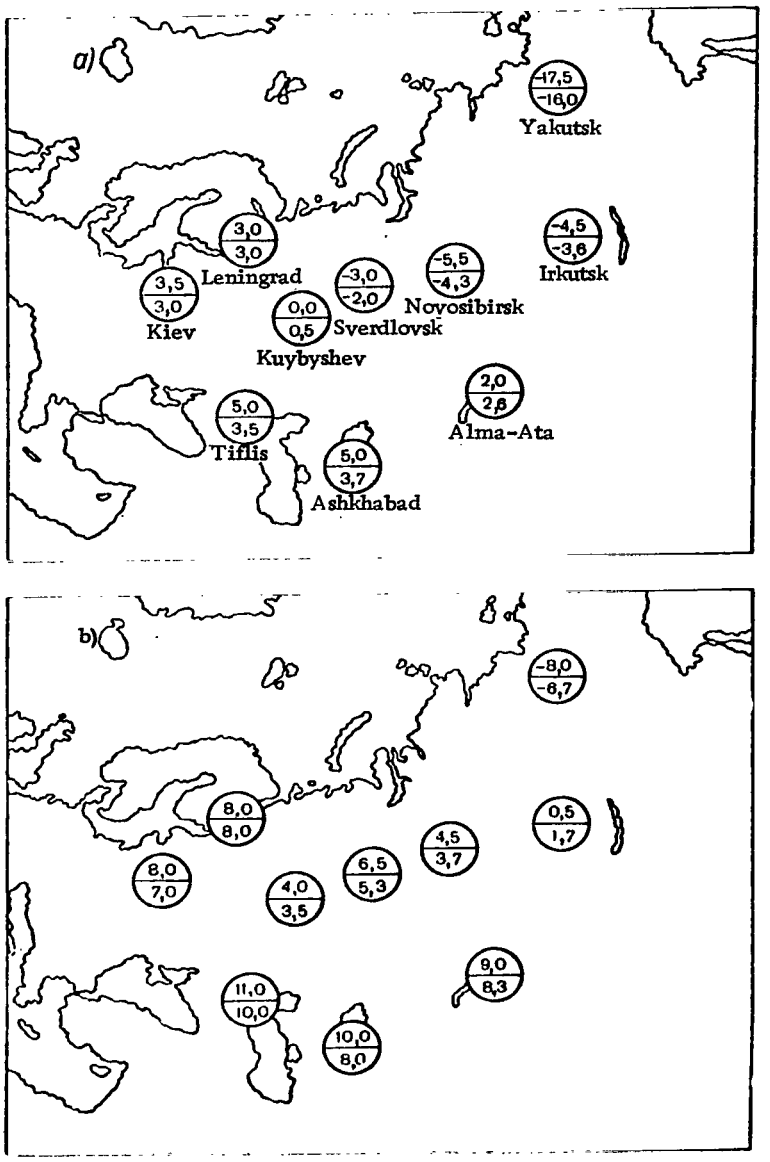

Figure 3.21. Radiation-Temperature Contrasts Between Underlying Surface and Clouds of Lower (a) and Middle (b) Levels for Various Regions of the Soviet Union. January. The numerators are values of ΔT_{rad} for λ = 3.5-4 μm, while the denominators are for λ = 8-13 μm.

For reliable interpretation of infrared cloud-cover pictures, it is extremely important to study the features of the

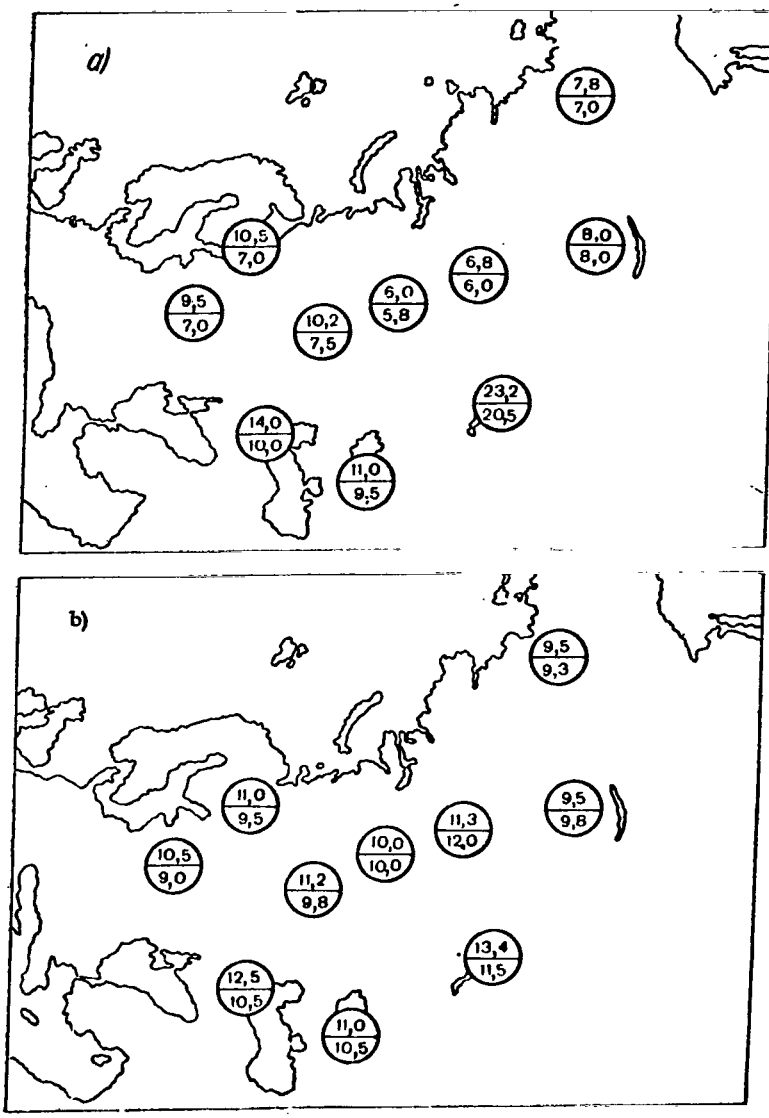

Figure 3.22. Radiation-Temperature Contrasts Between Underlying Surface and Clouds of Lower (a) and Middle (b) Levels for Various Regions of the Soviet Union. July.

geographical distribution of radiation-temperature contrasts at various times of the year. It is particularly important to investigate zones of inversion contrasts. In this context, the authors of [12] made temperature-contrast calculations that enabled them to construct charts of radiation-temperature-contrast geographical distribution for the 3.5-4.0 and 8-13-μm transparency windows for the territory of the USSR in various months.

TABLE 3.17. CONTRASTS BETWEEN UNDERLYING-SURFACE AND CLOUD RADIATION TEMPERATURES

Cloud level	Time of day	I	II	III	IV	V	VI	VII	VIII	IX	X.	XI	XII
Moscow													
Lower	Day	1,0	3,2	7,8	16,2	23,3	21,7	23,2	19,6	15,2	10,4	6,6	2,6
	Night	—1,0	—1,2	0,4	6,6	6,9	6,6	5,3	5,0	6,8	5,6	3,4	1,0
Upper	Day	4,6	6,4	8,2	10,6	12,7	13,4	14,0	12,0	9,4	8,0	7,6	4,6
	Night	3,4	3,6	4,4	7,4	6,3	6,5	6,7	6,4	7,3	6,4	5,8	6,2
Tiflis													
Lower	Day	15,6	20,0	25,2	30,0	39,2	37,3	40,4	41,2	31,0	24,6	20,2	16,0
	Night	3,2	6;8	8,8	8,8	10,8	12,4	11,6	10,7	9,0	8,8	8,8	5,6
Upper	Day	13,2	12,5	13,2	16,4	17,2	18,2	17,8	19,0	16,1	15,6	10,8	13,2
	Night	8,0	7,8	7,6	9,0	8,4	8,4	9,2	5,1	9,1	9,0	1,8	8,8
Riga													
Lower	Day	4,4	7,2	10,0	16,0	24,7	24,0	25,4	23,3	16,1	9,1	7,3	5,2
	Night	2,4	4,4	3,2	6,6	7,0	—	7,8	3,0	5,8	5,6	7,0	4,4
Upper	Day	8,4	9,2	8,0	9,6	13,8	14,2	13,4	13,0	10,1	9,1	7,1	6,8
	Night	7,6	6,0	4,0	6,6	7,4	6,9	7,4	6,7	6,9	6,8	8,7	6,4
Arkhangel'sk													
Lower	Day	0,0	1,6	6,8	14,6	18,9	24,0	22,4	18,8	12,8	9,0	—0,8	0,0
	Night	0,0	—1,6	0,0	3,0	9,6	8,6	6,2	4,2	6,8	6,4	3,1	0,8
Upper	Day	3,6	4,8	8,4	8,8	11,5	13,3	13,5	12,5	9,8	8,0	5,0	4,8
	Night	4,8	4,0	3,2	6,2	7,2	7,4	6,4	6,8	7,6	7,0	4,9	6,0
Omsk													
Lower	Day	—5,2	0,2	5,5	15,5	28,6	32,6	24,2	24,7	22,5	13,0	3,3	—2,2
	Night	—5,0	—5,2	—8,0	3,6	7,8	9,4	4,6	4,8	7,3	7,0	2,6	—5,0
Upper	Day	2,8	1,8	4,4	9,7	13,8	15,4	13,8	14,3	11,8	8,4	6,4	1,8
	Night	0,0	1,0	0,5	3,6	7,7	6,4	7,6	7,2	3,6	6,2	—8,8	1,0

Figures 3.21 and 3.22 show such charts for January and July. Features of the annual variation of the contrasts between cloud and underlying-surface radiation temperatures in the 8-13-μm transparency window for lower- and upper-level clouds were studied in [62]. Table 3.17 presents the corresponding calculated data for day and night, which simultaneously characterize the diurnal-variation features of these T_{rad} contrasts. Table 3.17 shows that the variability of the temperature contrasts is very weak.

On the Jaunary map (see Fig. 3.21), our attention is drawn to regions of negative (inversion) contrasts. At Yakutsk, for example, the negative contrasts reach -17.5° in winter for the 3.5-4.0-μm band and -16° for the 8-13-μm band. The calculations showed that, in general, there is a high degree of correlation between the radiation- and true-temperature contrasts. /179

Outgoing-radiation calculations made by Murav'yeva and N.Ye. Ter-Markaryants [54] for the 8-12-μm transparency window and various meteorological conditions (using data from aerological soundings at 24 stations in the Soviet Union) showed that for cloudless skies in the winter months, the outgoing-radiation intensities vary in the range from 1 to 1.8 $mW/cm^2 \cdot sr$ over most of the territory studied and reach 2-2.7 $mW/cm^2 \cdot sr$ in the south of the Soviet Union. In summer, the corresponding values are 3-4 and 5 $mW/cm^2 \cdot sr$. In the presence of clouds, the outgoing radiation varies from 1-2 $mW/cm^2 \cdot sr$ in winter to 2.5 $mW/cm^2 \cdot sr$ in summer. The maximum energy contrasts between the outgoing radiation of cloudless and cloudy skies occur in summer because of the maximum contrasts between the underlying-surface and cloud temperatures at this time of year. The radiation-temperature contrasts vary from -7 to 46° (they are small in winter). Inversion contrasts are sometimes observed at night. The minimum contrasts for lower-level clouds are 1-8°. In winter, it sometimes becomes difficult to trace cloudage on the basis of infrared-radiation measurements. Even in the absence of inversions, the equipment should have a temperature resolution of the order of 2-3°. During summer, resolutions of about 5-6° are adequate.

The temperature-contrast values discussed above were obtained by sighting at the nadir. As the nadir angle increases, there must obviously be a decrease in the contrasts because of the increasing importance of atmospheric attenuation. According to calculations for the 8-13-μm window, the average contrasts decrease to 7° or increase in inversions to 6° as the nadir angle increases from 0 to 82°. Here we observe a distinct annual variation: the contrast change as a function of sighting angle is smaller in winter than in summer. In practice, the angle dependence must be taken into account for angles exceeding 60-65°.

Optical properties (the emissivity of the underlying surface) are an important factor in determining temperature contrasts. Table 3.18 gives values of Δt, which characterize the decrease in

TABLE 3.18. DECREASE IN CONTRAST Δt OF CLOUDS AGAINST UNDERLYING SURFACE WITH CONSIDERATION OF SURFACE NONBLACKNESS

Spectral interval, μm	$J_{\Delta\lambda}$ μW/cm^2·sr, t_{rad} °Δt	Type of surface 1	2	3	4	5
3,5—4,0	$J_{\Delta\lambda}$	12,6	12,6	10,4	13,4	13,7
	t_{rad}	12,0	12,0	8,5	13,5	14,0
	Δt	2,0	2,0	5,5	0,5	
4,5—5,0	$J_{\Delta\lambda}$	55,1	58,3	55,8	60,7	61,7
	t_{rad}	8,5	10,5	9,0	11,0	11,5
	Δt	3,0	1,0	2,5	0,5	
8,0—13,0	$J_{\Delta\lambda}$	3440,9	3371,5	3151,6	3489,1	3555,0
	t_{rad}	8,0	6,5	3,0	8,5	9,5
	Δt	1,5	3,0	6,5	1,0	

the temperature contrasts with consideration of the earth's true emissivities according to [62, 63].

This table also gives absolute values of the outgoing radiation $J_{\Delta\lambda}$ and radiation temperature t_{rad} for various types of surfaces: 1) soil with vegetation cover, 2) desert, 3) sloping sandy beach, 4) water, 5) black body. As we see from the table, in the case of a sandy beach the decrease in temperature contrast in the 8-13-μm window reaches 6.5°. The Δt values given in Table 3.18 characterize the contrast decrease in the case of black-body clouds. If the clouds are partially transparent, the Δt become considerably smaller. /180

Adequate solution of the problem of detecting clouds against the background of the underlying surface by their thermal contrasts requires the use of statistical methods to interpret the results of measurements made with the infrared scanning apparatus. Precisely this approach to solution of the problem was taken in [105, 106].

G.P. Vimberg, Yu.A. Dranishnikov, V.I. Ivanov, and V.V. Puchkov [106] used data from the Kosmos 122 meteorological satellite to compute various statistical characteristics of the radiation field in the 8-12-μm window for various underlying-surface and cloud types (one-dimensional distribution laws of signal amplitudes, mathematical expectation, variance, third- and fourth-order central moments, autocorrelation and mutual correlation functions, etc.). The results of these calculations showed that different types of underlying surfaces and clouds differ first of all in their mathematical expectations and variances. Thus, for example,

the higher the elevation of the radiating surface, the smaller (as a rule) are the mathematical expectation (because of the lower temperature) and variance (because of the greater homogeneity). With increasing surface homogeneity, the distribution law approaches normal. In the presence of clouds above the surface of a continent or ocean, a sharp increase of the fourth-order central moments is observed, especially in the case of cumulus-shaped clouds with spaces between them. /181

Statistical reduction of recorded infrared-equipment signals from satellites enabled G.P. Vimberg, V.I. Ivanov, and V.V. Puchkov [105] to evaluate the performance of this equipment in detecting clouds. Table 3.19 presents calculated cloud-detection probabilities for various underlying surfaces as backgrounds. The last column of this table gives false-alarm probabilities $P_{f.a}$.

Analysis of Table 3.19 shows that the detection probability is quite close to unity in about 85% of cases. Low probability values occur when the ratios of the signal from the cloudage to the signal from the background are small and these signals have closely similar variances (accordingly, the video-signal distributions for these combinations of cloud and background are almost perfectly congruent).

F.F. Hauth and J.A. Weinman [153] discussed the possibilities for combined use of measured data on the angular intensity distribution of the outgoing radiation obtained with the five-channel radiometer on the Nimbus II weather satellite to solve the problem of distinguishing clouds against snow and ice backgrounds and determination of the type, altitude, and thickness of the cloud cover. The data examined pertain to the 10-11-μm and 0.2-4.0-μm bands and were obtained on 19 June 1966 over Greenland on two successive orbits.

It is shown in [153] that the brightness coefficients depend strongly in the case of shortwave radiation on the orientation of the snow-covered slopes reflecting the radiation. When the topography is known, this makes it possible to identify a snow-covered surface from features of the brightness-coefficient angular distribution. When reflection is from a horizontal snow-covered surface, the brightness coefficients (which amount to 62-66% in the cases considered) show a characteristic independence of scattering angle in the 110-135° angle range.

In the absence of clouds, the radiation-temperature field faithfully reflects the topographic peculiarities of the region under study. Cloudy zones are characterized by lower radiation temperatures and substantially greater variability of the reflection coefficient. Information on features of the brightness coefficient angular distribution, combined with data on radiation temperature, can be used for approximate determination of cloudage type.

TABLE 3.19. PROBABILITY OF DETECTING CLOUDS AGAINST BACKGROUND OF VARIOUS UNDERLYING SURFACES

Radiating surface	Object									
	Frontal clouds	Unbroken cloudage of stratus forms	Unbroken cloudage, cumulus & stratus forms	Cumulus cells	Unbroken cloudage in wake of low	Low	Cumulus clouds with gaps	Thick cumulus cloudage	Frontal clouds	$P_{f \cdot a}$
Surface of Pacific Ocean	0,005	0	0,204	0,660	0,835	0,228	0,670	0,205	0,880	10^{-3}
	0,186	0,650	0,663	0,814	0,910	0,615	0,780	0,540	0,998	10^{-1}
Mediterranean Sea	0,998	1,000	1,000	0,476	1,000	0,984	0,690	1,000	1,000	10^{-3}
	1,000	1,000	1,000	0,663	1,000	1,000	0,802	1,000	1,000	10^{-1}
Continent: North Africa	1,000	1,000	1,000	0,332	1,000	0,980	0,700	1,000	1,000	10^{-3}
	1,000	1,000	1,000	0,722	1,000	1,000	0,867	1,000	1,000	10^{-1}
Continent: Central South America	0,613	0,986	0,785	0,288	0,947	0,736	0,329	1,000	1,000	10^{-3}
	0,998	1,000	1,000	0,660	1,000	0,984	0,730	1,000	1,000	10^{-1}
Continent: Central Part of European Soviet Union	0,100	0,100	0,037	0,952	0,745	0,137	0,563	1,00	0,573	10^{-3}
	0,980	0,780	0,663	1,050	0,900	0,493	0,790	1,00	0,997	10^{-1}
Continent: Northeastern Caucasus	0,186	0,844	0,245	0,972	0,807	0,614	0,449	1,000	1,000	10^{-3}
	0,000	0,900	0,340	1,000	0,928	0,704	0,781	1,000	1,000	10^{-1}

Note. The first line of a pair gives probability values corresponding to $V_{cl} < V_b$, while the second gives values for $V_{cl} > V_b$ (V_{cl} and V_b are the amplitudes of the video signals from the clouds and the background).

Practical experience in the acquisition and interpretation /183
of infrared cloud-cover pictures has been exceptionally successful. A discussion of the problems of qualitative synoptic interpretation of the infrared pictures can be found in the monograph [57]. In a review of similar studies, V.P. Dombkovskaya [58] notes that although the basic criteria for deciphering both infrared (IR) and television (TV) pictures are the tone (brightness sensed by the eye) and structure (figure) of the picture, these characteristics are determined by totally different factors for IR and TV images; this is of fundamental importance for interpretation of the data and determines their specific application. Thus, for example, dense lower-level stratus clouds that are bright on TV pictures are difficult to distinguish from the underlying surface on the basis of IR tone.

Reference [58] considers possible ways to distinguish various types of underlying surfaces (lowlands and elevated regions, mountain ranges, water surfaces, etc.) on IR images as determined by inhomogeneities of the temperature field and the radiating properties of the underlying surface. It is shown that cloud formations are characterized by a wide variety of shapes, structures, and image tones. Lows, fronts, groups of cumulonimbus clouds, and other meteorological formations can be identified quite confidently from the shape of the cloud masses (corresponding examples are given). The belt, matte, and dome structures of IR cloud images are most clearly distinguished. Sometimes the effect of wind on the structure of upper-level cloudage is clearly seen (it is manifested, for example, in breaking up of dense cloud formations and their stretching out in the direction of the wind). V. P. Dombkovskaya considered examples of synoptic IR-image interpretation including the following groups of cloud forms: 1) cloud belts, 2) cloud vortices, 3) dense cloud sheets, and 4) indeterminate cloud formations with gaps.

Infrared images are particularly helpful for analysis of weather-forming processes in the tropical zone, where the vertically developed cloudage that is characteristic for these latitudes creates strong thermal contrasts that guarantee high contrast in infrared pictures. This makes the infrared picture a reliable tool for the analysis of such weather formations as, for example, tropical cyclones and the intertropical convergence zone. Using infrared images obtained with the Kosmos 122, Kosmos 144, Kosmos 156, and Kosmos 184 weather satellites, P.N. Belov [111] traced successive stages in the evolution of a number of tropical cyclones and analyzed the structure of the intertropical convergence zone above the oceans and continents. /184 An interesting example in which the birth and development of Typhoon Marie is analyzed in detail is discussed in [136]. The spatial-structure features of cloud cover that can be observed on infrared pictures are examined in [137].

L. Allison et al. [73] discussed various possible methods of meteorological interpretation of infrared pictures of the clouds and the earth's surface obtained with the high-resolution infrared radiometer on the Nimbus I satellite. They give a detailed analysis of infrared pictures of various regions of the globe showing a variety of meteorological situations: Hurricane Dora, Typhoon Ruby (following their movement and evolution); the onset of the monsoon over India (indicating the effectiveness of infrared pictures as a means of determining the height and vertical thickness of clouds); a meridional section along 140° E. long., including a frontal zone in the western Pacific Ocean, a strong polar jet stream, active Typhoon Wilda and a cloudless oceanic region of warm converging currents; a powerful frontal cloud system in Siberia. Also given is an example of planetary montage of fourteen infrared pictures that show the features of the global cloudage distribution and the synoptic situation in the Southern Hemisphere at the end of August 1964 (the intertropical convergence zone, Typhoon Ruby, and other features are clearly recorded). It is shown that the use of infrared cloud-cover pictures permits drastic refinement of analyses based on conventional meteorological observations. Examples are also given to illustrate the analysis of medium-scale processes (orographic cloudage).

Successful interpretation of infrared pictures with the object of investigating cloudage and underlying-surface features moved the authors of [55, 56, 154, 160] to examine the possibility of detecting ocean currents.

It is a well-known fact that ocean currents may undergo substantial changes not only over the course of a year, but also in a given month. Thus the problem of detecting ocean currents and following their dynamics from satellites is of great scientific and practical interest. Here we shall examine the warm Gulf Stream current in summer and winter (Figs. 3.23-3.24). The outgoing radiant fluxes in the 3.5-4.0 and 8-13-μm atmospheric transparency windows were computed on a Ural 4 electronic computer for the region of the Stream and the corresponding radiation temperatures were calculated. The initial data used for the outgoing-radiation calculation were the water-surface temperatures at five points (1-5) spaced at 100-km intervals (see Figs. 3.24-3.24); /185
the altitude distributions of air temperature and humidity were taken from the ARDC-1959 standard-atmosphere model. The calculation was made for a cloudless atmosphere and in the presence of unbroken clouds of the middle and upper levels. The emissivity coefficients used for the water were taken from [59]; spectral emissivities taken from [24] were introduced for the clouds.

According to [24], lower-level clouds can be regarded as practically black, i.e., as screening the water surface perfectly. For this reason, lower-level clouds were not considered in the calculation for the 3.5-4 and 8-13-μm transparency windows. The cloud-top height was assumed equal to 3.5 km for the middle-level

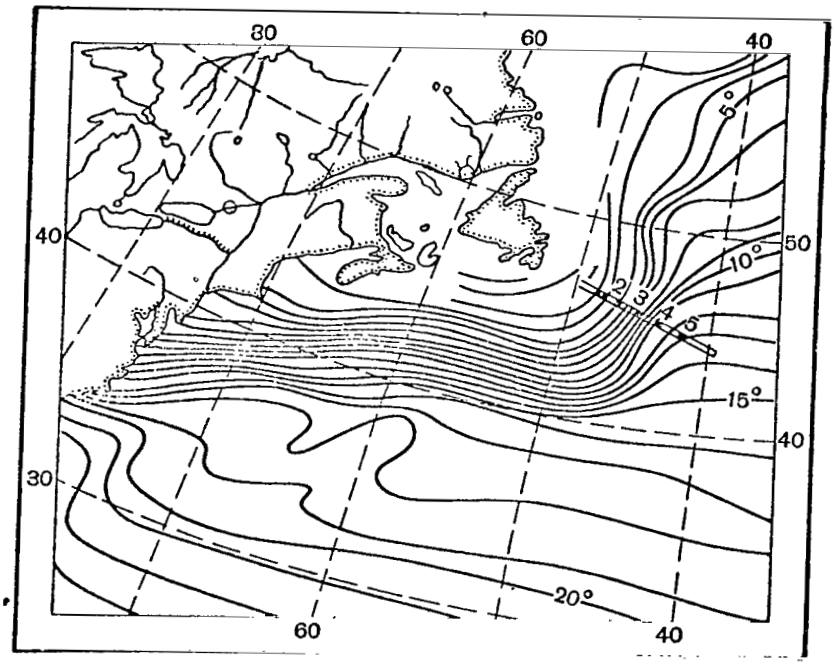

Figure 3.23. Isotherms of Atlantic Ocean Surface Water in the Region of the Gulf Stream. Winter.

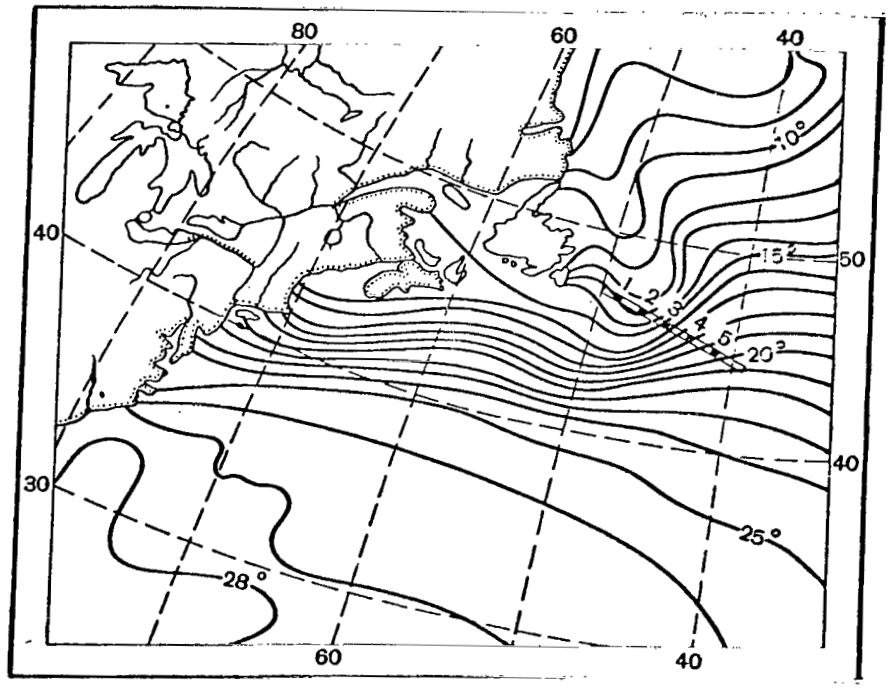

Figure 3.24. Isotherms of Atlantic Ocean Surface Water in the Region of the Gulf Stream. Summer.

TABLE 3.20. OUTGOING RADIANT FLUXES $J_{\Delta\lambda}$ IN THE 3.5-4-μm (LINE 1) AND 8-13-μm (LINE 2) TRANSPARENCY WINDOWS OVER OCEAN-CURRENT REGION AT POINTS 1-5 AND THE CORRESPONDING RADIATION TEMPERATURES T_{rad}, °C

Point No.	$J_{\Delta\lambda}$ μW/cm²·sr			t_{rad}°C			t °C
	cloudless	middle level	upper level	cloudless	middle level	upper level	
			Winter				
1	7,6	5,5	5,7	2,0	—4,0	—3,5	2,5
	3038,2	2699,7	2703,9	1,0	—5,5	—5,5	
2	8,4	5,8	6,2	3,7	—3,0	—1,7	4,5
	3136,8	2739,2	2780,9	3,0	—4,5	—4,0	
3	9,9	6,3	7,3	7,0	—1,5	0,5	8,0
	3315,0	2810,4	2919,9	6,0	—3,5	—1,5	
4	11,6	6,9	8,4	10,5	0,5	3,5	11,3
	3489,4	2880,2	3056,0	8,8	—2,0	1,3	
5	12,2	7,1	8,9	11,5	0,6	5,0	12,5
	3554,4	2906,2	3106,6	9,8	1,5	2,5	
			Summer				
1	12,5	7,2	9,1	12,0	1,0	5,2	13,0
	3581,7	2917,1	3127,9	10,3	—1,0	2,7	
2	13,7	7,6	9,9	14,2	2,0	7,0	15,0
	3692,4	2691,4	3214,3	12,0	—0,5	4,5	
3	15,1	8,1	10,9	16,5	3,2	9,0	17,2
	3816,9	3011,1	8311,4	13,8	0,5	6,0	
4	16,2	8,5	11,6	18,0	4,0	10,5	18,8
	3909,2	8048,1	3383,3	15,0	1,3	7,0	
5	17,0	8,8	12,2	19,0	4,5	11,5	20,0
	3979,4	3076,2	3438,1	16,0	2,0	8,0	

clouds and 7 km for the upper-level clouds. The calculated results appear in Table 3.20.

Table 3.20 presents values of the outgoing radiant fluxes above clouds in the current region at points 1-5 and the radiation temperatures that correspond to them in the 3.5-4 and 8-13- m transparency windows at various water-surface temperatures t, °C. /186

Table 3.21 gives radiation-temperature contrasts Δt between selected points of the stream, which are separated by a distance of 100 km (see Figs. 3.23-3.24). We see from Table 3.21 that with clear skies, the contrasts Δt between successive points of the stream are of the order of 1-3.5° in winter and 1-2.2° in summer. Here the contrasts between the radiation temperatures at two successive points increase from the periphery toward the center of the stream. Thus, for example, for cloudless winter skies, $\Delta t_{(2-3)} = 3.3°$ and $\Delta t_{(3-4)} = 3.5°$, while $\Delta t_{(1-2)} = 1.7°$ and $\Delta t_{(4-5)} = 1.0°$. It is also important to note that the temperature contrasts between points 1-3 and 3-5, which are separated by 200 km, are 4.5-5°.

TABLE 3.21. RADIATION-TEMPERATURE CONTRASTS (DEGREES) BETWEEN SUCCESSIVE POINTS 1-5 ABOVE THE OCEAN CURRENT REGION REPRESENTED IN FIGS. 3.23-3.24 IN THE 3.5-4-μm (LINE 1) AND 8-13-μm (LINE 2) TRANSPARENCY WINDOWS

Description of cloudage	1–2	2–3	3–4	4–5
	Winter			
Cloudless	1,7	3,3	3,5	1,0
	2,0	3,0	2,8	1,0
Middle Level	1,0	1,5	2,0	0,1
	1,0	1,0	1,5	0,5
Upper level	1,8	2,2	3,0	1,5
	1,5	2,5	2,8	1,2
	Summer			
Cloudless	2,2	2,3	1,5	1,0
	1,7	1,8	1,2	1,0
Middle level	1,0	1,2	0,8	0,5
	0,5	1,0	0,8	0,7
Upper level	1,8	2,0	1,5	1,0
	1,8	1,5	1,0	1,0

The radiation-temperature contrast is somewhat stronger in winter than in summer (see Table 3.21). Thus, for a clear sky, the winter Δt at the center of the stream are 3.3-3.5°, but they decrease to 2.2-2.3° in summer. /187

The contrasts Δt between adjacent points of the stream decrease markedly in the presence of clouds. Thus, the Δt values in the presence of upper-level clouds are 1.5-3.0° in winter and 1-2° in summer. Middle-level clouds reduce contrast especially strongly. The small contrasts Δt between these points of the stream indicate that it will be practically impossible to detect ocean currents from satellites in these spectral intervals when clouds are present.

Comparing corresponding temperature contrasts Δt in the two atmospheric transparency windows at 3.5-4.0 and 8-13 μm (Table 3.21), we see that the contrasts Δt are greater in the shorter-wavelength 3.5-4-μm window than in the 8-13-μm window. Thus, the maximum winter radiation-temperature gradient over 100 km is 3.5° in the 3.5-4-μm window and 2.8° in the 8-13-μm window; in summer, the Δt are 2.3° in the 3.5-4-μm band and 1.8° in the 8-13-μm band. /188

The results obtained indicate that in the absence of clouds, ocean currents can be detected from satellites in the 3.5-4 and 8-13-μm transparency windows with present-day apparatus having a temperature resolution of the order of 2-3°.

According to the calculations examined above, the warm Gulf Stream should appear on an infrared picture as a strip that is

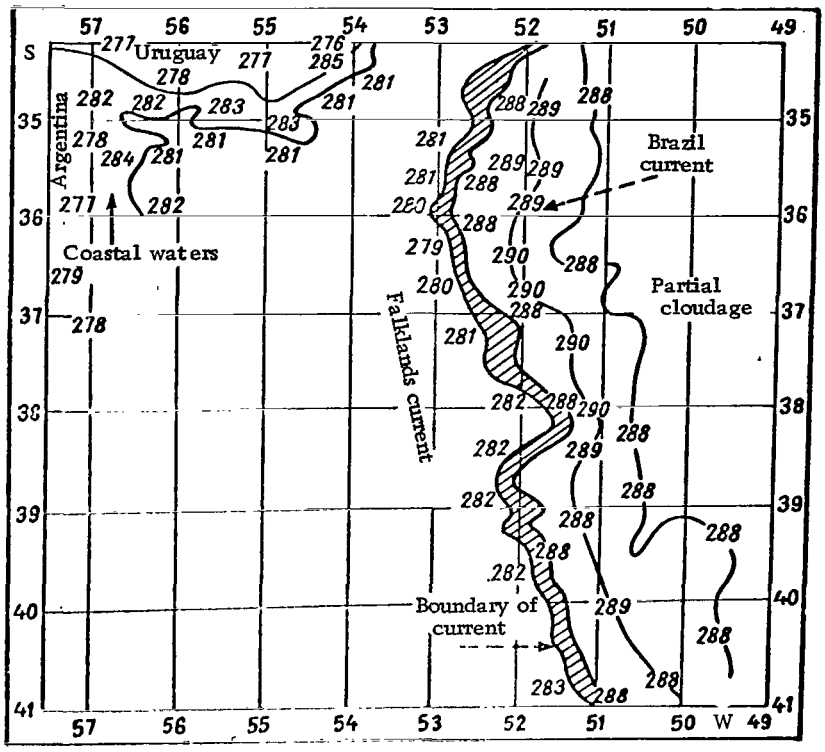

Figure 3.25. Radiation-Temperature Field in the Region of the Falkland and Brazil Currents According to Nimbus II Data (17 August 1966, 1248th Orbit).

darker than the areas surrounding it. And the Gulf Stream can indeed be traced as a dark band against the background of the colder Atlantic Ocean water on one of the thermal pictures obtained from the Nimbus II satellite in the 10-11-μm band and examined by W. Nordberg et al. [78].

Extensive experience in the detection of ocean currents on infrared pictures was acquired in analysis of Nimbus II satellite data [100]. Over 174 days of operation of the infrared scanning apparatus of this satellite, it was possible to locate the Gulf Stream in approximately 50 cases.

Figure 3.25 shows an example in which the cold Falkland and /189
the warm Brazil ocean currents were detected on the basis of Nimbus II data at midnight on 17 August 1966 (1248th orbit). As we see, the considerable temperature contrast between the two currents, which amounts to 6-8°, is enough to localize them quite dependably. In the upper left corner of the figure, our attention is drawn to the zone of warmer waters near the mouth of the Rio Plata.

When clouds are present, ocean currents can be detected from satellites only when there is a uniform veil of upper-level clouds above the region of the current, since such a veil transmits much of the thermal radiation emitted by the underlying surface. However, it should be noted that under real conditions, /190
the rule is that clouds of various levels are observed simultaneously, and in these cases it becomes practically impossible to trace thermal inhomogeneities of the underlying surface in the spectral bands under consideration unless the statistical approach to solution of the problem gives useful results.

It must also be remembered that the radiation-temperature contrast Δt_{cl} between clouds and the water surface may be comparable during the summer with the radiation contrasts Δt that are observed in study of ocean currents (as a rule, the Δt_{cl} are considerably greater, at 5-10°). This fact will also make it difficult to detect ocean currents in these spectral intervals when clouds are present. Then, like other thermal inhomogeneities of the earth's surface, ocean currents can apparently be detected in the centimeter radio band, for which clouds are practically transparent.

The progress that has been made in recent years in infrared measurement technique has made it possible to indicate very small temperature contrasts. This has made it possible not only to distinguish minute details of the earth's surface temperature field, but also to detect inhomogeneities in the atmosphere's temperature field. For example, a method is being developed successfully for detection of turbulence zones in the open atmosphere from inhomogeneities in the spatial distribution of infrared thermal radiation registered aboard aircraft [161].

§6. CERTAIN RESULTS FROM STUDY OF UNDERLYING-SURFACE TEMPERATURE, CLOUD TOP TEMPERATURE AND HEIGHT, AND TROPOSPHERIC MOISTURE CONTENT

The above methods of determining the temperatures of the underlying surface and cloud tops have been put to practical use and, in some cases, have been introduced into routine practical interpretation of satellite actinometric information and infrared images acquired with scanning IR radiometers (see [63-73, 97, 165]). Below we shall limit ourselves to discussion of a few examples of data interpretation that illustrate the fundamental possibilities at hand.

Before turning to the results, let us dwell briefly on methods of determining cloud-top heights. As was noted by H. Glahn [78], the following complicating factors must be taken /191
into account in solving the problem of determining cloud-top height from outgoing radiation measured in an atmospheric transparency window: 1) the nonblackness of the radiation from the

clouds (this pertains especially to cirrus clouds), 2) the influence of absorption of the radiation in the atmospheric layer above the cloud, 3) variations of the vertical temperature profile (especially those accompanied by inversions), 4) errors in geographical connection of the measured data, 5) measurement errors associated with changes in instrument sensitivity that elude detection, 6) the nonzero time constant of the outgoing-radiation sensor ("blurring" of the scanning spot), and 7) the inadequately high spatial resolution of the radiometer and its variation as a function of nadir angle. In [78], numerical experiments were performed with the object of detailed analysis of the effects of the last two factors. It is assumed that the satellite's radiometer is at an altitude of about 720 km and that its field covers a circle 9 km in diameter on the ground at the nadir. Within this field angle, 69 directions are defined and the outgoing radiation computed for them. The cloud distributions are assigned at random, assuming uniform heights, boundaries, and radii of individual clouds, which are circular in form. A total of nineteen cloud distribution models were examined. The calculations yielded data that characterize the variation of percentage cloudiness within the fixed radiometer field as a function of altitude and sighting nadir angle. It is shown that when the dimensions of individual clouds are somewhat smaller than the scanning spot at the nadir, large errors may result in determination of cloud heights and the amount of cloudage. The case of multilayered cloudage is most difficult for interpretation.

As for the influence of atmospheric thickness and the other factors listed above, they were discussed in detail in the earlier sections of this chapter. Here we shall consider only the possible methods of converting from the measured temperature of the top of the cloud to its height.

Naturally, solution of this problem is simplest if aerological sounding data are available. If the distribution of temperature over altitude is monotonic, the temperature value measured from the satellite that corresponds to the temperature measured with the radiosonde indicates the height of the cloud top. Usually, however, the aerological information is lacking, and this makes it necessary to use climatic or calculated data.

V.L. Gayevskiy and L.N. Guseva [79] discussed the possibilities of determining cloud-top heights from cloud radiation temperatures measured from a satellite when the vertical temperature distribution is unknown and it is therefore necessary to use a certain average value of the vertical temperature gradient. For this purpose, they used aircraft sounding data obtained in the Leningrad region (a total of 923 cases were considered) to compute vertical temperature gradients in the layer from the ground to cloud-top level. It was shown that in 80% of cases, the vertical temperature gradient ranges from 0.4 to 0.75 degree/100 m, and that only in the presence of stratus clouds was this range

/192

substantially broader (from -0.1 to 0.9 degree/100 m). If the average vertical temperature gradient is assumed equal to 0.55 degree/100 m, the errors of determination of the heights of clouds whose tops are at the 7- and 3-km levels will be 1 and 0.5 km, respectively, and will be largest for stratus clouds. It is reported that measured cloud surface radiation temperatures may differ by 3-10° from the true air temperature at this level. Such large differences limit the application of this method of determining cloud-top height, and the errors indicated above may be regarded as realistic only in the case of clouds that are at least 400 meters thick. Such clouds can be differentiated (although not in all cases) by reference to satellite photographs of the cloud cover.

Information on average climatic isotherm heights or the results of temperature calculations for specific levels in the atmosphere can be used together with climatic data on the average vertical temperature gradient. The error of cloud-height determinations based on such methods usually fluctuates from a few hundred meters to 1-2 km.

A method of determining the true temperature of the underlying surface from measured radiation-temperature data was discussed above in detail. The comparison of average monthly radiation-temperature charts constructed from Kosmos 144 weather satellite data for April and July of 1967 with monthly average climatological temperature charts of the ground surface and the atmosphere at various levels and cloudage charts made by I.V. Bugayeva and L.A. Ryazanova in [156] becomes highly interesting in this context. The radiation-temperature values were averaged over the areas of quadrangles measuring 10° in latitude and longitude. The numbers of observations for the individual quadrangles varied from 30 to 1000, exceeding 2000 in certain regions (for example, near the poles).

The data of [156] indicate that the polar regions of the Southern Hemisphere were the regions of lowest radiation temperature on the April chart (the absolute minimum near the South Magnetic Pole is -50°C). In the latitude range from 60 to 40° S., we observe a zonal distribution in which the temperature varies from -30 to -15°C. In the Northern Hemisphere, the lowest radiation temperatures occur over Greenland (-35°C), and the values in the polar region are around -30°C. In high and middle latitudes of the Northern Hemisphere, we observe considerable deviations from zonality (chiefly in the regions of Eastern Siberia and Indochina). The radiation temperature reaches 10-12°C in North Africa, and its distribution in the subtropics and tropics is distinguished by substantial departures from zonality. /193

Features of the continent and ocean distribution are clearly reflected in the outgoing-radiation field (higher radiation temperatures correspond to oceans). In July (by comparison with

April), the regions of minimum radiation temperatures over Antarctica become broader and, conversely, the temperatures rise in the Northern Hemisphere (thus, for example, Greenland ceases to be the coldest region). The regions of the radiation-temperature anomalies stand out more sharply.

Comparison of radiation-temperature charts with the corresponding cloudage and temperature-field charts demonstrates a clear relationship between nonzonal disturbances in the radiation-temperature field and the localization of cloud systems in various regions. The formation of certain radiation-temperature anomalies is determined to a major degree by orographic (accordingly, thermal) inhomogeneities of the earth's surface. The "influence zones" of elevation inhomogeneities of underlying-surface temperature and planetary charts of temperature isanomals at various levels were therefore analyzed in detail. Comparison of isanomal charts of the underlying-surface and radiation temperatures showed that the zones of the extrema were shifted and deeper in the radiation-temperature isanomal field.

An extensive series of studies has been devoted to the possibilities for use of outgoing-radiation data measured in the transparency windows in the interest of "quantitative" radiation synoptics (a survey of early studies in this field can be found in the monographs [1, 2]). Thus, for example, G. Warnecke [74-76] made a detailed analysis of outgoing-radiation data measured in the 8-12-μm transparency window on 16 July 1961 with the five-channel radiometer aboard the Tiros III weather satellite from the standpoint of their practical utilization in the preparation of weather forecasts. /194

Comparison of the outgoing-radiation field (expressed in effective radiation temperatures) in the region of Hurricane Anna, which was then in its infancy, with a television picture of the cloud cover over the same area showed full agreement between the results. The effective temperature changes by more than 50° as we pass from the highest clouds (238°K) to partial cloud cover (288°K). Use of radio sounding data together with measured outgoing-radiation results made it possible to determine the height of the cloud cover, which was about 12 km in the Dakar region. It was shown that measurements of the outgoing radiation in the transparency window can be used successfully not only to study detailed structural features of cloud-cover mesosystems, but also to characterize large-scale regularities in cloudage distribution. The combined use of data from conventional weather observations with the results of outgoing-radiation measurements makes it possible to characterize the synoptic situation much more precisely.

It was shown, for example, that an extended zone of very low temperatures in the southern and eastern parts of the USA that was detected in the radiation-temperature field corresponded to a cloud mass associated with a cold front. At the same time, cloud

masses over Lake Michigan (state of Wisconsin) and Minnesota did not produce such anomalies in the radiation-temperature field, since the clouds in this case were lower-level stratus with much warmer tops. This example shows that, in combination with satellite television pictures of the cloud cover and conventional meteorological information, radiation data for the transparency window are useful for determination of vertical cloud thicknesses. This conclusion is also illustrated by a comparative analysis of radiation data and the vertical profile for the region of the frontal cloud system, and by planetary radiation-temperature charts, which show clearly, for example, an equatorial cloudage belt associated with the intertropical convergence zone. However, it is essential to note that interpretation of the radiation data is sometimes made difficult by inadequate spatial resolution of the radiometer, since clouds of various levels are "mixed" in the instrument's field.

S. Fritz [77] discusses the possibilities for study of the diurnal variation of underlying-surface temperature, using analysis of Tiros II data for the 8-12-μm window as his example. Data from the Nimbus I weather satellite are discussed in detail in the work of W. Nordberg [71, 73] and other authors. /195

Black-body calibration of the radiometer on this satellite made it possible to determine the radiation temperatures of emitting objects with an error of the order of ±1°K. Calculation of the effective temperatures was based on the assumption that the radiating surfaces were homogeneous and isotropic. Knowledge of the underlying-surface relative emissivity is also important if it is smaller than 0.9. In this context, W. Nordberg [71] proposed a method for determining emissivity from daytime measurements of the outgoing thermal radiation and reflected solar radiation.

If we disregard transformation of the radiation by the layer of atmosphere, the daytime outgoing radiation J_d can be presented as the sum of the thermal radiation from the underlying surface δJ_B ($J_B = \sigma T^4$) and the reflected solar radiation $(1 - \delta)J_0$ ($J_0 =$ = 1.33 W/m^2 is the solar constant):

$$J_d = \delta B_s + rJ_0, \tag{3.13}$$

where the reflectivity $r = 1 - \delta$.

If $\delta = 0.5$ (and, accordingly, $r = 0.5$) and $T_s = 290°K$, then $J_B = 0.07$ and $rJ_0 = 0.7$ W/m^2. Hence it follows that the first term in the right member of (3.13) can be dropped if $\delta < 0.5$. In this case, the emissivity can be determined from the measured J_d and the known solar constant J_0. Values of $\delta > 0.5$ can be determined only if the underlying-surface temperature is known.

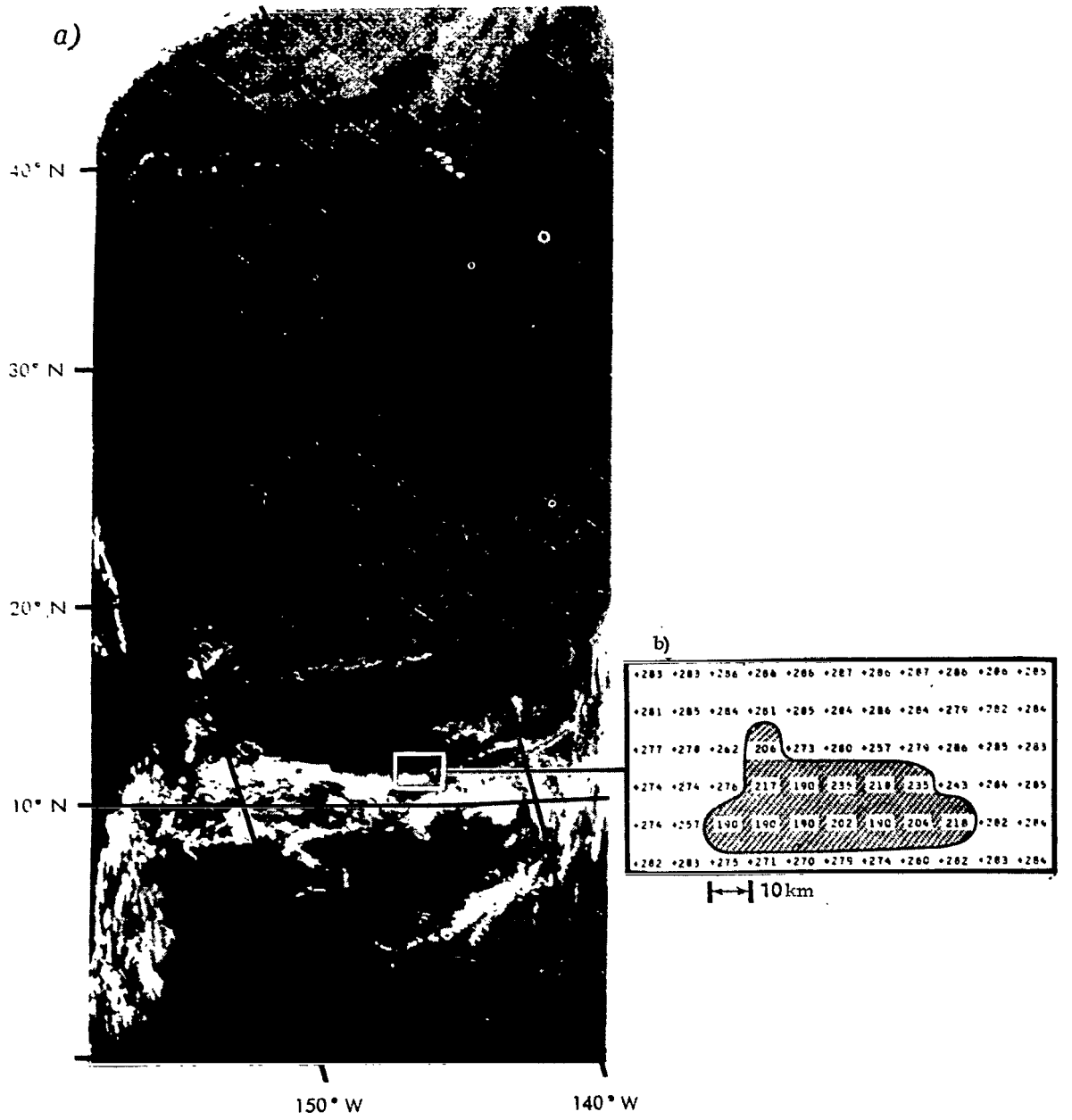

Figure 3.26. Infrared Image of Cloud Cover (Light Tones) in the North Pacific (Dark Tones) at Midnight on 20 September 1964 (a) and Spatial Distribution of Radiation Temperature in Region of High-Topped Clouds (b).

The observational data indicated emissivities greater than 0.9 for large areas of the surface (such as oceans). The possibility of emissivity determination and subsequent calculation of

underlying-surface temperature is of great importance for solution of such problems as the detection of ocean currents and fronts, the determination of soil moisture content, and study of other phenomena related to temperature-field inhomogeneity. W. Nordberg analyzed infrared cloudage pictures that illustrate the broad possibilities for analysis of the macro and mesostructures of the clouds and the topography of their tops.

Let us consider an example that demonstrates the topographic features of the cloud tops in the region of the intertropical convergence zone (ICZ) in the North Pacific on 20 September 1964 and other characteristic features of the synoptic situation (Fig. 3.26). In this case, cloud heights vary from 1 km (temperature 285°K) to 16 km (temperature 190°K) in the region of a broken ICZ cloud belt at about 10° N. lat. and an ocean-surface temperature of 293°K.

In this case, a major part of the Pacific equatorial waters /196
is covered with an enormous cloud mass occupying the latitude belt from 25 to 45° N. lat. The only areas of clear sky are found around 40° N. lat., 140° W. long. (the dark spots). At the upper left corner, we see part of a bright cloud belt associated with a strong cold front. The bright spots in the area of 38-40° N. lat., 137° W. long. correspond to very high cumulonimbus clouds, which reflect the presence of a zone of thunderstorm activity.

We note that for most of the cloudage types, the emissivity of the clouds was found to equal 0.75.

This means that a correction ranging from -5 to +10°, depending on cloud temperature and sighting angle, must be applied in calculating cloud-top temperatures from radiometric measurement data. W. Nordberg considered examples in which the temperatures of water basins are determined and demonstrated the possibility of identifying even comparatively small lakes on infrared pictures.

P.N. Belov and Yu.V. Kurilova made an interesting analysis of radiation-temperature-field features in a region of atmospheric fronts and at various stages in the development of cyclones, as well as in the intertropical convergence zone and tropical cyclones, on the basis of data from the Kosmos 122, Kosmos 144, and Kosmos 156 satellites [98].

The spatial structure of disturbances in the radiation-temperature field determined from outgoing radiation in the 8-12-μm transparency window is multiscale. Table 3.22 presents Kosmos 122 data that characterize the reproducibility of the horizontal dimensions of regions with low radiation temperatures (bounded by the -10°C isotherm) and illustrate this statement clearly.

As we see, large-scale disturbances (>200 km) account for 74% of all cases considered (228). Here, analysis shows that

TABLE 3.22. REPRODUCIBILITY OF HORIZONTAL DIMENSIONS OF REGIONS WITH LOW RADIATION TEMPERATURES

Size, km.	200	200-400	400-600	600-800	800
Reproducibility, %. .	26	47	15	5	7

disturbances in the form of elongated belts with depressed radiation temperatures and horizontal dimensions from 200 to 400 km are generally associated with cold fronts and intertropical convergence zones (occurring at a certain distance from the ground front), while disturbances with scales larger than 600 km correspond to cyclones.

E.I. Tolstikov [155] discussed the possibilities for automated acquisition of the fields of the basic meteorological elements from the outgoing-radiation field by the use of recognition-theory methods and examined the prospects for use of the starting notions of this theory — classes and realizations — to solve radiation-synoptic problems. In this context, the spatial statistical structure of 8-12-μm-window radiation fields corresponding to specific meteorological situations was analyzed in this context in [155] for two classes — cloudy and cloudless skies. Kosmos 144 satellite data for June 1967 were used as the starting materials; they pertain to times around noon (10-14 hours) in the Chukotka-Alaska region (50-70° N. lat., 170° E. long. to 130° W. long.). Seventeen realization charts were selected with consideration of available data from conventional meteorological observations. The quantitative characteristics used for the statistical structure of the radiation fields were the three-dimensional correlation and structure functions. Analysis of the behavior of these functions, which are characteristic for the various synoptic situations, made it possible to show that analysis of spatial statistical characteristics of the radiation-temperature field enables us to recognize situations to which various cloudage distributions correspond. /197

Analysis of television and infrared pictures opens the way to study of the morphology of snow and ice fields. It was found, for example, that the temperature of the snow surface in the polar-cap area near the South Pole varied from 210 to 215°K (29 August 1964). The temperature rises to 240°K near the edge of the Antarctic ice pack. Warm centers with temperature reaching 270°K were detected in the coastal strip of Victoria Land (they were probably areas of open water surface). Clouds with top temperatures 20° higher than the underlying-surface temperature (230°K) were recorded over Greenland. Analysis of infrared pictures of cloudless areas underlain by land showed a relationship between temperature-field inhomogeneities and variations in the heat capacity, thermal conductivity, and moisture of the soil. It is important here that in no case did the Nimbus I satellite data show manifestations of surface-emissivity inhomogeneity (it appears that detection of such inhomogeneities will be possible only

when radiometers with higher spatial and spectral resolutions are used). Analysis of infrared pictures permits investigation of the topography, temperature-field structure, and thermal characteristics of underlying surfaces. Determinations of temperature on areas of the ground surface with various elevations makes /198
it possible to estimate vertical temperature gradients. It has been shown that the possibility of clear differentiation of rivers less than 1 km wide on nighttime infrared pictures is governed by the higher temperatures of the land areas on the banks, where the moisture content of the soil (and, consequently, its heat capacity) is higher than at greater distances from the rivers.

Interest attaches to the method of quantitative radiation synoptics for study of hurricane cloud systems. Reference [68] gives an example in which the temperature and height of the cloud tops are determined for the area of Hurricane Gladys on 18 September 1964 (information on the vertical temperature profile from radio sounding data was used in determining the cloud heights). The temperature varied from 285°K in the "eye" of the hurricane to 210°K in the zones with the highest clouds.

Analysis of an infrared picture on which an old occluded low, an intertropical convergence zone, and Hurricane Dora were recorded simultaneously is a highly interesting example. Use of successive (taken over several days) infrared pictures made it possible to trace the evolution of this hurricane. The central part of the hurricane was covered by a homogeneous opaque cirrus cloud cover at 210°K, the lowest temperature that could be measured with the radiometer (apparently, the cloudage was inhomogeneous, but its inhomogeneities were smoothed out by the fact that the cloud-top temperature was below the measurement threshold).

A comparison with data from conventional weather observations showed that the underlying-surface temperature derived from satellite measurements over cloudless areas is approximately 5°K lower than the air temperature in the Stevenson screen, an observation that must be regarded as quite natural for nighttime conditions.

Determinations of cloud vertical thicknesses from infrared pictures taken over the Indian Ocean and Western Pacific regions made it possible to detect a heavily clouded zone over India and high clouds along the equator and over the Tibetan highlands.

Reference [68] gives a detailed analysis of the vertical atmospheric section along the meridian of 140° E. long., using an infrared picture of the cloud cover that reflects the existence at that point in time (19 September 1964) of a zone of frontal cloudage in the western Pacific, a strong polar jet stream, a developed Typhoon Winda, and a cloudless zone of warm-current convergence. It was found that, in accordance with known climatic data, the surface temperature ranged from 290°K to 300°K in the /199
area of the warm Kuro Siwo Stream. In another example, Hurricane Ruby was detected on infrared pictures for 31 August 1964 21 hours

before this could be done on the basis of weather-airplane data.

V.G. Boldyrev [35] considered an example in which the underlying-surface temperature was determined from Tiros III satellite data on the outgoing radiation for 15 July 1961, using transfer-function information (see §3 of this chapter). The mean deviation of the temperature values determined in this way from values taken from a synoptic chart was +0.9° (according to data for 25 points). If the mean annual (rather than the July) transfer function distribution chart is used to apply the corrections, the mean deviation increases to +2.0°. Reference [35] also proposed a procedure for determining the heights of cloud tops from top-temperature determinations using information on the geopotential to find the vertical temperature profile. An estimate of the error of cloud-top-height determination using data on the actual and prognostic geopotentials showed that vertical temperature profiles determined from the two potentials are approximately the same. It is also possible to use data on the climatic geopotential.

A series of papers by W. Bandeen and E. Raschke [81-84] was devoted to features of the space-time variability of the tropospheric humidity field, using the method set forth in the preceding section.

In [84], outgoing-radiation data measured from 8 February through 30 June 1962 with the five-channel radiometer aboard the Tiros IV weather satellite in the water-vapor band (5.7-6.9 μm) and the transparency window (8-13 μm) were used to plot nearly global distributions of the following parameters: 1) average relative humidity in the upper troposphere; 2) average surface radiation temperature (underlying surface or cloud tops); 3) water vapor content in the layer of atmosphere above the 500-mbar level.

As we have already noted, the method used to process the measured data is based on consideration of the fact that in the absence of clouds, the outgoing radiation in the 5.7-6.9-μm interval is generated chiefly by the 600-100-mbar layer of the atmosphere. In the presence of clouds with high tops, the latter also makes a substantial contribution to the outgoing radiation in this wavelength band. In this case, use of transparency-window measured data enables us to determine the temperature of the surface and, knowing this temperature, to "filter out" only the radiation of the atmospheric layer in the water-vapor band, which serves as an indicator of upper-troposphere relative humidity (relative humidity is assumed constant in the troposphere, and the specific humidity in the stratosphere is assumed equal to $2 \cdot 10^{-3}$ g/kg). /200

As for determination of the absolute moisture content of the atmosphere above the 500-mbar level, this quantity is determined by a somewhat generalized version of F. Möller's method that is due to W. Bandeen [87]. Bandeen pointed out that there is a good correlation between temperature at the 500-mbar level and the

moisture content of the atmosphere above this level at a relative humidity of 100%. The real moisture content can be found by multiplying the "saturation" moisture content found from the measured temperature by the relative humidity determined from satellite data. The most important factors that complicate the interpretation (and are not taken into account) include the influence of the nonblackness of the radiation from upper-level clouds, the radiation from aerosol layers, and the selectivity of the radiating properties of the underlying surface.

Only data pertaining to nadir angles smaller than 45° were processed, with separate analyses for the nadir-angle intervals from 0 to 26, 26 to 36, and 36-45°. The measured data were averaged over quadrangles measuring 5° in latitude × 5° in longitude, although this entailed the use of nonsimultaneous data for calculation of the averages (the need for averaging arose out of the strong influence of random noise in the 5.7-6.9-μm interval). The final results were obtained by averaging over 10-day and one-month periods.

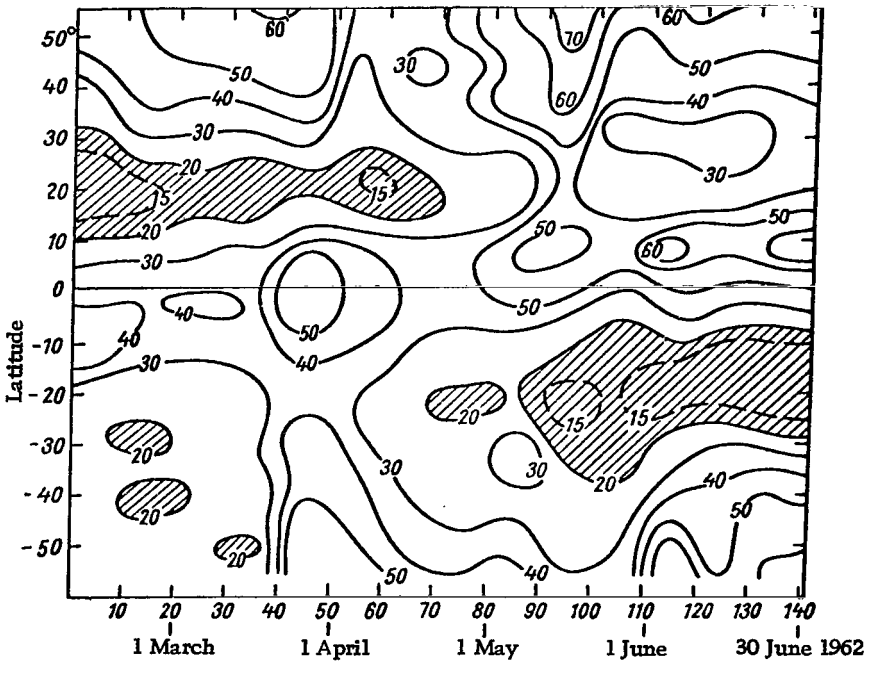

Figure 3.27. Zonal Average Distribution of Relative Humidity (%) in the Troposphere According to Tiros IV Data.

The quasiglobal distribution charts of relative humidity and radiation temperature obtained by E. Raschke and W. Bandeen demonstrate the presence of the chief regions of high humidity over South America, Central Africa, and the western Pacific near the

intertropical convergence zone. The subtropical high-pressure belts are characterized by low humidity. A narrow belt of minimum temperatures, coinciding with the position of the intertropical convergence zone, is observed in equatorial latitudes. On the whole, the radiation-temperature field faithfully reflects the climatic features of the underlying-surface and cloudage temperature distributions. Figure 3.27 presents data characterizing the zone-averaged humidity distributions for 10-day periods; they show clearly, for example, the motion of the moist (and dry) trans-equatorial belt from the Northern Hemisphere (February to April) to the Southern Hemisphere (May to June).

The spatial distribution of water-vapor content above the /201
500-mbar level reproduces the temperature field at this level almost perfectly. The upper-troposphere moisture contents diminish from 0.3-0.4 g/cm^2 near the equator to 0.02-0.04 g/cm^2 at middle latitudes. The authors of [84] stressed that use of the spectral outgoing-radiation data to be acquired in the near future with Nimbus satellites will be important for further improvement of the interpretation method.

W. Nordberg et al. [78] used Nimbus II data for a complex analysis in the interests of quantitative radiation synoptics. As we noted in the preceding section, the Nimbus II equipment made it possible to acquire pictures of the earth in various bands of the spectrum (6.4-6.9 μm, the region of the water-vapor band; 10-11 μm, atmospheric transparency window; 14-16 μm, carbon dioxide band; 5-30 μm, integrated longwave outgoing radiation; 0.2-4.0 μm, inte- /202
grated shortwave outgoing radiation). Reference [72] gives a detailed analysis of five simultaneous pictures acquired in various regions of the spectrum from data for 17 May 1966; they enable us not only to determine features of the spatial and vertical cloud-cover structure, but also to draw inferences as to the humidity of the upper troposphere and the average temperatures of the upper troposphere and lower stratosphere. The field of the outgoing radiation in the water-vapor band was found highly informative; it enables us to trace horizontal inhomogeneities in the water-vapor distribution and draw inferences as to the boundaries between air masses, zones of large-scale vertical movements, and perhaps the directions of jet streams. The case in which Hurricane Alma is analyzed as radiation-field inhomogeneities in five segments of the spectrum and a similar example of an intertropical convergence zone are also highly interesting.

A paper by L.F. Hubert, A. Timchalk, and S. Fritz [165] makes reference to the possibility of using infrared pictures of cloud cover to estimate maximum wind speeds in tropical storms by a method similar to that proposed above for reduction of television images.

§7. POSSIBILITIES FOR INTERPRETATION OF MEASURED DATA ON THE OUTGOING THERMAL RADIO EMISSION

Obviously, the possibilities that we have discussed above for interpretation of measured data on the infrared outgoing thermal radiation with the purpose of determining underlying-surface temperature or atmospheric moisture content also apply in principle to the outgoing microwave radiation. Further, when we consider that radio emission at wavelengths longer than 3 cm is virtually unattenuated by clouds, the high promise of the microwave band for solution of the underlying-surface-temperature problem becomes clear. As we know, high-precision measurements of the thermal radio emission present a serious problem in the smallness of the measured quantities (the radiant fluxes in the wavelength band around 10 cm are 10^8 times smaller than those for 10 μm). However, the use of modern microwave radiometers makes it possible to solve this problem quite successfully. This explains why a comparatively large number of papers (see, for example, [112, 132, 157, 166, 167]) have been devoted in recent years to study of the prospects for use of thermal radio emission to solve inverse problems of satellite meteorology. Leaving aside such problems as the identification of precipitation zones and study of ice cover, ocean waves, etc., we shall limit ourselves to matters involved in the determination of underlying-surface temperature and atmospheric moisture content. /203

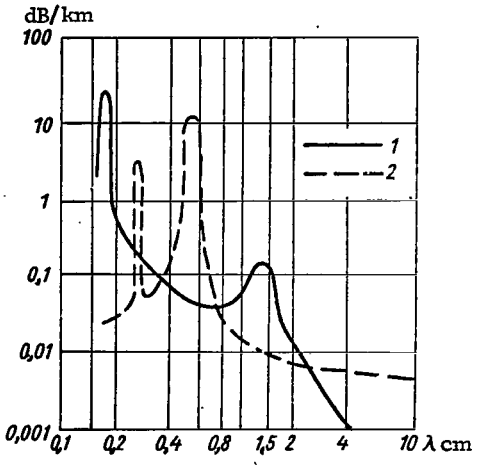

Figure 3.28. Microwave Absorption Spectra of Oxygen and Water Vapor. 1) Water vapor; 2) oxygen.

The microwave absorption spectrum of the atmosphere is comparatively poor [28, 164]. Among all of the atmosphere's components, only water vapor and oxygen, which have dipole moments (magnetic in the case of oxygen, electrical for water vapor), are active in absorption in this case. Oxygen has a system of lines around 0.5 cm. Water vapor has intense lines at $\lambda = 0.164$ and $\lambda = 1.348$ cm. Figure 3.28 gives an idea of the manner in which the oxygen and water vapor absorption coefficients depend on wavelength (we note that with the absorption coefficient α expressed in dB/km, the attenuation is determined by the formula $J = J_0 10^{-0,1\alpha x}$, where x is the distance traveled in kilometers). These data indicate that the region of wavelengths greater than 2-3 cm is an ideal transparency window for determination of the earth's surface temperature.

TABLE 3.23. EMISSIVITIES (%) OF VARIOUS SURFACES IN DIRECTION OF NORMAL FOR λ = 3.2 cm

Underlying Surface	Emissivity, %
Sea water	40
Forest	98-99
Swamp	85
Snowfield with thawed patches	75
Sea foam, surf	99-100
Soil	50

The fact that the emissivities of natural underlying surfaces are highly variable gives rise to serious difficulties. This is evident from Table 3.23, which gives data on surface-normal emissivities for a wavelength of 3.2 cm [112].

Table 3.23 shows that woodlands radiate as practically black bodies, while sea water is a very strong reflector. The latter otherwise depends very strongly on the state of the ocean surface (which becomes a black body in the presence of foam and surf). /204
The emissivity of water also depends on temperature, salinity, and the height of waves [130]. According to S.V. Pereslegin's calculations [119], the emissivity of water depends weakly on wavelength in the 3-15-cm band but increases rapidly toward shorter wavelengths. The presence of a strong temperature dependence, which is manifested in an increase in emissivity with decreasing temperature, is also characteristic for the millimeter band. The decimeter band is characterized by decreasing emissivity with increasing wavelength for salt water and by the absence of a wavelength dependence in the case of fresh water (the salinity effect is very strongly in evidence in this case).

It is quite important to consider the dependence of emissivity on the height of waves on a body of water; this can be seen from inspection of Fig. 3.29, which shows radiobrightness temperature as a function of sighting angle for various states of the ocean surface according to F.D. Jahns [115]. As we see, the sighting-angle dependence smooths out with increasing wave height (wind speed), with an accompanying increase in radiobrightness temperature. K.S. Shifrin and S.N. Ionina [123] showed that the dependence on wave height can be circumvented by using circular polarization in observations made at the nadir (the wind-speed variations of emissivity are in the opposite directions for the horizontal and vertical polarization components).

According to [115], the reflected solar radiation makes a substantial contribution in the daytime to the radiobrightness temperature of an agitated water surface at wavelengths around 1-2 cm. The resulting temperature variations may run to 10-20°K. /205
This conclusion is also confirmed by the experimental data of

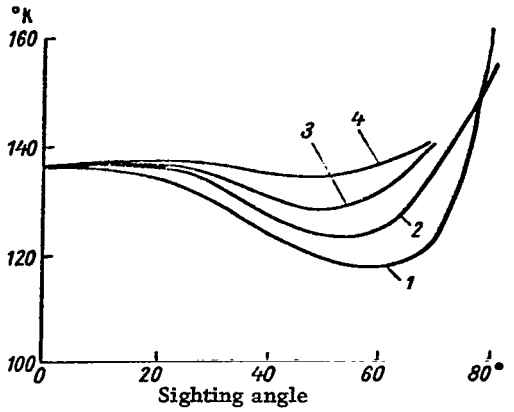

Figure 3.29. Radiobrightness Temperature as a Function of Sighting Angle for Various States of the Ocean Surface (Wavelengths 1-2 cm). 1) Smooth surface; 2) wind speed v = 4 m/sec; 3) v = = 8 m/sec; 4) v = 14 m/sec.

W.T. Kreiss [116].

The dependence of emissivity on the type and state of the underlying surface (soil moisture is important in the case of land), sighting angle, and type of polarization of the received radiation makes it quite difficult but by no means impossible to solve the problem of underlying-surface temperature determination.

The situation is simplest in the case of woodlands, which can be regarded as black-body radiators. Measurements made by D.T. Matveyev [121] over woodlands at a wavelength of 10 cm showed that in this case proper interpretation of the data is complicated by radiation from unwooded areas, which enters through side lobes of the antenna pattern (needless to say, this does not apply in the presence of a dense and extensive forested area).

The possibilities of determining water-surface temperatures have been investigated in greatest detail. In view of the difficulty of absolute brightness temperature measurements, A.S. Gurvich and S.T. Yegorov [117] made aircraft measurements of the radio emission at 9 cm in order to determine the variations of brightness temperature about a known temperature at a fixed point (the flights were made in November-December 1964 over the Caspian Sea). When the measured values were connected in this way, the /206
largest disagreement with the data of direct water-temperature measurements did not exceed 1.5-2.5°C with temperature contrasts up to 10-12°C. A similar method of connection with a known temperature was used by Yu.I. Rabinovich, G.G. Shchukin, and V.V. Melent'yev [113], who used radiometric apparatus working in the three-centimeter band (λ = 3.2 cm). The results of aircraft measurements over Lake Ladoga and the Caspian Sea using microwave and infrared radiometers were found to agree satisfactorily with direct water-temperature measurements.

Using a radiometer at 9 cm, D.T. Matveyev [120] showed that in this case, irrespective of flight altitude (transformation of the surface radiation by the layer of atmosphere is negligible), the errors of absolute surface-temperature measurements (as in other cases that are connected to a reference case) range from 1.5 to 2.5°C (the use of an antenna capable of receiving

circularly polarized radio emission excluded the effects of waves on the measurement results). This degree of accuracy was sufficient for construction of a highly detailed temperature chart of the surface of the Caspian Sea.

To a certain extent, the data of W. Nordberg, J. Conaway, and P. Thaddeus [158] stand in contradiction to the above results. These authors used a 1.55-cm radiometer for aircraft measurements (from altitudes from 20 meters to 12 km) of the microwave radiation of the ocean surface (only the horizontal polarization component was measured), and detected a very strong dependence of the emission on surface roughness (wave height), far in excess of the values predicted by theory. The difference between the radio brightness temperatures (which was practically independent of nadir angle) measured for calm and agitated (wind speed 14 m/sec) ocean surfaces was about 20°C. From this, the authors of [158] conclude that it is impossible to use data from such microwave measurements to determine the temperature of the ocean surface, and recommend that data of this kind be interpreted with a view to determining its state (roughness, wave height).

From the standpoint of determining atmospheric moisture content, useful information is, of course, available at wavelengths at which water-vapor absorption is strongly manifested. The 1.348-cm line is most convenient for use.

W.T. Kreiss [116] made extensive calculations of microwave transformation in the atmosphere; they permit quantitative estimates of the contribution made by surface radiation and the intervening atmosphere to the outgoing radiation at various wavelengths (frequencies). /207

Figure 3.30 presents the results of calculations for standard atmospheric conditions and a constant 60% relative humidity at altitudes up to 31 km. The upper part of the figure characterizes radio brightness temperature as a function of frequency for three different underlying-surface emissivities ε_s (the dashed vertical lines mark off the region around the 1.348-cm line). The bottom of the figure shows the frequency dependence of the contribution made by the surface to the outgoing radiation. /208

The data of Fig. 3.30 clearly confirm the conclusion drawn above to the effect that the atmosphere is practically transparent for radio emission at wavelengths greater than 3 cm (frequencies below 10 GHz). The radiobrightness temperature increase toward higher frequencies is due to oxygen absorption (at frequencies around 56 GHz, all three curves merge at the kinetic temperature corresponding to the lower layers of the troposphere, since the atmosphere becomes opaque here as a result of strong oxygen absorption). The influence of the water vapor line at λ = 22.235 GHz (1.348 cm) on absorption is most strongly manifest at small underlying-surface emissivities. This line is scarcely

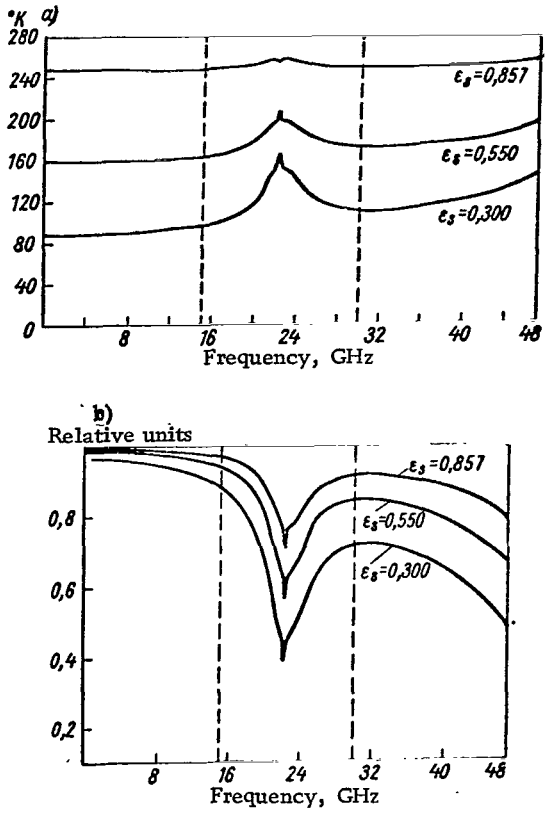

Figure 3.30. Transformation of Microwave Radiation by Intervening Atmosphere for Various Underlying-Surface Emissivities ε_s. a) Radiobrightness temperature (°C) as a function of frequency; b) contribution (relative units) of underlying-surface radiation to radiobrightness temperature after passage through thickness of atmosphere.

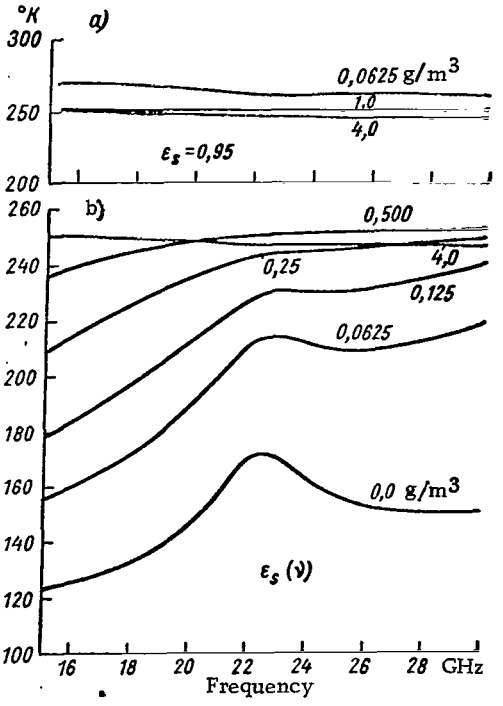

Figure 3.31. Spectral Distribution of Outgoing Radiation (Radiobrightness Temperature, °K) Over Land (a) and Sea (b) in the Presence of Cloudage 6557 Meters Thick and Various Water Contents (g/m³).

discernible at large ε_s. Since the same thing happens at high atmospheric humidities, this makes it difficult to distinguish the effects of surface emissivity (if it is unknown) and moisture content on the outgoing radiation.

D.L. Croom [126] calculated radiobrightness temperatures in the regions of the water vapor rotational lines at 1.35 cm and 0.164 cm. Special attention was given to an analysis of the influence of stratosphere stratification on the outgoing-radiation (brightness-temperature) values. The calculations were made for standard-atmosphere conditions, using two different vertical distributions of water-vapor concentration above 16 km. The calculations for the 1.35-cm line were made for various earth-surface

reflectivities (0, 0.1, 0.3, 0.5, and 1.0). The results showed that the outgoing radiation in the 1.35-cm region depends strongly on the nature of the underlying surface and is relatively insensitive to the moisture content of the entire intervening atmosphere.

While the 1.35-cm line manifests as an emission line, the line at 0.164 cm resembles an absorption line. Because absorption is very intense around 0.164 cm, the effective thickness of the radiating atmospheric layer drops off sharply as the frequency varies from the wings toward the center of this line. This is also accompanied by a decrease in effective temperature, since air temperature diminishes with altitude (if we disregard the influence of the stratosphere), i.e., a minimum is formed at the line center.

Even under the most favorable conditions (ocean surface), the variation of humidity in the stratosphere causes variations amounting to only 5°K in the effective temperature for the 1.35-cm line. At the center of the 0.164-cm line, these variations are much more strongly in evidence, reaching 45°K. In this case, however, the influence of stratosphere temperature on the outgoing radiation is very strong. For this reason, temperature data must /209
be available for determination of the stratospheric moisture content from the emission in the 0.164-cm line.

In the presence of clouds, the outgoing-radiation spectrum in the region of the 1.35-cm water-vapor line changes sharply, as can be seen from inspection of Fig. 3.31, which shows the results of W.T. Kreiss' calculations [116] for land ($\varepsilon_s = 0.95$) and sea (with consideration of the frequency dependence of ε_s) for a cloud thickness of 6557 meters and various water contents (from 0.0 to 4.0 g/m^3). At a water content of 4.0 g/m^3, the cloud becomes totally opaque and the outgoing radiation is identical to the black-body radiation at cloud-top temperature. Naturally, the properties of the underlying surface are not reflected in any way in the outgoing-radiation spectrum in this case.

Analysis of the data of Figs. 3.30-3.31 from the standpoint /210
of determination of atmospheric moisture content from the outgoing radiation leads at once to the conclusion that a solution to this problem can be found only for cloudless-sky conditions. And even in this case, the influence of the "hot" background presented by the underlying-surface radiation with its strongly varying emissivity creates a very difficult situation. Only over water surfaces is the presence of the water-vapor line clearly in evidence in the outgoing-radiation spectrum. The results of calculations made by Yu. I. Rabinovich and G.G. Shchukin [114] for the 1.35-cm wavelength and various stratifications of a cloudless atmosphere over the ocean indicate that in this case there is a distinct dependence of radiobrightness temperature on the moisture content of the intervening atmosphere. The effects of variations in

atmospheric stratification and salinity are comparatively minor. The total absolute error of the humidity determination is characterized by the following data:

Range of humidity variation	0-10	10-25	25-55
Absolute error, mm of precipitated water	2.5	3.5	4.5

K.S. Shifrin, Yu.I. Rabinovich, and G.G. Shchukin [163] made aircraft measurements of the ascending microwave fluxes using a four-channel radiometer working at wavelengths of 0.8, 1.35, 1.6, and 3.2 cm (the average sensitivity of the radiometers was 1.2°K with a time constant of 1 second). The data from measurements in the Caspian Sea and Lake Ladoga areas (the flight altitudes ranged up to 9-10 km) for the 1.35-cm wavelength were used to determine the humidity of the intervening cloudless atmosphere. Comparison with the results of aircraft soundings showed an average relative error of 8%, with maximum errors no greater than 16% (in absolute terms, this corresponds to 2.5 and 4.0 mm of precipitated water).

We note in conclusion that the possibility of determining humidity from measured radio-absorption data for the intervening atmosphere has been affirmed in a number of papers (see, for example, [118, 122, 124, 125, 127-129, 131] . W.B. Lenoir [132] demonstrated the possibility in principle of determining the average temperature of a 20-km layer of atmosphere centered at the 75-km level from measured data on the outgoing radiation in the 0.5-cm oxygen line.

The first direct measurements of outgoing microwave radiation at various frequencies were made on the Kosmos 249 satellite. Interpretation of these measurements has made it possible to determine a series of geophysical parameters, including the integrated moisture content of the atmosphere [140, 159].

Chapter 4

/211

SEMIEMPIRICAL INTERPRETATION OF MEASURED DATA ON THE OUTGOING THERMAL RADIATION

In the preceding chapter, we examined the possibilities for quantitative interpretation of measured outgoing thermal radiation data with the purpose of determining the temperature of the underlying surface or the cloud tops, as well as qualitative interpretation within the framework of radiation synoptics. Analysis of satellite actinometric information indicates the existence of a whole series of quite reliable correlation links between the characteristics of the radiation field and various meteorological parameters. Use of these relationships enables us to determine various meteorological elements from radiation data by the use of semiempirical interpretation methods. The object of the present chapter is to discuss these possibilities. We shall also consider the problem of determining stratosphere temperature from measured outgoing radiation data for a broad segment of the 15-μm carbon dioxide band, a problem with a clear physical basis.

§1. CORRELATION LINKS BETWEEN THE OUTGOING RADIATION AND CERTAIN METEOROLOGICAL PARAMETERS

The energetics of the atmosphere. Since the outgoing radiation is a component of the atmosphere's energy budget, it is natural to seek first of all relationships between the outgoing radiation and the energy-budget components, primarily the long-wave radiation budget (the long-wave radiant influx of heat for the entire thickness of the atmosphere). R.R. Sabatini and V.E. Suomi [1] used actinometric-sounding data to find the correlation link

/212

$$F_\infty = kF_a + b, \tag{4.1}$$

where F_∞ is the outgoing radiation, F_a is the long-wave radiation balance, and k and b are empirical coefficients.

K.Ya. Kondrat'yev and L.N. D'yachenko [2] showed that Relation (4.1) is satsified only when it is adapted for clear and cloudy sky conditions and the warm and cold seasons. The correlation of the (4.1) type is particularly high in the presence of low clouds of the FrNb, Ns, and Cb types, when the effective radiation from the underlying surface is practically zero (i.e., the outgoing radiation and the long-wave balance are similar in magnitude).

TABLE 4.1. VALUES OF COEFFICIENTS IN THE EMPIRICAL FORMULA (4.1)

	Summer		Winter	
	overcast	clear	overcast	clear
k	0,948 (0,76)	0,693 (0,65)	0,845	0,701
b	0,017 (0,097)	0,138 (0,152)	0,041	0,100
r	0,99 (0,85)	0,92 (0,87)	0,98	0,89
n	33	66	54	25

Table 4.1 gives the corresponding values of the coefficients in Formula (4.1), the correlation coefficients r, and the number of cases considered, n. The coefficients according to [1] are given in parentheses.

This table shows that for a given outgoing radiation, the long-wave balance is considerably larger for cloudy than for clear skies (the coefficient b is much smaller in the former case). This difference is about 0.08 cal/cm^{2}min or 30% of the outgoing radiation; this indicates the existence of differentiation between clear and cloudy sky conditions.

Use of the correlation formula (4.1) is of great interest from the standpoint of the possibility of determining the long-wave component of the radiant heat influx from satellite data on the outgoing radiation. However, it must be stressed that the raw observational material used to compute the coefficients of Formula (4.1) cannot be regarded as adequate. This formula requires a firmer statistical justification.

W.L. Smith, L.H. Horn, and D.R. Johnson [3] made an attempt to differentiate the correlation link between the outgoing radiation and the radiant heat influx for various layers of the atmosphere, using data from 64 series of vertical longwave radiant flux profiles measured with actinometric radiosondes and satellite (Tiros II) measurements of the outgoing radiation in the 7-13-μm transparency window and a broad region in the infrared (7-32 μm) for the period from 19 December 1960 to 18 January 1961. As a rule, the time difference between the satellite data and the actinometric radiosonde results did not exceed 4 hours (increasing to 7 hours only in a few cases). /213

The correlation between the radiant heat influx in 28 layers of the atmosphere and the outgoing radiation in the transparency window was found to be higher than that for the integrated long-wave radiation, partly as a result of the higher accuracy of the transparency-window measurements. In all cases, the correlation-coefficient values increased with increasing thickness of the layer for which the radiant heat influx is determined. If the thickness of the layer of atmosphere is increased from ground

level upward, the correlation coefficients become quite high even for a layer whose upper boundary is near 600 mbar.

Analysis of data for a clear sky or insignificant cloudiness indicated that in this case the outgoing radiation best characterizes the radiant heat influx in the layer from the ground to the 600-mbar level. In the presence of clouds, there is a negative correlation for the heat influx in the layer from the ground to the 700-mbar level, but a positive correlation if the upper boundary of the layer is raised to the 600-mbar level or higher. Because of this difference, the correlation link is question may be more reliable in the presence of independent data on the cloudage. It will probably also be necessary to take account of the difference between the correlation links as it depends on latitude and other factors. Needless to say, continued study using a larger volume of measured data will be even more necessary in this case.

P.A. Davies [4] also analyzed the possibilities for use of Tiros III weather satellite outgoing-radiation data to evaluate nonadiabatic heating and cooling of the atmosphere. In this case, the analysis was based on satellite data for four orbits in mid-July of 1961, which were averaged over squares measuring 4° in latitude × 4° in longitude; only results pertaining to nadir angles smaller than 45° were used in the reduction (at the nadir, the area covered by the radiometer's field is about 3700 km^2). Since the basic factor determining the generation of zonal available potential energy (the part of the potential energy that can be converted to kinetic) is meridional differential heating (or cooling), the basic attention in [4] was concentrated on this quantity. /214

The following components of the heat influx were computed on the basis of cloudage and atmospheric-stratification information: radiant cooling due to long-wave radiation, heating resulting from absorption of solar radiation, the heat influx due to phase transformations of water in the atmosphere, and turbulent heat exchange between the underlying surface and the atmosphere.

P.A. Davies noted that the correlation between the outgoing radiation and the atmosphere's long-wave balance is governed by the following circumstances. Both the outgoing radiation and the radiant heat influx are determined primarily by cloudage conditions. Cloud-top height is decisive for the outgoing long-wave radiation, and the position of the cloud bottoms for the effective radiation from the earth's surface. The radiant heat influx is determined, as the difference, by both factors: the positions of the bottom and top of the cloud cover. The largest radiant heat influx should be observed in the presence of a ground fog, when the effective radiation is zero and the outgoing radiation is quite large. The smallest values will occur under conditions such that the outgoing and effective radiations are small (for example, in the presence of vertically developed clouds, when the

cloud bottoms are low and the tops may reach the tropopause). It is obvious from the examples given here that the correlation between the outgoing radiation and the radiant heat influx cannot be perfect (for example, because the outgoing radiation undergoes almost no change in the presence of a ground fog, while there is a sharp discontinuity in the effective radiation).

The correlation between the quantities listed above and the outgoing radiation was analyzed in [4] on the basis of calculated results for the mean meridional profiles of the outgoing thermal radiation, the reflected solar radiation, radiant heat influx (total and long-wave component), and the total heat influx with consideration of radiation, phase transformations of water, and turbulent heat exchange. This analysis showed that the correlation between the outgoing radiation and the total heat influx is unsatisfactory. A high correlation obtains between such quantities as outgoing longwave radiation and radiation temperature, outgoing radiation or absorbed solar radiation and degree of cloud cover, and cloud-top altitude and radiation temperature. It is /215 interesting that the total radiant heat influx correlates much more strongly with the outgoing radiation than with the longwave radiant heat influx (the same applies to the corresponding correlation with ground-surface temperature).

The small negative correlation observed by P.A. Davies between the total radiant heat influx and total energy can be interpreted as a consequence of the generation of potential energy at the expense of radiant heat influx. It has been shown that very strong correlation is observed between the reflected solar radiation (outgoing shortwave radiation) and the following quantities: solar radiation absorbed by the atmosphere, radiation temperature; a parameter characterizing the thickness and top heights of clouds. Hence we may conclude that the results of outgoing shortwave radiation measurements are highly informative. Difficulties in quantitative evaluation of the heat influxes due to water phase transformations in the atmosphere and turbulent heat exchange made it impossible to obtain data on the coefficient of correlation between these quantities. Semiquantitative estimates based on climatological data resulted in the following conclusions: 1) negative correlation is observed between the heat of condensation and the total radiant heat influx (the same applies for the effective temperature); 2) the correlation between heat of condensation and cloud-top height is rather high; 3) there is a very definite relation between radiation temperature and total heat influx with consideration of radiation and condensation; 4) radiation temperature also correlates well with turbulent heat exchange between the earth's surface and the atmosphere. The principal conclusion obtained by P.A. Davies [4] is that the results of satellite measurements of effective temperature for the 8-12-μm transparency window and the outgoing shortwave radiation are of considerable interest for determination of heat influx and its components.

With the detection of correlation between the outgoing longwave radiation and the radiant heat influx, a number of attempts were made to analyze the influence of radiant cooling on the atmosphere's energy budget and dynamics and the possibilities for calculation of the atmosphere's thermodynamic parameters from measured outgoing radiation data.

Using the average-energy-level conception, Ye.P. Borisenkov [18] pointed out the possibility in principle of interpreting measured outgoing thermal radiation data in the interests of atmospheric-energetics research.

If T_0 is the underlying-surface temperature and T_a is the temperature corresponding to the mean energy level, the following relationship can be demonstrated: /216

$$\frac{T_0}{T_a} = 1 + \lambda_p, \tag{4.2}$$

where λ_p is the polytropic exponent, $T/T_0 = (P/P_0)^{\lambda_p}$; p is the atmospheric pressure.

T_0 can be determined from measured outgoing-radiation data for cloudless sky in the 8-12-μm transparency window. In the presence of clouds, only data on the radio emission, for which clouds are transparent, can be used. The temperature T_a is related as follows with the radiation temperature T* determined from the measured integrated longwave outgoing radiation:

$$T^* = kT_a, \tag{4.3}$$

where $k = \frac{1+\lambda_p}{\sqrt[4]{4\lambda_p+1}}$ varies from 1.009 to 1.036.

Applying (4.2) and (4.3), we have

$$\lambda_p = \frac{1}{4}\left[\left(\frac{T_0}{T^*}\right)^4 - 1\right]. \tag{4.4}$$

Having calculated the polytropic exponent λ_p, we can determine a whole series of important energy parameters.

Let us examine the following expressions for the internal I and potential II energies of a column of atmosphere of unit cross section:

$$I = \frac{jc_v}{g}\int_0^{p_0} T\,dp, \tag{4.5}$$

$$\Pi = \int_0^\infty gz\rho\, dz = \frac{R}{g}\int_0^{p_0} T\, dp. \qquad (4.6)$$

Here, j is the mechanical equivalent of work, g is the acceleration of gravity, ρ is the density, z altitude, p pressure, and p_0 the pressure at ground level; c_v is the specific heat at constant volume.

Using the polytropic equation, we obtain

$$I = \frac{jc_v}{g} T_0 p_0^{-\lambda_p} \int_0^{p_0} p^{\lambda_p} dp = \frac{jc_v T_0 p_0}{g(1+\lambda_p)}. \qquad (4.7)$$

Or, for the internal energy I_1 of a unit mass /217

$$I_1 = \frac{jc_v T_0}{1+\lambda_p}. \qquad (4.8)$$

Similarly, we obtain for the potential energy

$$\Pi = \frac{R}{g}\frac{T_0 p_0}{1+\lambda_p}, \qquad (4.9)$$

where R is the gas constant, or

$$\Pi_1 = \frac{RT_0}{1+\lambda_p}. \qquad (4.10)$$

The following expression is known for the useful potential energy L':

$$L' = \frac{(\lambda_p - \lambda) T_0 p_0}{\gamma_a (1+\lambda_p)(1+\lambda)}, \qquad (4.11)$$

where $\gamma_a = g/c_p$ is the adiabatic temperature gradient and $\lambda = R\gamma_a/g$.

Examination of Formulas (4.8), (4.10), and (4.11) shows that important components of the atmosphere's energy-budget equation can be found from known T_0, T_a (or T*) and p_0. The possibilities for determination of T_0 and T_a (or T*) and λ_p were indicated above. As concerns the ground pressure p_0, it is subject to the following relationship according to the mean-energy-level concept:

$$\frac{p_a}{p_0} = \left(\frac{1}{1+\lambda_n}\right)^{1/\lambda_p} = a. \qquad (4.12)$$

Here p_a is the pressure at the mean level. With the usually encountered λ_p, the coefficient $a \cong 0.395$, which corresponds to $p_a \cong 400$ mbar. Needless to say, use of directly measured p_0 gives the most reliable results.

Ye.P. Borisenkov [18] also derived the following approximate formulas for the mean temperature T_m of the p_0-400-mbar layer and the height H_{400}:

$$T_m = \frac{T_0 - T_a}{\ln \frac{T_0}{T_a}}, \tag{4.13}$$

$$H_{400} = R \frac{T_0 - T_a}{\ln \frac{T_0}{T_a}} \ln \frac{p_0}{400}. \tag{4.14}$$

Since the method proposed by Ye.P. Borisenkov for calculation of the atmosphere's thermodynamic variables is approximate, it requires careful experimental verification. Even in its present form, however, this method is unquestionably of interest from the standpoint of seeking correlation links with definite physical roots. Quantitative estimates of the individual energy-budget components are also important in this context. Table 4.2 presents Yu.V. Kurilova's calculated order-of-magnitude results [19] for various components in the energy equation and their diurnal variations for a unit column of atmosphere. All values were obtained as averages from more than 50 specific cases. The effective longwave radiation was computed for the 100-mbar level and can therefore be regarded as practically equivalent to the outgoing radiation. /218

TABLE 4.2. ORDERS OF MAGNITUDE OF THE COMPONENTS IN THE ENERGY EQUATION FOR A UNIT COLUMN OF ATMOSPHERE AND THEIR DIURNAL VARIATIONS

	Effective (outgoing) radiation	Energy			
		Internal	Potential	Kinetic	Total potential
Stored energy, 10^{10} ergs/cm^2		150	50	0.250	200
Diurnal amplitude, 10^{10} ergs/cm^2·day	1.0	0.7	0.3	0.05	1.0

It follows from Table 4.2 that the outgoing radiation is considerably (by a factor of four) greater than the stored kinetic energy, but much smaller than the stored potential and internal

energies. However, the variations of even the total potential energy (which equals the sum of the internal and kinetic energies) are comparable with the diurnal outgoing-radiation variation. In analyzing relationships to the outgoing radiation, therefore, it is important to isolate the "mobile" part of the total potential energy. The notion of the available (free) potential energy as the difference between the total potential energy of the real atmosphere and an atmosphere with horizontally stable stratification can be used for this purpose. An estimate of the order of magnitude of the available potential energy made by Yu.V. Kurilova [19] gave a value of $2 \cdot 10^{10}$ ergs/cm^2, which is comparable with the outgoing radiation. It will therefore be interesting to examine the zonal and vortical components of the available potential energy separately.

J.L. Corcoran and L.H. Horn [5] used Tiros II weather satellite data covering 27 days (from 26 November 1960 through 7 January 1961) to investigate the influence of atmospheric cooling governed by the long-wave radiation on the generation of the vortical component of available potential energy (that part of /219
the potential energy that can be converted to kinetic and is determined by the longitudinal variability of the temperature field). Reference [5] notes the contradiction inherent in published results of available potential energy determinations, which indicate that nonadiabatic processes may cause both generation and dissipation of potential energy. The calculation method that they used consisted in calculating the correlation of the deviations from the zone-averaged radiant-cooling values and the heights of the relative baric topography of the 1000-500-mbar layer for various wave disturbances at the 500-mbar level. In reduction of the experimental data, averaging was extended over ten or more discrete values, and only data for nadir angles no greater than 56° were used. The territory studied covered the 30-50° belt of northern latitudes from Europe westward to Japan. Values of the radiant heat influx (radiant cooling of the entire atmospheric thickness) were obtained from measured data on the outgoing radiation by applying a correlation formula derived from analysis of actinometric-radiosonde measurements of the longwave radiant fluxes.

J.L. Corcoran and L.H. Horn showed that the generation of potential energy is negative in the case of long waves and positive in the presence of shortwave disturbances. This wavelength dependence is apparently due to features of the cloudage distribution. They submitted the hypothesis that clouds also result in the generation of potential energy by heating of the air on absorption of solar radiation and liberation of latent heat of condensation. Turbulent heat conduction probably causes dissipation of potential energy. The direct generation of the vortical available potential energy component, which is governed by nonadiabatic processes, should be most important early in the development of baric disturbances (in the case of short wavelengths).

J.S. Winston [6] studied the patterns of outgoing-radiation variability as a function of features of the large-scale circulation and the reciprocal effect of radiant heat influx on circulation. The analysis was based on data on the latitude distribution of albedo and the outgoing longwave radiation as obtained from the Tiros IV weather satellite; they were averaged over five-day intervals during the spring of 1962 for the equatorial waters of the Pacific Ocean.

Reference [6] discusses the strong dependence of the type of meridional shortwave and longwave radiation profiles on atmospheric circulation features. Thus, for example, during a period of intense westerly transport from 29 March through 2 April 1962 /220 in the latitude zone from 30 to 45° N, a marked drop in albedo was observed as latitude decreased from 40 to 20° N, most of it taking place in the region of a strong anticyclonic wind shift on the south side of the west-east transport. The longwave radiant flux was observed simultaneously to vary in the opposite direction. All of this resulted from a transition from rather heavy clouds in the westerly-transport zone to relatively light cloudiness at the southern edge of this zone.

Examination of data characterizing the relationships between the spatial cloudage distributions, the solar radiation absorbed by the surface/atmosphere system, and the type of circulation indicated that nearly zonal circulations are characterized by a strong latitude gradient of absorbed radiation northward from 20° N. lat. Substantial disturbances to the zonality of circulation are accompanied by a marked weakening of this gradient in the latitude belt from 10 to 30° N and preservation of the steep gradient northward from 45° N. An estimate of the contribution of the latitudinal radiant-heating gradient to the generation of zonal available potential energy showed that this contribution is about 25% larger in the case of quasizonal circulation. This demonstrates that the cloudage distribution, which varies under the influence of circulation factors, and hence variations of absorbed radiation, exert substantial influence on the generation of available potential energy and the subsequent development of atmospheric circulation. This qualitative conclusion is confirmed by the results of a numerical Smagorinskiy experiment made using various data on the meridional absorbed-radiation profiles. It was shown, for example, that variations of the radiant heat influx may cause the length of the energy cycle to vary from 26 to 41 days and substantially reduce the amplitude of the available potential energy variations, i.e., produce important changes in the manner in which the atmospheric circulation varies. This effect is important for periods of the order of several weeks and possibly even for longer time intervals (months, seasons).

Precipitation. Since the temperature at cloud-top level is a factor on which cloud microstructure depends (for example, the presence or absence of ice crystals), it can be used as a

criterion for the existence (or absence) of clouds. In this context, A.Z. Chekirda and T.A. Yakovleva [7] studied the possibilities for determination of precipitation zones from outgoing radiation data measured in the 8-12-μm window with the Tiros II, Tiros III, and Kosmos 122 satellites, which reflect features of the underlying-surface or cloud-top temperature distribution. The results of ground observations of the cloudage and precipitation in meteorologically thoroughly explored regions were used for the comparisons (a total of 11 cases was studied). /221

The results obtained in [7] indicate that in middle latitudes and in the absence of a snow mantle, outgoing-radiation data can be used to determine precipitation zones, possible precipitation zones, zones without precipitation, and zones with cloud cover greater than 5. For example, precipitation zones occur in regions where the radiation temperature drops below 245°K. At temperatures above 265°K, precipitation is not, as a rule, observed. Since the indefiniteness of the situation in the intervening temperature range is determined to a substantial degree by the possible influence of partial cloudiness in the radiometer field, the availability of simultaneous television information (cloud pictures) is important for interpretation of the data.

MacLethbridge [8] made a similar study of the correlation of radiation temperature in the 8-12-μm transparency window and the amount of precipitation on the basis of Tiros IV data for the periods from 29 March through 3 April 1962 (12 orbits) and 30 May-9 June 1962 (20 orbits) over the USA, together with hourly data from ground weather observations of precipitation. It was shown in this study that the probability of precipitation within 3 hours after the time of a radiation-temperature determination increases sharply with diminishing temperature (i.e., in the presence of clouds, especially clouds with high tops), reaching 58% during the second of these periods at a temperature minimum no higher than 239°K. Similar results are obtained from precipitation data during the 12 hours following transit of the satellite. An even higher correlation with precipitation is obtained with simultaneous use of satellite data on the radiation temperature and cloud brightness in the wavelength range from 0.55 to 0.75 μm. The brightness information makes it possible to distinguish dense cirrus and cumulonimbus or multilayered clouds (the latter are brighter). In addition, the brightness data make it possible to judge at high temperatures whether clouds are absent (low brightness) or low cloudage is present (high brightness). The precipitation probability may reach 85% at maximum brightness and minimum temperature.

Large-scale vertical movements. W.E. Shenk [10] analyzed outgoing-radiation data measured in the 8-12-μm window with the Tiros II weather satellite in order to find possible ways to acquire information on the vertical temperature gradient fields and vertical movements in the atmosphere from these data. For this /222

purpose, he constructed a correlation diagram that characterizes the relation between cloudless-sky underlying-surface temperature (according to ground measurements made at 88 stations in the USA and Canada from 23 November through 23 December 1960) and the outgoing radiant flux in the transparency window (all of the outgoing-radiation measurements were made at night). This diagram and measured data on the outgoing radiation in the presence of clouds were used to calculate the difference between the outgoing radiant fluxes for clear and cloudy skies and to construct nine geographic-distribution charts of the radiant-flux difference for various synoptic situations.

It is not difficult to show that this outgoing radiant flux difference can be regarded as a characteristic of the temperature difference between the underlying surface and the cloud tops or, accordingly, of the vertical temperature gradient. On the other hand, cloud height and the vertical temperature gradient are among the factors associated with vertical movements (ascending movements occur under conditions of atmospheric instability, and descending movements in the presence of stability; the higher the cloud tops, the stronger should the vertical motions become). Hence follows the possibility of obtaining information on the nature of the vertical movements from data on the outgoing radiant flux difference.

Since the vertical motions are associated with the meridional component of atmospheric circulation, it is also possible to determine the latter quantity. Twelve-hour averages were computed for the vertical component of wind speed, using the adiabatic method, for the levels of the 700-, 500-, and 300-mbar isobaric surfaces (the standard deviation for the 700-mbar surface is about 1 cm/sec).

W.E. Shenk showed that a linear correlation is observed between the outgoing-radiation differences and the vertical velocities, with correlation coefficients of 0.768, 0.569, and 0.564, respectively, for the above levels. The poorer correlation for higher levels is due to the lower accuracy of the calculations in these cases. The fact that the 700-mbar surface can be regarded as a mean level to which the vertical velocity averaged over the entire layer pertains. Analysis of the correlation with reference to data from all measurements (irrespective of cloud height) showed that in this case the correlation coefficient is 0.721 for the 700-mbar surface and the vertical velocity can be determined reliably if the outgoing radiant flux differences are large enough and positive. /223

Linear correlation was detected between the outgoing-radiation difference and the meridional component of wind speed. Although the points are scattered very widely (correlation coefficient 0.557), it is nevertheless clearly seen from the diagram given in [10] that a south component of the meridional flow

obtains for outgoing radiant flux differences exceeding 10 W/m^2. In the case of the north component, the correlation is indefinite.

L.J. Allison and G. Warnecke [9] compared a chart of the vertical motions at the 650-mbar level for the territory of the USA at 12 hours 00 minutes Greenwich Mean Time on 16 July 1961 with simultaneous charts of the outgoing radiation in the 8-12-μm window according to Tiros III data and relative humidity according to conventional weather observations. This comparison led to the following conclusions.

1. Ascending movements at velocities from 0.1 to 0.9 cm/sec and the principal precipitation zones occur in zones of cold-front clouds and squall lines.

2. Descending movements at velocities from -0.1 to -1.7 cm/sec are observed where clouds are absent or lower-level clouds are overlaid by dry air.

Correlation between the outgoing radiation and the vertical-movement field is also confirmed by the data of Huang Ching-Hua, H.A. Panofsky and A. Schwalb [11]. They investigated the correlation of the outgoing radiation in various regions of the spectrum with certain meteorological parameters according to Tiros IV data, which were averaged over quadrangles measuring 5° in latitude × 5° in longitude for 13 April, 12 and 15 May 1962 (a total of five orbits), 14 May (6 orbits), 26 May (1 orbit), and 27 May (3 orbits) and with the results of conventional meteorological observations. It was shown that the 600-mbar vertical velocity and vorticity advection correlate with the difference between the underlying-surface temperature and the radiation temperature measured from the satellite (with dense high clouds, this difference may reach 70°C, and for a cloudless sky it is 10-20°C). The correlation coefficient between vertical velocity and temperature difference reaches -0.58 over the Atlantic Ocean, but does not exceed -0.40 over the Pacific Ocean. This disagreement is apparently due to substantial errors in calculation of the vertical velocities over the Pacific Ocean due to inadequate initial meteorological information.

The inference drawn in [11] to the effect that the vertical velocities are correlated with the outgoing radiation in the region of the 6.5-μm water vapor band at small temperature differences is highly interesting. /224 It was also found that there is a close relationship between the ground-level relative humidity, radiation temperature in the 8-12-μm transparency window, and brightness in the 0.55-0.75-μm range. The relative humidity varies from 39 to 81% as a function of these two factors (whose effects are of about the same order). Analysis of the relation between cloud bottom height, radiation temperature, and brightness showed that these two parameters, which can be measured with

weather satellites, can be used to estimate the amount of cloudage in the absence of television information (both predictors are equally strong).

Since the inhomogeneity of the outgoing thermal radiation field is determined primarily by cloudage conditions, the results obtained in a series of studies by Sh.A. Musayelyan et al. [13-17] are of great interest in connection with this problem of the correlation links.

For example, a successful attempt was made in these studies to represent the fields of the meteorological elements in the form of trigonometric series and correlate the harmonics of these series to compute the fields of the vertical movements or the vertical vorticity component from satellite television pictures of the cloudage taken at earlier times and used to determine the total-cloudage field (see also [36]).

In view of the successful solution of this problem, the following inverse problem can be formulated: if regression coefficients calculated from data on the total cloudage and geostrophic vorticity (or vertical velocities) are available for earlier points in time, can the corresponding cloud field be computed for a later point in time from the vorticity field (or the vertical motions)? This problem was set up for Tiros IX satellite data for all days from 14 May through 2 July 1965. The geostrophic vorticity was computed for the same points in time from the results of an objective analysis of absolute-topography data on the 500-mbar surface. The regression coefficients were computed for five points in time and used to determine the cloudage field for the first subsequent point in time (i.e., the sixth day in the series starting with the five). Analysis of 15 cloud charts computed in this way showed that the absolute error of determination of the total amount of cloudage varies from 2.9 to 3.6 points, averaging 3.1 points over all cases. The results of the calculation agree quite satisfactorily with factual data for the regions of Central and Southern Europe (unbroken clouds) and the areas in the north of the European USSR (unbroken clouds). There are also examples of good agreement for lightly clouded zones. In certain regions, however, the results were found to be unsatisfactory (as for the northern part of the Caspian Sea). The proposed calculation method can also be used prognostically if the vorticity-field data used to calculate the cloud field are obtained from a prognostic chart of the absolute topography of the 500-mbar surface. /225

The geopotential. Attempts to find correlation links between the outgoing-radiation and pressure fields are of great practical interest. Thus, for example, interclass correlation was used in [12] to investigate the relation between the height of the 500-mbar isobaric surface and the outgoing radiation field in the 8-12-μm transparency window. The analysis was based on measured

data for 45 days (March-June 1962) from the Tiros IV weather satellite, pertaining to the regions of North America and the Pacific Ocean. The measurement results were averaged over quadrangles measuring 5° in latitude × 5° in longitude. The unknowns were the linear correlation coefficients between the heights of the 500-mbar surface at 26 points and the outgoing-radiation values at 60 points, which covered a much larger area (the outgoing-radiation figures were obtained at some points by interpolation or extrapolation). A more general approach to solution of this problem was proposed by W.L. Smith [32].

Analysis of the geographic-distribution charts constructed in [12] for the correlation coefficients of the 500-mbar surface heights at the individual points with the outgoing-radiation values for the entire area considered (at 60 points) showed that the positions of regions with positive and negative correlation with respect to a fixed point may vary as a function of features of the synoptic situation. Regression equations were obtained for each of the 26 points, using as predictors the values of the outgoing radiation at 4 points selected from among the 60 by a "screening" process. Application of these equations to the same operational material permitted a more satisfactory reconstruction of the geopotential field from the outgoing-radiation field. However, the errors were found to be much larger when the regression equations were checked against independent data.

As we have already noted, qualitative synoptic analysis of weather-satellite television pictures of the cloud cover and weather maps has shown, for example, that large-scale cloud vortices reflect the characteristic features of the baric field quite faithfully. In this connection, we might pose the problem of reconstructing the wind and pressure fields from the cloud field, to be solved by correlating the harmonics of the trigonometric series used for analytical approximation of the fields of the meteorological elements [16]. A similar approach might also /226
be used in calculating the two-dimensional divergence of the velocity vector and the height field of the absolute topography AT_{500}. The availability of vorticity and divergence data makes it possible to determine the horizontal components of wind speed. In all cases, the results obtained have been encouraging. This is illustrated in [16], for example, by a determination of wind and absolute-topography height at one level of the atmosphere and any point in a hemisphere (except the pole) from cloudage-field data on the vorticity and divergence fields.

Contaminants in the atmosphere. A new field has recently emerged in the interpretation of spectral outgoing-radiation measurements with the purpose of studying atmospheric contaminants (see, for example, [34, 35]). Since this would range far afield from the subject matter of the present monograph, we note only that early progress indicates the feasibility of, for example, satellite methods for determining the atmosphere's contents of

such basic gaseous impurities as SO_2 and NO_2.

A method using correlation links between the outgoing radiation and various meteorological parameters would be of great practical interest from the standpoint of extensive utilization of weather-satellite radiation data in synoptic practice. However, it must be stressed that all of the links discussed above require much more reliable statistical justification.

§2. DETERMINATION OF STRATOSPHERE TEMPERATURE

One of the channels of the medium-angle five-channel radiometer on the Tiros VII and Nimbus II weather satellites was sensitive in the central part of the 15-μm carbon dioxide band. It was found that such measured data can be used effectively to determine the average temperature of the lower stratosphere [20-31].

The radiant intensity $J_{\Delta\lambda}$ measured by the radiometer within the spectral range of the channel's sensitivity (λ_1, λ_2) can be written

$$J_{\Delta\lambda} = \frac{1}{\pi}\int_{\lambda_1}^{\lambda_2} \Phi(\lambda) P_s(\lambda) B_\lambda(T_s)\, d\lambda + \frac{1}{\pi}\int_{\lambda_1}^{\lambda_2}\int_{h=0}^{h} \Phi(\lambda)\frac{\partial P(\lambda, h)}{\partial h} B(\lambda, T(h))\, dh\, d\lambda. \qquad (4.15)$$

Here $\Phi(\lambda)$ is the spectral sensitivity of the radiometer, $P_s(\lambda)$ is the transmission function of the entire thickness of the atmosphere, $P(\lambda, h)$ is the transmission function of the atmospheric layer above level h; T_s is the temperature of the ground surface or the cloud tops; $B(\lambda, T)$ is the Planck function.

/227

If we consider that $P_s(\lambda) \ll 1$ in the center of the 15-μm carbon dioxide band, we obtain, disregarding the first term in (4.15),

$$J_{\Delta\lambda} = \frac{1}{\pi}\int_{\lambda_1}^{\lambda_2}\int_{h=0}^{h} \Phi(\lambda)\frac{\partial P(\lambda, h)}{\partial h} B(\lambda, T(h))\, dh\, d\lambda. \qquad (4.16)$$

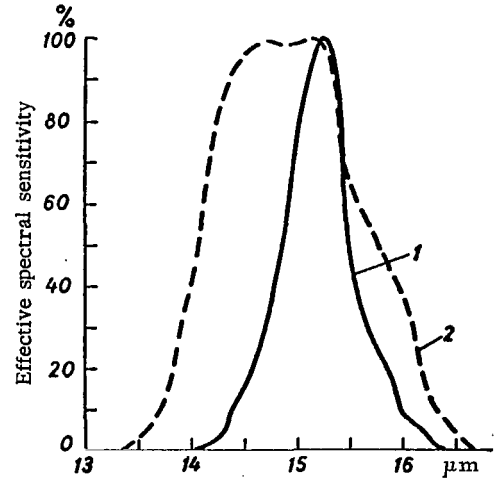

Figure 4.1. Normalized Spectral Sensitivity Function of 15-μm Channel of Tiros VII (1) and Nimbus II (2) Satellites.

Figure 4.1 shows normalized spectral-sensitivity curves of the corresponding channel in the radiometers used on the Tiros VII and Nimbus II satellites.

Introducing the notation

$$\psi(h) = \int_{\lambda_1}^{\lambda_2} \Phi(\lambda) B(\lambda, T(h)) \frac{\partial P(\lambda, h)}{\partial h} d\lambda, \tag{4.17}$$

we write (4.16) in the form

$$J_{\Delta\lambda} = \frac{1}{\pi} \int_{h=0}^{h} \psi(h)\, dh. \tag{4.18}$$

/228

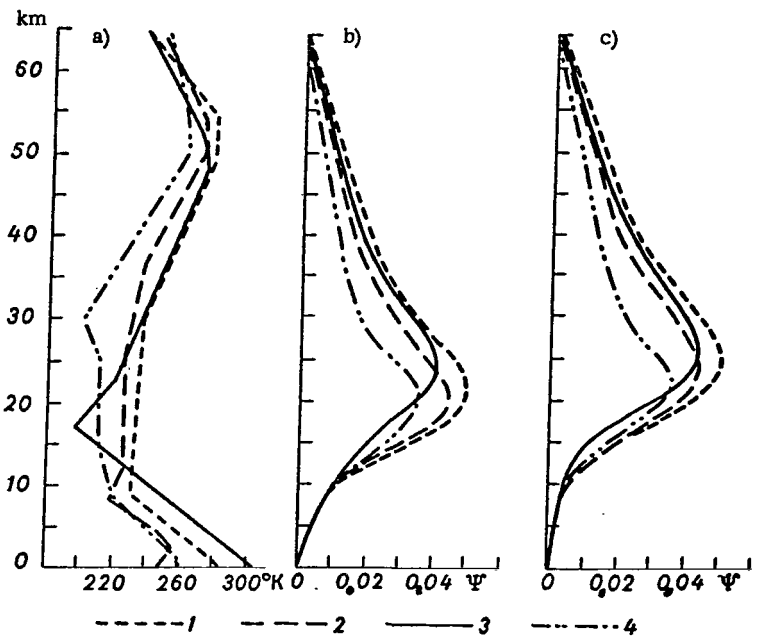

Figure 4.2. Typical Vertical Temperature Profiles Used to Compute the Weighting Functions (a), Weighting Function for Nadir Angle of 0° (b), and Weighting Function for Nadir Angle of 58° (c). 1) Summer, high latitudes; 2) warm winter, high latitudes; 3) tropics; 4) cold winter, high latitudes.

Here $\psi(h)$ is a weighting function that characterizes the contributions of various atmospheric layers to the outgoing radiation.

Figure 4.2 shows the weighting functions for the Tiros VII radiometer as computed for the vertical temperature profiles shown at the left in the figure [23]. As we see, the weighting functions have distinct maxima in the lower half of the stratosphere.

The radiation temperature T_{rad} determined from the relation

$$\int_{\lambda_1}^{\lambda_2} \Phi(\lambda) B(\lambda, T_{rad}) d\lambda = \pi J_{\Delta\lambda} \qquad (4.19)$$

can be assigned to the layer in which the maximum of the weighting function $\psi(h)$ occurs. An important feature of $\psi(h)$ is that its dependence on the vertical temperature profile is weak. For a measurement at the nadir, the maximum of $\psi(h)$ lies in the 20-25-km layer, with about 65% of the total "weight" falling to the 15-35 km layer and more than 96% to heights exceeding 10 km. /229

With increasing nadir angle, the $\psi(h)$ maximum shifts toward higher layers of the atmosphere, but is comparatively small. Thus, for example, when the angle is increased to 58° (see Fig. 4.2), the maximum shifts by less than 5 km. The presence of this shift makes it possible to obtain a qualitative notion of the vertical temperature gradient in the atmosphere from outgoing radiation data measured at various angles to the vertical. Estimates [29] indicate that the observational data are quite homogeneous from the standpoint of altitude attribution for nadir angles smaller than 40°.

The presence of the tropospheric "tail" on the weighting function requires special analysis of the possible influence of clouds on the results of stratosphere-temperature calculations. Calculations made in [31] indicate that clouds below 5 km do not influence the outgoing radiation in the 15-μm carbon dioxide band. However, the radiation of thick, dense cumulonimbus clouds with high tops may lower the radiation temperature by as much as 5-10°C, which would imply a greater height of the effective radiating layer.

To refine the localization of stratosphere-temperature values, the authors of [31] compared radiation temperatures with radiosonde data for the 100, 70, 50, 30, 20, and 10-mbar levels at 97 stations in the Northern Hemisphere for the period from 20 January through 17 February 1964 (the influence of clouds was not taken into account). The sounding data were averaged over areas measuring 5° along latitude circles and from 5° at the equator to 2.5° at 60° latitude along the meridians. The numbers of points from which the average values were determined was always greater than 10 and sometimes reached 200. Only data for nadir angles smaller than 40° were processed, and then only when reliable geographic connection was possible. Satellite data with time shifts of no more than 12 hours from the times of the aerological soundings (12 hours GMT) were used for the comparisons.

The results of this comparison indicate that the radiation temperature "dipped" sharply below the 30-mbar level. There was usually agreement with the radiosonde data for the 10-30-mbar

layer. The highest correlation coefficient (0.71-0.72) was obtained for the 20-30-mbar layer, i.e., near the weighting-function maximum for the 14.8-15.5-μm interval (Tiros VII). The vertical weighting-function profiles were found to be similar to those of the correlation coefficient. The correlation between the radiation and radiosonde temperatures deteriorates considerably as they decrease.

In principle, therefore, we may not expect any absolutely definite relation between radiation temperature and the actual temperature at any given level, since radiation temperature depends strongly on the weighting-function segment to which the observed temperature variations correspond. What is essential, however, is that the variations of the radiation and true temperatures are observed to coincide in time in the 10-30-mbar layer, and this enables us, for example, to use satellite data to detect and study sudden warmings of the stratosphere. Despite this simultaneity, there are differences in the absolute amounts by which the temperatures vary. /230

Quantitative estimates of the effect of clouds have led to the conclusion that the radiation-temperature decrease under the influence of clouds, by comparison with clear-sky conditions, reaches 2-3° at a 6-km cloud-top height and 5-6 and 8-13°, respectively, as this height increases to 10 and 15 km. This cloud effect can be taken into account if cloud height is determined, for example, from outgoing-radiation data measured in the 10-11-μm window with corrections for water-vapor and ozone absorption, assuming information is available on the vertical temperature profile.

A combined analysis of readings from the Nimbus II five-channel radiometer for the 14.0-15.8 and 10-11-μm channels indicated that the readings agree very closely in the equatorial region from 30° N. lat. to 30° S. lat. This can be explained by the influence of the very high, cold cloud tops in these latitudes and by the fact that the upper layers of the troposphere contribute appreciably to the outgoing radiation at wavelengths of 14-16 μm in this case. Thus, in interpreting outgoing-radiation data measured in the 14-16-μm band to obtain information on stratosphere temperature, it is necessary to apply a correction for the influence of high-topped clouds on the basis of measured transparency-window outgoing radiation. Under tropical conditions, this correction may be as large as 15°.

G. Warnecke [27] proposed a cloud-correction method based on calculated results for the outgoing radiation under various cloudage conditions. His calculations showed that the influence of clouds does not depend on atmospheric stratification for cloud heights not above 10 km. However, when the cloud tops are at higher altitudes, substantial differences are observed, depending on the geographic position of the region studied and on the time of year.

Figure 4.3 illustrates how the correction ΔT_{rad}, which characterizes the decrease in the radiation temperature under the influence of clouds, depends on cloud height at various nadir angles θ. As we see, the correction is about 4° in the direction of the nadir for a 10-km cloud height (the same value corresponds to middle-latitude conditions, see Fig. 4.4). If cloud height increases to 14 km, the result is an increase in the correction to 11° in the tropics but only 5° at middle latitudes.

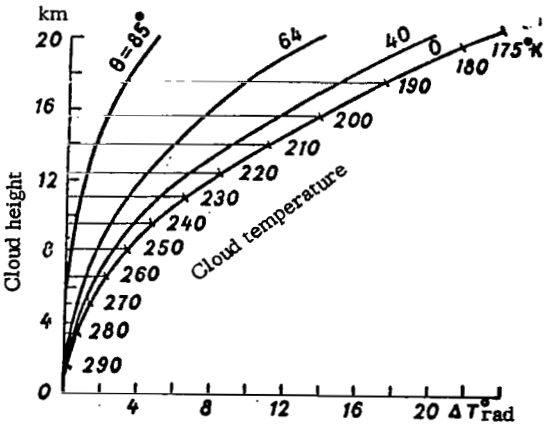

Figure 4.3. Influence of Unbroken Clouds in Field of Nimbus II Radiometer on Measured Radiation Temperature T_{rad} under the Conditions of the Tropical Atmosphere (15° N. lat.).

/231

Nomograms similar to those shown in Figs. 4.3-4.4 for various latitudes and months of the year make it possible to apply corrections for the cloud effect. Information on the temperature (height) of the cloud tops can be acquired from data measured in the 10-11-μm channel. As we showed in the preceding chapter, solution of this problem requires introduction of corrections for the intervening (below the clouds) layer of atmosphere to take account of absorption of the radiation emitted by the clouds, water vapor, and ozone. Special nomograms were constructed for calculation of these corrections. An example of a nomogram corresponding to tropical atmospheric conditions appears in Fig. 4.5.

The reliability of results obtained from outgoing-radiation data measured in the 15-μm carbon dioxide band has been tested in a number of studies.

Thus, for example, S. Teweles [26] compared results from stratosphere-temperature determinations using outgoing-radiation values measured in the 15-μm carbon dioxide band on Tiros VII with aerological soundings, with particular attention to registering temperature fluctuations. The data studied pertained to Campbell Island near New Zealand (53° S., 169° E.) for the period from 15 August (end of winter) through 15 November (beginning of summer) of 1963 and Wilkes Station in Antarctica (66° S., 11° E.) for the same period. In the first of these cases, the satellite data, averaged over 7-8 days, distinctly confirm the almost regular seven-day temperature periodicity detected in the aerological soundings. The observations from the Antarctic station do not indicate this periodicity and also demonstrate a substantial

/232

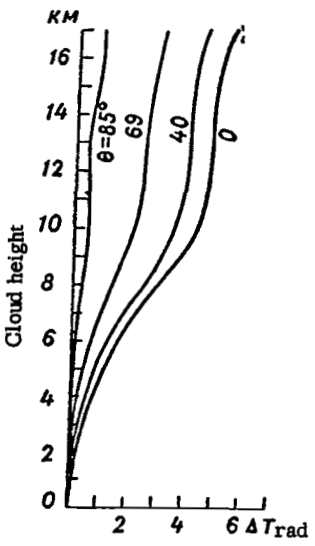

Figure 4.4. Influence of Unbroken Clouds in Field of Nimbus II Satellite Radiometer on Measured Radiation Temperature T_{rad} Under Conditions of the Atmosphere at Middle Latitudes (45° N. lat.). January. 1) $\theta = 85°$; 2) $\theta = 69°$, 3) $\theta = 40°$; 4) $\theta = 0°$.

difference in the nature of the atmospheric circulation as compared with middle latitudes. A temperature increase of approximately 20° registered in the aerological-station data for the 30-mbar level at the beginning of the interval studied is also brought out in analysis of the satellite data, along with other temperature variations. It may therefore be concluded that the satellite data characterize stratosphere-temperature variations reliably.

G. Warnecke [25] constructed a chart of the planetary distribution of stratosphere temperature at the 30-mbar level from aerological sounding data for 21-22 January 1964 and compared it with a similar chart based on radiation-temperature measurements in the 15-μm carbon dioxide band from the radiometer on the Tiros VII weather satellite. The principal features of the temperature fields agree satisfactorily in the two cases (the correlation coefficient is 0.9 in the Northern Hemisphere and reaches 0.94 in the Southern Hemisphere). This means that the radiation temperature field can be regarded as an equivalent of the true-temperature field at the 30-mbar level. Good correlation between radiation temperature and relative topography would probably be observed for the layer from 100 to 10 mbar, which determines the contribution of these wavelengths to the outgoing radiation. This opens prospects for the compilation of planetary topographic charts for the 10-mbar surface by use of this correlation and aerological-sounding data for the 100-mbar level. /233

Analysis of the variation of radiation temperature averaged over the periods from 15-22 January 1964 and 22-29 January 1964 showed substantial temperature contrast over these successive weeks, manifested primarily in the formation of a warm zone in the Caspian Sea region. Data from aerological soundings over Central Europe indicate that this was associated with stratospheric warming. Warming does not penetrate below the 10-mbar (30-km) level in the region of Central Europe. According to satellite data for the Near East, corrected with the weighting function, warming is observed in this region quite far below 30 km, reaching 30-50° for the 25- and 10-mbar levels, respectively. In the region of the Black and Caspian Seas, the directly measured /234

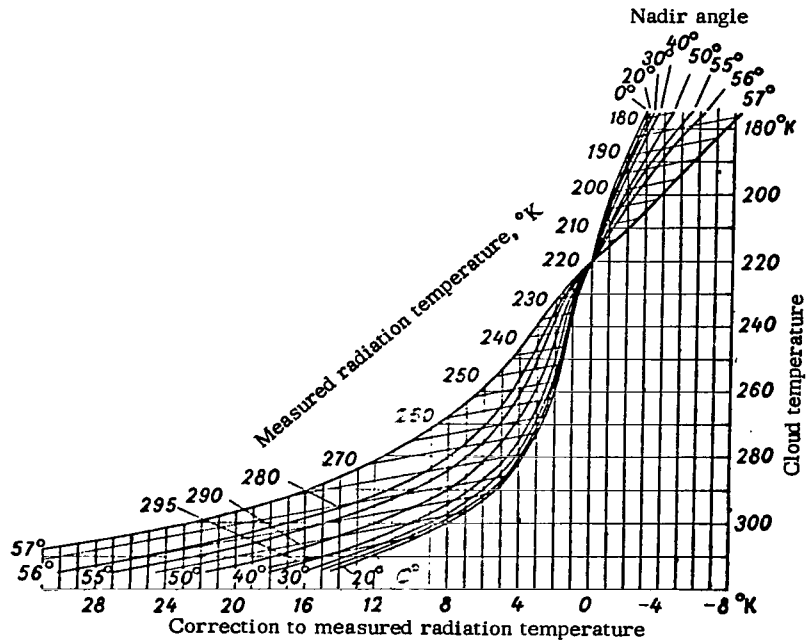

Figure 4.5. Nomogram for Determination of Correction for Intervening Atmospheric Layer in Determination of Cloud-Top Temperatures (Tropical Atmosphere, 15° N. lat.).

radiation temperature rose by 10°, which corresponds to more than a 30° increase in the true temperature. The results given here demonstrate the broad prospects for the use of outgoing radiation data measured in the 15-μm carbon dioxide band for study of the space-time variations of stratosphere temperature.

Using Tiros VII data, W. Nordberg [24] estimated the sensitivity of this method to variations of the stratospheric temperature. If, for example, the temperature in the 25-35-km layer increases by 10°, the directly measured radiation temperature increases from 228 to 331°K. When the same increase in true temperature occurs in the 33-43-km layer, the effective temperature reaches only 228.5°K (a 0.5° temperature change is outside the limits of measurement error). The data-analysis examples considered by W. Nordberg indicate the complex nature of the space-time variations of radiation temperature and a certain ambiguity of the results. However, despite the interpretation difficulties, the data acquired made it possible for the first time to analyze large-saale features of the planetary stratospheric-temperature field in the belt from 65° N. to 65° S. and agree quite satisfactorily with known (but thin) climatological radiosonde data for the Northern Hemisphere.

Satellite data indicate that the stratospheric temperature field in the Southern Hemisphere has an almost zonal character, and that the spatial variability of temperature in the Northern Hemisphere is incomparably more complex during the Northern Hemisphere winter (January), which shows a warm center (230°K) in the region of the Aleutian anticyclone and a very cold nucleus above the North Atlantic (210°K), the latter reflecting the influence of the circumpolar vortex. The stratospheric warming effect in the Near East was clearly discernible. In summer (August), the temperature distribution in the Northern Hemisphere approaches zonal, with a maximum of 236°K at 60° N. lat., while substantial anomalies are characteristic for the Southern Hemisphere.

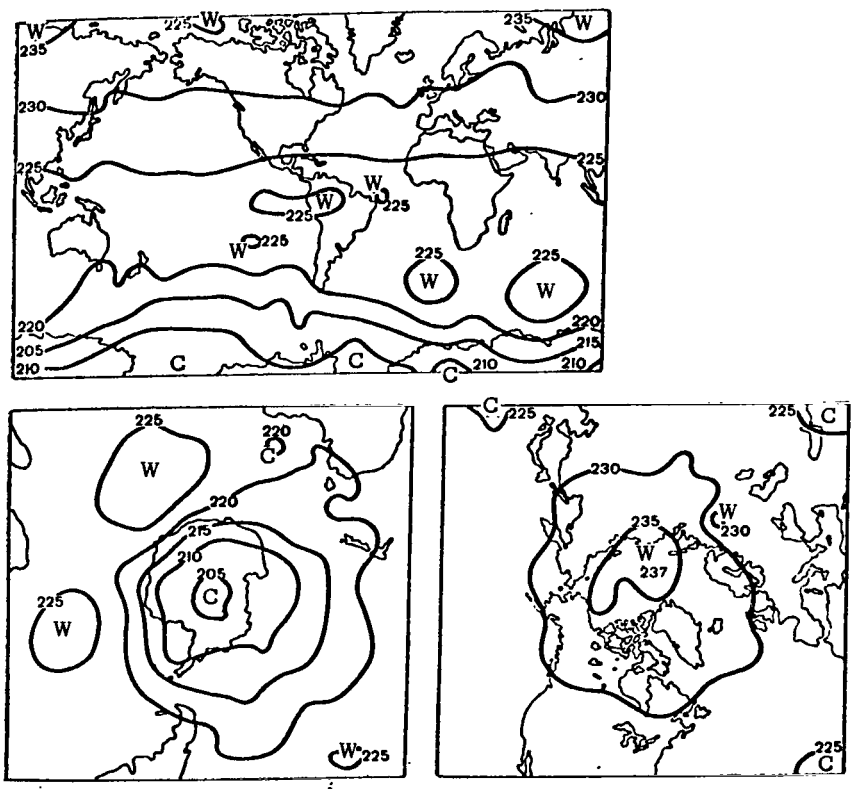

Figure 4.6. Global Distribution of Stratosphere Temperature on 21 May 1966.

Let us now turn to certain determinations of the stratospheric-temperature field from measurements of the outgoing radiation in the 15-μm carbon dioxide band that were obtained by G. Warnecke [27, 30] by the most correct method of interpreteting actinometric data from the Nimbus II satellite (with consideration of the cloud effect) and represent the first example of global data on the stratosphere's temperature field. /235

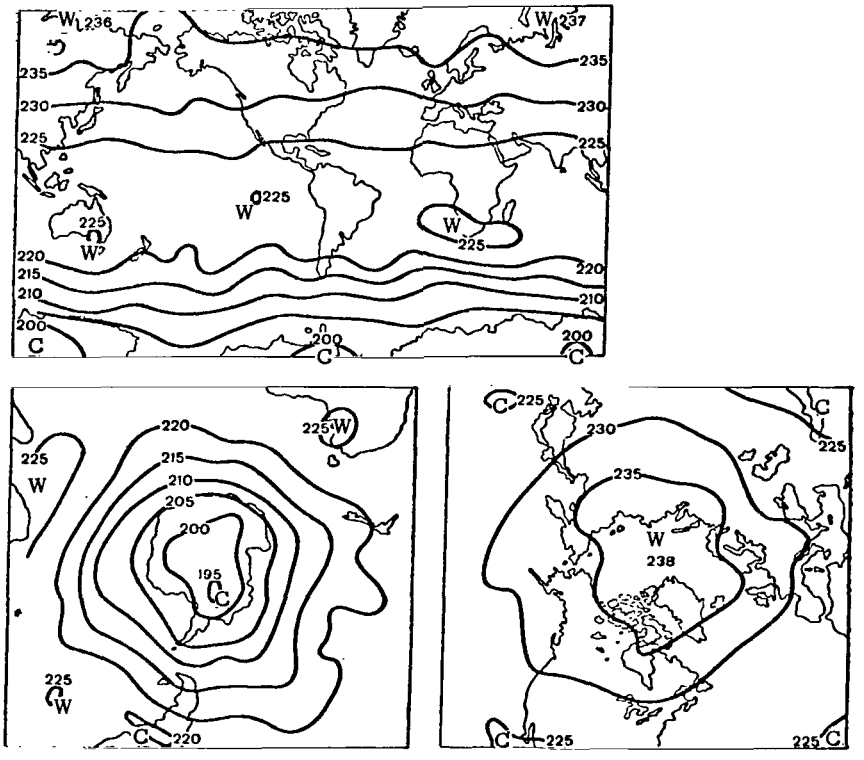

Figure 4.7. Global Distribution of Stratosphere Temperature on 24 July 1966.

Figures 4.6-4.7 are charts of the geographic distribution of stratosphere temperatures according to data for 21 May and 24 July 1966 (data on the 24-hour outgoing radiation were used in constructing these charts). During the span of time considered (end of May to end of July), the temperature field was comparatively stationary in the Northern Hemisphere. Thus, the highest temperatures remained above the North Arctic Ocean at all times. The horizontal temperature gradients were small over the entire hemisphere. The temperature maximum (240°K) was observed above the North Pole on about 1 July 1966. The stratospheric temperature in the tropical zone (30° S.-30° N.) was 220-225°K and rose slightly from south to north.

A more dynamic temperature field was observed in the stratosphere over the Southern Hemisphere. As we see from Fig. 4.6, a polar vortex appeared as early as 21 May over the South Pole and persisted throughout the entire interval studied. Over the first six weeks of this period, the temperature field exhibited a characteristic asymmetry. Thus, on 21 May 1966, a broad region of relatively warmer air extended toward the southern peripheries of the Atlantic and Indian Oceans, creating a strong meridional temperature gradient. The warm centers were observed to shift east- /236

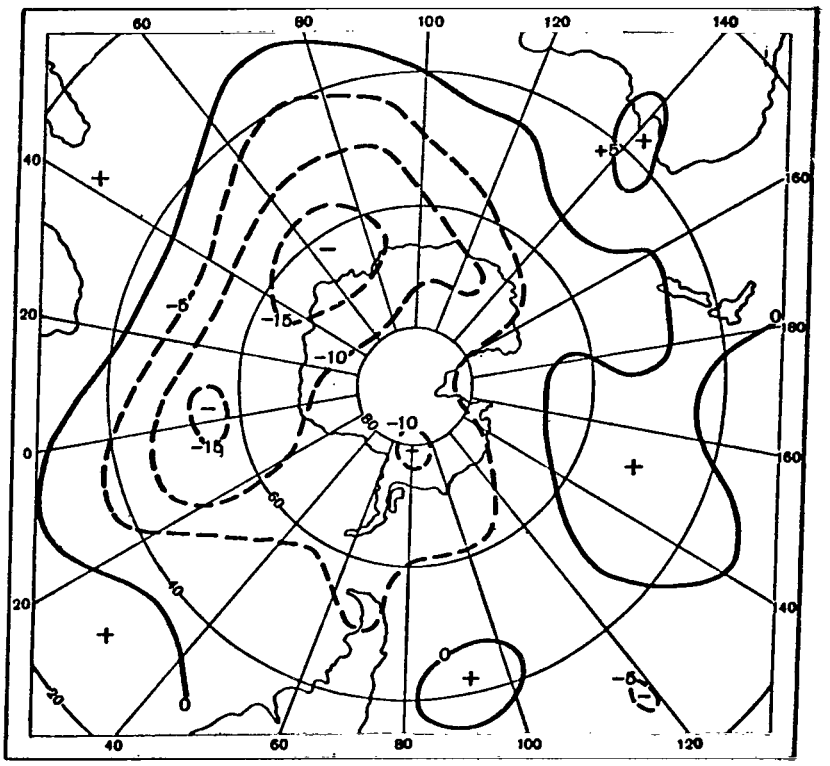

Figure 4.8. Variation of Stratosphere Temperature from 21 May Through 24 July 1966.

ward during the next three weeks, with the result that on 10 June, the warm air had reached Australia and the western sector of the Pacific Ocean's southern periphery. During the second half of June, however, the warm air withdrew to lower latitudes and the /237
polar vortex became thermally more symmetrical. This situation persisted until the end of July (see Fig. 4.7). This was accompanied by gradual cooling at the center of the vortex from the middle of May (about 205°K) to the beginning of July (196°K), after which the temperature drop ceased. However, maximum cooling was observed not in the zone of the polar night above Antarctica, but along the southern periphery of the Atlantic and Indian Oceans (55-65° S. lat., see Fig. 4.8). A detailed analysis of the temperature-field variations shows that the geographical-distribution features of this cooling are governed by a temperature wave that travels around the South Pole above the upper part of the middle-latitude zone and has an amplitude that decreases with time (practically to zero in July). This fact indicates the importance of dynamic processes as a factor in
winter cooling in the region of the polar vertex in the Southern /238
Hemisphere. The examples considered above merely illustrate the possibilities opened by the use of satellite data for study of the stratosphere's temperature field. A wealth of observational

material from the Tiros VII satellite for the period from June 1963 through July 1964 is available in the Atlas compiled by J.S. Kennedy [29] in the form of planetary-distribution charts of 10-day-average stratosphere temperatures. There is no doubt that subsequent application of the method described in this section will be very fruitful from the standpoint of investigation of large-scale processes in the stratosphere.

In a recent paper by M.N. Markov [33], an attempt was made to use rocket and satellite data on the angular distribution of the outgoing radiation in the 12.5-38-μm band to determine the water-vapor concentration in the mesosphere. However, the results of this study require further attentive analysis and confirmation by directly measured data.

Chapter 5

/239

THERMAL SENSING OF THE ATMOSPHERE

The preceding chapters have examined in detail the possibilities for determination of certain important parameters characterizing the state of the earth-atmosphere system: the temperature of the ground surface or cloud tops, total atmospheric moisture content, the average temperatures of specific atmospheric layers. Knowledge of these parameters is necessary for solution of many practically important problems. Moreover, some of these characteristics are used in solving more general and complex satellite problems — reconstruction of the vertical distributions of meteorological elements in the atmosphere. Problems of reconstructing temperature and humidity distributions in the atmosphere on the basis of interpretation of thermal-radiation measurements have been investigated most intensively in recent years. The two chapters that follow are devoted to solution of these problems.

§1. FORMULATION AND GENERAL CHARACTERIZATION OF THE PROBLEM

Knowledge of the three-dimensional fields of the principal characteristics of the atmosphere's physical state — pressure, temperature, density, and humidity — is extremely important for solution of a wide variety of scientific and applied problems. Among these problems, we make first mention of numerical weather forecasting. The above atmospheric variables are related by two familiar relationships [1]:

the equation of state of moist air

$$p = \rho R T, \tag{5.1}$$

and the static equation

$$dp = -\rho g\, dz. \tag{5.2}$$

Under the conditions of the earth's atmosphere, the virtual temperature T_v, which takes account of the water vapor present in the atmosphere, usually differs little from the kinetic temperature, i.e., $T_v \approx T$. (The largest differences between T_v and T are observed at high temperatures and high relative humidities [1].) Knowing the altitude distribution of one of the principal physical variables of state, we can apply (5.1) and (5.2) or relationships derived from them to find the distributions of other parameters. (This may, however, require certain additional

/240

information, e.g., on the pressure at a fixed level.) This raises the question of the optimum method for determining the atmosphere's characteristics of state. Various studies have proposed various methods for solution of this problem. For example, a number of investigators have proposed to determine the temperature distribution in the atmosphere by sounding for temperature, while others would determine the density distribution in the atmosphere from microwave refraction [2-4, 2.40]. The final selection among these methods is a rather complex problem and can be made only after careful analysis of the entire set of factors that characterize the particular experiment: the accuracy of reconstruction of the required characteristics, the range of their reconstruction in the atmosphere, the complexity and cost of the experiment, space and time resolution, the accuracy of measurement of the radiation characteristic needed, etc. The first step in solution of this complex problem might be to study the relationships among the errors of the parameters of interest to us by analyzing the equations of state and statics. Reference [5] compares the errors of two methods of acquiring the atmosphere's pressure distribution: from measured data on the temperature distribution (I) and from the distribution of air density (II). Information on the pressure at the ground with an error Δp = 1 mbar is used in both cases (Table 5.1).

TABLE 5.1. COMPARISON OF THE ERRORS OF PRESSURE ACQUISITION BY TWO METHODS

p(z) obtained by method	Measurement errors of original distributions	δ	z, km								
			0	0,5	1,0	5,0	10	20	30	40	50
I	$\delta_T = 3\%$	$\frac{\Delta p}{p}$ %	0,1	0,3	0,5	1,9	3,8	7,4	11,0	14,8	18,4
		Δp mb	1,0	3,0	4,51	0,21	0,1	4,1	1,3	0,4	0,2
	$\delta_T = 1\%$	$\frac{\Delta p}{p}$ %	0,1	0,16	0,22	0,7	1,3	2,5	3,7	4,9	9,2
		Δp mb	1,0	1,5	2,0	3,8	3,4	1,4	0,4	0,1	0,1
II	$\delta_\rho = 1\%$	$\frac{\Delta p}{p}$ %	0,1	0,16	0,2	1,0	3,0	20,0	100	100	100
		Δp mb	1,0	1,5	2,0	5,7	8,4	10,5	11,0		

We see from analysis of the data in Table 5.1 (the comparison has been made for relatively simple conditions) that even when temperature is reconstructed with relatively moderate accuracy (δ_T = 3%, $\Delta T \approx 7$-9°), the accuracy of pressure reconstruction by the first method is higher for z > 10 km than when density-distribution information is used. For given relative errors of the starting data (δ = 1%), the former method has the advantage over

the latter for practically the entire atmosphere.

Temperature sounding is a promising method of acquiring the atmosphere's principal characteristics from other points of view as well. At the present time, special instruments have been designed and tested successfully for solution of this problem (see Chapter II), and the difficulties of numerical radiation-data interpretation have been substantially overcome. Density determination by temperature-sounding experiments also has definite cost advantages over the "microwave" method. A system of satellites (4-6 in number) is required to obtain the density profile, while one is sufficient to determine temperature. /241

The idea of using the outgoing radiation of the earth-atmosphere system to find the temperature distribution was first advanced by J. King in 1956 [6]. In this paper, King proposed that the temperature profile be found by determining a source function B_ν from the measured angle dependence of the thermal radiation. However, this approach to study of the thermal structure of the atmosphere has a number of disadvantages, principal among which is the need to assume that the atmosphere is horizontally homogeneous. In 1959, L. Kaplan [7] proposed that measurements of the spectral curve of the outgoing thermal radiation at the nadir be used for the same purpose. The basic features of this proposal are valid today, although the temperature-sounding idea has been developed intensively in all of its aspects during the intervening decade.

G.I. Marchuk [101] formulated a general approach to solution of the inverse problems of atmospheric optics. Let us consider the radiant-transfer equation in its operator form

$$L\varphi = f. \tag{5.3}$$

Here L is, in the general case, the integrodifferential radiant-transfer operator; ϕ is the radiant intensity; f are the radiation sources. /242

Instrument readings are functionals of the radiation field and can be presented in the form

$$J_p(\varphi) = (p, \varphi). \tag{5.4}$$

The parentheses in (5.4) denote the scalar product, i.e., integration of the functions over the entire range of the problem's variables.

Let us now write the following adjoint equation for an arbitrary linear functional:

$$L^* \varphi_p^* = p, \tag{5.5}$$

the adjoint being understood in the Lagrangian sense.

It can be shown that this functional can be evaluated either with (5.4) or by the formula

$$J_p(\varphi) = (f,\ \varphi_p^*),$$

i.e., the functional J_p can be calculated either by solving the basic problem (5.3) or by solving the adjoint problem (5.5).

G.I. Marchuk invoked a standard atmosphere characterized by assigned distributions of the meteorological elements temperature, humidity, aerosols, etc. This atmosphere and the inverse problem corresponding to it might be referred to as "undisturbed." Generally, functionals measured from a satellite will pertain to the real, i.e., "disturbed" problem. The basic problem is to determine the variations of the atmosphere's characteristics from assigned variations of the functionals. This is done by constructing the appropriate formulas of disturbance theory for the functionals.

We write for the disturbance problem

$$L'\varphi' = f',$$
$$L' = L + \delta L,\quad f' = f + \delta f.$$

We can then derive the following expression to link the variations of the functional with those of the atmosphere's characteristics:

$$(\varphi_p^*,\ \delta L\varphi' - \delta f) = -\delta J_p.$$

Since the instrument produces measurements in various segments of the spectrum, we actually have a set of variations of functionals J_{p_n}, $n = 1, 2, \ldots, N$ and the functions $\varphi^*_{p_n}$ corresponding to them. Obviously, the information in the various functionals must be independent, i.e.,

$$\varphi^*_{p_n} \neq \varphi^*_{p_m}.$$

This general formulation of the atmospheric-optics problems was also used by G.I. Marchuk to formulate the thermal-sounding problem. /243

The basic relationship by which the measured quantity — radiant intensity — can be connected to the atmospheric temperature distribution is the integral form of the infrared or microwave radiant-transfer equation. Let us write an expression for the outgoing thermal radiation in the vertical direction at the top of the atmosphere in the form

$$J[\nu, 0, T(y), q_i(y)] = \int_{y_0}^{y'} B_\nu[T(y)] \frac{\partial P_\nu[y, q_i(y), T(y)]}{\partial y} dy +$$

$$+ B_\nu[T(y_0)] P_\nu[y_0, q_i(y), T(y)]. \qquad (5.6)$$

Here y is an arbitrary space variable, e.g., y = p or y = log p.

In the general case, radiant intensity is a complex functional of a number of atmospheric-parameter distributions: temperature T(y), absorbing substances $q_i(p)$, pressure p; it depends on the optical characteristics of the spectral intervals considered and on a number of other characteristics. The first term on the right in (5.6) is governed by the atmosphere's intrinsic emission, and the second by the contribution of underlying-surface radiation. (In writing (5.6), we assume that the emissivity of the underlying surface is unity; writing the corresponding expressions for other general hypotheses represents no difficulty.)

Calculation of the radiant intensity or other quantitative characteristics of the radiation field from assigned transmission functions and known atmospheric variable-of-state distributions is usually referred to as the direct problem. The inverse problems of infrared or microwave radiant transfer consist in determination of the distributions of the meteorological elements in the atmosphere — e.g., those of temperature, humidity, and the atmosphere's constituents — from assigned transmission functions (or, in the more general sense, from assigned absorption characteristics of the atmospheric gases) and measured radiation characteristics.

Measured radiation data simultaneously contain information on the distributions of many atmospheric variables. Generally speaking, it is not possible to determine the temperature distribution from such data. However, if the radiation measurements pertain to the absorption bands of gases whose distributions in the atmosphere are known and constant in time, and if all optical parameters that determine radiation are assigned, the only unknown function will be the distribution of temperature in the atmosphere. The transmission functions of such absorption bands and their derivatives for specific spectral intervals, which, as we see from (5.6), play a fundamental role in shaping the outgoing radiation and are needed for solution of the inverse problem, can be computed in advance. Very often, because of the dependence of the transmission functions on the unknown temperature distribution and the distributions of other absorbing gases (for example, water vapor), whose concentrations in the atmosphere are subject to wide variations, the transmission functions may differ under the specific conditions of an experiment from those computed for a definite model of the atmosphere. If the influence of all of these factors is weak, the inverse problem can still be solved,

/244

but the accuracy with which the unknown function is reconstructed will not be good enough (see §5 of this chapter). Then the information obtained on the atmosphere's thermal structure can be used, along with data on the absorbing-matter distribution, which can be determined from other radiation measurements, to improve the transmission functions and determine the temperature profile more accurately.

The fact that the radiation sensed by the instrument at different frequencies is generated by different layers of the atmosphere forms the physical basis for successful use of information on the atmosphere's thermal structure. Figure 5.1 shows typical kernels of Eq. (5.6), i.e., typical functions $\frac{\partial P_{\Delta\nu i}(\log p)}{\partial \log p}$ in this case corresponding to spectral intervals in the 15-μm carbon dioxide band for satellite observations. These functions, which are often known as "weighting functions," can be treated as the density distribution functions of the probability that a quantum of frequency ν in the range $\Delta\nu_i$ will arrive from a point with the coordinate log p. Weighting functions have the following characteristic properties: 1) finite thickness, 2) mutual correlation of functions corresponding to different $\Delta\nu_i$. Similar properties of the functions are also observed for other regions of the spectrum. The first property has as a consequence that spectral measurements carry information on the thermal state of atmospheric layers that are limited in thickness, although quite extensive. In the final analysis, the distribution-function thickness determines the temperature-profile vertical resolution attainable by indirect methods. Because of this property of the distribution functions and the presence of errors in the measurements, the thermal-sounding method does not yield information on the fine structure of the temperature profile. The second property of the distribution functions complicates solution of the corresponding mathematical /245

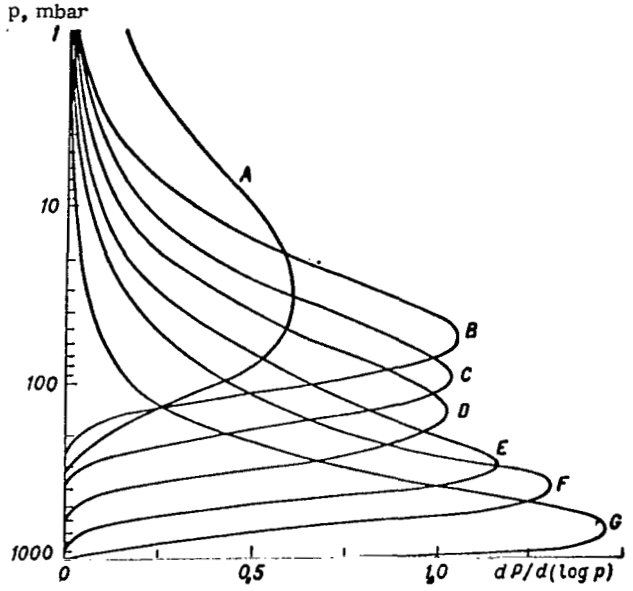

Figure 5.1. Kernels of Eq. (5.6) for Seven Spectral Intervals in the 15-μm CO_2 Band. A) ν = 669 cm^{-1}; B) ν = 677.5 cm^{-1}; C) ν = = 691 cm^{-1}; D) ν = 697 cm^{-1}; E) ν = 703 cm^{-1}; F) ν = 709 cm^{-1}; G) ν = 743 cm^{-1}.

problem on the one hand (the linear dependence of the equations of the algebraic system that approximates the integral equation) and, on the other, makes it possible to reconstruct the temperature profile, but not to determine the mean temperatures of specific atmospheric layers, as would be the case for totally uncorrelated distribution functions.

We note that it was the desire to isolate 5-7 spectral intervals within a specific absorption band with distribution functions having rather small correlation coefficients — which is equivalent to measuring the radiation arriving from appreciably differing heights in the atmosphere — that led the authors of the early papers to the conclusion that it was necessary to measure with high spectral resolution (~ 5 cm^{-1}). Actually, however, the problem of optimum measurement conditions must be solved on a more rigorous basis (see §2 of this chapter).

In practice, the problem of thermal sounding of the atmosphere reduces to solution of a Fredholm integral equation of the first kind: /246

$$\int_a^b K(x, y)\varphi(y)\,dy = f(x). \tag{5.7}$$

The conversion from the general expression (5.6) to concrete forms of the integral equation is accomplished differently in different methods. First of all, the unknown in many of the methods is not the temperature itself, but the temperature-dependent Planck function $B_\nu(y)$ of black-body radiation. Having determined the dependence of B_ν on some space variable by solving the equation, it is easy to convert to the spatial distribution of temperature using (1.11a). In all methods in which the Planck function is found, it is necessary to eliminate the frequency dependence of B_ν in order to reduce the problem to solution of integral equation (5.7). This is done by various methods at the present time.

1. The Planck function can be approximated in the form [8]

$$\widetilde{B}(\nu, T) = \alpha(\nu)B(\nu_r, T) + \beta(\nu), \tag{5.8}$$

where ν_r is a reference frequency, usually placed at the center of the spectral interval under consideration; $\alpha(\nu)$ and $\beta(\nu)$ are known functions.

In this case, the right member of (5.7) is $\frac{J(\nu) - \beta(\nu)}{\alpha(\nu)}$, and the unknown function is the Planck function for frequency ν_r. The accuracy of (5.8) depends on the width of the spectral interval

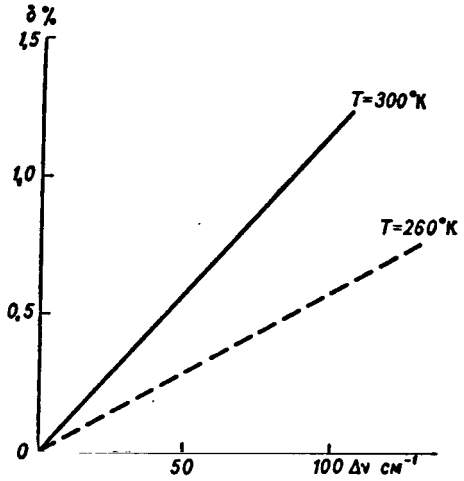

Figure 5.2. Error $\delta = \frac{|B(\nu, T) - \tilde{B}(\nu, T)|}{B(\nu, T)} \times 100\%$ of Approximation of Spectral Dependence of Black-Body Radiation as a Function of Distance to Reference Frequency ν_r = 700 cm^{-1}.

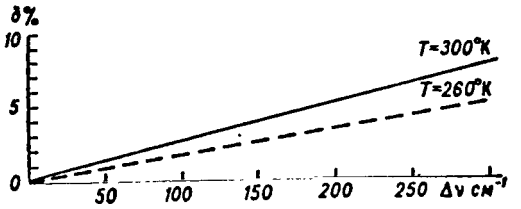

Figure 5.3. Error $\delta = \frac{|B(\nu, T) - \tilde{B}(\nu, T)|}{B(\nu, T)} \cdot 100\%$ of Approximation of Spectral Dependence of Black-Body Radiation as a Function of Distance to Reference Frequency ν_r at λ = 4.3 μm (CO_2 Absorption Band).

considered and the temperature range in which it is used. Figures 5.2 and 5.3 present data characterizing the error of (5.8). Here, values of $\delta = \frac{|B(\nu, T) - \tilde{B}(\nu, T)|}{B(\nu, T)}$ 100% are plotted against distance from ν_r in reciprocal centimeters for the two carbon dioxide bands centered on 15 and 4.3 μm; $\alpha(\nu)$ and $\beta(\nu)$ were found for T_1 = 280°K and T_2 = 240°K, and Relation (5.8) was tested for temperatures of 260 and 300°K. Analysis of Figs. 5.2 and 5.3 indicates that the errors that result from application of (5.8) in not very wide spectral intervals are small.

2. Another method of approximate allowance for the frequency dependence of the Planck function consists in reducing all intensities to a single frequency [9]. In this case, the brightness temperature is found for each $J(\nu_i)$ from the relation /247

$$T_{br}^{i} = \frac{1{,}43868\nu_i}{\ln\left(\frac{3{,}7403 \cdot 10^{-5}\nu_i^3}{B\pi} + 1\right)}. \qquad (5.9)$$

Then the Planck formula (1.11a) is used to find the radiant intensity corresponding to this radiation temperature for the reference frequency ν_r. The more exact relation /248

$$J_{\nu_r}(\nu_i) = B[\nu_r, T_{rad}^{i}] + \gamma(\nu). \qquad (5.10)$$

is sometimes used here; $\gamma(\nu)$ is an empirical correction factor, e.g., that obtained in [9] for measurements in the 15-μm CO_2 band.

TABLE 5.2. ERRORS ASSOCIATED WITH REDUCTION OF RADIANT INTENSITIES TO ν_r = 700 cm^{-1}

Center of frequency interval, cm^{-1}	Errors from use of (5.10) for various profiles [9], $erg \cdot cm^{-2} \cdot sec^{-1} sr^{-1} (cm^{-1})^{-1}$					
	Key West	Little Rock	Seattle	Churchill	Average error	$\gamma(\nu)$
669	0,116	0,11	0,08	0,12	0,10	0,12
677,5	0,07	0,04	0,02	0,02	0,03	0,04
691	0,03	0,02	0,01	0,01	0,01	0,02
697	0,01	0,00	0,01	0,00	0,01	0,00
703	—0,01	—0,01	—0,01	—0,01	0,00	—0,01
709	—0,07	—0,05	—0,03	—0,01	—0,04	—0,04
743	—0,34	—0,28	—0,24	—0,10	—0,23	—0,24

Table 5.2 lists errors resulting from the use of (5.10) and values of $\gamma(\nu)$ for a number of spectral intervals in the 15-μm band. As we see, the correcting term $\gamma(\nu)$ is small, so that we can set $\gamma(\nu) = 0$ in Expression (5.10). Furthermore — and this is most important — the mean error of reducing the radiation to the frequency ν_r = 700 cm^{-1} when (5.10) is used is smaller than 0.06% of the radiation values for the entire band at λ = 15 μm.

3. Another method of allowing for the frequency dependence of the Planck function for use in the carbon dioxide band at λ = = 4.3 μm was proposed in [10]. For this range of the spectrum, we can write

$$\frac{B(\nu, T)}{a\nu^3} = \left(e^{\frac{b\nu}{T}} - 1\right)^{-1} = X(T) Y(\nu) \delta(\nu, T), \qquad (5.11)$$

where $\delta(\nu, T) - 0(1)$.

As we see from Relation (5.11), the temperature dependence is expressed in the form $e^{-b\nu/T}$. Let us approximate the argument of the exponent $b\nu/T$ with the expression $c_1 + c_2\nu + (c_3/T)$ and find the coefficients c_j for the optimum root-mean-square representation of $b\nu/T$ within an assigned narrow range of variation of ν and T, i.e., let us require that /249

$$\frac{\partial}{\partial c_j} \int_{\nu'}^{\nu''} \int_{T'}^{T''} \left[\frac{b\nu}{T} - c_1 - c_2\nu - \frac{c_3}{T}\right]^2 dT\, d\nu = 0, \quad j = 1, 2, 3. \qquad (5.12)$$

The limits of integration depend on the frequency interval used in solving the problem and the range of temperature variation observed in the atmosphere. Solution of the three-equation system (5.12) yields the following expressions for the coefficients c_j:

$$c_1 = -b \frac{\ln \frac{T''}{T'}}{T'' - T'} \frac{\nu'' + \nu'}{2}, \tag{5.13a}$$

$$c_2 = b \frac{\ln \frac{T''}{T'}}{T'' - T'}, \tag{5.13b}$$

$$c_3 = b \frac{\nu'' + \nu'}{2}. \tag{5.13c}$$

Thus, the function X(T) can be written

$$X(T) = \exp\left(-c_1 - \frac{c_3}{T}\right), \tag{5.14}$$

and Relation (5.11)

$$\frac{B(\nu, T)}{a\nu^3} = X(T)\left[\frac{\exp\left(-\frac{b\nu}{T} + c_1 + \frac{c_3}{T}\right)}{1 - e^{-\frac{b\nu}{T}}}\right], \tag{5.15}$$

where the dependence of the function X(T) on temperature is several orders greater than the T-dependence of the second multiplier in (5.15) for the 4.3-μm region of the spectrum.

Finally, we note that solution of the microwave thermal sounding problem does not involve the use of these approximate methods, since the Rayleigh-Jeans approximation for the Planck black-body-radiation function is satisfied highly accurately in this region of the spectrum at the temperatures observed in the earth's atmosphere.

In a number of statistical methods of solving the thermal-sounding problem [11-13], and in R. McClatchey's method [14], the deviations of temperature from a certain assigned temperature profile are the unknown function. In statistical methods, this profile is the mean temperature distribution. In view of the fact that the T', the random variations of the temperature profile, are substantially smaller in magnitude than the mean temperatures $\overline{T}$, we can derive the following expressions for f(x), $\phi(y)$, and K(x, y) [11]: /250

$$\begin{aligned} f(\nu) &= J(\nu) - \overline{J}(\nu), \\ \varphi(p) &= T'(p), \end{aligned} \tag{5.16}$$

$$K(\nu, p) = \frac{\partial B_\nu [\bar{T}(p)]}{\partial p} \frac{\partial P_\nu (p)}{\partial p}, \qquad (5.16)$$

(Cont'd.)

where $\bar{J}(\nu)$ is the radiant intensity corresponding to the mean temperature profile.

A problem that arises in all methods for interpreting radiation data is that of allowing for the term outside the integral in (5.6). First, this term can be reduced to zero by special selection of spectral intervals. This applies in those cases in which $P_{\Delta\nu}(p_0) = 0$ for all of the intervals considered, i.e., the underlying-surface radiation does not reach the level of the radiation measurement. However, it must be noted that the term outside the integral in (5.6) will be governed by cloud emission when clouds are present. Another method of handling the term outside the integral is to eliminate it when the underlying-surface temperature and the ground-level pressure are known from independent measurements. Finally, the term can be brought under the integral sign in (5.6) by extending the atmosphere "fictively" to the p_0 level.

As we noted above, measurements of thermal radiation with the object of acquiring quantitative information on the atmosphere's temperature profile must be made in the absorption bands of those gases whose distributions remain constant in time. As a result, three regions of the spectrum are presently in use for purposes of thermal sounding: regions occupied by the absorption bands of carbon dioxide at $\lambda = 4.3$ and $\lambda = 15$ μm and the region around $\lambda \approx 5$ mm, where oxygen absorption is observed. Selection of the optimum spectral region is a complex problem and has not yet found its final solution. Let us discuss certain general advantages and disadvantages of various regions of the spectrum.

The carbon dioxide band at 4.3 μm lies in the spectral region in which black-body radiation depends strongly on temperature at the temperatures encountered in the atmosphere. As a consequence, /251 large changes in the radiation values correspond to small changes in the temperature of the radiating medium. Other conditions the same, this enables us to determine temperature from the Planck function $B_{\nu_r}(y)$ more accurately than for longer-wave regions of the spectrum, where the B(T) dependence is considerably weaker. On the other hand, this feature of the near infrared gives rise to certain experimental difficulties — it is difficult to measure with consistent relative errors a quantity that varies through approximately two orders within the spectral region under consideration. Another consequence of the same property is that the amount of radiation arriving at the registration level from various heights in the atmosphere depends not only on the form of the weighting functions (those given, for example, in Fig. 5.1), but also quite strongly on the temperature profile of the atmosphere

itself. Figure 5.4 shows the conventional weighting functions $\frac{\partial P}{\partial \ln p}$, and Fig. 5.5 the functions $\frac{\partial P}{\partial \ln p} B$, which characterize the contributions of various levels in the atmosphere to the outgoing radiation. The curves were plotted for a number of spectral intervals 20 cm^{-1} wide in the CO_2 band at $\lambda = 4.3$ μm for the following total contents of the absorbing substances: 256 cm-atm of CO_2, 0.22 cm-atm of N_2O_2, 0.06 cm-atm of CO, and 1.94 cm of precipitated water for H_2O. Comparison of the figures shows that consideration of B_ν results in a substantial change in the form of the corresponding functions. The effect of the Planck function is to narrow the weighting functions in the lower layers of the atmosphere and to change completely the form of the function $\frac{\partial P}{\partial \ln p}$ in the upper layers.

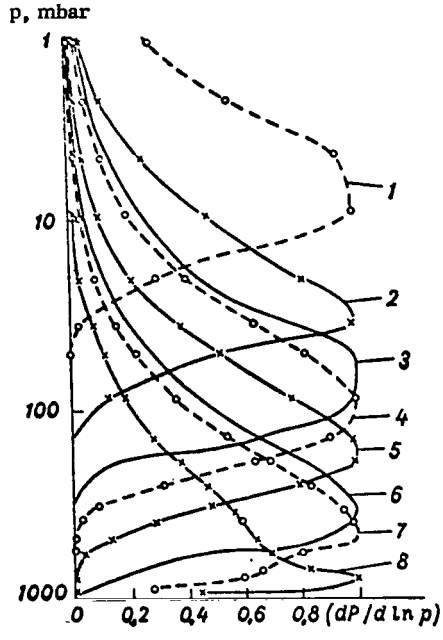

Figure 5.4. Kernels of Integral Equation (5.6) for a Series of Spectral Intervals in the CO_2 Band at $\lambda = 4.3$ μm.

1) ν=2360 см⁻¹, 2) ν=2340 см⁻¹, 3) ν=2315 см⁻¹, 4) ν=2295 см⁻¹, 5) ν=2275 см⁻¹, 6) ν=2255 см⁻¹, 7) ν=2235 см⁻¹, 8) ν=2215 см⁻¹.

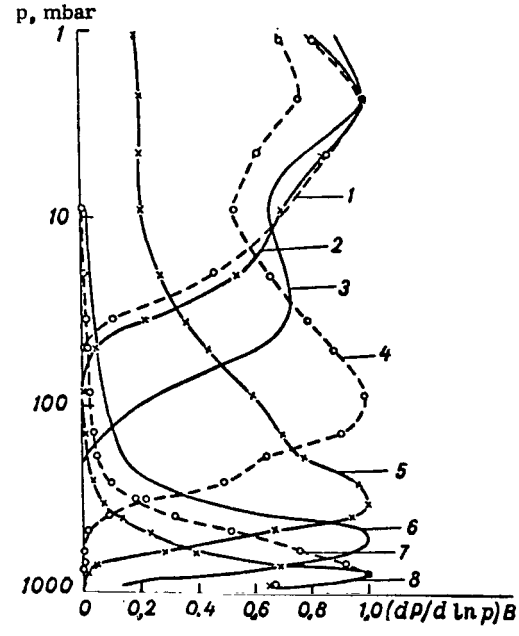

Figure 5.5. Kernels $\frac{dP}{d \ln p}$ of Integral Equation (5.6) for a Series of Spectral Intervals in the CO_2 Band at $\lambda = 4.3$ μm. For legend, see Fig. 5.4.

The basic disadvantage of the near infrared is the difficulty of using it in the daytime. As we noted in Chapter 1, the scattered solar radiation makes a significant contribution to the outgoing radiation in the 4-5-μm band under certain conditions (for

example, cloudiness), and this greatly complicates the problem of extracting information on the temperature profile from outgoing-radiation measurements. The regions of the 15-μm CO_2 band and the 5-mm O_2 band, in which the outgoing radiation is determined at any time of day by the intrinsic emission of the earth-atmosphere system, are more suitable from this viewpoint. The microwave region is still attractive in connection with the possibility in principle of sensing the atmospheric layers below clouds; this is because of the high penetrating power of radiation in this band. Moreover, the resolution presently attainable in the microwave region enables us to sound the atmosphere to altitudes of about 75 km [3, 132], while the upper sounding level is no higher than 50 km when the infrared is used, and most of the instruments that have been developed are capable of delivering information only on the lowermost layer of the atmosphere, up to 30 km. /253

The 15-μm region is most suitable from the standpoint of energy considerations because the atmosphere's intrinsic-emission maximum is observed in this region at atmospheric temperatures. Now, however, radiation detectors that permit measurement of the thermal radiation with approximately the same accuracy have been developed for all of the spectral regions in which we are interested.

The possibilities for use of all of these regions of the spectrum for purposes of thermal sounding are currently under both theoretical and experimental investigation. The possibility that it may be necessary to use measurements in a variety of absorption bands is not excluded. However, resolution of this question must be based on analysis of the information content of data measured in various parts of the spectrum.

We note in conclusion that our Expression (5.6) pertains to thermal radiant intensity. On the other hand, real instruments measure radiant fluxes in finite spectral and angle intervals. Naturally, this property must be taken into account in interpreting real measured data. Generally speaking, the frequency- and angular-sensitivity characteristics of the measuring instruments must be known. If they are, no particular difficulty is encountered in introducing them into the corresponding expressions. Let us illustrate this, referring to the spectral sensitivity of an instrument by way of example. The radiation registered in an interval $\Delta\nu$ is related to the true spectral distribution of the radiation as follows:

$$J_{\Delta\nu}(\bar{\nu}) = \int_{\bar{\nu}-\frac{\Delta\nu}{2}}^{\bar{\nu}+\frac{\Delta\nu}{2}} \varphi(\nu-\bar{\nu}) J(\nu)\, d\nu. \qquad (5.17)$$

Applying (5.6) for $J(\nu)$ and remembering that current instruments for thermal sounding have quite high resolutions, we replace

the Planck function $B(\nu)$ by its average value in the interval $\Delta\nu$ to obtain the expression

$$J_{\Delta\nu}(\bar{\nu}) = \int_{y_0}^{y_1} B_{\bar{\nu}}[T(y)]\,K'(\bar{\nu}, y)\,dy + B_{\bar{\nu}}[T(y_0)]\,P'(\bar{\nu}, y_0),$$

where /254

$$K'(\bar{\nu}, y) = \int_{\bar{\nu}-\frac{\Delta\nu}{2}}^{\bar{\nu}+\frac{\Delta\nu}{2}} \varphi(\nu - \bar{\nu}) \frac{\partial P_\nu(\nu, y)}{\partial y}\,d\nu$$

is the derivative of the transmission function and

$$P'(\bar{\nu}, y_0) = \int_{\bar{\nu}-\frac{\Delta\nu}{2}}^{\bar{\nu}+\frac{\Delta\nu}{2}} \varphi(\nu - \bar{\nu})\,P(\nu, y_0)\,d\nu$$

is the transmission function for the specific measuring instrument in frequency band $\Delta\nu$.

As we pointed out above, the influence of the instrumental function $\phi(\bar{\nu} - \nu)$ is small under certain conditions, enabling us to use the transmission function uncorrected for $\phi(\nu - \bar{\nu})$ in first approximation.

In principle, the angular dependence of instrument sensitivity can be taken into account in the same way. However, because of the relatively high angular resolution of the instruments and the high isotropy of the outgoing thermal radiation under cloudless-atmosphere conditions, this is not usually done. Radiation measured under partly-cloudy conditions, especially in the relatively transparent ranges, will be substantially nonisotropic, and the angle dependence of instrument sensitivity may influence the registered radiation quite considerably.

§2. MATHEMATICAL ASPECTS OF SOLUTION OF THE INVERSE PROBLEMS

From the mathematical standpoint, the thermal-sounding problem reduces to solution of a Fredholm integral equation of the first kind. Many other inverse problems of atmospheric optics can also be reduced to such equations, including the problem to be considered in the next chapter — that of reconstructing atmospheric humidity.

It is necessary to dwell in somewhat greater detail on a number of fundamental aspects of the mathematical methods used to solve these integral equations. This is the more necessary since, despite numerous specific features of the various inverse atmospheric-optics problems, they have not only formal similarity, but also closely similar kernels for the respective integral

equations. This gives rise to the hope that a number of numerical solution methods that have been used successfully in the thermal- /255
sounding problem may also be useful in solving other inverse problems. This similarity of the kernels can be illustrated by reference to Figs. 5.1 and 6.5, which show kernels encountered in problems of thermal sounding and atmospheric-humidity reconstruction.

The problem of solving the Fredholm integral equation of the first kind

$$\int_a^b K(x, y)\varphi(y)dy = f(x), \quad c \leqslant x \leqslant d \tag{5.18}$$

is one of the inverse problems of mathematical physics. The basic requirements made of the formulation and solution of mathematical-physics problems were stated by Hadamard (see [15]) in his definition of correctness.

Definition 1. Let Φ and F be complete metric spaces, and let A be a certain operator with a region of definition Φ and a region of values F. Consider the equation

$$A\varphi = f, \tag{5.19}$$

in which it is necessary to find a solution $\varphi \in \Phi$ from an assigned function $f \in F$. We shall assume that Problem (5.19) is correctly stated if the following conditions are satisfied:

1) a solution ϕ exists for any $f \in F$,

2) the solution ϕ is unique in region Φ, and

3) the solution ϕ is a continuous function of $f \in F$.

Thus, Problem (5.19) is correctly stated if there exists an operator B(f) that is defined and continuous on all F and the inverse of operator A. The first correctness requirement results from the need to avoid overdefinition in the problem (the presence of "extra conditions"). The second requirement excludes ambiguity in the solution, and the third arises out of the fact that the right member of (5.19) is known on the basis of measurements made with the specific instrument, i.e., with a certain error, when real problems are solved. Consequently, satsifaction of this condition guarantees proximity of a solution obtained from approximate values of the right side of (5.19) to the true solution.

Satisfaction of the first two correctness requirements and nonsatisfaction of the third is the usual situation for the inverse problems of mathematical physics. As we shall show below, the situation is the same with Problem (5.18).

To render correct a problem for which the requirement of inverse-operator continuity is not satisfied, we might introduce a sufficiently "strong" norm in space F or a sufficiently "weak" norm in space Φ. However, these approaches have the following disadvantages: in the former case, the statement does not cover those problems in which the errors can be regarded as small only in the usual norm of space F (but not in the "strong" one); in the latter case, functions that do not correspond to physical reality may be solutions of the problem. /256

A.N. Tikhonov [Tychonoff] offered another definition of correctness that makes it possible to approach the correctness problem from new aspects and generalizes on Hadamard's definition [15].

Definition 2. Let there be given, in addition to the spaces F and Φ and operator A, a certain closed space $M \subset \Phi$. We shall call Problem (5.19) Tikhonov correct if the following conditions are satisfied:

1) it is known a priori that a solution ϕ exists for a certain class of data and belongs to the assigned set $M \subset \Phi$;

2) the solution is unique in the class of functions M;

3) infinitesimally small variations of the solution ϕ correspond to infinitesimal variations of $\underline{f}$ that do not drive the solution ϕ beyond the limits of M. Denoting $M_A = A(M)$, we can formulate the third condition as follows.

The solution of (5.19) depends continuously on the right member $\underline{f}$ on M_A. The need to consider the spaces Φ and F along with M and M_A arises out of the fact that the errors in determining the right member $\underline{f}$ in real problems usually take the solution beyond the limits of $\overline{M}_A$. Examination of the problem in Tikhonov's formulation (assuming that $f \in M_A$, and, consequently, $\varphi \in M$) enables us to construct approximate solutions with a certain guaranteed accuracy despite the fact that the solution of Problem (5.19) with approximate data either does not exist at all or deviates sharply from the true solution.

It is found that the compactness of set M in space Φ enables us to affirm Tikhonov correctness. This follows from the following theorem.

Theorem 1. (Continuity of inverse mapping). Let a certain metric space M be mapped continuously and one-to-one onto another metric space N ($A: M \to N$). Then if space M is compact, the inverse mapping $A^{-1}: N \to M$ is also continuous.

Using this important fact, V.K. Ivanov [16] introduced the notion of the quasisolution of Problem (5.19). Let there be given

in addition to the principal spaces F and Φ and the operator A, a compact set M. Then the element $\tilde{\varphi} \in M$, which is defined by the equality $\rho(A\tilde{\varphi}, f) = \min_{\varphi \in M} \rho(A\varphi, f)$ (ρ is the metric in space F), is said to be a quasisolution of Problem (5.19). It is not assumed here that $f \in M_A$. In practice, a number of difficulties are encountered in finding quasisolutions — primarily in isolating the "necessary" compactum M. /257

The most general approach to solution of noncorrect problems of mathematical physics was formulated by A.N. Tikhonov in the concept of the regularizer.

Definition 3. Following A.N. Tikhonov [18], we shall say that any single-parameter family of operators $\{B_\alpha\}_{\alpha>0}$ with a definition region F and a region of values Φ is a regularizer of Problem (5.19) if these regions met the following conditions:

1) for any $\alpha > 0$, B_α is defined and continuous in space F, and

2) for any $\varphi \in \Phi$ $\lim_{\alpha \to 0} B_\alpha A\varphi = \varphi$.

The problem is considered regularizable if there exists at least one regularizer. The existence of a regularizer makes it possible to construct a solution with a certain guaranteed accuracy from an approximate value of the right member $f_\delta: \rho(f, f_\delta) < \delta$. This can be defended with the following theorem:

Theorem 2 (Regularizer Theorem). Let $\{B_\alpha\}_{\alpha>0}$ be a regularizer of Problem (5.19). Let us assume further that the sequence of elements $f_n \in F$ is such that $\rho(f, f_n) < \delta_n$ and $\delta_n \underset{n\to\infty}{\to} 0$. Then there exists a sequence of numbers $\alpha_n^* \underset{n\to\infty}{\to} 0$, such that $B^*_{\alpha_n}(f_n) \underset{n\to\infty}{\to} \varphi$. Indeed, let $\varphi_\delta^\alpha = B_\alpha f_\delta$, $\varphi^\alpha = B_\alpha A\varphi$. Then we have from the triangle inequality

$$\rho(\varphi, \varphi_\delta^\alpha) \leqslant \rho(\varphi, \varphi^\alpha) + \rho(\varphi^\alpha, \varphi_\delta^\alpha)$$

(ρ is a metric in space Φ). Then

$$\rho(\varphi, \varphi^\alpha) \leqslant a_1(\alpha); \quad \rho(\varphi^\alpha, \varphi_\delta^\alpha) \leqslant a_2(\delta, \alpha),$$

where $a_1(\alpha)$ is a function characterizing the speed of convergence of $B_\alpha A\varphi \to \varphi$ as $\alpha \to 0$; $a_2(\delta, \alpha)$ is the continuity modulus of operator B_α on element $A\phi$ for each $\alpha > 0$. Now let $\alpha = \alpha^*$ be a root of the equation $a_1^{-1}(\alpha) = a_2(\delta, \alpha)$; then

$$\rho(\varphi, \varphi_\delta^{\alpha^*}) \leqslant 2a_1(\alpha^*).$$

If we take some sequence $\delta_n \underset{n\to 0}{\to} 0$ and find for it, using the above method, the sequence α_n^*, which will also obviously tend to zero, we obtain $\rho(\varphi, \varphi_{\delta_n^*}^{\alpha_n^*}) \underset{\delta_n \to 0}{\to} 0$, since $a_1(\alpha_n^*) \to 0$ as $\alpha_n^* \to 0$. It should be noted that the notion of the regularizable problem, although more constructive, is also more general than the notion of the Tikhonov-correct problem. Indeed, if we take the contraction of operator A^{-1} on set M_A as B_α for each $\alpha > 0$, we revert to the notion of Tikhonov correctness. We note also that the process of successive determination of quasisolutions is the process of regularization of Problem (5.19). Indeed, let $\{M_\alpha\}$ $(\alpha > 0)$ be a single-parameter family of compacta: $M_{\alpha'} \subset M_{\alpha''}$ $(\alpha' < \alpha'')$; $\bigcup_{\alpha>0} M_\alpha = \Phi$, and let B_α be an operator that defines a quasisolution on M_α. According to theorem 1, operator B_α is continuous and defined over the entire space F. According to the theorems proven by V.K. Ivanov [19], the quasisolutions reduce to the true solution of Problem (5.19) on unlimited "expansion" of the compacta M_α. Thus, the values of $\{B_\alpha\}$ form a regularizer. /258

An important example of the Hadamard-incorrect problem is the Fredholm integral equation of the first kind (5.18). Let us consider the noncorrectness of this problem with reference to one simple example. Let us take the interval $[0, 2\pi]$ as the interval $[a, b]$. Let us assume further that the function ϕ belongs to a Hilbert space $L_2[0, 2\pi]$ and f to the space $L_2[c, d]$. We shall then assume that the first two correctness conditions are satisfied and that for any function $f \in L_2[c, d]$ there exists a unique solution $\varphi \in L_2[0, 2\pi]$. Further, let the function $K(x, y)$ be differentiable with respect to y and let the derivative $K'_y(x, y)$ be uniformly bounded:

$$|K'_y(x, y)| \leqslant c. \tag{5.20}$$

Let us consider the sequence $\phi_n(y) = \sin(ny)$. The corresponding sequence of f_n defined by the equality

$$f_n(x) = \int_0^{2\pi} K(x, y) \sin(ny)\, dy,$$

is (for each fixed x) a sequence of Fourier coefficients (in the sine expansion) of $K(x, y)$ as a function of y. Then, in virtue of Condition (5.20), the sequence $f_n(x)$ on $[c, d]$ converges uniformly to zero [17]. Quite clearly, the sequence of ϕ_n does not converge to zero. At the same time, convergence to zero must obtain whenever the inverse of a given operator is continuous, i.e., whenever the third correctness requirement is satisfied. It should be noted that the "smoother" the kernel $K(x, y)$ of integral

equation (5.18) (i.e., the smaller $\underline{c}$ in (5.20)), the more rapidly will the f_n converge to zero and, consequently, the "worse" will be the inverse operator of the problem.

In [20], A.N. Tikhonov constructed the regularizer $\{B_\alpha\}_{\alpha>0}$ /259 of Problem (5.18). For each value of $\alpha > 0$, B_α is an operator that transforms the given function $f \in F$ ($F = L_2[c, d]$) into an element $\varphi^\alpha \in \Phi$ ($\Phi = c^2[a, b]$), that realizes the minimum of the regularizing functional

$$M_\alpha(\varphi, f) = \int_c^d \left\{ \int_a^b K(x, y)\varphi(y)\,dy - f(x) \right\}^2 dx + \\ + \alpha \left\{ \int_a^b K_1(y)[\varphi(y)]^2 dy + \int_a^b K_2(y)\left[\frac{d\varphi}{dy}\right]^2 dy \right\} \qquad (5.21)$$

$$(K_1(y), K_2(y) > 0; \quad a \leqslant y \leqslant b).$$

An explicit expression for the operator B_α can be obtained from the Euler equation of the variational problem (5.21). We then have the following improvement of Theorem 2.

Theorem 2'. If the regularizer $\{B_\alpha\}$ is selected as described above, the sequence of elements $f_n \in F$, $f_n \underset{n\to\infty}{\to} f$ is such that $\int_c^d \{f_n(x) - f(x)\}^2 dx \leqslant \delta_n^2$, $\delta_n \underset{n\to\infty}{\to} 0$, and the number sequence $\alpha_n \to 0$ at speed $\alpha_n = 0(\delta_n^2)$, we have $B_{\alpha_n}(f_n) \underset{n\to\infty}{\to} \varphi$.

Introduction of the regularizing functional (5.21) actually introduces a metric that essentially separates "smooth" and "non-smooth" functions into the space of solutions Φ. The second part of the functional (5.21) determines the a priori "worth" of the given element $\varphi \in \Phi$: the smaller the value of the functional on this element, the greater will be its a priori "worth." We see from (5.21) that preference is given to smoother functions. This general method of regularizing Problem (5.18) and its basic ideas have formed the basis of many numerical methods for solution of this problem, which we shall henceforth call methods of α-parametric regularization.

The problem of thermal sounding of the atmosphere has been solved by a wide variety of mathematical methods. All of them have actually been designed for solution of the approximating (Eq. (5.18)) system of linear algebraic equations. Let us write this system in the form of the equality

$$A\varphi = f. \qquad (5.22)$$

where A is (in the general case) a square matrix of dimension mxn

that describes the transformation of the unknown atmospheric characteristic ϕ (n-dimensional vector) into the m-dimensional vector f of the measured quantity. The vector f is the sum /260

$$f=\bar{f}+\varepsilon \tag{5.23}$$

of the true value $\bar{f}$ of the quantity and the error vector ε, which we shall regard as a random vector whose uncorrelated components are normally distributed with zero mean and a variance σ^2. Together with Eq. (5.22), we shall examine the "undisturbed" problem (system)

$$A\bar{\varphi}=\bar{f}. \tag{5.24}$$

Detailed analysis of the various methods and comparisons with the general mathematical notion of the (Tikhonov) regularizer leads us to the conclusion that the solution of Problem (5.18) in connection with the present problem must incorporate three basic elements [90]:

1) mathematical introduction of a priori information on the solution;

2) selection of optimum conditions for measurements of the function f;

3) a stable solution of the algebraic-equation system, obtained on the basis of completed first and second steps.

The need to introduce a priori information on the solution results from the fact that within a small range of error in assignment of the function f, there exists an infinite set of solutions of the starting integral equation (5.18) and the approximating system of algebraic equations (5.22), which have widely varying structures and differ strongly in the corresponding metrics of the solution spaces.

The importance of optimum selection of measurement conditions for the function f proceeds from technical limitations on the possible number of measurements and the substantial mutual correlation of error-burdened measurements of f in different spectral intervals.

The derived algebraic-equation system is often not only poorly grounded (as a result of noncorrectness), but also often indeterminate (the number of equations does not agree with the number of unknowns). To solve this system, therefore, it is necessary to apply stabilizing methods that take account of a priori information on the unknown function ϕ.

A priori hypotheses as to the unknown function ϕ may be either quite general in nature (boundedness, smoothness), or quite

specific (property of belonging to an empirical probability population with an assigned mean ϕ and a correlation matrix D obtained by statistical reduction of numerous direct measurements of ϕ). It is these hypotheses that are used in the existing methods; they can be interpreted either as "deterministic" or probabilistically. /26 As a rule, this is done by introducing an a priori metric (explicitly or implicitly) determined by the scalar product

$$[\varphi, \varphi] H = (H\varphi, \varphi), \tag{5.25}$$

or introducing an a priori normal probability distribution with a density function

$$P(\varphi) = \frac{|H|^{1/2}}{(2\pi)^{n/2}} \exp\left\{-\frac{1}{2}(H\varphi, \varphi)\right\} \tag{5.26}$$

in the Euclidian solution space E_n. The specific form of the symmetrical positive-definite matrix H depends on the nature of the a priori hypotheses. For example, H may be a matrix that yields, in (5.25), an approximate value of the integral $\int_a^b [\varphi(y)]^2 dy$ or $\int_a^b [\varphi'(y)]^2 dy$ in cases in which the solution of (5.18) is assumed to be bounded or smooth, and may also be the inverse of the empirical correlation matrix D. Sometimes, "deterministic" smoothness hypotheses are interpreted probabilistically in order to use a more convenient mathematical apparatus. Certain authors [11, 12, 8] use concrete statistical information (a correlation matrix) in methods that should be classified as deterministic because of the use of analytical apparatus. The inadequacy of the apparatus used to the nature of the a priori information results in incomplete utilization of the information.

In most methods, the problem of selecting measurement conditions has been examined on the empirical level. Depending on the type of interpretation (deterministic or probabilistic), this problem can be stated as follows.

1. Select from among the practically possible measurements conditions for measurement of the function f such that the matrix A of System (5.22) that corresponds to them will be most stable in the sense of the a priori metric (5.25) with respect to the particular nature and magnitude of the "disturbances" in assigning f in the a priori class of solutions: $(H\phi, \phi) < C$ (the constant C must be suitably selected).

2. Treating ϕ as a normally distributed random variable (for example, distributed according to (5.25)) and selecting an adequate quantitative information measure, distribute the sounding spectral ranges in such a way as to extract the possible maximum

f information on ϕ as a random variable.

S. Twomey [23] made one attempt to solve the problem in a ormulation substantially simplified as compared to the determinis- ic formulation described above. We shall discuss his methods in /262 erms of the vector nomenclature that we have introduced. Let us erform scalar multiplication of the terms of (5.22) by some unit ector ξ: $\|\xi\|=1$. We obtain

$$(A\varphi, \xi)=(\overline{f}, \xi)+(\varepsilon, \xi).$$

Using indices to denote the individual components of the corresponding vectors, we obtain

$$\overline{f}_l=-\frac{1}{\xi_l}\sum_{\substack{l=1\\ l\neq l}}^{m}\overline{f}_l\xi_l+\frac{1}{\xi_l}\{(A\varphi, \xi)-(\varepsilon, \xi)\} \quad (l=1, 2, \ldots, m).$$

On examining the right member of this equality, we conclude hat for the measurements f_1 of the function $\underline{f}$ to carry more use- ul information than "noise," it is necessary that the relation

$$|(A\varphi, \xi)|>|(\varepsilon, \xi)| \tag{5.27}$$

e satisfied for all $\|\xi\|=1$.

Since the mathematical expectation of $|(\varepsilon, \xi)$ is σ for all $|\xi\|=1$, we find after a number of evaluations that (5.27) obtains nly when the inequality

$$\frac{\sigma}{n\overline{\varphi}_{av}}<\lambda_{min}, \tag{5.28}$$

s satisfied; here, $\overline{\phi}_{av}=\frac{1}{n}\sqrt{\sum_{j=1}^{n}\varphi_j}$, and λ_{min} is the minimum eigen- alue of the positive-definite matrix AA* (* is the transposition ymbol). When (5.28) is not satisfied, Twomey proposes that the orresponding row be struck from matrix A and that this operation e repeated until (5.28) is satisfied. The quantity $\overline{\phi}_{av}$ is to haracterize the sought solution. However, it is perfectly clear hat selection of measurement conditions must be oriented not to definite (perhaps characteristic) solution, but to the whole priori class or probability population of solutions. Moreover, womey is essentially concerned not with optimization of measure- ent conditions, but with isolation of $\underline{f}$-measurements that are inearly independent within the limits of error ε.

Probabilistic interpretation of the sought solution makes it ossible to use a convenient information apparatus. Using an in- ormation characteristic that he introduced, V.P. Kozlov examined

the problem of optimizing f-measurement conditions for the case in which concrete statistical information on the unknown characteristic is available (empirical correlation matrix D) [13]. We shall outline this method in its essentials farther on, since it is closely interrelated with the stabilization algorithm. /263

An algorithm for selection of f-measurement conditions is constructed on the basis of the classical Shannon measure of information in a paper of O.M. Pokrovskiy [24]; it can be used in cases corresponding to a broad range of a priori hypotheses as to ϕ (smoothness, boundedness, property of belonging to an empirical probability population). It is shown in the first segment of this work that the (Shannon) quantity of information contained in the measurements vector $f = \bar{f} + \varepsilon$ concerning a random variable ϕ that is normally distributed with the density function (5.26) is determined by the equality

$$J(\varphi, f) = \frac{1}{2} \log \frac{\det (AH^{-1}A^* + \sigma^2 I_m)}{(\sigma^2)^m}$$

(I_m is a unitary square matrix of order m).

Let us assume that we have at our disposal l spectral intervals, of which we must select m. Optimum selection of measurement conditions then requires $\frac{l!}{(l-m)!m!}$ calculations of the determinant in (5.28). When l is large (as is the case in practice), it may become impossible to perform this task. Accordingly, the paper proposes a method of successive selection of informative spectral intervals based on decomposition of the information-quantity increment extracted from the measurements on addition of a new, (m + 1)th spectral interval into two component parts: "noise" and useful information on the function ϕ:

$$\Delta J_{m+1} = \sigma^2 + \frac{\Gamma_\Phi(\tilde{a}_1, \tilde{a}_2, \ldots, \tilde{a}_m, \hat{a}_{m+1})}{\Gamma_\Phi(\tilde{a}_1, \tilde{a}_2, \ldots, \tilde{a}_m)}.$$

In this equality, the (1 + n)-dimensional vectors $\tilde{a}_i = (a_{i1}, a_{i2}, \ldots, a_{in}, \underbrace{0 \ldots 0}_{i-1}, \sigma, \underbrace{0 \ldots 0}_{l-i})$, $\hat{a}_i = (a_{i1}, \ldots, a_{in}, \underbrace{0 \ldots 0}_{l})$ $(i = 1, 2, \ldots, l)$, composed by the components of matrix $A = \{a_{ij}\}$, appear in the generalized Gramian

$$\Gamma_\Phi(a_1, \ldots, a_m) = \begin{vmatrix} (\Phi a_1, a_1)(\Phi a_1, a_2) \ldots (\Phi a_1, a_n) \\ \cdots\cdots\cdots\cdots \\ (\Phi a_n a_1)(\Phi a_n, a_2) \ldots (\Phi a_n, a_n) \end{vmatrix}$$

with the matrix

$$\Phi = \left(\begin{array}{c|c} H^{-1} & 0 \\ \hline 0 & I_l \end{array} \right).$$

On this basis, the i_1th interval, to which the $\Gamma_\Phi(\hat{a})$-maximizing vector $\hat{a}_{i_1}$ corresponds, should be taken as the first spectral interval. Thereafter, optimum selection of the (m + 1)th spectral interval with respect to the m intervals (m = 1, 2, ...) selected in the preceding steps consists in finding the number i_{m+1} to which the $\Gamma_\Phi(\tilde{a}_{i_1}, \ldots, \tilde{a}_{i_m}, \hat{a})$-maximizing vector $\hat{a}_{i_{m+1}}$ corresponds. /264

As a rule, stable-solution methods for algebraic equations are based on substitution of the unstable problem matrix operator by a stable operator that differs minimally (with consideration of a priori information on the solution) from the given operator. This is done in two ways: a) by contracting the given operator A to a certain subspace of smaller dimensionality (smaller than E_n); b) by distorting operator A in order to stabilize it throughout the entire space E_n. It must be noted here that methods based on the distortion principle are based on the ideas of the regularization method. Let us now examine the various methods in accordance with the above classification into two groups.

In one of the first papers devoted to the problem of temperature sounding of the atmosphere, G. Yamamoto [25] sought the solution of the problem in the form of an expansion in a system of orthogonal functions $\{e_k\}$

$$\varphi^{(l)} = \sum_{k=1}^{l} c_k e_k \quad (l \leqslant n). \tag{5.29}$$

This method is known as the method of moments in computational mathematics. On numerical realization of this method, we obtain the following equation system for the unknown coefficients c_k (k = 1, ..., l):

$$E^*A^*AEc = E^*A^*f, \tag{5.30}$$

in which the vector $c = (c_1, \ldots, c_l)$ and the matrix $E = (\bar{e}_1 | \ldots \bar{e}_l)$ is formed from the vectors $\{e_k\}$ corresponding to the functions $\{e_k\}$. In solving (5.30), G. Yamamoto encountered an unusual effect. As the number l of terms in the expansion (5.29) increased beyond a certain value, approximations $\phi^{(l)}$ that deviated increasingly from the exact solution were obtained. An approximation $\phi^{(l)}$ that takes account of only a few terms of the expansion (5.29) was found to be optimum; this optimum value of l decreases with increasing error ε in the assignment of f. This reflected the noncorrectness of the problem of solving the Fredholm integral equation of the first kind, as discerned in the poor conditionality of the matrix of (5.30). L. Kaplan [26] noted a similar effect in an attempt to solve the problem by another method.

A.M. Obukhov [27] showed that expansion of geophysical-field characteristics with respect to the basis formed by the eigenvectors of the empirical correlation matrix gives the optimum (in the statistical sense) approximation of these characteristics. Using A.M. Obukhov's results, M.S. Malkevich and V.I. Tatarskiy [12] proposed to find the solution ϕ of Problem (5.22) in the form of an expansion in empirical orthogonal vectors $\{e_k\}$ (the eigenbasis of correlation matrix D): /265

$$\varphi^{(l)} = \tilde{\varphi} + \sum_{k=1}^{l} \hat{c}_k \hat{e}_k \qquad (5.31)$$

where $\tilde{\phi}$ is the average vector). In this case, Eq. (5.22) is transformed to the system

$$\hat{E}^* A^* \hat{E} \hat{c} = \hat{E}^* A^* \left(f - A\tilde{\varphi}\right) \left(\hat{E} = \left|\hat{e}_1\right| \ldots \left|\hat{e}_l\right|\right) \qquad (5.32)$$

for determination of the vector of the unknown coefficients $\hat{c} = (\hat{c}_1, \ldots, \hat{c}_l)$. The determination of the optimum number of elements in the expansion (5.31) was based solely on a series of numerical experiments. An advantageous feature of this method, as compared with G. Yamamoto's method, was the use of the optimum statistical approximation. This made it possible to secure relatively good approximations of the solution while using a small number of terms of Expansion (5.31). However, staying within the framework of the deterministic algorithm (method of moments), the authors of [12] did not use the extensive information on the solution that was inherent in the empirical correlation matrix for rigorous definition of the optimum number of basis elements necessary for reconstruction of ϕ from the measurements vector $\underline{f}$ with an assigned level of error σ^2. This deficiency was corrected by V.P. Kozlov [13] in his statistical approach to solution of the problem. This method also proposes that the solution be sought in the form of the expansion (5.31), whose coefficients are determined from (5.32). Assuming that the errors ε in the measurements of $\underline{f}$ are Gaussian "white noise" with a variance σ^2, V.P. Kozlov introduced an information metric into the solution space by means of the equality

$$\rho^2(\varphi_1, \varphi_2) = \frac{1}{\sigma^2}(A^* A\varphi_1, \varphi_2), \quad \varphi_1, \varphi_2 \in E_n. \qquad (5.33)$$

The metric (5.33) has an important statistical implication: the two elements $\varphi_1, \varphi_2 \in E_n$ are practically indistinguishable at a given error level σ^2 if $\rho^2(\varphi_1, \varphi_2) \leq 1$. Kozlov assumes further that the solution belongs to a bounded a priori region (the scattering ellipsoid of the sought random variable ϕ, whose dimensions are determined by the elements of the empirical correlation matrix D) /266 and considers the extent of this region in various directions in units of the information metric. If in any direction the "thickness" of the a priori region in metric (5.33) does not exceed

unity, there is no point in concerning ourselves with projection of the solution onto this direction, since the error of possible determination will exceed the range of its possible variation in the a priori region. The average dimensions of the a priori region (in units of the information metric (5.33)) in mutually orthogonal directions are calculated as square roots of the eigenvalues λ_i of matrix $\frac{1}{\sigma^2} DA^*A$, while the directions themselves are determined by the corresponding eigenvectors. The author proposes the quantity $V = \sqrt[\lambda_i > 1]{\prod \lambda_i}$ as the measure of information for this method. It represents the number of distinguishable (by means of this method) elements of the a priori region within the limits of a given measurement-error level σ^2.

Within the framework of the method that he proposed for solution of the inverse problem, V.P. Kozlov considered the problem of selecting optimum measurement conditions for the function $\underline{f}$. Suppose that the matrix A in System (5.22) corresponds to all possible ($\underline{1}$) spectral intervals. The problem of evaluating the information potential of the method in the a priori region is solved by finding the eigenvalues $\{\lambda_i\}$ and vectors $\{u_i\}$ of the matrix $\frac{1}{\sigma^2} DA^*A$, which determine the information directions in this region:

$$\frac{1}{\sigma^2} DA^*Au_i = \lambda_i u_i.$$

The elements Au_i, which are eigenvectors of a matrix $\frac{1}{\sigma^2} ADA^*$ with the same eigenvalues $\{\lambda_i\}$, indicate the information directions in the space of signals $\underline{f}$. Kozlov combines the given spectral intervals on the basis of analysis of the components of the vectors Au_i corresponding to eigenvalues $\lambda_i > 1$. The quantitative criterion for this grouping of adjacent spectral intervals is maximization of the information quantity V for the new matrix A. With this combination of spectral intervals, V increases as a result of the increase in signal/noise ratio (concrete results of calculations by the Kozlov method are given on pages 263-265).

A method of isolating the stable part of the solution of (5.22) in the case of quite general a priori hypotheses as to the unknown ϕ (smoothness, boundedness) is proposed in O.M. Pokrovskiy's papers [28, 29]. The element $\bar{\varphi} \in E_n$ that has the minimum norm (see Formula (5.25)) /267

$$\|\bar{\varphi}\|_H^2 = (H\bar{\varphi}, \bar{\varphi})$$

among all of the elements that satisfy the "undisturbed" equation (5.24) is regarded as the exact solution. Let us denote by $\{e_k\}$ and $\{\lambda_k\}$ the eigenvectors and eigenvalues of the matrix $AH^{-1}A^*$.

It can be shown that the solution of Problem (5.22) is represented by the expansion

$$= \sum_{k=1}^{m} \tilde{c}_k \varphi_k, \qquad (5.34)$$

where $\tilde{c}_k = \frac{(f, e_k)}{\lambda_k}$, $\varphi_k = H^{-1}A^* e_k$ $(k=1, \ldots, m)$. Here, in virtue of (5.23), $\tilde{c}_k$ is a random variable. The same can be said of (5.34). We seek the stable solution of Problem (5.22) in the form

$$\hat{\varphi} = \sum_{k=k_1, \ldots, k_N} \tilde{c}_k \varphi_k, \qquad (5.35)$$

where the set of indices $k_1, \ldots, k_N$ is found to minimize the variance of the deviation from the exact solution $\bar{\phi}$

$$E\left(H\left(\bar{\varphi} - \hat{\varphi}\right), \bar{\varphi} - \hat{\varphi}\right)$$

(E is the sign of the mathematical expectation).

The criterion for selection of the set $(k_1, \ldots, k_N)$ is the inequality

$$\bar{f}_k = (\bar{f}, l_k) \geqslant \sigma^2. \qquad (5.36)$$

However, we do not know $\bar{f}_k$. Using the rule of confidence-interval estimation, we find that $\bar{f}_k$ satisfies the inequality

$$f_k - a\sigma \leqslant \bar{f}_k$$

with probability $\frac{1}{2} + \Phi(a)$, where $\Phi(a)$ is the probability integral. For example, for a = 0.5, the inequality $f_k \geq 1.5\sigma$ serves with a probability of $\sim$0.7 as a criterion of the hypothesis (5.36), which is usually a "threshold of discrimination" and can therefore be used in practice to test Hypothesis (5.36), which leads to selection of the solution $\hat{\phi}$ that is optimum according to (5.35). In contrast to V.P. Kozlov's method, the general nature of the a priori hypotheses as to the solution does not in this case enable us to isolate any bounded a priori region. The information /268 contained in H (in the case of a smoothness hypothesis) enables us merely to correlate the various components of the unknown vector ϕ. Hence the criterion that serves for isolation of the stable part of the solution is related only to the analysis of the given f. In the Kozlov method, isolation of the stable part of the basis is related to the magnitude of the error σ^2 and the characteristics of the a priori region, and is not linked in any

way to the specific realization f. Hence the described method may prove to be more flexible (in statistical interpretation, i.e., when $H = D^{-1}$) in cases in which the true solution of the problem differs significantly from the empirical statistics.

The error in assigning the matrix A can be taken into account in a definite sense by the method of expanding in eigenvectors of the operator $B = AH^{-1}A^*$. If the matrix A is assigned with a certain error, we obtain matrix B in the form $B = \overline{B} + \Delta$, where Δ is the symmetrical error matrix and $\overline{B}$ is the exact value of this matrix. Elementary bookkeeping [29] leads us to the inequality

$$\lambda^{\overline{B}}_{\min} \geqslant \lambda^{B}_{\min} - |\lambda^{\Delta}|_{\max},$$

in which the extreme eigenvalues of the matrices indicated by the indices appear. Hence we conclude that the eigenvalues λ_i of the "disturbed" matrix B, for which the inequality

$$\lambda^{B}_{i} \leqslant |\lambda^{\Delta}|_{\max} \tag{5.37}$$

is satisfied, are comparable with the zero eigenvalues (in the sense that the corresponding values of the true matrix $\overline{B}$ can equal zero), and hence that the terms associated with them in the expansion (5.34) must be eliminated from (5.35). Thus, (5.37) yields an independent criterion for stabilization of the solution with respect to errors in assigning the operator A.

The methods that we placed in the second group have been based on minimization of regularizing functionals of the form

$$\|A\varphi - f\|^2 + \alpha(H\varphi, \varphi) \quad (\alpha > 0). \tag{5.38}$$

The vector ϕ^{α} that realizes the minimum of Functional (5.38) is an approximation of the exact solution. The vector ϕ^{α} is determined from the Euler equation for (5.38)

$$(A^*A + \alpha H)\varphi^{\alpha} = A^*f. \tag{5.39}$$

Thus, the element that introduces stability into the solution of the initial problem is the matrix operator αH. The operator H is determined by the nature of the a priori hypotheses on the solution (see (5.25)).

The pivotal problem in practical solution using methods based /269 on the idea of α-parametric regularization is selection of the optimum α (to which the ϕ^{α} that deviates minimally from the exact solution $\overline{\phi}$ corresponds). Different interpretations of the problem data, a priori information, and sometimes even of the problem itself (as we shall show below) have resulted in different algorithms for selection of α. D. Phillips [30] and later

S. Twomey [31] proposed examination of the problem at a conditional extremum. That is to say, they proposed treating the vector $\check{\varphi}$ that minimizes the functional $(H\phi, \phi)$ (the matrix H corresponds to the smoothness hypothesis) as the solution ϕ of Problem (5.22) with the condition that $\|A\check{\varphi}-f\|^2 \leqslant \delta^2$, where the vector f, which is measured with an error, satisfies the condition $\|\bar{f}-f\|^2 \leqslant \delta^2$. On solving this problem by the Lagrange method of multipliers, we arrive at a functional of the form (5.38), in which $\alpha = 1/\lambda$ (λ is the Lagrange multiplier defined with the additional condition $\|A\hat{\varphi}-f\|^2=\delta^2$). With this formulation, we obtain as the solution a vector $\bar{\varphi}$ that approximates the smoothest of the acceptable functions that satisfy the starting equation (5.18) within the limits of error δ. This approach is purely deterministic.

D. Wark et al. [8] modified the Phillips-Twomey "smoothing" method for solution in the empirical orthogonal vector basis used in the methods of M.S. Malkevich and V.P. Kozlov. However, the deterministic apparatus of the Phillips-Twomey method did not permit extraction of the optimum value of the regularization parameter α from the concrete statistical information on the solution.

A.N. Tikhonov and V.B. Glasko [37] treated the problem of numerical realization of the regularization method (5.21) deterministically. Since the solutions of (5.38) and (5.39) depend in numerical realization of the regularization method on α, the criterion for selection of the optimum α was based on the idea of minimizing the variation of the "regularization" solution ϕ^α of Problem (5.39) with respect to α $\left\|\frac{\partial\varphi^\alpha}{\partial\alpha}\alpha\right\|$. The optimum parameter α is selected on the set $\{\alpha_i\}$ defined by the geometric progression $\alpha_{i+1} = \alpha_i q$ ($q < 1$) by finding the minimum of $\|\varphi^{\alpha_i}-\varphi^{\alpha_{i+1}}\|$, in view of the approximation

$$\Delta(\alpha_i) = \left\|\frac{\partial\varphi^\alpha}{\partial\alpha}(\alpha_i)\right\| \approx \frac{\|\varphi^{\alpha_i}-\varphi^{\alpha_{i+1}}\|}{1-q}. \qquad (5.40)$$

However (as the authors of [37] point out), the function $\Delta(\alpha)$ usually has several local minima. This leads to a certain indeterminacy in selection of α, and, in the case of large errors in assigning f, to erroneous conclusions regarding the optimum α. This is because the criterion (5.40) does not explicitly incorporate the dependence on the error in assignment of f. /270

O.M. Pokrovskiy [38] continued this investigation. Assuming that a priori information on the solution is introduced with (5.25) and that the error ε consists of "white noise" with a variance σ^2, the author treats the solution of the regularized

equation (5.43) as a function of α and ε: $\varphi^{\alpha}=\varphi(\alpha, \varepsilon)$. The solution $\bar{\varphi}$ of (5.24) with the minimum norm (5.25) is regarded as the exact solution of the problem. Obviously, $\bar{\varphi}=\varphi(0,0)=\lim_{\alpha\to 0}\varphi(\alpha, 0)$. Then the value of α that minimizes the quantity

$$\varphi(0, 0)-\varphi(\alpha, \varepsilon) \tag{5.41}$$

for the given ε will be optimum in solution of Problem (5.22) by means of (5.43). The only known characteristic of the random variable ε is its variance σ^2. Since the function $\phi(\alpha,\varepsilon)$ is smooth in the range $\{|(\alpha, \varepsilon)|\alpha\geqslant 0; \varepsilon\in E_m\}$ (if it is appropriately defined for $\alpha = 0$), the Taylor-series expansion can be used to evaluate the difference between the exact solution and the α-approximation. It is proposed that the first (complete) variation of the quantity (5.41) of interest be regarded as an approximation of that quantity. In view of the probabilistic nature of ε, the mathematical expectation of the first variation of the function $\phi(\alpha,\varepsilon)$ in the <u>a priori</u> metric (5.25) is determined by the equality

$$\gamma(\alpha)=\alpha^2\|L(A^*A+\alpha H)^{-1}H\varphi\|^2+\sigma^2\operatorname{tr}\{L(A^*A+\alpha H)^{-1}A^*A(A^*A+\alpha H)^{-1}L^*\}, \tag{5.42}$$

where the direct triangular matrix L is determined by the expansion $H = L^*L$. The first term in (5.42) represents $\left\|L\frac{\partial\varphi}{\partial\alpha}\alpha\right\|^2$, which is analogous to (5.40) as used in A.N. Tikhonov and V.B. Glasko's method. The second term, which represents the probable variation of the solution with respect to ε, is a decreasing function of α, and hence, in combination with the first term, introduces indeterminacy into the selection of α (in practice, it makes it possible to introduce indeterminacy into selection of the minimum of the function $\left\|\frac{\partial\varphi}{\partial\alpha}\cdot\alpha\right\|^2$). Moreover, the minimum value of the function $\gamma(\alpha,\varepsilon)$ with respect to α determines the approximate value of the deviation of the optimum regularized solution from the exact solution in the sense of the metric (5.25) and with consideration of the statistical nature of the error ε. /271

V.F. Turchin [32] used an idea similar to that proposed by D. Phillips, but treated the problem probabilistically. <u>A priori</u> hypotheses as to the sought solution are introduced with the aid of a parametric family of <u>a priori</u> probability distributions with density functions

$$P_{\tilde{\alpha}}(\varphi)=\frac{|H|^{1/2}}{(2\pi)^{n/2}}\tilde{\alpha}^{n/2}\exp\left\{-\frac{\tilde{\alpha}}{2}(H\varphi, \varphi)\right\}\quad(\tilde{\alpha}>0), \tag{5.43}$$

where the matrix H is selected by the same principles as in (5.26). Since the error vector of the measurements of f is assumed to be Gaussian "white noise" with a variance σ^2, the probability of

obtaining the vector $\underline{f}$ from the measurements with the condition that vector ϕ be the solution is determined by the density

$$P(f/\varphi) = \frac{1}{(2\pi\sigma^2)^{m/2}} \exp\left\{-\frac{\|A\varphi - f\|^2}{2\sigma^2}\right\}.$$

According to Bayes' formula [35], the a posteriori probability of the solution ϕ (provided that the vector $\underline{f}$ has been measured) is determined by the equality

$$P_{\tilde{\alpha}}(\varphi/f) = C \exp\left\{-\frac{1}{2}\left[\frac{\|A\varphi - f\|^2}{\sigma^2} + \tilde{L}(H\varphi, \varphi)\right]\right\} \qquad (5.44)$$

(C is a quantity selected from the normalization condition).

It is proposed that the mathematical expectation of the random variable ϕ according to the a posteriori distribution (5.44) be regarded as the solution to the problem. This quantity is defined as the element that minimizes the functional

$$\|A\varphi - f\|^2 + \tilde{\alpha}\sigma^2(H\varphi, \varphi). \qquad (5.45)$$

The value of $\tilde{\alpha}$ that is maximum among all values for which the variance according to the a posteriori distribution

$$\int_{E_n} \|A\varphi - f\|^2 P_{\tilde{\alpha}}(\varphi/f)\, d\varphi$$

does not exceed the variance σ^2 of the natural errors of measurement of $\underline{f}$ is regarded as optimum. Since the distributions (5.43) impose increasingly rigid limitations on "smoothness" with increasing $\tilde{\alpha}$, the optimum $\tilde{\alpha}$ determines the "smoothest" class of the family (5.43) that still permits solution of (5.22) with error σ^2. The analogy with the idea of D. Phillips, that of selection of the "smoothest" of the acceptable solutions, exists precisely in the sense of selection of the "smoothest" class. /272

Given concrete statistical information on the solution (the empirical average $\tilde{\phi}$ and the correlation matrix D), Turchin's method [32] uses as its a priori probability distribution the normal distribution with the density function

$$P(\varphi) = \frac{|D^{-1}|^{1/2}}{(2\pi)^{n/2}} \exp\left\{-\frac{1}{2}\left(D^{-1}\left(\varphi - \tilde{\varphi}\right), \varphi - \tilde{\varphi}\right)\right\}.$$

In this case, the functional that yields the solution of our problem will take the form

$$\|A\varphi - f\|^2 + \sigma^2\left(D^{-1}\left(\varphi - \tilde{\varphi}\right), \varphi - \tilde{\varphi}\right) \qquad (5.46)$$

On comparing (5.46) and (5.45), we note that in this case the concrete statistical information permits unique (at least statistically) solution of the problem of selecting the parameter $\tilde{\alpha}$: $\tilde{\alpha} = 1$.

The Euler equation for Problem (5.46) determines the unknown solution

$$\varphi = (A^*A + \sigma^2 D^{-1})^{-1} A^* (f - \tilde{f}) + \tilde{\varphi} \quad (A\tilde{\varphi} = \tilde{f}). \tag{5.47}$$

Calculation of D^{-1} involves certain difficulties because of the poor conditionality of matrix D. However, these difficulties can be overcome by use of the identity

$$(A^*A + \sigma^2 D^{-1})^{-1} A^* = DA^* (\sigma^2 I + ADA^*)^{-1}. \tag{5.48}$$

According to (5.48), the solution can be determined from the equality

$$\varphi = DA^* (\sigma^2 I + ADA^*)^{-1} (f - \tilde{f}) + \tilde{\varphi},$$

in which the matrix D^{-1} does not appear.

E. Westwater and O. Strand [35, 36] proposed a method for solution of the inverse problem in the case of availability of concrete statistical information on the solution; as we shall show below, it leads to the same result as V.F. Turchin's method.

Suppose that it is known that the unknown solution vector ϕ belongs to a normally distributed probability population with a correlation matrix D and a mean $\tilde{\phi}$. Further, let $\tilde{f} = A\tilde{\varphi}$, $\eta = \varphi - \tilde{\varphi}$, $h = f - \tilde{f}$. Our problem will then consist in solving the equation

$$A\eta = (\bar{f} - \tilde{f}) + \varepsilon \tag{5.49}$$

($\bar{f}$ is the exact value of the right member), in which ε is a "white noise" vector with variance σ^2. It is proposed that the linear unbiased estimate $\hat{\eta} = Bh_\varepsilon$ ($h_\varepsilon = \bar{f} - f + \varepsilon$), which is optimum in /273 the sense that it minimizes the variance $E\{(\hat{\eta} - \eta, \hat{\eta} - \eta)\}$ on the a priori distribution of the random variable η, be regarded as the solution of (5.49). It is known [33] that the optimum linear predictor in this problem is the matrix

$$B = DA^* (\sigma^2 I + ADA^*)^{-1}. \tag{5.50}$$

The correlation matrix of the solutions

$$S_{\eta - \eta} = \left(D^{-1} + \frac{1}{\sigma^2} A^*A\right)^{-1}$$

gives information on the probability distribution of the

reconstructed quantities η, where the quantity $\mathrm{tr}(S_{\hat{\eta}-\eta})$ ($\mathrm{tr}(A)$ is the trace of matrix A), which is the sum of the squares of the components of the random variable η to be reconstructed, can be regarded as a measure of the reconstruction error.

Comparing (5.47), (5.48), and (5.50), we arrive at the conclusion that the Bayes strategy leads to the same result as the linear estimate of least squares.

Within the framework of their proposed approach, E. Westwater and O. Strand [36] examined the problem of selecting optimum conditions for measurements of $\underline{f}$. Suppose that we have $\underline{l}$ spectral intervals (and hence $\underline{l}$ equations in a system of the form (5.49)), from which we must select $\underline{m}$ spectral intervals (and the corresponding equations). Obviously, it is possible to make $\frac{l!}{(l-m)!m!}$ different selections. Minimization of the quantity $\mathrm{tr}(S_{\hat{\eta}-\eta})$ (which corresponds to the various selection possibilities) is proposed as a criterion for selection of the optimum set of $\underline{m}$ spectral intervals. However, as the authors indicate, practical solution of the problem may be difficult when the number $\underline{l}$ is large.

J. King's "nonlinear method" [39] occupies a special position among the various regularization methods. This method was designed for approximate solution of an integral equation of the form

$$I\left(\frac{1}{\mu}\right) - B(0) = \int_0^\infty \frac{dB}{d\tau}(\tau) e^{-\frac{\tau}{\mu}} d\tau \qquad (5.51)$$

(the integral form of the transfer equation) for the function dB/dτ, which is represented in the form

$$\frac{dB}{d\tau} \sum_{j=1}^{n} \Delta B_j \delta(\tau - \tau_j) \quad (j = 1, 2, \ldots, n) \qquad (5.52)$$

(δ(τ) is the Dirac delta function), which corresponds to representing the unknown Planck function B(τ) in the form of a step function with increments ΔB_j at points τ_j (j = 1, 2, ..., n). In virtue of the known properties of the delta function δ(τ), substitution of (5.52) into (5.51) yields

$$I\left(\frac{1}{\mu}\right) - B(0) = \sum_{j=1}^{n} \Delta B_j x_j^{\frac{1}{\mu}} \quad x_j = e^{-\tau_j}. \qquad (5.53)$$

Selecting whole-numbered values of the variable 1/μ

$$\frac{1}{\mu_i} = i = 0, 1, 2, \ldots, 2n-1,$$

into (5.53), we obtain the equalities

$$I(i) - B(0) = \sum_{j=1}^{n} \Delta B_j x_j^i \quad (i = 0, 1, \ldots, 2n-1).$$

in which the right members formally represent the quadrature sums of the polynomials x^i (i = 0, 1, ..., 2n-1) and the left members are exact values of the integrals of (5.51) for $1/\mu$ = 0, 1, ..., 2n-1.

The values x_j, which have hitherto been arbitrary, are defined as nodes of the Gaussian quadrature formula, which is exact for all polynomials of degree no greater than 2n-1. At the same time, the unknown values ΔB_j are defined as the corresponding quadrature coefficients. An attractive feature of this method is the fact that the variables $1/\mu$ are uniquely defined within the algorithm (whether optimally or not is unclear). It is also highly important that the algorithm for finding the nodes x_j automatically stabilizes the system of algebraic equations for determination of the ΔB_j against errors in I ("unstable" nodes occur outside the range of integration in the complex plane). A certain generalization of this algorithm will be found in [9].

§3. CERTAIN INFORMATION ON THE ABSORPTION CHARACTERISTICS OF ATMOSPHERIC GASES

As we noted above, the carbon dioxide bands at λ = 4.3 μm and λ = 15 μm and the oxygen band at $\lambda \approx 5$ mm are presently used for thermal-sounding purposes. Since quantitative absorption characteristics are needed to obtain the corresponding integral-equation kernels, we present the basic data on these bands.

The CO_2 absorption band at λ = 15 μm is perhaps one of the most thoroughly studied regions of the infrared spectrum. This is primarily because of the strong influence of this band on shaping of the atmosphere's thermal-radiation field and the possibilities for its use in solution of the inverse problems of atmospheric optics. It consists of a series of vibrational-rotational bands, most important among which is the fundamental ν^2 band (00^00-01^10). Weak bands governed by transitions between excited levels also make an appreciable contribution to absorption, as do isotope bands. /275

Many theoretical and experimental studies have been devoted to the transmission functions of this band [1.1-1.3, 1.5]. However, far from all of them can be used to solve the thermal-sounding problem. This is because of a number of specific requirements made of absorption characteristics for solution of inverse problems. First of all, these characteristics must be

known with high accuracy (for greater detail, see §5 of this chapter).

It is also necessary in a number of interpretation methods to have information on the transmission functions for relatively narrow spectral intervals. The data of D. Burch et al. [40], which are usually used in one way or another for comparisons with theoretical calculations, rank among the best experimental studies. Among the theoretical investigations, we note those of L. Kaplan [41], G. Yamamoto and T. Sasamori [42, 44], and T. Sasamori [43], in which transmission functions are calculated for a broad range of pressures, temperatures, and absorbing-substance contents on the basis of fine-structure data on the band and with application of absorption-band models. The results of calculations [44] made for rather narrow spectral intervals have been used in a number of studies on the thermal-sounding problem (e.g., in [11]). V. Stull, P. Wyatt, and G. Plass [45] made extensive calculations of transmission functions with high spectral resolution with the aid of a quasirandom model. Calculations were made by a direct method for various conditions in [1.81]. We shall dwell briefly on the problem of comparing transmission functions obtained by different methods.

S.D. Andreyev and A.G. Pokrovskiy [1.83] compared the experimental data of D. Burch et al. with theoretical calculations by a quasirandom model [45] and with calculations made by the method proposed in [46]. Figure 5.6 presents an example of such a comparison for the band at 15 μm. The authors of this paper note — as S. Drayson [1.81] had noted previously — that the largest calculation errors of the quasirandom model are observed for the Q-branch of the band. On the whole, however, the calculated results from both of the methods investigated agree satisfactorily (with an error of 5-10%) with the experimental data. /276

S. Drayson derived real-atmosphere transformation characteristics by direct calculation of transmission functions [1.81]. Using fine-structure data from [1.31], he calculated transmission functions in the range from 500 to 859 cm^{-1} with 0.1 cm^{-1} resolution for 34 levels in the atmosphere and 6 zenith angles. The results of these calculations were applied in a number of papers devoted to solution of the thermal-sounding problem. Some time after S. Drayson, S. Li and C. Young [48] calculated transmission functions directly with the object of comparing them with the experimental data of D. Burch et al. Data on the positions and intensities of the spectral lines were taken from [47] for the calculations. Figures 5.7 and 5.8 present examples in which the calculations are compared with experiment. We see that the best agreement between theory and experiment is obtained in calculations with variable line half-widths. Data on the spectral-line half-widths as functions of rotational quantum number were obtained from analysis of available experimental data on the half-widths. (A recently published paper of G. Yamamoto, M. Tanaka, /278

and T. Aoki [49] gives results of theoretical calculations based on Anderson's theory of the half-widths of individual rotational lines in the 15-μm carbon dioxide band.) However, even the use of a constant 0.08-cm^{-1} atm^{-1} line half-width gave rather good results. We see from Fig. 5.8 that the experimental transmission data systematically exceed the theoretical values in the wings of the band. This may be due to departure of the line-contour shape from the Lorentzian expression (or, at low pressures, the Lorentz-Doppler expression) used in the calculations. The comparison given in [48] made it possible to improve the total-intensity value for one of the vibrational bands.

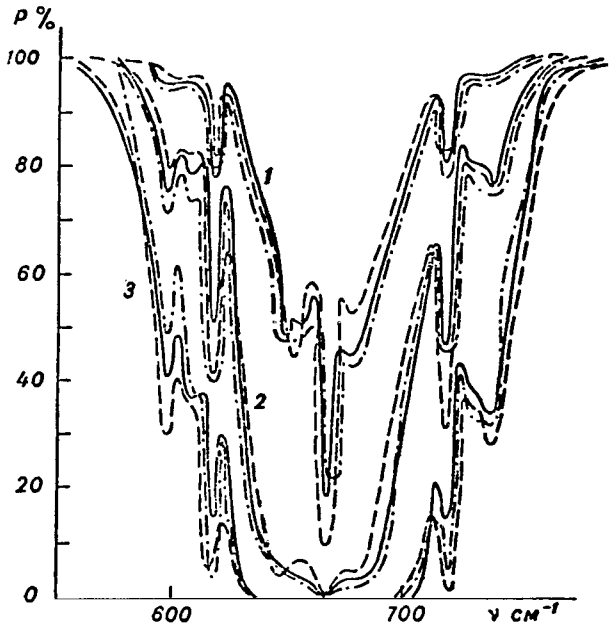

Figure 5.6. Comparison of Transmission Functions for the 15-μm CO_2 Band. 1) u = 0.748 atm-cm, p = 0.574 atm; 2) u = 6.15 atm-cm, p = 0.683 atm; 3) u = 46.4 atm-cm, p = 1.0 atm; the solid curves represent experimental data of [40], the dashed curves calculated results from [45], and the dot-dash curves results obtained from empirical formulas [1, 76]. /279

Transmission functions were computed directly by K.Ya. Kondrat'yev and Yu.M. Timofeyev [1.91] on the basis of fine-structure information taken from [1.31]. These calculations were used to investigate the transmission functions of a series of spectral intervals as functions of absorbing-substance content, pressure, and temperature. Figure 5.9 shows an example in which the results of these calculations are compared with calculations by the quasirandom model [45]. Comparisons of this kind indicated that good agreement is observed in some cases, but that sometimes the discrepancies become appreciable at low pressures and temperatures. Some of the disagreement may be due to errors of the interpolation that was necessary for comparison of the data. Comparison of calculations [1.91] with experimental transmission data [40] showed good agreement with experiment except for the region of the Q-branch of the CO_2 band.

Theoretical studies of the temperature dependence of the transmission function are of a certain amount of interest, especially for relatively narrow spectral intervals, since experimental data of this kind are not available. Such

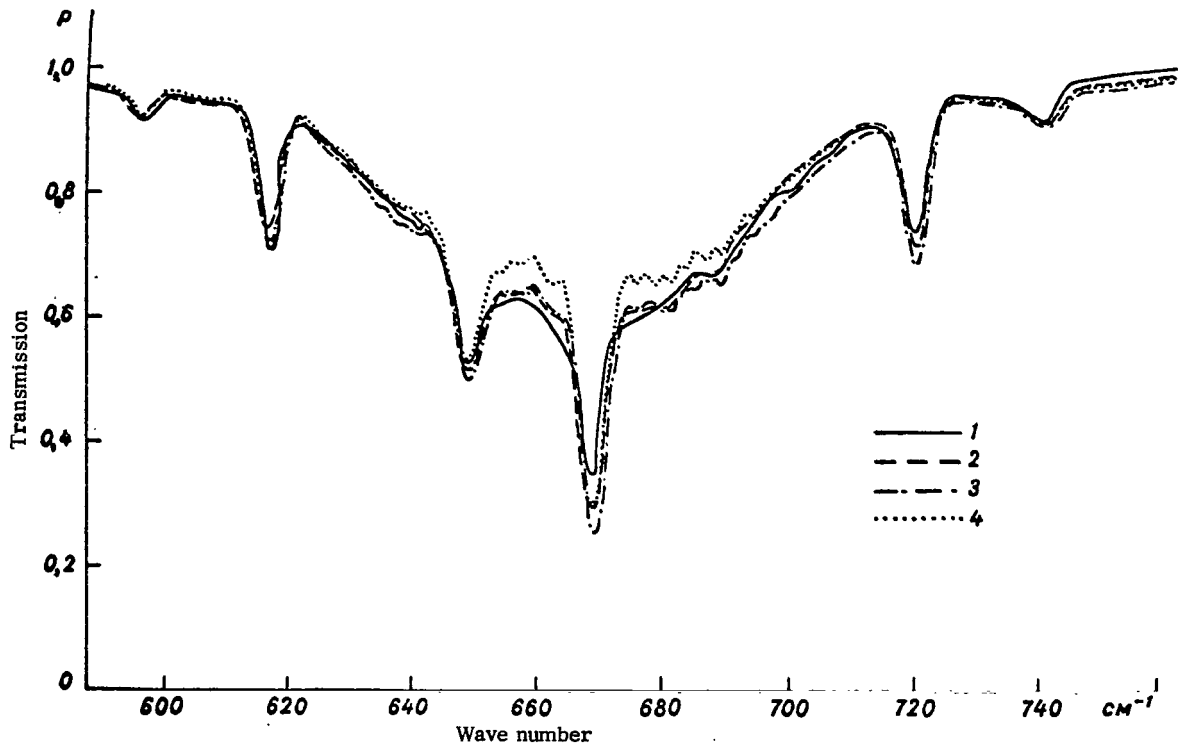

Figure 5.7. Comparison of Experimental Transmission Functions [40] (1) and Functions Obtained by Direct Method with Various Hypotheses as to Line Half-Widths [48]: Variable α (2), $\alpha = 0.08$ cm^{-1} (3), $\alpha = 0.06$ cm^{-1} (4), p = 0.02053 atm, u = 6.3 atm-cm, T = 300°K.

TABLE 5.3. VALUES OF THE EXPONENT m (FORMULA 1.47) FOR SPECTRAL INTERVALS 5 cm^{-1} WIDE IN THE 15-μm CO_2 BAND

Center of interval, cm^{-1}	669	667,5	691,5	697	703	709
$\bar{m}$	0,9	~0	1,9	2,9	3,9	4,3

investigations were made in [1.91]. Table 5.3 presents values of the exponent $\underline{m}$ (see Formula (1.47)), which permits approximate correction for the temperature variation of the transmission function for spectral intervals under consideration for atmospheric thermal sounding. Such data can also be obtained with satisfactory accuracy for other cases, using the functions η_1 and η_2 [1.55, 1.58].

Calculations were made in [1.91] for the case of an inhomogeneous atmosphere; the errors of approximate methods for consideration of atmospheric inhomogeneity were also analyzed. /280

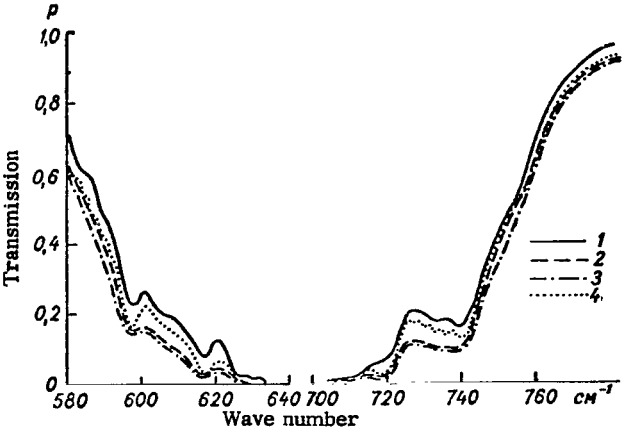

Figure 5.8. Comparison of Experimental Transmission Functions [40] (1) and Functions Obtained by Direct Method with Various Hypotheses as to Line Half-Widths [48]. p = 1 atm, u = = 106.2 atm-cm, T = 300°K. For legend, see Fig. 5.7.

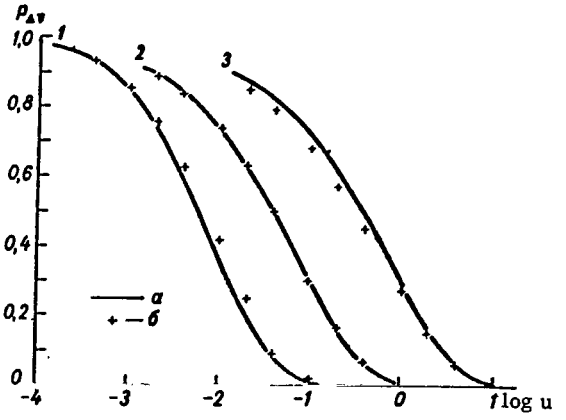

Figure 5.9. Comparison of Transmission Functions of a Spectral Interval 5 cm^{-1} Wide at ν = 703 cm^{-1}, as Obtained by Direct Method (a) and from Quasirandom Model [45] (b). T = 300°K. 1) p = 1000 mbar; 2) p = 100 mbar; 3) p = 10 mbar.

S. Drayson made direct calculations of real-atmosphere transmission functions specifically for the purpose of comparison with transparency measurements made by D. Murcray and T. Kiel using an aerostat-carried instrument [50]. The instrument's resolution was a few tenths of a reciprocal centimeter and made it possible to separate the individual spectral lines. The general structure and relative line intensities of the theoretical and experimental spectra agree well except for differences observed around 665.1 and 664.26 cm^{-1}. S. Drayson [50] notes that these discrepancies can be reduced substantially by an appropriate change in the vibrational energy of the higher-level state of one of the bands of the isotope $^{12}C^{16}O^{17}O$.

The data cited indicate that transmission functions can be obtained with satisfactory accuracy by direct calculation methods and, in a number of cases, by the use of such a detailed model of the absorption band as the quasirandom model. However, as will be shown in §5 of this chapter, even small errors in assigning the transmission functions may result in a marked increase in the error of temperature-profile reconstruction. This necessitates further efforts toward the acquisition of even more accurate transformation characteristics.

A certain amount of information on transmission-function accuracy can be acquired by comparing measured and calculated radiation values. This comparison is usually the first step in

investigating the possibilities for solution of an inverse problem. Indeed, if the measured radiation values and the theoretical values obtained by the use of the various transmission functions differ by more than the experimental error, it is difficult to expect successful solution of the inverse problem. The converse is generally untrue.

Indeed, the relation

$$J_{\text{theor}} - J_{\text{exp}} = \int B[T(p)] \frac{\partial}{\partial p} [P_{\text{theor}} - P]\, dp \leqslant \delta, \qquad (5.54)$$

where δ is the accidental measurement error, does not itself indicate proximity of P_{theor} and P. /281

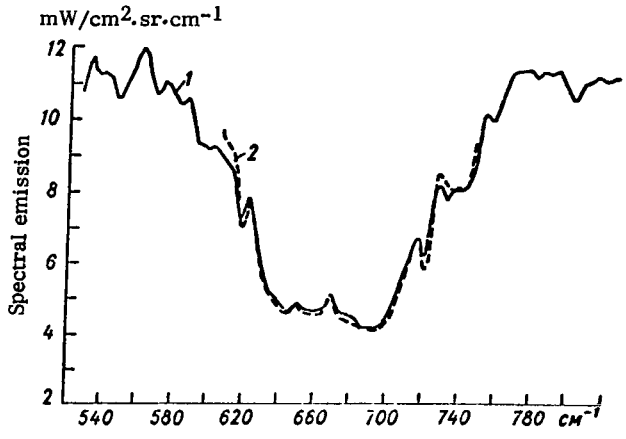

Figure 5.10. Comparison of Experimental (1) and Theoretical (2) Values of Outgoing Radiation in the 15-μm CO_2 Band [2.47].

According to the familiar lemma of the calculus of variations, it follows from the relation

$$\int \varphi(x)\, \delta P(x)\, dx = 0$$

that $\delta P(x) = 0$ only if the relation is satisfied for arbitrary functions ϕ. In this testing method, therefore, the comparison must be made under a variety of meteorological conditions. P_{theor} and P may agree accidentally under only some sets of measurement conditions as a result of compensation of errors at various levels in the atmosphere.

A number of authors have compared experimental and theoretical values of the outgoing radiation fluxes [2.47, 9]. Figure 5.10 shows such a comparison for a segment of the 15-μm band. Radiation measurements were made at an altitude of 33.5 km using a Michelson interferometer [51], and transmission functions obtained by the direct method were used in the calculations. As we see from Fig. 5.10, the agreement between theory and experiment is good; this also indicates high accuracy of the direct calculations. (Here, however, it is necessary to recall the remark made above concerning radiation comparisons.)

Reference [9] compares experimental and theoretical outgoing-radiation values by the use of various transmission functions. /282
The following transmission functions were used in the calculations:

TABLE 5.4. COMPARISON OF MEASURED AND CALCULATED RADIATION VALUES

Center of frequency interval, cm^{-1}	September 1964					
	Measured radiation values			Calculated radiation values		
	Time, h, min			D-Y	W-F	S-W-P
	07 57	08 24	15 02			
669	—	—	—	48,3	48,5	—
677,5	41,3	41,3	42,3	42,2	41,8	41,5
691,0	40,1	40,1	40,1	40,8	39,9	43,5
697,0	43,7	43,7	43,2	44,4	44,0	50,2
703,0	52,2	52,2	51,7	51,1	53,9	60,0
709,0	65,0	61,9	64,3	61,7	65,5	72,8

Center of frequency interval, cm^{-1}	May 1966						
	Measured radiation values				Calculated radiation values		
	Time, h, min				D-Y	W-F	S-W-P
	08 30	09 10	10 06	11 09			
669	52,1	51,0	52,5	51,1	52,7	53,1	—
677,5	46,2	45,7	46,5	45,7	46,1	45,9	45,0
691,0	42,2	43,0	44,7	43,2	42,5	42,3	43,4
697,0	43,6	43,8	46,0	44,1	43,2	42,9	46,9
703,0	49,4	50,7	51,4	50,7	46,7	48,9	54,0
709,0	59,2	59,9	60,4	59,7	54,8	58,3	65,3

Note. The letters denote the following transmission functions: D-Y) Drayson and Young's function; W-F) Wark and Fleming's function; S-W-P) Stull, Wyatt, and Plass' function.

those of V. Stull, P. Wyatt, and G. Plass (S-W-P) [47], S. Drayson and K. Young (D-Y), and D. Wark and G. Fleming (W-F) [10]. An advantageous feature of this comparison is the fact that it was made for two different cases of observations (Table 5.4). In their analysis of the results, the authors of [9] concluded that the S-W-P transmission functions yield distinctly high radiation values, which means high transmission functions for the comparison cases concerned. Calculations using the D-Y and W-F transmission functions give closely similar results, although better agreement between experiment and calculation is observed in some cases for the D-Y functions and in others for the W-F functions.

The absorption characteristics of the carbon dioxide band at $\lambda = 4.3$ μm have now also been studied in considerable detail. The total intensity of all vibrational-rotational bands in this region of the spectrum (the fundamental ν_3 bands of the molecules $C^{12}O_2^{16}$ and $C^{13}O_2^{16}$, the $02^00\text{-}10^01$ band of the principal isotope, and the bands corresponding to transitions between excited states) exceeds the total intensity of the bands at $\lambda = 15$ μm. In principle, with consideration of the strong $B_\nu(T)$ dependence in the near infrared, this would permit sounding of the atmosphere up to somewhat higher altitudes. High-resolution theoretical calculations /283

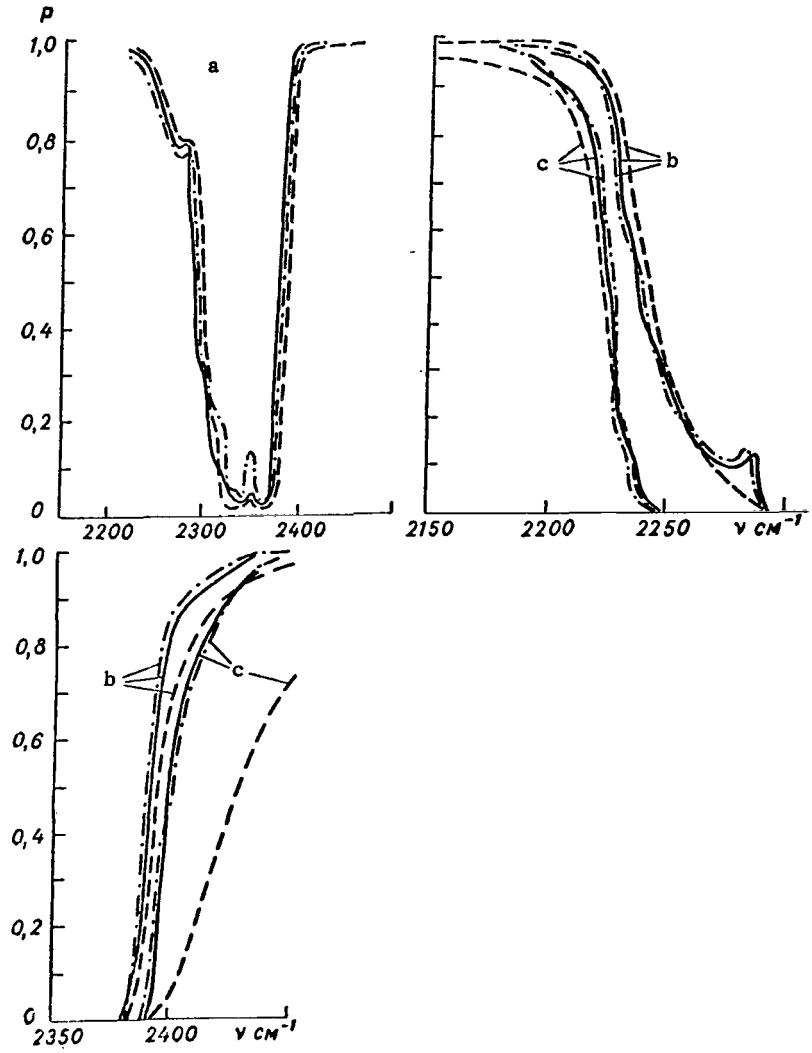

Figure 5.11. Comparison of Transmission Functions of the CO_2 Band at $\lambda = 4.3$ μm. a) $u = 0.649$ atm-cm, $p = 0.614$ atm; b) $u = 20$ atm-cm, $p = 0.6$ atm; c) $u = 100$ atm-cm, $p = 1.0$ atm; the solid curves represent experimental data [40], the dashed curves calculated data [45], and the dot-dash curves results obtained from empirical formulas [1.75].

have been made by V. Stull, P. Wyatt, and G. Plass [45] and by L. Gray and R. McClatchey [52]. A quasirandom model and various data on the fine structure of the absorption bands were used in these calculations. Here we present the results of a comparison made by S.D. Andreyev and A.G. Pokrovskiy [1.83] of the calculations of V. Stull, P. Wyatt, and G. Plass according to the quasirandom model, calculations based on an empirical method [46], and

the experimental transmission values [40]. As we see from Fig. 5.11, data obtained on the basis of the quasirandom model yield somewhat better accuracy than empirical data at small contents of the absorbing gas. The reverse is observed at high values. Calculation by the quasirandom model gives low transmission values in the wings of the band, especially in the short-wavelength zone. This may result either from the use of incorrect spectral-line contours or from errors in assigning the fine-structure parameters.

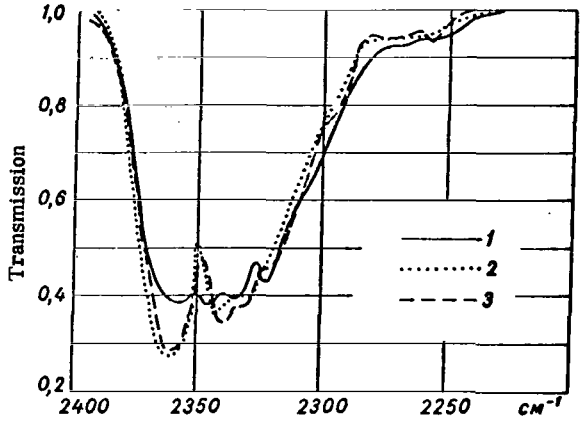

Figure 5.12. Comparison of Transmission Functions of CO_2 Band at $\lambda = 4.3$ μm ($T = 300°K$, $p = 0.180$ atm, $u = 0.195$ atm-cm). 1) Data of V. Stull, P. Wyatt, and G. Plass [45]; 2) data of L. Gray and R. McClatchey [52]; 3) experimental data [40].

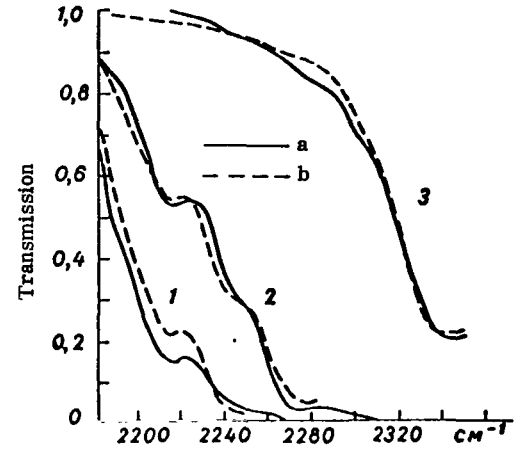

Figure 5.13. Comparison of Atmospheric Transparencies in the CO_2 Band at $\lambda = 4.3$ μm. a) Experimental data; b) theoretical calculation [14]; 1) $p = 497$ mbar, $\theta = 69.6°$; 2) $p = 245$ mbar, $\theta = 65°$; 3) $p = 18.6$ mbar, $\theta = 47.4°$.

Figure 5.12 presents the results of a comparison of experimental transmission functions with the calculations of W. Stull, P. Wyatt, and G. Plass [45] and L. Gray and R. McClatchey [52]. We note that the theoretical calculations of L. Gray and R. McClatchey agree more closely with experiment than does the calculation of [45]. Figure 5.13, where we have compared the transmission functions of [52] for cases of real inhomogeneous atmospheres with the measured results of Murcray et al. [53], also testifies to the high accuracy of the calculations in [52].

Let us now examine the absorption characteristics of the microwave range. By virtue of its symmetry, the oxygen molecule does not have an electrical dipole moment, but it does have a constant magnetic moment of two Bohr magnetons. Thus the oxygen spectrum is governed by magnetic rather than electrical interaction with the radiation field. Although the probability of

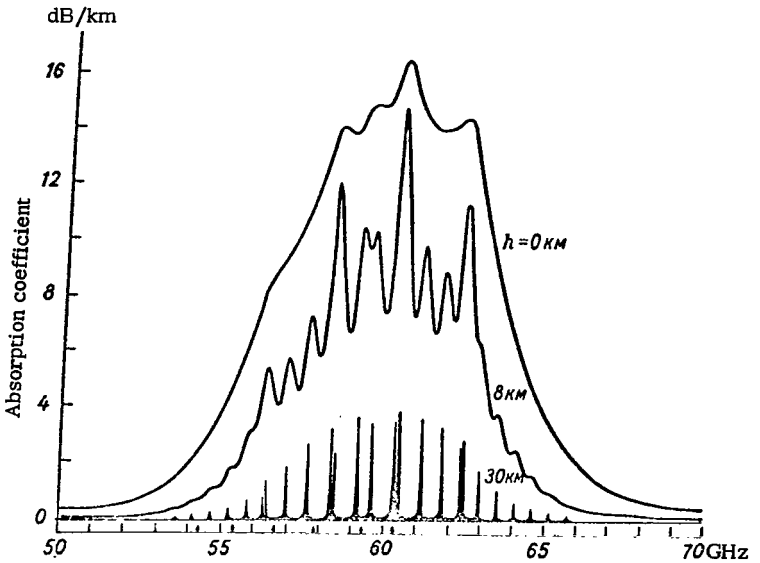

Figure 5.14. Theoretical Values of Absorption Coefficients in O_2 Band at Various Heights.

transitions is considerably lower in the case of magnetic than in the case of electrical interaction, the high oxygen content of the earth's atmosphere results in appreciable absorption in the corresponding segments of the spectrum. Interaction of the magnetic dipole moment with the rotational moment of the molecule results in the formation of many energy levels, which can be characterized by the quantum number of total momentum J. The total momentum J is composed of the spin momentum S and the rotational momentum N. /286
According to the selection rules, transitions between J = N levels and J = N + 1 and J = N - 1 levels are allowed. Thus, the oxygen spectrum under consideration is governed by transitions between fine-structure components of the same rotational level. Because of the high resolution of modern instruments in the microwave, use of absorption coefficients rather than transmission functions as quantitative characteristics of transformation is justified for this region. The spectral lines governed by the transitions considered above are spaced very close together in the region with $\lambda \approx 5$ mm, except for a line at $\lambda \approx 2.5$ mm. At a pressure of about 1 atm, the lines at $\lambda \approx 5$ mm cannot be resolved, and they form a continuous absorption region from 4 to 6 mm. The spectral lines can be resolved at low pressures. Figure 5.14 shows calculated results for the absorption coefficients of oxygen at various pressures and densities of the absorbing gases. The calculations were performed for a Van Vleck-Weisskopf spectral line contour. S.A. Zhevakin and A.P. Naumov [55, 56] made extensive calculations of the oxygen absorption coefficient for a line shape obtained from /287
the kinetic equation. Figure 5.15 compares these calculations and

those made using the Van Vleck-Weisskopf contour with experimental absorption-coefficient values. Good agreement between theory and experiment is observed around resonance for any contour shape. Data for the wings of the band are spotty and do not permit an altogether definite conclusion as to the contour shape of the absorption lines. According to results of low-pressure measurements and theoretical calculations, the average line half-width is $\alpha/p = 1.95$ MHz/mm Hg. Using this figure and the curve of line half-width as a function of pressure ($\alpha \sim p$) at a pressure of about 1 atm, we obtain $\alpha \approx 1.35$ GHz (0.045 cm^{-1}) for air — a value approximately twice the value for high pressures, as indicated by a number of experimental studies (for example, [54]). Empirical methods by which data from measurements at high and low pressures can be reconciled are proposed by M. Meeks and A. Lilley and C. Tolbert and A. Straiton [59]. In a number of cases, use of these methods has made it possible to obtain good agreement between measured and calculated values of the atmosphere's intrinsic emission in this interval of the spectrum. By way of example, we present Fig. 5.16, which has been borrowed from [60]. It compares measured and calculated antenna temperatures. (Antenna temperature is a quantitative characteristic of microwave radiation and takes account of the angle and spectral sensitivity variations of the specific measuring instrument.)

We note the presence of nonresonance oxygen absorption (γ_{n-r}), which is described in most papers by an expression of the Debye type derived by Van Vleck and Weisskopf [62]. We cite data indicating the relative importance of the two types of absorption. It is reported in [55] that the ratios γ_{n-r}/γ equal 0.4, 0.007, 0.2, and 0.0007 for λ = 2.0, 0.5, 4.3, and 5.0 mm, respectively.

Zeeman splitting of spectral lines occurs in the earth's magnetic field as a result of (2J + 1)-fold "magnetic" degeneration of molecular energy levels. The Zeeman effect becomes important in the atmosphere at heights above 40-50 km and makes it quite difficult to interpret radiation data because of the dependence of the transformation characteristics on geographic coordinates and polarization. The consequences of the Zeeman effect are analyzed in detail in the papers of W. Lenoir [3.132, 63].

Absorption in these regions of the spectrum is influenced /289
not only by the principal gases (CO_2 or O_2), but also by other components of the atmosphere: water vapor for the 15-μm CO_2 band and the oxygen band; H_2O, CO, and N_2O in the case of the carbon dioxide band at λ = 4.3 μm. This secondary absorption complicates the problem of interpreting measured data for determination of the temperature profile, because substantial variations are observed in the distribution of these absorbing gases in the atmosphere. To take precise account of the influence of these gases, the problems of reconstructing the atmosphere's thermal profile and composition must be solved simultaneously. This set of problems is solved for reconstruction of the water-vapor distribution

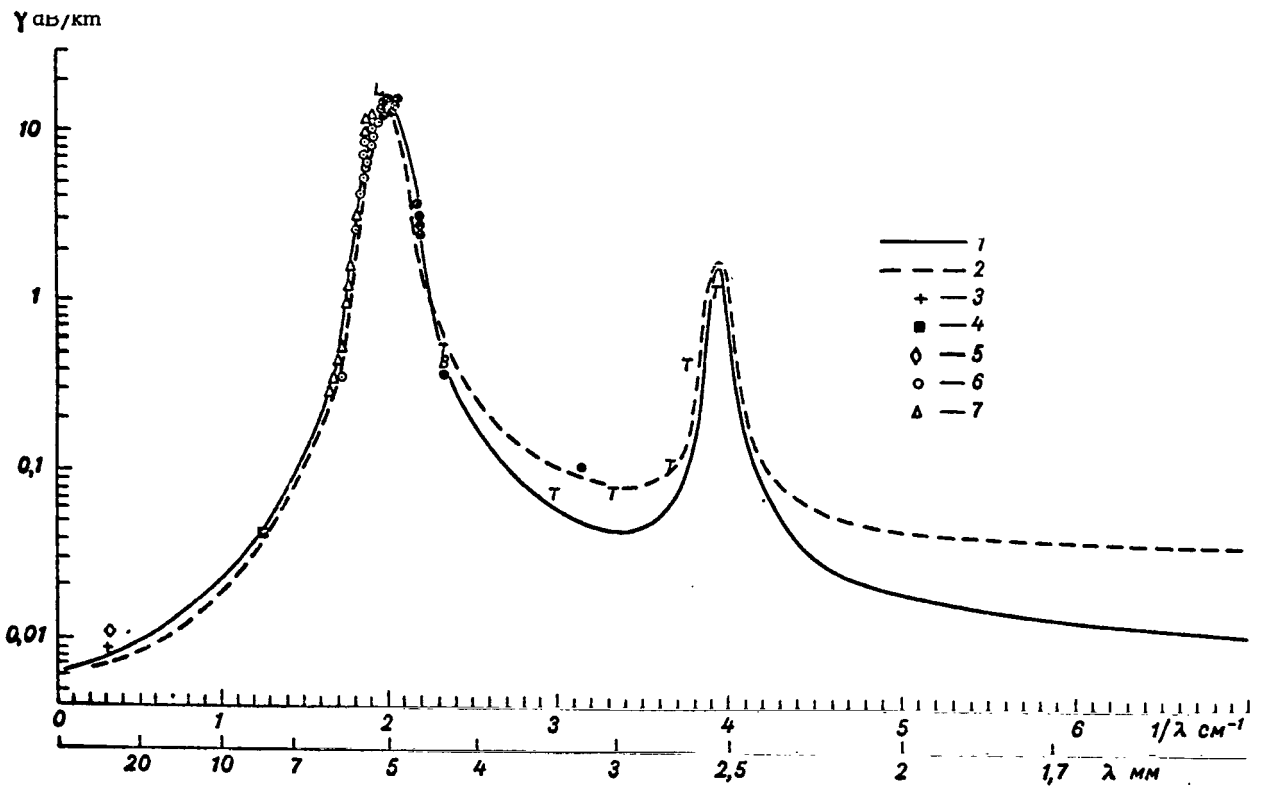

Figure 5.15. Comparison of Calculated Absorption Coefficients with Line Shape According to the Kinetic Equation $[(\alpha_k \pm)_{av} = 1.17$ MHz/mm Hg] (1) and with Line Shape According to Van Vleck-Weisskopf $[(\alpha_k \pm)_{av} = 1.39$ MHz/mm Hg] (2); with Experimental Results According to S.A. Zhevakin, V.S. Troitskiy, and N.M. Tseytlin (3); According to A.Ye. Solomonovich and O.M. Atayev (4); According to V.P. Lastochkin, K.S. Stankevich, and K.M. Strezhnev (5); According to Artman and Gordon (6); According to Crawford and Hogg (7); According to Lamotte (L); University of Texas (T).

and discussed in Chapter 6. Neglect of absorption by the gases listed above may result in substantial errors in determination of the temperature profile.

The absorption coefficients of water vapor in the microwave region have been measured and calculated by many authors. Recently, S.A. Zhevakin and A.P. Naumov [1.36, 48-50] published extensive calculations of this characteristic and compared the calculations with experiment. Quantitative transformation characteristics in the region of $\lambda = 4$ μm are examined in [45, 52]. The approach proposed in [95] may be used to study the atmosphere's absorption characteristics. Measurements of the radiation in the CO_2 and O_2 absorption bands under various sets of /290

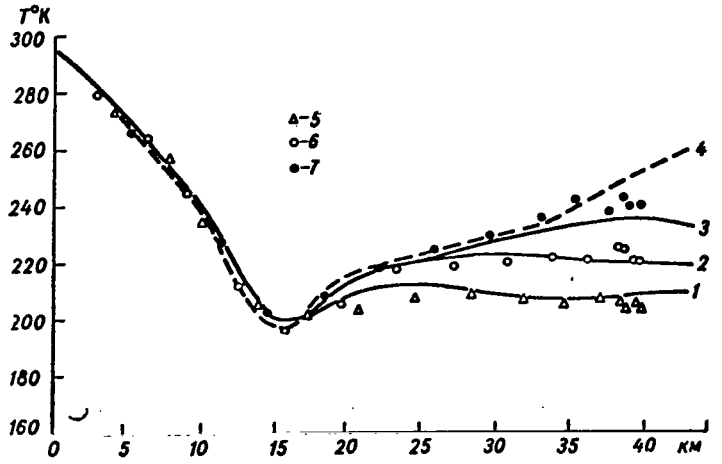

Figure 5.16. Comparison of Theoretical (1, 2, 3) and Experimental (5, 6, 7) Antenna-Temperature Values for Various Distances from the Center of the 61.151-GHz Line. Observations at the Nadir. 1, 5) For $\Delta\nu$ = 200 MHz; 2, 6) for $\Delta\nu$ = 60 MYz; 3, 7) for $\Delta\nu$ = = 2.0 MHz; 4) temperature distribution in the atmosphere.

meteorological conditions make it possible to determine the transmission-function derivatives of the real inhomogeneous atmosphere, assuming that its thermal structure is known. This requires solution of the inverse problem formulated in terms of the absorption characteristics.

§4. RESULTS OF NUMERICAL EXPERIMENTS TO DETERMINE THE TEMPERATURE PROFILE IN THE ATMOSPHERE

Under this heading, we shall examine the basic results of numerical experiments that have been carried out in the thermal-sounding problem. These experiments have usually been performed on a closed-circuit scheme: the thermal radiation is calculated on the basis of a defined model of the atmosphere that incorporates information on the atmosphere's thermal structure and the contents of the various absorbing gases, and with definite hypotheses as to the transmission functions or absorption coefficients. This radiation is then used to solve the inverse problem — reconstruction of the temperature profile. In studies of this type, it is easy to investigate the influence of a variety of factors (measurement errors, errors in assigning the kernel of the equation, radiation-measurement conditions, etc.) on the accuracy with which the temperature profile is recovered. A wide variety of methods have been used here to interpret the radiation data; the most important of these were examined in §2 of the

present chapter. The results, which will be submitted below, have played an important role in practical implementation of thermal sounding, since they have aided in clarifying and solving many problems associated with interpretation of radiation data. Further, these investigations have made it possible in a number of cases to formulate certain requirements that must be met by equipment designed to solve the problem.

The first numerical experiments in the thermal-sounding problem were performed by J. King [6], L. Kaplan [7, 26], D. Wark [65], and G. Yamamoto [25]. Without giving details of these studies, which are now of purely historical interest, we note only that it was their practical examples that brought out the instability of the problem, a consequence of which was that without the use of special methods, it was impossible to obtain a satisfactorily accurate reconstruction of the solution in the presence of accidental measurement errors.

The first papers to indicate realistic ways to overcome the difficulties that arise in numerical solution of the problem included those of D. Wark and H. Fleming [8] and M.S. Malkevich and V.I. Tatarskiy [11]. Their methods for solution of the problem were analyzed in §2 from the mathematical standpoint, and we shall present only the calculated results here. /291

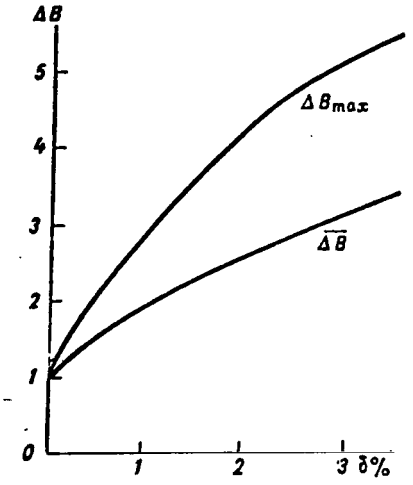

Figure 5.17. Error of Planck-Function Reconstruction as a Function of Measurement Error δ (ΔB ≈ ΔT for the 15-μm Band).

The basic features of the interpretation procedure can be characterized as follows. The thermal-state characteristics were sought in the form of the deviations of the Planck function B_ν from the functions corresponding to the mean profile for the particular locality. A priori statistical information was applied here in the form of an empirically orthogonal basis, which was used to decompose the unknown function. The algorithm also provided for smoothing, with the smoothing parameter selected on the basis of preliminary numerical experiments at various levels of the accidental measurement error.

Experiments to study the influence of accidental measurement errors on the accuracy of reconstruction were carried out for temperature distributions pertaining to various geographic regions. The calculations made use of weighting functions (except for $\nu = 743$ cm^{-1}) — the transmission-function derivatives $\partial P/\partial \log p$ shown in Fig. 5.1, which pertain to the 15-μm CO_2 band.

The experiment described in [8] was originally designed for determination of stratosphere temperature, and only later was the decision taken to add more transparent intervals with the purpose of more effective troposphere sounding. Figure 5.17 presents curves characterizing the reconstruction errors (maximum and mean) as they depend on measurement errors; they were plotted by averaging data pertaining to various temperature profiles. A typical feature of the curves in this figure is the fact that they originate from the point $(0, \Delta B_0)$ rather than $(0, 0)$. The value of ΔB_0 is actually the "null noise" of the algorithm, which characterizes the maximum attainable accuracy of temperature-profile reconstruction. Another behavioral feature of these curves is their relatively gentle slopes (especially for $\overline{\Delta B}$), indicating stability of the solution algorithm used for the integral equation. /292

TABLE 5.5. VALUES OF ERROR-AMPLIFICATION COEFFICIENT FOR VARIOUS LEVELS IN THE ATMOSPHERE

p mbar	1000	850	700	500	400	300	250	200	150	100
k_T ($n = N = 2$)	3,1	1,1	5,3	2,0	4,7	7,1	17,2	21,3	8,2	8,8
k_T ($n = 2, N = 13$)	1,8	1,0	1,4	0,5	1,3	2,3	6,0	8,0	2,6	2,5

The principal feature of the interpretation method used by M.S. Malkevich and V.I. Tatarskiy [11] is the use of an empirical orthogonal basis. In the numerical experiments of these authors, the corresponding algebraic system was stabilized by using only the first few terms of the unknown-function expansion (deviations of temperature from the mean profile) in this basis. In [11], the authors used the following spectral intervals (width 2 cm^{-1}): 696, 702, 708, 714, 730, 746, 750, and 752 cm^{-1}. To characterize the accuracy of temperature-profile reconstruction, they used an error amplification coefficient

$$k_T = \frac{\delta T}{\delta f},$$

where δT is the root-mean-square error of reconstruction of T and δf is the measurement error expressed in degrees of effective temperature.

Table 5.5 presents values of this coefficient for various heights in the atmosphere. It shows that they become quite large (up to 20), indicating, firstly, great instability of the corresponding algebraic system, and, secondly, the need for measurements of very high accuracy to attain high accuracy in the temperature reconstruction.

Amplification of the error can be reduced by using measurements in a number N of spectral intervals that is larger than the

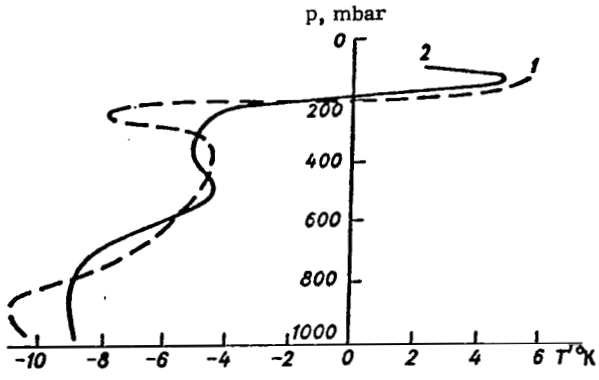

Figure 5.18. Reconstruction of Temperature Profile T'(p) by V.P. Kozlov's Method. 1) True profile; 2) reconstructed profile.

number n of basis vectors. In this case, k_T decreases by a factor of about $\sqrt{N/n}$. The data of [11] indicate certain advantages of the use of an empirically orthogonal basis as compared with a basis that has not been reconciled with the nature of the unknown distribution [25].

This method (which is sometimes referred to as the method of optimum approximation) was developed further by V.P. Kozlov [13] (see §2 of the present chapter). Figure 5.18 presents an example of temperature-profile /293 reconstruction for the numerical-experiment conditions of [11]. The measurement error was quite small in this case, amounting, in degrees of radiation temperature, to 0.4°. Interesting results with a bearing on optimum measurement conditions were obtained by V.P. Kozlov [13] and later by I.A. Gorchakova and V.P. Kozlov [66]. First, it was shown in [13] that measurements in the 8 spectral intervals proposed by M.S. Malkevich and V.I. Tatarskiy can be used more efficiently. Noting that only about 100 different temperature profiles can be distinguished in measurements in these spectral intervals with the error indicated above, V.P. Kozlov shows that combining ("gluing") these spectral intervals in a certain way into three broader spectral intervals simplifies the experiment on one hand and, on the other, increases the information content of the measurements. This last fact results from the increase in the signal/noise ratio under the conditions of the new measurements. For example, it is possible to distinguish more than 200 temperature profiles under these conditions and with the same measurement error.

A paper by I.A. Gorchakova and V.P. Kozlov [66] analyzes a segment of the band at λ = 15 μm (683-777 cm^{-1}). Transmission functions were assigned for this interval with a resolution of 2 cm^{-1}. First, it was shown that for a detector threshold sensitivity of the order of 10^{-8} W, it is possible to obtain information only on the first two coefficients in the expansion of the unknown temperature profile. The optimum spectral intervals are selected on the basis of an analysis of the rows of the corresponding matrix [13], two of whose rows appear in Fig. 5.19. It /294 can be shown on the basis of these data and estimates of information content that the optimum measuring system for this case will be a system consisting of two radiation detectors, one of which registers the radiation within the 683-753-cm^{-1} segment of the

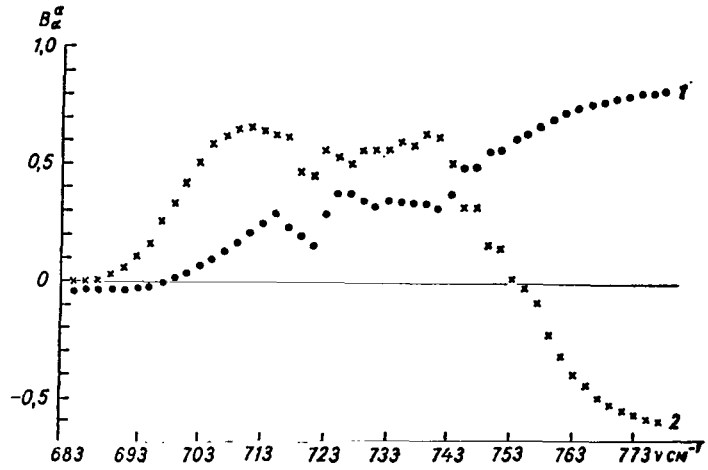

Figure 5.19. Method of Selecting Optimum Measurement Conditions According to V.P. Kozlov. 1, 2) First two rows of the corresponding matrix, which permit localization of the measurement spectral intervals.

spectrum, while the other senses it in the 755-777-cm^{-1} range (the boundary between them is determined by the null passage of the second-row elements [66]). The calculations show that the effectiveness of this optimum two-channel system is about 20 times that of a system designed to register the spectrum with high resolution (48 different channels). (The respective volumes of information are $V_2 = 196$ and $V_{48} = 11$.) This is because the narrow intervals that compose one of the combined segments introduce almost no independent information on the temperature distribution. As a result, combination of their energies results in an effective increase in the signal/noise ratio. These results indicate that when a statistical method is used for interpretation of the data, it is advantageous to measure the radiation in comparatively broad spectral intervals (in contrast to the measurement conditions for data reduction by D. Wark and H. Fleming's method [8], which is analyzed in [23]). We note in conclusion that it is desirable to make this analysis for the entire 15-μm band. It is also necessary to study the question of the seasonal and geographic variability of the optimum measurement conditions.

This last question requires special examination. The dependence of optimum measurement conditions on geographic location, time, and cloudiness, which is related to the dependence of the temperature correlation matrices on these factors, is characteristic not only for V.P. Kozlov's method for selection of measurement conditions, but also for other methods [35, 36] that use data on the statistical structure of the temperature field. This means that a satellite instrument designed for thermal sounding

must have variable characteristics. Naturally, the design and operation of such instruments constitutes a complex problem. On the other hand, if the dependence of optimum measurement conditions on the form of the correlation links is relatively weak, it is advantageous to use optimum measurement conditions obtained by use of certain averaged correlation matrices. However, this problem requires special study. Attention must also be drawn to the fact that cases in which V.P. Kozlov's method does not work effectively are possible with this approach. As we know, the inverse operator is stabilized in this method by cutting off the series on the basis of analysis of the a priori region of the expected solution. If an average (over time and space) correlation matrix is used for selection of measurement conditions, certain measurement ranges may, in principle, be superfluous in actual reduction of the data, so that the corresponding linear system becomes unstable. We note in this context that O.M. Pokrovskiy's algorithm (see §2), which is based on analysis of actual radiation measurements with consideration of the statistical nature of the errors and information on the expected region of the solutions, may have certain advantages.

For example, we might propose a totally different solution of this problem based on measured radiation data for the entire absorption band. In this case, radiation in certain intervals is to be taken into account in data interpretation in accordance with the optimum measurement conditions for the particular geographical location and time, and as a function of the observed measurement-error level.

Rather detailed a priori information on the unknown function — the mean profile and the correlation matrices — was used in the numerical-experiment examples considered above. However, this information has been used differently in different methods. V.F. Turchin and V.Z. Nozik [34] considered the same example of numerical temperature-distribution reconstruction as that in [11]. The results of all these investigations have not yet been compared, and it is therefore impossible to infer the superiority of any of them. /296

A number of studies have used the regularization method with rather general a priori hypotheses as to the unknown function (smoothness, boundedness). For example, V.B. Glasko and Yu.M. Timofeyev [5, 67] performed extensive numerical experiments toward this kind of solution of the thermal-sounding problem. These papers considered a somewhat idealized case of temperature sounding that can be characterized by the following hypotheses:

1) it is assumed that the spectral curve of the outgoing thermal radiation in the contour of an isolated Lorentz line is known;

2) the intensity and half-width of the line do not depend on the unknown temperature distribution, and the distribution of the

absorbing substance is known;

3) the data necessary to eliminate the contribution of the underlying surface from the registered radiation are available.

Despite its idealized character, this case of thermal sounding has all of the basic features of the problem of thermal sounding with the aid of radiation measurements made in finite spectral intervals. This can be seen in Fig. 5.20, which we have borrowed from [8]. This figure compares the kernels of the corresponding integral equations for various hypotheses as to the transmission functions. We also note that a situation similar to that considered in [5, 67] is observed in the microwave region of the spectrum, where contemporary instrument resolution makes it possible to measure within the contour of a spectral line.

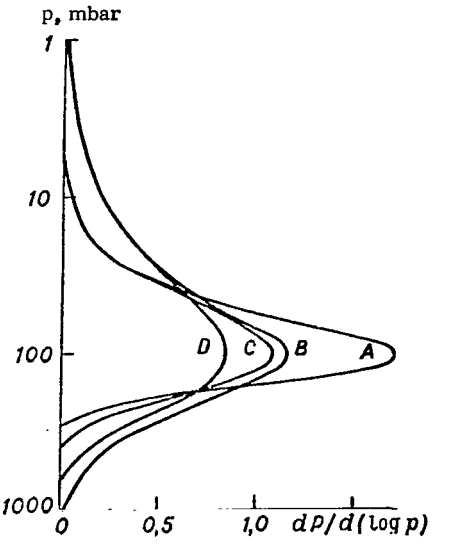

/297

Figure 5.20. Comparison of Kernels of Integral Equations Corresponding to Various Measurement Conditions. A) Measurement of monochromatic radiation in wing of Lorentz line; B) measurements of monochromatic radiation in the contour of the Lorentz line, $\nu - \nu_0 = \alpha$ (100 mbar); D) measurements in spectral interval with constant absorption coefficient; C) kernel corresponding to transmission function of Elsasser model.

With the above hypotheses, the corresponding integral equation can be written

$$U(x) = J(x) - B(\xi_0)P(x, \xi_0) = \int_0^{100} B(\xi)K(x, \xi)\,d\xi,$$

$$x = \nu - \nu_0, \quad \xi = \frac{p}{p_1}, \qquad (5.55)$$

where $J(x)$ is the measured radiation and $B(\xi_0)\cdot P(x, \xi_0)$ is the contribution of the underlying surface to the radiation,

$$K(x, \xi) = \frac{2\gamma\alpha_1^2\xi}{x^2 + \alpha_1^2\xi^2}\left[\frac{x^2 + \alpha_1^2}{x^2 + \alpha_1^2\xi^2}\right]^2, \qquad (5.56)$$

α_1 is the half-width of the spectral line at pressure p_1 (p_1 = 10 mbar), and γ is a parameter linearly related to line intensity and the volume concentration of the absorbing gas.

The numerical experiments were performed with the following functions:

$$B_1(\xi) = 70 + 35\left(\frac{\xi - 40}{39}\right)^2, \tag{5.57a}$$

$$B_2(\xi) = 100 - \frac{150}{\sqrt{\xi}} \sin\left(2\pi \frac{\xi}{100}\right), \tag{5.57b}$$

which describe the possible atmospheric temperature distributions rather well. The influence of many factors on the accuracy of solution reconstruction was investigated in solving Eq. (5.55): selection of the approximating nets, the range of measurement of the function J(x), assignment of boundary conditions, number of radiation measurements, etc. We note that the accuracy of reconstruction was found to depend strongly on the positioning of measurement frequencies within the spectral-line contour. Appropriate selection of the approximating nets permitted reconstruction with several times the accuracy obtained when uniform nets were used.

TABLE 5.6. INFLUENCE OF ACCIDENTAL MEASUREMENT ERRORS ON ACCURACY OF RECONSTRUCTION OF B_1

γ	δ	ε	ε*	γ	δ	ε	ε*
		B_1		99	10^{-2}	3,29	1,92
	10^{-2}	1,93	1,75		10^{-1}	3,36	1,91
1	10^{-1}	1,99	1,79		10^{0}	3,51	1,76
	10^{0}	6,35	2,79		10	5,59	3,18
1	10	56,0	10,7			B_2	
	10^{-2}	0,625	0,573		10^{-2}	2,37	2,10
	10^{-1}	0,657	0,600		10^{-1}	2,42	2,10
50	10^{0}	1,68	1,11	50	10^{0}	2,93	2,31
	10	6,09	4,09		10	8,79	8,33
						15,40	

The influence of accidental measurement errors was studied, using as the function U(x)

$$\tilde{U}(x_k) = U(x_k) + \delta\omega_k, \tag{5.58}$$

where /298

$$\omega_k = \frac{\eta_k}{\sqrt{h_1 \sum_{k=1}^{m} \eta_k^2}},$$

and $\{\eta_k\}$ is a random variable with uniform distribution on [-1, 1], and δ is the root-mean-square deviation of $\tilde{U}(x)$ from U(x).

Table 5.6 shows how $\varepsilon = \max_i |B^{\alpha_0}(\xi_i) - B(\xi_i)|$ depends on δ for certain numerical-experiment conditions.

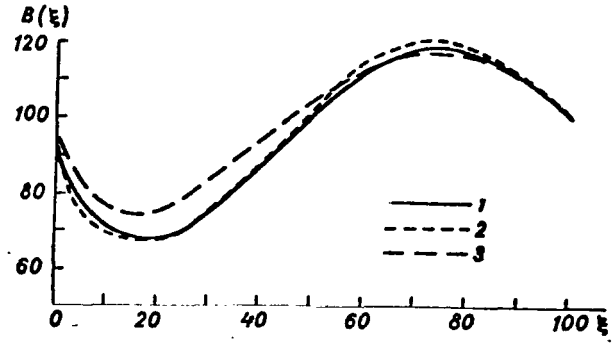

Figure 5.21. Reconstruction of Function $B_2(\xi)$ for Various Values of Accidental Measurement Error. 1) Exact solution; 2) with δ = = 1.0 erg/cm^2·sec·sr·cm^{-1}; 3) with δ = 10 erg/cm^2·sec·sr·cm^{-1}.

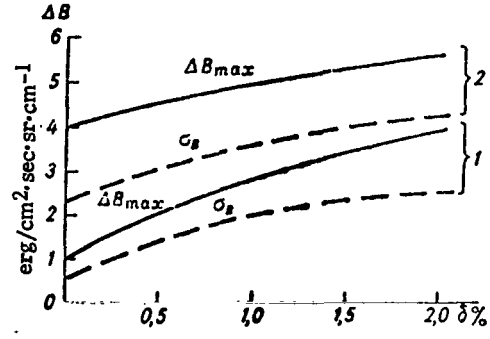

Figure 5.22. Reconstruction Errors as Functions of Accidental Radiation-Measurement Errors. 1) For exact assignment of equation kernel; 2) for assignment of kernel with an error (see §5 of this chapter).

Figure 5.21 presents a typical example of reconstruction of the profile $B_2(\xi)$ for various measurement-error levels.

We note that ε^*, which characterizes the theoretical reconstruction error (that obtained for a known function B), is given for comparison with ε (the quasioptimum value α_0 of the regularization parameter was selected from the algorithm described in §2 of this chapter). This comparison enables us to judge the effectiveness of applying the selection algorithm for quasioptimum approximations to the solution.

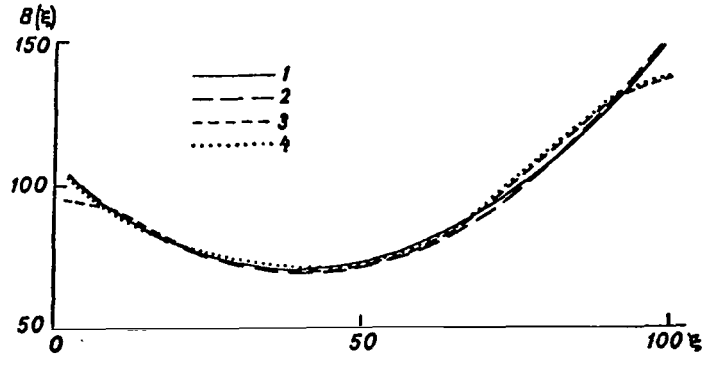

Figure 5.23. Influence of Boundary-Condition Assignment on Reconstruction Accuracy of the Function $B_1(\xi)$; γ = 50, δ =1.0. 1) Exact solution; 2) with known boundary values; 3) B(100) unknown; 4) B(1) and B(100) unknown.

We used the same regularization method and the same method for selection of the quasioptimum solution in numerical experiments with real kernels (Fig. 5.1). Figure 5.22 presents data characterizing the reproduction errors as they depend on accidental errors of measurement (ΔB_{max} is the maximum deviation from the true profile and σ_B is the standard deivation of the reconstruction error). This figure has about the same features as Fig. 5.17: algorithm null noise and a relatively weak dependence of the reconstruction errors on the measurement errors.

The influence of the type of boundary conditions on reconstruction accuracy has been studied in a number of papers. Figure 5.23 shows an example in which the function $B_1(\xi)$ is reconstructed with various boundary conditions. As we see from the figure, use of the trivial boundary conditions $\partial B/\partial \xi = 0$ distorts the solution conspicuously in the neighborhood of the boundary points. For this case, thermal structure can be reconstructed accurately with independent underlying-surface-temperature determinations. /299

In a departure from the methods examined above, W. Smith [69, 70] determines the tropospheric temperature profile with extremely rigid requirements imposed on the unknown profile. It is assumed that the unknown functions belong to a three-parameter family of curves of the form /300

$$T(p) = c_1 + c_2 \ln \frac{p}{p_0}, \quad p_c \leqslant p \leqslant p_0,$$

$$T(p) = c_1 + c_2 \ln \frac{p_c}{p_0} + c_3 \ln \frac{p}{p_c}, \quad p_t \leqslant p \leqslant p_c. \tag{5.59}$$

Here p_c is the level separating two atmospheric layers with constant temperature gradients, c_1, c_2, and c_3 are unknown parameters, $c_1 = T(p_0)$, and $p(t)$ is the pressure at tropopause level.

The level p_c is found from the condition

$$\sum_{i=1}^{4} [J_{msr}(\Delta\nu_i) - J_{clc}(\Delta\nu_i, p_c)]^2 = \min,$$

where J_{msr} are the measured radiation values in the ith spectral interval ($i = 1, 2, 3, 4$) and $J_{clc}(\Delta\nu_i, p_c)$ are the calculated values in the same spectral interval for various pressures p_c.

The overdefined equation system (four spectral intervals, three unknown coefficients c_j), which approximates the real integral equation, is solved by the method of least squares using smoothing algorithms. Smith's first paper [69] proposed that the problem be solved by an iteration method based on successive comparisons of calculated radiation values with values measured in /301

various spectral intervals. Smith's papers concentrate attention on cases in which data from real measurements are interpreted. The results obtained with Smith's method will be considered in §7 of this chapter.

T.L. Barnett [71] proposed that the vertical temperature profile be found by using a program for optimum root-mean-square estimation of the nonlinear parameters [72]. One distinctive feature of this program is the fact that both the temperature and height at which the solution is sought are varied in the process of selecting the solution. In Barnett's numerical experiments, the temperature profile was assigned by nine parameters: the value of T on the ground surface and four (T, z) pairs. Twelve intensity values in the range from 525 to 670 cm^{-1} were used in the calculations. The quantity

$$\sum_i [J_{msr}(\nu_i) - J_{clc}(\nu_i)]^2,$$

where $J_{msr}(\nu_i)$ and $J_{clc}(\nu_i)$ are the intensities measured by the instrument and calculated theoretically on the basis of the acquired temperature profile, was minimized in each iteration.

In the case of absolutely accurate measurements, the root-mean-square error of reconstruction of the T(z) profiles varies from 1.1 to 3.7°. The influence of accidental measurement errors and errors in assigning the kernel of the equation on the accuracy of temperature reconstruction was not investigated in [71], so that no inferences can be drawn as to the prospects of the method for interpretation of real radiation measurements.

Let us consider a study made for the band at $\lambda = 4.3$ μm. Several specific methods have been elaborated for solution of the thermal-sounding problem by interpreting data from radiation measurements in this band, but this does not ultimately signify that it is impossible to use the interpretation methods examined above. It is also necessary to consider the peculiarities of the near infrared, e.g., the strong temperature dependence of blackbody radiation in this region. In view of this fact, R. McClatchey [14] proposed an interpretation method that was originally designed for interpretation of measured thermal-radiation data for other planets. The a priori information on the unknown function must obviously be limited in this case, and McClatchey's method cannot be based on the statistical approaches that are natural in solving the thermal-sounding problem for the earth's atmosphere.

In approximation, the following equation system can be substituted for the corresponding integral equation: /302

$$\delta J(\nu_1) = J_1(\nu_1) - J_{msr}(\nu_1) = \sum_i \omega_{1i} \frac{\partial B(\nu_1 T_i')}{\partial T_i} \delta T_i',$$

. . . . . .

$$\delta J(\nu_N) = J_1(\nu_N) - J_{msr}(\nu_N) = \sum_i \omega_{Ni} \frac{\partial B(\nu_N T_i')}{\partial T_i} \delta T_i', \qquad (5.60)$$

where the $J_{msr}(\nu_i)$ are the measured radiation values in the ith spectral interval and the J_1 are the calculated values corresponding to the first approximation T' of the unknown temperature profile.

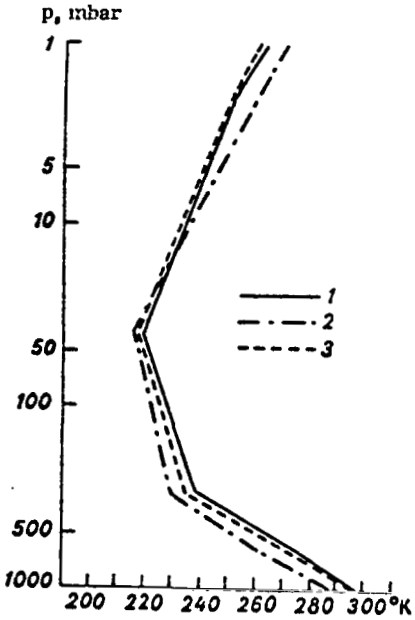

Figure 5.24. Reconstruction of Temperature Profile by McClatchey Method with 5% Systematic Measurement Error. 1) True profile; 2) first approximation; 3) reconstructed profile.

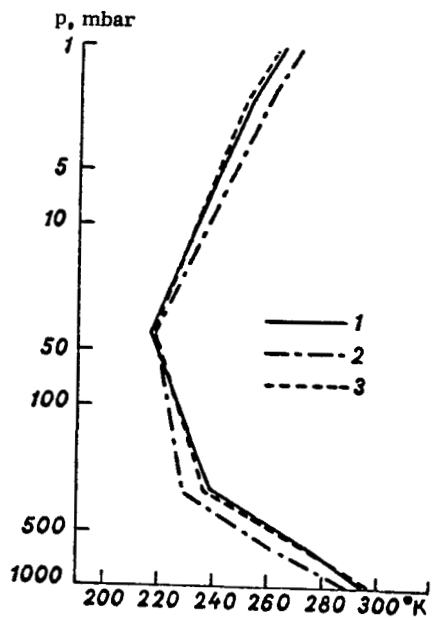

Figure 5.25. Reconstruction of Temperature Profile by McClatchey Method for 2% Accidental Measurement Error. For legend, see Fig. 5.24.

After determination of $\{\delta T_i'\}_{i=1}^n$, the solution is repeated for the new approximation T^2 and improved weights ω_{2i} and derivatives $\frac{\partial B(\nu_j T_i^2)}{\partial T_i}$. (The weight ω incorporates the transformation

characteristics, which depend generally on the unknown temperature distribution.) The smoothing method of [14] is used in a concrete solution. R. McClatchey showed that the algorithm described makes it possible to obtain a solution that converges toward the true temperature profile if the first approximation is "warmer" (or no more than 8% "cooler") than the temperature profile observed in reality. We note that use of a first approximation that meets this condition but departs widely from the true profile results in slow convergence of the iteration process. Figures 5.24 and 5.25 show examples of numerical temperature-profile-reconstruction experiments using this method with various measurement errors. McClatchey reports that a systematic measurement error of about 5% results in reconstruction errors of 2-3°. Accidental measurement errors of 2% produce approximately the same error. This relatively weak dependence of the temperature-profile-reconstruction error on the measurement errors is due to the strong temperature dependence of the function $B_\nu(T)$.

Chahine [10] proposed a unique method for interpretation of measured radiation data for the band at $\lambda = 4.3$ μm. Chahine reduces the thermal-sounding problem to discrete-level determinations of a function X(T), which describes the basic part of the temperature dependence of the Planck function (see page 224). After selection of the zeroth approximation of the unknown temperature profile, he makes use of an iteration process based on the relaxation relationship /304

$$X_i^n = X_i^{n-1} \frac{J_i}{J_i^{n-1}}, \qquad (5.61)$$

where X_i^n is the value of the function obtained at level i in the nth step, J_i is the radiation measured in the ith spectral interval, and J_i^{n-1} is the radiation calculated for the same interval on the basis of the (n-1)th approximation of the temperature profile.

Ten intervals in the 4.3-μm CO_2 band were selected for the numerical experiment (centers of intervals: 2180, 2235, 2245, 2260, 2290, 2295, 2305, 2315, 2360, 2370 cm^{-1}). The temperature was sought at 10 levels for p_i/p_0 values of 1.0, 0.85, 0.60, 0.20, 0.10, 0.04, 0.025, 0.0135, and 0.009. Naturally, selection of both the sounding frequencies and the temperature-determination levels is to a certain degree arbitrary. Figure 5.26 presents an example of temperature-profile reconstruction by Chahine's method. Good reconstructions were also obtained when a temperature profile departing strongly from the truth was used as the first approximation. Chahine reports that an average error of about 1° is attainable with

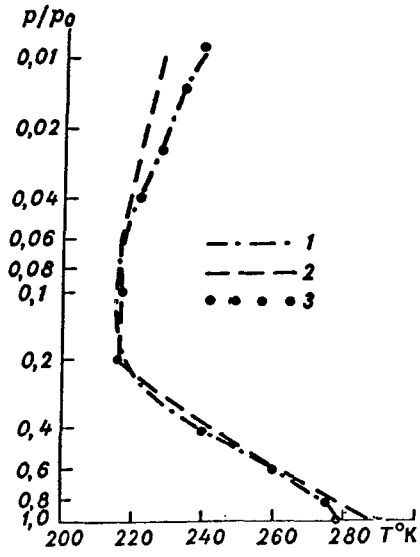

Figure 5.26. Reconstruction of Temperature Profile by Chahine Method. 1) True profile; 2) first approximation; 3) reconstructed profile.

$$\langle R^n\rangle_{\text{av}} = \frac{1}{i}\sum R_i^n = \frac{1}{i}\sum \frac{|J_i - J_i^n|}{J_i}, \quad (5.62)$$

which characterizes a measurement error of less than 3%. An average reconstruction error of 2-3° is attainable when $5\% < \langle R^n\rangle_{\text{av}} < 7\%$. As we have already noted, these high reconstruction accuracies result from the nature of the $B_\nu(T)$ dependence.

Let us turn to an analysis of the results of numerical thermal-sounding experiments relating to the microwave region. One of the first studies pertaining to this interval was E. Westwater's paper [73] on the problem of reconstructing temperature in the lower layer of the atmosphere (10-12 km) on the basis of oxygen-emission measurements made on the ground. To interpret the data, Westwater used an iteration method that takes account of the dependence of the transformation characteristics (in this case, absorption coefficients) on the unknown temperature profile. While the root-mean-square error of solution reconstruction is 2-2.5° for accurate measurements of radiobrightness temperature, reconstruction accuracy suffers considerably when various types of errors are taken into account. Examples of reconstruction in the presence of errors appear in Fig. 5.27. The errors were simulated by adding a) $(-1)^n|\delta T_B|$ at the nth frequency, and b) $(-1)^{n+1}|\delta T_B|$ to the exact brightness-temperature values. /305

Naturally, errors are quite detrimental to reconstruction accuracy, and when they are large (case a), $\delta T_B = 2.5°$), the iteration process may not converge to the true solution. Systematic errors were found to be less influential.

In later studies devoted to the same problem, E. Westwater and O. Strand used an improved method to interpret the measured data (see §2 of this chapter). Reference [36] submits examples of numerical reconstruction using this method. The process was run for various types of observations: measurements of radiation from the ground (with known and unknown underlying-surface temperatures), measurements of the ascending radiation at a height of 10 km. /306

The method developed by E. Westwater and O. Strand makes it possible to obtain quantitative estimates of the information content of indirect temperature measurements. The quantities

$$R = -\operatorname{tr}(S_T - X^{-1}), \qquad (5.63)$$

$$F = \frac{\operatorname{tr}(S_T - X^{-1})}{\operatorname{tr} S_T}, \qquad (5.64)$$

$$U = \left(\frac{\operatorname{tr} X^{-1}}{m}\right)^{1/2} \qquad (5.65)$$

may serve as a measure of this information content. Here, tr is the trace of the corresponding matrix and the quantity R characterizes the absolute quantity of information obtained through the indirect measurements, since $\mathrm{tr}S_T$ is the sum of the diagonal elements of the temperature correlation matrix and characterizes the uncertainty of knowledge of the temperature distribution in the absence of any additional information on the profile. The trace of matrix X^{-1} characterizes the error of temperature-profile reconstruction by interpretation of measured radiation data and, consequently, the uncertainty that remains after the indirect temperature measurements. Thus, R can be interpreted as the total decrease in the uncertainty of the temperature distribution or as the amount of information delivered by indirect temperature-determination methods. The quantity F characterizes the relative decrease in the uncertainty of the temperature, and the U are the mean deviations of the reconstructed solution from the true solution.

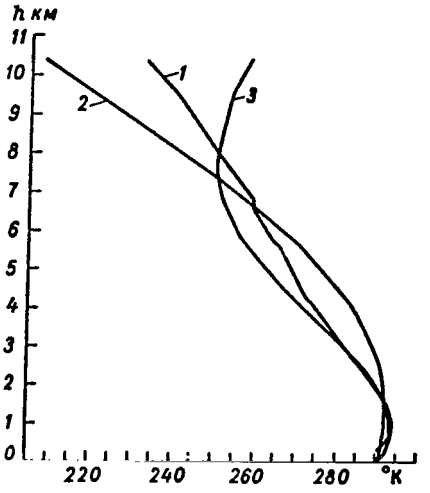

Figure 5.27. Example of Atmospheric Temperature Distribution Reconstructed From Measurements with Error of $|\delta T_B| = 1.25°K$. 1) True profile; 2, 3) reconstructed profiles with type a and b errors.

Table 5.7 presents results that can be used to analyze the dependence of R and F on accidental measurement errors (for radiation observations at the five frequencies 51.2, 53.3, 55.0, 57.3, and 61.193059 GHz). /307

We note that column 2 gives data characterizing the original error in the temperature distribution ($\mathrm{tr}S_T$), and that the numbers in columns 3-9 describe the residual uncertainty in T after application of radiation data with various errors σ. We note a number of interesting features that follow from analysis of the results in the table. First, our attention is drawn to the sharp decrease (to less than half) of tr S_T, which characterizes the a priori

TABLE 5.7. DEPENDENCE OF tr X^{-1} ON ACCIDENTAL MEASUREMENT ERRORS

	trS_T	tr. X^{-1} at σ of						
		0	0,01	0,1	0,5	1,0	1,5	2,0
Ascending radiation measurement	495,56	19,68	21,63	38,39	66,61	91,95	114,10	138,23
Descending radiation measurement	578,81	21,83	27,54	44,17	63,68	78,63	91,98	104,07
Descending radiation measurement with known T_{surf}	247,52	18,27	23,19	37,85	55,54	69,29	81,53	92,79

uncertainty of the temperature stratification, when data on underlying-surface temperature are used.

This effect is due to the relatively high correlation between underlying-surface temperature and the temperatures at various levels in the 10-km layer of atmosphere considered. The third column of the table presents data characterizing the residual uncertainty in the indirect determination of temperature stratification with absolutely accurate radiation measurements (case of five measurements). Although the values of trX^{-1} are small by comparison with trS_T, they differ appreciably from zero and are due both to the limited number of measurements and to the errors that are inevitable in numerical realization of algorithms for solution of integral equations. The data of Table 5.7 can be used to calculate all quantitative characteristics of information content and the accuracy of indirect measurements: R, F, and U.

TABLE 5.8. U AS A FUNCTION OF MEASUREMENT ERROR σ

σ° K	0	0,01	0,1	0,5	1,0	1,5	2,0
U	1,15	1,20	1,60	2,24	2,47	2,76	3,04

Let us analyze a case of atmospheric sounding with outgoing-radiation observations. Table 5.8 shows the dependence of U on the measurement error σ obtained on the basis of the data in the first line of Table 5.7.

As we see from Table 5.8, the "null noise" of the algorithm is about 1°, and U depends smoothly on σ.

The interpretation method proposed by E. Westwater and O. Strand enables us to solve the problem of selecting measurement conditions. For example, it can be used to determine the required

TABLE 5.9. DEPENDENCE OF trX^{-1} ON NUMBER OF MEASUREMENT FREQUENCIES USED AND ON ACCIDENTAL MEASUREMENT ERRORS

Number of measurement frequencies used	Type of observations	$\sigma = 0,0$	$\sigma = 0,1$	$\sigma = 0,5$	$\sigma = 1,0$
1	a	292,01	292,11	294,51	301,66
	b	136,26	136,36	138,74	146,01
	c	119,31	119,47	123,09	133,20
2	a	109,63	110,03	119,39	145,33
	b	65,50	65,89	74,18	82,93
	c	58,78	59,31	69,10	85,28
3	a	47,15	48,94	73,13	100,77
	b	50,10	53,57	71,11	88,90
	c	40,51	42,82	58,76	73,28
4	a	32,40	41,68	71,89	97,93
	b	36,18	46,28	65,62	80,89
	c	29,07	39,99	57,45	71,54
5	a	19,68	38,39	66,61	91,45
	b	21,83	44,17	63,68	78,63
	c	18,27	37,85	55,54	69,29

number of radiation measurements. The results of such an investigation are presented in Table 5.9 for all three radiation-measurement conditions: a) sounding of the atmosphere by measuring outgoing radiation at the 10-km level; b) sounding with the aid of ground measurements; c) ground sounding with known surface temperature and various measurement errors. /308

A number of interesting conclusions can be drawn from analysis of Table 5.9. With absolutely accurate measurements, the addition of each new measurement channel results in a marked decrease in the residual uncertainty of the temperature stratification $tr\ X^{-1}$. On the other hand, even at $\sigma \geq 0.1°K$, this decrease becomes insignificant at $n > 3$. This suggests that additional channels (more than three) bring relatively small amounts of new information under real measurement conditions. Similar conclusions had been drawn previously [13] in an analysis of the optimum observing conditions problem. This effect is due to the substantial mutual correlation between radiation data measured at different frequencies. The conclusions drawn by E. Westwater and O. Strand differ fundamentally from the results of [13, 23]. While [13, 23] indicate a necessary number of spectral intervals and establish that other intervals are superfluous, Westwater and Strand arrive at another conclusion. Any new interval reduces the uncertainty of the unknown temperature profile (see Table 5.9). That the addition of new intervals with large measurement errors does not appreciably reduce the uncertainty and is therefore irrational is another matter. /309

Moreover, the influence of measurement errors is extremely insignificant when a limited number of measurements (one or two) are used. Conversely, this influence is very strong in interpretation of data measured in four or five spectral intervals. This permits the conclusion that an instrument designed for determination of the temperature profile with moderate accuracy can be relatively simple: two radiation-measurement channels and moderate accuracy of radiation measurement.

Finally, the data of Table 5.9 enable us to study the comparative importance of the number of measurement channels and the accuracy of radiation measurement (for the specific conditions of the numerical experiment considered). It is found advantageous, for example (from the standpoint of the criteria of the paper under consideration), to build an instrument that has three measurement channels with a measurement error $\sigma_T = 0.5°K$ rather than a device with five channels but an error $\sigma_T = 1°K$ (the corresponding values of trX^{-1} will be 73.13 for the first instrument and 91.45 for the second, in case a)). Another similar example can be cited. For the case of atmospheric sounding from the ground, it is more advantageous to build an instrument with only two measurement channels and an error $\sigma_T = 0.5°K$ than a five-channel instrument with $\sigma_T = 1°K$. Such examples illustrate very clearly the importance of preliminary investigation of the entire set of observing conditions and careful selection of optimum conditions for the measurements.

E. Westwater and O. Strand suggest that their method for estimating the information content of observations by used to select observing conditions. In practice, however, numerical implementation of this method becomes an extremely cumbersome problem. Thus, it is necessary to compute approximately $2 \cdot 10^6$ matrix traces to select 5 sounding channels from a total of 50 possible spectral intervals. Finally, we note that Reference [36] compared results from selection of optimum measurement conditions by S. Twomey's method and the method proposed by E. Westwater and O. Strand. This investigation showed that the two methods yield substantially different results, apparently because of their different a priori hypotheses as to the unknown function.

The possibilities for determination of the temperature profile in arctic regions by interpretation of microwave radiation were examined by T.I. Bazlova [89, 91]. The problem was solved by an optimum-approximation method. Successive approximations were used to take account of the temperature variations of the absorption characteristics. Like the number of basis vectors, the sounding frequency was selected empirically. On the basis /310
of numerical experiments made with a large number of temperature profiles, T.I. Bazlova arrives at the conclusion that the reconstruction error would be 1-3° with the presently attainable measurement accuracy.

The possible uses of thermal-sounding results will depend to a major degree on the accuracy that can be obtained in the actual temperature reconstruction. The data given above permit estimation of the method's possible error. Despite the existing variety of interpretation methods, most of them give about the same reconstruction errors. For example, the root-mean-square error of reconstruction using absolutely accurate radiation values is about 0.5°. The existence of this error is explained by a number of factors: the errors of the quadrature formulas used in substituting the algebraic system for the integral equation; errors resulting from approximate consideration of the frequency dependence of the Planck function; rounding errors; poor conditionality of the system; regularization-parameter selection algorithms; nature of the a priori information, etc. Under real measurement conditions, we may expect reconstruction errors of 2-3° at the presently attainable radiation-measurement accuracy (~1%). Somewhat higher accuracy (1-2°) is attainable in interpretation of radiation measurements in the CO_2 band at $\lambda = 4.3$ μm. This is because of the high sensitivity of black-body radiation to temperature variations in this region of the spectrum.

The accuracy requirements for determination of meteorological elements used in various systems for numerical weather forecasting have been indicated in a number of papers (for example, in [96]). For example, the accuracy required for temperature is 0.5-1.0°. The attainment of such accuracy in indirect temperature determination by thermal sounding requires very high measurement accuracy and the development of methods with small algorithm errors and a number of special methods that will make it possible to improve the solution by invoking additional information. It can be said that the solution of each of these problems represents a highly complex and laborious task.

§5. INFLUENCE OF ERRORS IN ASSIGNMENT OF INTEGRAL-EQUATION KERNELS ON ACCURACY OF TEMPERATURE-PROFILE RECONSTRUCTION

In the preceding section, we examined the results of numerical experiments in the reconstruction of temperature in the atmosphere on the assumption that the kernels of the respective integral equations are known with absolute accuracy (an exception is found in [73, 89], where the temperature dependence of the transformation characteristics is taken into account but its influence on reconstruction accuracy is not analyzed). Actually, it is necessary in real reconstructions to use a kernel that is burdened by both accidental and systematic errors. Before passing to a direct study of the influence of these errors on the accuracy of solution of the thermal-sounding problem, let us analyze their causes in detail. /310

The kernels of integral equations incorporate the transformation characteristics of the thermal radiation in any formulation of the thermal-sounding problem: transmission functions for

the infrared and absorption coefficients for the microwave region. (Use of absorption coefficients implies the use of the exponential representation of the transmission functions.) In practice, they are never exactly known. The causes of errors in the kernel of the equation can be classified into two groups. The first includes errors associated with the methods used to acquire the transformation characteristics. Experimental errors are incurred in experimental acquisition of transmission functions or absorption coefficients. These errors may vary in magnitude depending on experimental conditions. They are largest when transmission is investigated under conditions of low pressures and low absorbing-substance contents, under conditions of high spectral resolution. On the average, they vary from 1 to 10%, depending on the quality of the experiment.

The errors of theoretically calculated absorption characteristics have many causes. When the transmission functions are calculated directly, the basic error source is imprecise knowledge of fine-structure parameters and the contour shape of the spectral line. Errors arise from similar causes when such absorption-band models as the quasirandom model are used. Inadequacy of the model to the real spectrum may give rise to other errors. When models are used as approximating formulas to represent the experimental data, the accuracy of the resulting transmission functions will not, of course, be any better than the accuracy of the experimental material used.

Use of the various approximate methods of earth-atmosphere radiative-transfer theory may be another source of errors of this type (§4 of Chapter 1).

Errors stemming from the instability of the atmosphere must be included in the latter class. Because the absorption characteristics depend on the temperature of the atmosphere and its composition, they are not constant, even for the CO_2 and O_2 absorption bands used in the thermal-sounding problem. In a concrete solution of the problem, it is necessary to use the absorption characteristics of a particular model of the atmosphere. The magnitudes of errors of this type depend both on the observed variability of the atmospheric parameters and on the sensitivity of the absorption characteristics to changes in these parameters. /312

Let us take note of a fundamental difference between errors of the first and second types. While errors of the first type can be reduced by appropriate experimental and theoretical investigations of the absorption characteristics, errors of the second type will always attend solution of the inverse problems. These errors result from the very nature of radiative transfer and must be taken into account in the development of inversion algorithms.

Let us consider errors of the second type in somewhat greater detail. All contemporary methods for indirect determination of

the temperature distribution from thermal-radiation measurements are based on the assumption that the spatial distribution of the basic absorbing gas does not vary. While this hypothesis is apparently satisfied very closely for oxygen, the content of carbon dioxide is subject to conspicuous time and space variations. A large body of data on the CO_2 content at the surface of the earth is now available [68, 74-76, 82-85]. The influence of natural and artificial carbon dioxide sources and sinks is being studied. A number of papers have reported substantial variations of the CO_2 concentrations at various stations. Thus, measurements were made in the Pacific and Indian Oceans on the research vessel "Vityaz'" [68]. It was observed that the carbon dioxide content increases appreciably at low latitudes as compared with middle and high latitudes. The CO_2 content depends on the types of the air masses and on wind direction. Measurements made along the coast of the Black Sea also indicated substantial variability of the content of this gas (its concentration varied from 0.0240 to 0.0380%). Various investigations have detected annual, monthly, and diurnal variations of carbon dioxide content at the ground surface. At average concentration values of about 0.031-0.033%, conspicuous fluctuations can be observed, ranging to about 0.01% even within a given day [76]. However, these fluctuations are usually small, averaging 0.001%. It appears that deviations of 10-20% from the average concentration values may be considered quite realistic, especially near carbon dioxide sources and sinks (large masses of vegetation, industrial and metropolitan complexes, etc.).

The altitude distribution of carbon dioxide concentration has not yet been studied in such detail [81, 85, 76]. A slight decrease in the relative content of the gas is noted with increasing distance from the ground surface, along with a narrowing of the range of possible CO_2-content variations. It is reported in [74] that the influence of vegetation is appreciable up to altitudes of about 1 km. References [76, 78, 80, 83] contain extensive data on the spatial contents of carbon dioxide at various elevations. Space and time fluctuations of CO_2 content amounting to 2-4% of the averages have been detected. Thus, there can be no doubt that the basic effect of CO_2 concentration variability on the transmission functions will be observed in transparent spectral intervals, since the maximum variations of CO_2 content are observed at the ground surface. /313

Errors in the kernel of the equation may also result from the temperature variation of the absorption characteristics: the transmission functions or absorption coefficients. Most of the temperature dependence of these characteristics is accounted for by the temperature variation of line intensity, methods for approximate consideration of which were set forth in §4 of Chapter 1. The detrimental influence of errors resulting from the temperature variation of absorption characteristics can be reduced by using a method of successive approximations in which the

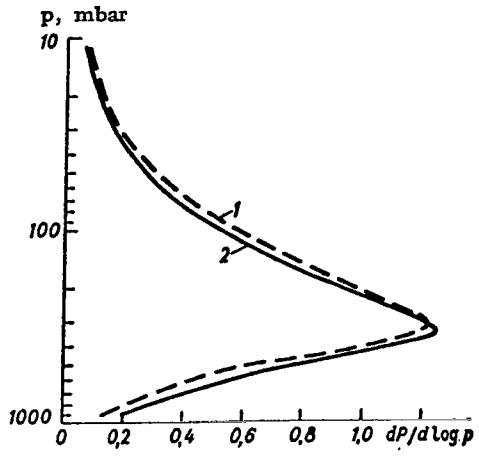

Figure 5.28. Temperature Dependence of the Functions dP/d log p (ν = 705.8 cm). 1) $T(p) = T_s(p) + 10°$; 2) $T_s(p)$, standard atmosphere.

temperature profile found with the aid of the kernel corresponding to the average temperature distribution is used to improve the kernel and subsequent solution of the inverse problem.

Estimates of the effect of temperature on the transmission function of the 15-μm CO_2 band were obtained in [1.91, 50]. Figure 5.28 [50] gives weighting functions $dP_{\Delta\nu}/d \log p$ for a spectral interval 5.2 cm^{-1} wide centered on ν = 705.8 cm^{-1}. As we see from the figure, the weighting-function variations are relatively small, but calculation indicates that they are still sufficient to change the outgoing radiation by 2-3%. /314

Despite the fact that most of the absorption in the spectral regions selected for solution of the thermal-sounding problem is governed by carbon dioxide or oxygen, whose distributions are relatively stable, absorption in these intervals is also influenced by other gases (H_2O, CO, N_2O, O_3). Although the influence of these gases is often relatively weak, the errors resulting from failure to consider them may increase the errors of temperature reconstruction. In view of the variability of the contents of these gases, they can be allowed for correctly on independent determination of their distributions in the atmosphere. At the present time, this problem is solved only for H_2O and O_3 (see Chapter 4). Average distributions of the absorbing components are most frequently used in the reconstruction, and this substantially reduces the errors that appear in the kernels when they are left totally out of account.

S. Drayson [50] was the first to evaluate the influence of absorption by ozone (ν_2 band at λ = 14 μm) in the region of the 15-μm carbon dioxide band. It was found that O_3 absorption may range up to 5% in the thermal-sounding channels. Drayson therefore concludes that O_3 must be taken into account for accurate transmission-function calculations, at least on the basis of climatological data.

Numerical experiments to investigate the influence of errors in assigning the integral-equation kernel on the accuracy of temperature-profile reconstruction have been made on a number of occasions. I.A. Gorchakova and M.S. Malkevich [86] investigated

the sensitivity of the spectral curve of the outgoing radiation in the carbon dioxide bands at 15 and 4.3 μm to changes in various parameters. The analysis for the 15-μm band was especially thorough: the sensitivity of the radiation to variations in the vertical temperature profile, CO_2 concentration, changes in observation angle, underlying-surface emissivity, and atmospheric water-vapor content was studied. Such research has made it possible to estimate the possible effects of various factors on the accuracy with which the inverse problem is solved. Gorchakova and Malkevich performed numerical experiments to solve the inverse problem in which they used various transmission functions. (The problem was solved by the optimum-approximation method.) Use of "bad" transmission functions, i.e., functions deviating from those used in radiation calculations, increases the maximum reconstruction error by a factor of 1.3 to 1.7. /315

In solving the inverse problem, Gorchakova and Malkevich also investigated the influence of water-vapor absorption. Numerical experiments showed that water vapor strongly influences the accuracy of temperature-profile reconstruction when spectral intervals of weak CO_2 absorption are used. Use of data on radiation in the strongly absorbing spectral intervals or in intervals of both types has little influence on the accuracy of inverse-problem solution. On the basis of these results, they infer the possibility of selecting segments of the band at $\lambda = 15$ μm in which the influence of water vapor can be disregarded in solving the thermal-sounding problem. We note that none of the present methods for selection of optimum experimental conditions takes account of the possible errors in the kernel of the equation.

V.B. Glasko and Yu.M. Timofeyeva [5] investigated the influence of accidental and systematic errors of kernel assignment on the accuracy of reproduction of the Planck function $B(\xi)$ for the case of thermal sounding considered in the previous section, which used radiation data measured in the contour of an isolated Lorentz line. The influence of accidental errors was studied by solving (5.55) with the kernel

$$\tilde{K}(x_k, \xi_j) = K(x_k, \xi_j) + \delta_K \omega_{kj}, \qquad (5.66)$$

where

$$\omega_{kj} = \frac{\eta_{kj}}{\sqrt{h \sum_{j=1}^{n} \eta_{kj}^2}},$$

and the $\{\eta_{kj}^2\}$ are values of a random variable (different sets for different $\underline{k}$) that is uniformly distributed in the interval [-1, 1].

The values of δ_K were varied to span the entire possible range of errors in the kernel as governed by various physical factors. Figure 5.29 shows the calculated results for the case of

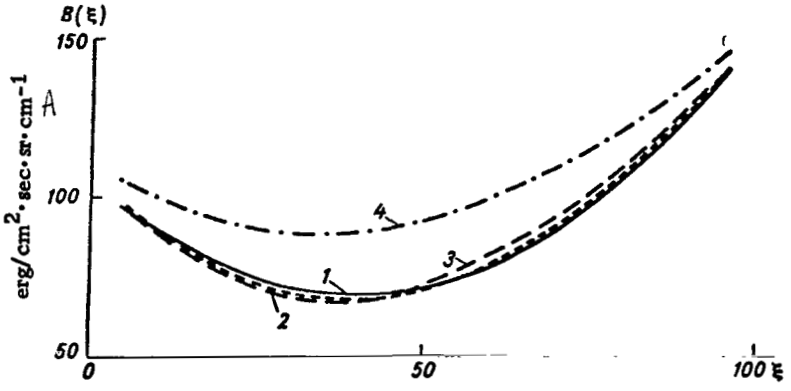

Figure 5.29. Reconstruction of the Function $B_1(\xi)$ ($\gamma = 1.0$) for Various Values of the Accidental Error in the Kernel. 1) Exact solution; 2) $\delta_K = 10^{-3}$; 3) $\delta_K = 10^{-2}$; 4) $\delta_K = 10^{-1}$.

$B_1(\xi)$ and $\gamma = 1.0$. We note that reconstruction accuracy deteriorates insignificantly at relatively low accidental-error levels, but strongly when $\delta_K > 10^{-2}$. This suggests that the accidental error may not exceed a certain level, which depends on the type of the kernel, the nature of the unknown function, the type of approximating net, etc., if the desired reproduction accuracy is to be attained. In selecting spectral intervals for thermal sounding, therefore, it is necessary to consider not only their optical properties, but also the possible level of the errors that arise from the causes considered above. /316

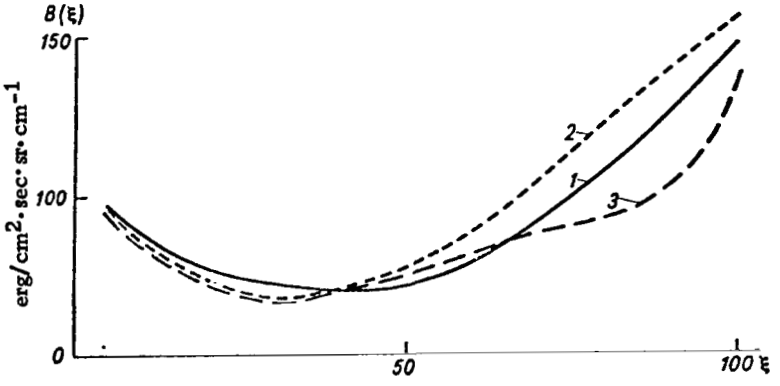

Figure 5.30. Reconstruction of the Function $B_1(\xi)$ when Kernel of Eq. (5.55) is Assigned with a Systematic Error. 1) Exact solution; 2) $\gamma = 0.9$; 3) $\gamma = 1.1$.

The influence of systematic errors on reconstruction accuracy was investigated as follows. Radiation values corresponding to

$\gamma = 1.0$ were interpreted with kernels for $\gamma = 0.9$ and 1.1. The calculated results appear in Fig. 5.30. As we see, the accuracy of reconstruction of $B_1(\xi)$ deteriorated markedly, especially for large ξ, i.e., near the ground surface, as a result of strong distortions of the kernels at these values of ξ.

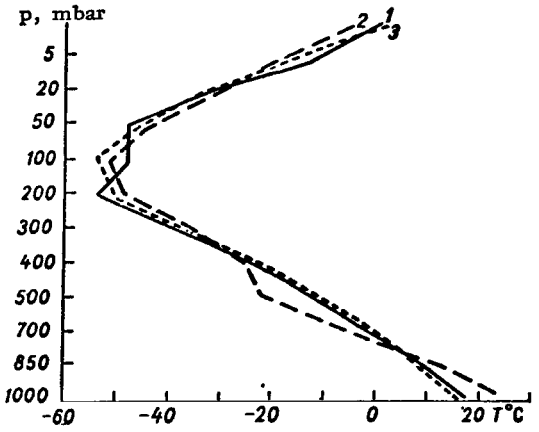

/317

Figure 5.31. Influence of Errors in Kernel of Integral Equation on Accuracy of Vertical Temperature Profile Reconstruction by the Regularization Method. 1) True profile; 2) $\delta_K = 0.1$; 3) $\delta_K = 0.01$.

O.S. Bogomolov [87] also studied the influence of errors in assigning the kernel of the equation. Figure 5.31 presents an example of reconstruction of the temperature profile T(p) for two kernel errors that retained the same signs, but diminished with increasing altitude and varied over the spectrum. At tropospheric levels, they were 0.01 and 0.1 for transparent intervals. In the former case, the solution differs little from that obtained when the kernel is assigned accurately, but in the latter we begin to observe a substantial increase in the reconstruction error (8-10°). Bogomolov also showed that neglect of water-vapor absorption also substantially increases the reconstruction errors (7-10°). However, the accuracy of reconstruction of the vertical temperature profile can be improved substantially with even an approximate estimate of the atmosphere's moisture content. A relative error of ~20% in the moisture-content determination produces errors of 1-2° in the temperature-profile reconstruction.

The combined influence of radiation-measurement and kernel-assignment errors observed in actual thermal-state reconstructions was investigated by O.M. Pokrovskiy and Yu.M. Timofeyev [21]. /318
Numerical experiments were performed with the weighting functions shown in Fig. 5.1, which pertain to the conditions of solution of the thermal-sounding problem with a six-channel instrument for the 15-μm band. Figure 5.22 shows the variance and maximum error of the B(p) reconstruction as functions of the accidental measurement error for cases of an accurately assigned kernel and a kernel assigned with a systematic error, with the nature of the error corresponding to the case of inaccurate assignment of the distribution of the basic absorbing gas or temperature. This error reaches maximum values of 0.025 in transparent intervals of the spectrum near the ground surface. As we see from Fig. 5.22, the accuracy of reconstruction diminishes appreciably, indicating the

importance of the most accurate possible assignment of the kernel. All of the examples given above testify that the accuracy of kernel assignment determines the accuracy of reconstruction of the atmosphere's thermal structure to a substantial degree. This calls for experimental and theoretical research with the object of obtaining accurate information on absorption characteristics.

Use of special methods of successive approximations in solution of the problem is also important. To use these methods effectively, it is necessary to develop accurate procedures for correcting the kernels of the integral equations and to use additional information, such as data on the water-vapor distribution. Finally, we note that attainment of the accuracy of temperature-profile determination that is necessary in a number of problems is an extremely complex task.

§6. THERMAL SOUNDING UNDER THE CONDITIONS OF A CLOUDY ATMOSPHERE

Most of the research that has been done in the thermal-sounding problem pertains to the case of a clean and cloudless atmosphere. However, clouds (with various shapes and optical properties) and layers of aerosols and haze may be observed at various levels in the real atmosphere. These factors may complicate the already quite difficult problem of reconstructing the temperature profile under clean-atmosphere conditions, and in some cases even make it impossible to obtain the T(z) profile, at least in certain layers of the atmosphere. Indeed, the presence of clouds, aerosols, etc. in the atmosphere may make it necessary to take account of additional radiation-transformation mechanisms, and this would require a review of the mathematical model and complicate the problem. However, consideration of these factors, and cloudiness in /319
particular, is absolutely necessary, since 50-75% of the area of the globe is shrouded by clouds at various times. The present section is devoted to the problem of taking clouds into account in schemes for solution of our inverse problem. The few other papers devoted to this important problem have appeared only recently [9, 21, 69, 70].

Let us first consider the problem of reconstructing the temperature profile for the case of solid cloud cover. The emissivities of many types of clouds (for greater detail, see §1, Chapter 3) approach unity in the infrared. This means that from the optical standpoint, the presence of continuous cloud cover at a certain level in the atmosphere is equivalent to a temperature profile in which isothermy is observed downward from cloud level with $T = T_{cld}$. Let us study the possibility of reconstructing the temperature distribution for solid cloud cover. Figure 5.32 shows an example in which the Planck function has been reconstructed for high clouds. Reconstruction was by the regularization method, and the errors of the radiation measurements in the 15-μm CO_2 band were 1%. The kernels given in Fig. 5.17 were used in the

numerical experiment. The figure shows that the maximum reconstruction errors are observed around the cloud-top level, in the range of the sharp transition to isothermy. The maximum reconstruction errors are $\Delta B_m = 4.8$ and $\Delta B_m = 5.25$ erg/cm^2·sec·sr·cm^{-1}, respectively, for $\delta = 1.0\%$ and $\delta = 2\%$. An important feature of the reconstructed B(p) profile is satisfactory agreement between the reconstructed and true profiles above and below the inflection point. Thus, the presence of clouds does not exclude the possibility of temperature reconstruction in the upper layers of the atmosphere by the regularization method. In the absence of any additional information other than radiation data measured in the thermal-sounding channels, the resulting profiles can, in principle, be regarded as genuine. However, if the bare fact of the existence of solid clouds is known, it will be possible in certain cases to determine their top height.

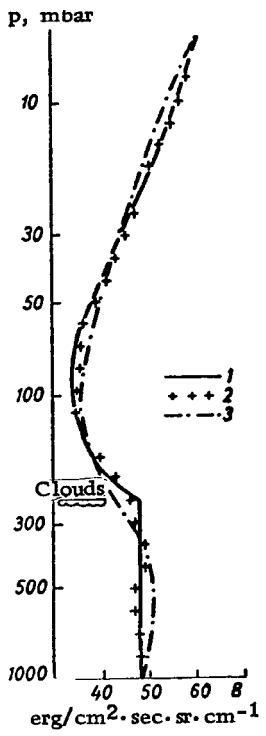

/320

Figure 5.32. Reconstruction of Planck-Function Distribution for Solid Cloud Cover. 1) True profile; 2) profile reconstructed using absolutely accurate radiation measurements; 3) profile reconstructed with accidental error $\delta = 1\%$.

Reconstruction of the temperature distribution under partly cloudy conditions is a difficult problem. On the other hand, it is a highly important one. Even relatively small "windows" in continuous cloud cover can be used in solving the problem to determine the temperature distribution in the layer of atmosphere below the clouds. A number of papers have proposed that the difficulties of solving the thermal-sounding problem under partly cloudy conditions be overcome by sharply narrowing the fields of the instruments. This would indeed increase the probability of observations under the conditions of unbroken cloud cover or a clean atmosphere. However, since the spatial dimensions of cloud formations vary extremely widely, this method does not eliminate the need for radiation measurements under partly cloudy conditions (in the instrument field) and, consequently, does not eliminate the need for development of methods for interpretation of radiation measurements under these conditions.

We cite examples in which the atmosphere's thermal structure is reconstructed from radiation measurements made under various cloudage conditions in the absence of any information on the

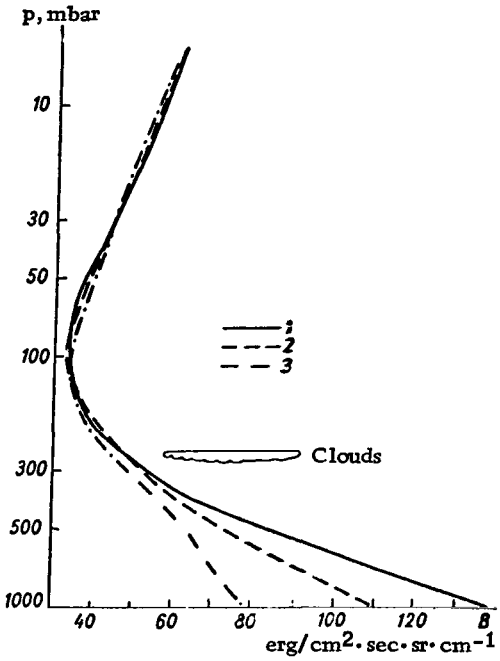

Figure 5.33. Reconstruction of Planck Function Distribution under Conditions of Partial Cloud Cover in the Absence of Any Information on the Cloud Cover. 1) True profile observed in the atmosphere; 2) for N = 0.33 (δ = 0.5%); 3) for N = 0.66 (δ = 0.5%).

nature of the clouds. Figure 5.33 presents examples of Planck-function reconstruction for two different percentage cloud covers: N = 0.33 and N = 0.66. The problem was solved by the regularization method and the accidental error of the measurements was 0.5% (case of thermal sounding corresponding to the kernels shown in Fig. 5.1). Figures 5.32 and 5.33 show curves for the true profile and the profiles corresponding to various cloudage conditions. As we see from these figures, an extremely important property of the interpretation method employed comes to light here: the upper parts of the profile are reconstructed very accurately. Thus, the presence of partial cloud cover in the lower atmosphere does not make it impossible to reconstruct the thermal structure of its upper layers even in the absence of any auxiliary data. Naturally, we can take the B(p) distributions obtained (see Fig. 5.33) as the true temperature stratification in the atmosphere in the absence of information on cloudage and its characteristics. We note that the presence of clouds can be detected on comparison of the temperature profiles for closely spaced successive measurements under partly cloudy conditions because of the strong spatial variation of the lower part of the profile in observations under cloudy conditions with various values of N. /321

To illustrate further the reconstruction possibilities under partly cloudy conditions, we present Fig. 5.34, which we have borrowed from [88]. This reconstruction used a nonlinear method, assuming absolute accuracy in the radiation measurements.

Let us now examine a number of methods that have been proposed for thermal sounding under parly cloudy conditions. These methods differ from one another in various ways, but our basic classification for them will be based on the use of additional information, which is necessary for practical application of these methods. We note first of all that in the absence of all information on the clouds, it becomes practically impossible to

reconstruct the temperature distribution in the layer below the clouds with satisfactory accuracy. The same conclusions can be arrived at from analysis of the results given in [9].

This report was devoted to a study of the possibilities for reconstruction of B(p) under the conditions of a cloudy atmosphere solely on the basis of conventional measurements corresponding to cloudless-atmosphere thermal-sounding conditions. For example, it was assumed that radiation measurements in the 15-μm band were made with a six-channel instrument or a modified instrument with a larger number of channels. Reference [9] also proposed a so-called direct thermal sounding method especially adapted for sounding under cloudy-atmosphere conditions. (A direct method has also been used for numerical experiments under cloudless-atmosphere conditions [92, 93].) We note that in so doing, the authors of [9] dispensed with the nonlinear interpretation method, which shows how strongly the cloudage problem may influence the selection of interpretation method.

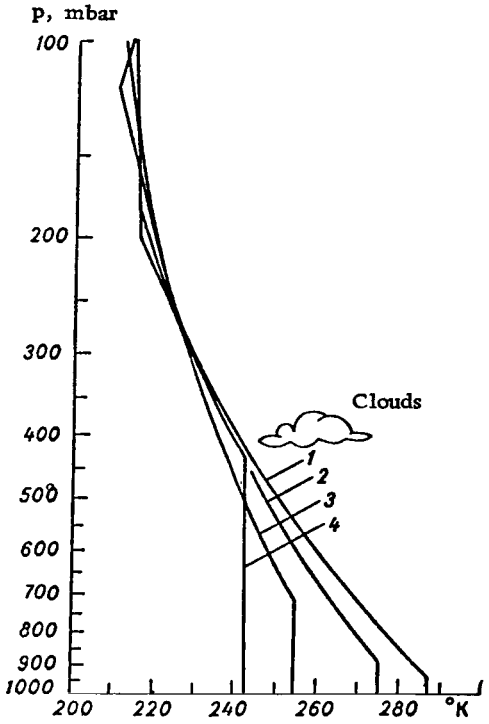

/322

Figure 5.34. Reconstruction of Temperature Profile Under Various Cloudage Conditions by Means of Nonlinear Interpretation Method. 1) Cloudless atmosphere; 2) N = 0.3; 3) N = 0.7; 4) N = 1.0.

The principal features of the direct interpretation method are as follows. First of all, the temperature profile is reconstructed separately for various layers of the atmosphere. The atmosphere is divided between the troposphere and stratosphere, and it is assumed that clouds can be present only in the troposphere. The first step is to reconstruct the thermal structure of the stratosphere. This is done on the basis of measurements made in three spectral intervals centered at 669, 677.5, and 691 cm^{-1}. Then a series of possible temperature distributions in the troposphere is established in the presence of clouds. The following hypotheses may be included among the other distinctive features of this method.

/323

1. The temperature profile is assumed to be known above a certain level (for example, from climatological estimates). For

example, it was assumed in [9] that it is known for $p \leq 20$ mbar.

2. The pressure at ground level, and in some cases the ground temperature, which might be obtained from radiation measurements in a transparency window, are assumed to be known.

3. The unknown temperature profile or Planck function is approximated by straight-line segments. The points at which these segments meet are specially selected.

Thermal structure in the troposphere is evaluated by using the three (or four where the modified instrument is concerned) remaining thermal-sounding channels. This estimate is based on selection of the tropospheric temperature profile at which the following quantity has its minimum:

$$R = \left\{ \frac{\sum_{i=1}^{n} [J_c(\nu_i) - J_{msr}(\nu_i)]^2}{n} \right\}^{1/2} \qquad (5.67)$$

where J_c and J_{msr} are the calculated and measured radiation values.

Here, the following profile parameters are varied: altitude of tropopause, thermal structure of ground layer (gradient in ground layer), temperature at top of troposphere, transmission of clouds or percentage cloud cover, underlying-surface temperature. In the concrete numerical experiments performed in [9], it was assumed that the temperature of the underlying surface was known. The remaining parameters were varied stepwise; for example, the authors considered 135 different possible temperature profiles with 9 different tropopause-level temperatures (the tropopause level was placed at altitudes ranging from 6 to 15 km), three temperatures at the 932-mbar level, and five cloud transmissions or five cloud-cover percentages. As we see from the data cited, the direct method proposed in [9] is characterized by /324
rather rough approximations of the temperature profile and rather rigid conditions imposed on the sought solution. These conditions were selected from analysis of a large number of real profiles observed in the atmosphere, but are undoubtedly arbitrary to a certain degree.

The results of the numerical experiments performed in [9] indicate that in many cases the minimum of R is obtained on profiles quite remote from the true thermal stratification observed in the atmosphere. By way of example, we present Fig. 5.35, which shows a case of unsuccessful temperature-profile reconstruction for a situation with clouds at two levels ($N = 0.3$ at $p = 297$ mbar and $N = 0.5$ at $p = 700$ mbar). This example and others given in [9] indicate that thermal conditions in the troposphere may be determined with large errors (up to 15°) when the direct interpretation method is used. In some cases, there are also wide disagreements between the real cloudage characteristics (percentage cover and

height of cloudage) and those determined by the direct method. From our point of view, the results of [9] show that it is necessary to use additional information on the cloudage situation in order to reconstruct the tropospheric temperature profile with satisfactory reliability. Examples in which the direct method is used to interpret data from actual measurements will be given in §7.

W. Smith [69, 70] proposes another approach to solution of the thermal-sounding problem under partly cloudy conditions. First, Smith proposes the use of scanning instruments with substantially higher spatial resolution for thermal sounding. This resolution would, for example, make it possible to obtain about 100 frames for the area that usually forms the horizontal averaging element. A sharp reduction in the instrument's field angle would require a substantial decrease in its spectral resolution in order to preserve a high signal/noise ratio. Even with the higher angular resolution, however, observations are quite often made under partly cloudy conditions.

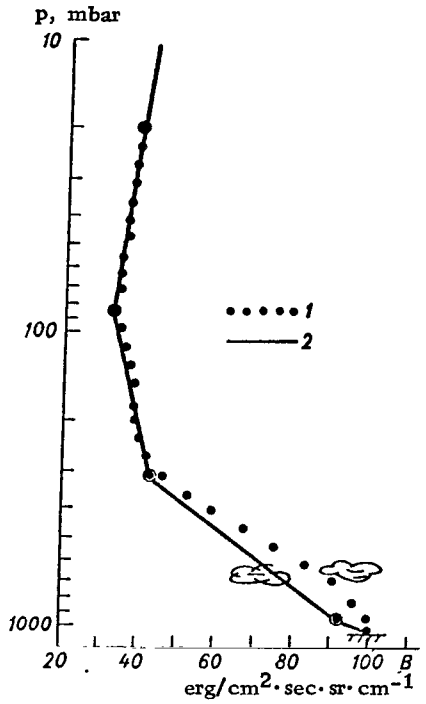

Figure 5.35. Reconstruction of Planck-Function Profile by Direct Method for Clouds at Two Levels. 1) True profile; 2) reconstructed profile.

/325

Direct acquisition of data on the temperature profile in the area below clouds is an extremely difficult problem, since its solution requires knowledge of such parameters as cloud height, amount of clouds, and their optical properties. Smith therefore proposes a method that permits extraction of the radiation corresponding to a clean, cloudless atmosphere from the registered radiation data. Smith then determines the temperature profile on the basis of the interpretation method that we described in §4 of this chapter. The method used to separate the cloudless-atmosphere radiation is as follows. For the radiation measured above a certain elementary area on the earth's surface under partly cloudy conditions we can write

$$J(\Delta\nu_i) = NJ_{\text{cld}}(\Delta\nu_i) + (1 - N)J_{\text{clr}}(\Delta\nu_i), \qquad (5.68)$$

where N is the percentage cloud cover for the particular instrument reading and $J_{\text{cld}}(\Delta\nu_i)$ and $J_{\text{clr}}(\Delta\nu_i)$ are the radiations in the ith spectral interval for cloudy and cloudless atmospheres, respectively.

Having at least two sets of measurements obtained over different areas of the surface, we can write the following system of equations:

$$J_1(\Delta\nu_l) = N_1 J'_{\text{cld}}(\Delta\nu_l) + (1 - N_1) J'_{\text{clr}}(\Delta\nu_l),$$
$$J_2(\Delta\nu_l) = N_2 J_{\text{cld}}(\Delta\nu_l) + (1 - N_2) J'_{\text{clr}}(\Delta\nu_l). \qquad (5.69)$$

If we assume that

$$J'_{\text{cld}}(\Delta\nu_l) = J''_{\text{cld}}(\Delta\nu_l),$$
$$J'_{\text{clr}}(\Delta\nu_l) = J''_{\text{clr}}(\Delta\nu_l) = J_{\text{clr}}(\Delta\nu_l), \qquad (5.70)$$

the cloudless-atmosphere radiation can be found from this system. We then have from the solution of System (5.69) for $N_1 \neq N_2$

$$J_{\text{clr}}(\Delta\nu_l) = \frac{J_2(\Delta\nu_l) - N^* J_1(\Delta\nu_l)}{1 - N^*} \qquad (5.71)$$

where $N^* = N_1/N_2$.

It is proposed that N^* be determined from $J(\omega)$ data measured in the transparency window. Solving the corresponding system, which is similar to (5.69), for N^* in the case of transparency-window observations, we obtain /326

$$N^* = \frac{J_1(\omega) - J_{\text{clr}}(\omega)}{J_2(\omega) - J_{\text{clr}}(\omega)}, \qquad (5.72)$$

where $J_{\text{clr}}(\omega)$ is to be determined by some independent method, e.g., with an ultrahigh-angular-resolution radiometer [70]. The requirement that (5.70) be satisfied implies identical optical properties of the clouds and identical top heights for adjacent readings. It must be satisfied quite frequently for the condition of high spatial resolution, which is an indispensible element of W. Smith's scheme. It is also proposed that the radiation from the clear atmosphere be determined by using various pairs from a large set (about 100) of measurements made above the volume of atmosphere under study. In this case, J_{clr} is found from the relation

$$\overline{J}_{\text{clr}}(\Delta\nu_l) = \frac{\sum_{j=0}^{n} \omega_j J_{\text{clr}\,j}(\Delta\nu_l)}{\sum_{j=1}^{n} \omega_j}, \qquad (5.73)$$

where $\omega_j = 1 - N^*_j$.

With this averaging, we may expect the influence of accidental measurement errors and errors resulting from differences in cloud optical properties to be weaker. References [69, 70] present examples of numerical experiments and real reconstruction under partly cloudy conditions. The most interesting data

pertaining to the case of a real temperature-profile reconstruction will be given in the next section. Here we note only that these examples demonstrated the promise of Smith's method for data interpretation under partly cloudy conditions.

O.M. Pokrovskiy and Yu.M. Timofeyev [21] proposed another method for solution of the same problem. In developing it, they proceeded from the necessity of maximum utilization of existing thermal-sounding instruments. In this sense, their method occupies a position intermediate between that of W. Smith and the method proposed in [9]. For solution of the thermal-sounding problem under partly cloudy conditions, W. Smith proposes the use of a new instrument with higher spatial resolution and a special radiometer for determination of underlying-surface temperature. The method of House et al. [9] uses no measured results /327 other than data acquired from an instrument with normal spatial resolution. The method proposed by O.M. Pokrovskiy and Yu.M. Timofeyev is based on use of a thermal-sounding spectrometer with a wide field and a special radiometer (as in W. Smith's method) for determination of underlying-surface and cloud-top temperatures (or, more precisely, the ground and cloud radiations). The method itself is based on the linearity of the relation linking the measured radiation and the atmospheric distribution of Planck's function. We can write for the clear-atmosphere radiation

$$J_{\text{clr}}(\Delta\nu_i) = \int B_{\text{clr}}(x) K(\Delta\nu_i, x)\, dx. \tag{5.74}$$

where $\underline{x}$ is the corresponding space variable.

At the same time, we have the following equality for radiation under solid-overcast conditions (the case considered is that of clouds with $\varepsilon \approx 1$):

$$J_{\text{cld}}(\Delta\nu_i) = \int B_{\overline{\text{cld}}}(x) K(\Delta\nu_i, x)\, dx. \tag{5.75}$$

Using the linearity property of the integral equations involved, we can write

$$J(\Delta\nu_i) = (1-N) J_{\text{clr}} + N J_{\text{cld}} = \int [(1-N) B_{\text{clr}} + N B_{\text{cld}}] K(\Delta\nu_i, x)\, dx, \tag{5.76}$$

where $J(\Delta\nu_i)$ is the radiation measured under partly cloudy conditions.

Thus, solution of the equation

$$J(\Delta\nu_i) = \int B(x) K(\Delta\nu_i, x)\, dx \tag{5.77}$$

enables us to determine the function B(x), which is a superposition

of the profiles of the corresponding clear and solid-cloudy atmospheres. Consequently, we have

$$B(x) = (1 - N) B_{clr}(x) + N B_{cld}(x). \quad (5.78)$$

Hence we obtain for the Planck-function profile for the clear atmosphere

$$B_{clr}(x) = \frac{B(x) - N B_{cld}}{1 - N}. \quad (5.79)$$

The unknown profile $B_{clr}(x)$ and, consequently, the temperature T(x) can be determined if we know the percentage cloud cover and the profile under cloudy-atmosphere conditions. Let us examine the possibilities for determining these quantities from satellite observations. The percentage cloudiness can be obtained from observations of the state of the cloud cover that are now being conducted from many weather satellites. On the other hand, this characteristic might be determined from measured transparency-window data with the same spatial resolution as measurements intended for direct use in solving the thermal-sounding problem. We can write for the transparency-window radiation

/328

$$J(\omega) = N B_{cld} + (1 - N) B_{grd}, \quad (5.80)$$

whence we have

$$N = \frac{B_{grd} - J(\omega)}{B_{grd} - B_{cld}}, \quad (5.81)$$

where B_{grd} is the radiation from the ground surface.

Relations (5.80) and (5.81) do not account for transformation of the radiation by the atmosphere, but this can be considered by the methods set forth in Chapter 3. Using measurements made with an ultrahigh-spatial-resolution radiometer to determine the cloud- and ground-surface radiations, we can determine the percentage cloud cover from (5.81).

The cloudy-atmosphere profile of the Planck function, which appears in (5.79), can be determined if the cloud-top $B(p_{cld})$ is known (for example, from measurements made with the ultrahigh-spatial-resolution radiometer). Indeed, as we see from Fig. 5.32, B_{cld} is equivalent to the cloudless-atmosphere profile for $p < p_{cld}$ (p_{cld} is the pressure at cloud-top level) and $B(p) \approx B[T(p_{cld})]$ for $p > p_{cld}$. Thus, knowing $B[T(p_{cld})]$, we can obtain $B_{cld}(p)$ from the reconstructed B(p) profile. On the other hand, the profile for solid-overcast conditions can be obtained in the process of solving the inverse problem for observations under conditions of solid cloud cover (Fig. 5.32).

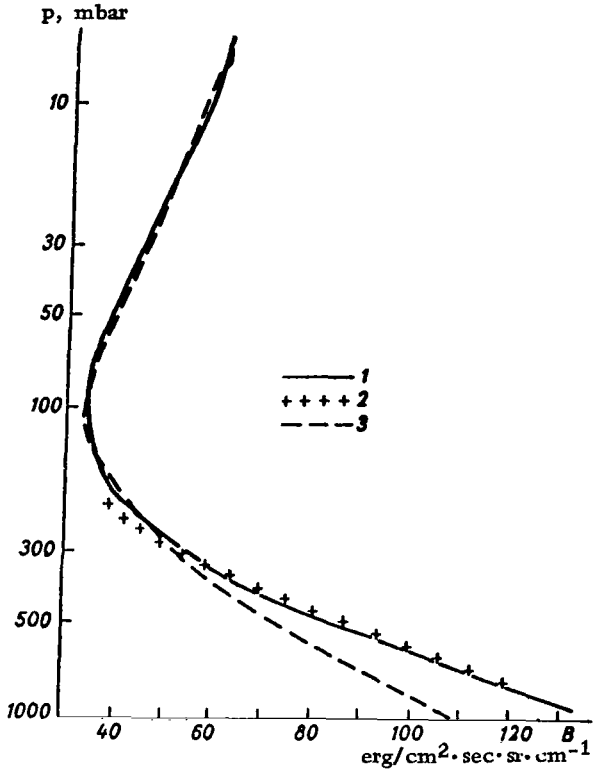

Figure 5.36. Reconstruction of Planck-Function Profile for Partly Cloudy Conditions (N = 0.33). 1) True profile; 2) profile in cloudless atmosphere (δ = 0.5%, ΔT_{cld} = 1°K); 3) profile B(p) obtained by solving Eq. (5.77).

We now present a few examples to illustrate results obtained from the proposed method [21]. Figure 5.36 shows an example of reconstruction of B(p) under partly cloudy conditions (N = 0.33) and with an accidental measurement error of 0.5%. In this example, it was assumed that the temperature at cloud-top level was known with an error ΔT_{cld} = 1°K. Reconstruction of B(p) from profile data obtained by solving the solid-overcast inverse problem leads to approximately the same results. Numerical experiments have shown that the reconstruction error increases with increasing percentage cloudiness because of the smaller amount of radiation /329 arriving from layers of the atmosphere below the clouds. The maximum reconstruction errors are 3-4 erg/cm^2·sec·sr·cm^{-1} at N = = 0.33 and 5-6 erg/cm^2·sec·sr·cm^{-1} for N = 0.66, corresponding to 2-3 and 3.0-4.5°, respectively, under the conditions of the experiment.

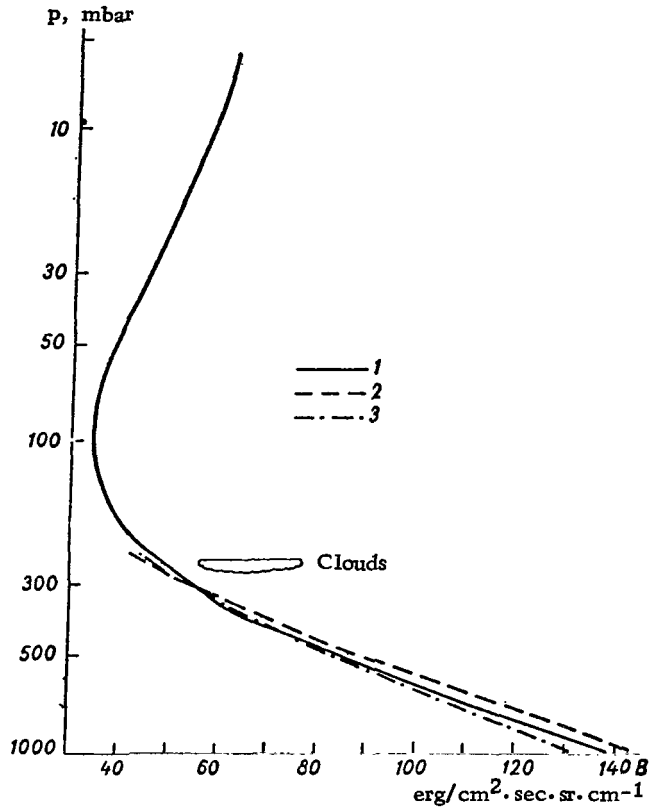

Figure 5.37. Reconstruction of Planck-Function Profile for Partly Cloudy Conditions (N = 0.33). Case of Interpretation of Data when N is Assigned with Error. 1) True profile; 2) reconstructed for N = 0.38; 3) reconstructed for N = = 0.28.

Under real conditions, N may be known with an error. We estimated the influence of errors in assigning percentage cloud cover on the accuracy of Planck-function profile reconstruction in the layer below the clouds. Figure 5.37 shows an example in which B_{clr} is reconstructed for the case N = 0.33 and δ = 0.5. The values N = 0.38 and N = 0.28, which correspond to errors of about 15% in assignment of N, were used in reducing the data. As /330 we see from the figure, the maximum errors are observed near the ground surface and amount to 6-7 erg/cm^2·sec·sr·cm^{-1} (4-5°).

We performed such numerical experiments not only for high clouds (Figs. 5.32-5.37), but also for middle- and lower-level clouds. It was found that reconstructions of the temperature stratification under the conditions of solid and partial cloud cover at middle and lower levels on the basis of data measured in

six thermal-sounding channels (see Fig. 5.1) are burdened with appreciably larger errors, especially for the case of low clouds. This is because measurements in these six channels give us very little information on the thermal situation in the lower levels of the troposphere. The addition of more transparent sounding channels, e.g., at $\nu = 750$ cm^{-1} or $\nu = 743$ cm^{-1}, yields a substantial improvement in the accuracy of the B(p) reconstruction. In the method proposed, as we noted above, it is assumed that the cloud emissivities are close to unity. Its applications are therefore more limited than those of W. Smith's method. It will subsequently be necessary to generalize the method, extending it to cases of cloud cover whose emissivities differ appreciably from unity. /331

The methods examined above for reconstruction of the atmosphere's thermal state under partly cloudy conditions have been based on the assumption of constant angular sensitivity of the measuring instruments (Relations (5.68), (5.76)). If the deviations from this hypothesis are large, interpretation of the data under partly cloudy conditions becomes much more complicated. For example, cases may be observed in which different radiation values are obtained for the same cloud cover (assuming differing angular structures of the outgoing radiation).

§7. EXAMPLES OF RECONSTRUCTION OF THE THERMAL-STRUCTURE CHARACTERISTICS OF THE ATMOSPHERE UNDER REAL CONDITIONS

The first experimental determination of the temperature distribution in the atmosphere from measurements of the outgoing radiation in the 15-μm carbon dioxide band at high altitude was made in 1964 in Texas and described in [2.4]. A U.S. Weather Bureau six-channel spectrometer was used in this experiment. It had been preceded by an experiment to determine the atmosphere's temperature distribution by means of ground infrared radiation measurements [97]. Let us note first of all that the possibilities of determining temperature profiles by interpretation of measured incoming-infrared data are quite limited. This is because the major part of the radiation is formed in the lower, dense layers of the atmosphere if the measurements are made in spectral intervals 5-10 cm^{-1} in width. Considerably more favorable conditions for ground-based sounding prevail in the microwave region because of the higher spectral resolutions of existing microwave instruments.

In the experiment described in [97], the incoming radiation was measured in eight spectral intervals in the 15-μm CO_2 band. The centers of these intervals were located as follows: 667.5, 677.5, 688.5, 694.5, 702.5, 727.5, 747.5, and 899 cm^{-1}, and the instrument had a spectral resolution of 5 cm^{-1}. The transmission functions of the respective intervals were acquired experimentally in the laboratory, using an instrument with the same spectral resolution. The temperature variation of the transmission /332

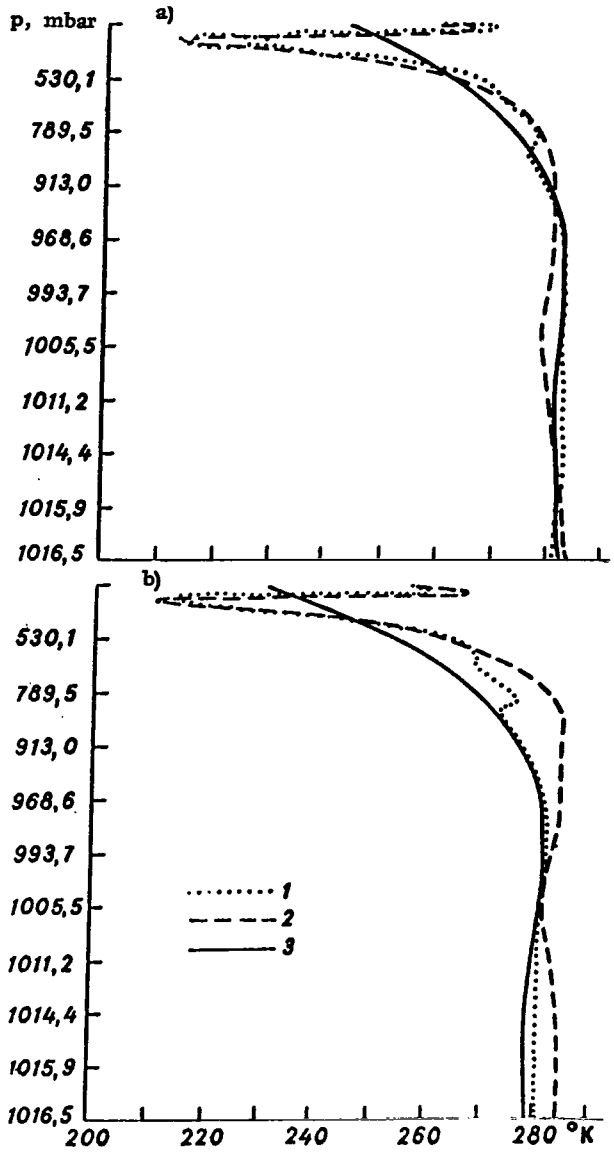

Figure 5.38. Reconstruction of Temperature Profile from Incoming-Radiation Measurements Made in the 15-μm CO_2 Band. a) 21 September 1962; b) 22 September 1962; 1) radio sounding data; 2) solution using empirical orthogonal basis; 3) solution using trigonometric basis.

functions was taken into account theoretically. The Curtis-Godson method was used to obtain the real-atmosphere transmission functions. The influence of water vapor absorption was also taken into account in calculating them. Transmission functions corrected for the combined carbon dioxide and water vapor absorptions were obtained by cross-multiplication (see §4 of Chapter 1), using experimental data for continuum absorption and theoretical data to account for absorption in individual spectral lines in calculation of the water-vapor transmission functions. The temperature profile was reconstructed by a method in which the unknown function was expanded in a certain basis and smoothing mechanisms were applied in solving the corresponding algebraic equation system (see §2 of this chapter). In [97], the expansion was performed with respect to two bases; a trigonometric basis and a basis of empirical orthogonal functions (vectors). Eight terms of the series were used in the trigonometric-basis expansion, and four in the expansion in the empirically orthogonal basis. Figure 5.38 shows examples of reconstruction using these two bases. We see that the agreement with radiosonde data is better in the case of the trigonometric basis up to p = = 850 mbar; above this level, use of the empirically orthogonal basis gives better results. The authors of [97]

note, however, that this agreement is of relatively little importance, since very little information is available on the temperature profile above $p < 850$ mb in radiation data measured in these intervals. In their opinion, it is more important that none of the approaches made it possible to detect a temperature inversion at about $p = 850$ mbar.

The authors of [97] made similar reconstructions of the temperature profile on the basis of data measured in four spectral intervals (667.5, 694.5, 712.5, and 747.5 cm^{-1}). The resulting temperature profile showed practically no differences from that shown in Fig. 5.38. This fact suggests that most of the information on the thermal state of the lower atmospheric layers is present in no more than four radiation measurements (needless to say, for a given temperature profile and a given experimental error).

Reference [98] offers a detailed analysis of the results of temperature-profile reconstructions from outgoing radiation data measured in the 15-μm CO_2 band on a high-altitude aerostat (May 1966, Texas and Six Falls, USA). The radiation measurements were made with a U.S. Weather Bureau six-channel spectrometer. For all spectral intervals except that centered on $\nu = 669$ cm^{-1}, the transmission functions of carbon dioxide were computed from a random-superposition model of Elsasser bands, using the Curtis-Godson method to account for the inhomogeneity of the real atmosphere. The transmission functions were compared with laboratory transmission measurements to check the accuracy of the calculated results. The transmission function for the segment at $\nu = 669$ cm^{-1} was obtained through special laboratory experiments with the same 5-cm^{-1} spectral resolution. The water vapor transmission functions were calculated using the random model (to describe the absorption due to the spectral lines of water vapor) and experimental values of the absorption coefficients to account for continuum absorption. Data from radiosonde measurements of temperature and humidity distribution were also used to obtain the real-atmosphere transmission functions. The authors of [98] report that for reconstruction under real conditions, it is necessary to use averaged temperature profiles and successive approximations to take account of the temperature variation of the transmission functions and to have independent indirect estimates of the atmospheric water vapor distribution. /334

An empirical orthogonal basis constructed from radio sounding data for neighboring stations and corresponding times of year was used in reconstructing the temperature profile. Five empirical orthogonal functions were used to reduce data obtained at Palestine, Texas and six for measurements at Six Falls. Figures 5.39 and 5.40 show examples of temperature-profile reconstruction together with temperature data from radiosondes. (It should be noted that the results of direct temperature measurements pertain to adjacent radio sounding stations.) The reconstructed temperature profile for the measurement at Palestine differs

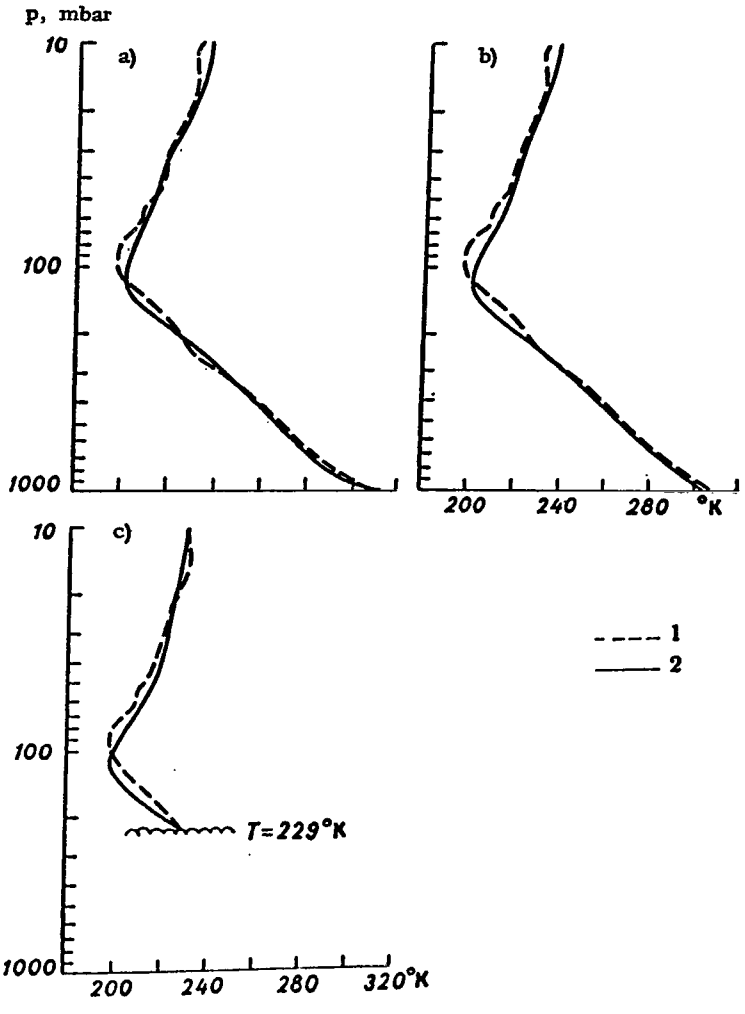

Figure 5.39. Reconstruction of Temperature Profile. Palestine, Texas. a, b) Clear sky; c) solid cloud cover; 1) radiosonde data; 2) reconstructed profile.

appreciably from the true profile around the tropopause. After analyzing a number of possible causes for these deviations from true distribution, the authors of [98] concluded that the errors resulted from use of the empirically orthogonal basis. It was found that the situation observed during the radiation measurements at Palestine was noncharacteristic with respect to the set of temperature distributions used in constructing this basis, so that it was practically impossible to obtain an accurate solution with this basis. In this context, the authors of [98] draw attention to the importance of careful construction of the empirical orthogonal basis. On the other hand, this suggests the possibility of major reconstruction errors resulting from the use of a priori statistical information that is inadequate to the /335

realization under study (pertains to another time of year, another location, or different cloudage conditions). Thus, the results of the analysis given in [98] do not agree with M.S. Malkevich's conclusion [11] to the effect that the "poor" orthogonal basis that he obtained by analysis of numerical-experiment results could be used in temperature reconstructions.

Figure 5.39b presents an example of temperature-profile reconstruction for solid-overcast conditions. In this case, the authors of [98] solved the integral equation

$$g(\nu_l) = \frac{J(\nu_l) - \beta(\nu_l)}{\alpha(\nu_l)} + \int_1^{P(\nu_l, t_c)} B(\nu_r, t)\, dP(\nu_l, t) -$$

$$- B(\nu_r, t) P(\nu_l, t_c) = \sum_{j=1}^{N} c_j \int_1^{P(\nu_l, t_c)} \Phi_j(t)\, dP(\nu_l, t),$$

where $t = \log p$ and t_c is the level of the clouds.

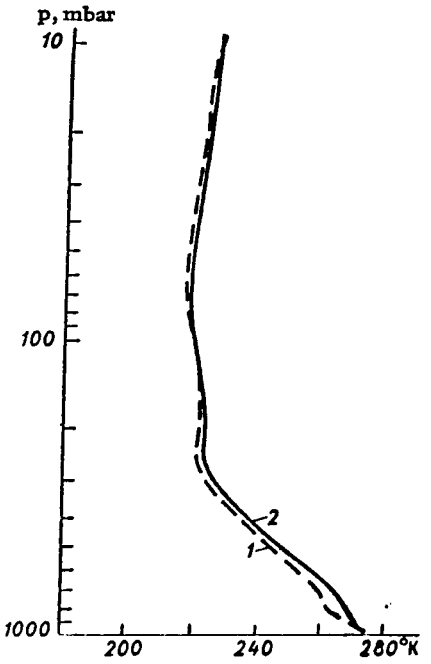

/336

Figure 5.40. Example of Temperature-Profile Reconstruction. Six Falls, (USA). 1) Radiosonde data; 2) reconstructed profile.

Since t_c, and, consequently, the cloud-top pressure p_c are unknown, the iterative solution method was used. The first estimate for p_c was used to find the temperature distribution T'(p). Then, using this profile and independent cloud top temperature measurements made in the transparency window, the pressure at cloud-top level was improved and the solution of the inverse problem repeated.

The measured radiation data for the case of Palestine, Texas were also reduced by Yu.M. Timofeyev and O.M. Pokrovskiy [95]. They used no a priori statistical information on the unknown profile. The problem was solved with five radiation values in the 669, 677.5, 691, 697, and 703 cm^{-1} channels, which belong to the 15-μm CO_2 band, and radiation in the transparency window ($\nu \approx 899$ cm^{-1}) to determine underlying-surface temperature. The regularization method was used in reducing the data, and the quasioptimum approximation was selected on the basis of Criterion (5.40). The value of B at the radiation-measurement level was also used in reconstructing the temperature profile to assign a boundary condition at the profile upper limit. Figure 5.41 presents curves that characterize the temperature-profile reconstruction error. It is

/337

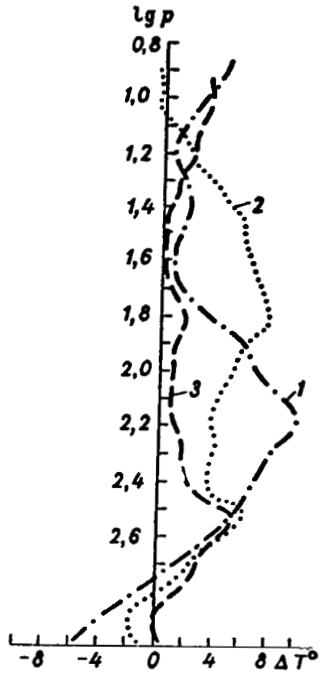

Figure 5.41. Accuracy of Temperature Profile Reconstruction by Regularization Method, $\Delta T = T_{rad} - T_{recon}$. 1) Data of [98]; 2) reconstruction by regularization method; 3) reconstruction from corrected radiation values.

a plot of the deviations of the solutions from radiosonde data: $\Delta T = T_{rad} - T_{recon}$. As we see from the figure, the error is approximately the same for both methods when it is averaged over the entire range of reconstruction. Curve 2 is somewhat closer to the true profile in the range from 1000 to 100 mbar, and slightly farther from it at $p < 100$ mbar.

The accidental errors of the experiment used to determine the temperature profile were about 2%. It was found on theoretical calculation of the outgoing-radiation values from the known temperature profile and known transmission functions that the measured values differ from the calculated results by 6-10%. Naturally, such a substantial disagreement cannot be accounted for entirely by accidental experimental errors. Moreover, it was found that the disagreement between theory and experiment is systematic in nature. It may be due either to errors in assigning the transmission functions or systematic errors in the measurements, for example, errors in the absolute calibration of the spectrometer. (In addition, certain errors may arise as a result of numerical integration in the theoretical calculations.) If we assume that systematic errors were incurred in the measurements and correct the radiation values, for example by reducing all values by a constant 4 $erg/cm^2 \cdot sec \cdot sr \cdot cm^{-1}$, we obtain a substantial improvement in the accuracy of reconstruction (the maximum error becomes 5° instead of ∿8°; curve 3 in Fig. 5.41). In a certain sense, this improvement is, of course, fudged, since it can be obtained only if the systematic error is known, which is usually not the case. /338

A Michelson interferometer was also used to measure the outgoing thermal radiation on a high-altitude aerostat in a broad frequency range. These measurements, which were conducted in the range from 5 to 20 μm with an absolute error of the order of 0.5 $erg/cm^2 \cdot sec \cdot sr \cdot cm^{-1}$ [51], contained, in principle, information on the atmosphere's thermal profile and on the altitude distributions of water vapor and ozone. These measured data were used to solve

the thermal sounding problem by various methods in several of the studies to be discussed below.

Figure 5.42, which we have borrowed from [2.47], examines an example of temperature-profile reconstruction based on interpretation of radiation data measured in the 15-μm CO_2 band [51]. An iterative solution method was used in inverting [sic; reducing] the data. The zeroth approximation of the solution was the monthly average temperature profile. As we see from the figure, the reconstruction errors do not exceed 4°. The largest errors are observed in the tropopause region.

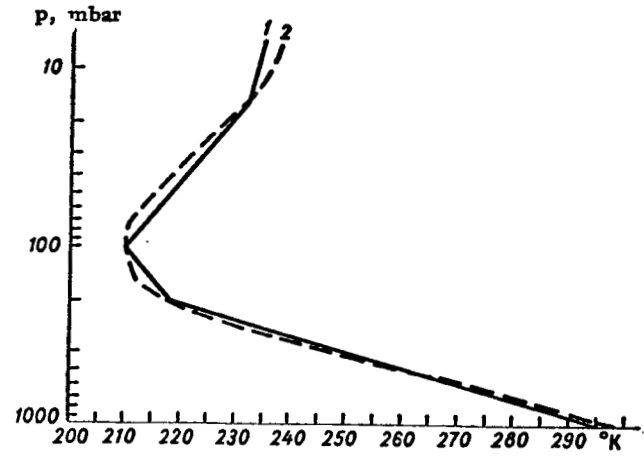

Figure 5.42. Example of Temperature-Profile Reconstruction. 1) Reconstructed profile; 2) radio sounding data.

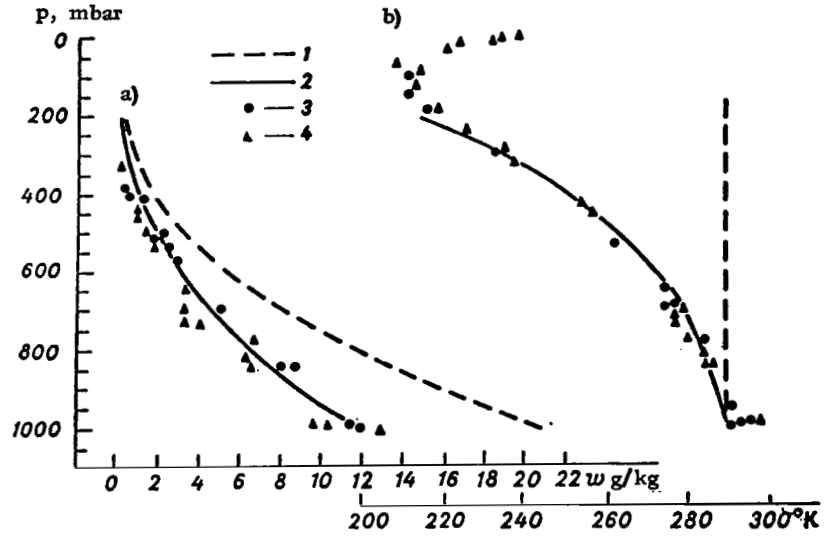

Figure 5.43. Reconstruction of Humidity (a) and Temperature (b) Profiles in the Troposphere. Palestine, Texas, June 1968. 1) Zeroth approximation; 2) reconstructed profiles; 3, 4) data from direct measurements.

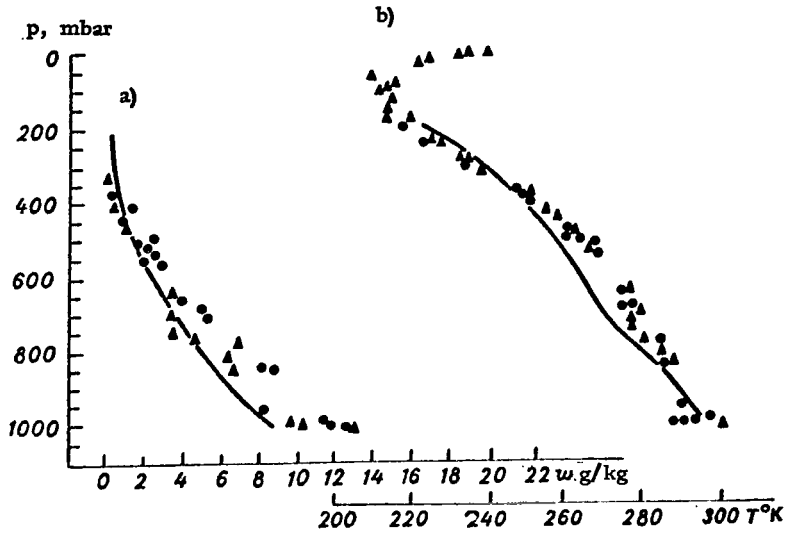

Figure 5.44. Reconstruction of Humidity (a) and Temperature (b) Profiles in the Troposphere. For Legend see Fig. 5.43.

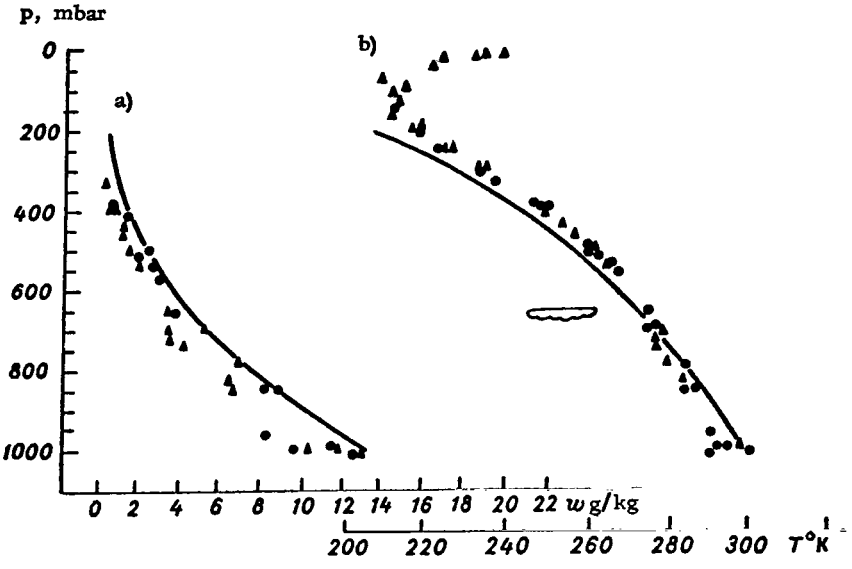

Figure 5.45. Reconstruction of Humidity (a) and Temperature (b) Profiles in the Troposphere from Observations Under Partly Cloudy Conditions. For legend see Fig. 5.43.

W. Smith [69, 70] also used Michelson-interferometer outgoing-radiation measurements to solve the thermal-sounding problem. The interpretation method proposed by Smith (which we discussed in §4 of the present chapter) provides for radiation measurements in the

spectral intervals 825-975, 740-780, 730-770, and 717.5-757.5 cm^{-1}. These data were obtained by summing over the corresponding radiation values obtained with higher spectral resolution, using the relation

$$J(\Delta\nu_i) = \frac{\int_{\Delta\nu_i} \varphi_i(\nu) J(\nu)\, d\nu}{\int_{\Delta\nu_i} \varphi_i(\nu)\, d\nu}, \quad i = 1, 2, \ldots,$$

where $\phi_i(\nu)$ is the instrumental function of the measuring device, for which the expression

$$\varphi_i(\nu) = \cos^2\left[\frac{\pi(\nu - \bar{\nu}_i)}{\Delta\nu}\right]$$

was used.

Figures 5.43-5.45 show examples of temperature-profile reconstruction by the Smith method. Figure 5.43 shows a profile reconstruction based on radiation values averaged over three measurements. The solution was obtained for a smoothing-parameter value of 10^{-7}. Five iterations were used to obtain the profile shown in Fig. 5.43. (The curves on the left in Figs. 5.43-5.45 pertain to the tropospheric humidity profile and will be analyzed in the next chapter.) Figure 5.44 shows an example of a less successful reconstruction for different experimental conditions. The substantial deviations of the resulting temperature profile from the radiosonde data in Fig. 5.44 were due, in Smith's opinion, to large errors observed at the time of measurement.

W. Smith used radiation data measured under partly cloudy conditions to check his proposed method for interpretation of measurements made under cloudy-atmosphere conditions (see §6 of this chapter). Measurements made at times at which there were varying amounts of clouds in the instrument's field were used for this purpose. Figure 5.45 shows an example of temperature-profile reconstruction under partly cloudy conditions by Smith's method. The reconstruction was based on measurements corresponding to three instrument readings. The value of N* obtained from analysis of cloud-cover photographs was 0.363. It was quite close to the figure (0.386) obtained from radiation in the transparency window /341 (see §6 of this chapter). W. Smith considers that the tropospheric temperature profile could be reconstructed even more accurately with improved measurement accuracy and the use of a considerably larger number of frames.

To illustrate application of the direct method described in the preceding section, we present Fig. 5.46, which shows the results of reduction of real data obtained from measurements under cloudy-atmosphere conditions (September 1964, Texas, USA). The errors become quite large even in the case of reconstruction of

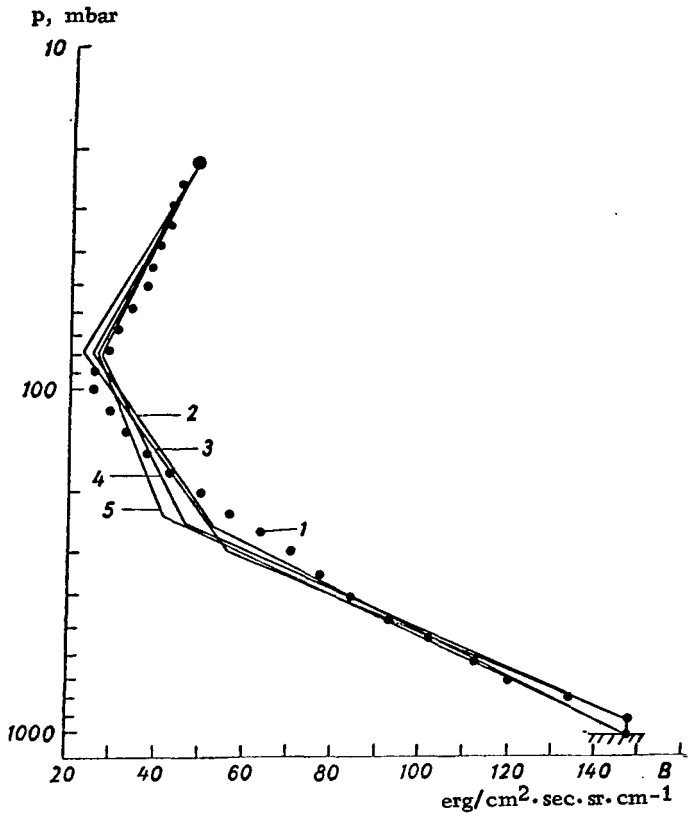

Figure 5.46. Reconstruction of Planck Function by Direct Interpretation Method. 1) Radio sounding data; 2) reconstruction from theoretical radiation values; 3) from measurements under cloudless conditions; 4, 5) from measurements in the presence of broken clouds.

the B(p) profile from exact theoretical radiation data for the cloudless atmosphere (curve 1): -4° at p = 260 mbar and 5° at p = = 100 mbar. Curve 2 also pertains to cloudless conditions, but was obtained by reducing real measurements. The reconstruction errors are substantially larger for interpretation of observations made in the presence of clouds (curves 3, 4).

V.F. Turchin, M.S. Malkevich, and I.A. Gorchakova [99] processed aerostat measurements by the statistical-regularization method. The problem was inverted by two schemes: scheme A_1, in which theoretical radiation values obtained by calculation were used in the inversion, and scheme A_2, in which the inversion was performed with real measured data. This enabled the authors of [99] to make a careful analysis of error sources in temperature-profile reconstruction. Reconstruction-accuracy characteristics /342

TABLE 5.10. ERRORS $\sigma_T = T_c - T_{true}$ IN °C RESULTING FROM ACTUAL ERRORS OF INITIAL DATA

p, mbar	σ_j, °C	Palestine, 7h 57m		Palestine, 15h 02m		Six Falls, 12h 02m		Palestine, 8h 30m		Palestine, 13h 30m
		A_1	A_2	A_1	A_2	A_1	A_2	A_1	A_2	A_2
1000	0,1	0,6	—14,5	0,3	1,3	0,2	—1,3	0	1,3	—0,8
900	1,7	5,2	—5,6	3,2	3,7	1,8	3,5	0,7	0,8	—5,9
850	1,7	4,8	—4	3	3,2	2,4	4,9	1,1	—0,7	—5,2
800	1,8	5,1	—2	3,5	3,4	4,4	7,7	0,2	—2,3	5,4
700	1,3	4,3	0,1	2,4	2,2	3,1	5,7	—0,9	—4,3	—4,5
600	1,1	0,5	—1,3	1,0	0,7	2,0	5,4	—2,8	—6,8	—5,5
500	1,0	—0,5	—1,9	—0,2	—1,0	1,2	6,7	1,7	—1,9	—1,4
400	1,0	—0,7	—2,6	—1,8	—2,9	—1,4	5,3	4,5	—2,3	—2,8
300	1,1	—0,3	—5,7	2,0	—0,5	—4,6	1,1	1,1	0,3	0,9
250	2,6	—1,6	—6,3	—1,7	—5,4	—2,6	—0,6	1,6	2,6	7,8
200	1,9	1,3	2,9	—0,4	—0,2	2,9	5,3	—2,2	4,3	—1,0
150	1,3	—4,4	—0,8	—4,2	—3,4	1,0	1,9	0,1	4,5	—0,5
100	1,1	4	7,8	5,6	7,2	—0,2	—0,3	2,6	5,4	1
50	1,2	2,4	3,1	2	2,6	—0,1	0,5	2,8	4,3	2,1
10	0,7	—3	—6,1	—2,4	—2,1	0,3	—2,6	—7,2	—8,6	—4,5

can be obtained for several cases of measurements by analysis of Table 5.10, which presents the reconstruction errors for solution of the problem by schemes A_1 and A_2. As we see from the table, the values of the theoretical root-mean-square error σ_j of the method used do not exceed 3°, but the errors of inverting the problem by scheme A_1 and especially by scheme A_2 are substantially larger in certain specific cases.

Comparison of the theoretical and experimental radiation values showed that the actual errors in the initial data exceed 1% in most cases. This accounts for the several cases of considerable errors in the reconstruction of T from real measured data and substantial disagreements between results calculated by schemes A_1 and A_2.

The maximum differences between the true deviations of T' from the mean profile $\overline{T}$ and the reconstructed values, which are observed at the earth's surface (Table 5.10, columns 3 and 4), are due, in the opinion of the authors of [99], to the fact that the problem was inverted by scheme A_2 for morning radiation measurements, while the noon temperature profile was taken for comparison. On this basis, they conclude that the thermal-sounding /343 method can be used to obtain the diurnal temperature variation, at least in the boundary layer of the atmosphere, where the time variations of T are quite wide.

The studies made in [99] indicated that when the statistical-regularization method is used, increasing the number of spectral intervals used from 9 to 45 has practically no effect on the reconstructed function (with a measurement error of 1%). The solution

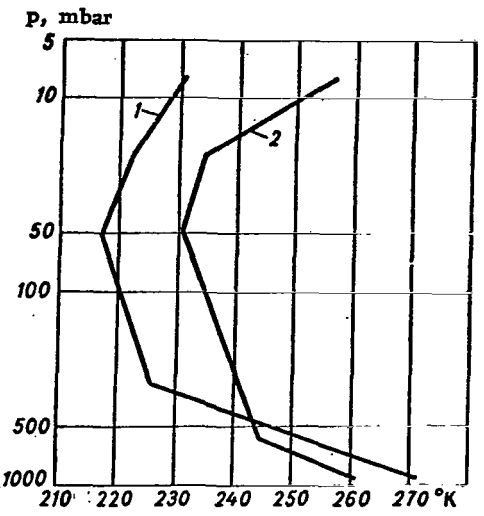

Figure 5.47. Example of Temperature-Profile Reconstruction Using Measurements in the CO_2 Band at $\lambda = 4.3$ μm. 1) Radio sounding data; 2) reconstructed profile.

becomes unstable for low error levels when many intervals are used.

Figure 5.47 shows an example in which the thermal-sounding problem is solved with outgoing-radiation measurements at a height of ∿30 km in the CO_2 band at $\lambda = 4.5$ μm [100]. The large reconstruction errors (25° at p = 8 mbar, 10° near the ground) are due basically to substantial measurement errors. (According to rough estimates made in [100], the errors ranged from 20 to 300% in the various spectral intervals.)

The above examples in which the thermal-sounding problem is solved by interpretation of real measured data indicate, on the one hand, the practical possibility of acquiring information on the thermal structure by this method and, on the other, the need for improvement of the method to obtain the temperature profile with higher accuracy. In the cases that we have considered, the basic sources of reconstruction errors were relatively large errors of measurement and of assignment of integral-equation kernels. In certain cases, reconstruction accuracy is adversely influenced by the interpretation methods. All of this indicates that attainment of the desired temperature-determining accuracy will require further effort, both theoretical and experimental. /344

§8. EXAMPLES OF INTERPRETATION OF SATELLITE MEASUREMENTS

Let us briefly examine the results from the first satellite experiments in thermal sounding of the atmosphere. The Nimbus III weather satellite, which carried several instruments designed for solution of this problem, was launched on 14 April 1969. Preliminary results of interpretation of outgoing thermal radiation measurements made in the 15-μm carbon dioxide band were published in [102, 103].

D. Hilleary and D. Wark's paper [102] is devoted to reduction of measurements made with the satellite infrared spectrometer (SIRS) (see Chapter 2). Table 5.11 presents data that characterize the positions and widths of the spectral intervals and the radiation values measured in these intervals with the SIRS. It is reported in [102] that an absolute measurement error of /345

TABLE 5.11. CHARACTERISTICS OF SIRS AND MEASURED RADIATION VALUES

Channel No.	Position of spectra interval		Width of spectra interval		J, erg/cm^2·sec·sr·cm^{-1} (see Fig. 5.48)				
	cm^{-1}	μm	cm^{-1}	μm	a	b	c	d	e
1	899,3	11,12	5,353	0,0662	111,26	107,90	58,20	74,92	48,58
2	750,0	13,33	5,988	0,1065	105,60	99,69	69,31	83,66	62,56
3	714,3	14,00	5,357	0,1050	74,40	68,25	59,26	63,30	55,44
4	706,3	14,16	5,221	0,1047	58,94	53,91	52,23	52,79	51,29
5	699,3	14,30	5,102	0,1043	46,33	45,09	47,01	45,73	50,00
6	692,3	14,44	4,986	0,1040	40,96	42,73	46,78	44,85	50,83
7	677,8	14,75	4,748	0,1033	53,16	46,64	48,94	47,10	52,17
8	669,3	14,94	4,604	0,1028	55,34	57,50	58,97	56,02	58,34

±2 ergs/cm^2·sec·sr·cm^{-1} was attained in the measurements, and that the relative errors of simultaneous measurements made in different spectral intervals ranged around 0.5 erg/cm^2·sec·sr·cm^{-1}. A special program of checkouts and tests was run during the first two weeks of the instrument's operation. Special radiosonde launchings were arranged, both from the continental USA and from the western Pacific Ocean. This permitted careful comparisons of the reconstructed profiles with data from direct temperature measurements.

Figure 5.48 presents examples in which the temperature profiles obtained from indirect measurements from the satellite and direct radiosonde measurements are compared. Our attention is drawn first of all to the proximity of the temperature profiles obtained by the two methods (the largest differences between T_{recon} and T_{rad} are ∿6%, and the mean errors are considerably smaller). The most important differences between the profiles are observed in the middle troposphere, where the indirect measurements indicate higher temperatures. As D. Hilleary and D. Wark point out, the most probable cause of this effect may be transmission-function errors. It is suggested that the real transmission values are 3% lower than those used in solving the inverse problem. This fact indicates once again (see §5 of this chapter) the importance of accurate assignment of the integral-equation kernel.

Figure 5.48b presents an example of reconstruction of T from radiation measurements in which there were many high clouds in the instrument's field. Despite this, the profiles agree closely, and this moves D. Hilleary and D. Wark to the conclusion that such high clouds have little influence on the outgoing radiation in the thermal-sounding channels and, consequently, on the solution of the inverse problem. The reconstructed temperature profile shown in Fig. 5.48c pertains to observations made with solid cloud cover. From the 640-mbar level to the ground, the

/346

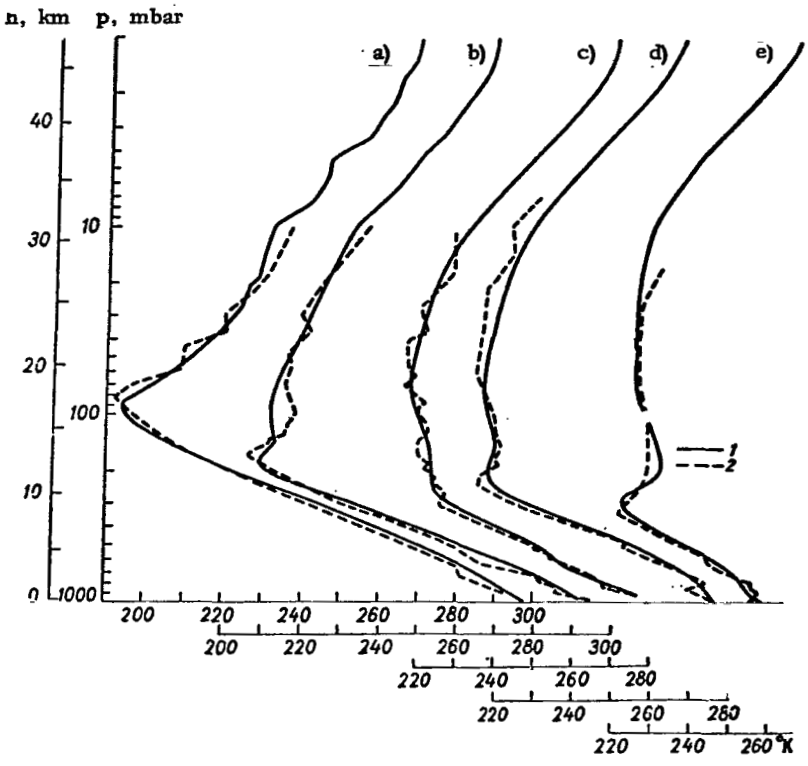

Figure 5.48. Examples of Temperature-Profile Reconstruction on the Basis of Satellite Radiation Measurements. a) 14 April 1969, Kingston, Jamaica; b) 25 April 1969, Omaha, Nebraska; c) 27 April 1969, North Platte, Nebraska; d) 19 April 1969, Green Bay, Wisconsin; e) 18 April 1969, Resolute, northwestern Canada; 1) reconstructed profiles; 2) radio sounding data.

temperatures were obtained by interpolation between the satellite data and the known surface-temperature value. Figure 5.48, d and e, presents other T-reconstruction examples.

D. Hilleary and D. Wark note that the SIRS sounding results /347
do not conform to meteorological requirements in 20% of cases. But even this relatively small percentage may be reduced further by improvements to the instrument and the data-reduction method. The authors of [102] indicate advantages of satellite temperature-profile determination: the use of one instrument to acquire global temperature-field information, thus eliminating the errors that arise when this function is performed by instruments that differ in working principle, reliability, calibration, and manufacture; the absence of the radiation effects to which radiosondes are subject, especially in the stratosphere. It is stressed in [102]

that the success of the experiment was due primarily to the high quality of the instrument and was the outcome of intense effort spanning the preceding decade.

The Nimbus III also carried a Michelson interferometer (see Chapter 2), which was used to measure the outgoing radiation in the range from 5 to 25 μm (2000-400 cm^{-1}). The instrument had a spectral resolution of 5 cm^{-1}, and the accidental error of the measurements was 0.5-1.0 $erg/cm^2 \cdot sec \cdot sr \cdot cm^{-1}$. The paper by R. Hanel and B. Conrath [103] presents preliminary results from interpretation of these measurements. The temperature profile was reconstructed by M.T. Chahine's method (see §4 of this chapter). An example in which the reconstructed temperature profile is compared with radio sounding data appears in Fig. 5.49.

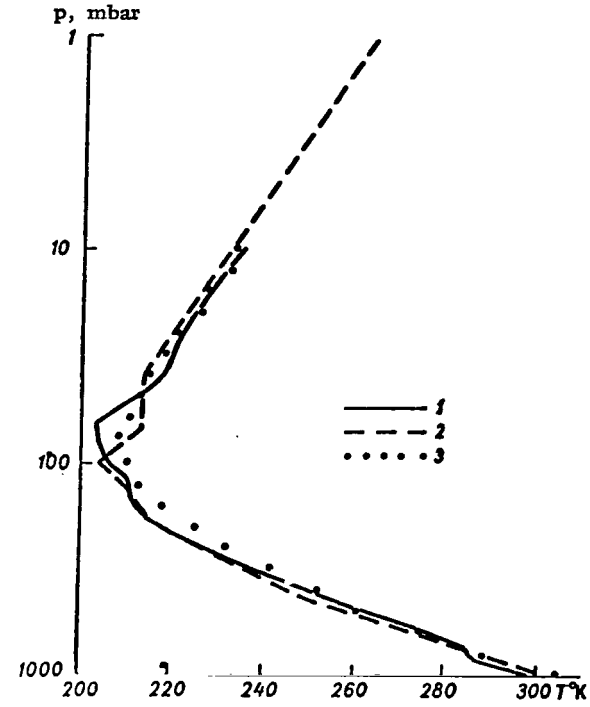

Figure 5.49. Example of Temperature-Profile Reconstruction Based on Satellite Radiation Measurements. 1) Reconstructed profile [103]; 2) radio sounding data; 3) reconstruction by regularization method.

We note the proximity of the direct and indirect temperature measurements, but, at the same time, substantial discrepancies (up to 10°) between them in the region around 100 mbar. R. Hanel and B. Conrath note that future plans call for improvement of the spectral (to 3 cm^{-1}) and spatial resolutions of the instrument, lowering of the measurement errors, and a change in the range of measurement (6.25-50 μm).

The same measured radiation data were reduced by O.M. Pokrovskiy and Yu.M. Timofeyev's regularization method. The largest temperature-reconstruction errors were ∿8° (Fig. 5.49).

§9. CERTAIN PROBLEMS IN ROUTINE PROCESSING OF RADIATION DATA

Weather satellites equipped with special instruments for solution of the thermal-sounding problem enable us to acquire global data on the atmospheric temperature field. Since radiation is the quantity directly measured, it is necessary to use the various interpretation methods described above to obtain the temperature field. Naturally, because of the massive numbers of

measurements concerned, the data must be processed on electronic computers (EC's) by programs specifically designed for operational reduction of the radiation data. The specific scheme used for such processing will depend to a major degree on the algorithm used to invert the problem.

Various special instruments for acquisition of the radiation measurements needed for the particular interpretation method have now been built or are in preparation. As yet, practically no comparisons have been drawn between the various methods; nor have the fields of their optimum application been investigated. Obviously, such investigations permit an approach to the development of effective methods for interpretation of radiation data and will /349 make possible a more rigorous solution to the problem of optimum measurement conditions. Here, of course, it must be remembered that the multitude of interpretation methods and experimental approaches to the thermal-sounding problem also results from a number of objective causes: the complexity of the problem, the possibility of using various methods in its solution, the varying requirements made of the unknown characteristic (for example, of the range of reconstruction), the use of varying a priori information, etc.

For example, attention should be drawn to the fact that in the methods that use large amounts of a priori information in one form or another (Kozlov, Smith), radiation measurements in rather broad spectral intervals are acceptable, while a number of other methods require rather high spectral resolution. This problem requires further careful study. The immediate future will hardly see the development of a universal interpretation method and the system of measurements corresponding to it that will meet the entire variety of requirements made as to knowledge of the temperature distribution in various problems. On the other hand, the variety of methods presently in existence is such as to raise the important question of studying and comparing them with the purpose of determining their actual possibilities, disadvantages, and advantages. Research on the combined use of various bands of the spectrum for thermal sounding is also necessary.

Numerical experiments to reconstruct the temperature profile are among the methods of comparative analysis of the various interpretation methods. Let us cite certain results obtained in this trend by O.S. Bogomolov [87]. He examined the following methods of determining the atmospheric temperature distribution:

a) a statistical method based on use of correlation links between the radiations in various spectral intervals and the temperature values at various levels;

b) the optimum-approximation method;

d) the method using A.N. Tikhonov's regularization algorithm.

The statistical method made use of the regression equation

$$T_i = \overline{T}_i + r\frac{\sigma_{T_i}}{\sigma_{T_j}}(T_j^* - \overline{T}_j^*)$$

to find the temperature distribution; here T_i is the unknown and $\overline{T}_i$ is the average temperature at the ith level, r is the coefficient of correlation between the radiation temperature in the jth spectral interval and the actual temperature at the ith level, $\overline{T}_{j*}$ and $\overline{T}_{j*}$ are the measured temperature and the radiation temperature corresponding to the mean temperature profile in the jth spectral interval, and σ_{T_i} and σ_{T_j} are the corresponding root-mean-square deviations. /350

TABLE 5.12. ACCURACY CHARACTERISTICS OF STATISTICAL TEMPERATURE-DETERMINATION METHOD

Error, °C	p, mbar						
	1000	850	700	500	400	300	200
σ	1,5	2,5	2,3	2,0	2,5	2,9	3,6
$\|\Delta\|_{max}$	4,2	7,1	5,2	4,5	7,6	8,3	9,0

Table 5.12 presents accuracy (error) characteristics of the statistical temperature-determining method: σ is the root-mean-square deviation of the temperature from the exact values, and $|\Delta|_{max}$ is the maximum reconstruction error. We note that the numerical experiment was performed on the assumption of absolutely accurate radiation measurements. The presence of measurement errors will no doubt increase the reconstruction errors substantially.

The optimum-approximation method yielded higher reconstruction accuracies. For example, in most cases (30 different vertical temperature profiles were considered), the root-mean-square error of temperature reconstruction in the 1000-100-mbar layer amounted to 1.7°C over all of the cases considered, and the maximum errors were observed around the tropopause, amounting to 4-5° in occasional cases. A considerable increase in the reconstruction errors was observed for complex temperature profiles (with an inversion or isothermy in the lower layers of the atmosphere).

The regularization method enabled O.S. Bogomolov to obtain an average reproduction error of about 1° over all cases; it varied from 0.1 to 1.8°. The largest errors incurred in use of

this interpretation method came to 2-3° near the tropopause or at the upper limit of the layer under consideration. Thus, O.S. Bogomolov's analysis indicates certain advantages of the interpretation method based on the regularization algorithm. However, it must be stressed that this conclusion pertains to absolutely accurate radiation measurements. On the other hand, O.S. Bogomolov [87] notes that the reconstruction of relatively simple, nearly linear temperature profiles proceeds in practically the same way with either the regularization or the optimum-approximation method. In the case of more complex temperature distributions, the regularization method has certain advantages. /351

Certain indirect comparisons can be made between interpretation methods with reference to the results of reduction of the same experimental data. However, such comparisons are rendered somewhat difficult by the fact that most authors do not give careful error analyses for their temperature-profile reconstructions. The results of inverse-problem solution using the two methods are given in Fig. 5.41 (for details, see page 301). On the average, both methods give about the same reconstruction errors. The maximum reconstruction error is slightly smaller when the regularization method is used.

We may conclude that the above example did not award the advantage to either approach to solution of the problem. M.S. Malkevich [94] arrives at approximately the same conclusion from a comparison of interpretations of real measured data by the optimum-approximation method and a method proposed by Hilleary, D. Wark, and D. James [2.44].

Comparison of the results obtained by the nonlinear method in interpreting real radiation data [11] in the case of a simple exponential kernel with results obtained by other methods does not come out in favor of the nonlinear method. The principal error source is the use of an inaccurate approximation for the integral-equation kernel. Use of a more general method [9] improves the reconstruction results markedly. As we have already noted, the results of using data obtained by the Chahine method (see §4) and the regularization method for reduction are quite similar, although a somewhat smaller maximum reconstruction error is observed in this case when the latter method is used.

The isolated examples of comparison between various interpretation methods that were given above do not, of course, permit clear inferences as to the advantages and disadvantages of the approaches considered. More thorough research is necessary in this direction. The specific scheme used for routine data processing will depend to a major degree on solution of this problem. Even now, however, we can indicate a number of features that should be inherent to this system.

1. The solution methods used in the routine system must carry insignificant errors in the algorithm itself.

2. The numerical interpretation methods must be stable to the various errors of measurement and assignment of the equation kernel.

3. The interpretation method must work effectively for both cloudy and cloudless atmospheres. Naturally, additional information may be required here.

4. The system must permit adequate flexibility in the use of various kinds of supplementary information on the unknown profile. It must be remembered that the thermal sounding method itself will yield an enormous quantity of information on the thermal situation of the atmosphere and that this information can be used in subsequent work.

5. The scheme must contain a block in which the equation kernels are corrected to permit use of successive-approximation methods. Effective performance of this block requires independent determinations of the atmospheric distribution of water vapor (or other absorbing gases).

Further expanded research is necessary in regard to many of the points enumerated above.

Chapter 6

/353

RECONSTRUCTION OF ATMOSPHERIC HUMIDITY DISTRIBUTION

The present chapter is devoted to a brief discussion of the possibilities for indirect determination of the humidity distribution in the atmosphere. We shall examine only a single method based on an interpretation of outgoing thermal radiation data.

§1. GENERAL CHARACTERISTICS OF THE PROBLEM. PROPERTIES OF WATER VAPOR ABSORPTION

Solution of the problem of thermal sounding of the atmosphere will make it possible in principle to solve other inverse problems, e.g., those of reconstructing the distributions of absorbing constituents in the atmosphere. At present, the possibilities for determination of the atmosphere's humidity characteristics have been most thoroughly investigated. This has been due both to the fundamental role of water vapor in various physical processes that unfold in the atmosphere and to the need to know this characteristic for accurate solution of the thermal-sounding problem. The possibilities of acquiring such important information as the spatial distribution characteristics of ozone from outgoing thermal radiation data have also been studied.

As we showed in the preceding chapter, combined absorption by water vapor and CO_2 or O_2 is observed in a number of the spectral intervals used in solution of the thermal-sounding problem. In this case, the temperature profile can be reconstructed accurately only with independent determinations of the atmosphere's water-vapor concentration. The notion that it was necessary to solve a set of inverse problems was first advanced by L. Kaplan [5.26]. He proposed that the humidity distribution be found after determination of the temperature profile without considering the effect of water vapor and used in turn to obtain a more accurate solution of the thermal-sounding problem. This process can be continued until the results obtained in successive steps become practically equivalent.

/354

Formally, if we know the temperature distribution in the atmosphere, the problem of reconstructing its composition characteristics reduces to solution of a Fredholm nonlinear integral equation of the first kind. For example, we can write for the outgoing radiation at level p_1

$$J(\nu, p_1) = \int_{p_0}^{p_1} B_\nu [T(p)] \frac{\partial P[\nu, p_1, q(p)]}{\partial p} dp +$$

$$+ B_\nu [T(p_0)] P[\nu, p_0, q(p)]. \qquad (6.1)$$

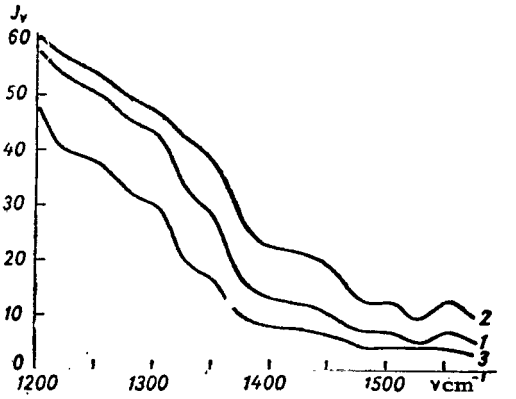

Figure 6.1. Spectral Curves of Outgoing Radiation J_ν, erg/cm·sec·sr·cm^{-1}, in Absorption Band at λ = 6.3 μm for Various Water-Vapor Distributions in the Atmosphere. 1) Ordinary summer temperature and humidity profiles $q_1(p)$; 2) $q_2(p) = 10^{-1}q_1(p)$; 3) $q_3(p) = 10q_1(p)$. /355

In measurements of radiation in the water vapor absorption bands with a known T(p), the measured radiation data will carry information on the distribution q(p) in the atmosphere. By solving the direct problem — calculating the intensities of the ascending or outgoing radiation in the H_2O bands —, we can study the sensitivity of the radiation characteristics due to variations in the distribution q(p) and hence the possibilities for solution of the inverse problem. Figure 6.1 presents a simple example of such calculations. It gives spectral curves of the outgoing radiation (z ≈ 30 km) in the absorption band at λ = = 6.3 μm for various distributions of water vapor in the atmosphere. Curve 1 corresponds to the normal summer temperature and humidity profiles, while curves 2 and 3 were obtained after changing the specific humidity of the atmosphere by one order of magnitude, i.e., $q_2(p) = 10^{-1}q_1(p)$ and $q_3(p) = 10q_1(p)$. As we see from the figure, the variations of the radiation are quite substantial. In this method of estimating the sensitivity of radiation to humidity-characteristic variations, it is, of course, necessary to take account of the real range of humidity variations in the atmosphere. For example, it is shown in [1] that $\delta_q/\bar{q}$ (where δ_q is the variance and $\bar{q}$ is the mean humidity profile), which characterizes the relative variability of specific humidity, may reach 50-90%.

The solution of this inverse problem has a number of noteworthy properties. For convenience in analysis, let us rewrite (6.1) in the following form (integrating (6.1) by parts):

$$J(\nu, p_1) = B_\nu [T(p_1)] - \int_{p_0}^{p_1} \frac{\partial B_\nu [T(p)]}{\partial p} P[\nu, p, q(p)] dp. \qquad (6.2)$$

In approximation, the variability of the radiation as a function of variations in atmospheric composition can be written

$$\delta J(\nu, p_1) = \int_{p_0}^{p_1} \frac{\partial B_\nu [T(p)]}{\partial p} \times \int_{p'}^{p_1} \frac{\delta P [p, p', \nu, q(p)]}{\delta q(p')} \Big|_{q = q(p')} \delta q(p') \, dp' \, dp, \qquad (6.3)$$

where $\frac{\delta P [p, p', \nu, q(p)]}{\delta q(p)}$ is the variational derivative of the functional P, whose explicit form is not important in our case.

Relation (6.3) links the radiation variations δJ to those of the distribution of the absorbing substance. First of all, we draw attention to the fact that for $dB_\nu/dp \equiv 0$, i.e., under isothermal-atmosphere conditions, $\delta J \equiv 0$ for all $\delta q(p)$. Under isothermal-atmosphere conditions, therefore, the radiant intensity does not depend on the distribution of the absorbing substance. This means, of course, that we cannot speak of the possibility of determining q(p) under such distribution conditions either. It is clear from this that determination of the distributions of absorbing constituents in the atmosphere from thermal-radiation spectra will depend to a major degree on the thermal state of the gaseous medium. It is understandable from the physical viewpoint that strong thermal inhomogeneity of the atmosphere will help solve this inverse problem. On the other hand, it is evident from (6.3) that the radiation variations are related to those of moisture content distribution by a rather complex relationship and — a particularly important point — the function $\delta q(p)$ is smoothed twice. Reconstruction of the atmospheric humidity distribution on the basis of (6.3) encounters major difficulties because of the complexity of the relationship itself and the cumbersome explicit expressions for the variational derivatives $\delta P/\delta q$ even in relatively simple cases. It is therefore necessary to simplify the problem substantially. All existing methods for determining the humidity distribution from outgoing-radiation spectra are based on approximate substitution of the real inhomogeneous atmosphere's transmission functions by those of a homogeneous atmosphere. The reduced-mass method (see Chapter 1, §4) is normally used here. In this formulation, the unknown function is the distribution of the reduced mass of the absorbing constituent in the atmosphere. /356

Naturally, the radiation characteristics will be found most sensitive to water-vapor variations in the atmosphere in the H_2O absorption bands. Water vapor has a great many absorption bands scattered over the entire infrared region of the spectrum. However, from the standpoint of our problem, the absorption bands at $\lambda = 6.3$ μm and the rotational band that extends from $\lambda \approx 10$ μm to radio wavelengths will attract special attention. The strong vibrational-rotational band corresponding to the fundamental ν_2 vibration lies in the region of $\lambda = 6.3$ μm. This band has been studied experimentally in [2, 3, 6, 7]. Theoretical transmission calculations and empirical methods for calculating transmission

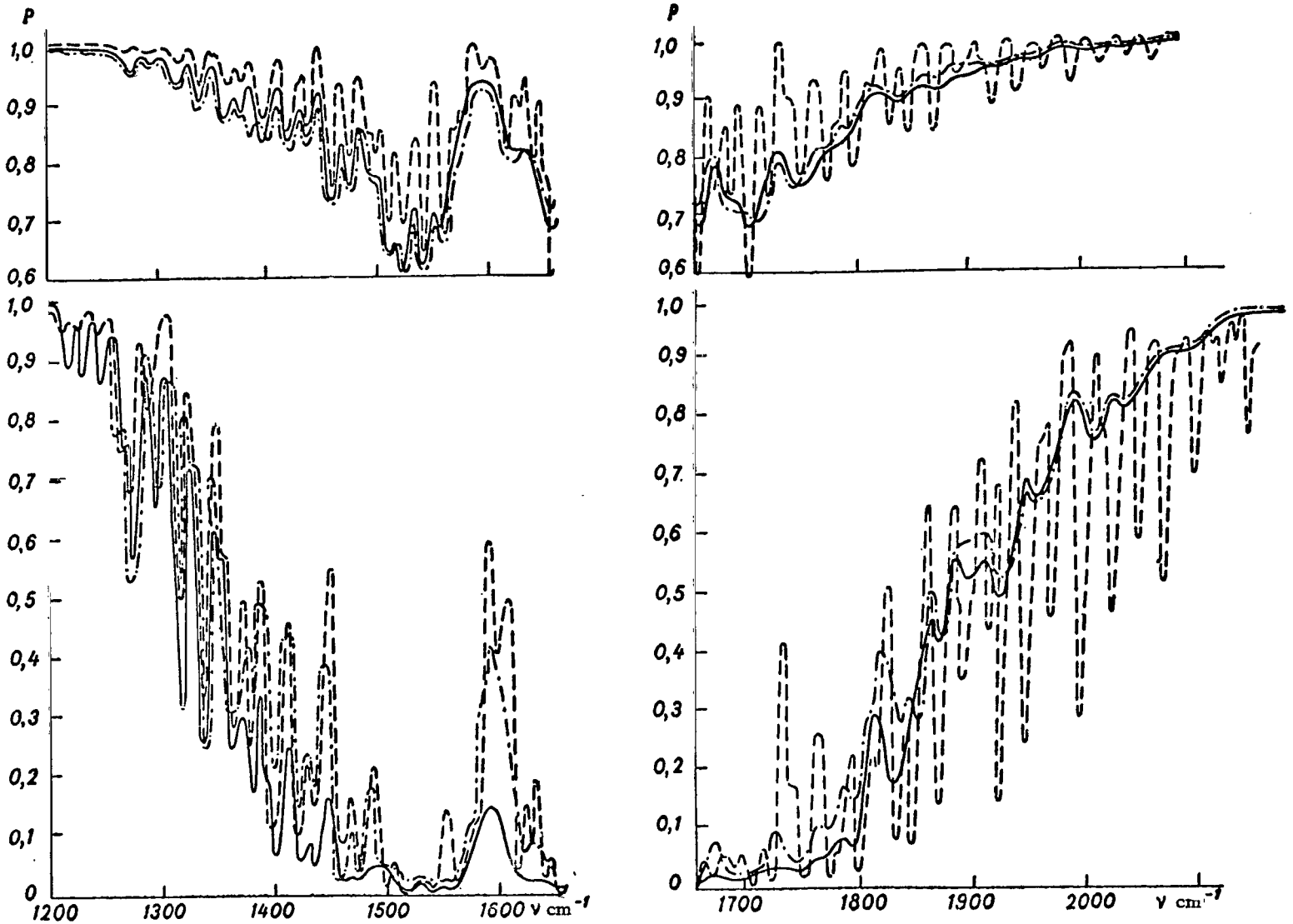

Figure 6.2. Comparison of Experimental Data (Solid Curves) According to Transmission Functions of 6.3-μm Band with Calculation by Quasirandom Model (Dashed Curves) and Calculation by Empirical Method (Dot-Dash Curves). Top: u = 0.002 g/cm^2, p = 0.26 atm; bottom: u = 0.077 g/cm^2, p = 1.06 atm.

are given in [4, 5]. Figure 6.2 compares experimental data with the theoretical calculations of Stull, Wyatt, and Plass based on their quasirandom model and with calculations by the empirical method proposed by B.M. Golubitskiy and I.I. Moskalenko. This figure, which we have borrowed from S.D. Andreyev and A.G. Pokrovskiy's paper [1.83], indicates that calculations based on the quasirandom model reflect the structure of the real spectrum satisfactorily. However, the theoretical data tend to exaggerate (by 5-15%) the transmission in the central parts of the bands. Calculations by the empirical method describe the experimental spectra with transmission errors no greater than 5-7%. The transmission-function data obtained by F. Möller and E. Raschke [18] have been used in a number of studies of humidity-distribution reconstruction. In this paper, it is proposed that the transmission function be approximated as follows: /357

$$P(\nu, u) = \exp\left[-\frac{1{,}97\underline{l}_{\nu}}{(1+6{,}57\underline{l}_{\nu}u)^{1/2}}\right], \qquad (6.4)$$

where $\underline{l}_{\nu}$ is the generalized absorption coefficient and $\underline{u}$ is the amount of absorbing substance.

Reference [1.28] gives all data on the fine structure of the 6.3-μm band that are needed for direct calculations of the transmission functions: spectral-line positions, intensities, and half-widths. Direct calculations are given in [1.60] and compared with calculations based on the random model.

As we have already noted, the rotational band of water vapor occupies a broad range of wavelengths from $\lambda \approx 10$ μm to the radio range. There are possibilities for solution of this problem by use of either the interval from $\lambda \approx 17$ to 50 μm or individual water-vapor lines in the microwave region. References [8-9] investigated the transmission functions in the infrared part of the rotational band. On the basis of these studies, B.M. Golubitskiy and N.I. Moskalenko proposed an empirical method for computing transparency; McClatchey [1.99] presented the same data in a convenient form. Benedict and Kaplan obtained data on the fine-structure parameters (certain information concerning their accuracy was given in Chapter 1). Transmission functions for the far infrared were computed directly in [19, 10]. Figure 6.3 shows an example in which the calculations of [19] are compared with Palmer's experimental results as well as those of Stauffer and Walsh [8, 9]. Using the Van Vleck-Weisskopf expression for the absorption-line shape, it was possible to obtain good agreement between theory and experiment in the 250-500-cm^{-1} region (40-20 μm). The disagreements are appreciable when the Van Vleck-Weisskopf formula is used in the 500-700-cm^{-1} region. K. Ya. Kondrat'yev and Yu.M. Timofeyev calculated the transmission functions directly for narrow spectral intervals in the water-vapor rotational band for homogeneous and inhomogeneous propagation

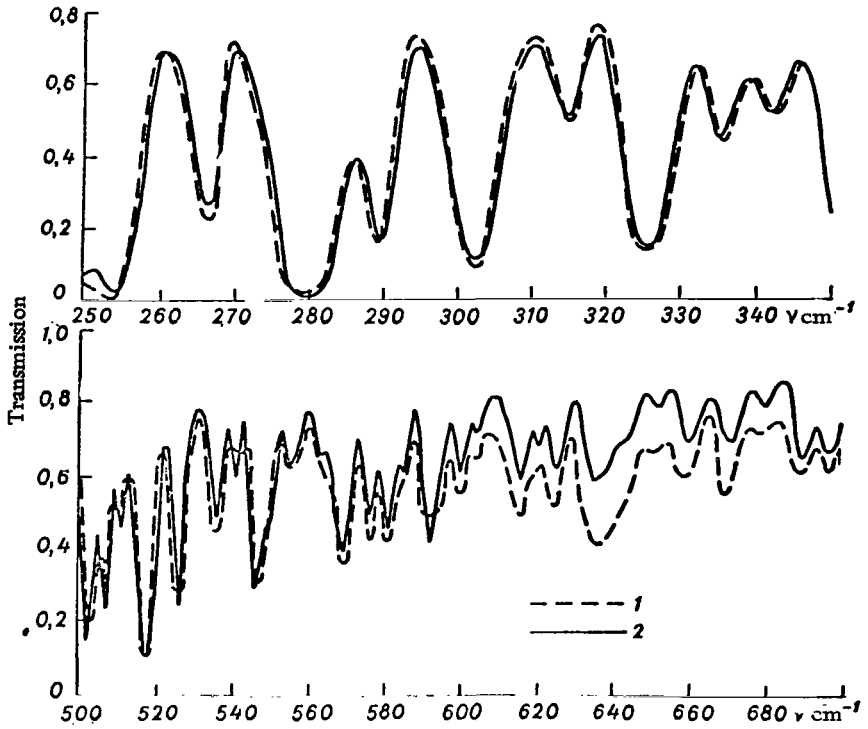

Figure 6.3. Comparison of Experimental Transmission Functions (1) with Functions Calculated by the Direct Method (2) for the Rotational Band of Water Vapor. a) T = 285°K, u = 0.0147 g/mg, p = = 0.263 atm; b) T = 306°K, u = 0.149 g/mg; p = = 0.263 atm.

conditions. They also studied the errors of the various approximate methods for taking atmospheric inhomogeneity into account (for details, see Chapter 1), for example, the reduced-mass method; this is especially important in view of the extensive use of this method in solving problems of atmospheric-humidity reconstruction.

The absorption coefficients of water vapor in the microwave region have been investigated theoretically and experimentally in many papers. Extensive calculations and an analysis of the present state of the problem will be found in a series of papers by /360
S.A. Zhevakin and A.P. Naumov [1.48-1.50]. Calculating the absorption coefficient of water vapor in a broad range of wavelengths from 10 μm to 32 cm, they used a line-shape expression derived from the kinetic equation. This enabled them to bring the results of theoretical absorption-coefficient calculations closer to the experimental data. (The excess of the experimental values over theory was reduced in the centimeter, millimeter, and near submillimeter transparency windows by factors ranging from 3-4 to

1.5-2.) Consideration of water vapor dimer absorption makes it possible to obtain even better agreement between theory and experiment for $\lambda > 0.7$ mm.

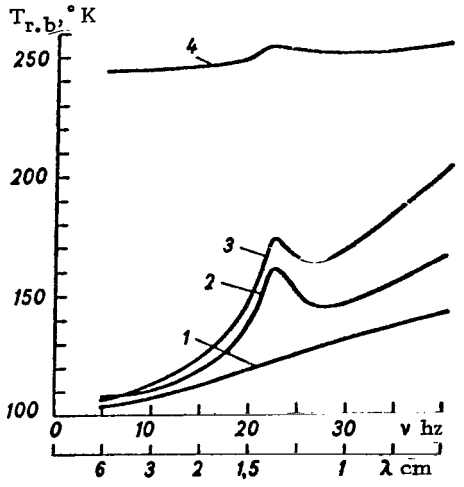

Figure 6.4. Distribution of Brightness Temperature in the Region of the Water-Vapor Line at $\lambda = 1.35$ cm. 1) Radiation from underlying surface (water); 2) radiation of earth-atmosphere system ($H_2O + O_2$); 3) radiation of earth-atmosphere system with consideration of clouds; 4) radiation over land surface ($H_2O + O_2$ + clouds).

It has been suggested that /361
the spectral line at $\lambda = 1.35$ cm be used to determine the atmospheric humidity distribution. Figure 6.4 shows the distribution of radio brightness temperature in the region of the 1.35-cm line [11] according to satellite observational data. As we see from the figure, the influence of the water-vapor absorption line on the amount of outgoing radiation is quite strong over the oceans; it may therefore be hoped that determination of q(p) from satellite measurements will prove possible. The same figure contains curves from which the influence of oxygen and cloud absorption on the outgoing radiation in this region can be estimated. Reference [11] proposed a method for consideration of cloudage which, in principle, permits sounding in the layers of the atmosphere below clouds. The upper curve in Fig. 6.4, which corresponds to observations made over land, indicates that the influence of water vapor absorption is insignificant in this case. (We recall that the emissivities of land and water surfaces differ substantially in the microwave, and this is responsible for the substantial differences in the brightness-temperature values.)[1]

As we noted above, the problem of reconstructing the atmospheric humidity distribution from thermal-radiation spectra can be reduced to solution of Fredholm integral equations of the first kind. The weighting functions dP/d log p, which have a simple /363
physical interpretation, figure as the kernels of these equations. They indicate regions in the atmosphere that are responsible for shaping the radiation for the spectral interval under consideration and characterize the sensitivity of the outgoing thermal radiation to changes in the atmosphere's humidity characteristics.

[1]Experimentally measured data on the ascending radiation for this region of the spectrum are given in [12].

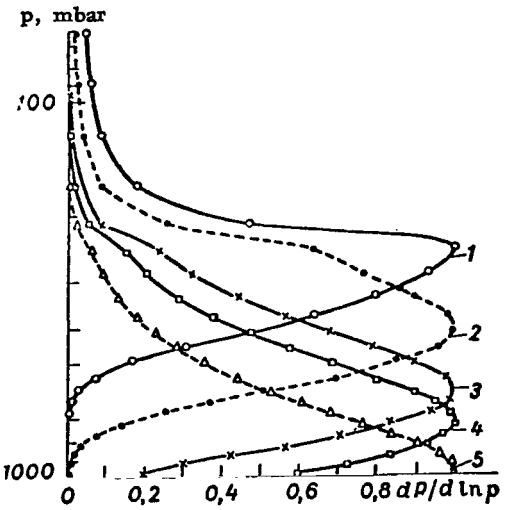

Figure 6.5. Weighting Functions dP/d ln p for a Series of Spectral Intervals in the Water Vapor Band at λ = 6.3 μm. 1) ν = 1680-1700 cm^{-1}; 2) ν = 1780-1800 cm^{-1}; 3) ν = 1800-1820 cm^{-1}; 4) ν - 1880-1900 cm^{-1}; 5) ν = 1960-1980 cm^{-1}.

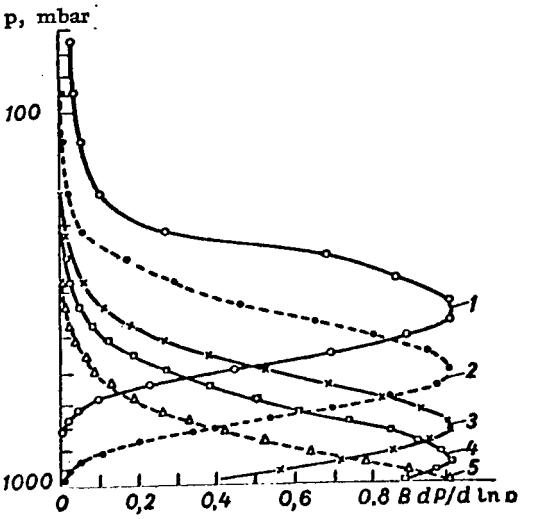

Figure 6.6. Weighting Functions $B\frac{dP}{d\ln p}$ for a Series of Spectral Intervals in the Water Vapor Band at λ = = 6.3 μm. For legend, see Fig. 6.5.

In some formulations of the problem, they may be derivatives of the transmission functions with respect to the reduced mass of the absorbing substance. Figure 6.5 presents typical curves characterizing these weighting functions for the band at λ = 6.3 μm. In view of the properties of this region of the spectrum, it is also helpful to use the functions $B\frac{dP}{d\ln p}$, shown in Fig. 6.6 to characterize the contributions of layers to the outgoing radiation. We see that the functions $B\frac{dP}{d\ln p}$ lie for the most part in the troposphere for these spectral intervals, and that they are somewhat narrower than the weighting functions dP/d ln p.

Because of the sharp decrease in the amount of water vapor in the atmosphere with increasing height,

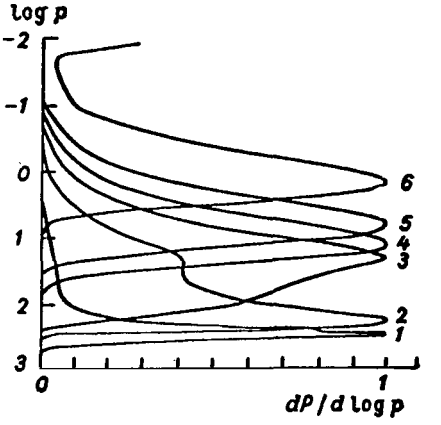

Figure 6.7. Weighting Functions dP/d log p for Spectral Intervals of Varying Width Around the Center of the Water Vapor Line at 202.67 cm. 1) ν = 190-215 cm^{-1}; 2) ν = = 202.67±1.0 cm^{-1}; 3) ν = = 202.67±0.5 cm^{-1}; 4) ν = = 202.67±0.1 cm^{-1}; 5) ν = = 202.67±0.05 cm^{-1}; 6) ν = = 202.67±0.01 cm^{-1}.

the possibilities for sounding the upper layers of the atmosphere by this method are rather severely limited. The sounding ceiling can be raised considerably by the use of narrow spectral intervals in the vicinity of strong spectral lines. Figure 6.7, which shows the weighting functions dP/d log p for spectral intervals of varying width around the center of the line at $\nu_0 = 202.67$ cm^{-1}, may be cited as an illustration of this. However, measurements of the thermal radiation in such narrow intervals are presently practically impossible because of the small energy values. /364

§2. METHODS OF SOLVING THE PROBLEM OF ATMOSPHERIC-HUMIDITY-DISTRIBUTION RECONSTRUCTION. EXAMPLES OF NUMERICAL EXPERIMENTS

J. King examined the possibilities for extracting various kinds of meteorological information from measured data on the thermal radiation of the earth-atmosphere system in [14]. With certain simplifications, for example, he considered the problem of reconstructing the distribution of an absorbing substance. He developed methods for the case of interpretation of monochromatic radiation values that make it possible to determine the relative distributions of various absorbing gases. Assuming that the atmospheric distribution of one of these gases is known, the distribution of another can be determined. In one variant of this approach, the function of a source (or black-body radiation) is reconstructed as it depends on the reduced mass of the absorbing substance. Having determined $B(\tilde{u})$ on the basis of measurements in the water vapor absorption bands (where $\tilde{u}$ is the reduced mass of H_2O) and having information on the atmosphere's thermal structure B(p), these data can be used to find the function u(p). This approach was used, for example, by Yamamoto and Tanaka [15] in an analysis of the possibilities for extraction of atmospheric humidity characteristics from outgoing radiation measurements made in the water vapor rotational band. Investigations of this method showed that rough estimates of the water-vapor distribution in the atmosphere can be obtained if radiation measurements in the 6.3-μm band are used. However, it is difficult to acquire solutions without using some sort of statistical or empirical information on the unknown profile.

M.S. Malkevich and V.I. Tatarskiy [5.12; 16] developed a method for solving this problem that is based on use of statistical information on the unknown specific-humidity profile. These papers gave particular attention to the mathematical aspects of solution of the problem. The transmission functions used were expressions that can be derived for the transmission functions of the corresponding regular absorption-band model. In this case, we can write

$$P_\nu(x) = 1 - \Phi\left[\sqrt{-\frac{\gamma}{2} w_0 \tilde{\mu}(x)}\right], \qquad (6.5)$$

where $x = p/p_0$, $w_0 = p_0 q_0/g$ is the mass of water vapor in the air column, reduced to normal pressure p_0, $\underline{l}_\nu$ is the generalized absorption coefficient, $\Phi(y)$ is the probability integral, $\tilde{u}(x) = \int_0^x t q(t)\,dt$ is the reduced mass of water vapor. /365

The specific humidity q(x) can be represented as the sum of its average value $\bar{q}(x)$ for the particular region and time and the accidental deviation q'(x) from the mean profile:

$$q(x) = \bar{q}(x) + q'(x). \qquad (6.6)$$

A system of orthogonal functions (or vectors) ψ_k that ensure optimum parametrization of any realization of q'(x) can be constructed on the basis of existing statistical data on humidity characteristics in the atmosphere. Figure 6.8 shows examples of the first three orthogonal vectors (summer, Bismarck station). Assuming that the temperature distribution T(x) and the atmosphere's mean humidity profile $\bar{q}(x)$ are known and that $\bar{q}(x) \gg q'(x)$, we can obtain the equation

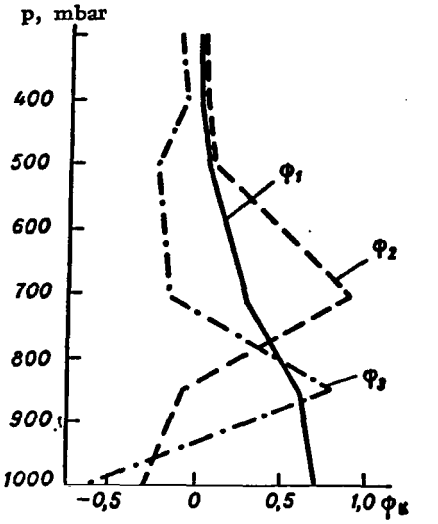

Figure 6.8. Eigenvectors $\psi_k(p)$ Calculated from Correlation Matrix $B_q(p_k, p_l)$ for Bismarck Station.

$$f_\nu = -B_\nu[T(1)]\frac{\partial \psi_\nu\left[\bar{\tilde{u}}(1)\right]}{\partial \tilde{u}}\tilde{u}'(1) + \int_0^1 B_\nu[T(x)]\,d\left\{\frac{\partial \psi_\nu\left[\bar{\tilde{u}}(x)\right]}{\partial \tilde{u}}\tilde{u}'(x)\right\}, \qquad (6.7)$$

where $f_\nu = J_\nu - \bar{J}_\nu$; $\bar{J}_\nu$ is the outgoing radiant intensity corresponding to the mean profile $\bar{q}(x)$; $\bar{\tilde{u}}(x) = \int_0^x t\bar{q}(t)\,dt$, and $\tilde{u}'(x) = \int_0^x t q'(t)\,dt$.

To solve (6.7), which is linear in q'(x), the unknown function is presented in the form /366

$$q'(x) = \sum_{k=1}^{n} q_k \psi_k(x). \qquad (6.8)$$

Substituting (6.8) into (6.7), we obtain a system of algebraic equations for determination of the coefficients q_k:

$$\sum \Gamma_{\nu k} q_k = f_\nu, \quad \nu = 1, 2, \ldots, N, \tag{6.9}$$

where

$$\Gamma_{\nu k} = B_\nu [T(1)] \frac{\partial \Phi_\nu \left[\tilde{\tilde{u}}(1)\right]}{\partial \tilde{u}} g_k(1) + \\ + \int_0^1 B_\nu [T(x)]\, d\left\{ \frac{\partial \Phi_\nu \left[\tilde{\tilde{u}}(x)\right]}{\partial \tilde{u}} g_k(x) \right\},$$

$$g_k(x) = \int_0^x t \psi_k(t)\, dt. \tag{6.10}$$

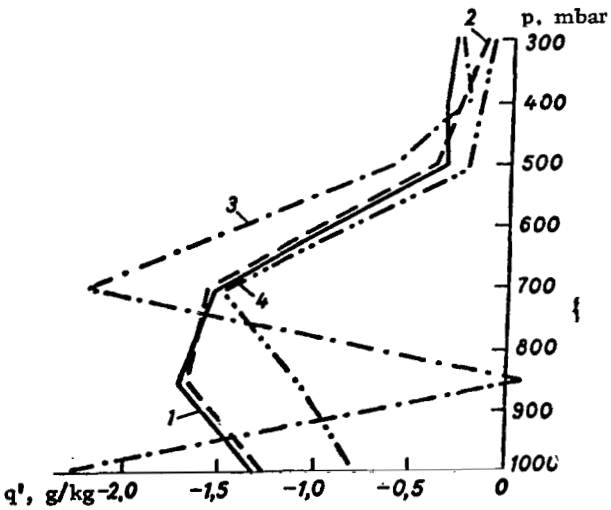

Figure 6.9. Reconstruction of Humidity Profile [16]. 1) True profile; 2) optimum approximation of profile (n = 3); 3) from system (6.10); 4) second approximation of q'(p).

The numerical experiment in solution of this inverse problem was performed by the closed scheme. Several spectral intervals of width $\Delta\nu$ = = 25 cm^{-1} in the frequency interval from ν_1 - 1241 cm^{-1} to ν_2 = 1512.5 cm^{-1} (6.3-μm band) were used. Figure 6.9 presents the results of a numerical experiment to reconstruct humidity for n = 3 and N = 3. As we see from the figure, the discrepancies between the true and calculated humidity profiles are large near the earth's surface. This is evidently because the values of q' are comparable with the mean profile near the surface of the earth and consideration of only the linear terms in (6.7) produces appreciable errors.

TABLE 6.1. COEFFICIENT k_q AS A FUNCTION OF LEVEL IN THE ATMOSPHERE

p mbar	1000	850	700	500	400	300
k_q ($n = N = 3$)	6,2	7,6	5,0	0,61	0,4	0,1
k_q ($n = 3$, $N = 8$)	5,4	2,5	1'8	0,3	0,1	—

By way of improving the solution of the problem, it is proposed that the general Newtonian method, generalized by L.V. Kantorovich for nonlinear operators, be used in solving the nonlinear equation. Calculated results (see Fig. 6.9) indicate that this

brings the reconstructed q' profile close to the true profile. The root-mean-square error of the solution does not exceed 10% provided that absolutely accurate radiation values were used in solving the inverse problem. The influence of radiation-measurement errors is characterized by introduction of the error amplification factor

$$k_q(p) = \frac{\sigma_q}{\sigma_t}, \tag{6.11}$$

where σ_t is the variance of the radiation-measurement error and /367
σ_q is that of the error in reconstructing q'(p). Table 6.1 lists values of k_q calculated for the numerical experiments examined above.

As we should expect, the values of the error amplification factor are largest near the earth's surface. The values of $k_q(p)$ can be reduced by solving the problem with a number of radiation measurements larger than the number of basis vectors n. In this case, k_q is reduced by a factor of about $\sqrt{N/n}$ (third line of Table 6.1, n = 3, N = 8).

Conrath [17] proposed another method for reconstructing atmospheric humidity. Treating the transmission function of the real inhomogeneous atmosphere as the atmospheric distribution /368
function of the reduced mass of H_2O, we can write in approximation

$$P[u(x)] = P[u_0(x)] + \left(\frac{\partial P}{\partial u}\right)_{u_0(x)} \delta\tilde{u}(x). \tag{6.12}$$

Substituting the Taylor-series expansion (6.12) into (6.2), we obtain the integral equation

$$g'(\nu) = \int_0^{x_s} K(\nu, x)\,\delta\tilde{u}(x)\,dx, \tag{6.13}$$

where

$$K(\nu, x) = \frac{\partial B_\nu}{\partial x}\left(\frac{\partial P}{\partial \tilde{u}}\right)_{\tilde{u}_0(x)}, \tag{6.14}$$

$$g'(\nu) = J(\nu, p) - B_\nu(p) - \int_0^{x_s} \frac{\partial B_\nu}{\partial x} P_\nu[\tilde{u}_0(x)]\,dx. \tag{6.15}$$

Here $\tilde{u}_0(x)$ is the initial approximation of the unknown reduced-mass profile and x is the corresponding space variable, e.g., p or log p.

Physically, the kernel of Eq. (6.13) can be interpreted as a measure of the sensitivity of outgoing radiation at frequency ν to small variations in the total reduced-mass water-vapor content above level $\underline{x}$. In solving the inverse problem by this method, Conrath proposes use of M. Chahine's iteration method, in which solutions of (6.13) are used to improve the kernel (6.14) and subsequently to determine the unknown function more accurately. The proposed method permits determination of the distribution u(x), and such humidity characteristics as the mixture ratio can be obtained by differentiating the final solution.

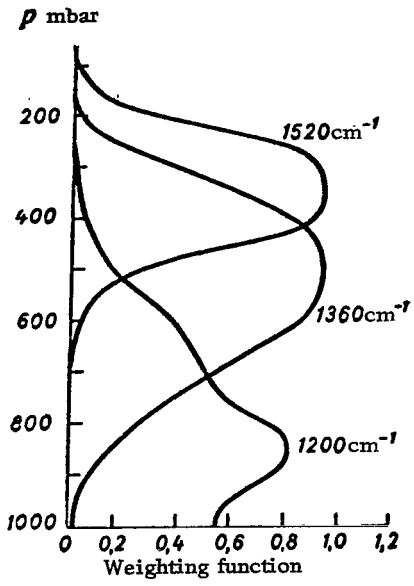

Figure 6.10. Weighting Functions of Eq. (6.13) for Spectral Intervals Centered on ν of 1520, 1360, and 1200 cm^{-1} (Humid-Atmosphere Model for Middle Latitudes).

Numerical experiments indicating the possibilities of the proposed method were performed in [17]. Expression (6.4) was used for the transmission functions, and values of the generalized absorption coefficients were taken from [18]. The reduced mass was determined by the expression

$$d\tilde{u} = \left(\frac{p}{p_0}\right)^{0,72}\left(\frac{T_0}{T}\right)^{0,5} du.$$

The band from 1520 to 1200 cm^{-1} was used in solving the problem. By way of example, Fig. 6.10 shows equation kernels for intervals centered on ν of 1520, 1360, and 1200 cm^{-1} (the middle-latitude humid-atmosphere model was used in the calculations). In a specific solution of the problem, Conrath seeks the solution in the form of the following simple expression: /369

$$w = w_s\left(\frac{p}{p_s}\right)^k, \qquad (6.16)$$

where w_s and p_s are the mixture ratio and pressure at the surface of the earth.

Thus, the problem reduces to determination of the two parameters w_s and $\underline{k}$ from the radiation data. A similar representation of the unknown function was used by Smith [5.69, 5.70]. Two spectral intervals centered at ν = 1520 cm^{-1} and ν = 1200 cm^{-1} were used in the numerical experiments whose results appear in Figs. 6.11 and 6.12. Figure 6.11 shows an example of humidity reconstruction for a tropical model of the atmosphere, while Fig. 6.12 pertains to a polar model (winter). The solutions were obtained after two or three iterations even when the zeroth approximation

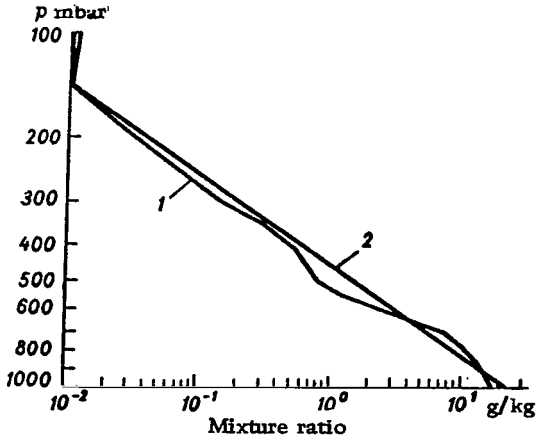

Figure 6.11. Reconstruction of Humidity for Tropical Atmospheric Model. 1) True profile; 2) reconstructed profile.

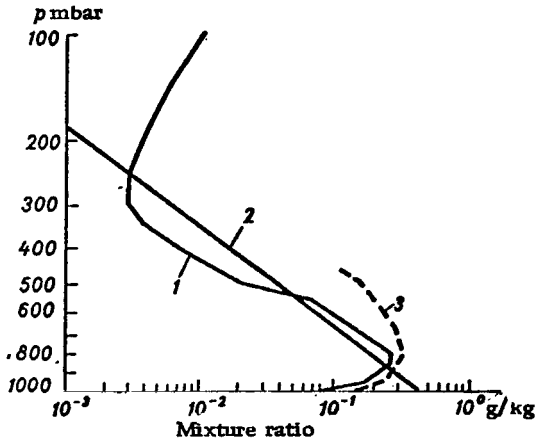

Figure 6.12. Reconstruction of Humidity for Polar Atmosphere (Winter). 1) True profile; 2) reconstructed profile; 3) mixture-ratio distribution corresponding to saturated water vapor.

of the solution was quite far from the truth. This indicates that the method converges well. However, we see from these figures, and especially from Fig. 6.12, that the approximation of humidity with Expression (6.16) does not yield a sufficiently accurate solution in a number of cases. As Conrath observes, the strong variability of the mixture ratio is an obstacle to its use as the unknown function (it varies through several orders of magnitude in the altitude range from the ground surface to the tropopause). In addition, the form of Function (6.16) depends on the temperature distribution, and this leads to additional difficulties in reconstruction (see Fig. 6.12). It is therefore proposed that the distribution of relative humidity in the atmosphere, f(p), be sought. For this purpose, we present f(p) in the form of an expansion in a certain basis $\{\Phi_i(p)\}$ /371

$$f(p) = \sum_{i=1}^{n} c_i \Phi_i(p), \tag{6.17}$$

where the c_i are the unknown coefficients of the expansion.

Then, using the relation between relative humidity and the mixture ratio

$$w(\text{g/kg}) = 622 \frac{e_s}{p} f, \tag{6.18}$$

where e_s is the saturation vapor pressure, we obtain the integral

equation

$$g'(\nu) = \sum_{i=1}^{n} \Delta c_i \int_0^{p_s} \frac{\partial B(\nu, p)}{\partial p} \frac{\partial P(\nu, p)}{\partial p} \psi_i(p)\, dp, \qquad (6.19)$$

where

$$\psi_i(p) = \frac{622}{g} \int_0^{p} \left(\frac{p'}{p_0}\right)^{0.72} \sqrt{\frac{T_0}{T}} \frac{e_s(T)}{p'} \Phi_i(p')\, dp'. \qquad (6.20)$$

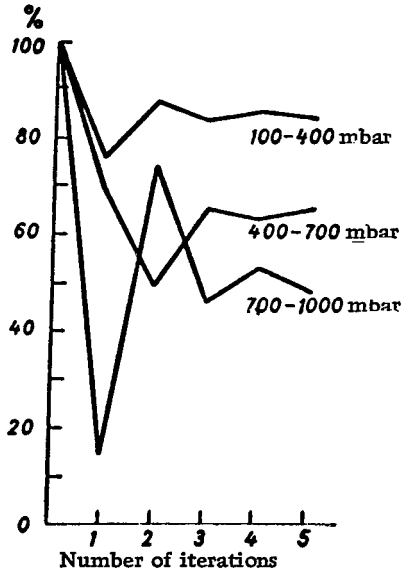

Figure 6.13. Reconstruction of Relative Humidity (%) after Various Numbers of Iterations.

Having a set of measurements in N spectral intervals, we can use (6.19) and (6.20) to obtain a system of linear algebraic equations for determination of the corrections Δc_i to the coefficients used as the zeroth approximation. The proposed method was used in numerical experiments for rather simple atmospheric humidity distribution conditions: relative humidity in the 100-400-mbar layer 85%, reduced to 65% in the 400-700-mbar layer and to only 50% in the 700-1000-mbar layer. Figure 6.13 presents the results of solution of the problem after various numbers of iterations. The zeroth approximation f = 100% was used for all layers. The figure shows that the convergence /372 to the sought solution is quite fast. However, the oscillating nature of the solution sometimes produces negative relative-humidity values. This property of the algorithm must be appropriately neutralized.

Numerical experiments were also performed in [17] to investigate the influence of measurement errors on the accuracy of humidity reconstruction. For this purpose, the problem was solved with various error levels (two types of errors were assigned with two distortion levels: 0.1 and 0.2 erg/cm^2·sec·sr·cm^{-1}) for a humidity distribution observed during Michelson-interferometer radiation measurements in Texas [5.51]. Either three or nine radiation values were used in reconstructing the relative humidity (n = 3). In the latter case, the method of least squares was used to solve the equation system. Table 6.2 presents the results of a study to determine the influence of the number of measurements for the two types of errors (I and II).

TABLE 6.2. INFLUENCE OF ERRORS AND NUMBER OF MEASUREMENTS ON ACCURACY OF RELATIVE-HUMIDITY RECONSTRUCTION

Error, erg/cm2	Number of measurements	125–425 mbar		425–725 mbar		725–1000 mbar		Total water vapor content	
		f %	Error	f %	Error	f %	Error	u(cm ppdt water)	Error
0	3	29	—	36	—	52	—	2,31	—
0,1 (I)	3	34	+5	29	—7	66	+14	2,71	+0,40
0,1 (II)	3	26	—3	43	+7	39	—13	1,93	—0,38
0,2 (I)	3	39	+10	22	—14	82	+30	3,18	+0,87
0,2 (II)	3	22	—7	50	+14	26	—26	1,57	—0,74
0,1 (I)	9	30	+1	35	—1	55	+3	2,39	+0,08
0,1 (II)	9	29	0	37	+1	49	—3	2,23	—0,08
0,2 (I)	9	31	+2	34	—2	58	+6	2,47	+0,16
0,2 (II)	9	28	—1	38	+2	47	—5	2,16	—0,15

As we see from the table, use of nine radiation measurements improves the accuracy of the solution substantially as compared to the case in which only three are used. Thus, the implication of these results is that the proposed method, which is based on the use of simple approximations of the unknown humidity characteristics, can be used to bring out the general features of the sought characteristic.

§3. EXAMPLES OF RECONSTRUCTION OF HUMIDITY DISTRIBUTION IN THE ATMOSPHERE UNDER REAL CONDITIONS /373

There are few available examples of reconstruction of the atmosphere's humidity distribution that are based on interpretation of measured thermal radiation data. We cite the results of two studies [17, 5.70] in which measurements of the ascending thermal radiation made at an altitude of 33.5 km in a broad range of wavelengths from 5 to 20 μm using a Michelson interferometer [5.51] were used as the initial data on the radiation. W. Smith's papers [5.69, 5.70] are devoted to the problem of determining the temperature and humidity distributions in the troposphere. The method proposed by Smith for determining the tropospheric temperature distribution was examined at considerable length in the preceding chapter. Here we note that a method by which the approximate type of the water-vapor distribution in the troposphere can be determined is a constituent part of the general algorithm used by Smith. Like B. Conrath, W. Smith assumes that the unknown function has the simple form

$$w(p) = w(p_0)\left(\frac{p}{p_0}\right)^{\lambda}, \qquad (6.21)$$

where (in contrast to B. Conrath's method) the constant λ is regarded as known. Thus, the problem actually reduces to extraction

of only the single parameter $w(p_0)$ from the radiation data. The value of λ is taken from climatological data. The 500-570 cm^{-1} interval in the water vapor rotational band is used in solving the problem. The radiation in this interval is generated by the troposphere under practically all conditions observed in the earth's atmosphere. The actual method by which the unknown parameter is extracted is also based, as with B. Conrath, on the reduced-mass concept, expansion of the transmission function in Taylor series, and successive iterations that permit improving the temperature and humidity distributions at each step. The only differences from Conrath's method, which was treated in detail in the preceding section, are certain details of the specific algorithm — most importantly, the fact that the temperature profile is not considered to be known, but is found in the process of solving the problem.

Assignment of the unknown function in the form of (6.21) imposes severe limitations on the possibilities of the method. It cannot be used to determine the fine structure of the humidity distribution, yielding only somewhat raw data, especially when the type of distribution differs substantially from the functional form (6.21). However, it is still accurate enough for determination of total atmospheric moisture content and is quite suitable /374
for correction of the thermal-sounding-channel transmission functions. Results of application of Smith's method appear in Figs. 5.43-5.45. It was necessary to use five iterations to obtain the results shown in Fig. 5.43, which convey the true atmospheric humidity characteristics quite faithfully. Figure 5.44 shows a less successful reconstruction of the unknown distribution. In Smith's opinion, the trouble arose out of rather large errors that were observed at the time of the measurements. Major errors in determination of the humidity profile also resulted from errors in the temperature-profile reconstruction in this case (see Fig. 5.44). While errors in determining the atmospheric humidity distribution have little influence on the accuracy with which the atmosphere's thermal structure is determined, errors in our knowledge of the temperature profile result in large errors in determination of atmospheric humidity. Thirteen iterations were used in constructing the curves shown in Fig. 5.44. Smith observes that the accuracy of the solution correlates with the number of iterations required, so that unsuccessful reconstructions can be identified by this criterion.

Figure 5.45 presents a tropospheric humidity distribution reconstructed under partly cloudy conditions. The method considered in Chapter 5, §6 was used to separate the cloudless-atmosphere radiation. We note that there is no substantial deterioration of humidity-reconstruction accuracy as compared with cases of cloudless-atmosphere reconstruction.

B. Conrath [17] used the method described above to process data obtained in a different band during the same radiation

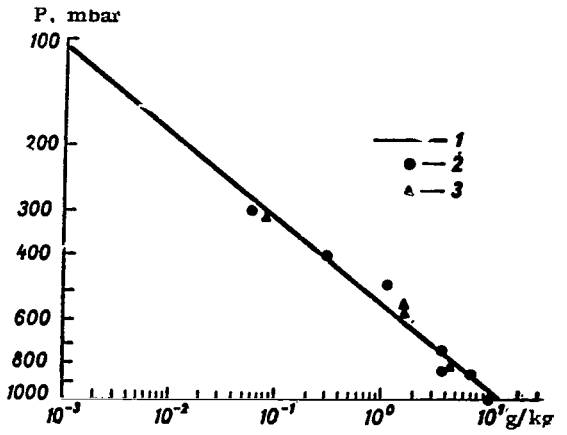

Figure 6.14. Reconstruction of Humidity Profile (g/kg) under Real Conditions. 1) Reconstructed profile; 2, 3) radio sounding data at 12 and 18 hours, respectively.

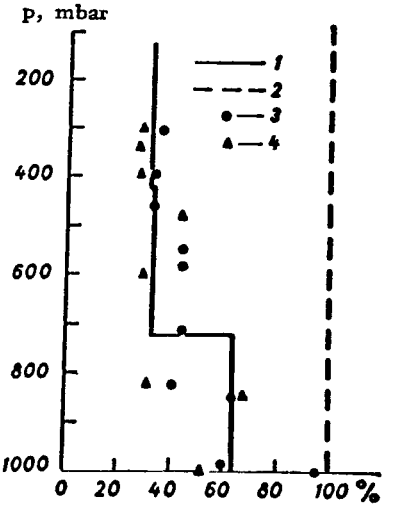

Figure 6.15. Reconstruction of Relative-Humidity Profile (%) under Real Conditions. 1) Reconstructed profile; 2) zeroth approximation to unknown profile; 3, 4) radio sounding data at 12 and 18 hours.

measurements. Figure 6.14 presents an example in which the inverse problem is solved with the water-vapor mixture-ratio distribution regarded as the unknown function. Two spectral intervals $\sim$40 cm^{-1} wide and centered at ν = 1520 and ν = 1200 cm^{-1} were used in solving the problem. The circles and triangles on the diagram represent data from radiosonde measurements. As we see from the figure, the agreement between the sought function and the real distribution is not at all bad. Figure 6.15 presents results from solution of the same problem for the case in which relative humidity is treated as the unknown function. Three terms of the expansion in (6.17) were used here. The same data are presented in Fig. 6.16, this time in the form of the pressure curve of water-vapor mixture ratio. Because of the type of humidity distribution observed in the atmosphere, the latter method of determining the humidity characteristics has no major advantages over the former. On the whole, the results can be rated good, since the measurement errors were quite large — 3-4% — in the spectral interval considered. /375

In reconstructing the humidity, Conrath used a temperature profile obtained with a radiosonde. In the satellite version of this problem, it would, of course, be necessary to use temperature-profile data obtained indirectly. This raises the question as to the influence of errors in assigning T(p) on the accuracy of humidity-profile reconstruction. Figure 6.17 presents results

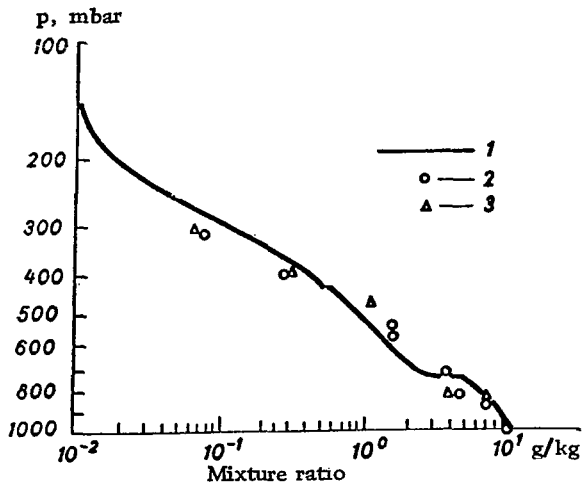

Figure 6.16. Humidity Profile Reconstruction Data shown in Fig. 6.15, in the Form of a Plot of Water Vapor Mixture Ratio as a Function of Pressure in the Atmosphere. For legend see Fig. 6.14.

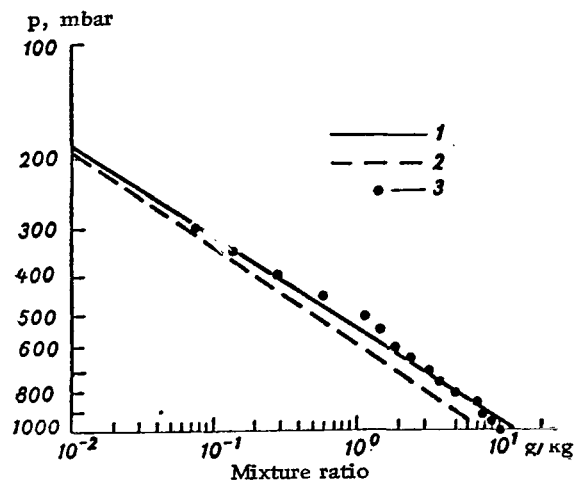

Figure 6.17. Influence of Errors in Assignment of Atmospheric Temperature Profile on Accuracy of Humidity Distribution Reconstruction. 1) Reconstruction using accurate T(p) profile; 2) reconstruction with T(p) profile assigned with 2° error; 3) radio sounding data.

from reconstruction of the water-vapor mixture ratio using a temperature profile assigned with a systematic error of -2°C. As we see from the figure, the reconstruction error is appreciably larger. We may expect a somewhat weaker influence of temperature-assignment errors on the solution of this inverse problem when relative humidity is used as the unknown function. This is because a certain amount of error compensation will result from the temperature variations of both the relative humidity itself and the black-body radiation. Nevertheless, it may be concluded that the errors arising in reconstruction of the temperature profile will be one of the basic sources of errors in determination of the atmosphere's humidity characteristics. /377

The examples given here indicate the possibility of extracting the basic characteristics of tropospheric humidity from measured thermal radiation data. In a number of problems, it will, of course, be necessary to have more detailed information in a broader altitude range. This requires further improvement of the method. The problems that must be solved include the use of more accurate methods of correction for atmospheric inhomogeneity in the solution, selection of the optimum band of the spectrum, investigation of optimum measurement conditions, development of improved interpretation methods, etc.

CONCLUSION /378

The last decade has been pivotal in the development of meteorology. Progress made in computer techniques has made possible the rapid development of numerical weather-forecasting methods and the first numerical experiments to study the laws governing the general circulation of the atmosphere. The technical possibility of quantitative description of processes on the planetary scale and the acute need for the development of numerical methods for long-range weather forecasting have made the problem of developing a planetary system for the acquisition of meteorological information (initial data) a pressing one. It is this problem that constitutes the principal content of the plan advanced by the World Weather Organization for a World Weather Watch (WWW) and its research aspect — the Global Atmospheric Research Program (GARP).

The advances made over the last decade in the development of satellite meteorology have shown that weather satellites must be the basic link in a planetary system of weather observations. However, this has not yet become a practical reality, since television and infrared pictures of the cloud cover have been, until very recently, the sole and principal form of information obtained with weather satellites and used in the weather services. The absence of quantitative data on the fields of the basic meteorological elements needed for application of numerical forecasting methods has created a situation in which results obtained by means of present-day engineering facilities have only been of help in the development of a semiquantitative synoptic method.

The first progress in thermal sounding of the atmosphere and in approximate determination of the vertical water-vapor and ozone concentration profiles, which was made in 1969, marks a crucial /379
stage in the development of satellite meteorology in that it has opened the way to practical acquisition of information on the fields of the principal meteorological elements in quantitative form. Although it is quite clear that the conventional weather-observation methods will be just as important in the future, recent advances in satellite meteorology indicate the need for formulation and solution of the problem of the optimum mix of conventional and satellite methods of acquiring meteorological information.

There is no doubt that the results obtained in the first stage of solving the thermal-sounding problem can be improved upon greatly. This will require, first of all, further development with the purpose of solving the problem for arbitrary cloudage conditions. Since the basic directions to be taken in overcoming this difficulty are more or less clear, most of our attention should be focused on the instrumental aspect of the problem. The

problem of the optical characteristics of the atmosphere, clouds, and underlying surface is of no lesser importance. A broad program of research in atmospheric spectroscopy must be implemented here.

The most efficient way to solve inverse problems of satellite meteorology will undoubtedly be to use complex formulations in which, for example, the vertical profiles of temperature and humidity are determined simultaneously and information on the transmission functions (kernels of the fundamental integral equation) is improved. This implies the need for outgoing-radiation measurements in various regions of the spectrum, and it must be stressed in this context that the microwave outgoing radiation deserves the most diligent attention as a source of meteorological information.

The development of methods for indirect sounding of the atmosphere from satellites is only in its infancy. The problems mentioned above as requiring attention are no more than isolated illustrations of the unsolved problems. The next stage in the development of satellite meteorology, which will involve practical solution of various inverse problems, will require major efforts, but it is, at the same time, highly promising from the standpoint of solving the cardinal problem of acquiring weather data on the global scale.

REFERENCES

/382

To Chapter 1

1. Kondrat'yev, K.Ya. Luchistyy teploobmen v atmosfere (Radiant Heat Transfer in the Atmosphere), Gidrometeoizdat, Leningrad, 1956.
2. Kondrat'yev, K.Ya. Aktinometriya (Actinometry), Gidrometeoizdat, Leningrad, 1965.
3. Gudi (Goody), R.M. Atmosfernaya radiatsiya. I. Osnovy teorii (Atmospheric Radiation. I. Fundamentals of Theory), Izd-vo "Mir", Moscow, 1966.
4. Sobolev, V.V. Kurs teoreticheskoy astrofiziki (Textbook of Theoretical Astrophysics), Izd-vo "Nauka," Moscow, 1967.
5. Zuyev, V.Ye. Prozrachnost' atmosfery dlya vidimykh i infrakrasnykh luchey (Atmospheric Transparency for Visible and Infrared Light), Izd-vo "Sov. Radio," Moscow, 1966.
6. Chandrasekar (Chandrasekhar), S. Perenos luchistoy energii (Transfer of Radiant Energy), IL, Moscow, 1953.
7. Dzhemison, Dzh.E. (Jamison, J.E.), et al. Fizika i tekhnika infrakrasnogo izlucheniya (Physics and Engineering of Infrared Radiation), Izd-vo "Sov. Radio," Moscow, 1965.
8. Popov, O.I. et al. Experimental studies of the ascending radiation spectra in the free atmosphere in the 2-6-μm band. Aktinometriya i optika atmosfery. Trudy Shestogo mezhvedomstvennogo soveshchaniya po aktinometrii i optike atmosfery (Actinometry and Atmospheric Optics. Transactions of the Sixth Interdepartmental Conference on Actinometry and Atmospheric Optics), Izd-vo "Valgus," Tallin, 1968.
9. McClatchey, R.A. Temperature Sounding with the 4.3 Micron CO_2 Band. Proceedings of a Specialist Conference on Molecular Radiation and its Application to Diagnostic Techniques. NASA TMX-53711, 1968.
10. Kondrat'yev, K.Ya. and Filipovich, O.P. Teplovoy rezhim verkhnikh sloyev atmosfery (Thermal Regime of the Upper Layers of the Atmosphere), Gidrometeoizdat, Leningrad, 1950.
11. Tauns, Ch. (Townes, C.) and Shavlov, A. Radiospektroskopiya (Radiospectroscopy), IL, Moscow, 1959.
12. Curtis, A.R. and Goody, R.M. Thermal Radiation in the Upper Atmosphere, Proc. Roy. Soc. A236, 193, 1956.
13. Shved, G.M. A method of accounting for deviations from Kirchhoff's law in the mesosphere for radiant transfer in the 15-micron carbon dioxide band. Vestn. LGU, seriya fiziki i khimii, No. 1, Vol. 67, 1965.
14. Burn, J.W. Determination of Atmospheric Temperature Profiles from Satellite Radiance Measurements at the Limb of the Earth. Proceedings of a Specialist Conference on Molecular Radiation and its Application to Diagnostic Techniques, NASA TMX-53711, 1968.

15. Kondrat'yev, K.Ya. et al. Pole izlucheniya Zemli kak planety (The Radiation Field of the Earth as a Planet), Gidrometeoizdat, Leningrad, 1967.
16. Feygel'son, Ye.M. Spectral reflection of radiation by clouds. Trudy GGO, No. 166, 1964.
17. Novosel'tsev, Ye.I. Emissivities of clouds of various levels. Aktinometriya i optika atmosfery. Trudy Shestogo mezhvedomstvennogo soveshchaniya po aktinometrii i optike atmosfery. Izd-vo "Valgus," Tallin, 1968.
18. Gertsberg, G. Kolebatel'nyye i vrashchatel'nyye spektry mnogoatomnykh molekul (Vibrational and Rotational Spectra of Polyatomic Molecules), IL, Moscow, 1949.
19. Yel'yashevich, M.A. Atomnaya i molekulyarnaya spektroskopiya (Atomic and Molecular Spectroscopy), Fizmatgiz, Moscow, 1962. /383
20. Penner, S.S. Kolichestvennaya molekulyarnaya spektroskopiya i izluchatel'naya sposobnost' gazov (Quantitative Molecular Spectroscopy and the Emissivity of Gases), IL, Moscow, 1963.
21. Gordi, V. Smit, V. and Trambarulo, R. Radiospektroskopiya (Radiospectroscopy), GITTL, Moscow, 1955.
22. Ingram, D. Spektroskopiya na vysokikh i sverkhvysokikh chastotakh (Spectroscopy at High and Superhigh Frequencies), IL, Moscow, 1956.
23. Mirtov, B.A. Gazovyy sostav atmosfery Zemli i metody yego analiza (The Gaseous Composition of the Earth's Atmosphere and Methods for its Analysis), Izd. AN SSSR, Moscow, 1961.
24. Raschke, E. and Tannhauser, J. Investigation of Atmospheric Properties Based upon Evaluation of Infrared Radiation Data Obtained from the Tiros Satellite. Part II. Influence of Minor Constituents on the Outgoing Radiation. Final Report, NASA Research Grant NsG-305, May 1965.
25. Viktorova, A.A. and Zhevakin, S.A. Absorption of microwaves in air by water vapor dimers, DAN SSSR, 171, No. 5, 1966.
26. Viktorova, A.A. and Zhevakin, S.A. The dimer of water vapor and its spectrum, DAN SSSR, 171, No. 4, 1966.
27. Dianov-Klokov, V.I. and Matveyeva, O.A. The absorption spectrum of atmospheric oxygen in the 1.3-0.23-μm band and the role of short-lived $[O_2]_2[O_2-N_2]$ complexes. Izv. AN SSSR, seriya fiziki atmosfery i okeana, Vol. IV, No. 4, 1968.
28. Filimonov, V.N. Induced molecular absorption of infrared radiation, UFN, Vol. 69, No. 4, 1959.
29. Zuyev, V.Ye. On the error of determining line positions in the spectra of atmospheric gases to evaluate absorption of laser light in the atmosphere, Izv. vuzov, fizika, No. 3, 1967.
30. Madden, R.P. A High Resolution Study of CO_2 Absorption Spectra between 15 and 18 Microns. J. Chem. Phys., Vol. 35, No. 6, 1961.
31. Young, C.A. Study of the Influence of Carbon Dioxide on Infrared Radiative Transfer in the Stratosphere and Mesosphere. Technical Report 04682 - 1-t University of Michigan. College of Engineering, Department of Meteorology and Oceanography, 1964.
32. Benedict. W.S.,and Calfee, R.F. Line Parameters for 1.9 and 6.3 Micron Water Vapor Bands. ESSA Professional Paper 2. US

Department of Commerce, Washington, D.C., June 1968.
33. Ben Aryeh, Y. Line Widths and Intensities in the Wings of the ν_2 Water Vapor Band at 400°K and 540°K. Journ. Quant. Spectr. Rad. Transfer, Vol. 7, No. 1, 1967.
34. Vasilevskiy, K.P., Kazbanov, V.A. and Dervich, T.Ye. Intensity and half-width of CO_2 lines in the $4\nu_2 + \nu_3$ band. Optika i spektroskopiya, Vol. 23, No. 6, 1967.
35. Sanderson, R.B. and Ginsburg, N. Line Widths and Line Strengths in the Rotational Spectrum of Water Vapor. J. Quant. Spectr. Rad. Transfer, Vol. 3, No. 1, 1963.
36. Zhevakin, S.A. and Naumov, A.P. Propagation of centimeter, millimeter, and submillimeter radio waves in the earth's atmosphere, Izv. vuzov, radiofizika, Vol. X, No. 9-10, 1967.
37. Babrov, H.I. and Casden, F. Strengths of Forty-Two Lines in the ν_1 and ν_3 Bands of Water Vapor. J. Opt. Soc. Amer., Vol. 58, No. 2, 1968.
38. Oppenheim, U.P. and Devir, A.D. Determination of CO_2 Line Using a CO_2-N_2-Ne Laser. J.Opt. Soc. Amer., Vol. 58, No. 4, 1968.
39. Benedict, W.S., Herman, R., Moore, G.E. and Silverman, S. The Strengths, Widths and Shapes of Infrared Lines. Canad. J. Phy., 1956, Vol. 34, No. 830.
40. Benedict, W.S., Herman, R., Moore, G.E., and Silverman, S. The Strengths, Widths and Shapes of Infrared Lines. Canad. J. Phy., 1956, Vol. 34, No. 851.
41. Benedict, W.S., Herman, R., Moore, G.E., and Silverman. S. /384 The Strengths, Widths and Shapes of Lines in the Vibration-Rotation Bands of CO_2. Astrophys. J., Vol. 135, No. 277, 1962.
42. Sobel'man, I.I. Vvedeniye v teoriyu atomnykh spektrov (Introduction to the Theory of Atomic Spectra), Fizmatgiz, Moscow, 1963.
43. Rautian, S.G. and Sobel'man, I.I. Influence of collisions on spectral line broadening, UFN, Vol. 90, No. 2, 1966.
44. Chen, M. and Takeo, M. Broadening and shift of spectral lines due to foreign gases, UFN, Vol. 66, 1958.
45. Breen, R.C. The Shift and Shape of Spectral Lines. Pergamon Press, London, 1961.
46. Plass, G.N. The Absorption of Laser Radiation Along Atmospheric Slant Paths. Appl. Opt., Vol. 5, No. 1, 1966.
47. Winters, B.M., Silverman, S., and Benedict, W.S. Line Shape in Wing Beyond the Band Head of the 4.3 μ Band CO_2. Journ. Quant. Spectr. and Rad. Transfer, Vol. 4, 527, 1964.
48. Zhevakin, S.A. and Naumov, A.P. Absorption of electromagnetic radiation by H_2O vapor at wavelengths from 10 μm to 2 cm in the upper layers of the atmosphere. Geomagnetizm i aeronomiya, Vol. 3, No. 3, 1963.
49. Zhevakin, S.A. and Naumov, A.P. Absorption of centimeter and millimeter radio waves by water vapor. Radiotekhnika i elektronika, Vol. 9, No. 8, 1964.
50. Zhevakin, S.A. and Naumov, A.P. Coefficient of water vapor absorption of electromagnetic waves in the band from 10 μm to 2 cm. Izv. vuzov, radiofizika, Vol. 6, No. 4, 1963.

51. Harris, D.L. On the Line-Absorption Coefficient Due to Doppler Effect and Damping. Astrophys. J., 108, 112, 1948.
52. Baryshev, V.A. and Krylov, G.N. Calculation of certain integrals in absorption theory. Problemy fiziki atmosfery (Problems of Atmospheric Physics), Izd. LGU, No. 3, 1965.
53. Young, C. Calculation of the Absorption Coefficient for Lines with Combined Doppler and Lorentz Broadening. J. Quant. Spectr. Rad. Transfer, Vol. 5, No. 3, 1965.
54. Armstrong, B.M. Spectrum Lines Profiles: The Voight Function. J. Quant. Spectr. Rad. Transfer, Vol. 7, No. 1, 1967.
55. Chiarella, C. and Reiche, A. On the Evaluation of Voight Spectral Line Functions. Mon. Not. Roy. Astr. Soc., Vol. 134, No. 1, 1966.
56. Surtees, W.J. Calculation of Combined Doppler and Collision Broadening. J. Opt. Soc. Am., Vol. 55, No. 7, 1965.
57. Gersten, I.I. and Foley, H.M. Combined Doppler and Collision Broadening. J. Opt. Soc. Amer., Vol. 58, No. 7, 1968.
58. Finn. G.D. and Mugglestone, D. Tables of the Line Broadening Function H(a,v). Mon. Not. Roy. Astr. Soc., Vol. 129, No. 2, 1965.
59. Young, C. Tables for Calculating the Voight Profile. Technical Report. University of Michigan. Contr. No. NASr-541 (03), July 1965.
60. Anderson, P.W. Pressure Broadening in the Microwave and Infrared Regions. Phys. Rev., Vol. 76, No. 5, 647, 1949.
61. Tsao, C.J. and Curnette, B. Line Width of Pressure Broadened Spectral Lines. J. Quant. Spectr. Rad. Transfer, Vol. 2, No. 41, 1962.
62. Mason, A.A. and Nielsen, A.H. Rotational Spectrum of Hydrogen Fluoride. J. Opt. Soc. Am., Vol. 57, No. 12, 1967.
63. McCubin, T.K. and Mooney, T.K. Study of the Strengths and Widths of Lines in the 9.4 and 10.4 μ CO_2 Bands. J. Quant. Spectr. Rad. Transfer, Vol. 8, No. 5, 1968.
64. Benedict, W.S. and Kaplan, L.D. Calculations of Line Widths in H_2O-N_2 Collisions. J. Chem. Phys., Vol. 30, No. 388, 1959.
65. Benedict, W.S. and Kaplan, L.D. Calculations of Line Widths in H_2O-H_2O and H_2O-O_2 Collisons. J. Quant. Spectr. Rad. Transfer, Vol. 4, No. 453, 1964. /385
66. Vasilevskiy, K.P. Effect of foreign gases on water vapor absorption of infrared radiation. Optika i spektroskopiya, Vol. II, No. 2, 1961.
67. Anderson, A., Chai, A., and Williams, D. Self-Broadening Effects in the Infrared Bands of Gases. J. Opt. Soc. Amer., Vol. 57, No. 2, 1967.
68. Patty, R.R., Manring, E.R., and Gardener, J.A. Determination of Self-Broadening Coefficients of CO_2 Using CO_2 Laser Radiation of 10.6μ. Appl. Opt., Vol. 7, No. 11, 1968.
69. Reiche, H.G., Jr. The Effect of Several Infrared Transparent Broadening Gases on the Absorption of Infrared Radiation in the 15μ Band of Carbon Dioxide. Technical Rep. PRA Project 05863. Univ. Michigan, May 1969.
70. Burch, D.E., Singleton, E.B., France, W.L. and Williams, D. Absorption Line Broadening in the Infrared. Appl. Opt., Vol. 1, No. 3, 1962.

71. Burch, D.E., Gryvnak, D. Patty, R.R. and Barthy, C.E. The Shape of Collision Broadened CO_2 Lines. Aeronutronic Division Philco-Ford Corp., Publication U-3203, 1968.
72. Gryvnak, D.A. and Shaw, J.H. Study of the Total Absorption by Two Samples of CO as their Total Pressures and CO Concentrations were Independently Varied. J. Opt. Soc. Am., Vol. 52, No. 539, 1962.
73. Abels, L.L. and Shaw, J.H. Study of Total Absorption Near 4.5μ by Two Samples of N_2O as their Total Pressures and N_2O Concentrations were Independently Varied. J. Opt. Soc. Amer., Vol. 53, No. 7, 1963.
74. Zachar, A.S. Equation for the Transmittance of the 2μ CO_2 Bands. J. Quant. Spectr. Rad. Transfer, Vol. 8, No. 6, 1968.
75. Moskalenko, N.I. Spectral transmission functions in certain IR bands of H_2O vapor, CO, and CH_4. Izv. AN SSSR, seriya fiziki atmosfery i okeana, Vol. IV, No. 7, 1968.
76. Golubitskiy, B.M. and Moskalenko, N.I. Spectral transmission functions in H_2O vapor and CO_2 bands. Izv. AN SSSR, seriya fiziki atmosfery i okeana, Vol. IV, No. 3, 1968.
77. Smith, W.L. A Polynomial Representation of Carbon Dioxide and Water Vapor Transmission. ESSA Tech. Rep. NESC, 47, Febr. 1969.
78. Shved, G.M. Isolated-line approximation in radiant energy transfer in the upper atmosphere. Vestnik LGU, seriya fiziki i khimii, No. 1, 1964.
79. Timofeyev, Yu.M. Applicability of the isolated spectral line model. Izv. AN SSSR, seriya fiziki atmosfery i okeana, Vol. 1, No. 12, 1965.
80. Wyatt, P.J., Stull, V.R., and Plass, G.N. Quasi-Random Model of Band Absorption. J. Opt. Soc. Amer., 52, 1209, 1962.
81. Drayson, S.R. Atmospheric Transmission in the CO_2 Band between 12 and 18μ. Appl. Opt., Vol. 5, No. 3, 1966.
82. Drayson, S.R. Atmospheric Slant Path Transmission in the 15μ CO_2 Band. Technical Report ORA, Project 05863, Univ. Michigan, 1964.
83. Andreyev, S.D. and Pokrovskiy, A.G. Comparison of calculated infrared spectra of H_2O and CO_2 with laboratory measurements, Izv. AN SSSR, seriya fiziki atmosfery i okeana, Vol. IV, No. 11, 1968.
84. Goldman, A. and Kyle, T.G. A Comparison between Statistical Model and Line by Line Calculation with Application to the 9.6μ Ozone and the 2.7μ Water Vapor Bands. Appl. Opt., Vol. 7, No. 6, 1968.
85. Auman, J., Jr. The Infrared Opacity of Hot Water Vapor. Proceedings of Specialist Conference in Molecular Radiation and its Application to Diagnostic Techniques. NASA TMX-53711, 1968.
86. Pokrovskiy, A.G. A method of calculating the spectral absorption of infrared radiation in the atmosphere. Problemy fiziki atmosfery (Problems of Atmospheric Physics), No. 5, Izd. LGU, 1967. /386
87. Kondrat'yev, K.Ya. and Timofeyev, Yu.M. A numerical experiment to investigate the transmission functions of atmospheric

gases. Aktinometriya i optika atmosfery. Trudy Shestogo mezhvedomstvennogo soveshchaniya po aktinometrii i optike atmosfery. Izd-vo "Valgus," Tallin, 1968.
88. Kondrat'yev, K.Ya. and Timofeyev, Yu.M. Direct methods of calculating the transmission functions of atmospheric gases (a survey), Izv. AN SSSR, seriya fiziki atmosfery i okeana. Vol. III, No. 2, 1967.
89. Shaw, J.H. Empirical Methods for Computing the Integrated Absorptance of Infrared Bands of Atmospheric Gases at Nonuniform Pressures. Appl. Opt., Vol. 2, No. 6, 1963.
90. Timofeyev, Yu.M. The transmission functions of the real atmosphere. Problemy fiziki atmosfery [Problems of Atmospheric Physics]. No. 5, Izv. LGU, 1967.
91. Kondrat'yev, K.Ya. and Timofeyev, Yu.M. Numerical simulation of transmission functions for narrow spectral intervals in the 15-μm CO_2 band, Izv. AN SSSR, seriya fiziki atmosfery i okeana, Vol. V, No. 4, 1969.
92. Timofeyev, Yu.M. On the accuracy of approximate methods of accounting for atmospheric inhomogeneity. Problemy fiziki atmosfery, No. 6, Izv. LGU, 1968.
93. Niylisk, Kh. Yu. Toward improvement of atmospheric thermal radiation calculations, Aktinometriya i optika atmosfery. Trudy Shestogo mezhvedomstvennogo soveshchaniya po aktinometrii i optike atmosfery. Izd-vo "Valgus," Tallin, 1968.
94. Walshaw, C.D. and Rodgers, C.D. The Effect of the Curtis-Godson Approximation in the Accuracy of the Radiative Heating-Rate Calculations. Quart. J. Roy. Meteorol. Soc., 89, 122-130, 1963.
95. Goody, R.M. The transmission of Radiation through an Inhomogeneous Atmosphere. J. Atm. Sci., Vol. 21, No. 6, 1964.
96. Kondrat'yev, K.Ya. and Timofeyev, Yu.M. Applicability of approximate methods of accounting for atmospheric inhomogeneity in computing transmission functions for the water vapor rotational band. Izv. AN SSSR, seriya fiziki atmosfery i okeana, Vol. III, No. 3, 1967.
97. Armstrong, B.H. Analysis of the Curtis-Godson Approximation and Radiation Transmission through Inhomogeneous Atmospheres. J. Atm. Sci., Vol. 25, No. 2, 1968.
98. Kaplan, L.D. A Method for Calculation of Infrared Flux for Use in Numerical Models of Atmospheric Motion. In: The Atmosphere and the Sea in Motion. Rockefeller Inst. Press, page 170.
99. McClatchey, R.A. Infrared Heat Transfer by Atmospheric Water Vapor. Department of Meteorology, Massachusetts Institute of Technology, Cambridge, Massachusetts, August 1961.
100. Lavrent'yev, M.A. and Lyusternik, L.A. Kurs variatsionnogo ischisleniya (Textbook of Variational Calculus), GITTL, Moscow-Leningrad, 1950.
101. Tatarskiy, V.I. Rasprostraneniye voln v turbulentnoy atmosfere (Wave Propagation in the Turbulent Atmosphere), Izd-vo "Nauka," Moscow, 1967.
102. Burch, D.E., Howard, J.N., and Williams, D. Infrared Transmission of Synthetic Atmospheres. V. Absorption Laws for

Over-Lapping Bands, J.Opt. Soc. Amer., 46, 452 (1956).
103. Hoover, G.H., Hathway, C.F., and Williams, D. Infrared Absorption by Over-Lapping Bands of Atmospheric Gases. Appl. Opt., Vol. 6, No. 3, 1967.
104. Tubbs, L.D., Hathway, C.E., and Williams, D. Further Studies of Over-Lapping Bands. Appl. Opt., Vol. 6, No. 8, 1967.
105. Kuznetsova, E.S., and Podkladenko, M.V. Emissivity of a mixture of CO_2 and H_2O at temperatures up to 1000°K, Zh. prikladnoy spektroskopii, Vol. VI, No. 5, 1967.
106. Timofeyev, Yu.M. Gas-mixture transmission. Problemy fiziki atmosfery. No. 7, Izd. LGU, 1969. /387
107. Plass, G.N. and Fivel, D.I. Influence of Doppler Effect and Damping on the Line-Absorption Coefficient and Atmospheric Radiation Transfer. Astrophys. J., Vol. 117, No. 1, 1953.
108. Shved, G.M. and Tsaritsyna, I.V. Transmission functions for infrared radiation in the mesosphere and upper stratosphere. Problemy fiziki atmosfery, No. 2, Izd. LGU, 1963.
109. Rodgers, C.D. and Walshaw, C.D. The Computation of Infrared Cooling Rate in Planetary Atmospheres. Quart. J. Royal Met. Soc., Vol. 92, No. 391, 1966.
110. Yamada, H.Y. Total Radiance and Equivalent Widths of Isolated Lines with Combined Doppler and Collision Broadening Profiles. J. Quant. Spect. and Rad. Transfer, Vol. 8, No. 8, 1968.
111. Johnson, P.A. and Korb, C.L. A Table of the Equivalent Widths of Isolated Lines with Combined Doppler and Collision Broadening Profiles. J. Quant. Spectr. and Rad. Transfer, Vol. 8, No. 7, 1968.
112. Kyle, T.G. Absorption by Doppler-Lorentz Atmospheric Lines. J. Quant. Spectr. and Rad. Transfer, Vol. 8, No. 8, 1968.

To Chapter 2

1. Aver'yanov, I.P. et al. Measurement of the earth's thermal radiation into space from a high-altitude automated geophysical station during the total solar eclipse of 15 February 1961. ISZ (Artificial Earth Satellites), No. 14, Izd. AN SSSR, 1962.
2. Kasatkin, A.M. A high-altitude optical station for atmospheric studies. ISZ, No. 15, Izd. AN SSSR, 1963.
3. Markov, M.N., Merson, Ya.I., and Shamilev, M.R. Investigation of the thermal radiation field of the stratosphere and troposphere in the infrared from geophysical aerostats. Kosmicheskiye issledovaniya, Vol. 1, No. 2, 1963.
4. Liventsov, A.V. et al. Investigation of the angular distribution of the earth's thermal radiation into space from a geophysical rocket launched on 27 August 1968. Kosmicheskiye issledovaniya, Vol. IV, No. 4, 1966.
5. Markov, M.N., Merson, Ya.I. and Shamilev, M.R. Investigation of the angular and spectral distributions of the earth's radiation in the infrared from the Kosmos 45 artificial earth

satellite, Kosmicheskiye issledovaniya, Vol. IV, No. 4, 1966.
6. Markov, M.N., Merson, Ya.I. and Shamilev, M.R. Investigation of the angular distribution of radiation from the earth and its atmosphere from geophysical rockets and aerostats. Issledovaniya kosmicheskogo prostranstva (Investigation of Cosmic Space), Izd-vo "Nauka," Moscow, 1965.
7. Bazhulin, P.A., Kartashev, A.V., and Markov, M.N. Angular and spectral distributions of the earth's infrared radiation. Issledovaniya kosmicheskogo prostranstva. Izd-vo "Nauka," Moscow, 1965.
8. Markov, M.N., Merson, Ya.I., and Shamilev, M.R. Layers of the upper atmosphere that radiate in the infrared. Issledovaniya kosmicheskogo prostranstva. Izd-vo "Nauka," Moscow, 1965.
9. Markov, M.N. Infrared radiation of the upper atmosphere and its structure. FIAN, Preprint No. 70, Moscow, 1968.
10. Lebedinskiy, A.I. et al. Infrared spectrophotometry of the earth's thermal radiation. Issledovaniya kosmicheskogo prostranstva. Izd-vo "Nauka," Moscow, 1965.
11. Lebedinsky, A.I., Boldyrev, V.G., Tulupov, V.I. et al. The Spectrum of the Earth's Heat Radiation According to Observation from the Cosmos 45, Cosmos 65, and Cosmos 92 Satellites, Space Research, Vol. 7/2, Amsterdam, N.-Holl. Publ. Co., 1967, pp. 905-914.
12. Lebedinskiy, A.I. et al. Statistical characteristics of the earth's radiation into space in the 7-26-μm wavelength band. Geomagnetizm i aeronomiya, Vol. VII, No. 3, 1967. /388
13. Lebedinskiy, A.I. et al. Correlation relationships of the spectral intensity of the earth's outgoing infrared radiation. Geomagnetizm i aeronomiya, Vol. 8, No. 1, 1968.
14. Lebedinskiy, A.I. et al. Latitude variations of the spectral intensities of the earth's radiation into space according to observations from the Kosmos 45 and Kosmos 65 satellites. Geomagnetizm i aeronomiya, Vol. 8, No. 2, 1968.
15. Lebedinskiy, A.I. et al. Meteorological interpretation of outgoing-radiation spectra registered by the Kosmos satellites. Geomagnetizm i aeronomiya, Vol. 8, No. 1, 1968.
16. Lebedinskiy, A.I., Polyakova, T.G., and Tulupov, V.I. Angular and spectral distributions of the earth's infrared radiation into space near the horizon according to satellite observations. Geomagnetizm i aeronomiya, Vol. 8, No. 2, 1968.
17. Livantsov, A.V. et al. Experimental determination of the earth's outgoing radiation. DAN SSSR, Vol. 146, No. 2, 1962.
18. Markov, M.N., Merson, Ya.I., and Shamilev, M.R. The radiation of the ionosphere's layers in the infrared. DAN SSSR, Vol. 167, No. 4, 1966.
19. Walker, R.G., Cuniff, C.V., and D'Agati, A.D. Measurement of the Infrared Horizon of the Earth. AFCRL-66-631, Environm. Res. Pap. No. 223, Sept. 1966.
20. Kondrat'yev, K.Ya. Satellites and meteorology. Uspekhi fiz. nauk, Vol. 74, No. 2, 1961.
21. Kondratyev, K.Ya. Radiation in the Atmosphere. Academic Press, New York, 1969.

22. Girard, A. Experimental analysis of the infrared contrast between the earth and space, Space Res., Vol. 7/2, North Holl. Publ. Co., Amsterdam, 1967, pp, 934-952.
23. Lienesh, J.H. and Wark, D.Q. Infrared Limb Darkening of the Earth from Statistical Analysis of Tiros Data. J. Appl. Meteor., Vol. 6, No. 4, 1967, pp. 674-682.
24. Ruff, I., Koffler, R., Fritz, S., Winston, J.S., and Rao, P.K. Angular Distribution of Solar Radiation Reflected from Clouds as Determined from Tiros IV Radiometer Measurements. J. Atm. Sci., Vol. 25, No. 2, 1968, pp. 323-332.
25. Wexler, R. Infrared and Visual Radiation Measurements from Tiros III. Appl. Opt., Vol. 3, No. 2, 1964.
26. Anthony, R. and Smiley, V.N. Infrared Horizon Measurements from Near-Orbiting Altitudes. Gen. Dynam. Astronaut., San Diego, Calif., 1962.
27. Block, L.C. and Zachor, A.S. Inflight Satellite Measurements of Infrared Spectral Radiance of the Earth. Appl. Opt., No. 2, Vol. 3, 1964.
28. Larsen, S.H.H., Fujita, T., and Fletcher, W.L. Evaluation of Limb Darkening from Tiros III Radiation Data. Dept. Geophys. Sci. Univ. Chicago, Res. Pap., No. 18, August 1963.
29. Burn, J.W. The Application of the Spectral and Spatial Characteristics of the Earth's Infrared Horizon to Horizon Scanners. IEEE Trans. on Aerospace, Vol. AS-1, No. 2, 1963.
30. Vetlov, I.P. Meteorological observations from artificial earth satellites. Meteorologiya i gidrologiya, No. 4, 1967.
31. Vetlov, I.P. Meteorological research using artificial earth satellites. Meteorologiya i gidrologiya za 50 let Sovetskoy vlasti (Meteorology and Hydrology after 50 Years of The Soviet Regime), Gidrometeoizdat, Leningrad, 1967.
32. Beskin, V.A. et al. Actinometric instruments of Soviet weather satellites. Trudy GGO, No. 221, 1968.
33. Krasil'shchikov, L.B. Calibration principles for long wave actinometric instruments on weather satellites. Trudy GGO, No. 221, 1968. /389
34. Kondrat'yev, L.Ya. Meteorologicheskiye issledovaniya s pomoshch'yu raket i sputnikov (Meteorological Research Using Rockets and Satellites), Gidrometeoizdat, Leningrad, 1962.
35. Kondrat'yev, K.Ya. Meteorologicheskiye sputniki (Weather Satellites), Gidrometeoizdat, Leningrad, 1963.
36. Kondrat'yev, K.Ya., Borisenkov, Ye.P. and Morozkin, A.A. Prakticheskoye ispol'zovaniye dannykh meteorologicheskikh sputnikov (Practical Utilization of Data from Weather Satellites), Gidrometeoizdat, Leningrad, 1966.
37. Bandeen, W.R. Experimental Approaches to Remote Atmospheric Probing in the Infrared from Satellites. Goddard Space Flight Center, Greenbelt, Maryland, Preprint X-662-68-146, May 1968.
38. Nimbus II Users Guide. Goddard Space Flight Center, NASA, Greenbelt, Md., July 1966.
39. Bartman, F.L. The Calibration and Interpretation of Data from the 0.55-0.85 Micron and 0.2-0.4 Micron Channels of the F-1

and F-4 MRIR Radiometers. Univ. Michigan. ORA Project 05863, Ann Arbor, February 1966.
40. Kondrat'yev, K.Ya. and Timofeyev, Yu.M. Inverse problems of satellite meteorology. Meteorologiya i gidrologiya, No. 11, 1967.
41. Kondrat'yev, K.Ya. and Timofeyev, Yu.M. Certain problems of atmospheric thermal sounding. Problemy fiziki atmosfery (Problems of Atmospheric Physics), No. 5. Izd. LGU, 1967.
42. Dreyfus, M.G. and Hilleary, D.T. Satellite Infrared Spectrometer Design and Developments. Aerospace Engineering, Vol. 21, No. 42, 1962.
43. Hilleary, D.T., Heacock, E.L., Morgan, W.A., et al. Indirect Measurements of Atmospheric Temperature Profiles from Satellites. III: The Spectrometers and Experiments. Mon. Wea. Rev., Vol. 94, No. 6, 1966.
44. Hilleary, D.T., Wark, D.Q., and James, D.G. An Experimental Determination of the Atmospheric Temperature Profile by Indirect Means. Nature, Vol. 205, No. 4970, 1965.
45. Hanel, R.A. and Chaney, L.W. The Merits and Shortcomings of a Michelson Type Interferometer to Obtain the Vertical Temperature and Humidity Profile. Proceedings of the XVII IAF Congress, Madrid, 9-15 Oct. 1966.
46. Chaney, L.W. Fundamentals of Fourier Transform Spectroscopy. The University of Michigan. ORA Project 05863, Ann Arbor, February 1967.
47. Chaney, L.W., Drayson, S.R., and Young, C. Fourier Transform Spectrometer-Radiative Measurements and Temperature Inversion. Appl. Optics, Vol. 6, No. 2, 1967.
48. Hilleary, D.T., Wark, D.Q., and Saiedy, F. Indirect Measurements of Atmospheric and Surface Temperatures. Proceedings of the XVII IAF Congress, Madrid, 9-15 October 1966, Vol. 11 (Application Satellites). Polish Scientific Publishers, Warsaw, 1967.
49. Heidemann, M. A study of the use of Fabry-Perot interferometers for resolution of the infrared water vapor spectrum in the upper atmosphere. Meteor. Inst. der Ludwig-Maximilians-Universität Munchen, Research Report W66-02, Nov. 1966.
50. Houghton, J.T. and Smith, S.D. Satellite-Borne Meteorological Experiments. Space. Res. U.K. University Reports, 1962-1963, London, Roy. Soc., 1964.
51. Smith. S.D. and Pidgeon, C.R. Application of Multiple-Beam Interferometric Methods to the Study of CO_2 Emission at 15 Micron. Les Spectres infra-rouges des astres (The Infrared Spectra of the Stars), Mem. de la soc. roy. des sci. de Liege. 5th Series, Vol. IX, Cointe Sclessin, 1964.
52. Houghton, J.T. and Shaw, J.H. The Deduction of Stratospheric Temperature from Satellite Observations of Emission by the 15 Micron CO_2 Band. Ibid.
53. Houghton, J.T. The Meteorological Significance of Remote Measurements of Infrared Emission from Atmospheric Carbon Dioxide. Quart. J. Roy. Met. Soc., Vol. 87, No. 371, 1961. /390
54. Peckham, G., Rodgers, C.D., Houghton, J.T., and Smith S.D. Remote Temperature Sensing of the Earth's Atmosphere Using a

Selective Chopper Radiometer. Proceedings of the Symposium on Electromagnetic Sensing of the Earth from Satellites. Miami Beach, Florida, 22-24 Nov. 1965, Brooklyn Polytechn. Inst. Press, New York, 1967.
55. Houghton, J.T., Smith, S.D., Peckham, G., and Williamson, E.J. Remote Temperature Sensing of the Earth's Atmosphere Using a Selective Chopper Radiometer. Space Res., Vol. 7/2, (p. 933), Amsterdam, North-Holl. Publ. Co., 1967.
56. Drummond, A.J., Hickey, J.R., Scholes, W.J., and Lane, E.G. Multi-Channel Radiometer Measurements of Solar Irradiance. Journal of Spacecraft and Rockets, Vol. 4, No. 9, 1967.
57. Nordberg, W. Inference of Properties of the Earth from Satellite Measurements of Infrared Emission. In: Thermophys. Spacecraft and Planet. Bodies. New York-London, Acad. Press, 1967.
58. Meteorology. COSPAR Trans., No. 5, 1968, pp. 364-381.
59. Thelen, A. Circularly Wedged Optical Coatings. I: Theory. Appl. Opt., Vol. 4, No. 6, 1965.
60. Apfel, S.N. Circularly Wedged Optical Coatings. II: Experimental. Appl. Opt., Vol. 4, No. 6, 1965.
61. Albert, E.G. The Improved Tiros Operational Satellite. NESC, Techn. Memorandum, No. 7, Wash., Aug. 1968.
62. Corliss, W.R. Scientific Satellites. NASA SP-133, 1967.
63. Condron, T.P. Optical Radiation Measurements Program, AFCRL in Space. A Summary of AFCRL Rocket and Satellite Experiments. January 1966-July 1967, AFCRL, Bedford, Mass., 1967.
64. Kondrat'yev, K.Ya., and Yakushevskaya, K.Ye. Angular distribution of the outgoing thermal radiation in various regions of the spectrum, ISZ (Artificial Earth Satellites), No. 14, 1962.
65. Kondrat'yev, K.Ya. and Yakushevskaya, K.Ye. Angular distribution of the thermal radiation of the earth-atmosphere system in various regions of the spectrum. Trudy GGO, No. 166, 1964.
66. Kondrat'yev, K.Ya. and Yakushevskaya, K.Ye. The spectral distribution of the outgoing radiation. Problemy fiziki atmosfery, No. 2, Izd. LGU, 1963.
67. Yakushevskaya, K.Ye. On the angle dependence of the spectral distribution of the outgoing thermal radiation. Problemy fiziki atmosfery, No. 3, Izd. LGU, 1965.
68. Kondrat'yev, K.Ya. and Niylisk, Kh.Yu. Certain results of theoretical calculations of the angular distribution of the thermal radiation of the earth as a planet under real conditions. Trudy GGO, No. 166, 1964.
69. London, J. The Use of Satellite Observations for Atmospheric Radiation Studies. Archiv für Meteorologie, Geophysik und Bioklimatologie, Ser. B., Vol. 12, No. 1, 1962.
70. Koprova, L.I. and Malkevich, M.S. The thermal radiation of the spherical atmosphere, Kosmicheskiye issledovaniya, Vol. II, No. 6, 1964.
71. McGee, R.A. An Analytical Infrared Radiation Model of the Earth. Appl. Opt., Vol. 1, No. 5, 1962.
72. McGee, R.A. Far Infrared Radiation Model of the Earth. AIAA

(American Institute of Aeronautics and Astronautics) J., Vol. 1, No. 9, 1963.
73. Hanel, R.A., Bandeen, W.R., and Conrath, B.J. The Infrared Horizon of the Planet Earth. J. Atm. Sci., Vol. 20, No. 2, 1963.
74. Wark, D.Q., Yamamoto, G. and Lienesch, J.H. Methods of Estimating Infrared Flux and Surface Temperature from Meteorological Satellites. J. Atm. Sci., Vol. 19, No. 5, 1962.
75. Wark, D.Q., Alishouse, J. and Yamamoto, G. Variation of the Infrared Spectral Radiance Near the Limb of the Earth. Appl. Opt., Vol. 3, No. 2, 1964. /391
76. Woestman, J.W. Earth Radiation Model for Infrared Horizon Sensor Applications. Infrared Physics, Vol. 3, No. 2, 1963.
77. Yakushevskaya, E.Ya. Comparison of experimental and theoretically calculated values of the atmosphere's nonisotropic thermal radiant intensity. Problemy fiziki atmosfery, No. 3, Izd. LGU, 1965.
78. Yakushevskaya, K.Ye. Influence of the angular dependence of the reflectivity of a smooth water surface on the angular distribution of the thermal outgoing radiation. Problemy fiziki atmosfery, No. 4, Izd. LGU, 1966.
79. Yakushevskaya, K.Ye. Angular distribution of the long wave outgoing radiation with various methods of taking the pressure variation of absorption into account. Problemy fiziki atmosfery, No. 6, Izd. LGU, 1968.
80. Goldberg, I.L.A. A Very High Resolution Radiometric Experiment for ATS F and G. Goddard Space Flight Center. Preprint. X-622-68-26, Jan. 1968.
81. Yakushevakaya, K.Ye. Contribution of the earth's surface, clouds, and the various atmospheric layers to the outgoing radiation. Problemy fiziki atmosfery, No. 3, Izd. LGU, 1965.
82. Bates, J.C. Spectral Analysis of the Spatial Distribution of the Earth's 15μ Carbon Dioxide Horizon Profile. Infrared Physics, Vol. 7, No. 4, 1968.
83. Bertram, F.-W. Thermal emission of the atmosphere in the spectral region between 3.1 and 4.2 μm. Pure and Appl. Geophys., Vol. 68, No. 3, 1967.
84. Wetmore, W.C. Nimbus 3 Soundings Exceed Expectations. Aviat. Week and Space Technol., Vol. 90, No. 18, 1969.
85. Hanel, R.A. and Chaney, L. The Merits and Shortcomings of a Michelson Type Interferometer to Obtain the Vertical Temperature and Humidity Profiles. XVII IAF Congress, Madrid, 1966. Proc. Vol. 2, Applic. Sat. Paris et al., 1967.
86. Hickey, J .R., Garvey, J.A., Scholes, W.J., et al. Calibration of the Earth Albedo Experimental Package of the OSO Satellite Series. XVII IAF Congress, Madrid, 196q. Proc. Vol. 2, Applic. Sat. Paris et al. 1967, pp. 237-246.
87. Drummond, A.J., Hickey. J.R., Scholes, W.J., and Lane, E.G. The Calibration of Multi-Channel Radiometers for Application in Spacecraft and Space Simulation Program. XVII IAF Congress, Belgrade, 1967, Proc. Vol. 2, Spacecraft Syst. Educ. Oxford et al., 1968, pp. 407-422.

88. Hilleary, D.T., Anderson, S.P., Caroli, A.R., and Hickey, J.R. The Calibration of a Satellite Infrared Spectrometer. XVIII IAF Congress, Belgrade, 1967. Proc. Vol. 2. Spacecraft Syst. Educ. Oxford et al., 1968, pp. 423-437.
89. Girard, A. and Lemaitre, M.-P. Experimental profiles of the earth's infrared horizon. Tacit Experiment 2. Communication Presented at the 13th Plenary Session of COSPAR, Prague, 19-24 May 1969.
90. Hilleary, D.T., Wark, D.Q., and Saiedy, F. Indirect Measurements of Atmospheric and Surface Temperatures. XVII IAF Congress, Madrid, 1966. Prov. Vol. 2, Applic. Sat. Paris et al., 1967, pp. 219-225.
91. Nordberg, W. Development of Meteorological Satellites in the United States. WMO Bull., Jan. 1969.
92. Rados, R.M. Atmospheric Measurements from Satellites. AIAA Paper, No. 9, 1969.
93. Porter, P.W. Meteorological Research Satellites — Nimbus D. Aeronaut. J., Vol. 73, No. 700, 1969.
94. Suomi, V., Krauss, R. and Haar, T.V. On the Possibility of Sounding the Atmosphere from Geostationary Altitude. Special Report No. 1, Contr. NAS5-11542, Univ. Wisconsin, Febr. 21, 1969.
95. Suomi, V., Hanson, K.J. and Haar, T.V. The Theoretical Basis /392 for Low-Resolution Radiometer Measurements from a Satellite. Studies in the Atmospheric Energetics Based on Aerospace Probings. Annual Rept. 1966. Dept. Meteorol., Univ. Wisconsin, March 1967, pp. 79-100.
96. Nelson, D.F. and Parents, R. The Prototype Flat-Plate Radiometers for the ESSA III Satellite. Ibid., pp. 119-129.
97. Parents, R.J. and Nelson, D.F. Design of a Flat-Plane Radiometer for Tiros-M Spacecraft. Studies in Atmospheric Energetics Based on Aerospace Probings. Annual Rept. 1967. Dept. of Meteorol. Univ. Wisconsin, May 1968, pp. 179-190.
98. House, F.B. On the Interpretation of Long-Wave Radiation Data from Explorer VII Satellite. Meteorological Satellite Instrumentation and Data Processing. Final Sci. Rept. on MASw-65, 1958-1968, Dept. Meteorol. Univ. Wisconsin, Dec. 1968, pp. 151-164.
99. Bartman, F.L. Earth Reflectance Patterns Measured by Radiometer on High Altitude Balloon Flights. Techn. Rept. Contr. NASr-54(03). Univ. Michigan, Dec. 1968.
100. Lebedinskiy, A.I. et al. Estimation of measurement-nonsimultaneity corrections to be applied to correlation formulas between spectral intensities of the earth's radiation. Geomagnetizm i aeronomiya, Vol. IX, No. 2, 1969.
101. Belov, P.N., Kurilova, Yu.V., and Berkovich, L.V. Certain characteristics of the outgoing-radiation fields. Trudy GMTs, No. 30, 1968.
102. Thomas, J.R., Jones, E.E., and Peterson, R.E. Two Promising Empirical Techniques for Closed Form Functional Representation of 14-16 Micron Radiance Profiles. Infrared Phys., Vol. 8, No. 2, 1968.

103. Haar, T.H.V. Variations of the Earth's Radiation Budget. Meteorological Satellite Instrumentation and Data Processing. Final Sci. Rept. on NASw-65, 1958-1968. Dept. Meteorol. Univ. Wisconsin, Dec. 1968, pp. 31-107.
104. Ganopol'skiy, V.A. et al. The scientific program and scientific instrument package of the Kosmos 149 artificial earth satellite. Izv. AN SSSR, seriya fiziki atmosfery i okeana, Vol. 5, No. 3, 1969.
105. Klimchuk, Ye.F. et al. Instruments for measurement of the earth's brightness from the Kosmos 149 satellite. Izv. AN SSSR, seriya fiziki atmosfery i okeana, Vol. 5, No. 3, 1969.
106. Krasovskiy, V.I. On the infrared radiation of the upper atmosphere. Kosmicheskiye issledovaniya, Vol. VI, No. 6, 1968.

To Chapter 3

1. Kondratyev, K.Ya. et al. Radiative Factors of the Heat Regime and Dynamics of the Upper Atmospheric Layers. Les Problemes Meteorologiques de la stratosphere et de la mesosphere (Meteorological Problems of the Stratosphere and Mesosphere), Presses universitaires de France, Paris, 1966.
2. Kondratyev, K.Ya. Radiation in the Atmosphere. Academic Press, New York, 1969.
3. Zuyev, V.Ye. Prozrachnost' atmosfery dlya vidimykh i infrakrasnykh luchey (Transparency of the Atmosphere for Visible and Infrared Light), Izd-vo "Sov. Radio," Moscow, 1966.
4. Kondrat'yev, K.Ya. et al. Certain results from ground studies of the infrared absorption spectrum and the atmosphere's thermal radiation. Izvestiya AN SSSR, Seriya fiziki atmosfery i okeana, Vol. 1, No. 4, 1965.
5. Kondratyev, K.Ya. et al. Direct Solar Radiation up to 30 km and Stratification of Attenuation Components in the Stratosphere. Appl. Opt., Vol. 6, No. 2, 1967.
6. Kondrat'yev, K.Ya. and Nikol'skiy, G.A. The direct solar radiation and the aerosol structure of the troposphere and stratosphere during the IQSY. Trudy Vsesoyuznoy konferentsii po itogam MGSS (Transactions of the All-Union Conference on IQSY Results), Moscow, Izd-vo "Nauka," 1968.
7. Kondratyev, K.Ya. and Nikolsky, G.A. Direct Solar Radiation and Aerosol Structure of the Atmosphere from Balloon Measurements in the Period of the IQSY. Sveriges Met. och Hydrol. Inst. Meddel., Ser. B, No. 28, 1968. /393
8. Elterman, L. Parameters for Attenuation in the Atmospheric Windows for Fifteen Wavelengths. App.. Opt., Vol. 3, No. 6, 1964.
9. Bertram, F.-W., Bolle, H.-J., Rabus, D., Seeger, W. Untersuchungen zur Emission, Transmission und Reflexion infraoter Strahlung in der Bodennahen Atmosphare (Studies of the emission, transmission, and reflection of infrared radiation in the atmosphere near the ground), Meteor. Inst. der Univ. München, 1967.

10. Bolle, H.-J. Infrarotspektroskopie als Hilfsmittel und Gegenstand meteorologischer und planetischer Forschung (Infrared spectroscopy as a tool in and object of meteorological and planetary research), Met. Inst. Univ. München, BWWF-FB W 67-17, München, July 1967.
11. Tannhauser, J. On the Influence of Atmospheric Transmission Functions on Infrared Measurements in Planetary Atmospheres. Met. Inst. Univ. München, NSG-305, München, Jan. 1967.
12. Zhvalev, V.F., Kondrat'yev, K.Ya., and Ter-Markaryants, N.Ye. Calculation of spectral outgoing-radiation values and contrasts between underlying-surface and cloud radiation temperatures in the context of the problem of detecting clouds from artificial earth satellites. Trudy GGO, No. 203, 1967.
13. Kostyanoy, G.N. Influence of the underlying-surface reflectivity on the longwave radiant fluxes in the free atmosphere. Izv. AN SSSR, seriya fiziki atmosfery i okeana, Vol. 1, No. 9, 1965.
14. Hovis, W.A. Jr. Optimum Wavelength Intervals for Surface Temperature Radiometry. Appl. Opt., Vol. 5, No. 5, 1966.
15. Hovis, W.A. Jr. and Tobin, M. Spectral Measurements from 1.6 to 5.4 Microns of Natural Surfaces and Clouds. Appl. Opt., Vol. 6, No. 8, 1967.
16. Gayevskiy, V.L. Large-area surface temperatures. Trudy GGO, No. 26(88), 1951.
17. Kellog, W.W., Buettner, K.J.K., and May, E.C. Meteorological Satellite Observation of Thermal Emission (Part II of an Examination of the Application to Satellite Meteorology of Various Segments of the Electromagnetic Spectrum). Memorandum RM-4392-NASA, The Rand Corp., Santa Monica, Calif., Dec. 1964.
18. Buettner, K.J.K., Kern, C.D. The Determination of Infrared Emissivities of Terrestrial Surfaces. Journ. Geophys. Res., Vol. 70, No. 6, 1965.
19. Bramson, M.A., Zel'manovich, I.L., and Kuleshova, G.I. The infrared emissivity of water. Trudy GGO, No. 152, 1964.
20. Feygel'son, Ye.M. Radiatsionnyye protsessy v sloistoobraznykh oblakakh (Radiation Processes in Stratus Clouds), Izd-vo "Nauka," Moscow, 1964.
21. Bauer, E. The Scattering of Infrared Radiation from Clouds. Appl. Opt., Vol. 3, No. 2, 1964.
22. Yamamoto, G., Tanaka, M., Kamitani, K. Radiative Transfer in Water Clouds in the 10-Micron Window Region. Journ. Atm. Sci., Vol. 23, No. 3, 1966.
23. Gayevskiy, V.L. Certain results from albedo measurements of stratus clouds in the 8-12-micron region of the spectrum. Trudy GGO, No. 152, 1964.
24. Novosel'tsev, Ye.P. On the emissivities of upper- and middle-level clouds. Trudy GGO, No. 196, 1966.
25. Chapurskiy, L.I. Experimental studies of the spectral brightness characteristics of the clouds, atmosphere, and underlying surface in the 0.3-2.5-μm wavelength range. Trudy GGO, No. 196, 1966.

26. Espinola, R.P. and Blau, H.H. Near Infrared Optical Properties of Sunlit Terrestrial Clouds. Trans. Am. Geophys. Un., Vol. 47, No. 1, 1966.
27. Kondrat'yev, K.Ya. The planetary atmospheric research program; radiation factors in weather and climate. Meteorologiya i gidrologiya, No. 6, 1968.
28. Burroughs, W.J., Harries, J.E., and Gebbie, H.A. Submillimetre Absorption by Isotopic and Vibrationally Excited Forms of Water Vapor. Nature, Vol. 222, No. 5194, 1969, pp. 658-660.
29. Shaw, J.H., Chapman, R.N., Howard, J.N., and Okholm, M.L. A Grating Map of the Solar Spectrum from 3.0 to 5.2 Microns. Astrophys. J., 113(2); 268-298, March 1951. /394
30. Kunde, V.G., Theoretical Relationship Between Equivalent Black-Body Temperatures and Surface Temperatures Measured by the Nimbus High-Resolution Infrared Radiometer. Observations from Nimbus I Meteorological Satellite, NASA SP-89, 1965.
31. Hovis. W.A. Jr., Blaine, L.R., and Callahan, W.R. Infrared Aircraft Spectra over Desert Terrain 8.5 to 16μ. Appl. Opt., Vol. 7, No. 6, 1958.
32. Kuhn, P.M., Suomi, V.E. Airborne Radiometer Measurements of Effects of Particulars on Terrestrial Fluxes. J. Appl. Met., Vol. 4, No. 2, 1965.
33. Zdunkowski, W., Henderson, D., and Hales, J.V. The Influence of Haze on Infrared Radiation Measurements Detected by Space Vehicles. Tellus, Vol. 17, No. 2, 1965.
34. Lorenz, D. Measurements of ground surface temperature from a helicopter. Ber. der Deutsche Wetterd., Vol. 11, No. 82, 1962.
35. Novosel'tsev, Ye.P. Selection of spectral range for determination of underlying-surface and cloud temperatures from satellites by means of a radiometer. Trudy GGO, No. 196, 1965.
36. Kondrat'yev, K.Ya., Novosel'tsev, Ye.P., and Ter-Markaryants, N.Ye. Determination of underlying-surface and cloud temperatures from weather satellites. Trudy GGO, No. 196, 1966.
37. Gayevskiy, V.L. and Rabinovich, Yu.I. Correcting for the influence of the atmosphere on the results of ground-surface radiation-temperature measurements from artificial earth satellites. Trudy GGO, No. 166, 1964.
38. Malkevich, M.S. Certain problems in the interpretation of the earth's outgoing radiation field. I. Determination of underlying-surface temperature and cloud top height. Trudy GGO, No. 166, 1964.
39. Boldyrev, V.G. On the use of outgoing radiation measurements to calculate the temperature of the earth's surface and cloud top heights. Trudy MMTs, No. 8, 1965.
40. Boldyrev, V.G. Calculation of atmospheric transfer functions in the 8-12-μm interval for the northern hemisphere. Izv. AN SSSR, seriya fiziki atmosfery i okeana, Vol. 1, No. 7, 1965.
41. Boldyrev, V.G., Koprova, L.I., and Malkevich, M.S. Correction for the variations of the vertical temperature and humidity profiles in determining underlying-surface temperatures from

the outgoing radiation. Izv. AN SSSR, seriya fiziki atmosfery i okeana, Vol. 1, No. 7, 1965.
42. Boldyrev, V.G. Computer compilation of surface-temperature and cloud-top-height maps from weather satellite data. Trudy MMTs, No. 11, 1966.
43. Malkevich, M.S. Certain problems in the interpretation of radiation measurements from satellites. Kosmicheskiye issledovaniya, Vol. II, No. 2, 1964.
44. Wark, D.Q., Yamamoto, G. and Lienesh, J.H. Methods of Estimating Infrared Flux and Surface Temperature from Meteorological Satellites. J. Atm. Sci., Vol. 19, No. 5, 1962.
45. Lönnqvist, O. Window Radiation Chart for Estimating Surface Temperature from Satellite Observations. Tellus, Vol. 15, No. 3, 1963.
46. Möller, F. Atmospheric Water Vapor Measurements at 6-7 Microns from a Satellite. Planet. Space Sci., Vol. 5, 1961.
47. Möller, F. Certain preliminary results from reduction of radiation measurements from Tiros II. Arch. Meteor. Geophys. Biokl., Ser. B. Vol. 12, No. 1, 1962.
48. Möller, F. and Raschke, E. Evaluation of Tiros III Radiation Data. Meteor. Inst. München, NsG-305, July 1963.
49. Raschke, E. Tropospheric Water Vapor Content and Surface Temperatures from Tiros IV Radiation Data. NASA Contr. Rep. 595, Washington, D.C., September 1966.
50. Marlatt, W.E. Remote and in Situ Temperature Measurements of Land and Water Surfaces. J. Appl. Met., Vol. 6, No. 2, 1967. /395
51. Raschke, E. Reduction of infrared radiation measurements from the weather satellite Tiros III. Part II. Beitr. Phys. Atm., Vol. 38, No. 3-4, 1965.
52. Raschke, M. and Tannhäuser, I. Investigation of Atmospheric Properties Based upon Evaluation of Infrared Radiation Data Obtained from Tiros Satellites. Fin. Rep., Univ. Munich, May 1965.
53. Saiedy, F. and Hilleary, D.T. Remote Sensing of Surface and Cloud Temperatures Using the 899 cm^{-1} Interval. Appl. Opt., Vol. 6, No. 5, 1967.
54. Murav'yeva, L.V. and Ter-Markaryants, N.Ye. On the possibility of cloudage observations on the dark side of the earth from weather satellites. Trudy GGO, No. 196, 1966.
55. Gayevsky, V.L., Guseva, L.N., Kondratyev, K.Ya. et al. Meteorological Interpretation of Infrared Pictures of the Earth from Space. Pure and Appl. Geophys., Vol. 69, 1968/I.
56. Zhvalev, V.F., Kondrat'yev, K.Ya., and Ter-Markaryants, N.Ye. On the possibility of using infrared pictures of the earth to follow the dynamics of ocean currents and detect jet streams and noctilucent clouds. Izv. AN SSSR, seriya fiziki atmosfery i okeana, Vol. III, No. 11, 1967.
57. Kondrat'yev, K.Ya., Borisenkov, Ye.P., and Morozkin, A.A. Practical utilization of weather satellite data. Gidrometeoizdat, Leningrad, 1966.
58. Dombkovskaya, V.P. Reading and synoptic interpretation of infrared (IR) cloud-cover photographs. Trudy GMTs, No. 11, 1967.

59. Novosel'tsev, Ye.P. and Ter-Markaryants, N.Ye. The emissivities of water surfaces. Trudy VNMS, Gidrometeoizdat, Leningrad, 1963.
60. Gandin, L.S. and Boltenkov, V.P. Toward a method of objective analysis of actinometric information from weather satellites. Trudy GGO, No. 166, 1964.
61. Puchkov, V.V. and Titov, S.I. Use of outgoing-radiation data to reconstruct temperature and humidity fields. Izv. AN SSSR, seriya fiziki atmosfery i okeana, Vol. II, No. 1, 1966.
62. Gayevskiy, V.L. et al. Meteorological interpretation of infrared pictures of the earth from space. Meteorologiya i gidrologiya, No. 4, 1968.
63. Guseva, L.N. et al. Problems in the interpretation of infrared cloud-cover pictures from weather satellites. Trudy GGO, No. 221, 1968.
64. Fritz, S. and Rao, P.K. On the Infrared Transmission through Cirrus Clouds and the Estimation of Relative Humidity from Satellites. J. Appl. Met., Vol. 6, No. 6, 1967.
65. Krishnamurti, T.N., Papetty, A., Torres, M.E.S. On the Transmissivity of the Atmosphere in the Water Vapor Absorption (6.0-6.5 Microns) Band. Pure and Appl. Geophys., Vol. 59, No. 3, 1964.
66. Adem, J. Preliminary Model for Computing Midtropospheric and Surface Temperatures from Satellite Data. J. Geophys. Rev., Vol. 70, No. 12, 1965.
67. Kondrat'yev, K.Ya. and Ter-Markaryants, N.Ye. The possibility of detecting clouds on the night side of the earth from measurements of the outgoing thermal radiation in the atmosphere's "transparency window." Trudy GGO, No. 170, 1965.
68. Kondrat'yev, K.Ya. Interpretation of weather-satellite radiation data. Issledovaniya kosmicheskogo prostranstva, Izd-vo "Nauka," Moscow, 1965.
69. Kondratyev, K.Ya. Interpretation of Meteorological Satellite Radiation Data. Space Research IV, North-Holl. Publ. Co., Amsterdam, 1964.
70. Kondratyev, K.Ya. The Interpretation of Meteorological Satellite Radiation Data. Proc. Inter-regional Seminar on Interpretation and Use of Meteorological Satellite Data. Jap. Met. Agency, Tokyo, 1965. /396
71. Kondrat'yev, K.Ya. Meteorologicheskiye issledovaniya. Razvitiye nauk o Zemle v SSSR za 50 let (Meteorological Research. Development of Earth Science in the USSR over 50 Years), Izdvo "Nauka," Moscow, 1967.
72. Kondratyev, K.Ya. Meteorological Space. Atomes, No. 5, 1967.
73. Allison, L.J., Nicholas, G.W., and Kennedy, J.S. Examples of the Meteorological Capability of the High Resolution Infrared Radiometer on the Nimbus I Satellite. J. Appl. Met., Vol. 5, No. 3, 1966.
74. Nordberg, W. Research with Tiros Radiation Measurements. Astronaut. and Aerospace Engin., Vol. 1, No. 3, 1963.
75. Nordberg, W., Bandeen, W.R., Conrath, B.J. et al. Preliminary Results of Radiation Measurements from the Tiros III Meteorological Satellite. J. Atm. Sci., Vol. 19, No. 1, 1962.

76. Kern, C.D. Desert Soil Temperature and Infrared Radiation Received by Tiros III. J. Atm. Sci., Vol. 20, No. 2, 1963.
77. Nordberg, W. The Nimbus I Meteorological Satellite Geophysical Observations from a New Perspective. Science, Vol. 150, No. 3696, 1965.
78. Nordberg, W., McCulloch, A.W., Foshee, L.L., and Bandeen, W.R. Preliminary Results from Nimbus II. Bull. Am. Met. Soc., Vol. 47, No. 11, 1966.
79. Nordberg, W., and Samuelson, R.E. Terrestrial Features Observed by the High Resolution Infrared Radiometer. Observations from the Nimbus I Meteorological Satellite, NASA, SP-89, 1965.
80. Warnecke, G. Synoptic Applications of Satellite-Borne Infrared Window Measurements. NCAR Techn. Notes, No. 11, 1966.
81. Warnecke, G. Satellites and Meteorology, Ann. Meteor., No. 3, 1967.
82. Allison, L.J., and Warnecke, G. Synoptic Interpretation of Tiros III Radiation Data Recorded on 16 July 1966. Bull. Am. Met. Soc., Vol. 47, No. 5, 1966.
83. Fritz, S. The Diurnal Variation of Ground Temperature as Measured from Tiros II. J. Appl. Met., Vol. 2, No. 5, 1963.
84. Glahn, H.R. On the Usefulness of Satellite Infrared Measurements in the Determination of Cloud Top Heights and Areal Coverage. J. Appl. Met., Vol. 5, No. 2, 1966.
85. Gayevskiy, V.L. and Guseva, L.N. Determination of cloud-top heights from weather satellite data. Trudy GGO, No. 170, 1965.
86. Martin, G.E. and Rubin, L. Automatic Processing of Nimbus Infrared Radiometer Data. Met. Sat. Lab. Rep., No. 28, U.S. Weather Bureau, Washington, July 1964.
87. Bandeen, W.R. Atmospheric Water Vapor Content from Satellite Radiation Measurement. NCAR Techn. Notes, No. 11, 1966.
88. Raschke, E. A Quasi-Global Analysis of the Mean Relative Humidity of the Upper Atmosphere. Tellus, Vol. 19, No. 2, 1967.
89. Raschke, E. and Bandeen, W.R. A Quasi-Global Analysis of Tropospheric Water-Vapor Content and its Temporal Variations from Radiation data of the Meteorological Satellite Tiros IV. Space Res., Vol. 7/2, North-Holl. Publ. Co., Amsterdam, 1967.
90. Raschke, E. and Bandeen, W.R. A Quasi-Global Analysis of Tropospheric Water Vapor Content from Tiros IV Radiation Data. J. Appl. Met., Vol. 6, No. 3, 1967.
91. Yamamoto, G. Radiative Transfer in Aerosols and Clouds. Symposium on Radiation, Bergen, August 1968.
92. Valovcin, F.R. Infrared Measurements of Jet-Stream Cirrus. S. Appl. Met., Vol. 7, No. 5, 1968.
93. Arlt, H. and Bolle, H.-J. Investigation of the Infrared Emission Spectrum of the Atmosphere and Earth. Final Scientific Rep. AF 61(052)-778, Meteorol. Inst., München, August 1968. /397
94. Grant, L.P. and Hunt, G.E. Calculations Relating to Infrared Radiation Emerging from the Earth's Atmosphere in the Presence of Cirrus Clouds. Symposium on Radiation, Bergen, August 1968.

95. Hall, F.F. Jr. The Effect of Cirrus Clouds on 8-13 Micron Infrared Sky Radiation. Appl. Opt., Vol. 7, No. 5, 1968.
96. Panin, B.D. Determination of radiating-surface temperature and total atmospheric moisture content from satellite radiation measurements. Trudy GGO, No. 221, 1968.
97. Belov, P.N., Kurilova, Yu.V., and Berkovich, L.V. Certain characteristics of outgoing-radiation fields. Trudy NIIGMTs, No. 30, 1968.
98. Belov, P.N. and Kurilova, Yu.V. Radiation fields of large-scale atmospheric disturbances. Trudy NIIGMTs, No. 30, 1968.
99. Belov, P.N. and Kurilova, Yu.V. Certain possibilities for the use of satellite radiation data in synoptic analysis. Meteorologiya i gidrologiya, No. 7, 1967.
100. Warnecke, G., Allison, L.J., and Foshee, L.L. Observations of Sea Surface Temperatures and Ocean Currents from Nimbus II. Goddard Space Flight Center, X-622,67-435, August 1967.
101. Clark, H.L. Some Problems Associated with Airborne Radiometry of the Sea. Appl. Opt., Vol. 6, No. 12, 1967.
102. Lorenz, D. Temperature Measurements of Natural Surfaces Using Infrared Radiometer. Appl. Opt., Vol. 7, No. 9, 1968.
103. Barashkova, Ye.P. and Gayevskiy, V.L. Experiment in the comparison of results from ground, aircraft, and satellite measurements. Trudy GGO, No. 221, 1968.
104. Barashkova, Ye.P. et al. An experiment in the simultaneous investigation of the atmosphere's three-dimensional radiation-field structure with instruments on aircraft, aerostats, and satellites. Trudy GGO, No. 235, 1970.
105. Vimberg, G.P., Ivanov, V.I., and Puchkov, V.V. Probability of detection of clouds and underlying surface from infrared-system signals. Trudy GGO, No. 221, 1968.
106. Vimberg, G.P. Statistical characteristics of signals from infrared scanning apparatus. Trudy GGO, No. 221, 1968.
107. Gorodetskiy, A.K., Gurvich, A.S., and Migulin, A.V. Determination of underlying-surface temperature from aircraft measurements of outgoing radiation in the 8-12-μm band. Izv. AN SSSR, seriya fiziki atmosfery i okeana, Vol. III, No.6, 1967.
108. Nigulin, A.V. Determination of underlying-surface temperature from aircraft measurements of outgoing radiation in the 10-12-μm band. Izv. AN SSSR, seriya fiziki atmosfery i okeana, Vol. IV, No. 6, 1968.
109. Panin, B.D. Determination of atmospheric humidity from the outgoing radiation of the earth-atmosphere system in the spectral band from 6 to 6.5 μm. Izv. AN SSSR, seriya fiziki atmosfery i okeana, Vol. III, No. 2, 1967.
110. Rakipova, L.R. Statistical links between the outgoing radiation and the atmosphere's meteorological elements. Izv. AN SSSR, ser. fiz. atm. i okeana, Vol. III, No. 8, 1967.
111. Belov, P.N. Tropical Zone Weather in Infrared Rays. U.N. Conference on Exploration and Peaceful Uses of Outer Space, Vienna, Aug. 1968.
112. Shifrin, K.S., Rabinovich, Yu.I., and Izukin, G.G. Investigation of the microwave radiation field in the atmosphere.

Trudy GGO, No. 222, 1968.
113. Rabinovich, Yu.I., Shchukin, G.G., and Melent'yev, V.V. Determination of water-surface temperature from radio emission in the centimeter band. Trudy GGO, No. 222, 1968.
114. Rabinovich, Yu.I. and Shchukin, G.G. Determination of water-vapor content in the atmosphere from measurements of microwave radiation. Trudy GGO, No. 222, 1968. /398
115. Buettner, K.J.K., Dara, R., Katsaros, K., Kreiss, W., and Martin, L. On the Uses of Intermediate Infrared and Microwave Infrared in Meteorological Satellites. Semi-Annual Rep. on Contract NASA NgG-632. Dept. Atm. Sci., Univ. Washington, June 1968.
116. Kreiss, W.T. Meteorological Observations with Passive Microwave Systems. A Dissertation. Dept. Atm. Sci., Univ. Washington, Febr. 1968.
117. Gurvich, A.S. and Yegorov, S.T. Determining the temperature of the ocean surface from its thermal radio emission. Izv. AN SSSR, seriya fiziki atmosfery i okeana, Vol. II, No. 3, 1966.
118. Gurvich, A.S. and Time, N.S. Variations of the atmosphere's absorption and brightness temperature. Izv. AN SSSR, seriya fiziki atmosfery i okeana, Vol. II, No. 8, 1966.
119. Pereslegin, S.V. Relationship between thermal and radio-brightness contrasts of the ocean surface. Izv. AN SSSR, seriya fiziki atmosfery i okeana, Vol. II, No. 1, 1967.
120. Matveyev, D.T. An experimental study of the temperature field of the ocean surface based on its thermal radiation in the radio range. Izv. AN SSSR, seriya fiziki atmosfery i okeana, Vol. IV, No. 5, 1968.
121. Matveyev, D.T. Measurement of the diurnal variations of woodlands brightness temperature at the 10-cm wavelength. Izv. AN SSSR, ser. fiz. atm. i okeana, Vol. II, No. 7, 1966.
122. Plechkov, V.M. Preliminary results from the determination of the humidity of the atmosphere from measurements of its thermal radio emission around $\lambda = 1.35$ cm. Izv. AN SSSR, seriya fiziki atmosfery i okeana, Vol. IV, 1968.
123. Shifrin, K.S. and Ionina, S.N. Thermal radiation and reflection from an undulating ocean surface in the microwave region. Trudy GGO, No. 222, 1968.
124. Naumov, A.P. A method for determination of atmospheric humidity with measurements of radio-wave absorption around $\lambda =$ = 1.35 cm. Izv. AN SSSR, seriya fiziki atmosfery i okeana, Vol. IV, No. 2, 1968.
125. Basharinov, A.Ye. and Kutuza, B.G. Investigation of the radio emission and absorption of the cloudy atmosphere in the millimeter and centimeter bands. Trudy GGO, No. 222, 1968.
126. Croom, D.L. The Possibile Detection of Atmospheric Water Vapor from a Satellite by Observations of the 13.5 mm and 1.64 mm H_2O Lines. J. Atm. Terr. Phys., Vol. 28, No. 3, 1966.
127. Croom, D.L. Microwave Studies of the Stratosphere and Mesosphere. Proc. Roy. Soc., A, Vol. 288, 1965.

128. Croom, D.L. Stratospheric Thermal Emission and Absorption Near the 22.235 GHz (1.35 cm) Rotational Line of Water Vapor. J. Atm. Terr. Phys., Vol. 27, No. 2, 1965.
129. Croom, D.L. Stratospheric Thermal Emission and Absorption near the 183.311 GHz (1.64 mm) Rotational Line of Water Vapor. J. Atm. Terr. Phys., Vol. 27, No. 2, 1965.
130. Sirounian, V. Effect of Temperature, Angle of Observation, Salinity, and Thin Ice on Microwave Emission of Water, J. Geophys. Rev., Vol. 73, No. 14, 1968.
131. Staelin, D.H. Measurement and Interpretation of the Microwave Spectrum of the Terrestrial Atmosphere near 1-cm Wavelength. Proceedings of the Symposium on Electromagnetic Sensing of the Earth from Satellites. Polytechnic Press, Brooklyn, N.Y., 1967.
132. Lenoir, W.B. Remote Sounding of the Atmospheric Temperature by Microwave Measurement. Proceedings of the Symposium on Electromagnetic Sensing of the Earth from Satellites, Polytechnic Press, Brooklyn, N.Y., 1967.
133. Hovis, W.A. Jr., Blaine, L.R., and Callahan, W.R., Infrared Aircraft Spectra Over Desert Terrain 8.5 mkm to 16 mkm. Appl. Opt., Vol. 7, No. 6, 1968. /399
134. LaViolette, P.E. and Chabot, P.L. Nimbus II Satellite Sea Surface Temperatures Versus Historical Data in a Selected Region: A Comparative Study. Deep-Sea Res., Vol. 15, No. 5, 1968.
135. Lorenz, D. Temperature Measurements of Natural Surfaces Using Infrared Radiometers. Appl. Opt., Vol. 7, No. 9, 1968.
136. Warnecke, G., Allison, L.J., Kreins, E.R., and McMillin, L.M. A Satellite View of Typhoon Marie 1966 Development. NASA Techn. Note D-4757, Nov. 1968.
137. Nayshuller, M.G., Sonechkin, D.M., and Yakovleva, T.A. Analysis of cloud cover based on infrared photographs of the earth from satellites of the "Meteor" experimental system. Meteorologiya i gidrologiya, No. 11, 1968.
138. Belov, P.N., Kurilova, Yu.V., and Berkovich, L.V. Certain characteristics of the outgoing radiation fields. Trudy GMTs, No. 30, 1968.
139. Griggs, M. Emissivities of Natural Surfaces in the 8-14-Micron Spectral Region. Journ. Geophys. Res., Vol. 73, No. 24, 1968.
140. Basharinov, A.Ye., Gurvich, A.S., and Yegorov, S.T. Determination of geophysical elements for measurements of the thermal radio emission on the Kosmos 243 satellite. DAN SSSR, Vol. 188, No. 6, 1969.
141. Hoidale, G.B. and Blanco, A.J. Infrared Absorption Spectra of Atmospheric Dust over an Interior Desert Basin. PAGEOPH, Vol. 74, 1969, pp. 151-164.
142. Buettner, K.J.K., Dana, R., Katsaros, K. et al. On the Use of Intermediate Infrared and Microwave Infrared in Weather Satellites. Fourth Annual Rept. Contr. NsG-632 and NGR 48-002-009. Dept. Atm. Sci., Univ. Washington, March 1969.

143. Sparkman, B.A., Cherrix, G.T. and Tobin, M.S. Preliminary Results from an Aircraft-Borne Medium Resolution Radiometer. Goddard Space Flight Center. X-622-67-445, Sept. 1967.
144. Hale, F.F. Jr. A Physical Model of Cirrus 8-13 Micron Infrared Radiance. Appl. Opt., Vol. 7, No. 11, 1968.
145. Conel, J.E. Infrared Emissivities of Silicates: Experimental Results and a Cloudy Atmosphere Model of Spectral Emission from Condensed Particulate Mediums. J. Geophys. Rev., Vol. 74, No. 6, 1969.
146. Lorenz. D. Temperature Measurements of Natural Surfaces Using Infrared Radiometers. Appl. Opt., Vol. 7, No. 9, 1968.
147. Kattawar, G.W. and Plass, G.N. Infrared Cloud Radiance. Appl. Opt., Vol. 8, No. 6, 1969.
148. Peterson, J.T. Measurement of Atmospheric Aerosols and Infrared Radiation over Northwest India and their Relationship. Techn. Rept. No. 38, Dept. Meteorol., Univ. Wisconsin, Jan. 1968.
149. Griggs, M. Measured and Calculated Earth-Atmosphere Radiance in the 8-14 Micron Window as a Function of Altitude. Appl. Opt., Vol. 8, No. 1, 1969.
150. Tannhauser, I.O. Overlapping effects in the infrared spectrum. Beitr. Phys. Atm., Vol. 41, No. 4, 1968.
151. Gorodetskiy, A.K., Klimchuk, Ye.F., and Malkevich, M.S. Method of and certain results from determination of underlying-surface temperature from the Kosmos 149 satellite. Izv. AN SSSR, seriya fiziki atmosfery i okeana, Vol. V, No. 4, 1969.
152. Möller, F. and Raschke, E. Problems of Meteorological Observations from Satellites. Space Science Review, Vol. 9, 1969, pp. 90-148.
153. Hauth, F.F. and Weinman, J.A. Investigation of Clouds Above Snow Surface Utilizing Radiation Measurements Obtained from the Nimbus II Satellite. Remote Sensing of Environment, Vol. 1, No. 1, 1969.
154. Rao, P.K. Sea Surface Temperature Measurements from Satellites. Mariners Weather Log, Vol. 12, No. 5, 1968, pp. 152-154.
155. Tolstikov, E.I. Experience in the recognition of baric formations from the statistical structure of radiation-temperature fields obtained from artificial earth satellites. Meteorologiya i gidrologiya, No. 3, 1969. /400
156. Bugayeva, I.V. and Ryazanova, L.A. Preliminary results from analysis of monthly average radiation charts based on earth satellite data. Meteorologiya i gidrologiya, No. 4, 1969.
157. Shifrin, K.S., Rabinovich, Yu.I., and Shchukin, G.G. Use of thermal radar in meteorology. Meteorologiya i gidrologiya, No. 6, 1969.
158. Nordberg, W., Conaway, J., and Thaddens, P. Microwave Observations of Sea State from Aircraft. Goddard Space Flight Center, X-620-68-414 , Nov. 1968.
159. Obukhov, A.M. and Tatarskaya, M.S. The atmosphere's integrated humidity field above the southern hemisphere

according to thermal radio sounding measurements made on the Kosmos 243 satellite. Meteorologiya i gidrologiya, No. 11, 1969.
160. Pickett, R.L. An Infrared Technique for Tracking the Gulf Stream. Proc. 5th Symp. on Remote Sensing of Environment. Univ. Michigan, Sept. 1968, pp. 549-554.
161. Weis, M. and Mather, G.K. Evaluation of an Infrared Spectrometer as a Clear Air Turbulence Detector. Proc. 5th Symp. on Remote Sensing of Environment. Univ. Michigan, Sept. 1968, pp. 587-608.
162. Merritt, E.S., Chang, D. and Beran, D. Cirrus Cloud Influence on 6.4-6.9 Micron Observations. Proc. 5th Symp. on Remote Sensing of Environment. Univ. Mighigan, Sept. 1968, pp. 631-654.
163. Shifrin, K.S., Rabinovich, Yu.I., and Shchukin, G.G. Certain results from measurements of microwave radiation in the free atmosphere. Meteorologiya i gidrologiya, No. 7, 1969.
164. Zhevakin, S.A. and Naumov, A.P. Propagation of centimeter, millimeter, and submillimeter radio waves in the earth's atmosphere. Izv. VUZ, seriya radiofiziki, Vol. X, No. 9-10, 1967.
165. Hubert, L.F., Nimchalk, A., and Fritz, S. Estimating Maximum Wind Speed of Tropical Storms from High Resolution Infrared Data, ESSA Techn. Rept. NESC 50, Washington, D.C., May 1969.
166. Cummings, C.A. and Hull, J.W. Microwave Radiometric Meteorological Observations. Proc. 4th Symp. on Remote Sensing of Environment, Univ. Mighican, June 1966, pp. 263-271.
167. Chalfin, G.T. and Ricketts, W.B. 3.2 mm Thermal Imaging Experiments. Proc. 4th Symp. on Remote Sensing of Environment, Univ. Michigan, June 1966, pp. 859-871.

To Chapter 4

1. Sabatini, R.R. and Suomi, V.E. On the Possibility of Infrared Cooling Estimates from Satellite Observations. J. Atm. Sci., Vol. 19, No. 4, 1962.
2. Kondrat'yev, K.Ya., and D'yachenko, L.N. Correlation links between the atmosphere's longwave budget values and the outgoing radiation. Trudy GGO, No. 184, 1966.
3. Smith, W.L., Horn, L.H., and Johnson, D.R. On the Relation Between Tiros Radiation Measurements and Atmospheric Infrared Cooling. J. Appl. Met., Vol. 5, No. 4, 1966.
4. Davies, P.A. Tiros III Radiation Measurements and Some Diabatic Properties of the Atmosphere. Mon. Wea. Rev., Vol. 93, No. 9, 1965.
5. Corcoran, J.L. and Horn, L.H. The Role of Synoptic Scale Variations of Infrared Radiation in the Generation of Available Potential Energy, J. Geophys. Res., Vol. 70, No. 18, 1965.
6. Winston, J.S. Radiative Heating. NCAR Techn. Notes, No. 11, 1966.

7. Chekirda, A.Z. and Yakovleva, G.A. Use of satellite information on the outgoing radiation for determination of precipitation zones. Meteorologiya i gidrologiya, No. 6, 1967.
8. Lethbridge, Mac. Precipitation Probability and Satellite Radiation Data. Mon. Wea. Rev., Vol. 95, No. 7, 1967. /401
9. Allison, L.J. and Warnecke, G. The Interpretation of Tiros Radiation Data for Practical Use in Synoptic Weather Analysis. Beitr. z. Phys. der Atm., Vol. 39, No. 2-4, 1966.
10. Shenk, W.E. Tiros II Window Radiation and Large-Scale Vertical Motion. J. Appl. Met., Vol. 2, No. 6, 1963.
11. Huang Ching-Hua, Panofsky, H.A., and Schwalb, A. Some Relationships Between Synoptic Variables and Satellite Radiation Data. Mon. Wea. Rev., Vol. 95, No. 7, 1967.
12. Jensen, C.E., Winston, J.S., and Taylor, V.R. 500mb Heights as a Linear Function of Satellite Infrared Radiation Data. Mon Wea. Rev., Vol. 94, No. 11, 1966.
13. Musayelyan, Sh.A. Certain aspects of the interpretation and use of cloudage data obtained from weather satellites. DAN SSSR, Vol. 163, No. 5, 1965.
14. Musayelyan, Sh.A., Khazizova, N.S., and Chuzavkova, N.L. Certain results from calculation of vertical motion fields from cloudage distribution. Trudy MMTs, No. 11, 1967.
15. Musayelyan, Sh.A. and Fatkhullayeva, Z.N. A method of using cloudage data obtained from weather satellites. Trudy MMTs, No. 11, 1967.
16. Musayelyan, Sh.A., Belinskaya, A.A., and Khazizova, N.S. Calculation of wind and pressure fields at one atmospheric level from cloudage data obtained from weather satellites (numerical experiment). In: "Dinamika krupnomasshtabnykh protsessov" (Dynamics of Large-Scale Processes), Izd-vo "Nauka," Moscow, 1967.
17. Musayelyan, Sh.A. and Aprausheva, N.N. Combined use of observational data from satellites and a separate network of aerological satellites to reconstruct the fields of the meteorological elements. Trudy NIIGMTs, No. 30, 1968.
18. Borisenkov, Ye.P. Solution of certain inverse problems of satellite meteorology. Meteorologiya i gidrologiya, No. 3, 1967.
19. Kurilova, Yu.V. Possibilities for meteorological interpretation of long wave radiation. Trudy MMTs, No. 8, 1965.
20. Bandeen, W.R., Haley, M., and Strange, J.A. Radiation Climatology in the Visible and Infrared from the Tiros Meteorological Satellites. Goddard Space Flight Center, NASA, X-651-64-218, August 1964.
21. Bandeen, W.R., Conrath, B.J., and Hanel, R.A. Experimental Confirmation from the Tiros VII Meteorological Satellite of the Theoretically Calculated Radiance of the Earth Within the 15-Micron Band of Carbon Dioxide. J. Atm. Sci., Vol. 20, No. 6, 1963.
22. Nordberg, W., Bandeen, W.R., Warnecke, G., and Kunde, V. Stratospheric Temperature Patterns Based on Radiometric Measurements from the Tiros VII Satellite. Goddard Space Flight Center, X-651-64-115, May 1964.

23. Nordberg, W., Bandeen, W.R., Warnecke, G., and Kunde, V. Stratospheric Temperature Patterns Based on Radiometric measurements from the Tiros VII Satellite. Space Res. Y. Proc. of the Fifth Intern. Space. Sci. Symp., North-Holl. Publ, Co., Amsterdam, 1965.
24. Nordberg, W. Satellite Radiation Measurements in Spectral Regions. NCAR Techn. Notes, No. 11, 1966.
25. Warnecke, G. Tiros VII 15-Micron Radiometric Measurements and Mid-Stratospheric Temperatures. NCAR Techn. Notes, No. 11, 1966.
26. Teweles, S. Radiometer Data in the 15-Micron Band. NCAR Techn. Notes, No. 11, 1966.
27. Warnecke, G. The Remote Sensing of Stratospheric Temperatures and Some Results from the Nimbus II Satellite Experiment. Goddard Space Flight Center, X-622-67-471, September 1967.
28. Kondrat'yev, K.Ya. Relation between outgoing thermal radiation /402 and tropospheric and lower-stratospheric mean temperature field. Meteorologiya i gidrologiya, No. 1, 1966.
29. Kennedy, J.S. An Atlas of Stratospheric Mean Isotherms Derived from Tiros VII Observations. Goddard Space Flight Center, X-622-66-307, July 1966.
30. Warnecke, G. and McCulloch, A.W. Stratospheric Temperature Pattern Derived from Nimbus II Measurements. Goddard Space Flight Center, X-622-67-436, August 1967.
31. Belmont, A.D., Nicholas, G.W. and Shen, W.C. Comparison of 15-Micron Tiros VII Data with Radiosonde Temperatures. J. Appl. Met., Vol. 7, No. 2, 1968.
32. Smith, W.L. Statistical Estimation of the Atmosphere's Geopotential Height Distribution from Satellite Radiation Measurements. ESSA Techn. Rept., NECS 48, Washington, D.C., April 1969.
33. Markov, M.N. Water vapor in the mesosphere (according to measurements made from geophysical rockets and the Kosmos 45 and Kosmos 65 satellites). Kosmich. issled., Vol. VII, No. 2, 1969.
34. Ludwig, C.B., Bartle, R., and Griggs, M. Study of Air Pollutant Detection by Remote Sensing. Contr. NAS 12-630, San Diego, Calif., 113 pp. Dec. 1968.
35. Barringer, A.R., Newbury, B.C., and Moffat, A.J. Surveillance of Air Pollution from Airborne and Space Platforms. Proc. 5th Symp. on Remote Sensing of Environment, Univ. of Michigan, Sept. 1968, pp. 123-155.
36. Brodrick, H.J. and McLain, E.P. Synoptic/Dynamic Diagnosis of a Developing Low-Level Cyclone and Its Satellite-Viewed Cloud Patterns. ESSA Techn. Rept. NESC 49, Washington, D.C., May 1969.

To Chapter 5

1. Matveyev, L.T. Osnovy obshchey meteorologii. Fizika atmosfery (Fundamentals of General Meteorology. Atmospheric Physics),

Gidrometeoizdat, Leningrad, 1965.
2. SPINMAP (Standard Proposal for an International Network for Meteorological Analyses and Prediction) Final Report, June 1966.
3. Graves, M.E. and Fischbach, F.F. Analysis of Microwave Occultation Techniques for Atmospheric Soundings. Technical Report, ORA Project 05863, Univ. Michigan, Jan. 1969.
4. Kondratyev, K.Ya. and Timofeyev, Yu.M. Inverse Problems of Satellite Meteorology. Pure and Applied Geophysics, Vol. 71, No. 3, 1968.
5. Glasko, V.B. and Timofeyev, Yu.M. Possibilities of the regularization method for solution of the problem of atmospheric thermal sounding. Izv. AN SSSR, seriya fiziki atmosfery i okeana, Vol. 4, No. 12, 1968.
6. King, Y.J.F. The Earth Satellite Vehicle as a Stratospheric Temperature Probe. Proc. VII Intern. Astron. Congress, 1956.
7. Kaplan, L.D. Inference of Atmospheric Structure from Remote Radiation Measurements. J. Opt. Soc. America, Vol. 49, 10, 1959.
8. Wark, D.Q. and Fleming, H.E. Indirect Measurements of Atmospheric Temperature Profiles from Satellites. I. Introduction. Monthly Weather Review, Vol. 94, No. 6, 1966.
9. House, F.B., Florance, E.T., Harrison, R., and King, J.I.F. Meteorological Inferences from Radiance Measurements. Final Report Contract NO CNB-11317 G.C.A. Corporation, Bedford, Massachusetts, Sept. 1968.
10. Chahine, M.T. Determination of the Temperature Profile in an Atmosphere from Its Outgoing Radiation. J. Opt. Soc. America, Vol. 58, No. 12, 1968.
11. Malkevich, M.S. and Tatarskiy, V.I. Determination of the atmospheric vertical temperature profile from the outgoing radiation in the CO_2 absorption band. Kosmicheskiye issledovaniya, Vol. 3, No. 3, 1964.
12. Malkevich, M.S. and Tatarskiy, V.I. Determination of the temperature and humidity of the earth's atmosphere from satellite measurements of the earth's radiation. In: "Issledovaniya kosmicheskogo prostranstva" (Investigation of Cosmic Space), Izd-vo "Nauka," 1965. /403
13. Kozlov, V.P. Reconstruction of the altitude profile of temperature from the outgoing radiation spectrum. Izv. AN SSSR, seriya fiziki atmosfery i okeana, Vol. 2, No. 3, 1966.
14. McClatchey, R.A. The Use of 4.3μ CO_2 Bands to Sound Planetary Atmosphere of the Earth. Proceedings of the Symposium on the Electromagnetic Sensing of the Earth from Satellites, Brooklyn, 1965 [sic], N.Y., 1967.
15. Lavrent'yev, M.M. Nekorrektiyye zadachi matematicheskoy fiziki (Noncorrect Problems of Mathematical Physics), Novosibirsk, 1962.
16. Ivanov, V.K. Noncorrectly formulated problems. Matem. sb., Vol. 61, No. 2, 1963.
17. Bokhner, S. Lektsii ob integralakh Fur'ye (Lectures on Fourier Integrals), Fizmatgiz, 1962.

18. Tikhonov, A.N. Regularization of noncorrectly formulated problems. DAN SSSR, Vol. 153, No. 1, 1963.
19. Kolmogorov, A.N. and Fomin, S.V. Elementy teorii funktsiy i funktsional'nogo analiza (Elements of the Theory of Functions and Functional Analysis), Izd-vo "Nauka," 1968.
20. Tikhonov, A.N. Solution of noncorrectly formulated problems and the regularization method. DAN SSSR, Vol. 151, No. 3, 1963.
21. Pokrovskiy, O.M. and Timofeyev, Yu.M. Thermal sounding of the atmosphere. Problemy fiziki atmosfery (Problems of Atmospheric Physics), No. 8, Izd. LGU, 1969.
22. Tikhonov, A.N. Solution of poorly conditional algebraic equation systems. Zh. vychislitel'noy matematiki i matematicheskoy fiziki, Vol. 5, No. 4, 1965.
23. Twomey, S. Mathematical Aspects of the Inverse Problem. Mon. Wea. Rev., Vol. 94, 6, 1966.
24. Pokrovskiy, O.M. Optimum conditions for indirect sounding of the atmosphere. Izv. AN SSSR, seriya fizika atmosfery i okeana, No. 12, 1969.
25. Yamamoto, G. Numerical Method for Estimating the Stratospheric Temperature Distribution from Satellite Measurements in the CO_2 Band. J. Meteorol., Vol. 18, 5, 1961.
26. Kaplan, L.D. The Spectroscope as a Tool for Atmospheric Sounding by Satellites. Instrum. Soc. Amer. Confer. Preprint, New York 9 — No. 460.
27. Obukhov, A.M. Statistically orthogonal expansions of empirical functions. Izv. AN SSSR, seriya geofizicheskaya, No. 3, 1960.
28. Pokrovskiy, O.M. Certain mathematical problems in the solution of inverse problems in atmospheric optics. Problemy fiziki atmosfery, No. 8, Izd. LGU, 1969.
29. Pokrovskiy, O.M. A stable solution method for the inverse problems of atmospheric optics. Problemy fiziki atmosfery, No. 8. Izd. LGU, 1969.
30. Phillips, D.A. Technique for the Numerical Solution of Certain Integral Equations of the First Kind. J. Assoc. Comput. Machinery, Vol. 9, No. 1 (1962).
31. Twomey, S. On the Numerical Solution of Fredholm Integral Equations of the First Kind by the Inversion of the Linear System Produced by Quadrature. J. Assoc. Comput. Machinery, Vol. 10, No. 1 (1963).
32. Truchin, V.F. Solution of the Fredholm equation of the first kind in a statistical ensemble of smooth functions. Zh. vychislitel'noy matematiki i matematicheskoy fiziki, Vol. 7, No. 6, 1967.
33. Pao, C.P. Lineynyye statisticheskiye metody i primeneniya (Linear Statistical Methods and Applications), Izd-vo "Nauka," 1968.
34. Turchin, V.F. and Nozik, V.Z. Statistical regularization of the solutions of certain problems. Izv. AN SSSR, seriya fiziki atmosfery i okeana, Vol. 5, No. 1 (1969).
35. Westwater, E. and Strand, O. Minimum-rms Estimation of the Numerical Solution of a Fredholm Integral Equation of the /404

First Kind. Siam J. Numer. Anal., Vol. 5, No. 2, 1968.
36. Westwater, E. and Strand, O. Statistical Information Content of Radiation Measurements Used in Indirect Sensing. J. Atmosph. Sci., Vol. 24 (1968).
37. Tikhonov. A.N. and Glasko, V.B. Approximate solution of the Fredholm integral equation of the first kind. Zh. vychislitel'noy matematiki i matematicheskoy fiziki, Vol. 4, No. 3 (1964).
38. Pokrovskiy, O.M. On the problem of α-parametric regularization. Vestnik LGU, seriya matematicheskaya (in preparation).
39. King, J.I.F. Inversion by Slabs of Varying Thickness. J. Atm. Sci., 21, 1964.
40. Burch, D.E., Gryvnak, D., and Williams, D. Infrared Absorption by Carbon Dioxide. Report on Project 778, Ohio State Univ. Research Foundation, 1960.
41. Kaplan, L.D. Line Intensities and Absorption for the 15-Micron Carbon Dioxide Band. J. Chem. Phys., Vol. 18, No. 186, 1950.
42. Yamamoto, G. and Sasamori, T. Calculations of the Absorption of the 15-Micron Carbon Dioxide Band. Sci. Rep., Tohoku Univ., Series 5, Geophysics, Vol. 10, No. 2 (1958).
43. Sasamori, T. The Temperature Effect on the Absorption of 15μ Carbon Dioxide Band. Sci. Rep. Tohoku Univ. Series 5, Geophysics, Vol. 11, No. 3, 1959.
44. Yamamoto, G. and Sasamori, T. Further Studies on the Absorption by the 15-Micron Carbon Dioxide Bands. Sci. Rep. Tohoku Univ., Series 5, Geophysics, 13, 1961.
45. Stull, V.R., Wyatt, P.J., and Plass, G.N. The Infrared Absorption of Carbon Dioxide. Infrared Transmission Studies, Final Report, Vol. III, Contract AF 19(604)-7479, Aeronutronic Division, Ford Motor Company, Jan. 1963.
46. Golubitskiy, B.M. and Moskalenko, N.I. Measurements of the spectral absorption of CO_2 under synthetic-atmosphere conditions. Izv. AN SSSR, seriya fiziki atmosfery i okeana, Vol. 4, No. 1, 1968.
47. Drayson, S.R. and Young, C. The Frequencies and Intensities of Carbon Dioxide Absorption Lines Between 12 and 18 Microns. Technical Report, Univ. Michigan, November 1967.
48. Drayson, S.R., Li, S.Y., and Young, C. Atmospheric Absorption by Carbon Dioxide, Water Vapor, and Oxygen. Univ. Michigan, Final Report, ORA Project 08183, 1968.
49. Yamamoto, G. H., Tanaka, M., and Aoki, T. Calculation of the Line Widths of the 15μ CO_2 Bands. Report Tohoku Univ., Sendai, Japan, 1968.
50. Drayson, S.R. Investigation of Atmospheric Absorption for Remote Sensing Applications. Final Report ORA Project 01427, Univ. Michigan, May 1969.
51. Chaney, L.W., Loh, L.T., and Surh, M.T. A Fourier Transform Spectrometer for the Measurement of Atmospheric Thermal Radiation. Technical Report, Contract NASr-54(03), College of Engineering, Univ. Michigan, Ann Arbor, May 1967.
52. Gray, L.D. and McClatchey, R. Calculations of Atmospheric Radiation from 4.2μ to 5μ. Appl. Opt., 4, No. 12, 1965.

53. Murcray, D.G., Murcray, F.H., and Williams, W.I. Comparison of Experimental and Theoretical Slant Path Absorption in the Region from 1400-2500 cm^{-1}. Opt. Soc. America, 55, 5, 1965.
54. Meeks, M.L. and Lilley, A.E. The Microwave Spectrum of Oxygen in the Earth's Atmosphere. J. Geophys. Res., Vol. 68, No. 6, 1963.
55. Zhevakin, S.A. and Naumov, A.P. Absorption of electromagnetic waves in the band from 3 mm to 7.5 cm in the earth's atmosphere. Izv. VUZov, radiofizika, Vol. IX, No. 3, 1966.
56. Zhevakin, S.A. and Naumov, A.P. Calculation of centimeter- and /405 millimeter-radio-wave absorption coefficients in atmospheric oxygen. Radiotekhnika i elektronika, Vol. 10, No. 6, 1965.
57. Hill, R.M. and Gordy, W. Zeeman Effect and Line Breadth Studies of the Microwave Lines of Oxygen. Phys. Rev., 93, No. 5, 1954.
58. Zimmerer, R.W. and Mizushima, M. Precise Measurement of the Microwave Absorption Frequencies of the Oxygen Molecule and the Velocity of Light. Phys. Rev., 121, No. 1, 1961.
59. Tolbert, C.W. and Straiton, A.W. Synoptic Investigation of 58 to 62 KMC Frequencies in the Earth's Atmosphere. Proceedings of the IEEE, Vol. 51, No. 12, 1963.
60. Barrett, A.N., Juiper, J.W., and Lenoir, W.B. Observations of Microwave Emission by Molecular Oxygen in the Terrestrial Atmosphere. J. Geophys. Res., 71, 20, 1966.
61. Lenoir, W.B., Barrett, J.W., and Papa, D.C. Observations of Microwave Emission by Molecular Oxygen in the Stratosphere. J. Geophys. Res., Vol. 73, No. 4, 1968.
62. VanVleck, J.H. and Weisskopf, V.F. On the Shape of Collision-Broadened Lines. Review of Modern Physics, Vol. 17, No. 2-3, 1967.
63. Lenoir, W. Microwave Spectrum of Molecular Oxygen in the Mesosphere. J. Geophys. Res., Vol. 73, No. 1, 1968.
64. Zhevakin, S.A. and Naumov, A.P. Certain problems in the calculation and measurement of millimeter and submillimeter radio wave absorption in atmospheric water vapor. Izv. VUZov, Radiofizika, Vol. 8, No. 6, 1965.
65. Wark, D.Q. On Indirect Temperature Sounding of the Stratosphere from Satellites. J. Geophys. Res., Vol. 66, No. 1, 1961.
66. Gorchakova, I.A. and Kozlov, V.P. Selection of spectral segments in the atmospheric thermal sounding problem. Trudy VII Vsessoyuznogo soveshchaniya po aktinometrii i atmosfernoy optike (Transactions of the Seventh All-Union Conference on Actinometry and Atmospheric Optics), Leningrad, 1968. Gidrometeoizdat, Leningrad, 1969.
67. Glasko, V.B. and Timofeyev, Yu.M. Use of the regularization method for solution of the atmospheric thermal sounding problem. Izv. AN SSSR, seriya fiziki atmosfery i okeana, Vol. 4, No. 3, 1969.
68. Bruyevich, S.V. and Lyutsarev, S.V. The CO_2 content in the atmosphere above the Pacific and Indian Oceans and in the Black Sea region. DAN SSSR, Vol. 136, No. 2, 1961.

69. Smith, W.L. An Iterative Method for Deducing Tropospheric Temperature and Moisture Profiles from Satellite Radiation Measurements. Mon. Wea. Rev., Vol. 95, No. 6, 1967.
70. Smith, W.L. An Improved Method for Calculating Tropospheric Temperature and Moisture from Satellite Radiometer Measurements. Mon. Wea. Rev., Vol. 96, No. 6, 1968.
71. Barnett, T.L. Application of a Nonlinear Least-Squares Method to Atmospheric Temperature Sounding. J. Atm. Sci., Vol. 26, No. 3, 1969.
72. Marquardt, D.W. An Algorithm for Least-Squares Estimation of Nonlinear Parameters. J. Soc. Ind. Appl. Math., 11, 431, 1963.
73. Westwater, E.R. Ground-Based Passive Probing Using the Microwave Spectrum of Oxygen. Radio Science, Vol. 69, D., No. 9, 1965.
74. Lieth, N. The Role of Vegetation in the Carbon Dioxide Content of the Atmosphere. J. Geophys. Res., Vol. 68, No. 13, 1963.
75. Bischof, W. Periodical Variations of the Atmospheric CO_2 Content in Scandinavia. Tellus, Vol. XII, No. 2, 1960.
76. Bischof, W. Variations in Concentration of Carbon Dioxide in the Free Atmosphere. Tellus, Vol. XIV, No. 1, 1962.
77. Kelley, J.J. Jr. and LaChapelle. Atmospheric Carbon Dioxide Variation on Mount Olympus, Washington. J. Geophys. Res., Vol. 71, No. 8, 1966.
78. Bischof, W. and Bolin, B. Space and Time Variation of the CO_2 /406 Content of the Troposphere and Lower Stratosphere. Tellus, Vol. XVIII, No. 2-3, 1966.
79. Georgii, H.W. CO_2 Over the Atlantic. Die Umschau, Frankfurt a.M. 67(12) 391-92, 1967.
80. Hageman, F., Cray, J., Machta, L. and Turkey, M.A. Stratospheric Carbon-14, Carbon-Dioxide Science, Vol. 130, Nc. 3375, 1959.
81. Rohrbough, S.F. Determination of the Mixing Ratios of Water Vapor and Carbon Dioxide in the Atmosphere. Science, Vol. 137, No. 3530, 1962.
82. Eriksson, E. Periodical Variation of the Atmospheric CO_2 Content in Scandinavia. Tellus, Vol. 12, No. 2, 1960.
83. Keeling, Ch.D., Heriss, T.B., and Wiekins, E.M. Concentration of Atmospheric Carbon Dioxide at 500 and 700 Millibars. J. Geophys., Vol. 73, No. 14, 1968.
84. Pales, J.C. and Kelling, C.D. The Concentration of Atmospheric Carbon Dioxide in Hawaii. J. Geophys. Res., Vol. 70, No. 24, 1965.
85. Brown, G.W. and Kelling, C.D. The Concentration of Atmospheric Carbon Dioxide in Antarctica. J. Geophys. Res., Vol. 70, No. 24, 1969.
86. Gorchakova, I.A. and Malkevich, M.S. Variability of the outgoing radiation in the 15-μm carbon dioxide absorption band. Izv. AN SSSR, ser. fizika atmosfery i okeana, Vol. II, No. 6, 1966.
87. Bogomolov, O.S. Nekotoryye voprosy chislennoy interpretatsii dannykh meteorologicheskikh i.s.z. (Certain Problems in Numerical Interpretation of Weather Satellite Data), Author's

abstract of dissertation, Leningrad, 1968.
88. House, F.B. Clouds and Inversion Problem. J. Quant. Spectr. and Rad. Transfer., Vol. 8, No. 1, 1968.
89. Bazlova, T.I. Determination of the vertical temperature profile in the Arctic atmosphere from the outgoing microwave radiation. Problemy Arktiki and Antarktiki, Vol. 30, 1968.
90. Kondrat'yev, K.Ya., Pokrovskiy, O.M. and Timofeyev, Yu.M. Thermal sounding of the atmosphere from satellites. Meteorologiya i gidrologiya, No. 9, 1969.
91. Bazlova, T.I. Temperaturnoye zondirovaniye atmosfery v Arktike po ukhodyashchemu mikrovolnovomu izlucheniyu (Thermal Sounding of the Atmosphere in the Arctic from the Outgoing Microwave Radiation), Dissertation, AANII, Leningrad, 1969.
92. Florance, E.T. Numerical Study of Nonlinear Inversion Molecular Radiation and its Application to Diagnostic Techniques. Proceed. Spec. Cont. Huntsville, Alabama, 1967, NASA TMX-53711.
93. Florance, E.T. Application of Nonlinear Inversion Techniques to Radiometric Sensing of Atmospheric Temperatures. Proc. Third Interdiscip. Workshop on Inversion of Radiometric Meas. Tallahassee, Florida, May 1968. Ed. C. Gille.
94. Malkevich, M.S. Methods of interpretating radiation measurements from satellites. Trudy Shestogo mezhvedomstvennogo soveshchaniya po aktinometrii i optike atmosfery. Izd-vo "Valgus," Tallin, 1968.
95. Timofeyev, Yu.M. and Pokrovskiy, O.M. A real example of atmospheric temperature profile reconstruction. Izv. AN SSSR, Vol. 5, No. 10, 1969.
96. Dobryshman, Ye.M. Accuracy and frequency requirements for hydrometeorological information. Meteorologiya i gidrologiya, No. 11, 1968.
97. Wolk, M. Van Cluf, F., and Yamamoto, G. Indirect Measurements of Atmospheric Temperature Profiles from Satellites: V. Atmospheric Soundings from Infrared Spectrometer Measurements at the Ground. Mon. Wea. Rev., Vol. 95, 7, 1967.
98. Wark, D.Q., Saiedy, F., and James, D.Q. Indirect Measurements of Atmospheric Temperature Profiles from Satellites. VI High-Altitude Balloon Testing. Mon. Wea. Rev., Vol. 95, 7, 1967.
99. Turchin, V.F., Malkevich, M.S., and Gorchakov, I.A. Application of statistical regularization to determination of the atmosphere's vertical temperature profile. Izv. AN SSSR, seriya /407
fiziki atmosfery i okeana, Vol. V, No. 5, 1969.
100. Shaw, J.H., McClatchey, R.A., and Schaper, P.W. Balloon Observations of the Radiance of the Earth Between 2100 cm^{-1} and 2700 cm^{-1}. Appl. Opt., Vol. 6, No. 2, 1967.
101. Marchuk, G.I. The equation for the importance of information from weather satellites and formulation of inverse problems. Kosmicheskiye issledovaniya, Vol. II, No. 3, 1964.
102. Hileary, D. and Wark, D. A Successful Test of Remote Probing of the Atmospheric Temperature. Science, Vol. 165, No. 3899, 1969.
103. Hanel, R. and Conrath, B. Preliminary Results from the Interferometer Experiment on Nimbus III. Science, Vol. 165, No. 3899, 1969.

To Chapter 6

1. Komarov, V.S. Statistical structure of vertical humidity profiles. Izv. AN SSSR, seriya fiziki atmosfery i okeana, Vol. IV, No. 1, 1968.
2. Howard, J.N., Burch, D.E., and Williams, D. Infrared Transmission of Synthetic Atmospheres. J. Opt. Soc. Amer., 46, 186, 237, 334, 452, 1956.
3. Burch, D.E., Singleton, E.B., France, W.L., and Williams, D. Infrared Absorption by Minor Atmospheric Constituents. Report on RF Project 778, The Ohio State University Research Foundation, 1960.
4. Stull, V.R., Wyatt, P.J., and Plass, G.N. The Infrared Absorption of Water Vapor. Report SSD-TDR-62-127, Vol. II, Space Systems Division, Air Force Systems Command, Los Angeles, California, 1962.
5. Wyatt, P.J., Stull, V.R., and Plass, G.N. The Infrared Transmittance of Water Vapor. Appl. Opt., 3, 229, 1964.
6. Burch, D.E., Gryvnak, D., Singleton, E.B., et al. Infrared Absorption by Carbon Dioxide, Water Vapor, and Minor Atmospheric Constituents. Ohio State University, Research Report, Contract AF-19 (604), 2633 July 1962.
7. Golubitskiy, B.M. and Moskalenko, N.I. Measurement of spectral absorption in the H_2O vapor bands. Izv. AN SSSR, seriya fiziki atmosfery i okeana, Vol. 4, No. 1, 1968.
8. Palmer, C.H. Jr. Experimental Transmission Functions for the Pure Rotational Band of Water Vapor. J. Opt. Soc. Am., Vol. 50, 1232, 1960.
9. Stauffer, F.R., and Walsh, T.E. Transmittance of Water Vapor — 14 to 20 Microns. J. Opt. Soc. Am., Vol. 56, No. 401, 1966.
10. Kondrat'yev, K.Ya. and Timofeyev, Yu.M. Transmission functions for the water vapor rotational band. Izv. AN SSSR, seriya fizika atmosfery i okeana, Vol. II, No. 3, 1966.
11. Staelin, D.H. Measurements and Interpretation of the Microwave Spectrum of the Terrestrial Atmosphere near 1 cm. Proceedings of the Symposium on the Electromagnetic Sensing of the Earth from Satellites. Brooklyn, 1965, No. 4, 1967.
12. Hyatt, H.A. The Airborne Detection of Microwave Emission from Earth's Surface and Atmosphere. Proceedings of the Symposium on the Electromagnetic Sensing of the Earth from Satellites. Brooklyn, 1965, No. 4, 1967.
13. Möller, F. Atmospheric Water Vapor Measurements at 6-7 Microns from a Satellite. Planet. Space Sci., 5, 202-206, 1961.
14. King. J.I.F. Meteorological Inference from Satellite Radiometry. I. J. Atm. Sci., Vol. 20, No. 4, 1963.
15. Yamamoto, G. and Tanaka, M. Estimation of Water Vapor Distribution in the Atmosphere from Satellite Measurements. Proceedings of the XVII Congress of the International Astronautical Federation, 1966.
16. Malkevich, M.S. Determination of meteorological elements with satellites. Paper at Scientific Conference on the Problem of "The General Circulation of the Earth's Atmosphere." Moscow, 1964. /408

17. Conrath, B.J. Remote Sensing of Atmospheric Water Vapor and Ozone Using Interferometry. Molecular Radiation and Its Application to Diagnostic Techniques. Proceed. Spec. Conf. Huntsville, Alabama, 1967, NASA TMX 53711.
18. Möller, F. and Raschke, E. Evaluation of Tiros III Radiation Data. Final Report. NASA Research Grant NsG-305, March 1964.
19. Drayson, S.R. Methods of Calculating Atmospheric Transmission Functions. Molecular Radiation and Its Application to Diagnostic Techniques. Proceed. Spec. Conf. Huntsville, Alabama, 1967, NASA TMX-53711.

NASA-Langley, 1971 – 13
Coml., Phila., Penn.

NATIONAL AERONAUTICS AND SPACE ADMINISTRATION
WASHINGTON, D. C. 20546

OFFICIAL BUSINESS
PENALTY FOR PRIVATE USE $300

FIRST CLASS MAIL

POSTAGE AND FEES PAID
NATIONAL AERONAUTICS A
SPACE ADMINISTRATION

07U 001 38 51 3DS 71166 00903
AIR FORCE WEAPONS LABORATORY /WLOL/
KIRTLAND AFB, NEW MEXICO 87117

ATT E. LOU BOWMAN, CHIEF, TECH. LIBRARY

POSTMASTER: If Undeliverable (Section 15 Postal Manual) Do Not Ret

"The aeronautical and space activities of the United States shall be conducted so as to contribute . . . to the expansion of human knowledge of phenomena in the atmosphere and space. The Administration shall provide for the widest practicable and appropriate dissemination of information concerning its activities and the results thereof."

—NATIONAL AERONAUTICS AND SPACE ACT OF 1958

NASA SCIENTIFIC AND TECHNICAL PUBLICATIONS

TECHNICAL REPORTS: Scientific and technical information considered important, complete, and a lasting contribution to existing knowledge.

TECHNICAL NOTES: Information less broad in scope but nevertheless of importance as a contribution to existing knowledge.

TECHNICAL MEMORANDUMS: Information receiving limited distribution because of preliminary data, security classification, or other reasons.

CONTRACTOR REPORTS: Scientific and technical information generated under a NASA contract or grant and considered an important contribution to existing knowledge.

TECHNICAL TRANSLATIONS: Information published in a foreign language considered to merit NASA distribution in English.

SPECIAL PUBLICATIONS: Information derived from or of value to NASA activities. Publications include conference proceedings, monographs, data compilations, handbooks, sourcebooks, and special bibliographies.

TECHNOLOGY UTILIZATION PUBLICATIONS: Information on technology used by NASA that may be of particular interest in commercial and other non-aerospace applications. Publications include Tech Briefs, Technology Utilization Reports and Technology Surveys.

Details on the availability of these publications may be obtained from:

SCIENTIFIC AND TECHNICAL INFORMATION OFFICE

NATIONAL AERONAUTICS AND SPACE ADMINISTRATION

Washington, D.C. 20546